



**UNIVERSIDAD NACIONAL AUTÓNOMA DE MÉXICO
POSGRADO EN CIENCIAS BIOLÓGICAS**

**FACULTAD DE MEDICINA
BIOLOGÍA EXPERIMENTAL**

**CARACTERIZACIÓN ESTRUCTURAL Y FUNCIONAL DE LA MUTANTE
delta-g DE LA F₁F₀-ATP SINTASA DE *Ustilago maydis***

TESIS

**QUE PARA OPTAR POR EL GRADO DE:
DOCTORA EN CIENCIAS**

PRESENTA:

M. EN C. ESPARZA PERUSQUÍA MARÍA DE LAS MERCEDES

**TUTOR PRINCIPAL DE TESIS: DR. OSCAR FLORES HERRERA
FACULTAD DE MEDICINA, UNAM**

**COMITÉ TUTOR: DRA. MARIETTA TUENA SANGRI
INSTITUTO DE FISIOLÓGIA CELULAR, UNAM**

**DR. SALVADOR URIBE CARVAJAL
INSTITUTO DE FISIOLÓGIA CELULAR, UNAM**



Universidad Nacional
Autónoma de México



UNAM – Dirección General de Bibliotecas
Tesis Digitales
Restricciones de uso

DERECHOS RESERVADOS ©
PROHIBIDA SU REPRODUCCIÓN TOTAL O PARCIAL

Todo el material contenido en esta tesis esta protegido por la Ley Federal del Derecho de Autor (LFDA) de los Estados Unidos Mexicanos (México).

El uso de imágenes, fragmentos de videos, y demás material que sea objeto de protección de los derechos de autor, será exclusivamente para fines educativos e informativos y deberá citar la fuente donde la obtuvo mencionando el autor o autores. Cualquier uso distinto como el lucro, reproducción, edición o modificación, será perseguido y sancionado por el respectivo titular de los Derechos de Autor.

COORDINACIÓN DEL POSGRADO EN CIENCIAS BIOLÓGICAS
FACULTAD DE MEDICINA
OFICIO CPCB/517/2020
ASUNTO: Oficio de Jurado

M. en C. Ivonne Ramírez Wence
Directora General de Administración Escolar, UNAM
Presente

Me permito informar a usted que en la reunión virtual del Subcomité de Biología Experimental y Biomedicina del Posgrado en Ciencias Biológicas, celebrada el día **30 de marzo de 20** se aprobó el siguiente jurado para el examen de grado de **DOCTORA EN CIENCIAS** de la estudiante **ESPARZA PERUSQUÍA MARÍA DE LAS MERCEDES** con número de cuenta **511021118** con la tesis titulada **"CARACTERIZACIÓN ESTRUCTURAL Y FUNCIONAL DE LA MUTANTE delta-g DE LA F₁F₀-ATP SINTASA DE Ustilago maydis"**, realizada bajo la dirección del **DR. OSCAR HERRERA FLORES**, quedando integrado de la siguiente manera:

Presidente: DRA. MINA KONIGSBERG FAINSTEIN
Vocal: DR. RICARDO JASSO CHÁVEZ
Secretario: DR. SALVADOR URIBE CARVAJAL
Suplente: DR. DIEGO GONZÁLEZ HALPHEN
Suplente: DR. MANUEL GUTIÉRREZ AGUILAR

Sin otro particular, me es grato enviarle un cordial saludo.

ATENTAMENTE
"POR MI RAZA HABLARÁ EL ESPÍRITU"
Cd. Universitaria, Cd. Mx., a 28 de agosto de 2020

COORDINADOR DEL PROGRAMA



DR. ADOLFO GERARDO NAVARRO SIGÜENZA



AGRADECIMIENTOS

A la Universidad Nacional Autónoma de México y al Posgrado en Ciencias Biológicas, UNAM por todo el apoyo brindado durante la realización del presente trabajo.

Durante el desarrollo de esta tesis recibí beca de para estudios de Doctorado otorgada por el Consejo Nacional de Ciencia y Tecnología (CONACyT) con número de becario 254400.

Este proyecto fue financiado por el Programa de Apoyo a Proyectos de Investigación e Innovación Tecnológica (PAPIIT IN214914-OFH, IN222617-OFH, IN215518-FMM, IN222117-JPP), así como por el CONACyT con el proyecto 168025.

Esta tesis se realizó bajo la dirección del Dr. Oscar Flores Herrera en el laboratorio 4Bis del Departamento de Bioquímica de la Facultad de Medicina de la Universidad Nacional Autónoma de México.

Especialmente deseo agradecer a los miembros del Comité Tutorial: Dra. Marietta Tuena de Gómez-Puyou y Dr. Salvador Uribe Carvajal, por las valiosas aportaciones a este trabajo.

La sección de Biología Molecular se realizó en el laboratorio del Instituto de Microbiología de la Universidad Heinrich-Heine en Düsseldorf, Alemania, bajo la asesoría de los doctores Michael Feldbrügge y Thorsten Langner.

Agradezco también a la M. en C. Sara Teresa Méndez del Instituto Nacional de Pediatría, torre de investigación “Dr. Joaquín Cravioto” por la ayuda en las técnicas de Biología Molecular.

Un especial agradecimiento a la Dra. Guadalupe Zavala del Instituto de Biotecnología, UNAM por su apoyo en microscopía de transmisión electrónica.

Agradezco por sus valiosas aportaciones a este trabajo al jurado del Examen Doctoral que estuvo conformado por:

Presidente	Dra. Mina Konigsberg Fainstein	Universidad Autónoma Metropolitana
Vocal	Dr. Ricardo Jasso Chávez	Instituto Nacional de Cardiología
Secretario	Dr. Salvador Uribe Carvajal	Instituto de Fisiología Celular, UNAM
Suplente	Dr. Diego González Halphen	Instituto de Fisiología Celular, UNAM
Suplente	Dr. Manuel Gutiérrez Aguilar	Facultad de Química, UNAM

A Oscar, por tu compromiso y dedicación, por tu apoyo incondicional, por tu confianza, por nunca perder la fe en mí, por permitirme ser parte de este gran grupo de trabajo que comenzó con nosotros dos y que fue creciendo con el tiempo, pero sobre todo por tu gran paciencia. A lo largo de este camino me enseñaste que los datos se dan con emoción, que cuando te aprendes todas las respuestas te cambian todas las preguntas, que ser investigador era el mejor trabajo del mundo porque te pagaban por aprender y que sin importar lo que hiciera en la vida tenía que apasionarme. Y aquí estoy esperando estar siempre a tu altura, agradeciendo a la vida haberte puesto en mi camino, por tomar mi mano cuando más lo necesitaba, por enseñarme a usar la densidad y por levantarme los ánimos con cafecito. Durante estos 11 años no solo tuve al mejor tutor, sino también al mejor amigo. “Gracias Tlanepantla”.

A mis compañeros del laboratorio Giovanni, Jaime, Ixchel, Paola, Luis, Toño, y todos aquellos con quién he compartido, ideas, experimentos, enseñanzas y experiencias de vida. Mil gracias a todos porque sin ustedes este trayecto no hubiera sido tan divertido.

A ti mamá por hacerme una mujer de valores y que sabe luchar para alcanzar sus sueños. Por darme siempre ese ejemplo de lucha, de tenacidad, de amor y comprensión. Por escucharme cada que contaba de mis experimentos, ahora se que lo hice bien porque ya me hablas de los “catiónicos”. Porque a pesar de lo largo de los años y lo pesado nunca has soltado mi mano, tus brazos siempre serán mi lugar favorito Todo lo que soy te lo debo a ti. Te amo mami.

A mi papá por todo su amor. ¡Gracias pá!

A la memoria de Manuel Perusquía, mi abuelo que me enseñó a cuestionarme y a pensar más allá de lo lógico, por fomentar mi inquietud y curiosidad y transformarla en ese pensamiento crítico y científico que desconocía que tenía. Gracias por creer en mí Pipito, ojalá estuvieras aquí. Besos hasta el cielo.

A la familia Perusquía González por siempre ser la mejor porra, porque siempre dan los mejores abrazos y por tener ese lugar de amor que hacen mi segunda casa, donde siempre me siento tan feliz. Los amo!

Marlén y Aránzazu a quienes les pertenece la mitad del miocardio, porque sin importar lo difícil de los años, día con día mi alma se siente tranquila de saberse segura entre sus manos. ¡Male y Gogoro gracias por este par!

Abuela de Batman gracias por cuidarme tanto, por ayudarme con las tareas, por estudiar conmigo y por ser la mejor abuela del mundo, se que me miras desde donde estés. Te llevo como una chispita en el corazón.

A mi hermosa familia Perusquía, que me vio crecer, física, emocional y académicamente, que nunca nos abandono aún en los momentos mas difíciles, a todos ustedes muchas gracias.

A mis segundas mamás Patita y Conchitas no tengo palabras para describir cuan emocionada estoy de llegar hasta aquí, pero no hubiera sido posible de no ser por ustedes, que nos arroparon, que nos mimaron, que nos cuidaron y muchas veces nos llenaron la pancita. Gracias por confiar en mi e impulsarme siempre a seguir mis sueños. ¡Las amo!

Mensa eres mi pilar y mi fortaleza, gracias por estar ahí siempre, por compartir conmigo no sólo mis momentos felices, sino también los más desastrosos, vergonzosos y tristes. Quiero dar gracias por todas las veces que nos hemos reído, por las que nos hemos peleado también y porque siempre sacas lo mejor de mí. Por hacer que estos 17 años en los que hemos sido amigas parezcan mucho más de los que son. Porque durante estos años hemos creado recuerdos para toda una vida. Gracias por recordarme que no tengo que preocuparme por los demás, sino que sólo por aquellos que me quieren y por ser mi fiel escudero. Pero sobre todo, gracias por darme todas estas razones y por ser mi persona. Te adoro hermana!

A Alejandra Sánchez por ser mi hermana de corazón. Porque eres parte fundamental de mi ser, por tomar mi mano y consolarme, por enseñarme a luchar, eres la persona más amorosa y valiente que conozco. Eres ese pequeño rayo de luz cálida que ilumina mi corazón, eres mi mayor ejemplo de amor. Gracias por adoptarme como hermanita y por enseñarme que no hace falta ser la misma sangre para ser familia. A Blanca, por compartirme a su hermosa y valiosa hermana, besos hasta el cielo. ¡Arriba la laguna!... literal.

A Fernando Garrido “el hombre de la casa” por cuidar no solo de mi hermana si no también de nosotras. Gracias por compartirnos tu maravillosa familia, te amamos y lo hacemos extensivo a Mariel y mamá Flor.

A Sofía por tu amistad, confianza y por estar cerca de mí siempre. Tu ayuda ha sido fundamental, has estado conmigo hasta en los momentos mas turbulentos. Este proyecto no fue nada fácil y estuviste apoyándome, motivándome y soportándome, creo que lo ultimo fue lo más difícil. Aunque la vida nos ha hecho diferentes en actitud y comportamiento, el cariño siempre va a ser más fuerte. ¡Te quiero 4ever!

A Montse y sus alocados chinos, eres de las mejores personas que conozco, amo tu locura, tu pasión por la vida, tu entusiasmo, tu gran sentido del humor y sobre todo tu fuerza de voluntad para no darte por vencida, ese es mi mejor ejemplo y motor. Gracias por siempre tomar mi mano, por ser ese hombro que seca mis lagrimas y por siempre siempre devolverme la sonrisa. Te mega adoro amiga.

Amore mío, compañero de aventuras, este trabajo también te lo dedico a ti. Eres esa parte de amor, locura y sensatez que me hacen el día a día. A tu lado siento que nada me falta y que todo se torna más ligero. Apúrate que las vegas no esperan. Te amo nene!

A Thorsten Langner for German Classes and Molecular Biology coaching.
Thank you Guapo.

A Roselia porque contigo aprendí la responsabilidad de dirigir alumnos, por ahí dicen que “echando a perder se aprende”, pero sobre todo a tener paciencia a las necesidades, muuucha paciencia (Oscar: aquí donde pague todas las que te hice pasar jajajaja). Nunca te detengas, que eso me encanta de ti, eres una persona muy lista, loca, siempre valiente, entusiasta, decidida y una gran amiga. Te quiero mucho güera!

A Héctor Miranda por aguantar mi estrés, siempre darle una explicación lógica a mi alocado pensamiento, por las revisiones críticas y severas, por las ideas de madrugada, por consolarme cuando se me caía el mundo, por los abrazos que me reiniciaban el alma y sobre todo por sacarme tantas sonrisas. Nos debemos esas duvel.

A Norma Silvia, por ese consejo siempre tan atinado acompañado de un buen vino. Eres mi ejemplo a seguir, eres una gran maestra y una excelente amiga, no miento cuando te digo que cuando sea grande quiero ser como tú, o cuando menos la mitad de feliz, de inteligente, de tenaz, de comprensiva y cariñosa. Te admiro mucho y te quiero más.

A Sara Teresa Méndez por enseñarme la magia de la biología molecular y por trabajar hombro a hombro conmigo, aunque nos dieran las 11pm, pero sobre todo por ser esa mamá cariñosa y atenta que me cuidaba no solo los experimentos. Mil gracias por todo, te adoro.

A Juan Pablo Pardo por su aportación a este trabajo, por la revisión del artículo y por el p(ashe) osho osho. Te quiere la pinshe Meshe.

A Federico Martínez por permitirnos vivir a su lado tantos años formando el fabuloso 5Bis, gracias por aceptarme como su alumna ese octubre de 2006, por confiar en mi pequeño talento de investigador que fue creciendo a lo largo de los años y ahora todo se concentra en esta tesis.

A TODOS USTEDES MIL GRACIAS.

DEDICATORIAS

A Viridiana, porque gracias a ti comencé a subir la escalera...

¡y ya llegamos hasta arriba!

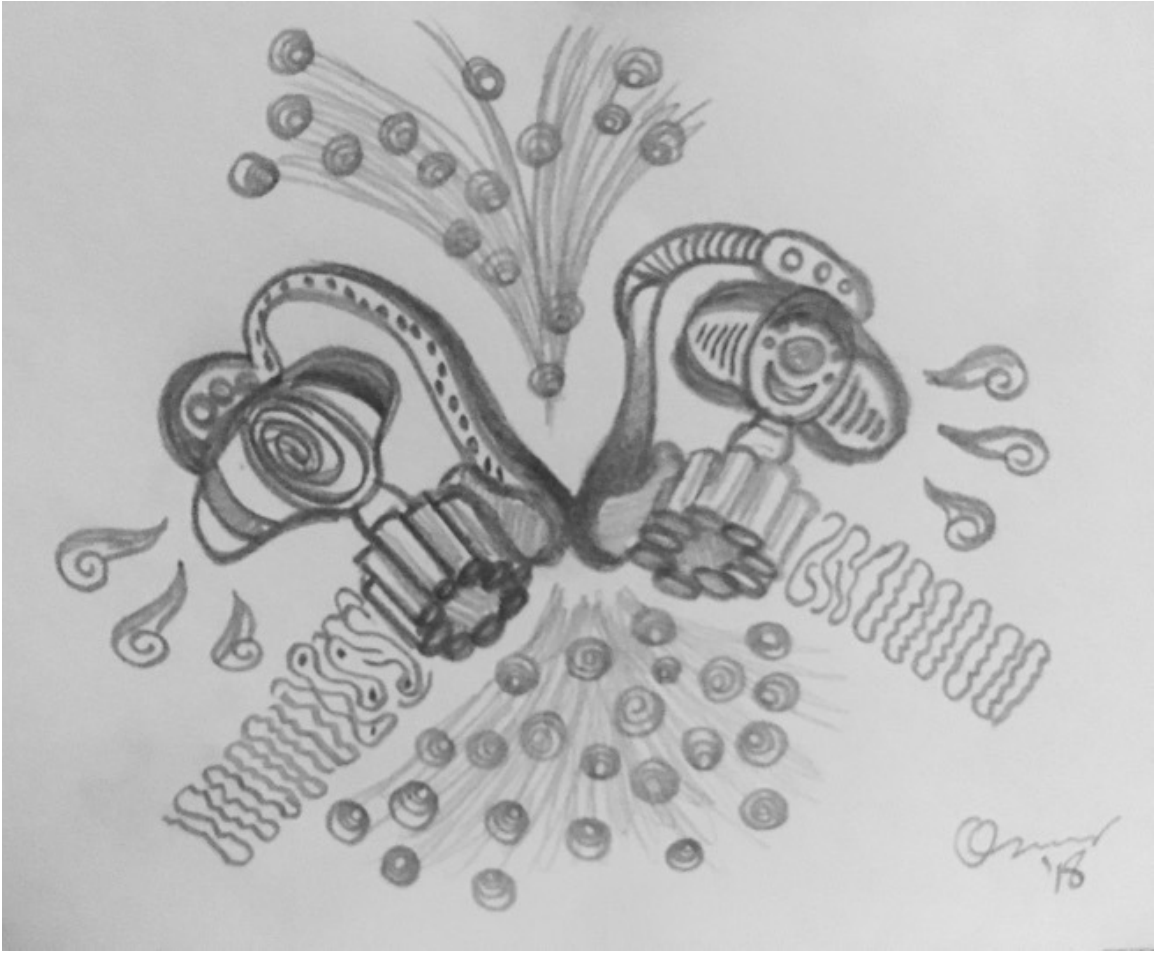
En ti tengo ese espejo de fortaleza en donde algún día me quiero reflejar, pues tus virtudes infinitas y tu gran corazón me llevan a admirarte cada día más.

Gracias por no dejarme perder la fe en la humanidad, por curarme el estrés con cacahuates enchilados y coca-cola, por despertarme con un beso a media noche, por ser la mejor amiga y sobetodo por ser la persona más buena que conozco, haces del mundo un lugar mejor o por lo menos mi mundo.

Hay días que cuando me duele mirar hacia atrás y me da miedo mirar hacia enfrente tengo la seguridad de que al voltear a la derecha o izquierda tu siempre estas a mi lado.

Gracias Dios por concederme a la mejor de las hermanas,

Eres mi luz al final del túnel. Te amo chiquitina.



"La ATP sintasa" Dr. Oscar Flores-Herrera, 2018.

Índice

ÍNDICE	página
LISTA DE FIGURAS	
LISTA DE TABLAS	
ABREVIATURAS	
RESUMEN	1
ABSTRACT	2
1. INTRODUCCIÓN	4
1.1. Generalidades.	4
1.2. Arquitectura y función de la F₁F₀-ATP sintasa.	10
1.3. Las crestas mitocondriales.	17
1.4. La F₁F₀-ATP sintasa como dímero y su papel en el plegamiento de las crestas mitocondriales,	20
1.5. Otros factores que participan en la formación de las crestas mitocondriales.	33
1.6. Efecto de la eliminación de las subunidades dimerizantes y su repercusión en la arquitectura mitocondrial	35
1.7. <i>Ustilago maydis</i> como modelo experimental.	37
2. JUSTIFICACIÓN	41
3. OBJETIVOS	43
3.1. General	
3.2. Particulares	
4. MATERIALES Y MÉTODOS	45
5. RESULTADOS	64

6. DISCUSIÓN	100
7. CONCLUSIONES	107
8. PERSPECTIVAS	109
9. REFERENCIAS BIBLIOGRÁFICAS	111
10. ANEXOS	129
10.1. Oligonucleótidos usados para la formación del knock-out para la transformación de <i>U. maydis</i>.	129
10.2. Transformación por biobalística.	129
10.3. Solución de sales.	130
10.4. Elementos traza.	130
10.5. Cuantificación de la cantidad de F₁F₀-ATP sintasa en las muestras V_{1WT}, V_{2WT}, V_{Δg}.	130
10.6. Cuantificación de la cantidad de F₁F₀-ATP sintasa en las mitocondrias de las cepas WT y Δg.	139
11. ARTÍCULOS	145
11.1. Artículo de requisito.	
• STRUCTURAL AND KINETICS CHARACTERIZATION OF THE F ₁ F ₀ -ATP SYNTHASE DIMER. NEW REPERCUSSION OF MONOMER-MONOMER CONTACT (2017) Mercedes Esparza-Perusquía , Sofía Olvera-Sánchez, Juan Pablo Pardo, Guillermo Mendoza-Hernández, Federico Martínez, and Oscar Flores-Herrera. <i>BBA-Bioenergetics</i> . 1858(12):975-981. doi: 10.1016/j.bbabi.2017.09.002.	148

11.2. Publicaciones directas.

- DELETION OF SUBUNIT G FROM F₁F₀-ATP SYNTHASE AFFECTS THE STABILITY OF ITS DIMERIC STATE AND THE MITOCHONDRIAL ATP SYNTHESIS. **Esparza-Perusquía M**, Langner T, Feldbrügge M, Pardo JP, Martínez F, and Flores-Herrera O. *En preparación*. **155**
- DELETION OF THE NATURAL INHIBITORY PROTEIN INH1 FROM USTILAGO MAYDIS ATP SYNTHASE DOES NOT INCREASE THE ACTIVITY OF THE DIMERIC STATE OF F₁F₀-ATP SYNTHASE. Romero-Aguilar Lucero*, **Esparza-Perusquía Mercedes***, Langner Thorsten, García Giovanni, Feldbrügge Michael, Pardo Juan Pablo, Martínez Federico, and Flores-Herrera Oscar. *En preparación*. **178**

11.3. Otras publicaciones.

- MITOCHONDRIAL PROTEASES ACT ON STARD3 TO ACTIVATE PROGESTERONE SYNTHESIS IN HUMAN SYNCYTIOTROPHOBLAST (2015) **Mercedes Esparza-Perusquía**, Sofía Olvera-Sánchez, Oscar Flores-Herrera, Héctor Flores-Herrera, Alberto Guevara-Flores, Juan P Pardo, María T Espinosa-García y Federico Martínez. *BBA-General Subjects*. 1850(1):107-17. doi: 10.1016/j.bbagen.2014.10.009. **204**
- MEMBRANE POTENTIAL REGULATES THE MITOCHONDRIAL ATP-DIPHOSPHOHYDROLASE ACTIVITY BUT IT IS NOT INVOLVED IN THE PROGESTERONE BIOSYNTHESIS IN HUMAN SYNCYTIOTROPHOBLAST CELL (2015) Oscar Flores-Herrera, Sofía Olvera-Sánchez, **Mercedes Esparza-Perusquía**, Juan Pablo Pardo, Juan Luis Rendón, Guillermo Mendoza- **215**

- Hernández, and Federico Martínez. *BBA-Bioenergetics*. 1847(2):143-52. doi: 10.1016/j.bbabi.2014.10.002.
- MULTIPLE FUNCTIONS OF SYNCYTIOTROPHOBLAST MITOCHONDRIA IN PREGNANCY (2015) Federico Martínez, Sofía Olvera-Sánchez, **Mercedes Esparza-Perusquía**, Erika Gómez-Chang, Oscar Flores-Herrera. *Steroids*, 103:11-22. doi: 10.1016/j.steroids.2015.09.006. 225
 - STREPTOZOTOCIN INDUCED ADAPTIVE MODIFICATION OF THE MITOCHONDRIAL SUPERCOMPLEXES IN LIVER OF WISTAR RATS AND THE PROTECTIVE EFFECT OF *MORINGA OLEIFERA* LAM (2018) Alejandra Sánchez-Muñoz, Mónica A Valdez-Solana, Mara I Campos-Almazán, Oscar Flores-Herrera, **Mercedes Esparza-Perusquía**, Sofía Olvera-Sánchez, Guadalupe García-Arenas, Claudia Avitia-Domínguez, Alfredo Téllez-Valencia and Erick Sierra-Campos. *Biochemistry Research International*. 1-15. ID 5681081. doi:10.1155/2018/5681081. 237
 - CARDIOPROTECTIVE STRATEGIES PRESERVE THE STABILITY OF RESPIRATORY CHAIN SUPERCOMPLEXES AND REDUCE OXIDATIVE STRESS IN REPERFUSED ISCHEMIC HEARTS (2018) Ixchel Ramírez-Camacho, Francisco Correa, Mohammed El-Hafidi, Alejandro Silva-Palacios, Marcos Ostolga-Chavarría, **Mercedes Esparza-Perusquía**, Sofía Olvera-Sánchez, Oscar Flores-Herrera and Cecilia Zazueta. *Free Radical Biology and Medicine*. 129:407-417. doi: 10.1016/j.freeradbiomed.2018.09.047. 254
 - MITOCHONDRIAL RESPIRASOME WORKS AS A SINGLE UNIT AND THE CROSSTALK BETWEEN COMPLEXES I, III₂ AND IV STIMULATES NADH DEHYDROGENASE ACTIVITY (2019) Meztli Reyes-Galindo, Roselia Suarez, **Mercedes Esparza-** 265

Perusquía, Jaime de Lira-Sánchez, Juan Pablo Pardo, Federico Martínez, and Oscar Flores-Herrera. *BBA-Bioenergetics*. 1860(8):618-627. doi: 10.1016/j.bbabi.2019.06.017.

- ASPECTOS GENERALES DEL TRANSPORTE DE COLESTEROL EN LA ESTEROIDOGÉNESIS DE LA PLACENTA HUMANA (2019) Sofía Olvera-Sánchez, **Mercedes Esparza-Perusquía**, Oscar Flores-Herrera, Viviana A. Urban-Sosa y Federico Martínez. *TIP Revista Especializada en Ciencias Químico-Biológicas*, 22:1-9. DOI: 10.22201/fesz.23958723e. **275**
- STEADY-STATE PERSISTENCE OF RESPIRATORY SYNCYTIAL VIRUS IN A MACROPHAGE-LIKE CELL LINE AND IDENTIFICATION OF NON-SYNONYMOUS MUTATIONS THROUGH SEQUENCING OF THE PERSISTENT VIRAL GENOME. Ximena Ruiz-Gómez, Joel Armando Vázquez-Pérez, Oscar Flores-Herrera, **Mercedes Esparza-Perusquía**, Carlos Santiago-Olivares, Jorge Gaona, Beatriz Gómez, Carmen Méndez, Evelyn Rivera-Toledo. *MDPI-viruses*, Manuscript ID: 842162. **284**

12. CAPITULOS DE LIBRO **306**

- “*Proteomics of lignocellulosic substrates bioconversion in anaerobic digesters to increase the carbon recovery as methane*” Alicia Guadalupe Talavera-Caro, María Alejandra Sánchez-Muñoz, Inty Omar Hernández-De Lira, Lilia Ernestina Montañez-Hernández, Jesús Antonio Morlett-Chávez, **María de las Mercedes Esparza-Perusquía**, Nagamani Balagurusamy. *Biological Approaches for the Management of Agro-industrial Residues Applied Environmental Science and Engineering for a Sustainable Future*. (2020) Editor: Zainul Akmar Zakaria, Ramaraj **307**

Boopathy, Julian Rafael Dib, Reeta Rani Singhania. Springer,
Cham. ISBN 978-3-030-39137-9.

LISTA DE FIGURAS	página
Figura 1. Morfología mitocondrial.	4
Figura 2. Cadena de transporte de electrones.	8
Figura 3. La F_1F_0 -ATP sintasa.	11
Figura 4. Mecanismo para la síntesis de ATP.	13
Figura 5. Mecanismo de los sitios catalíticos de la porción F_1 de la ATP sintasa durante la síntesis de ATP.	15
Figura 6. Estructura de la subunidad a y la translocación de protones.	16
Figura 7. Representación esquemática de la fosforilación oxidativa en una cresta plegada.	18
Figura 8. Mecanismos propuestos para la formación de las crestas.	19
Figura 9. Actividad de ATPasa en gel de los oligómeros de la F_1F_0 -ATP sintasa.	20
Figura 10. Densidad de protones al interior de la cresta.	21
Figura 11. Estructura del dímero de la F_1F_0 -ATP sintasa de <i>Polytomella sp.</i>	24
Figura 12. Dímero de la F_1F_0 -ATP sintasa porcina y sus sitios de unión.	27
Figura 13. Ultraestructura mitocondrial de las células de placenta Humana.	28
Figura 14. Estructura de la F_1F_0 -ATP sintasa mitocondrial de <i>S. cerevisiae</i> a 25 Å de resolución.	31
Figura 15. Reconstrucción tomográfica de una cresta tubular mitocondrial de hígado de rata.	32
Figura 16. Dímeros aislados observados por microscopía de transmisión electrónica.	32
Figura 17. Elementos proteicos involucrados en la formación de las crestas mitocondriales.	34
Figura 18. Diferencias estructurales en las mitocondrias de <i>Saccharomyces cerevisiae</i> .	35

Figura 19. Ultraestructura mitocondrial de las células Hela.	36
Figura 20. Ciclo de Vida de <i>U. maydis</i> .	38
Figura 21. Cadena de transporte en electrones de <i>U. maydis</i> .	39
Figura 22. Amplificación de los fragmentos UF y DF para la construcción del plásmido KO.	65
Figura 23. Transformación de <i>U. maydis</i> con el DNA exógeno.	66
Figura 24. Comprobación de la cepa mutante Δg .	67
Figura 25. Southern Blot.	68
Figura 26. Curva de crecimiento en YPD.	69
Figura 27. Curva de crecimiento en MM-EtOH.	70
Figura 28. Curva de crecimiento en MM-Glucosa.	71
Figura 29. Microscopia de las células WT y Δg (fase logarítmica).	72
Figura 30. Microscopia de las células WT y Δg (fase estacionaria).	73
Figura 31. Diluciones seriadas (1:10) de las cepas WT y Δg de <i>U. maydis</i> .	74
Figura 32. Ultraestructura de las células de <i>U. maydis</i> .	75
Figura 33. Consumo de oxígeno de las células cultivadas en medio rico YPD.	76
Figura 34. Consumo de oxígeno de las células cultivadas en MM-EtOH.	77
Figura 35. Consumo de oxígeno de las células cultivadas en MM-Glucosa.	78
Figura 36. Consumo de glucosa.	81
Figura 37. Células permeabilizadas de <i>U. maydis</i> .	82
Figura 38. Potencial de membrana ($\Delta\psi_m$) generado por las células de <i>U. maydis</i> .	82
Figura 39. Síntesis de ATP mitocondrial en las células WT y Δg .	83
Figura 40. Producción de radicales libres en las mitocondrias de <i>U. maydis</i> .	84

Figura 41. Actividad en gel de los supercomplejos y complejos respiratorios.	86
Figura 42. 2D-Tricina-SDS-PAGE.	87
Figura 43. Purificación de los oligómeros de la F_1F_0 -ATP sintasa mitocondrial de la cepa WT.	89
Figura 44. Purificación del monómero de la F_1F_0 -ATP sintasa mitocondrial de la cepa Δg .	90
Figura 45. Caracterización cinética o de la F_1F_0 -ATP sintasa Mitocondrial aislada.	92
Figura 46. Titulación de la actividad de ATPasa del V_2 con DDM.	93
Figura 47. Actividad de la F_1F_0 -ATP sintasa mitocondrial en presencia de DDM.	94
Figura 48. Actividad de ATPasa de los oligómeros de la F_1F_0 -ATP sintasa mitocondrial aislados de las cepas WT y Δg .	95
Figura 49. Efecto de la oligomicina en la actividad de ATPasa.	97
Figura 50. Efecto de la temperatura en la actividad de ATPasa.	98
Figura S1. SDS-Tricina-PAGE de V_1 y V_2 .	132
Figura S2. SDS-Tricina-PAGE de las mitocondrias WT y Δg .	139

LISTA DE TABLAS	página
Tabla 1. Composición de la F ₁ F ₀ -ATP sintasa mitocondrial de <i>S. cerevisiae</i> , <i>B. taurus</i> y <i>Ustilago maydis</i> .	12
Tabla 2. Diferencias metabólicas de las cepas WT y Δg .	79
Tabla 3. Parámetros cinéticos para la actividad de hidrólisis de ATP para el dímero y el monómero de la F ₁ F ₀ -ATP sintasa de <i>Ustilago maydis</i> .	105
Tabla 4. Oligonucleótidos utilizados para generar el plásmido knock-out y para verificar la cepa mutante Δg .	129
Tabla 5. Cuantificación del contenido de las subunidades α y β del V _{1WT} de la F ₁ F ₀ -ATP sintasa (4 diferentes muestras).	133
Tabla 6. Cálculo del contenido de F ₁ F ₀ -ATP sintasa en diferentes muestras de V _{1WT} aislados.	134
Tabla 7. Cuantificación del contenido de las subunidades α y β del V _{2WT} de la F ₁ F ₀ -ATP sintasa (4 diferentes muestras).	135
Tabla 8. Cálculo del contenido de F ₁ F ₀ -ATP sintasa en diferentes muestras de V _{2WT} aislados.	136
Tabla 9. Cuantificación del contenido de las subunidades α y β del V _{1Δg} de la F ₁ F ₀ -ATP sintasa (4 diferentes muestras).	137
Tabla 10. Cálculo del contenido de F ₁ F ₀ -ATP sintasa en diferentes muestras de V _{1Δg} aislados.	138
Tabla 11. Cuantificación del contenido de las subunidades α y β de la F ₁ F ₀ -ATP sintasa total en las mitocondrias de la cepa WT.	140
Tabla 12. Cálculo del contenido de F ₁ F ₀ -ATP sintasa total en las mitocondrias de la cepa WT.	141
Tabla 13. Cuantificación del contenido de las subunidades α y β del Δg de la F ₁ F ₀ -ATP sintasa total en las mitocondrias de la cepa Δg .	142
Tabla 14. Cálculo del contenido de F ₁ F ₀ -ATP sintasa total en las mitocondrias de la cepa Δg .	143

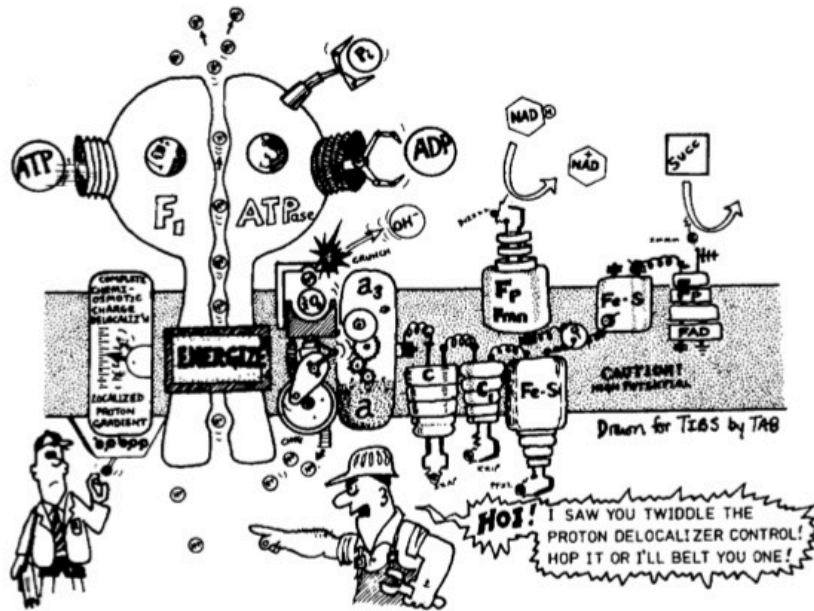
ABREVIATURAS

ADP	Adenosín 5'-difosfato.
AMPc	Adenosín 3',5'- monofosfato cíclico.
anti-DIG-AB	Anticuerpo contra digonexina marcada.
AOX	Oxidasa alterna mitocondrial.
ASA	del inglés "ATP Synthase-Associated protein"
ATP	Adenosín 5'-trifosfato.
Bis-Tris	2,2-Bis(hydroxymethyl)-2,2',2"-nitrilotriethanol, 2-Bis(2-hydroxyethyl)amino-2-(hydroxymethyl)-1,3-propanediol, Bis(2-hydroxyethyl)amino-tris(hydroxymethyl)methane.
BN-PAGE	Electroforesis en condiciones nativas en geles azules.
BrEt	Bromuro de 3,8-diamino-5-etil-6-fenilfenantridinio.
<i>C. reinhartii</i>	<i>Chlamydomonas reinhartii</i>
CCCP	Carbonyl cyanide 3-chlorophenylhydrazone.
CJ	Uniones de Cresta.
DAB	3, 3'-Diaminobenzidine.
DDM	<i>n</i> -Dodecil β -D-maltósido.
DF	Downstream flank (secuencia río abajo del gen).
DMSO	Dimetilsulfóxido.
dNTP's	Desoxinucleótidos trifosfato.
DNA	Ácido desoxirribonucleico .
DOC	Ácido 3 α , 12 α -Dihidroxi-5 β -colan-24-oico.
EDTA	Ácido 2-({2[bis(carboximetil)amino]etil}(carboximetil)amino)acético.
FADH ₂	Flavín adenín dinucleótido reducido.
Fcj1	Proteína formadora de la unión de cresta.
G-6P-DH	Glucosa-6-fosfato deshidrogenasa.
gDNA	DNA genómico.
GOD	Glucosa oxidasa.

EGTA	Ácido etilenglicol-bis(2-aminoetiléter)-N,N,N',N'-tetraacético
H ₃ BO ₃	Ácido trioxobórico (III).
HEPES	Ácido 4-(2-hidroxietil)-1-piperazina-etanosulfónico.
HK	Hexocinasa.
hrCN-PAGE	Electroforesis en condiciones nativas en geles claros en presencia de DDM y DOC.
HygR	Cassette de resistencia a la higromicina.
K_m	Constante de Michaelis-Menten.
KO	Knock-out.
Kpb	Kilo pares de bases.
LB	Luria Bertani medio.
LB ^{Amp}	Luria Bertani medio suplementado con ampicilina.
LDH	Lactato deshidrogenasa.
M_{app}	Masa molecular aparente.
MEM	Membrana Externa Mitocondrial.
MIM	Membrana Interna Mitocondrial.
MM-EtOH	<u>Medio Mínimo</u> -Etanol.
MM-Glucosa	<u>Medio Mínimo</u> -Glucosa.
MOPS	3-(N-morpholino)propanesulfonic acid.
MTT	1.2 mM de bromuro de 3-[4,5-dimetiltiazol-2-yi]-2,5-difeniltetrazolio.
NADH	Nicotinamida adenina dinucleótido reducido.
NADP	Nicotinamida adenina dinucleótido fosfato.
NADPH	Nicotinamida adenina dinucleótido fosfato reducido.
natgO ₂	Nanoatomo gramo de Oxígeno.
nOg	n-octil-galato (inhibidor de la oxidasa alterna).
OPA1	del inglés "Optic atrophy type 1".
OSCP	del inglés "Oligomycin - Sensitivity Conferring Protein".
pb	Pares de bases.
PBS	Amortiguador de fosfato salino.

PCR	Reacción en cadena de la polimerasa.
PEP	Fosfoenolpiruvato.
PHU	Pushion polimerasa.
PK	Piruvato cinasa.
PMS	5-Methylphenazinium methyl sulfate, <i>N</i> -Methylphenazonium methyl sulfate.
PMSF	Fluoruro de fenilmetilsulfonilo.
POD	Peroxidasa.
pUMa	Plásmido de <i>Ustilago maydis</i> .
RNA	Ácido ribonucleico.
ROS	del inglés "Radical Oxidative Species".
<i>S. cerevisiae</i>	<i>Saccharomyces cerevisiae</i>
SC	Supercomplejos.
SCS	Amortiguador para resuspender células de <i>U. maydis</i> .
STC	Amortiguador para resuspender protoplastos de <i>U. maydis</i> .
STC/PEG	Amortiguador para resuspender protoplastos de <i>U. maydis</i> con polietilenglicol.
STET	Medio para resuspender células (Obtención del DNA plasmídico).
TAE	Amortiguador para electroforesis en geles de agarosa, formada por Tris, acetato y EDTA.
TBE	Amortiguador para electroforesis en geles de agarosa, formada por Tris, borato y EDTA.
TOPO	pCR2.1-TOPO vector.
<i>U. maydis</i>	<i>Ustilago maydis</i>
UF	Upstream flank (secuencia río arriba del gen).
V ₁	Monómero de la F ₁ F ₀ -ATP sintasa.
V _{1Δg}	Monómero de la F ₁ F ₀ -ATP sintasa de la mutante Δg.
V ₂	Dímero de la F ₁ F ₀ -ATP sintasa.
V _{2Δg}	Dímero de la F ₁ F ₀ -ATP sintasa de la mutante Δg.

V_{max}	Velocidad enzimática máxima.
<i>Y. lipolitica</i>	<i>Yarrowia lipolitica</i>
(v)	Velocidad de la reacción.
$\Delta\Psi_m$	Potencial de membrana mitocondrial.
$\Delta\psi_m$	Potencial eléctrico de membrana.
$\Delta\mu_{H^+}$	Gradiente Electroquímico de Protones.
Δg	Cepa mutante de <i>U. maydis</i> (eliminación del gen ATP20).
ΔpH	Diferencial de pH .
4-AF	4-aminofenazona.



“La cadena respiratoria mitocondrial y la ATP sintasa: los años 1970 y 1980 debaten si los protones viajan en el circuito quimiosmótico deslocalizado o por vías más localizadas” Bioenergetics3, Nicholls, D. G. et al., 2002

RESUMEN

La espectrometría de masas demuestra que el dímero y el monómero de la F_1F_0 -ATP sintasa de *Ustilago maydis* contienen las 14 subunidades canónicas, pero además, el dímero contiene en el sector F_0 -estator las subunidades *e* y *g*, las cuales se sugiere son proteínas dimerizantes.

El dímero del complejo V tiene un papel importante en la formación de las crestas de la membrana interna mitocondrial y al eliminar la subunidad *g* la proporción de dímero disminuye y se modifica la arquitectura mitocondrial. En *U. maydis* la eliminación genética de la subunidad *g* no impide la dimerización del complejo V manteniéndose la misma proporción entre dímero y monómero. Por otro lado, observamos que la actividad de ATPasa del dímero es lenta, demostrando que la subunidad *g* no es esencial para la dimerización pero que podría tener un papel importante para de la actividad de la enzima. Aunado a esto, en la cepa Δg la AOX aparece a partir de la primera fase de crecimiento, lo que sugiere que la célula podría entrar en un estrés oxidativo.

El consumo de oxígeno durante la fase logarítmica de crecimiento fue alrededor de 108 natgO/mg/min para la cepa silvestre y 120 natgO/mg/min para la cepa Δg . Por otro lado, en las células recuperadas de la fase estacionaria el consumo de oxígeno para la cepa WT fue de 348 natgO/mg/min y de 168 natgO/mg/min para la Δg . La síntesis de ATP en ambas cepas es similar, para la cepa WT es de 0.34 $\mu\text{molas de ATP/g peso húmedo/min}$ y para la Δg es de 0.31 $\mu\text{molas de ATP/g peso húmedo/min}$.

Aunado a esto, el análisis de la arquitectura mitocondrial de la cepa Δg de *U. maydis* mostró crestas tubulares y lamelares, y no los anillos de cebolla descritos para *S. cerevisiae*. Asimismo, la síntesis de ATP y $\Delta\Psi_m$, en la cepa Δg y WT fueron similares y lo que sugiere que su estado bioenergético no fue afectado.

ABSTRACT

Mass spectrometry reveals that the dimer and monomer of F₁F₀-ATP synthase from *Ustilago maydis* contain the 14 canonic subunits, but in addition the dimer contains the subunits *e* and *g* at F₀-membrane-stator which are suggested to play a role in dimerization.

F₁F₀-ATP synthase plays a central role in the creation of internal membrane cristae, and therefore in mitochondrial architecture. In *U. maydis* genetical removal of the *g* subunit does not prevent dimerization of the V complex maintaining the same ratio of dimer to monomer. On the other hand, we observed that the ATPase activity of the dimer is slow, demonstrating that the subunit is not essential for dimerization but might play an important role in the enzymatic activity. In addition, in the Δg strain the AOX is expressed in the early stages of growth, which suggest that the cell oxidative stress is present since premature phases in contrast to the WT strain.

Oxygen consumption in the logarithmic phase was about 108 natgO/mg/min for the wild-type strain and 120 natgO/mg/min for the Δg strain. On the other hand, in cells recovered from the steady state oxygen consumption for the WT strain was 348 natgO/mg/min and 168 natgO/mg/min for the Δg . The synthesis of ATP in both strains was similar; for the WT strain 0.34 μ moles ATP/g wet weight/min and for Δg is 0.3134 μ moles ATP/g wet weight/min.

Mitochondrial architecture from the of *U. maydis* Δg -strain showed a tubular and lamellar crista, and not the onion ring morphology previously described in *S. cerevisiae*. Also, ATP synthesis, and $\Delta\Psi_m$, in the Δg and WT-strain were similar; suggesting that, although the ATPase activity of dimer was inhibited, its role in cristae structure and bioenergetics was not affected.



"Mitochondrial Membranes II" Odra Noel

Introducción

1. INTRODUCCIÓN

1.1. Generalidades

Las mitocondrias son organelos que adaptan su arquitectura y metabolismo a los requerimientos celulares, consiguiendo así producir más del 90% del ATP necesario para alejar a la célula del equilibrio termodinámico. Las mitocondrias están constituidas por dos membranas cuya composición proteica y lipídica varía enormemente: la membrana externa mitocondrial (MEM) es relativamente permeable para la mayoría de las moléculas, mientras que la membrana interna mitocondrial (MIM), es impermeable a los iones y a muchas moléculas orgánicas. La MIM incrementa su área de superficie al proyectarse hacia el interior de la matriz mitocondrial en forma de invaginaciones que se denominan crestas mitocondriales. La biogénesis y el mantenimiento de las crestas dependen de los procesos de fisión y fusión, así como de los cambios en la composición proteica y lipídica (Figura 1) (Hackenbrock *et al.*, 1986; Frey *et al.*, 2002).

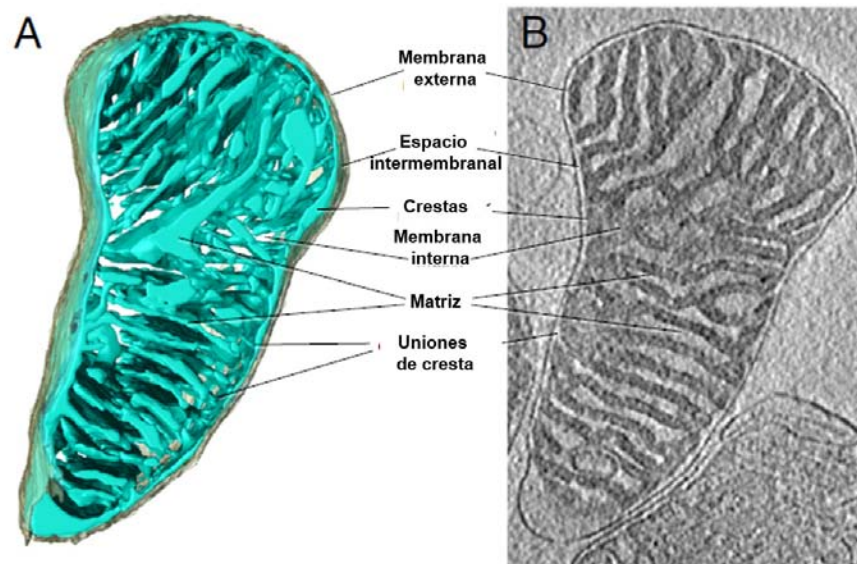


Figura 1. Morfología mitocondrial. Mitocondrias aisladas de *Saccharomyces cerevisiae*. **(A)** Se muestra la reconstrucción tridimensional. **(B)** Se muestra un corte histológico por criotomografía, en el cual se muestran las membranas mitocondriales, la matriz, las crestas, las uniones de cresta y el espacio intermembranal (Modificado de Kühlbrandt, 2015).

Los cambios morfológicos de las crestas son reflejo del nivel energético de la mitocondria, los cuales se clasifican en dos estados: el ortodoxo (alta concentración de ATP y baja de ADP), donde el número de crestas es bajo y las uniones de cresta son mínimas; y el condensado (baja concentración de ATP y alta de ADP), en el que hay un incremento en el número de las crestas al igual que de las uniones de cresta, provocando la contracción de la matriz mitocondrial (Mannella, 2006). En el estado condensado donde el consumo de oxígeno aumenta, se acopla con el bombeo de protones y la síntesis de ATP.

La respiración celular aeróbica, es el proceso mediante el cual las células transfieren poder reductor generado a partir de la degradación de azúcares, grasas y proteínas hasta el oxígeno molecular (O_2), es fundamental para el metabolismo energético de todas las células eucariontes y algunas procariontes. En las eucariontes las etapas finales de la respiración aeróbica se llevan a cabo en las mitocondrias, donde ocurren diversas vías metabólicas relacionadas con la obtención de energía, entre las cuales podemos mencionar a la β -oxidación, el ciclo de Krebs, la generación del gradiente electroquímico y la síntesis de ATP. El poder reductor (representado por el NADH y $FADH_2$) que se genera en la β -oxidación, la descarboxilación del piruvato y el ciclo de Krebs, pueden ser utilizados por la cadena de transporte de electrones para la generación del gradiente electroquímico de protones ($\Delta\mu_{H^+}$), el cual dirige la síntesis del ATP por la F_1F_0 -ATP sintasa (Cardol *et al.*, 2009; Letts *et al.*, 2019).

Los complejos de la cadena de transporte de electrones se encuentran embebidos en la membrana interna mitocondrial y catalizan las reacciones terminales de transferencia de electrones. Ésta se compone de cuatro grandes complejos proteicos: (1) la bomba de protones NADH-CoQ oxidorreductasa (complejo CI), (2) la succinato- CoQ oxidorreductasa (complejo CII), (3) el dímero obligado de la bomba de protones $CoQH_2$ -citocromo c-oxidorreductasa (complejo CIII₂) y (4) la bomba de protones citocromo c oxidasa (complejo CIV) responsable

de la reducción del oxígeno en agua (Figura 2) (Cardol *et al.*, 2009; Letts *et al.*, 2019).

El complejo I (NADH-CoQ oxidorreductasa) es el primero de los complejos de la cadena respiratoria, tiene una masa molecular alrededor de ~1 MDa y está formado por 45 subunidades de proteína dispuestas en dos "brazos": un brazo extrínseco que se extiende hacia la matriz mitocondrial y un brazo de membrana que está incrustado en el MIM. La transferencia de electrones es estimulada por K^+ e inhibida por rotenona. El transporte de electrones comienza en el complejo I, el cual acepta los electrones cuando se pierde el ion hidronio del NADH y los transfiere hacia el flavín mononucleótido (FMN), y varios centros hierro-azufre hasta la ubiquinona (Q) convirtiéndola en ubiquinol ($CoQH_2$). Durante este proceso, se obtiene la energía necesaria para el bombeo de 4 H^+ al espacio intermembranal o interior de la cresta (lado P). El sitio de oxidación del NADH se encuentra expuesto hacia la cara interna de la MIM, así como el sitio para la reducción de la $CoQH_2$ (lado N). Si tomamos en cuenta que la MIM es impermeable al NADH, el complejo I debe oxidar a los equivalentes reductores que provienen de las deshidrogenaciones de los sustratos del ciclo de Krebs, la descarboxilación oxidativa del piruvato y de la β -oxidación de los ácidos grasos, todas localizadas en la matriz mitocondrial; además de consumir el poder reductor producido en la glucólisis, empleando las lanzaderas de aspartato-malato (Hirst, 2013; Sazanov, 2015).

El complejo II (succinato- CoQ oxidorreductasa) es un tetrámero de 140 kDa, que tiene un FAD como grupo prostético y además tiene tres centros hierro-azufre. Esta enzima forma parte del ciclo de Krebs, oxidando al succinato en fumarato. El sitio activo de la succinato deshidrogenasa se encuentra situado en el lado N de la MIM. Por lo tanto, en mitocondrias íntegras, el succinato debe ser generado en la matriz, o bien ser transportado hacia ese EIM para su oxidación. La succinato deshidrogenasa, que reduce a la CoQ, es inhibida por el oxaloacetato y malonato (Chávez *et al.*, 2013).

La coenzima Q es una benzoquinona liposoluble que contiene una cadena lateral constituida por 11 unidades de isoprenos (Q₁₀). Esta quinona es reducida por los complejos CI y CII a ubiquinol (CoQH₂) y es oxidada por el CIII. Durante su reducción en el CI se realiza el bombeo de H⁺ al espacio intermembranal, mientras que en el CIII se realiza el ciclo-Q, donde ocurre la oxidación de dos moléculas de CoQH₂ y la reducción de una Q, con la formación de una semiquinona (HQ[•]). Además, durante el ciclo-Q, el CIII acopla la energía libre disponible de la reacción de transferencia de electrones con el bombeo de H⁺ al espacio intermembranal. Los electrones transferidos de la CoQH₂ al citocromo c1 del CIII son translocados al citocromo c, el cual actúa como agente reductor del CIV (Figura 2) (Chávez *et al.*, 2013).

La CoQH₂-citocromo c-oxidoreductasa (CIII₂) es un homodímero, cuyo monómero tiene un peso molecular de 500 kDa y está formado por 10 subunidades, en donde se encuentran 3 centros de óxido-reducción formados por un centro [2Fe-2S] y los grupos hemo b562, b566 y c1 (Chávez *et al.*, 2013). El complejo III acepta los electrones del CoQH₂ y el poder reductor es transferido al citocromo c, el cual es una proteína pequeña de 13 kDa, que se encuentra situada hacia el lado P de la MIM; este citocromo transporta los electrones del complejo III al complejo IV y se libera de la membrana a alta fuerza iónica, utilizando soluciones con altas concentraciones de sales como el KCl. Este complejo es el tercer sitio de acoplamiento, bombea 4 protones y puede inhibirse con Antimicina A y Mixotiazol (Chávez *et al.*, 2013).

La citocromo c oxidasa (CIV) tiene una masa molecular alrededor de 240 KDa, se reconoce como la oxidasa terminal y comprende a los citocromos a y a₃, está formado por 13 subunidades y contiene tres átomos de cobre iónico (2 CuA y 1 CuB) y los grupos hemo necesarios para la función redox de la enzima. La citocromo oxidasa oxida al citocromo c, reduce al oxígeno molecular (O₂) produciendo 2 H₂O y bombea 4 H⁺ al espacio intermembranal. La citocromo oxidasa es inhibida por cianuro, azida de sodio o monóxido de carbono (Chávez *et al.*, 2013).

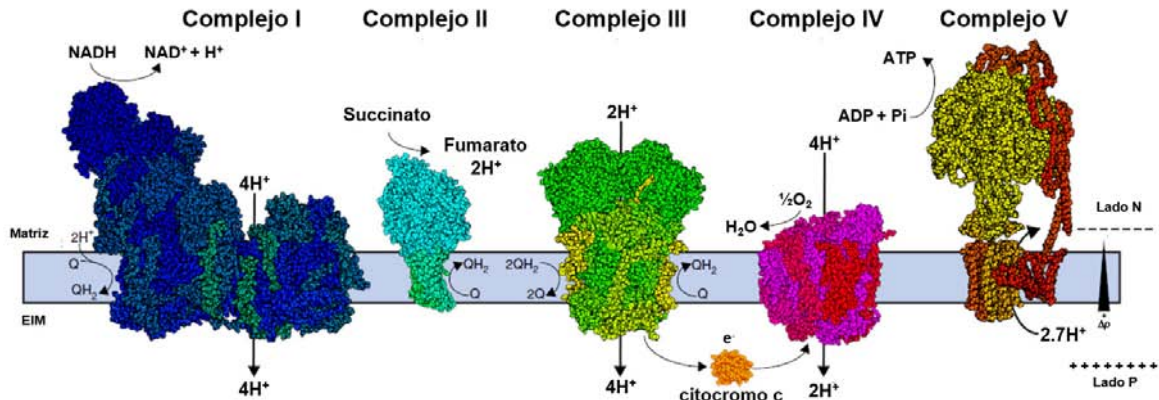


Figura 2. Cadena de transporte de electrones. Esquema general de la cadena de transporte de electrones, la teoría quimiosmótica propone que los protones se conducen desde la matriz mitocondrial a través de la membrana interna y dentro del espacio intermembranal por el mecanismo de transporte electrónico para generar un gradiente, el cual es aprovechado para la síntesis de ATP por la ATP sintasa. Δp = fuerza protón matriz. EIM = Espacio InterMembranal (Modificado de Letts *et al.*, 2017).

Estos complejos se asocian entre si para formar supercomplejos que pueden ser aislados de la membrana cuando se solubilizan con un detergente suave, como la digitonina. Gracias a esto, se ha propuesto un modelo de estado sólido para la transferencia de los electrones, el bombeo de H^+ y el consumo de O_2 ; sin embargo, algunos estudios han demostrado que los supercomplejos no son la entidad funcional esencial de la cadena respiratoria, ya que los complejos respiratorios pueden encontrarse en su forma monomérica (modelo de plasticidad) (Acín-Pérez *et al.*, 2008) y llevar así la transferencia de los electrones y formar el $\Delta\mu_{H^+}$ necesario para la síntesis de ATP por medio de la F_1F_0 -ATP sintasa, proceso que se conoce como fosforilación oxidativa (Schägger, 2000).

La teoría quimiosmótica, que explica la fosforilación oxidativa, fue descrita por Peter Mitchell en 1961. En esta se describe que el transporte de electrones de una serie de reacciones de oxido-reducción entre los grupos prostéticos (hemos, flavinas, FeS y Cu^{2+}) de los diferentes complejos respiratorios, que convierten la energía de las coenzimas NADH y $FADH_2$ en energía electroquímica representada por el $\Delta\mu_{H^+}$. Manipulando la ecuación de Nernst, Mitchell (1961) definió el término conocido como fuerza protón-matriz (Δp), la cual está compuesta por un componente químico (ΔpH) y un componente eléctrico ($\Delta\Psi$) de los protones separados por la membrana interna mitocondrial de las células eucariotas o la

membrana plasmática de las bacterias. De esta manera, se reconoce como lado positivo (P) a la cara de la membrana interna hacia donde se bombean de forma vectorial los protones (H^+), mientras que el lado negativo (N) es la cara de la membrana donde la $[H^+]$ disminuye. Posteriormente, el $\Delta\mu_{H^+}$ se traduce en energía química en forma de ATP a partir de ADP y fosfato (P_i), gracias al flujo de H^+ desde el lado P al lado N de la membrana a través del nanomotor conocido como F_1F_0 -ATP sintasa, lo cual se interpreta como la conversión de la energía libre almacenada en el $\Delta\mu_{H^+}$ (Mitchell, 1961; Boyer, 2000; Nicholls *et al.*, 2013).

1.2. Arquitectura y función de la F₁F₀-ATP sintasa

La F₁F₀-ATP sintasa o complejo V desempeña un papel central al acoplar su actividad al $\Delta\mu_{H^+}$ para llevar a cabo la síntesis de ATP necesaria para realizar todos los procesos metabólicos incluyendo fusión y fisión (Alfonzo *et al.*, 1981). Esta enzima es considerada un nanomotor y la podemos describir estructuralmente por un sector hidrofílico denominado F₁ y un sector hidrofóbico llamado F₀; mientras que funcionalmente la podemos dividir en un rotor y un estator. Al considerar ambas clasificaciones se ha definido que el dominio catalítico hidrofílico F₁-estator está compuesto por las subunidades solubles α y β ; mientras que el dominio F₁-rotor contiene las subunidades γ , δ , y ϵ , con una estequiometría general para la F₁ de 3:3:1:1:1 (α , β , γ , δ , y ϵ , respectivamente). En la interfase de cada par de subunidades α y β se forma un sitio activo, por lo que se tiene un total de 3 (Habersetzer *et al.*, 2013).

La estructura de los segmentos catalíticos muestra un alto grado de conservación evolutiva; por ejemplo, se ha determinado que las subunidades de mayor masa molecular de la enzima de las mitocondrias de bovino y de *Escherichia coli*, comparten un 72% de identidad en sus secuencias. A pesar de su alto grado de complejidad estructural, la F₁F₀-ATP sintasa mitocondrial es la enzima más estudiada (Yoshida *et al.*, 2001).

El dominio F₁ está unido al dominio hidrofóbico F₀ por el F₀-estator-tallo periférico el cual está constituido por las subunidades ATP4/*b*, OSCP, *h*(F6), *d* y *f*, mientras que la porción F₀-estator-membranal contiene a las subunidades ATP6(*a*), ATP8(A6L), *i*, *j* y entre 9-11 subunidades ATP9/*c* componen el F₀-rotor (Figura 3). Las subunidades de dimerización son las *e*, ATP20 (*g*) y *k* (Tabla 1) (Walker *et al.*, 2006; Devenish *et al.*, 2008; Watt *et al.*, 2010; Couoh-Cardel *et al.*, 2010).

Se han reportado otras proteínas asociadas al sector F₀ cuya función aún se desconoce, pero se sugiere que podrían estar relacionadas con mecanismos de regulación o que tiene un papel estructural. Adicionalmente, existe una proteína

cuyo papel es el de inhibir y/o regular la actividad de hidrólisis de ATP, la cual en *Saccharomyces cerevisiae* es denominada Inh1 e IF_1 en mamíferos. Mientras que en *Paracoccus denitrificans*, miembro de las α -proteobacterias, se encontró el inhibidor denominado subunidad ζ (Morales-Ríos *et al.*, 2010). La F_1F_0 -ATP sintasa de los mamíferos y las levaduras cuentan con la subunidad OSCP (del inglés “Oligomycin - Sensitivity Conferring Protein”) que le confiere la susceptibilidad al inhibidor oligomicina (Racker, 1963; Pullman *et al.*, 1963; Ebner *et al.*, 1977; Arselin *et al.*, 1996; Minauro-Sanmiguel *et al.*, 2005; Bisetto *et al.*, 2007; Strauss *et al.*, 2008; Vonk *et al.*, 2009;). La F_1F_0 -ATP sintasa es una enzima altamente conservada, sobre todo en aquellas subunidades involucradas en la catálisis y el bombeo de protones (Tabla 1) sin embargo, existen subunidades especie-específicas (Strauss *et al.*, 2008); por ejemplo, las subunidades *i/j* y *k* en levadura (Racker, 1963).

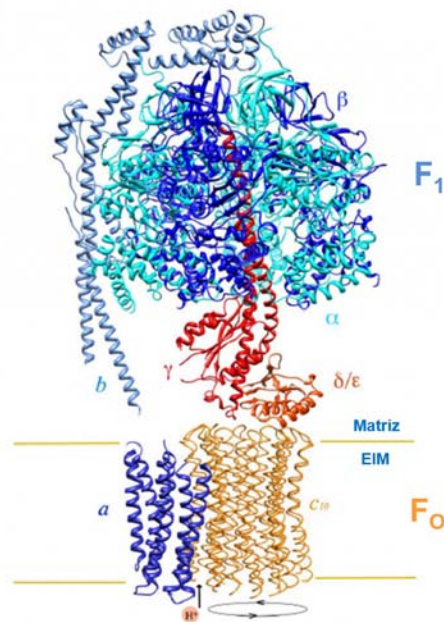


Figura 3. La F_1F_0 -ATP sintasa. Es la enzima encargada de la síntesis de ATP a partir de ADP y P_i , a través de un mecanismo rotatorio acoplado al gradiente de protones generado por el proceso oxidativo. El flujo de protones desde el EIM hacia la matriz mitocondrial impulsa la rotación de las subunidades c del dominio F_0 y el tallo del dominio F_1 formado por las subunidades γ y ϵ , alrededor de la cual se encuentran localizadas las tres subunidades α y las tres subunidades β que tienen una distinta conformación y diferentes afinidades para los nucleótidos, impuestas por la asimetría del tallo central.

Tabla 1. Composición de la F₁F₀-ATP sintasa mitocondrial de *S. cerevisiae*, *B. taurus* y *U. maydis*.

Sector	Función	Subunidad	<i>S. cerevisiae</i>		<i>B. taurus</i>		<i>U. maydis</i>	
			Tamaño (aa)	ID	Tamaño (aa)	ID	Tamaño (aa)	ID
F ₁	F ₁ -estator	α (ATP1)	510 (545)	P07251	510 (553)	P19483	510 (543)	UMAG_10213
		β (ATP2)	480 (511)	P00830	480 (528)	P00829	472 (540)	UMAG_10397
		γ (ATP3)	278 (311)	P38077	273 (298)	P05631	279 (312)	UMAG_05090
	F ₁ -rotor	δ (ATP16)	138 (160)	Q12165	146 (168)	P05630	139 (168)	UMAG_01103
		ε (ATP15)	61 (62)	P21306	50 (51)	P05632	65 (65)	UMAG_10754
F ₀	F ₀ -rotor	c (ATP 9)	76 (76)	P61829	75 (136)	P32876/07926	73 (73)	Q0H8W9
		OSCP (ATP5)	195 (212)	P09457	190 (213)	P13621	202 (218)	UMAG_06324
		b (ATP 4)	209 (244)	P05626	214 (256)	P13629	205 (240)	UMAG_10548
	Estator- tallo periférico	h (F ₆) (ATP14)	92 (124)	Q12349	76 (108)	P02721	99 (132)	UMAG_02360
		d (ATP7)	173 (174)	P30902	160 (161)	P13620	139 (170)	UMAG_12050
		f (ATP17)	95 (101)	Q06405	87 (88)	Q28851	69 (114)	UMAG_10180
		a (ATP6)	249 (259)	P00854	226 (226)	P00847	254 (254)	Q0H8Y6
	Estator de membrana	ATP 8 (A6L)	48 (48)	P00856	66 (66)	Q7JAT2	48 (48)	Q0H8Y5
		ijj (ATP18)	59 (59)	P81450	-	-	62 (62)	UMAG_11576
		e (TIM11)	95 (96)	P81449	70 (71)	Q00361	64 (92)	UMAG_10374
	Subunidades de dimerización	g (ATP20)	115 (115)	Q12233	102 (103)	Q28852	132 (159)	UMAG_00975
		k (ATP19)	68 (68)	P81451	-	-	82 (82)	UMAG_10479
		(s)	-	-	175 (200)	P22027	-	-
	Regulación	IF1 (INH1) (ATP5IF1)	63 (85)	P01097	84 (109)	P01096	64 (91)	UMAG_02361

Los números corresponden al número de aminoácidos de la proteína madura y, entre paréntesis la inmadura (Modificado de Habersetzer *et al.*, 2013; Esparza-Perusquía *et al.*, 2017). El ID fue recopilado de la base de datos de Uniprot (<http://www.uniprot.org>) y KEGG (https://www.genome.jp/kegg-bin/show_organism?org=uma).

La función de la F_1F_0 -ATP sintasa es producir el ATP a través de un sistema acoplado entre el sector F_1 y F_0 . Esto es posible debido a que la energía almacenada en el $\Delta\mu_{H^+}$ impulsa el flujo de los H^+ desde el interior de la cresta hacia la matriz mitocondrial, a través del sector F_0 -rotor (Figura 4) (Junge *et al.*, 1997; Allegretti *et al.*, 2015; Guo *et al.*, 2017). El $\Delta\mu_{H^+}$ tiene dos componentes: un diferencial de pH (ΔpH) y un potencial eléctrico de membrana ($\Delta\psi_m$) ambos componentes forman la fuerza protón-motriz (Mitchell, 1961; Boyer, 2000). Cuando los protones atraviesan la membrana acoplados al dominio F_0 , provocan el giro de un anillo formado por 9 - 15 subunidades c (Cox *et al.*, 1984; Wittig *et al.*, 2008. Kühlbrandt *et al.*, 2016), esta rotación hace girar al tallo central (subunidades δ y ϵ del rotor F_1) (Boyer *et al.*, 1981) en movimientos de 120° , provocando cambios conformacionales consecutivos en las subunidades catalíticas (subunidades α y β del estator F_1) e induciendo la unión de sustratos (ADP + P_i), la síntesis de ATP y la liberación de éste (Figura 5) (Walker, 1998; Itoh *et al.*, 2004).

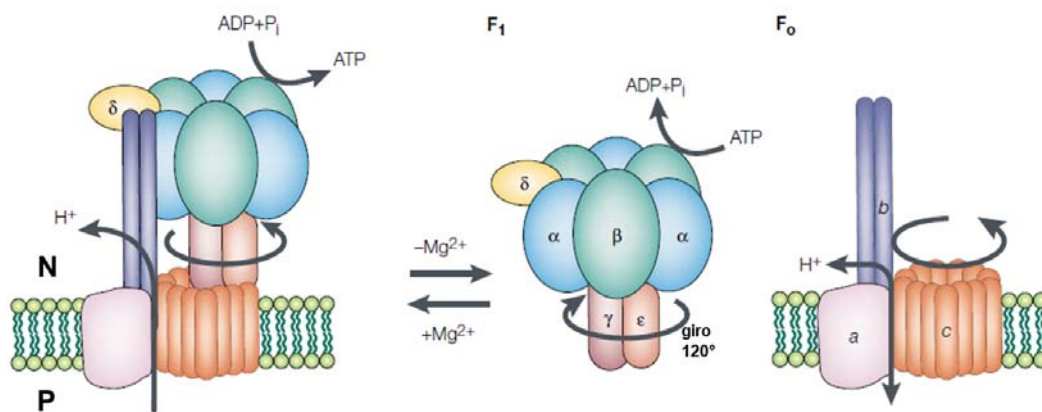


Figura 4. Mecanismo para la síntesis de ATP. Los protones atraviesan la membrana del lado P al lado N a favor del $\Delta\mu_{H^+}$ a través de un hemicanal formado entre la subunidad a y el anillo de subunidades c generando una rotación en la dirección indicada (flechas). En el modelo aceptado en la actualidad, cada subunidad c contiene un grupo carboxilo de un glutámico que contacta el hemicanal a través del cual pasan los protones. Una vez aceptado el protón por la subunidad c , esta gira dentro de la membrana lipídica y la rotación se completa por una atracción entre el residuo glutámico, con carga negativa, y un residuo de arginina, con carga positiva, de la subunidad a (Modificado de Yoshida *et al.*, 2001).

Las subunidades γ , δ , ϵ y c están involucradas en el movimiento del rotor de la enzima durante la catálisis, mientras que el estator lo forman las subunidades del tallo periférico (Tabla 1), las cuales se mantienen estáticas durante la síntesis de ATP y a su vez mantienen fijas a las subunidades catalíticas α y β (Weber *et al.*, 2003).

Para la síntesis de ATP, el sector F_1 (heterohexámero α/β) es donde se lleva a cabo la catálisis alternando cambios estructurales (Cabezón *et al.*, 2003; Glendhill *et al.*, 2005). Mediante cristalografía de rayos X se resolvió que el sitio activo de la enzima se encontraba principalmente en la subunidad β en cada uno de los sitios (uno en cada β) y que estos muestran cooperatividad. Esto significa que uno de estos sitios está en la conformación β_3 ó sitio T (cerrado que une al ATP fuertemente) y es considerado el sitio catalítico activo, un segundo está en la conformación β_1 o sitio L (relajado y con el ADP y Pi unidos) y un tercero está en la conformación β_2 o sitio O (abierto-vacío de unión muy débil por el ATP, pero afín por el ADP y Pi) (Abrahams *et al.*, 1994; Orriss *et al.*, 1998).

La fuerza protón-motriz hace que el eje central rote (subunidad γ), el cual se pone en contacto con cada par de subunidades α/β de forma sucesiva. Esto produce un cambio conformacional cooperativo en el que el sitio β_3 se convierte en la conformación β_2 y el ATP se disocia; simultáneamente el sitio β_1 se convierte en la conformación β_3 , que promueve la condensación del ADP-Pi unidos para formar ATP; y el sitio β_2 se convierte en un sitio β_1 , donde se lleva a cabo la unión del ADP y Pi. Por lo que el $\Delta\mu_{H^+}$ sirve para el giro de la enzima (cambio conformacional) pero no para la unión del Pi al ADP.

La estequiometría H^+/ATP puede variar dependiendo del número de subunidades c que forman el semicanal de protones en la membrana, aquí se muestra la estequiometría $3H^+/ATP$ para la F_1F_0 -ATP sintasa de corazón de bovino (9 subunidades c). La flecha central indica la rotación de la subunidad γ impulsada por el $\Delta\mu_{H^+}$ (Figura 5) (Walker, 1998). Este mecanismo que describe la síntesis de ATP también puede ocurrir en sentido contrario durante la hidrólisis del ATP (Adachi *et al.*, 2007).

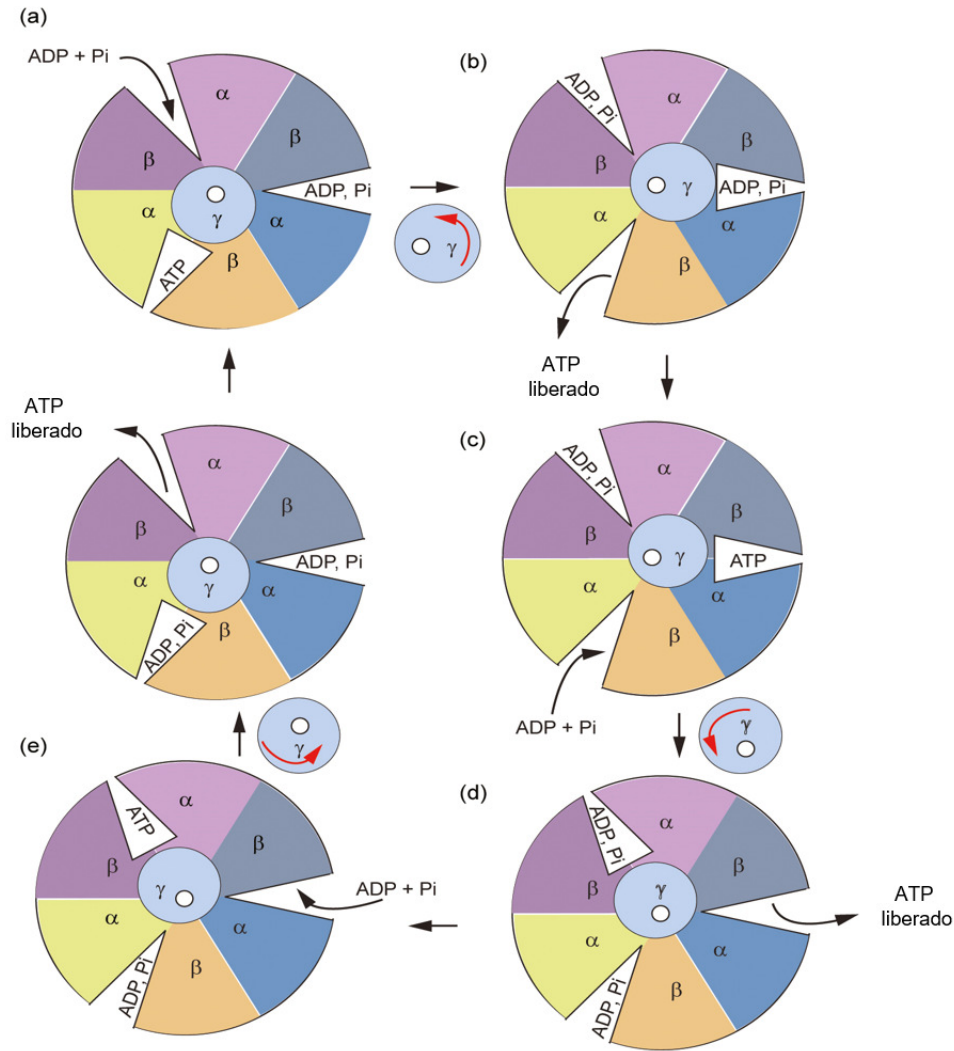


Figura 5. Mecanismo de los sitios catalíticos de la porción F₁ de la ATP sintasa durante la síntesis de ATP. Las tres subunidades catalíticas β adquieren diferentes estados conformacionales durante la síntesis de ATP: Abierta (O), semiabierta (L) y cerrada (T). Este ciclo se repite alternadamente en cada una de las subunidades β que componen el dominio catalítico de la enzima (Modificado de Nicholls *et al.*, 2013)

Utilizando técnicas de criomicroscopía, se obtuvo un mapa tridimensional de las subunidades involucradas en la translocación de protones, en el cual se pudo observar que la subunidad *a* tiene una interacción particular con la membrana y con el anillo de subunidades *c*, ya que presenta un grupo de hélices integrales de membrana, las cuales forman dos horquillas, éstas se acomodan casi de forma paralela a la membrana y parecen abrazar al anillo *c* (Figura 6A) (Allegretti *et al.*, 2015; Guo *et al.*, 2017; Guo *et al.*, 2018).

En el modelo propuesto se observa que la disposición de las subunidades *a* y *c* da lugar a dos semicanales, cuyas cavidades son hidrofílicas y que permiten la entrada y salida de protones, respectivamente (Figura 6B). Los residuos involucrados en la asociación entre las subunidades *a* y *c* están altamente conservados por lo que se considera que el evento ocurre en todas las ATPasas de este tipo (Allegretti *et al.*, 2015; Guo *et al.*, 2018).

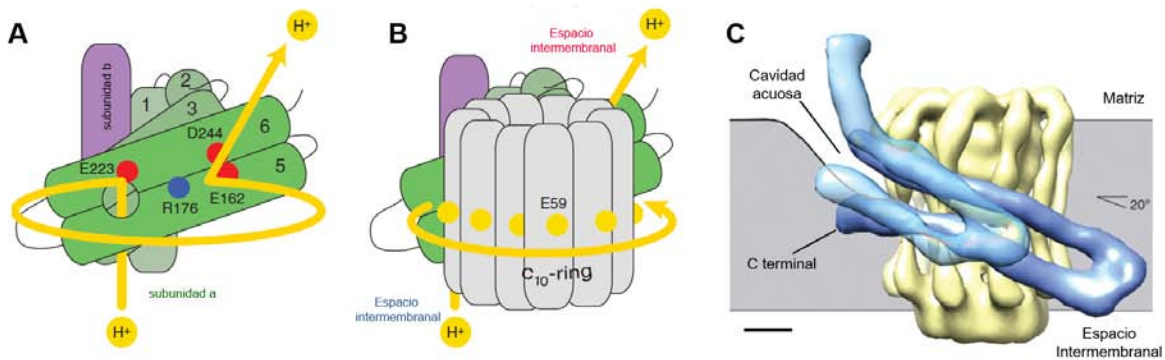


Figura 6. Estructura de la subunidad *a* y la translocación de protones. (A) Durante la translocación de protones estos siguen el camino indicado por la línea amarilla (izquierda), ingresando al semicanal desde el espacio intermembranal por las hélices 5 y 6 de la subunidad *a* y saliendo a través del semicanal de la matriz entre las hélices 5 y 6 del anillo *c* (B). (Modificado de Guo *et al.*, 2017). (C) Mapa tridimensional propuesto para la subunidad *a* de *Polytomella sp.* En este mapa se representa a la subunidad *a* en color azul y el anillo de subunidades *c* en color amarillo (Modificado de Allegretti *et al.*, 2015).

1.3. Las crestas mitocondriales

Las crestas mitocondriales pueden ser estructuras tubulares, lamelares o discoides, las cuales tienen un diámetro de 12 a 40 nm y una longitud de 30 a 50 nm y se conectan con la membrana interna por medio de estructuras tubulares denominadas uniones de cresta. Dichas estructuras limitan el compartimento que corresponde a la cresta con la membrana interna, de esta manera, las uniones de cresta podrían representar barreras para la difusión de moléculas entre el espacio de la cresta y el espacio intermembranal, lo que tendría un impacto en la fosforilación oxidativa (Mannella, 2000; Mannella *et al.*, 2001; Frey *et al.*, 2002; Zick *et al.*, 2009; Mannella *et al.*, 2013).

Es en la membrana de las crestas donde se encuentran integrados los complejos de la fosforilación oxidativa, los cuales son responsables de consumir oxígeno y de generar la energía para la síntesis de ATP a través de la F_1F_0 -ATP sintasa. La distribución de los complejos respiratorios y de la F_1F_0 -ATP sintasa también sugiere la presencia de dos compartimientos delimitados por las uniones de crestas, el interior de la cresta y el espacio intermembranal (Figura 7) (Zick *et al.*, 2009; Cogliati *et al.*, 2016). Así, la membrana interna mitocondrial se encuentra dividida en dos secciones, aquella que forma la crestas, donde se encuentran los componentes de la fosforilación oxidativa así como las proteínas encargadas de la síntesis de los centros hierro-azufre y el resto de la membrana interna, donde se encuentran los translocadores que participan en el transporte de proteínas (Wurm *et al.*, 2006). Al igual que con el retículo mitocondrial, la morfología de las crestas varía de una célula a otra e inclusive dentro de la misma célula; sin embargo, los factores que determinan esta morfología aún están por definirse (Zick *et al.*, 2009; Mannella *et al.*, 2013).

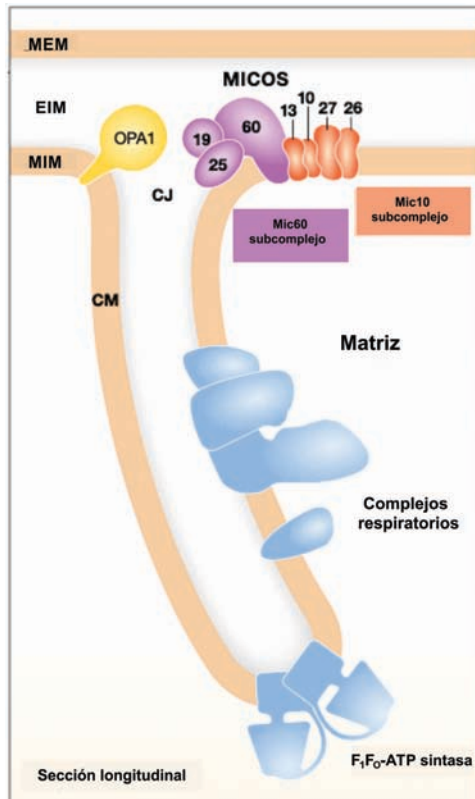


Figura 7. Representación esquemática de la fosforilación oxidativa en una cresta plegada. Los complejos se ensamblan en diferentes supercomplejos de composiciones muy dinámicas a lo largo de la membrana (en las crestas). Los dímeros de la ATP sintasa están organizados en largas filas en el canto de las crestas y el citocromo *c* se mantiene dentro de ellas. Así, la cadena de transporte de electrones funciona eficientemente y el gradiente de protones se forma a través de las membranas de las crestas, para ser aprovechado por la ATP sintasa. El espacio delimitado para la cresta se forma con ayuda del complejo MICOS, la proteína OPA, entre otras. MEM = Membrana Externa Mitocondrial; EIM = Espacio InterMembranal; MIM = Membrana Interna Mitocondrial; CM = Cresta Mitocondrial; CJ = Uniones de cresta (Crista Junction) (Modificado de McArthur *et al.*, 2020).

Diversos modelos explican la formación de las crestas, como el modelo de invaginación y el modelo de globo. El modelo de invaginación propone que, debido a la mayor producción de membrana interna, hay una tendencia a su plegamiento termodinámicamente favorable; una vez que se inicia este plegamiento, se reclutan las proteínas involucradas en la formación de las uniones de cresta (Figura 8A) (Zick *et al.*, 2009; Song *et al.*, 2014; Milenkovic *et al.*, 2015). En el modelo del globo, hay un agrupamiento inicial de los componentes proteicos de las uniones de cresta (CJ) y a partir de éstos se inicia la formación de la cresta (Figura 8B) (Legros *et al.*, 2002).

Asimismo, la topología de las crestas cambia con el estado energético de la mitocondria. En el estado III de la respiración mitocondrial (Chance *et al.*, 1956), cuando la concentración de ADP es alta y la mitocondria entra en el modo de

síntesis de ATP, este organelo adopta una conformación o estado condensado, con un espacio muy grande entre las crestas (Mannella, 2006). Por otro lado, cuando la concentración de ADP baja (estado IV de la respiración), la mitocondria cambia al estado ortodoxo, en el cual el volumen entre las crestas disminuye (Mannella, 2006). Esta transición entre el estado ortodoxo y condensado se relaciona con un balance dinámico entre la fusión y la fisión de las crestas.

Distintas proteínas “esenciales” generan las crestas, tales como las prohibitinas (PHB1 y PHB2), la proteína OPA1 (Optic atrophy 1), la proteína formadora de la unión de cresta (Fcj1), el complejo MICOS, entre otros componentes que aún no están del todo identificados. Aunado a esto, se reconoce al dímero de la F_1F_0 -ATP sintasa como la principal entidad responsable de la formación de los bordes y las puntas de las crestas (Figura 7) (Zick *et al.*, 2009; Song *et al.*, 2014; Milenkovic *et al.*, 2015).

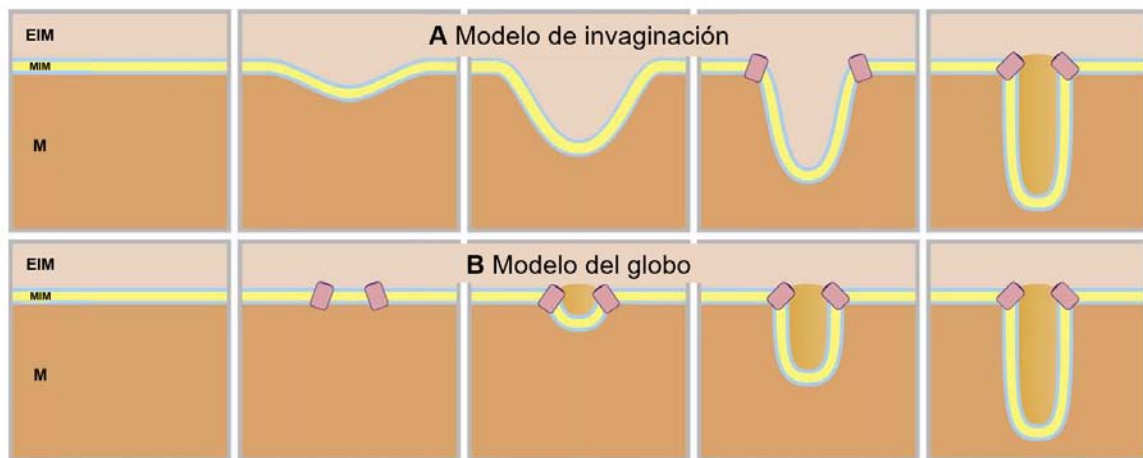


Figura 8. Mecanismos propuestos para la formación de las crestas. A) El modelo de invaginación supone el inicio de la cresta previo a la incorporación de los elementos proteicos de las uniones de cresta (CJ); en contraste, en el modelo del globo **(B)** el reclutamiento de los elementos proteicos de la CJ es previo a la formación de la cresta. M = Matriz mitocondrial EIM = Espacio InterMembranal; MIM = Membrana Interna Mitocondrial (Modificado de Zick *et al.*, 2009).

1.4. La F_1F_0 -ATP sintasa como d\u00edmero y su papel en el plegamiento de las crestas mitocondriales

La F_1F_0 -ATP sintasa no s\u00f3lo tiene la funci\u00f3n bioenerg\u00e9tica de producir ATP, sino que tambi\u00e9n puede desempe\u00f1ar un papel morfo-funcional dentro de la arquitectura mitocondrial. En este sentido, se ha reportado que la F_1F_0 -ATP sintasa puede formar homo-olig\u00f3meros (Zick *et al.*, 2009), siendo los estados monom\u00e9ricos y dim\u00e9ricos los m\u00e1s estudiados. Se ha sugerido que los d\u00edmeros se asocian formando largas filas, las cuales forzan a la membrana a asumir una curvatura positiva, conservando as\u00ed la morfolog\u00eda de las crestas mitocondriales (Strauss *et al.*, 2008).

La manera por la cual se ha estudiado a los olig\u00f3meros de la F_1F_0 -ATP sintasa es solubiliz\u00e1ndolos con un detergente suave como la digitonina y separ\u00e1ndolos por medio de electroforesis en condiciones nativas en presencia de azul brillante de Coomassie\u2122 G250 (BN-PAGE) o de *n*-dodecil β -D-malt\u00f3sido (DDM) y desoxicolato de sodio (DOC) (hrCN-PAGE). La ubicaci\u00f3n del complejo V en el gel se determina por medio de una tinci\u00f3n que revela la actividad de ATPasa (Figura 9) (Sch\u00e4gger *et al.*, 1991; Wittig *et al.*, 2006).

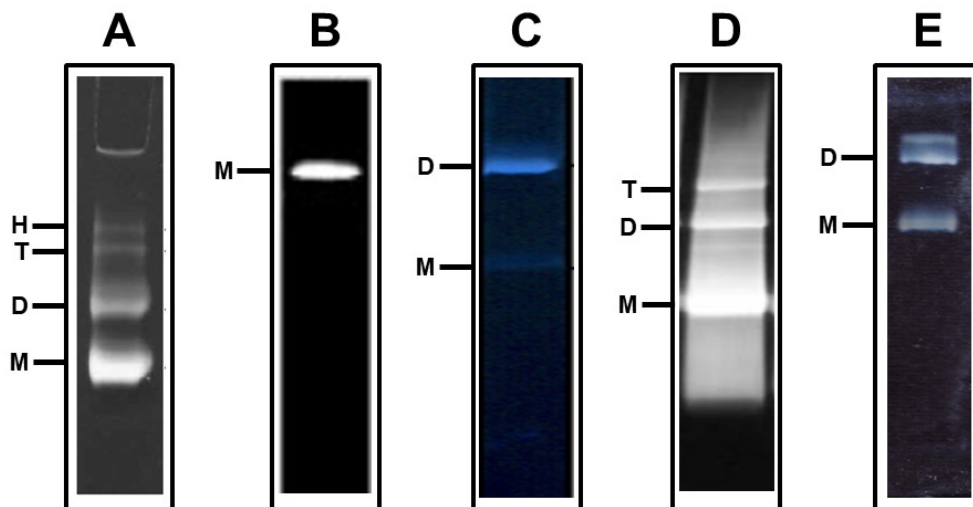


Figura 9. Actividad de ATPasa en gel de los olig\u00f3meros de la F_1F_0 -ATP sintasa. Mitocondrias solubilizadas con digitonina donde se muestra la formaci\u00f3n de distintos olig\u00f3meros de la F_1F_0 -ATP sintasa en **A)** Coraz\u00f3n de Bovino (Modificado de Strauss *et al.*, 2008), **B)** *Chlamydomonas reinhardtii* (Modificado de van Lis *et al.*, 2003), **C)** *Yarrowia lipolytica* (Modificado de Wittig *et al.*, 2008), **D)** *Saccharomyces cerevisiae* (Modificado de Guerrero-Castillo *et al.*, 2012), **E)** *Ustilago maydis* (Modificado de Esparza-Perusqu\u00eda *et al.*, 2017). La figura muestra la actividad de ATPasa de los Hex\u00e1meros (H), Tetr\u00e1meros (T), D\u00edmeros (D) y Mon\u00f3meros (M) que fueron resueltos en gels nativos azules (C) o claros (A, B, D y E).

Aunque aún se desconoce el papel bioenergético de los diferentes estados oligoméricos de la F_1F_0 -ATP sintasa, se ha demostrado que el dímero tiene un papel importante en la arquitectura de las crestas de la membrana interna mitocondrial (Arnold *et al.*, 1998).

Debido a la asociación angular de dos monómeros, la dimerización conduce a la flexión de la membrana interna mitocondrial, es decir, al plegamiento de las crestas mitocondriales. La presencia de la F_1F_0 -ATP sintasa dimérica en el vértice de las crestas crea una fuerte curvatura positiva que genera una trampa de protones; esto es, la curvatura de la membrana permite que incremente el número de H^+ translocados por unidad de área de la MIM, lo que produce el aumento de la $[H^+]$ local y por consiguiente una mayor densidad de cargas positivas (Figura 10). En consecuencia, la contribución de la fuerza protón-motriz aumenta en las regiones curvadas (punta y borde de la cresta); suponiendo que la fuerza protón-motriz a lo largo de la membrana interna es constante, todos los protones en las crestas mitocondriales tendrían el mismo potencial químico, pero la contribución del ΔpH a la fuerza protón-motriz será más grande para los protones que se encuentran en el ápice y el borde, ya que al plegarse la membrana interna el espacio donde se encuentran almacenados los protones se reduce, lo que incrementa la concentración local de los protones que se traduce en una mayor disponibilidad de energía para la síntesis de ATP (Strauss *et al.*, 2008, Rabl *et al.*, 2009).

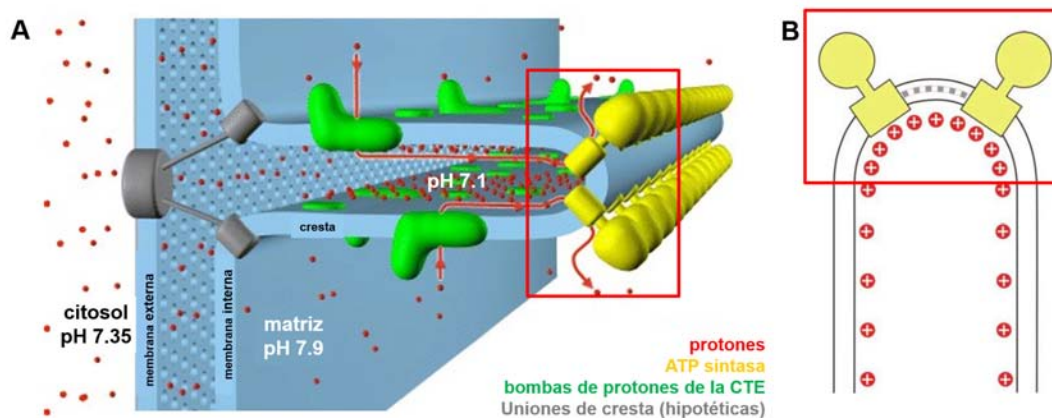


Figura 10. Densidad de protones al interior de la cresta. El esquema representa la densidad de protones dentro de la cresta, (A) la presencia del dímero de la F_1F_0 -ATP sintasa crea una fuerte curvatura positiva que genera una trampa de protones; lo que produce el aumento aparente de la $[H^+]$ dentro de la cresta y por consiguiente una mayor densidad de cargas positivas (B) (Modificado de Strauss *et al.*, 2008, Rabl *et al.*, 2009).

Aunque la estructura de la F_1F_0 -ATP sintasa es altamente conservada y el plegamiento de las crestas es fundamental para la bioenergética mitocondrial, se ha demostrado que las proteínas involucradas en la interacción monómero-monómero y en la estabilidad del dímero son diferentes en cada sistema biológico.

A continuación, se describe la composición proteica del dímero del complejo V en diferentes reinos biológicos.

El dímero de la F_1F_0 -ATP sintasa en las algas clorofíceas.

Chlamydomonas reinhardtii y *Polytomella* sp son algas clorofíceas o algas verdes. El análisis de la composición peptídica de la F_1F_0 -ATP sintasa en estas especies mostró ocho péptidos canónicos: α , β , γ , ϵ , δ , OSCP, a (ATP6) y c (ATP9), las subunidades en paréntesis corresponden a las subunidades en mamífero, pero no se encontraron homólogos para las subunidades b, d, e, f, g, IF_1 , A6L, y F6, que se han reportado como parte del estator de la enzima en el resto de los eucariontes. Tampoco se encontraron aquellas involucradas en la dimerización del complejo; sin embargo se identificaron 10 subunidades que conforman al brazo periférico y alguna de ellas posiblemente son responsables de la dimerización (ASA10). Todas estas subunidades son diferentes a otras proteínas, y han sido denominadas subunidades ASA (del inglés “ATP Synthase-Associated protein”) (Figura 11) (Funes *et al.*, 2002; Cardol *et al.*, 2005; Vázquez-Acevedo *et al.*, 2006; van Lis *et al.*, 2007, Colina-Tenorio *et al.*, 2018).

Las F_1F_0 -ATP sintasas de las algas clorofíceas (Figura 11A) tienen un tallo periférico muy robusto formado principalmente por las subunidades ASA, donde éstas tienen diferentes interacciones; esto se ha comprobado mediante experimentos llevados a cabo con subunidades recombinantes. De esta forma se encontró que las subunidades ASA4 y ASA7 interactúan por medio de sus extremos carboxilos y su vez interactúan con ASA2 (Miranda-Astudillo *et al.*, 2014). Por otro lado, se ha reportado que ASA6, ASA8 y ASA9 pueden tener cruces

transmembranales y podrían estar encargadas de la dimerización (Sánchez-Vázquez *et al.*, 2017).

Existen interacciones típicas de una ATP sintasa mitocondrial como OSCP con γ y δ las cuales se asocian extrínsecamente con ASA2, ASA4 y ASA 7 (Cano-Estrada *et al.*, 2010). Colina-Tenorio *et al.*, (2016) demostró que la subunidad ASA1 es la subunidad del tallo periférico más grande uniéndose desde la subunidad OSCP hasta ASA3, que a su vez mantiene interacción con las subunidades ASA2, ASA7 y ASA8.

A pesar de que las subunidades catalíticas presentan alta similitud con el resto de las ATP sintasas, éstas presentan diferentes extensiones en la secuencia de aminoácidos; por ejemplo, la subunidad α cuenta con aproximadamente 20 aminoácidos en el extremo N-terminal y la subunidad β contiene 60 aminoácidos extras en el extremo C-terminal. Aunque aún no es clara la función de esta última extensión, se ha propuesto que podría desempeñar un papel regulador de la actividad del complejo, ya que aún no se ha identificado el homólogo de la proteína inhibidora IF_1 (Villavicencio-Queijeiro *et al.*, 2009).

El dímero de la ATP sintasa de estas especies pesa aproximadamente 1600 kDa y es altamente estable (van Lis *et al.*, 2003; Cano-Estrada *et al.*, 2010), siendo las subunidades Asa2/Asa4/Asa5/Asa8 las que estabilizan la unión entre los sectores F_0 y F_1 (Villavicencio-Queijeiro *et al.*, 2015). Cuando el dímero se disocia en sus respectivos monómeros, se ha observado una disminución en la proporción de las subunidades ASA6, ASA8 y ASA9, que probablemente están involucradas en la dimerización (van Lis *et al.*, 2007).

Todas estas nuevas subunidades están involucradas en la formación del estator de la enzima, aunque todavía no es clara la función de cada una de ellas dentro del complejo enzimático. Se ha sugerido que podrían ser esenciales para el

buen ensamble del complejo, estabilizando una forma dimérica necesaria para mantener la morfología de las crestas mitocondriales (van Lis *et al.*, 2007).

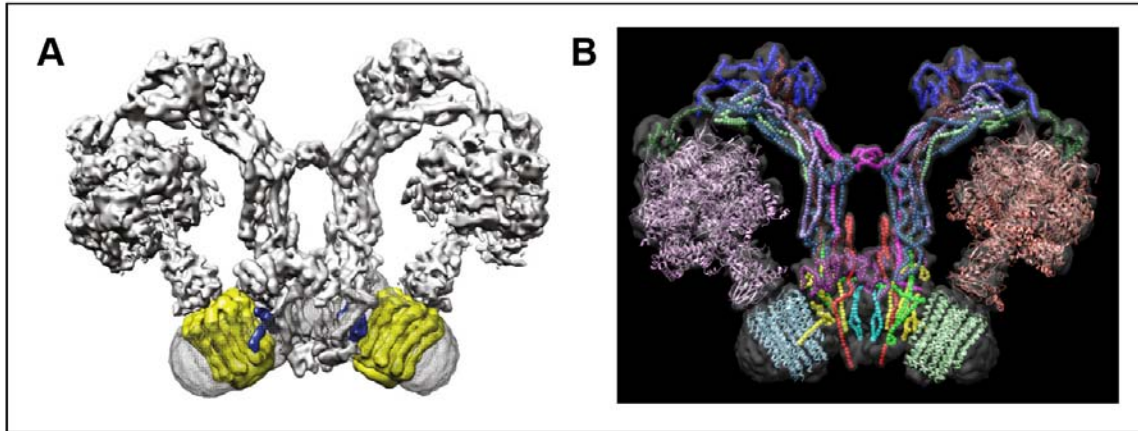


Figura 11. Estructura del dímero de la F_1F_0 -ATP sintasa de *Polytomella sp.* Las proteínas involucradas en la asociación entre los monómeros son altamente conservadas en las algas clorofíceas, éstas cuentan con nueve subunidades ASA, las cuales sustituyen a las subunidades clásicas que forman el estator de la enzima. **(A)** Estructura tridimensional generada a partir de criomicroscopía electrónica (Modificado de Kühlbrandt *et al.*, 2016; Allegretti *et al.*, 2015). **(B)** Mapa de densidad electrónica de la F_1F_0 -ATP sintasa dimérica de *Polytomella sp.* El mapa de densidad electrónica corresponde al generado por Allegretti *et al.*, 2015 (EMD-2852) (Colina-Tenorio *et al.*, 2018).

El dímero de la F_1F_0 -ATP sintasa en los mamíferos.

La F_1F_0 -ATP sintasa del corazón de bovino presenta las subunidades catalíticas homólogas a *E. coli*, así como las subunidades que conforman el rotor de la enzima, el cual está compuesto por las subunidades *b*, *d*, *F₆*, *OSCP* y como proteína reguladora a la proteína inhibidora *IF₁*. Además, cuenta con las subunidades supernumerarias membranales *e*, *g*, *A6L* y *f*. Se ha reportado que las subunidades *a* y *A6L* (ATP8) también tienen un papel importante dentro de la estabilización del homo-dímero (Wittig *et al.*, 2010).

Se ha reportado que la subunidad *IF₁* promueve la dimerización de la F_1F_0 -ATP sintasa (Cabezón *et al.*, 2000; García *et al.*, 2006; Couoh-Cardel *et al.*, 2010; De los Rios-Castillo *et al.*, 2011). Experimentos de entrecruzamiento demostraron que la *IF₁* interactúa con el dominio C-terminal de una subunidad β . Durante años, esto ha hecho suponer que el mecanismo de inhibición de la *IF₁* es el de interferir con los cambios conformacionales de las interfases catalíticas necesarios para la síntesis y la hidrólisis de ATP (Minauro-Sanmiguel *et al.*, 2002). Se ha logrado

resolver la estructura de la proteína inhibidora aislada, la cual resultó ser una larga α hélice extendida con un dominio inhibitorio localizado en la región N-terminal. En el extremo C-terminal la IF_1 contiene un dominio de dimerización con la cual se auto-asocia, y que podría inducir la dimerización de la F_1 -ATPasa soluble (Cabezón *et al.*, 2000; Cabezón *et al.*, 2003). Aunque la presencia de la IF_1 no es esencial para la dimerización (Tomasetig *et al.*, 2002), podría inducir la formación de un puente dimérico que conecta las dos F_1 solubles (Cabezón *et al.*, 2000; Cabezón *et al.*, 2003). Por otra parte, la sobreexpresión y/o reconstitución de la IF_1 modifica la relación monómero/dímero a favor de los complejos diméricos. Lo anterior sugiere que la IF_1 podría cumplir un papel estabilizador en las mitocondrias de corazón de bovino mediante la formación de un puente $\leq 12\text{\AA}$ que la conecta con las subunidades γ del rotor central de la F_1 (Minauro-Sanmiguel *et al.*, 2002; Bravo *et al.*, 2004).

Mediante microscopía electrónica, Minauro-Sanmiguel *et al.*, (2005) resolvieron la estructura de la F_1F_0 -ATP sintasa dimérica aislada de las mitocondrias de corazón de bovino y encontró que la interfase del dímero está formada por el contacto tanto entre los dominios F_1 como entre los dominios F_0 , que además pueden conectarse a través de la proteína IF_1 . Por otro lado, se encontró que el dímero de bovino presenta dos puentes: uno que une a los sectores F_1 y otro a los sectores F_0 ; se propuso que éstos corresponden a la dimerización de la IF_1 y la subunidad e , respectivamente (Minauro-Sanmiguel *et al.*, 2005). Dado que la proteína inhibidora promueve y estabiliza a la estructura dimérica de la F_1F_0 -ATP sintasa en corazón de bovino y en el hígado de rata, se sugiere que la IF_1 forma una estructura cruzada en la interfase del dímero que explica tanto su papel inhibitorio como su participación en la dimerización (García *et al.*, 2006).

Otros estudios han demostrado que al eliminar la subunidad IF_1 se pierden los dímeros y simultáneamente la arquitectura mitocondrial se ve afectada, particularmente en la formación de crestas (Campanella *et al.*, 2008). Lo anterior apoya la hipótesis de la IF_1 como proteína dimerizante (Campanella *et al.*, 2008).

Recientemente Gu *et al.*, (2019) aislaron la ATP sintasa tetramérica porcina (*Sus scrofa domestica*) y resolvieron su estructura a 6.2 Å (Figura 12A) utilizando un método de criomicroscopía crioelectrónica (Cryo-EM). Demostraron que dos dímeros de la F_1F_0 -ATP sintasa se encuentran antiparalelos entre sí para formar un tetrámero unido por un dímero de IF_1 .

Los dos dímeros están unidos entre sí a través de seis sitios (Figura 12B). Para los sitios de unión 1 y 6, dos proteínas IF_1 forman un dímero antiparalelo que interactúa con los sectores F_1 dentro de la matriz mitocondrial (Figura 12B). Los sitios 2 y 4 están por encima de la membrana, incluyen el bucle N-terminal de la subunidad k y la hélice N-terminal de la subunidad b de dos dímeros adyacentes. El sitio 3 incluye dos hélices N-terminales de subunidades g de dímeros opuestos dentro del tetrámero, colocadas en paralelo en el centro de la estructura (Figura 12B). El sitio 5 está dentro de la membrana interna, donde dos subunidades e que interactúan entre sí, mantienen al tetrámero unido (Figura 12C).

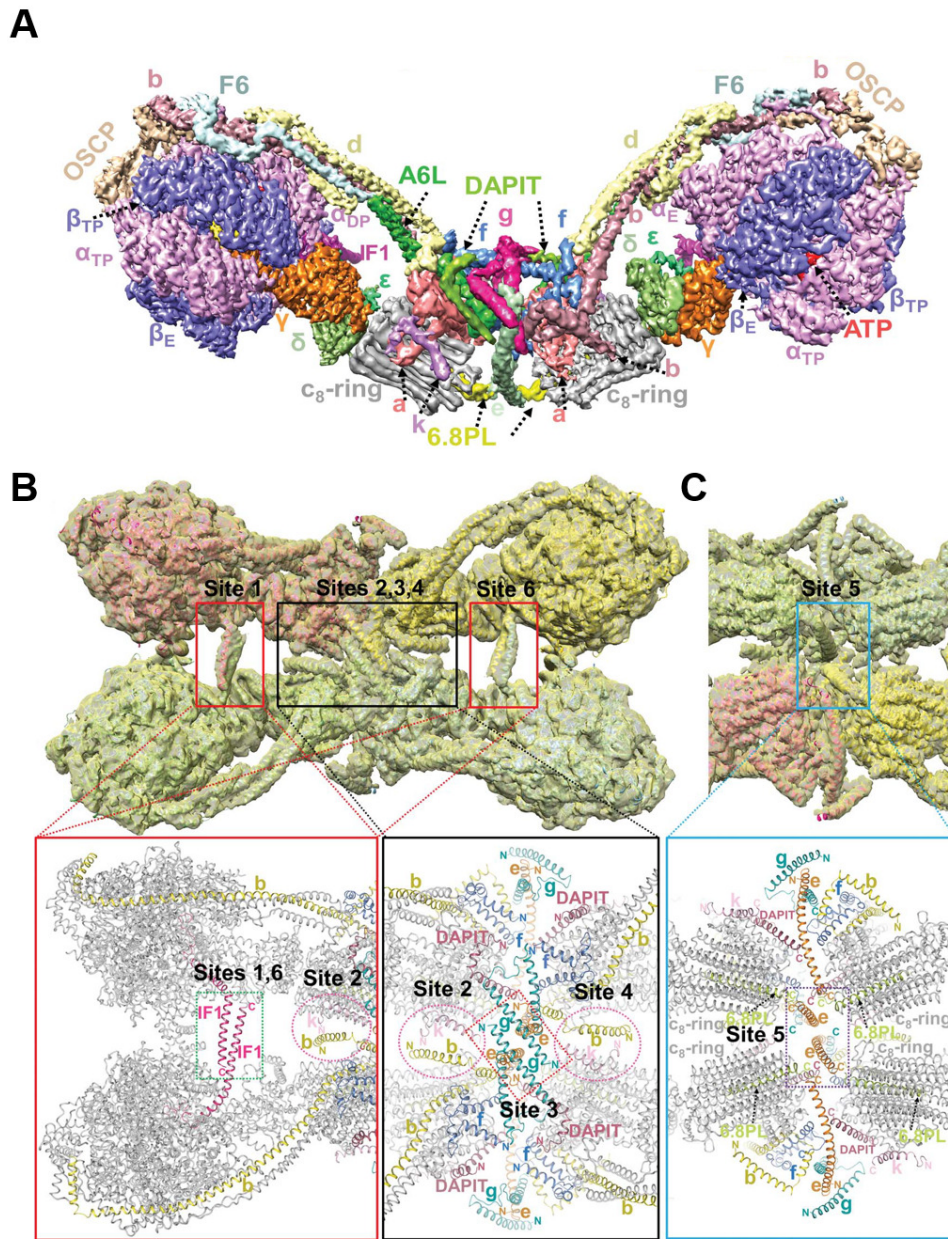


Figura 12. Dímero de la F_1F_0 -ATP sintasa porcina y sus sitios de unión. (A) Modelo cristalográfico del dímero de la F_1F_0 -ATP sintasa obtenido a 6.2 Å. (B) Sitios de interacción de los tetrameros vistos desde el lado de la matriz. Los modelos de alta resolución se ajustaron a los mapas de tetramero con un coeficiente de correlación de 0.85. (C) Vista desde el espacio intermembranal (Modificado de Gu *et al.*, 2019).

El dímero de la F_1F_0 -ATP sintasa en un tejido humano.

Adicionalmente, se ha demostrado que la expresión de la IF_1 y su repercusión en la dimerización del complejo V está asociada a procesos de diferenciación celular; por ejemplo, la transformación del citotrofoblasto en sincitiotrofoblasto y la adquisición del fenotipo esteroideogénico (Figura 13) (De los Rios-Castillo *et al.*, 2011). Las microfografías electrónicas de las vellosidades de la placenta humana a

término, muestran que la arquitectura mitocondrial del citotrofoblasto obedece a la estructura tradicional, tienen forma redondeada y presenta crestas lamelares en una configuración ortodoxa (Figura 13B) y que el dímero del complejo V se encuentra en alta concentración (Figura 13C). Por otra parte, el sinciciotrofoblasto contiene mitocondrias pequeñas de forma irregular con protuberancias de la membrana interna y externa, con una matriz condensada (Figura 13B) y las crestas en forma de vesículas, debido a que la F_1F_0 -ATP sintasa se encuentra principalmente como monómero (Figura 13C) (De los Ríos-Castillo *et al.*, 2011). Se determinó que la cantidad de la IF_1 es mayor en las mitocondrias de citotrofoblasto, lo que está directamente relacionado con la formación del dímero y la arquitectura mitocondrial observada.

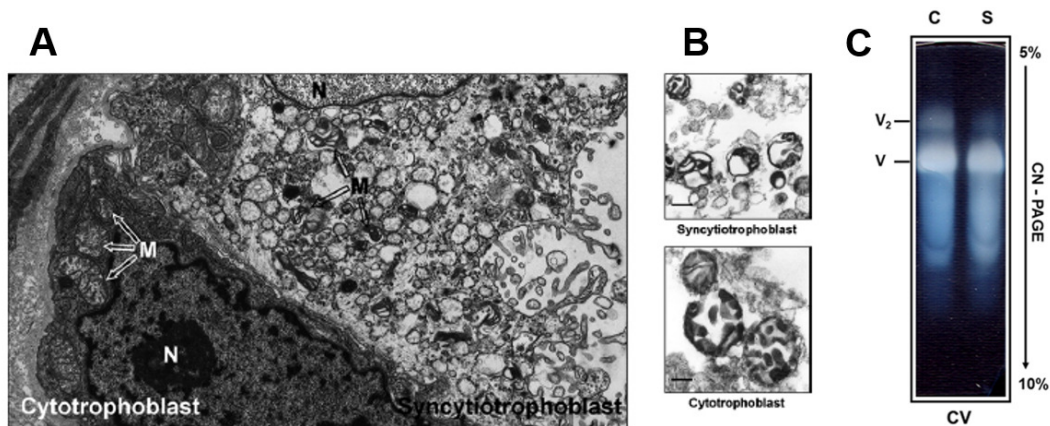


Figura 13. Ultraestructura mitocondrial de las células de placenta humana. Las micrografías muestran que la arquitectura de las mitocondrias es diferente aun tratándose del mismo tejido. **(A)** Corte de la placenta humana donde se muestra el cito y el sinciciotrofoblasto, las flechas hacen referencia las mitocondrias. **(B)** Mitocondrias aisladas del cito y del sinciciotrofoblasto. **(C)** La actividad de ATPasa de los complejos solubilizados de los dos tipos mitocondriales, donde se muestra que el dímero solo está presente en las mitocondrias del citotrofoblasto (Modificado de De los Ríos-Castillo *et al.*, 2011).

De los Ríos-Castillo *et al.*, (2011) reportó que los valores de control respiratorio se encuentran entre 2.85 y 12 natgO/mg/min, y la síntesis de ATP por la F_1F_0 -ATP sintasa fue de 151 ± 16 y 153 ± 13 nmol/mg/min para las mitocondrias del citotrofoblasto y sinciciotrofoblasto respectivamente, lo que demuestra un acoplamiento entre la respiración mitocondrial y la síntesis de ATP. Esto indica que las mitocondrias esteroideogénicas y no esteroideogénicas de la placenta humana son capaces de sintetizar ATP aún sin mostrar la misma arquitectura de sus crestas.

Esto sugiere que aunque el dímero tiene un papel estructural importante, el monómero puede cubrir el papel bioenergético (De los Ríos-Castillo *et al.*, 2011).

El dímero de la F₁F₀-ATP sintasa en las levaduras.

La F₁F₀-ATP sintasa de las levaduras presentan algunas subunidades conservadas entre bacterias, algas y mamíferos y también pueden adoptar estructuras supramoleculares. A diferencia de los dímeros de mamífero, el dominio de interacción entre los monómeros de *S. cerevisiae* es el sector F₀.

Se ha establecido que las subunidades *e*, *g* y *k* están asociadas únicamente al dímero de la F₁F₀-ATP sintasa de *S. cerevisiae* y no a su forma monomérica (Arnold *et al.*, 1998). También se ha sugerido que la subunidad *a* tiene un papel importante formando parte de la base para la dimerización ya que se le ha predicho un alto número de hélices transmembranales (Wittig *et al.*, 2008). Junto con la subunidad *a*, las subunidades del tallo estator y subunidades accesorias (*e*, *g*, *b*, *i*, *k* y *δ*) estabilizan la interfaz del homo-dímero (Figuras 14A) (Wittig *et al.*, 2008; Wittig *et al.*, 2010, Couch-Cardel *et al.*, 2010).

Se ha demostrado que una alteración en los componentes arriba descritos desestabiliza las estructuras oligoméricas, lo que conduce a la aparición de especies monoméricas y morfologías anómalas en las crestas mitocondriales, que se describen como aros de cebolla (Velours *et al.*, 2009). Sin embargo, en las mutantes de las subunidades *e*, *g* y *k* no se eliminan del todo las crestas mitocondriales, pero hacen sensible al dímero, lo cual sugiere que no son esenciales para la dimerización, pero sí para su estabilidad (Figura 14B). En contraste, se ha podido demostrar que la subunidad Inh1 (proteína inhibidora de la F₁F₀-ATP sintasa de levadura) no es necesaria para la oligomerización (Arnold *et al.*, 1998; Dienhart *et al.*, 2002; Wittig *et al.*, 2008; Wagner *et al.*, 2010).

Por su parte, la subunidad *g* tiene dos α hélices en el extremo N-terminal que se encuentran expuestas en la superficie del sector F_0 y una única α hélice transmembrana que interactúa con la subunidad *e*, probablemente a través de los motivos conservados Gly-XXX-Gly de las dos proteínas (Figura 14C) (Bustos *et al.*, 2005; Saddar *et al.*, 2005). La estructura curva del dominio formado por las subunidades *e*, *g* y *b* sugiere cómo las subunidades *e* y *g*, con el apoyo adicional de la subunidad *k*, crean una estructura que refuerza la curvatura de la bicapa lipídica (Figura 14D) (Guo *et al.*, 2017) y porqué la supresión de los genes que codifican a estas subunidades en la levadura conduce a defectos en la formación de crestas (Paumard *et al.*, 2002).

Como se puede observar, cada reino biológico ha desarrollado una estrategia diferente para formar y/o estabilizar los dímeros del complejo V y plegar así la membrana interna mitocondrial en crestas, lo que podría ser un evento de convergencia evolutiva. Por lo tanto, es importante ampliar el conocimiento sobre la composición del dímero de la F_1F_0 -ATP sintasa en otros organismos y determinar cuáles son sus subunidades dimerizantes.

Por otro lado, mediante el empleo de la microscopía de fuerza atómica se ha analizado la formación de los oligómeros de la F_1F_0 -ATP sintasa de *S. cerevisiae* desde la membrana interna-cresta, lo cual permitió detallar la posición espacial de los canales de protones y de 3 densidades circulares que corresponden a los dominios transmembranales de las otras subunidades que conforman los segundos dominios de los sectores F_0 . Así mismo, se describió la existencia de dos tipos de dímeros cuyos puntos más distantes de los anillos de sub *c* miden 15 y 10 nm; con esto se propuso que el dímero con una mayor distancia corresponde a un estado activo que sintetiza ATP y que es capaz de unirse a otros dímeros para oligomerizarse, mientras que el dímero más cerrado se forma durante la inhibición de la hidrólisis de ATP y es incapaz de oligomerizarse (Buzhynskyy *et al.*, 2007).

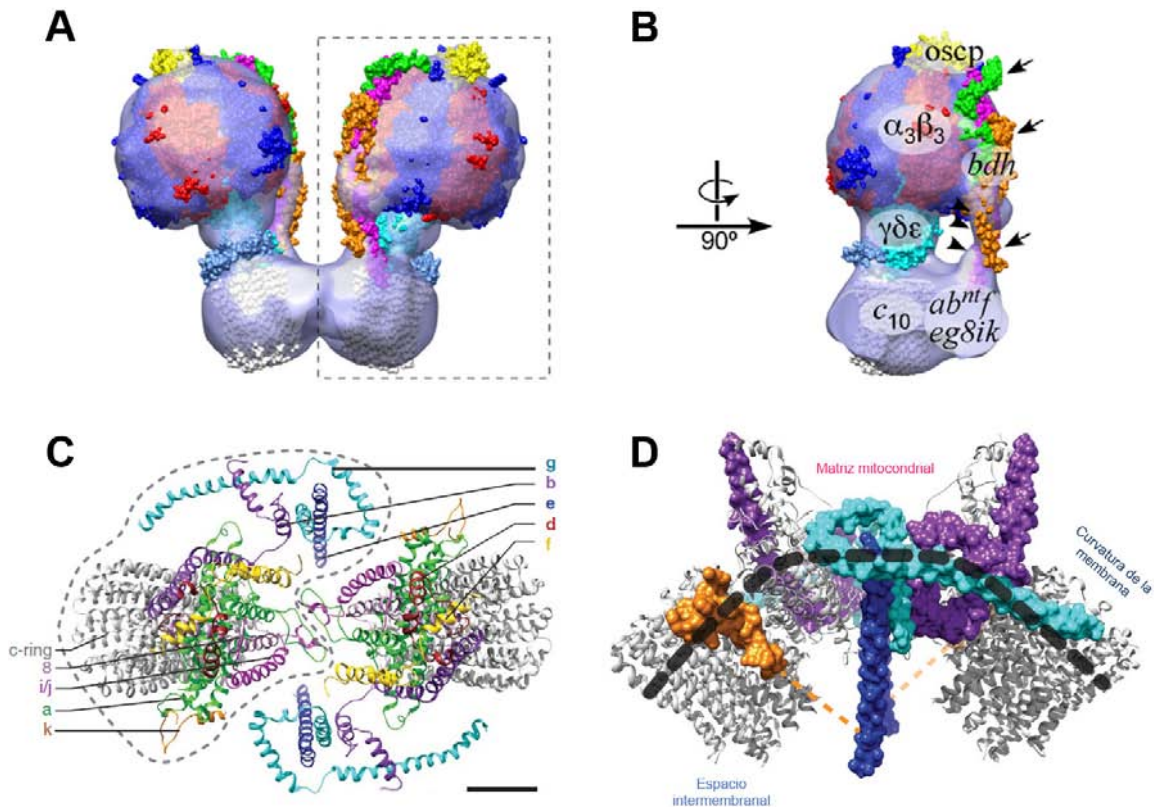


Figura 14. Estructura de la F₁F₀-ATP sintasa mitocondrial de *S. cerevisiae* a 25 Å de resolución. (A) Reconstrucción tridimensional de la F₁F₀-ATP sintasa dimérica por microscopía electrónica, donde se muestra la disposición de las subunidades propuesta según su densidad electrónica (Modificado de Couoh-Cardel *et al.*, 2010). **(B)** Identificación de las subunidades que componen al monómero (Modificado de Couoh-Cardel *et al.*, 2010). **(C)** Vista superior del dímero F₀, que revela la disposición de las subunidades e, g y b. El monómero se perfila con una línea punteada. Resolución a una escala de 25 Å (Modificado de Guo *et al.*, 2017). **(D)** Vista lateral del dímero F₀ muestran que las subunidades b, e, g y k crean la estructura que dobla la bicapa lipídica casi 90°. La línea naranja discontinua indica la longitud completa de la subunidad k. Resolución a una escala de 25Å (Modificado de Guo *et al.*, 2017).

Papel del dímero en las crestas.

En la actualidad, se cuenta con la primera reconstrucción tomográfica de una cresta tubular mitocondrial de hígado de rata con un diámetro de 34 nm, a partir de la cual se ha determinado que el dímero de la F₁F₀-ATP sintasa tiene un ángulo de 70°, con una distancia entre F₁ - F₁ de 28 nm y entre los centros F₀-F₀ de 13 nm (Figura 15) (Strauss *et al.*, 2008). En corazón de bovino el ángulo oscila entre 55° y 95°, aunque la microscopía electrónica permitió definir un ángulo de 40° entre los cuellos centrales de los monómeros (Minauro-Sanmiguel *et al.*, 2005; Strauss *et al.*, 2008). En *S. cerevisiae*, se observaron dos familias de ángulos, una de 35° y otra de 90°; y en *Polytomella sp*, la formación dimérica tiene un ángulo de 70°. Estudios recientes han definido la existencia de al menos 6 tipos diméricos en *S. cerevisiae* (Figura 16) (Thomas *et al.*, 2008).

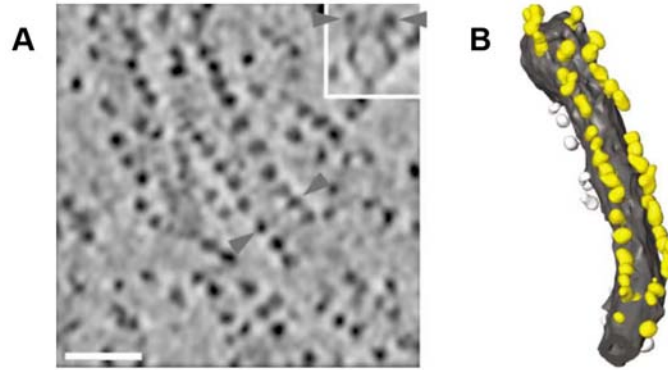


Figura 15. Reconstrucción tomográfica de una cresta tubular mitocondrial de hígado de rata. (A) Tomografía de membranas mitocondriales de hígado de rata. Las flechas grises indican los mismos pares de cabezas de F_1F_0 -ATP sintasas ordenadas linealmente. Barra de escala en panel A, 50 nm. (B) Reconstrucción tridimensional de una cresta tubular. Las cabezas de F_1 son amarillas, mientras que la membrana es gris. Las partículas no asignadas a las cintas de dímero se muestran en gris más claro. La longitud del tubo en el panel B es de 280 nm, y el diámetro de las vesículas es 51 nm (Modificado de Strauss *et al.*, 2008).

Se ha sugerido que los diferentes ángulos dependen de la forma en la que el detergente solubiliza a los oligómeros, los cuales se definen como dímeros verdaderos (estructuras abiertas) y pseudo-dímeros (estructuras cerradas). Los cuellos periféricos de éstos últimos no son observables debido a que, probablemente, se localizan detrás de los cuellos centrales mientras que en el dímero verdadero son visibles en una vista lateral (Dudkina *et al.*, 2006).

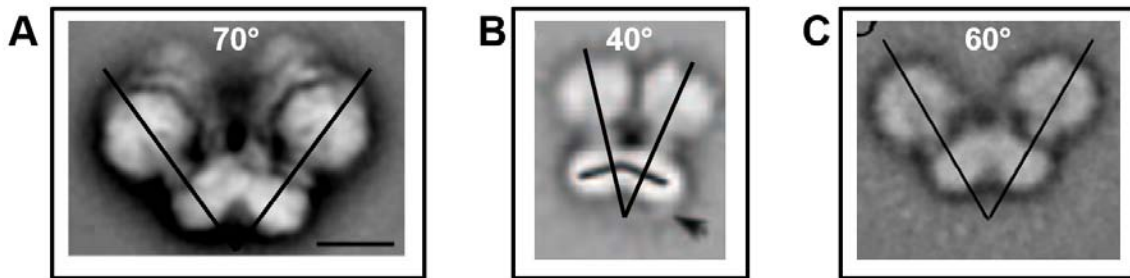


Figura 16. Dímeros aislados observados por microscopía de trasmisión electrónica. Los dímeros de diferentes especies han sido aislados a través de gradientes de glicerol o sacarosa. (A) *Polytomella sp.* presentó un dímero con una amplitud de 70° (Modificado de Dudkina *et al.*, 2006). (B) *Bos Taurus* tiene una amplitud de 40° , se propone que el puente generado por las F_0 's (flecha negra) es debido a la dimerización de la subunidad *e* mientras que el formado por las F_1 's, la dimerización de IF_1 (Modificado de Minauro-Sanmiguel *et al.*, 2005). (C) *S. cerevisiae* presenta un ángulo de 60° dado por las interacciones entre las subunidades *e* y *g* (Modificado de Couho-Cardel *et al.*, 2010).

1.5. Otros factores que participan en la formación de las crestas mitocondriales

Como ya se mencionó, las crestas están formadas por dos hojas de la membrana interna, que están paralelas y muy próximas, dejando entre sí un espacio estrecho llamado lumen de la cresta. Estas hojas de membrana interna están unidas en sus bordes formando puntas o cantos, en donde la bicapa lipídica se dobla con una curvatura positiva. En su base la cresta tiene forma tubular y se conecta a la membrana interna en una región conocida como frontera de la membrana interna. Estas conexiones están limitadas por las uniones de cresta y en ellas la bicapa lipídica tiene una curvatura negativa provocada por una proteína denominada Fcj1 (proteína formadora de la unión de cresta); estas uniones de cresta controlan la apertura de la cresta hacia el espacio intermembranal (Rabl *et al.*, 2009).

Se ha propuesto que la arquitectura de la cresta depende del equilibrio entre la concentración del dímero de la F_1F_0 -ATP sintasa y la proteína Fcj1. Así pues, las puntas de las crestas y los cantos están formados por los dímeros de la F_1F_0 -ATP sintasa, los cuales imponen una curvatura positiva a la membrana (Rabl *et al.*, 2009) y donde la proteína Fcj1 está ausente; por el contrario, en las uniones de cresta los dímeros están virtualmente ausentes, lo que permite una curvatura negativa de la membrana provocada por la presencia de la proteína Fcj1. La cara de la cresta contiene tanto a la proteína Fcj1 como al dímero de la F_1F_0 -ATP sintasa, lo que puede determinar su forma plana (Figura 17).

Aunque esta hipótesis trata de explicar la distribución dinámica del dímero de la F_1F_0 -ATP sintasa y la proteína Fcj1, no se puede excluir que otros componentes tales como las prohibitinas, la proteína OPA1 u otros componentes que aún no se identifican, participen en la formación de las uniones o las puntas y cantos de las crestas (Paumard *et al.*, 2002; Rabl *et al.*, 2009).

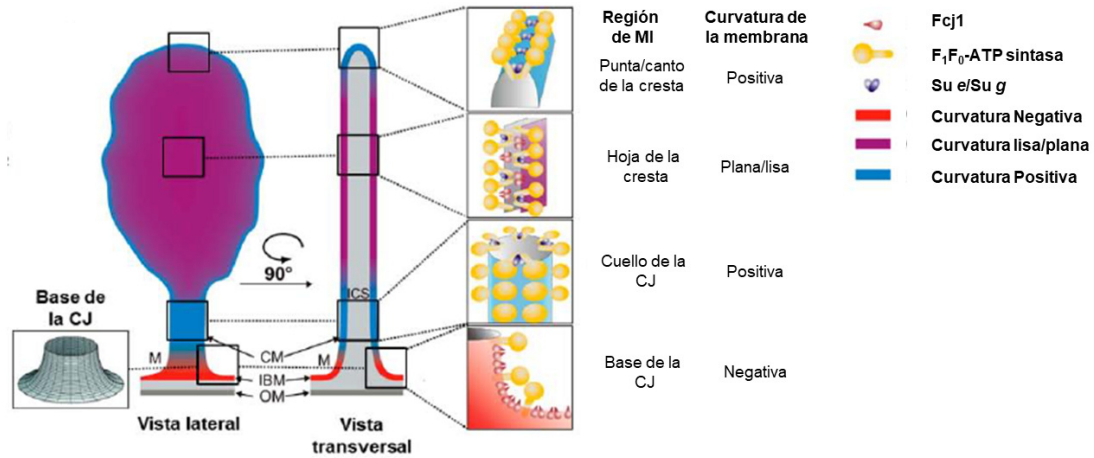


Figura 17. Elementos proteicos involucrados en la formación de las crestas mitocondriales. Representación esquemática de la curvatura de la membrana en las diferentes regiones de la cresta y la localización submitocondrial de la proteína Fcj1 y las subunidades e y g. La curvatura positiva de la membrana está indicada en azul, la curvatura negativa en rojo, y las regiones con ambas curvaturas o ninguna en especial está en púrpura. El esquema representativo de una cresta con una sola CJ se muestra en su vista lateral (izquierda) y su sección transversal después de un giro de 90° (en el medio). Las ampliaciones del área enmarcada muestran el arreglo propuesto de Fcj1, Sub e/Sub g, y la F₁F₀-ATP sintasa y su influencia en la curvatura de la membrana. El recuadro de la izquierda muestra la estructura tubular propuesta para la unión de las crestas (CJ) a la membrana interna mitocondrial. (Modificado de Rabl *et al.*, 2009).

1.6. Efecto de la eliminación de las subunidades dimerizantes y su repercusión en la arquitectura mitocondrial

Como se mencionó, dentro de las proteínas necesarias para la formación de las crestas mitocondriales se encuentran las formas oligoméricas de la F_1F_0 -ATP sintasa. Al eliminar los genes que codifican para las subunidades *e* y *g* en *S. cerevisiae* se producen solamente monómeros de la F_1F_0 -ATP sintasa, se altera la arquitectura de las crestas y las mitocondrias adquieren morfologías o formas inusuales (Paumard *et al.*, 2002; Rabl *et al.*, 2009; Velours *et al.*, 2009). En estas condiciones *S. cerevisiae* crece lentamente en medios no fermentables y las crestas mitocondriales se observan como discos concéntricos en forma de “aros de cebolla” (Figura 18) (Arselin *et al.*, 2004). Sin embargo, no se ha realizado un estudio sistemático de la síntesis e hidrólisis de ATP en estas cepas mutantes. También la formación de los supercomplejos III_2IV se ve afectada (Saddar *et al.*, 2008) y el potencial de membrana disminuye, motivo por el cual cerca de 40% del ADN mitocondrial se pierde (Bornhövd *et al.*, 2006; Duvezin-Caubet *et al.*, 2006).

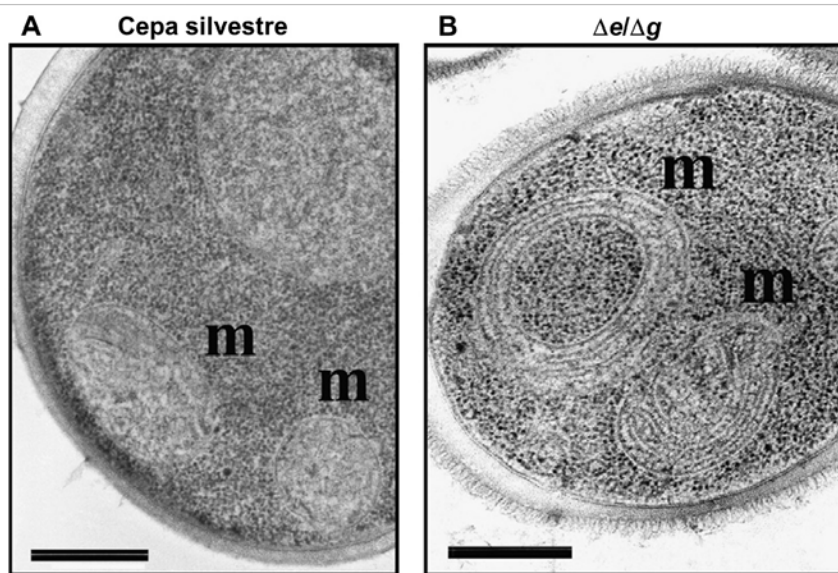


Figura 18. Diferencias estructurales en las mitocondrias de *Saccharomyces cerevisiae*. Micrografía de las mitocondrias de *Saccharomyces cerevisiae* (A) cepa WT y (B) cepa mutante $\Delta e/\Delta g$, en la cual se observan las estructuras anómalas de las mitocondrias, crestas en forma de aros de cebolla. m=mitocondria. La barra indica 500nm (Modificado de Velours *et al.*, 2009).

Aunado a esto, se ha propuesto que la oligomerización de la F_1F_0 -ATP sintasa puede estar involucrada de manera directa en la actividad catalítica de la enzima y de manera indirecta también puede afectar el estado metabólico de las células, ya que cuando se impide la dimerización de la F_1F_0 -ATP sintasa eliminando genéticamente a las subunidades *e* y *g*, las mitocondrias presentan una morfología alterada en las crestas. Así pues, el rearrreglo de las crestas durante la regulación bioenergética de la mitocondria supone el cambio en la proporción dímero/monómero del complejo V (Velours *et al.*, 2009).

En el caso de las mitocondrias de las células HeLa, Campanella *et al.*, (2008) demostraron que al eliminar la subunidad IF_1 se pierden los dímeros y simultáneamente la arquitectura mitocondrial se ve afectada; en particular disminuye el número de crestas por mitocondria y por μm^2 y la muerte celular inducida incrementa hasta en un 40% (Figura 19). Cuando la respiración celular se ve comprometida, la célula permite la despolarización mitocondrial para promover la liberación de inductores proapoptóticos que desencadenan las vías de muerte celular. Sin embargo, cuando se sobreexpresa a la subunidad IF_1 , se observa un aumento en los niveles del dímero del complejo V y en la actividad de síntesis de ATP (Campanella *et al.*, 2008).

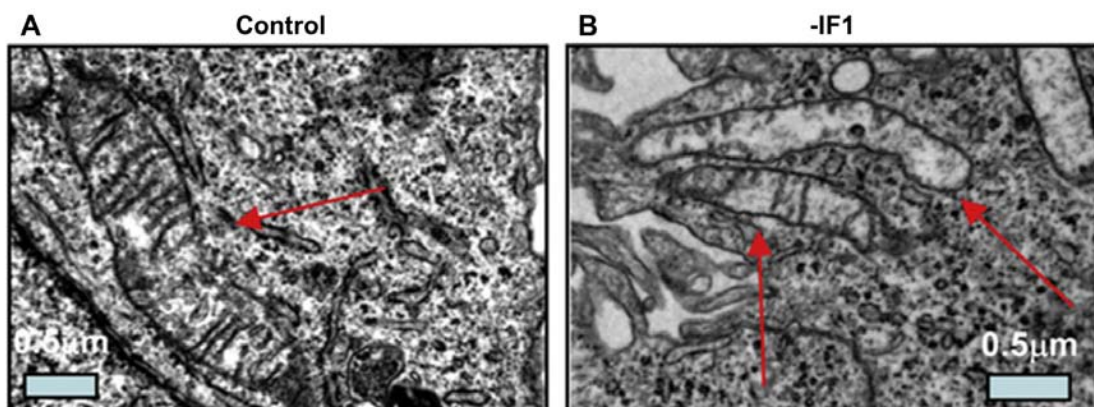


Figura 19. Ultraestructura mitocondrial de las células HeLa. (A) Mitocondrias control y **(B)** cepa mutante $-IF_1$, donde se puede observar que el interior de la mitocondria está desorganizado y con disminución de las crestas mitocondriales. Las flechas rojas señalan las mitocondrias por campo. Simultáneamente se reportó la pérdida del $\Delta\Psi$ y la síntesis de ATP (Modificado de Campanella *et al.*, 2008).

1.7. *Ustilago maydis* como modelo experimental.

U. maydis es un hongo biotrófico que causa el carbón del maíz, comúnmente llamado cuitlacoche o huitlacoche. Se presenta como agallas negras en el maíz y se ha utilizado como un ingrediente tradicional en la gastronomía mexicana. *U. maydis* ha sido un modelo ejemplar en los estudios de fitopatogenicidad, dimorfismo, eventos de recombinación homóloga e interacciones planta-patógeno (Vollmeister *et al.*, 2012).

U. maydis durante su ciclo de vida transita por tres diferentes etapas morfológicas: saprofítica, en la que crece en forma de levadura o basidiospora haploide no patógena; el micelio dicariótico que aparece cuando dos basidiosporas compatibles se fusionan, que es la forma infecciosa del organismo, y la teliospora o esporas binucleadas de latencia, de gran resistencia a cambios ambientales adversos y que constituye el mecanismo de diseminación del hongo (Herrera *et al.*, 1990; Feldbrugge *et al.*, 2004).

El ciclo de vida se inicia cuando las teliosporas germinan sobre la superficie del tejido del hospedero produciendo el promicelio, a partir del cual se liberan las esporidias haploides o levaduras. Cuando éstas son compatibles (A1B1-A2B2), se fusionan y se forma el micelio dicariótico que invade a la planta y que finalmente dará origen a las teliosporas. Estas permanecen viables en el ambiente hasta que se presentan las condiciones favorables para su germinación (Figura 20) (Herrera *et al.*, 1990; Bölker *et al.*, 1992; Bölker, 2001). Los cambios en la patogenicidad, la morfología y la invasión a la planta se regulan por las vías de la MAPK y del AMPc (Mendoza-Mendoza *et al.*, 2009; Kahmann *et al.*, 1999; Doehlemann *et al.*, 2008; Feldbrugge *et al.*, 2004; Lengeler, 2000; Reifschneider *et al.*, 2005; Rexroth *et al.*, 2004; Marques *et al.*, 2007).

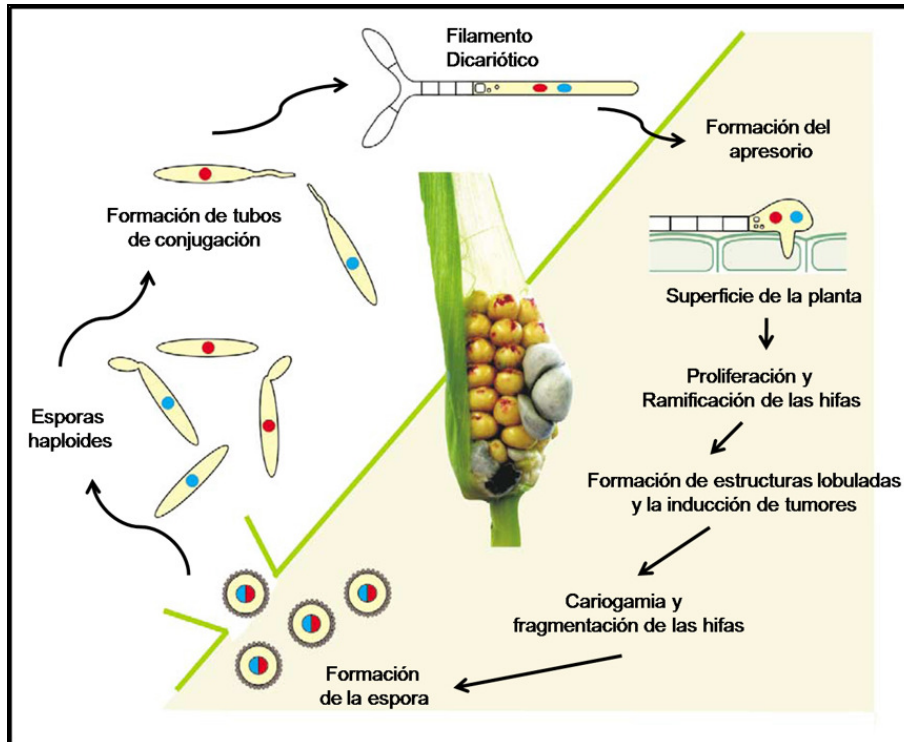


Figura 20. Ciclo de vida de *U. maydis*. El área sombreada en verde claro indica los procesos que son absolutamente dependientes de la presencia de la planta. Los núcleos azules y rojos indican los diferentes tipos de apareamiento en el locus A y B y se utiliza para visualizar las fases haploide y diploide dicarióticas durante el ciclo de vida. En el centro del diagrama se muestra una mazorca de maíz infectada con síntomas de la enfermedad típica. En la parte inferior, el tumor se rompe y revela cantidades masivas de teliosporas negras. Cuando las esporas diploides germinan sufren meiosis y producen esporidios haploides. En este trabajo se emplearon a las levaduras haploides (Modificado de Feldbrügge *et al.*, 2004).

U. maydis ofrece grandes ventajas como modelo biológico, por ejemplo, aunque requiere a la planta para completar su ciclo de vida, en el laboratorio es posible obtener levaduras o micelio en función de las condiciones de crecimiento. Así mismo, se pueden producir cepas mutantes nulas carentes de genes de interés (*knock-out*); este proceso es relativamente sencillo, debido a la alta eficiencia con que la recombinación homóloga se lleva a cabo en este hongo.

Por otra parte, debido a que *U. maydis* presenta un metabolismo aerobio estricto, de tipo no fermentativo y que depende totalmente de la fosforilación oxidativa para el suministro de ATP, la mitocondria es parte esencial para el crecimiento de la levadura. La cadena de transporte de electrones y fosforilación oxidativa de *U. maydis* está compuesta por los 5 componentes clásicos, el complejo I (NADH: ubiquinona oxidorreductasa), el complejo II (succinato: ubiquinona oxidorreductasa), el complejo III (ubiquinol: citocromo c oxidorreductasa), el

complejo IV (citocromo c oxidasa) y el complejo V (F₁F₀-ATP sintasa). Además de éstos, cuenta con otros componentes alternos como la oxidasa alterna (AOX) y las deshidrogenasas alternas externas (Nde1 y 2) e interna (Ndi1). La AOX es una enzima respiratoria que cataliza una reacción de oxidación terminal a nivel de la poza de quinonas, de manera similar a lo que harían en conjunto los complejos III y IV en la vía citocrómica, pero sin generar una diferencia de potencial de membrana, por lo que dicha enzima no participa en la síntesis de ATP (Figura 21).

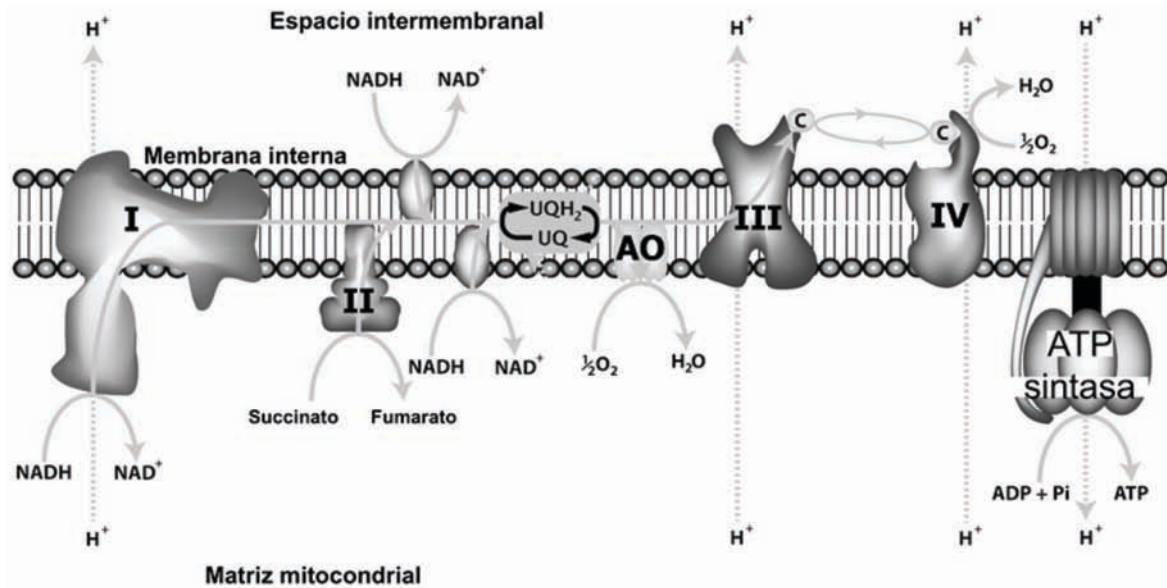


Figura 21. Cadena de transporte de electrones en *U. maydis*. Esquema general de la cadena de transporte de electrones, en el cual podemos localizar los cuatro complejos respiratorios clásicos, la F₁F₀-ATP sintasa, un par de deshidrogenasas alternas (externa e interna) y la oxidasa alterna (AOX) (Modificado de Rogov *et al.*, 2014).



"Mitonulceus" Odra Noel

Justificación

"Lo importante es que la ciencia avance" Dr. Edmundo Chávez

2. JUSTIFICACIÓN

U. maydis es un basidiomiceto fitopatógeno del maíz que provoca grandes pérdidas económicas a nivel mundial. Otros ustilaginales infectan plantas como el arroz (*Oryza sativa*) y el sorgo (*Sorghum bicolor*). Es importante incrementar el conocimiento sobre esta familia, a fin de contar con más herramientas para ayudar a su control biológico.

Se ha reportado que el dímero de la F₁F₀-ATP sintasa tiene un papel importante en la formación de las crestas de la membrana interna mitocondrial, y su ausencia provoca crestas anormales, y pérdida del potencial de membrana ($\Delta\Psi_m$) y de la síntesis de ATP, es importante mencionar que debido a que *U. maydis* es un organismo aerobio, de tipo no fermentativo, que depende totalmente de la fosforilación oxidativa para el suministro de ATP, *U. maydis* es un organismo aerobio, de tipo no fermentativo, que depende totalmente de la fosforilación oxidativa para el suministro de ATP. La mitocondria es la encargada de oxidar los equivalentes reductores provenientes de la glucólisis, el ciclo de Krebs y la β -oxidación y así alimentará la cadena de transporte de electrones y convertir el poder reductor en ATP.

El dímero de la F₁F₀-ATP sintasa de *U. maydis* tiene 17 subunidades homólogas a las reportadas para *S. cerevisiae*, incluyendo a las subunidades dimerizantes *g* y *e* (Arnold *et al.*, 1998; Wittig *et al.*, 2008; Esparza-Perusquía *et al.*, 2017). Con base en lo anterior, se decidió construir la cepa mutante de la subunidad *g* en *U. maydis* y determinar la repercusión de la eliminación de dicha subunidad (Δg) sobre la formación del dímero de la ATP sintasa, el plegamiento de las crestas, el retículo mitocondrial y el estado bioenergético ($\Delta\Psi_m$, consumo de oxígeno y síntesis de ATP). Asimismo, se pretende caracterizar la actividad de ATPasa de los dímeros ($V_{2\Delta g}$) y en los monómeros ($V_{1\Delta g}$) aislados de la cepa mutante.



Odra Noel

Objetivos

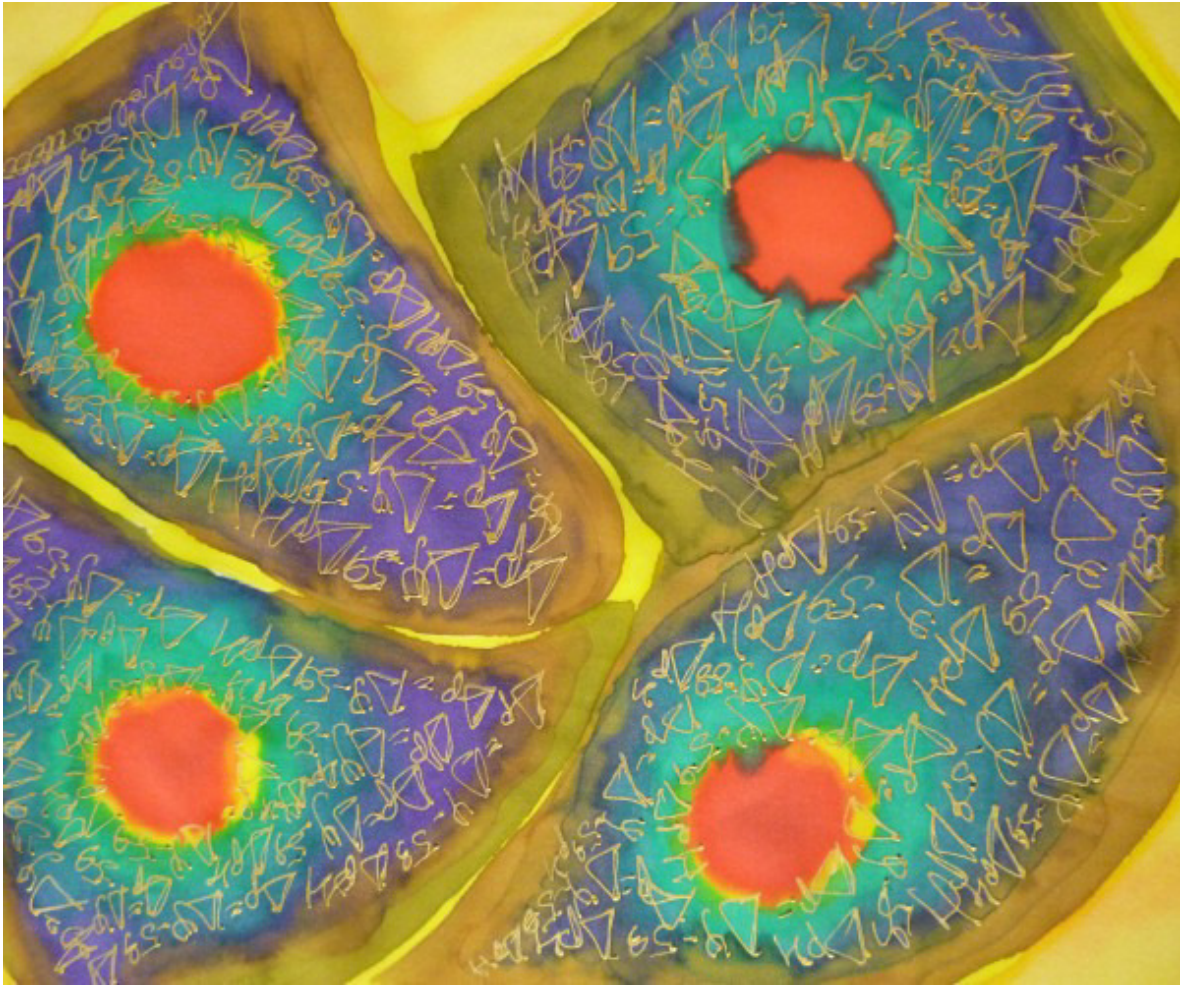
3. OBJETIVOS

3.1. OBJETIVO GENERAL

Determinar la repercusión de la eliminación de la subunidad *g* en la oligomerización y la actividad enzimática de la F₁F₀-ATP sintasa de *Ustilago maydis*, así como su papel en la formación de crestas mitocondriales y en el estado bioenergético mitocondrial.

3.2. OBJETIVOS PARTICULARES

- Generar la cepa mutante Δg de la F₁F₀-ATP sintasa de *Ustilago maydis*.
- Determinar la presencia del V_{2 Δg} y V_{1 Δg} .
- Aislar los oligómeros (V_{2 Δg} y V_{1 Δg}) de F₁F₀-ATP sintasa.
- Caracterizar la actividad de hidrólisis de ATP de los oligómeros aislados de la F₁F₀-ATP sintasa.
- Determinar la morfología de crestas mitocondriales de la cepa Δg en comparación con la cepa silvestre (WT).
- Cuantificar el potencial de membrana, la respiración y síntesis mitocondrial de ATP en las cepas WT y Δg de *Ustilago maydis*.



"Mitchell's equation 1" Odra Noel

Materiales y métodos

"Si modifica el protocolo le puede costar sangre" Dr. Armando Gómez-Puyou

4. MATERIALES Y METODOS

Cultivo celular para biología molecular. La cepa silvestre FB2 (a2b2-WT; ATCC 201384) de *Ustilago maydis* se sembró en un medio sólido de YPD (0.5% (p/v) extracto de levadura, 0.25% (p/v) bactopectona, 0.5% (p/v) de glucosa, 2% (p/v) de agar), se incubó por 18 horas a 28°C. A partir de ese cultivo se inoculó una azada de células en 3 mL de YPD y se incubaron durante 12 h a 28°C en agitación orbital constante.

Obtención del DNA genómico (gDNA) de la cepa WT de U. maydis. El cultivo anterior se centrifugó a 15,700 g durante 2 min para recuperar las células. Éstas se rompieron con perlas de vidrio (0.5 mm) en 500 µL de amortiguador de lisis (10 mM Tris-HCl pH 8.0, 10 mM NaCl, 1% (p/v) SDS, 2% (v/v) Tritón X100, 1 mM EDTA) y 500 µL de la solución de fenol/cloroformo en una relación 1:1, en agitación constante durante 10 min. El DNA se recuperó de la fase acuosa (400 µL), el cual se transfirió a un tubo que contenía 1 mL de etanol al 100% para lavar el DNA; dicho volumen se centrifugó para compactar el DNA. Finalmente, se incubó en agitación orbital constante (400 rpm) durante 10 min a 50°C en presencia de 50 µL de TE/Rnase (1.31 mM Tris-Base, 8.69 mM Tris-HCl, 10 mM Na₂-EDTA y 10 mg/mL de Rnase-A para remover el RNA).

Para corroborar la integridad del DNA genómico (gDNA), las muestras se resolvieron en un gel de agarosa al 0.8% (p/v), 1x-TBE (89 mM Tris-base, 89 mM ácido bórico, 2 mM EDTA, pH 8.0), 25 µg/mL bromuro de etidio (BrEt) y la concentración se determinó en un NanoDrop 2000c (Thermo Scientific).

Diseño de los oligonucleótidos. Para la construcción del *knock-out* (KO) se amplifican los fragmentos UF (upstream flank) y DF (downstream flank) de aproximadamente 1000 pares de bases flanqueando al gen que codifica para la subunidad g (ATP20), el diseño de los oligonucleótidos se realizó en el programa SnapGene versión 2.0.1 y se sintetizaron en Ludwig-Maximilians Universität München, Alemania.

Para el caso del fragmento UF los oligonucleótidos correspondientes para las diferentes PCR son denominados U1-Fw (aproximadamente 20 pb antes de UF) 5'-GCGTAGTCGATGTCCTTGG-3', U2-Fw (aproximadamente 1000 pb antes del gen ATP20) 5'-atttaaatGCTTCCTTGTATTCGGC-3' (las letras en minúsculas indican el sitio de corte para la enzima *SwaI*), U3-Rv (aproximadamente 20 pb antes del gen ATP20) 5'-ggccatctaggccGATGACCGTATTACCCGAAAGAC -3' (las letras en minúsculas indican el sitio de corte para la enzima *SfiI*) y P1-Fw (aproximadamente 20 pb al final del UF) 5'- TCCTCACACCATCCCCTT-3'.

Para el fragmento DF se diseñaron los oligonucleótidos D1-Fw (aproximadamente 20 pb después del gen ATP20) 5'-ggcctgagtgccACGCTCGACAATTGAATTCG -3' (las letras en minúsculas indican el sitio de corte para la enzima *SfiI*), D2-Rv (aproximadamente 1000 pb después del gen ATP20) 5'- atttaaatCTGGCATGTGCTCACC -3' (las letras en minúsculas indican el sitio de corte para la enzima *SwaI*) y D3-Rv (aproximadamente 1020 pb después del gen ATP20) 5'- GGCCTGCCGTATCAAGTC -3'.

Los oligonucleótidos U2, U3, D1, D2 fueron diseñados con sitios de corte para las enzimas de restricción específicas, ya que el cassette de resistencia a la higromicina (HygR) cuenta con esos sitios para la ligación y formación del plásmido KO. P2-Rv (aproximadamente 20 pb al inicio del gen ATP20) 5'-GGGAGCAGCAGCTCGGC -3', MF167-Rv (aproximadamente 20 pb al final del HygR) 5'- AACTCGCTGGTAGTTACCAC -3' y MF168-Fw (aproximadamente 20 pb al inicio del HygR) 5'- ACTAGATCCGATGATAAGCTG -3'.

Amplificación de los fragmentos UF y DF. Para la construcción del KO se amplifican los fragmentos UF y DF mediante PCR punto final en un termociclador MAXYGENE II (THERM-1000), siguiendo los protocolos de temperatura variable y tamaño del producto para la polimerasa Phusion High-Fidelity (New England Biolabs, Cat. E0553L). El medio de reacción contiene gDNA (aproximadamente 1 µg), 10 mM dNTP's, 1X Phusion HF buffer, 5% (v/v) DMSO y 10 mM MgCl₂.

Preparación de células competentes TOP10 de Escherichia coli. Para la preparación de las células competentes de *E. coli* se siguió el método Kushner utilizando cloruro de rubidio (RbCl) (Kushner, 1978).

Se sembró una colonia de *TOP10* de *E. coli* en 25 mL de medio LB (1.6% (p/v) bacto-triptona, 1% (p/v) extracto de levadura, 0.5% (p/v) NaCl) y se incubó durante 16 horas a 37°C con agitación orbital constante. Las células se cosecharon a 1,690 g por 20 min a 4°C, el precipitado se resuspendió en 1 mL de LB sin antibióticos. Se inocularon 30 mL de LB con la suspensión anterior hasta una densidad óptica (D.O._{600nm}) de 0.1 y se crecieron por 2 horas a 37°C en agitación orbital constante hasta alcanzar una D.O._{600nm} de 0.6. Las células se recuperaron a 1,690 g por 30 min a temperatura ambiente.

El botón se resuspendió en 20 mL de solución TFB1 frío (30 mM acetato de potasio, 50 mM MnCl₂, 100 mM RbCl, 10 mM CaCl₂, 15% (v/v) glicerol, pH 5.8, esterilizado por filtración), y se incubó por 2 h a 4°C. Las células se recuperan a 1,690 g por 30 min a 4°C y se resuspendieron cuidadosamente en 4 mL de solución TBF2 frío (10 mM MOPS, 75 mM CaCl₂, 10 mM RbCl, 15% (v/v) glicerol, pH 6.8, estéril por filtración) y se incubaron por 1 h a 4°C. Finalmente, las células se conservaron en alícuotas de 100 µL a -70°C hasta su uso.

Formación y clonación de los plásmidos TOPO (TA cloning) para UF y DF. Ya que los amplificadores UF y DF provienen de una PCR donde se utiliza la polimerasa Phusion, a éstos se les debe añadir extensiones de adenina para que sean reconocidos por el plásmido TOPO para poder integrarse. En la reacción se añadió 1 µL de Taq polimerasa, 0.5 µL dNTP's y 5 µL del amortiguador 10x y se incubaron por 15 min a 72°C. Una vez finalizada la proyección, los fragmentos UF y DF se ligaron a un vector pCT2.1-TOPO (pCR2.1-TOPO plásmido. Invitrogen Cat. 45-0641) en presencia de 3.5 µL del PCR modificado, 1 µL de solución salina (incluida en el Topo-kit), 0.2 µL del Topo-vector y se ajusta a un volumen final de 5

μL con H_2O , se incubaron por 5 min a temperatura ambiente y se clonaron en TOP10 *E. coli*.

La transformación de las células TOP10 con los plásmidos UF y DF se llevó a cabo por choque térmico siguiendo el método descrito en Sambrook *et al.*, (2001) con algunas modificaciones. Las células se incubaron por 30 min a 4°C , seguido de un choque térmico a 37°C durante 5 min; éstas se recuperan en 1 mL de LB a 37°C durante 1 hora; al término de la incubación las células se centrifugan a $13,800\text{ g}$ por 1 minuto y se resuspenden en $100\ \mu\text{L}$ de LB. Posteriormente, se sembraron en medio LB sólido, suplementado con ampicilina (LB^{Amp} contiene: 1.6% (p/v) bacto-triptona, 1% (p/v) extracto de levadura, 0.5% (p/v) NaCl y 0.1 mg ampicilina/mL) y se incubaron por 16 h a 37°C .

Obtención del DNA plasmídico. Una colonia de la cepa TOP10 transformada se sembró en 3 mL de LB^{Amp} y se incubó por 12 h a 37°C con agitación orbital constante. Para obtener el DNA plasmídico, 1 mL de la muestra se centrifugó a $15,700\text{ g}$ durante 2 min, el sobrenadante se descartó y las células fueron resuspendidas en $200\ \mu\text{L}$ del amortiguador STET (100 mM NaCl, 10mM Tris-HCl pH 8.0, 1 mM EDTA, 5% (v/v) Tritón X100) y 0.1% (p/v) lisozima; se incubaron por 60 seg a 95°C y se centrifugó a $15,700\text{ g}$ durante 10 min.

Al sobrenadante, que contenía al RNA y al DNA plasmídico, se le añadieron $20\ \mu\text{L}$ de solución Mini III (3 M NaOAc) y $500\ \mu\text{L}$ de 2-propanol para precipitar a los ácidos nucleicos. Las muestras se centrifugaron a $15,700\text{ g}$ durante 10 min, el precipitado que contenía los ácidos nucleicos se lavó con $200\ \mu\text{L}$ de etanol al 70% (v/v). Finalmente, se centrifugó a $15,700\text{ g}$ durante 2 min y se eliminó el sobrenadante, al precipitado se le agregaron $100\ \mu\text{L}$ TE-RNase para obtener una muestra libre de RNA. La concentración de DNA se determinó en un NanoDrop 2000c (Thermo Scientific).

Purificación del DNA. El DNA se purificó con un kit JET Quick Spin Column Technique de Genomed. Al DNA plasmídico se le adicionó 400 μ L del amortiguador M1 (hidroxicloruro de guanidina e isopropanol), se mezcló por inversión y se transfirió a una columna de sílica de purificación, la cual se centrifugó a 15,700 g por 1 min y se descartó el filtrado. La columna se lavó dos veces con 400 μ L del amortiguador M2 (etanol, NaCl, EDTA y Tris-HCl) y se centrifugó a 15,700 g por 1 min eliminando el filtrado. Para eluir el plásmido de la columna se le adicionó 50 μ L de TE (10 mM Tris-HCl, pH 8.0) y se centrifugó a 15,700 g por 2 min. Se determinó concentración de DNA obtenido.

Secuenciación del DNA. La mezcla de reacción fue compuesta por: 250 ng de la muestra, 3.2 pmoles del cebador MF963/MF964 y 10 mM Tris-HCl, pH 8.0, en un volumen final de 7 μ L; la secuenciación fue realizada y registrada en Ludwig-Maximilians Universität München, Alemania (Sequencing LMU <http://www.gi.bio.lmu.de/sequencing/index.html>); se verificaron las secuencias obtenidas y los sitios de corte.

Construcción del plásmido knock-out. Las mutaciones se realizaron como lo describió Brachmann *et al.*, (2004). La digestión del plásmido que contiene el cassette de resistencia a higromicina (HygR) (pUMa_198, donado por el Dr. Michael Feldbrügge del Instituto de Microbiología, Universidad Heinrich-Heine, Düsseldorf, Alemania) así como aquellos que contienen los fragmentos UF y DF fueron digeridos con la enzima de restricción *Sfi*I. El DNA fue purificado del gel mediante un Zymoclean Gel DNA Recovery kit de Zymo Research (USA). El plásmido KO (pUMa_1704) se obtuvo a partir de la ligación de los fragmentos de DNA empleando una relación 1:1:3 de UF:DF:HygR, durante 3 h a temperatura ambiente en presencia de 200 unidades de DNA ligasa (Invitrogen).

*Generación de la cepa mutante (Δ g) de *U. maydis*.* Para la obtención de la cepa Δ g se realizó por medio de *transformación química* como se describe a continuación.

Formación de protoplastos. Se inoculan 3 mL de medio YPD con la cepa WT y se incubaron 24 h a 28°C en agitación orbital constante. Posteriormente, el preinóculo se diluyó hasta 0.4 unidades de D.O._{600nm} y se cultivó hasta alcanzar las 0.8 unidades de D.O._{600nm}. Se comprobó la pureza celular por microscopía, se centrifugó un volumen de 50 mL de las células a 1,700 g durante 5 min; el paquete celular se resuspendió con 25 mL del amortiguador SCS (20 mM ácido cítrico, 1 M sorbitol, pH 5.8) y se centrifugó a 1,700 g durante 5 min. El precipitado se recuperó y resuspendió con una solución de Novoenzima (7 mg/2 mL SCS); posteriormente se incubó de 10 a 20 min a temperatura ambiente; la permeabilización celular se observó con el microscopio como la aparición de burbujas en el ápice celular; cuando el 40% de las células fueron permeabilizadas, se continuó con la transformación genética de *U. maydis*.

Se añadió 10 mL de SCS y se centrifugó a 1,100 g durante 5 min a 4°C; el precipitado se resuspendió con 10 mL de SCS para eliminar las enzimas y nuevamente se centrifugó a 1,100 g durante 5 min; el precipitado se resuspendió en 10 mL del amortiguador STC (1 M sorbitol, 10 mM Tris-HCl, 100 nM CaCl₂, pH 7.5) y se centrifugó a 1,100 g durante 5 min (este paso se repitió dos veces). Posteriormente se desechó el sobrenadante y el precipitado se resuspendió en 1 mL de STC. Finalmente, las muestras se almacenaron a -70°C en alícuotas de 100 µL.

Del mismo modo se intentó realizar la transformación por biobalística para eliminar el gel ATP21 que codifica para la subunidad e (mutante Δe). No se obtuvieron resultados positivos (ver anexo 10.1).

Incorporación del genoma Δg exógeno a los protoplastos de U. maydis. Para la transformación de la levadura se utilizaron cajas de Petri con YPD agar (suplementado con 18.22% (p/v) sorbitol y 50 µg higromicina B/mL de PBS). Se adicionó 10 mL de YPD agar con 80 µL de higromicina (aproximadamente 4 mg) y finalmente a los 15 min se agregó 10 mL de YPD agar (sin higromicina). A los

protoplastos se les añadió 15 μg de heparina (15 mg/mL) y 5 μL del plásmido *KO* (pUMa_1704), y se incubaron por 10 min a 4°C; posteriormente se añadieron 500 μL del amortiguador STC/PEG (60% (v/v) STC-amortiguador, 40% (p/v) polietilenglicol, Sigma P-3640) y se incubaron por 15 min a 4°C. Finalmente, las células transformadas se dispersaron muy suavemente en la placa y se incubaron por 7 días a 28°C.

Comprobación por PCR de la cepa Δg (eliminación del gen ATP20). Se sembró una azada de la cepa transformada en medio CM-Hyg agar (0.25% (p/v) casaminoácidos, 0.1% (p/v) extracto de levadura, 1% solución Holliday de vitaminas, 6.25% solución Holliday de sales, 0.05% DNA (sigma D-3159), 0.15% (p/v) NH_4NO_3 , 18.22% (p/v) sorbitol, 1.5% (p/v) bacto-agar, 5 $\mu\text{g}/\text{mL}$ Hyg, pH 7.0) en forma de estría para obtener cepas independientes y se incubó por 24 h a 28°C.

Una vez multiplicadas las células, se tomó una azada de cada una de las colonias (aproximadamente 10) y fueron sembradas en medio YPD líquido e incubadas por 24 h a 28°C en agitación orbital constante; posteriormente se tomaron 5 μL del cultivo y se sembraron en una caja con CM-Agar para mantener la línea celular, el cultivo restante se empleó para aislar gDNA (ver arriba el procedimiento descrito para aislar el gDNA de la cepa WT).

Para comprobar que el gen ha sido sustituido por el HygR se realizó una PCR con el gDNA Δg de las colonias aisladas en el paso anterior, utilizando los oligonucleótidos P1 y P2; la migración del producto de PCR se realizó en un gel de agarosa al 0.8% (p/v), 1x-TBE, 25 $\mu\text{g}/\text{mL}$ BrEt. Para comprobar que el gen ATP20 ya no estaba presente se incluyó como control negativo el gDNA de la cepa WT, las clonas que no amplificaron fueron usadas como positivas para una segunda PCR donde se comprobó la presencia del cassette HygR.

Para comprobar que el cassette se insertó en el lugar correcto después de la recombinación homóloga, se realizó una PCR utilizando un par oligonucleótidos que flanquearon las regiones UF (U1 y el MF167) y DF (MF168 y D3), usando como control negativo el gDNA de la cepa WT. Las muestras se resolvieron en un gel al 0.8% de agarosa, 1x-TBE, 25 µg/mL BrEt/mL.

Southern Blot. Para llevar a cabo las réplicas tipo Southern se digirió el gDNA con una enzima de restricción, cuidando de que la enzima reconociera un sitio de corte dentro del cassette HygR sin cortar en la secuencia del gen de interés. En este caso la reacción contenía 10 unidades de *Nco-I*, 1 µg DNA, 1X NEBuffer, 39 µL dH₂O y se incubó por 1 h a 37°C. Posteriormente, las muestras se corrieron en un gel de agarosa al 0.8% (p/v) con 25 µg BrEt/mL en 1x de TAE (40 mM Tris-Base, 40 mM ácido acético, 1 mM EDTA pH 8.0), a 90V/2 h. Al finalizar la corrida, el gel se lavó con 250 mM HCl durante 20 min, posteriormente se lavó 2 veces con dH₂O por 5 min y se incubó en la solución DENAT (1.5 M NaCl, 0.4 M NaOH) por 20 min; se lavó con dH₂O y se incubó con la solución RENAT (1.5 M NaCl, 282 mM Tris-HCl, 218 mM Tris-Base) por 20 min.

El gel se colocó sobre papel filtro Whatman en una base plana, y se humedeció con una solución 20x de SSC (3 M NaCl, 0.3 M citrato de sodio) cuidando que el papel siempre estuviera en contacto con la solución. Se colocó la membrana Hybond-N+Nylon (GE Healthcare) sobre el gel y se sellaron los bordes con una película plástica flexible (parafilm). Se colocaron papeles Whatman sobre la membrana, luego una pila de 5 cm de altura de papel absorbente y encima una placa de aproximadamente 500 gr para producir presión sobre el gel y la membrana para permitir que el DNA se movilizara del gel a la membrana por capilaridad. Al finalizar la transferencia después de 48 h, la membrana se humectó con 2x de SSC y se dejó secar por 15 min; el DNA se fijó a la membrana irradiando con UV-crosslinker directamente, cuidando siempre de no exponer la cara de la membrana que estuvo en contacto directo con el gel para no dañar el DNA.

Se prehibridizó la membrana en un tubo para Southern blot con el amortiguador de hibridación 26% (v/v) SSPE (3 M NaCl, 200 mM fosfato de sodio, 20 mM EDTA, pH 7.4), 20% (v/v) solución Denhardt (1% (v/v) ficoll, 1% (p/v) polivinilpirrolidona, 1% (p/v) BSA, 5% (p/v) SDS) durante 15 min a 65°C (Southern, 1975; Rybicki *et al.*, 1996).

Para la detección del fragmento de interés, la membrana se incubó toda la noche con una sonda de DNA complementaria al sector de DNA buscado y marcada con digonexina (Feinberg *et al.*, 1983); el marcaje, la hibridación y el revelado se realizaron siguiendo las instrucciones del fabricante (New England Biolabs). Posteriormente, se retiró la sonda y la membrana se lavó con diferentes concentraciones de la solución SSPE. Se realizó un primer lavado con 10 mL del amortiguador DIG1 (100 mM ácido málico, 150 mM NaCl, pH 7.5) por 5 minutos; y el segundo con 10 mL del amortiguador DIG2 (DIG1, 10% leche en polvo desgrasada) durante 30 min para bloquear la membrana, posteriormente se incubó en 10 mL de DIG2 que contenía el anticuerpo anti-DIG-AB en una relación 1:10,000, por 3 h a 60°C.

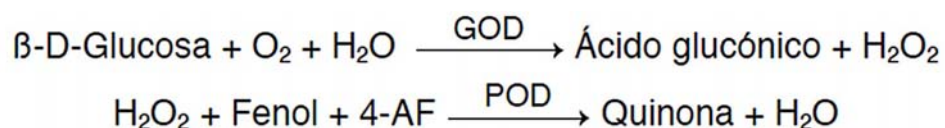
La membrana se lavó dos veces por 15 min con el amortiguador DIG-wash (DIG1, 0.3% (v/v) Tween-20); se incubó con 20 mL del amortiguador DIG3 (100 mM Tris-HCl, 100 mM NaCl), y finalmente se incubó en presencia de la solución CDP-Star® Reagent de NEB labs (CDP-Star 1:100 en DIG3) por 5 min. Se retiró la solución y se detectó la señal de quimioluminiscencia con una cámara ImageQuant LAS4000 de GE Healthcare.

Curva de crecimiento. Las cepas WT y Δg de *U. maydis* se sembraron en un medio sólido de YPD y se cultivaron por 48 h a 28°C. A partir de este cultivo se preparó un inóculo en 100 mL de YPD y se incubó durante 24 h a 28°C, en agitación orbital constante. Las células se lavaron y se resuspendieron en 5 mL de agua destilada estéril. Se inoculó el equivalente a 40 unidades de absorbancia (600 nm) de esta suspensión a un litro de YPD, Medio Mínimo-Etanol (0.3% (p/v) sulfato de

amonio, 1% (v/v) etanol absoluto, 1x solución de sales (ver anexo 10.2), 1x elementos traza (ver anexo 10.3) y Medio Mínimo-Glucosa (0.3% (p/v) sulfato de amonio, 1% (p/v) glucosa, 1x solución de sales, 1x elementos traza). Las levaduras fueron cultivadas a 28°C, en agitación orbital constante y se tomaron alícuotas de 1 mL cada 2 h para determinar la D.O._{600nm}, el pH y la concentración de glucosa.

Curva de crecimiento en placa (diluciones seriadas). Las cepas WT y Δg de *U. maydis* fueron sembradas en 100 mL YPD y cultivadas por 24 h a 28°C. Se tomó 1 mL de *U. maydis*, se centrifugó a 12,000 g por 5 min y se descartó el sobrenadante. Las células fueron resuspendidas en 1 mL de agua destilada estéril, se tomaron 10 mg (peso húmedo) de las mismas y se realizaron 5 diluciones seriadas (1/10).

Determinación cuantitativa de glucosa (método enzimático colorimétrico para la cuantificación de glucosa en medios de levadura). La concentración de glucosa se determinó mediante un “Glucose-LQ kit”, siguiendo las instrucciones del fabricante. La glucosa oxidasa (GOD) cataliza la oxidación de glucosa a ácido glucónico. El peróxido de hidrógeno (H₂O₂) producido se detecta mediante un aceptor cromogénico de oxígeno, fenol, 4-aminofenazona (4-AF), en presencia de la peroxidasa (POD):



La intensidad del color formado es proporcional a la concentración de glucosa presente en la muestra ensayada. Para la determinación se tomó 1 mL de células y se centrifugaron a 16,100 g por 5 min. Se recuperaron 500 μ l del sobrenadante y se continuó con la técnica como la reportó el fabricante, realizando las lecturas a 505 nm.

Microscopía de transmisión electrónica. La microscopía electrónica se realizó en el Instituto de Biotecnología de la UNAM, mediante la técnica LR White, usando 2.5% (v/v) glutaraldehído (GTA) y 4% (v/v) paraformaldehído (PFA) como fijador, las muestras se incubaron en 160 mM de cacodilato de Na/K, pH 7.4 por 1 hora a temperatura ambiente, una vez transcurrido el tiempo se lavaron dos veces con el amortiguador de cacodilato y se incubaron toda la noche a 4°C. Las muestras fueron deshidratadas gradualmente en etanol al 70, 80 y 96 %. Se usó una mezcla 50:50 de LR White-EtOH absoluto y se incubó 1 hora.

Se realizaron cortes ultrafinos (60-80 nm) en un ultramicrotomo (UltraCut-R, Leica), los cortes se recogieron en rejillas Formvar® recubiertas de cobre (EMS) y se tiñeron con 2% (p/v) de acetato de uranilo y 0.3% (p/v) de citrato de plomo. Las muestras se analizaron en un microscopio de transmisión electrónica (ZEISS Libra 120 Oberkochen Alemania) equipado con un dispositivo de carga acoplada (CCD) (300 W de doble visión; Gatan, Pleasanton, CA, EE. UU.) a la cámara. Las imágenes fueron capturadas a una tensión de aceleración de 80 kV.

Consumo celular de oxígeno. Se realizó la determinación del consumo de oxígeno en las células WT y Δg cosechadas en la fase logarítmica de crecimiento (8 hrs) y en la fase estacionaria (24 hrs); las células se recuperaron de 50 mL de cada cultivo por centrifugación a 2,300 g por 5 min, y se resuspendieron en 3 mL de 10 mM K_2PO_4 , pH 7.4. La concentración de oxígeno se determinó polarográficamente usando un electrodo tipo Clark acoplado a un oxímetro YSI-5300 y una cámara de incubación manteniendo la temperatura constante a 30°C (Estambrook, 1967, Guerrero-Castillo *et al.*, 2012, Affourtit *et al.*, 2012). La respiración se inhibió con 5 mM de KCN (inhibidor del complejo IV) y/o 10 mM de *n*-octil-galato (*n*Og - inhibidor de la oxidasa alterna) (Juárez *et al.*, 2006).

Permeabilización de las células para ensayos bioenergéticos. Se centrifugaron 50 mL de células (fase estacionaria), las cuales fueron resuspendidas en 3 mL del amortiguador de permeabilización (300 mM sorbitol, 10 mM HEPES, 1

mM EGTA, 10 mM KH₂PO₄, 10 mM MgSO₄, 150 mM KCl, pH 7.4) y se incubaron por 20 min en presencia de 0.02% (p/v) de digitonina. Se verificó en el oxímetro la permeabilización de las células y se estimuló la respiración adicionando 10 mM de succinato (Esparza-Perusquía *et al.*, en preparación). La respiración se inhibió con KCN o nOg.

Monitoreo del potencial de membrana mitocondrial ($\Delta\Psi_m$). Para determinar el potencial de membrana mitocondrial se utilizó 10 μ M safranina O (Akerman *et al.*, 1976), el cual es un colorante lipofílico catiónico que se transporta (internaliza) a la matriz mitocondrial cuando la membrana interna está energizada, aumentando su absorbancia. Cuando se abate el $\Delta\Psi_m$, el colorante sale de la matriz y la señal disminuye. Estos cambios se determinan en un espectrofotómetro de doble longitud de onda con agitación orbital constante, en modo dual (AMINCO DW 2000, Olis, Inc., Bogart, GA, EUA) a 511 nm, utilizando de referencia el punto isobéptico 533 nm, para determinar el cambio en la absorción de la safranina O.

Para la cuantificación del potencial de membrana mitocondrial se utilizaron células permeabilizadas (ver permeabilización de las células para ensayos bioenergéticos). La reacción se llevó a cabo en un amortiguador que contenía 300 mM sorbitol, 10 mM HEPES, 1 mM EGTA, 10 mM MgSO₄, 150 mM KCl y 10 mM KH₂PO₄ a pH 7.4. El potencial de membrana se generó mediante la adición de 10 mM de succinato en presencia de 10 μ M safranina O. El $\Delta\Psi_m$ se abatió con 5 μ M de CCCP.

Síntesis de ATP mitocondrial. Para la cuantificación de la producción de ATP mitocondrial se utilizaron las células permeabilizadas con digitonina (0.02% p/v) y se incubaron con agitación con 10 μ M de P1, P5-Di(adenosine-5')pentaphosphate penta-ammonium (Inhibidor de la miocinasa de ADP) por 5 minutos en el amortiguador de permeabilización. Las mitocondrias se energizaron con 10 mM succinato.

Una vez transcurrida la incubación se tomó una muestra para determinar el T₀; posteriormente, se les adicionó 5 mM de ADP y se tomaron muestras diferentes tiempos (10, 20, 30, 40, 50 y 60 seg). Para detener la reacción se adicionó ácido perclórico (0.7 M) y se centrifugaron a 16,100 g por 1 min. Se recuperaron 900 μ L del sobrenadante y se amortiguaron con 0.5 M KOH para neutralizar al ácido perclórico. El KClO₄ es una sal que se precipita, la que puede ser removida al centrifugar a 16,100 g por 1 min. Se recuperaron nuevamente 900 μ L del sobrenadante y se les ajustó el pH a 7.0

La concentración de ATP sintetizado se determinó por medio de un sistema enzimático acoplado a la reducción de NADP⁺. La mezcla de reacción contenía 0.5 mM NADP⁺, 5 mM ADP, 6 unidades/mL de la glucosa-6-fosfato deshidrogenasa (G-6P-DH), 16 unidades/mL de hexocinasa (HK) y 10 mM de glucosa. En este proceso enzimático la hexocinasa produce glucosa-6-fosfato a partir de glucosa y ATP, la glucosa-6-fosfato deshidrogenasa oxida a la glucosa-6-fosfato y genera δ -gluconolactona y NADPH.

Los resultados se analizaron determinando el cambio de absorbancia tomando en cuenta el coeficiente de extinción molar del NADP⁺ ($\epsilon_{\text{NADPH}} = 6.22 \text{ mM}^{-1} \text{ cm}^{-1}$) en función del tiempo, para obtener la velocidad de síntesis de ATP (Trautschold *et al.*, 1995; De los Ríos-Castillo *et al.*, 2011). El ajuste de los datos para determinar los parámetros cinéticos se realizó en el programa Sigma Plot versión 10.0.

Aislamiento de las mitocondrias. Las mitocondrias de *U. maydis* fueron aisladas como lo describió Juárez *et al.*, (2004) con algunas modificaciones (Guérin *et al.*, 1979; Díaz-Ruiz, *et al.*, 2008, Esparza-Perusquía, *et al.*, 2017). Las células fueron cosechadas por centrifugación a 5,500 g durante 5 min a 4°C; se resuspendieron y se lavaron dos veces con agua destilada. Posteriormente las levaduras se resuspendieron en 0.6 M de sulfato de amonio, 20 mM KH₂PO₄, en una relación de 100 mL por cada 8 g de células; para degradar la pared celular se

adicionaron las enzimas líticas de *Trichoderma harzianum* (0.016 g/g de peso húmedo de células) (Sigma-Aldrich L1412) y se incubaron durante 60 min a 30°C.

Para eliminar las enzimas líticas, los protoplastos se centrifugaron a 5,500 g durante 10 min a 4°C; se resuspendieron y lavaron con una solución compuesta por 0.8 M sacarosa, 10 mM Tris, 2 mM EDTA, 20 mM KH₂PO₄, 0.3% (p/v) albúmina sérica de bovino desgrasada, pH 7.0 y se recuperaron por centrifugación a 5,500 g durante 10 min a 4°C. Los protoplastos se resuspendieron en 40 mL de una solución de 0.4 M sacarosa, 10 mM Tris, 2 mM EDTA, 20 mM KH₂PO₄, 0.3% (p/v) albúmina sérica de bovino desgrasada, pH 7.0 y se homogenizaron con 15 ± 30 golpes con un homogeneizador Potter, en presencia de 1 mM PMSF y coctel de inhibidores de proteasas (Sigma-Aldrich P-8340). Al finalizar, el homogenado se diluyó a un volumen final de 130 mL y se centrifugó a 5,500 g durante 10 min a 4°C.

Para recuperar a las mitocondrias, el sobrenadante se centrifugó a 17,300 g durante 10 min a 4°C; finalmente las mitocondrias se resuspendieron en 0.4 M sacarosa, 10 mM Tris, 2 mM EDTA, 20 mM KH₂PO₄, 0.3% (p/v) albúmina desgrasada, pH 7.0, con el menor volumen posible.

Determinación de la concentración de proteína. La concentración de concentración de proteína se determinó por medio del método de Lowry (Lowry, 1951) con algunas modificaciones (Mahuran *et al.*, 1983). Las muestras fueron tratadas con 0.4% (p/v) desoxicolato de sodio (DOC) y se continuó con el método tradicional. La absorbancia de las muestras se determinó a 660 nm usando albúmina sérica de bovino (BSA) como estándar. Para conocer la concentración de proteína en mg/mL, se utilizó el método de regresión lineal o mínimos cuadrados (Waterborg *et al.*, 1984).

Producción mitocondrial de peróxido de hidrogeno. La cuantificación de la producción de H₂O₂ se realizó con el kit Amplex® Red (Invitrogen, Molecular Probes, EE. UU.), siguiendo las instrucciones del fabricante. Se utilizaron 30 µg de

proteína mitocondrial en presencia de 600 μ M de 2, 6-Dimethoxy-1, 4-benzoquinona (DBQ), 10 mM de Citocromo c de corazón de caballo (SIGMA C2037) y 3 mM NADH. La reacción se inició 10 min después de haber añadido el NADH y se incubó por 30 min. La fluorescencia se determinó en un lector Varioskan LUX (Thermo Scientific) a 530-590nm.

Solubilización de los supercomplejos y complejos mitocondriales. Para solubilizar las membranas mitocondriales liberando así los complejos y supercomplejos respiratorios embebidos en la membrana interna, las mitocondrias se incubaron en presencia de diferentes concentraciones del detergente digitonina (0.5, 1, 2, 3, 5 g/g proteína), en una solución de 50 mM Bis-Tris, 500 mM de ácido aminocaproico, pH 7.0, 10 mM succinato y 10 mM de ATP; el detergente (solucion stock 500 mg/mL en DMSO) se añadió mientras la solución se agita lentamente. La solución se incubó durante 30 min a 4°C, posteriormente se ultracentrifugó a 100,000 g durante 35 min a 4°C. Los complejos y supercomplejos respiratorios se recuperaron en el sobrenadante (Schägger *et al.*, 1991; Esparza-Perusquía *et al.*, en preparación).

Electroforesis en condiciones nativas (BN-PAGE y hrCN-PAGE). Los complejos respiratorios de las mitocondrias de *U. maydis* se resolvieron por medio de la electroforesis azul en condiciones nativas (BN-PAGE) y la electroforesis clara en condiciones nativas (hrCN-PAGE) en geles en gradiente de poliacrilamida (4 – 10%) (Schägger *et al.*, 1991; Wittig *et al.*, 2006). Para la BN-PAGE el amortiguador del ánodo contenía 50 mM Bis-Tris/HCl, pH 7.0; el amortiguador del cátodo contenía 50 mM tricina, 15 mM Bis-Tris, pH 7.0 y el colorante aniónico Coomassie® G250 (0.02%). Para la hrCN-PAGE el amortiguador del ánodo contenía 25 mM imidazol-HCl, pH 7.0; el amortiguador del cátodo contenía 50 mM tricina, 7.5 mM imidazol, pH 7.0, 0.05% (p/v) desoxicolato de sodio (DOC) y 0.01% (p/v) *n*-dodecil β -D-maltósido (DDM) (Wittig *et al.*, 2007). Se utilizó como marcador del frente de corrida al colorante rojo de Ponceau. Se aplicaron 100 μ g de proteína por carril y las condiciones de la corrida electroforética fueron 30 V durante 16 horas a 4°C.

El peso molecular de los complejos respiratorios y supercomplejos fue determinado a partir de su movilidad electroforética y el revelado de su actividad catalítica en gel, utilizando como estándares de peso molecular los complejos mitocondriales de corazón de bovino solubilizados con digitonina en las mismas condiciones que los complejos de *U. maydis*.

Actividad en gel de los complejos y supercomplejos respiratorios. La actividad de los complejos respiratorios se realizó como los reportó Wittig *et al.*, (2007).

**Actividad de NADH deshidrogenasa.* Al concluir la electroforesis nativa, los geles se incubaron en una solución de 10 mM tris-HCl pH 7.4, 0.5 mM NADH como sustrato y 1.2 mM bromuro de 3-[4,5-dimetiltiazol-2-yi]-2,5-difeniltetrazolio (MTT) como agente oxidante. En esta reacción el NADH es oxidado por la flavina unida a las deshidrogenasas y ésta última reduce directamente al tetrazolio. Mediante esta tinción es posible detectar la actividad del complejo I y de las deshidrogenasas alternas. La presencia de actividad se observó como un depósito violeta y la reacción se detuvo con una solución de 40% de metanol y 10% de ácido acético (Wittig *et al.*, 2007).

**Actividad de succinato deshidrogenasa.* Los geles se incubaron en una solución de 10 mM KH_2PO_4 , pH 7.4, 10 mM succinato, 0.19 mM 5-metilfenazinium metil sulfato (PMS), 5 mM MTT y 4.5 mM EDTA. La presencia de actividad se observó como un precipitado violeta y se detuvo la reacción con una solución de 40% de metanol y 10% de ácido acético (Wittig *et al.*, 2007).

**Actividad de citocromo c oxidasa.* La actividad en gel del complejo IV se determinó utilizando 3, 3'-diaminobenzidina (DAB) como agente reductor y citocromo c como donador de electrones (Zerbetto *et al.*, 1997). El gel se incubó en una solución de 10 mM KH_2PO_4 pH 7.4, 4.66 mM DAB, 4 mg citocromo c y 1.8 KU catalasa, ésta última se añade para evitar que peróxidos contaminantes oxiden a la diaminobencidina, evitando así que la reacción sea inespecífica. La presencia de

actividad se observó como un depósito marrón. La reacción se detuvo con una solución de 40% (v/v) metanol y 10% (v/v) ácido acético (Wittig *et al.*, 2007).

**Actividad de ATPasa.* La ubicación en el gel de los oligómeros del complejo V fue determinada por medio de su actividad de hidrólisis de ATP. El gel se incubó en una solución de 50 mM de glicina, 10 mM MgCl₂, 0.2% (p/v) Pb(NO₃)₂, 5 mM ATP, pH 8.0; ajustando el pH con trietanolamina para evitar la precipitación inespecífica del plomo. La presencia de actividad de hidrólisis de ATP se observó como un depósito blanco del fosfato de plomo, sobre un fondo oscuro (Jung *et al.*, 2000). La reacción se detuvo con una solución de 40% (v/v) metanol y 10% (v/v) ácido acético (Wittig *et al.*, 2007).

Purificación del dímero y del monómero de la F₁F₀-ATP sintasa de U. maydis. Los supercomplejos y complejos respiratorios solubilizados con digitonina (2:1 digitonina/proteína) se aislaron por medio de un gradiente continuo de sacarosa de 0.5 - 1.5 M, en presencia de 20 mM KCl, 15 mM tris-base, pH 7.4 y 0.2% (p/v) digitonina; se añadieron aproximadamente 48 mg de proteína (3.5 mL del solubilizado) a 24 mL del gradiente y se centrifugaron a 131,000 g durante 16 h a 4°C. Se colectaron fracciones de 500 µL; la densidad de cada fracción se determinó por medio de un densitómetro ATAGO N1 (Brix 0~32%). La presencia de los supercomplejos se determinó por medio de una electroforesis nativa (hrCN-PAGE). Las fracciones de interés se equilibraron con 30 mM HEPES, 5% (v/v) glicerol, pH 8.0 y se concentraron en filtros Amicon de 10 K (Esparza-Perusquía *et al.*, 2017).

Ensayo enzimático de la actividad de ATPasa. La actividad de ATPasa del complejo V se ensayó en presencia de un sistema regenerador de ATP acoplado a la oxidación del NADH; el medio de reacción contenía 30 mM HEPES, pH 8.0, 5 mM fosfoenolpiruvato (PEP), 1 mM Mg²⁺ (MgSO₄) libre, 50 unidades de la piruvato cinasa (PK), 30 unidades de la lactato deshidrogenasa (LDH), 90 mM KCl, 0.01% (p/v) DDM, 150 µM NADH y 100 µg de muestra; se empleó una solución equimolar de Mg-ATP.

La reacción de hidrólisis de ATP se inició agregando el ATP a una celda de cuarzo la cual contenía todo el sistema regenerador y al V_1 o V_2 del complejo V. Se realizaron lecturas cada 0.5 seg por 15 min a 340 nm. Los resultados se analizaron tomando en cuenta el coeficiente de extinción del NADH ($\epsilon = 6.22 \text{ mM}^{-1}\text{cm}^{-1}$) y la región lineal del trazo espectrofotométrico (Penefsky *et al.*, 1960; Andrianaivomananjaona *et al.*, 2011; Esparza-Perusquía *et al.*, 2017).

Sensibilidad a la oligomicina. En los ensayos enzimáticos también se determinó la sensibilidad a la oligomicina de la F_1F_0 -ATP sintasa. Debido a que la oligomicina es un inhibidor lento pero fuertemente unido, los oligómeros de la F_1F_0 -ATP sintasa fueron incubados en el medio de reacción durante 5 min en presencia de diferentes concentraciones del inhibidor (0.1, 0.25, 0.5, 1, 5, 10, 20 $\mu\text{g}/\text{mg}$ proteína). Al término de este tiempo la reacción fue iniciada como se describió arriba (Esparza-Perusquía *et al.*, 2017).

Estabilidad térmica. Para determinar la termoestabilidad del V_1 y V_2 la F_1F_0 -ATP sintasa se incubó la enzima por 15 min a diferentes temperaturas, al término de este tiempo la reacción de hidrólisis de Mg-ATP se realizó a 25°C como se describió en el apartado *ensayo enzimático* (Esparza-Perusquía *et al.*, 2017).

Análisis Estadísticos. Los datos de la actividad enzimática se procesaron con un análisis de regresión no lineal, robusto, ponderado, usando el programa Systat Software, Inc., versión 10.0, a partir de un promedio de 3 réplicas de 5 a 7 preparaciones independientes. Las imágenes derivadas de la tinción de las proteínas con azul de Coomassie® R250 de los geles de Tricina-SDS-PAGE para la cuantificación de la F_1F_0 -ATP sintasa fueron escaneadas y la intensidad de las bandas se determinó utilizando el programa My Image Analysis 2.0 (ThermoScientific). El ajuste de todos los datos cinéticos se realizó con el programa Sigma Plot versión 10.0.



"Mitochondrial Membranes 1" Odra Noel

Resultados

"Que Dios la lleve y la virgen la acompañe" Dr. Antonio Peña

5. RESULTADOS

La construcción de los plásmidos y la transformación para generar la cepa mutante Δg se realizó en el Instituto de Microbiología de la Universidad Heinrich-Heine en Düsseldorf, Alemania, bajo la asesoría del Dr. Michael Feldbrügge.

Construcción y clonación de los plásmidos UF y DF. Se amplificaron los fragmentos UF (1.06 kpb) y DF (1.36 kpb), flanqueando al gen ATP20, el cual codifica para la subunidad *g*, mediante un PCR punto final acoplado a la polimerasa Phusion (PHU), tomando como molde al gDNA de la cepa WT (Figura 22A). Dichas secuencias fueron insertadas en el plásmido TOPO (pCR2.1-TOPO vector. Invitrogen Cat. 45-0641) usando un Topo TA Cloning Kit. Las células competentes TOP10 de *E. coli* fueron transformadas con los plásmidos UF (pUMa_1706) y DF (pUMa_1705) para obtener múltiples copias idénticas y aislar el DNA. Una vez obtenido el DNA plasmídico se realizó una digestión controlada mediante enzimas de restricción, donde se verificó el estado del plásmido y la orientación de la secuencia; finalmente, el DNA se secuenció para comprobar que no tenía mutaciones inespecíficas y posteriormente se continuó con el proceso de construcción del plásmido knock-out (KO).

Construcción del plásmido Knock-out (KO). La mutación se realizó como lo describió Brachmann *et al.*, (2004), digiriendo los plásmidos UF y DF con 20 unidades de las enzimas de restricción *SfiI* y *ScaI-HF*, los productos de la restricción para UF y DF que nos interesan corresponden a 3.1 y 3.0 kpb, los sitios para cortar el pUMa_198 y liberar completamente a HygR son reconocidos por la enzima *SfiI* liberando un fragmento de 1.8 kpb (Figura 22B).

Al finalizar la digestión, las bandas correspondientes a UF, DF e Hyg se purificaron del gel. Los fragmentos obtenidos se colocaron en una reacción de ligación manteniendo la relación 1:1:3 (UF:DF:HygR). Al finalizar la ligación se llevó a cabo la transformación y clonación en *E.coli*.

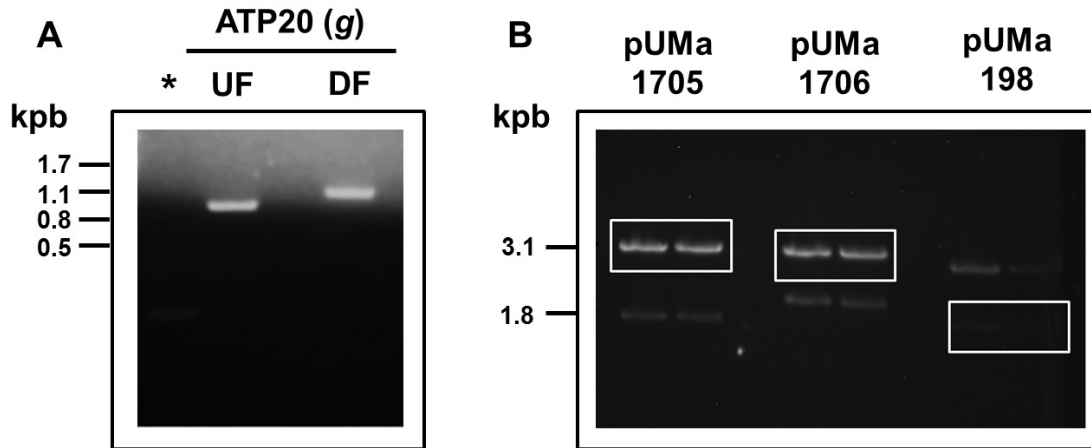


Figura 22. Amplificación de los fragmentos UF y DF para la construcción del plásmido KO. (A) Los amplificadores UF (1.06 kpb) y DF (1.36 kpb) se resolvieron en un gel de agarosa al 1% en presencia de bromuro de etidio. El control negativo (*) no contiene oligonucleótidos. (B) Los plásmidos fueron digeridos con las enzimas *SfiI-ScaI*-HF. Se obtuvieron los fragmentos de 3.1 y 3.0 kpb para UF y DF respectivamente y 1.88 kpb para el HygR.

Verificación del plásmido *Knock-out* (KO). Para verificar la correcta ligación en el plásmido KO, el DNA bacteriano fue extraído y digerido con la enzima *SfiI*, la cual produce dos bandas que corresponden al HygR con un tamaño de 1.88 kpb y al resto del plásmido con un tamaño de 6.37 kpb (Figura 23A).

Los plásmidos se analizaron en la unidad de Secuenciación de DNA Ludwig-Maximilians Universität München, Alemania (Sequencing LMU <http://www.gi.bio.lmu.de/sequencing>) utilizando los oligonucleótidos MF167 y MF168, los cuales amplifican parte del HygR y los oligonucleótidos universales M13R y M13F, que reconocen una parte de la secuencia del vector TOPO; se obtuvieron aproximadamente 1000 pb de cada uno sin mutaciones inespecíficas.

Transformación química de Ustilago maydis. Una vez que se secuenció el plásmido KO para verificar su correcta construcción, se linealizó mediante una digestión controlada con la enzima *SwaI*. Este plásmido lineal es usado para la transformación química de *U. maydis* como DNA exógeno (Figura 23B). La transformación significa que el DNA digerido se incorporó a los protoplastos y se llevó a cabo la recombinación homóloga, donde el DNA endógeno se intercambia por el DNA exógeno, conservando las regiones UF y DF del DNA original.

Cabe mencionar que *U. maydis* requiere que los fragmentos UF y DF sean de 1000 pb aproximadamente para que se lleve a cabo el reconocimiento eficiente de las secuencias durante la recombinación homóloga. Para comprobar la transformación de los protoplastos, estos son esparcidos en una caja de YPD agar suplementado y se incubaron a 30°C por 7 días hasta observar el crecimiento de la cepa (Figura 23C).

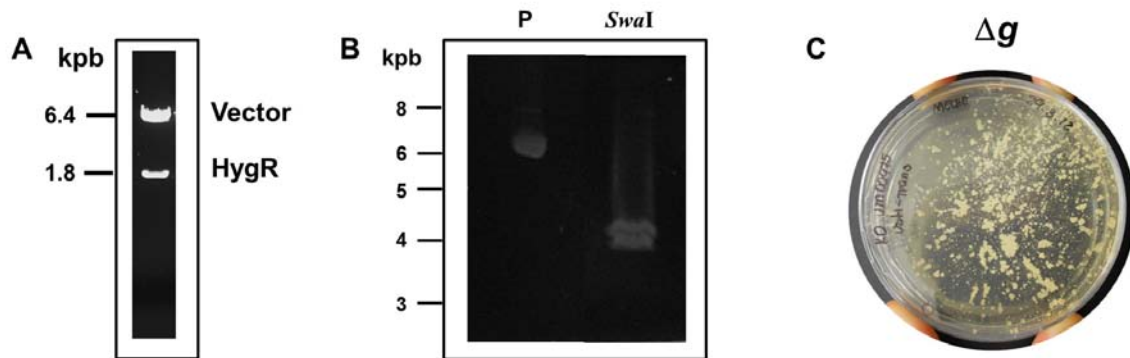


Figura 23. Transformación de *U. maydis* con el DNA exógeno. (A) El plásmido se digirió con *SfiI* y se obtuvieron dos fragmentos, uno de 1.88 kpb correspondiente al HygR y otro de 6.4 kpb correspondiente al resto del plásmido. (B) El plásmido fue digerido con *SwaI* obteniendo el fragmento UF-Hyg-DF (3.98 kpb). P= plásmido no linealizado y *SwaI*= plásmido digerido. (C) Las células transformadas después de 7 días de crecimiento sembradas en medio YPD agar suplementado con higromicina para la selección de la cepa mutante. El crecimiento sugiere la incorporación del gen de resistencia a higromicina y la pérdida de la subunidad *g*.

Comprobación de la cepa mutante Δg . Se tomaron diferentes colonias de las cepas transformadas, se resembraron en medio YPD a 28°C por 48 horas. Se aisló el gDNA de las cepas seleccionadas para comprobar por PCR que el gen ATP20 fue sustituido por el HygR usando los oligonucleótidos P1 y P2 y como control negativo el gDNA de la cepa WT. Si las bandas tienen el mismo tamaño que derivado de la cepa WT, se descartan, ya que el oligonucleótido P2 está hecho diseñado directamente sobre una secuencia del gen, lo que demuestra que en esas muestras el gen no fue sustituido por el HygR. Los productos de PCR separaron en un gel al 0.8% agarosa, 1x-TBE, BrEt (Figura 24A).

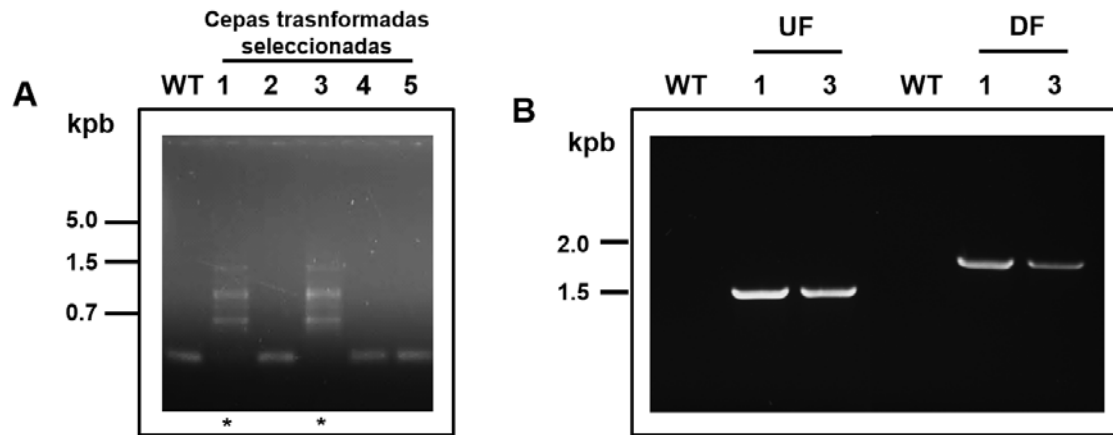


Figura 24. Comprobación de la cepa mutante Δg . (A) Las muestras 1 y 3 presentaron diferente patrón electroforético a la cepa WT, lo que se comprueba que el gen ATP20 fue sustituido por el gen HygR. (B) Se comprobó por PCR la integridad de los flancos UF y DF, ambos unidos al gen HygR. Se utilizó como control negativo el gDNA WT. En la figura se muestran dos amplificados de 1.5 y 1.7 kpb para UF y DF respectivamente de las cepas positivas 1 y 3.

Las muestras 1 y 3 presentaron un patrón electroforético diferente al del gDNA WT, lo que sugiere la incorporación del gen HygR. Dichas muestras se usaron para realizar otro ciclo de PCR con los oligonucleótidos U1 y D3 (ambos cuentan con aproximadamente 20 pb dentro de gDNA pero fuera de las construcciones UF y DF, respectivamente), así como los oligonucleótidos MF167 y MF168, los cuales se alinean 20 pb al inicio y 20 pb al final del gen HygR, respectivamente. Se observó un amplificado de aproximadamente 1.5 kpb para el UF y 1.7 kpb para el DF. El DNA de las muestras se resolvió en un gel de agarosa al 8% (Figura 24B), el gDNA mutante fue secuenciado para demostrar que fue sustituido por HygR y que no había otras mutaciones inespecíficas.

Southern Blot. Para el análisis por Southern Blot, se realizó un PCR con dNTP's marcados con digoxigenina, la cual permite su detección por medio de anticuerpos específicos marcados con fosfatasa alcalina y detectados con CDP-Star. Se identificaron bandas correspondientes a 8.3 kpb para la cepa WT, 5.07 y 4.1 kpb para la cepa mutante Δg (Figura 25). Se obtuvieron 5 muestras positivas para la mutante, las cuales fueron cultivadas nuevamente en medio YPD y conservadas en glicerol esteril (25%) a -70°C . Finalmente después de 24 horas se sembraron en un medio sólido y se cultivaron a 28°C durante 24 horas.

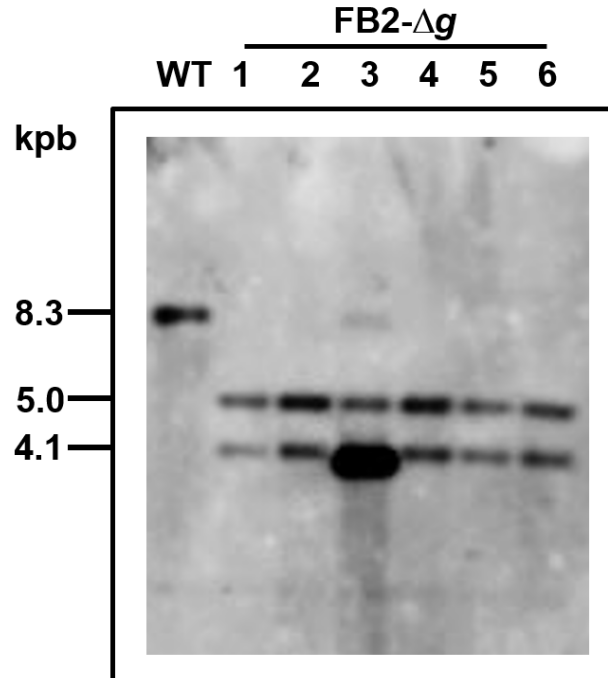


Figura 25. Southern Blot. Detección de los fragmentos de 5.07 y 4.1 kpb para la cepa mutante y se utilizó como control negativo el gDNA WT observando una banda de 8.3 kpb. En el primer carril se encuentra la cepa WT y 5 clonas positivas para la Δg .

Curva de crecimiento. Se analizó la curva de crecimiento de la cepa WT y Δg a partir del inóculo de 40 U D.O. de células/L de medio de cultivo y se monitoreó su crecimiento cada 2 horas en medio líquido YPD, medio mínimo con etanol (MM-EtOH) y medio mínimo con glucosa (MM-glucosa).

- *Crecimiento en medio YPD.* Se observó que durante la fase logarítmica de crecimiento (8 horas) las cepas WT y Δg presentaron un comportamiento similar; se tomaron lecturas a 600 nm cada 2 horas y se calculó el tiempo de duplicación celular, observando para la WT un valor de 2 horas con 7 min y para la Δg de 2 horas con 45 minutos. Sin embargo, a partir de las 20 horas podemos ver un desfase en el crecimiento de la cepa Δg , obteniendo una absorbancia para la cepa WT de 1.81 D.O. (Figura 26, círculos llenos) y de 1.31 para la cepa Δg (Figura 26, círculos vacíos). Las células se fijaron con formaldehído y se observaron al microscopio para verificar su estructura. El tamaño de la WT en la fase logarítmica fue de $18.8 \pm 1.8 \mu\text{m}$ mientras que la cepa Δg fue más grande ($28.1 \pm 6.5 \mu\text{m}$) (Figuras 29A y 29B); en la fase estacionaria fue de 22.6 ± 3.9 y $30.0 \pm 5.9 \mu\text{m}$

respectivamente (Figuras 30A y 30B). Otro parámetro útil para la caracterización de las cepas mutantes es determinar su capacidad de acidificar el medio. En este caso, ambas cepas producen un cambio en el pH de 6.63 (fase logarítmica) a 6.0 (fase estacionaria) (Figura 26). Sin embargo, la cepa Δg (Figura 65, triángulos vacíos) inicia la acidificación del medio inmediatamente, mientras que la WT (Figura 26, triángulos llenos) muestra un periodo de lenta acidificación (0 - 5 hrs). Esto sugiere que la cepa Δg es más grande y es capaz de acidificar el medio ligeramente más rápido que la WT.

Aunque no es clara la relación entre el tamaño de la célula con la velocidad de acidificación del medio, ambos fenómenos pueden estar relacionados con una posible aceleración del catabolismo.

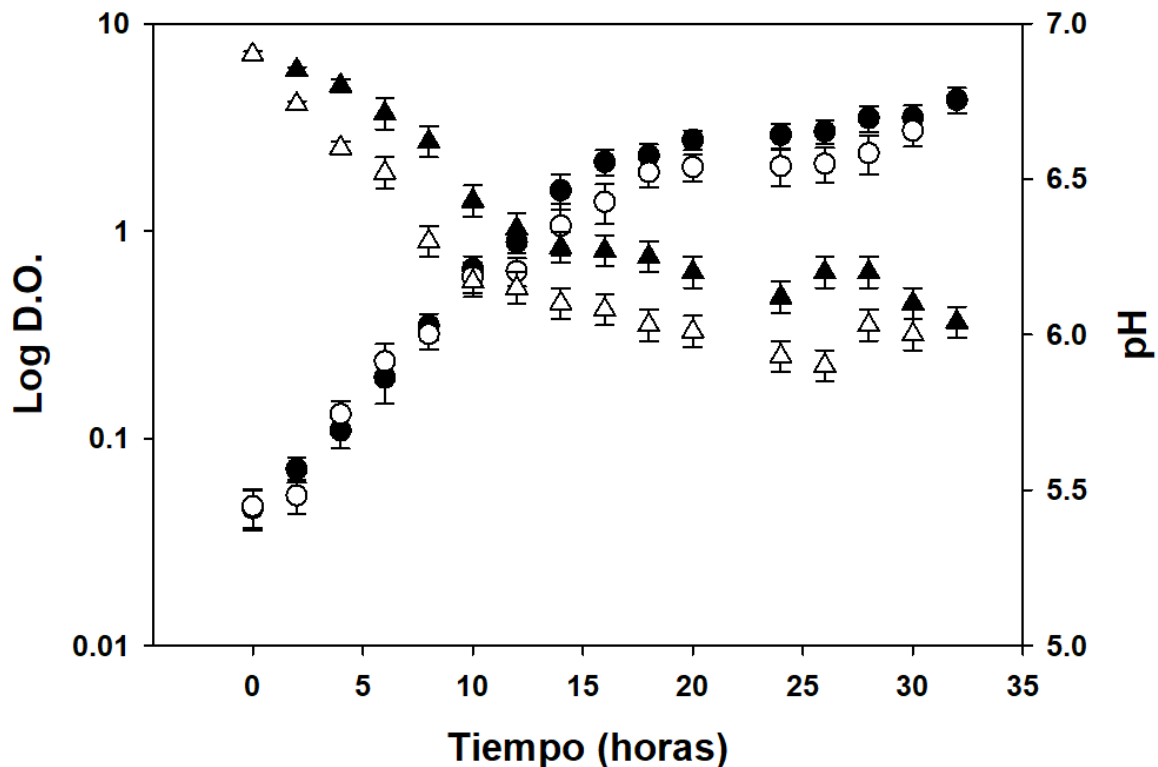


Figura 26. Curva de crecimiento en YPD. Las cepas WT (●) y Δg (○) se cultivaron en un medio de YPD y se determinó su crecimiento a 600nm. Se observó un comportamiento similar durante la fase logarítmica y un ligero decremento del crecimiento para la Δg en la fase estacionaria. También se determinó el pH durante las diferentes fases del crecimiento para las cepas WT (▲) y Δg (△), donde se observó una acidificación del medio de 6.63 a 6.0 respectivamente. Los datos son el promedio de tres repeticiones de cuatro preparaciones independientes. Las barras de error representan S.D.

Para tener una aproximación al efecto de la mutante sobre su adaptación metabólica, se decidió estudiar el efecto de la fuente de carbono sobre el crecimiento.

-Crecimiento en MM-EtOH. Se observó que el crecimiento de ambas cepas durante la fase logarítmica es similar (Figura 27); también se observó que el crecimiento en este medio es más lento para ambas cepas siendo el tiempo de duplicación celular de la WT de 2 horas 43 minutos (Figura 27, círculos llenos) y para la Δg de 3 horas 18 minutos (Figura 27, círculos vacíos). Las células se fijaron con formaldehído y se observaron al microscopio para verificar su estructura.

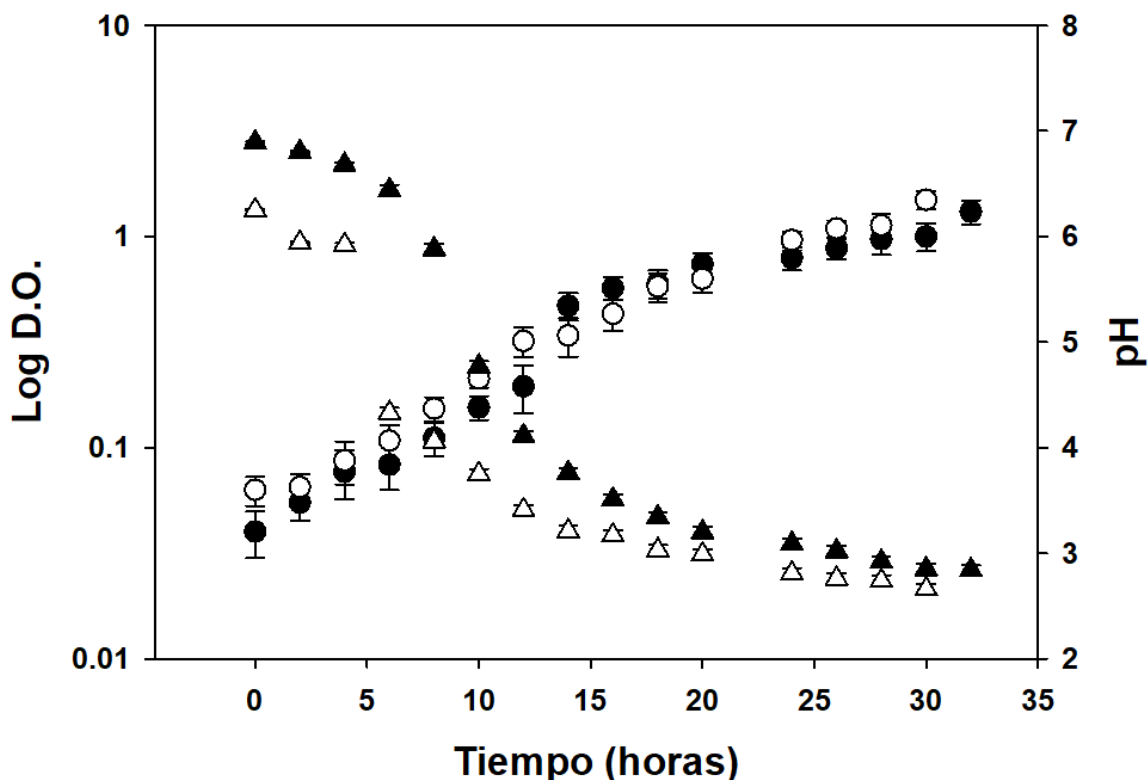


Figura 27. Curva de crecimiento en MM-EtOH. Las cepas WT (●) y Δg (○) se cultivaron en un medio mínimo con 1% de etanol y se determinó su crecimiento a 600 nm. Se observó un comportamiento similar durante el crecimiento en ambas cepas y se determinó el pH de las cepas WT (\blacktriangle) y Δg (\triangle) en los tiempos señalados. Los datos son el promedio de tres repeticiones de cuatro preparaciones independientes. Las barras de error representan S.D.

El tamaño de la cepa WT fue de $19.9 \pm 1.9 \mu\text{m}$ y para la cepa Δg de $29.3 \pm 3.7 \mu\text{m}$ en la fase logarítmica (Figuras 29C y 29D) y en la fase estacionaria de 26.1 ± 7.2 y $39.2 \pm 10.4 \mu\text{m}$, respectivamente (Figuras 30C y 30D). Ambas cepas son

capaces de producir un cambio en pH del medio de 6.63 (fase logarítmica) a 2.68 (fase estacionaria) (Figura 27). Debido a que la cepa Δg es más activa en la acidificación del medio, nuevamente se sugiere un metabolismo más activo respecto a la WT.

-Crecimiento en MM-Glucosa. El crecimiento de ambas cepas durante la fase logarítmica es similar (Figura 28). La WT tiene un tiempo de duplicación de 3 horas 8 minutos (Figura 28, círculos llenos) y la Δg de 3 horas 17 minutos (Figura 28, círculos vacíos). El tamaño de la cepa WT fue de $26.40 \pm 7.96 \mu\text{m}$ mientras que para la cepa Δg fue de $37.24 \pm 12.07 \mu\text{m}$ en la fase logarítmica (Figuras 29E y 29F) y en la fase estacionaria fue de 41.37 ± 5.25 y $46.25 \pm 8.41 \mu\text{m}$, respectivamente (Figuras 30E y 30F).

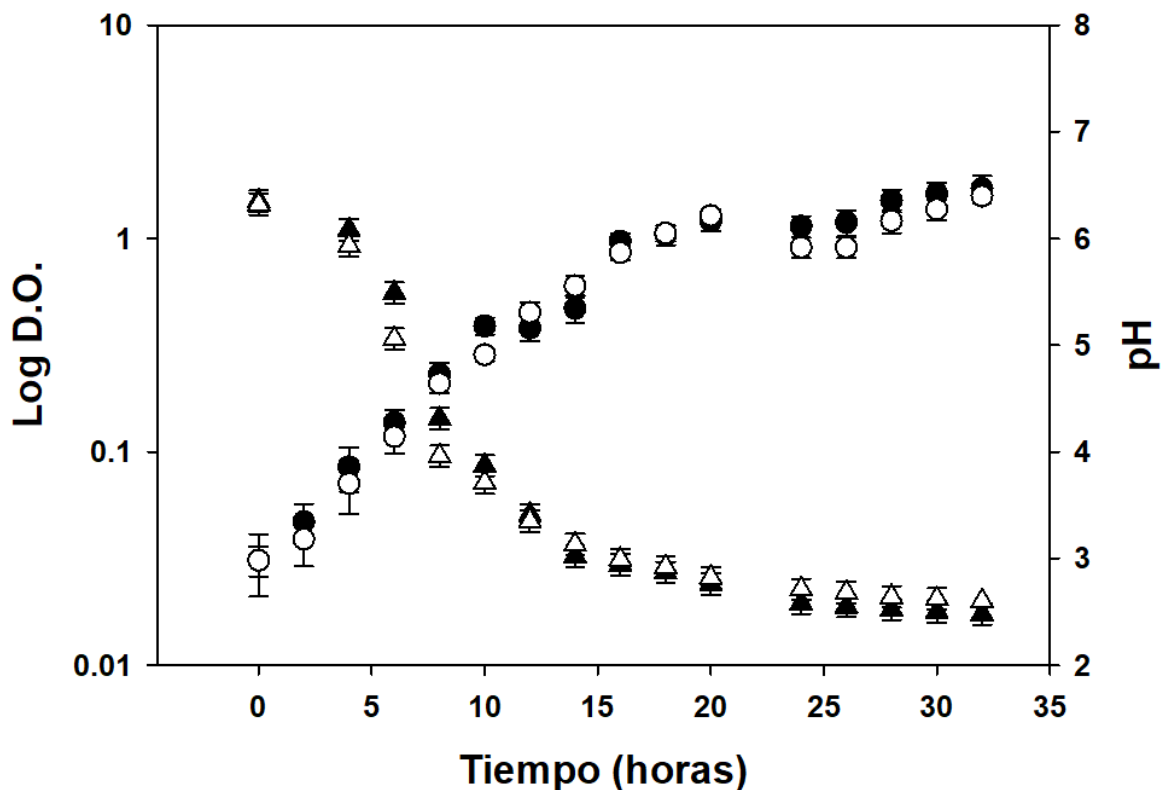


Figura 28. Curva de crecimiento en MM-Glucosa. Las cepas WT (●) y Δg (○) se cultivaron en un medio mínimo con 1% de Glucosa y se determinó su crecimiento a 600nm. Se observó un comportamiento similar durante el crecimiento en ambas cepas y se determinó el pH de las cepas WT (▲) y Δg (△) durante la curva de crecimiento. Los datos son el promedio de tres repeticiones de cuatro preparaciones independientes. Las barras de error representan S.D.

Ambas cepas producen un cambio en el pH de 6.35 (fase logarítmica) a 2.48 (fase estacionaria) (Figura 28). En este caso, la velocidad de acidificación es similar en ambas cepas, lo que sugiere que el aumento del tamaño de la cepa Δg no es el único factor que acelera el catabolismo con la subsecuente acidificación.

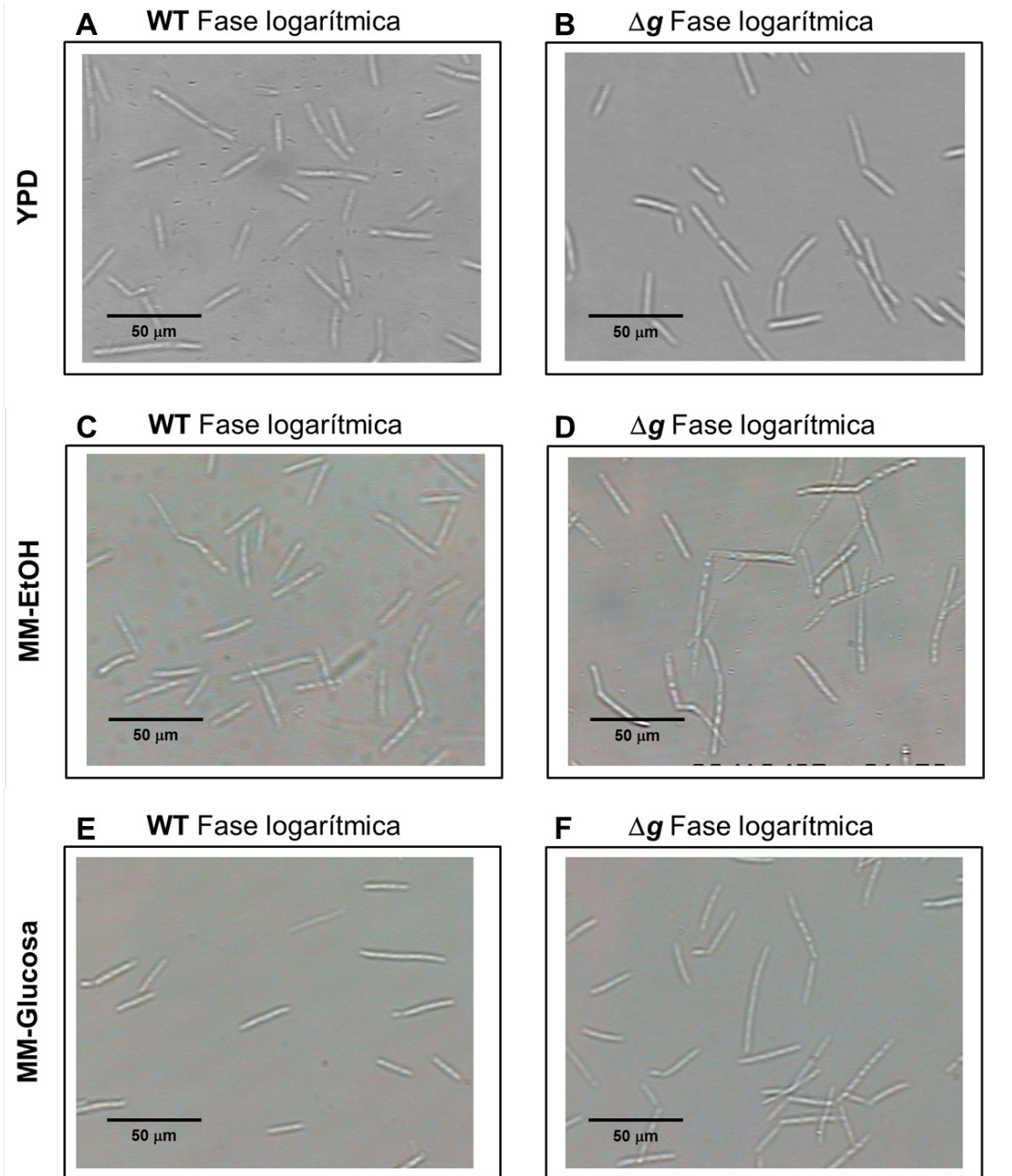


Figura 29. Microscopia de las células WT y Δg (fase logarítmica). Microscopia de las células WT y Δg en la fase logarítmica de crecimiento con un objetivo 40x, dilución 1:100. **A)** WT en YPD. **B)** Δg en en YPD. **C)** WT en MM-EtOH. **D)** Δg en en MM-EtOH. **E)** WT en MM-Glucosa. **F)** Δg en en MM-Glucosa.

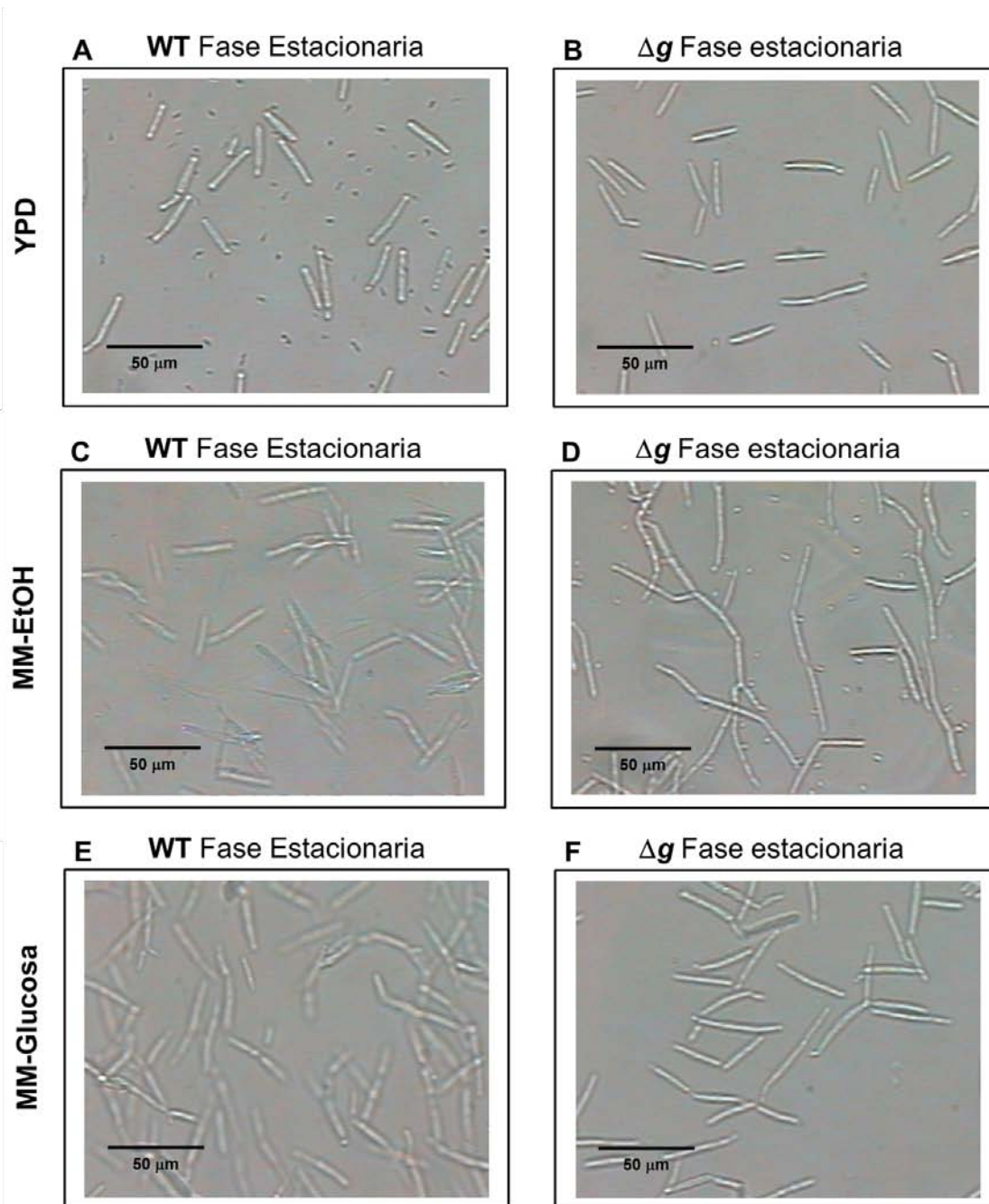


Figura 30. Microscopia de las células WT y Δg (fase estacionaria). Microscopia de las células WT y Δg en la fase Estacionaria de crecimiento con un objetivo 40x, dilución 1:100. **A)** WT en YPD. **B)** Δg en en YPD. **C)** WT en MM-EtOH. **D)** Δg en en MM-EtOH. **E)** WT en MM-Glucosa. **F)** Δg en en MM-Glucosa.

Aunado a esto se determinó la resistencia de la cepa Δg a la dilución. La figura 31 muestra el crecimiento a las 48 horas en medio sólido. Se observa que el fenotipo de crecimiento en medios respiratorios, como el MM-EtOH, es similar aún con la eliminación del gen ATP20. Esto sugiere que la mutación no afecta el crecimiento, apoyando lo que se observó en las figuras 25-27, tampoco repercute en la viabilidad de las células para duplicarse y formar colonias.

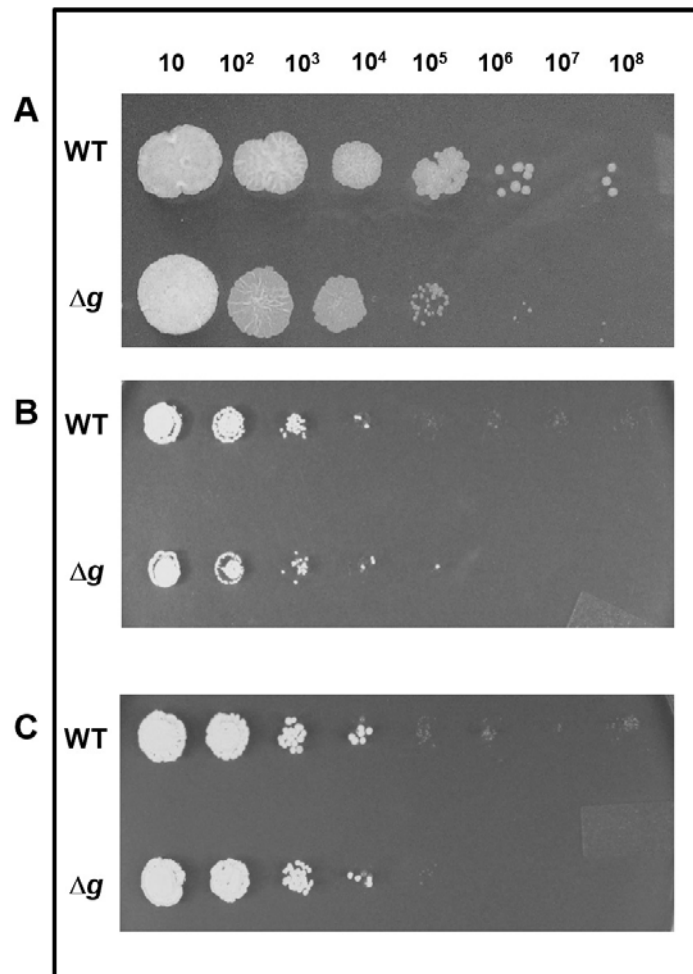


Figura 31. Diluciones seriadas (1:10) de las cepas WT y Δg de *U. maydis*. Se realizaron diluciones seriadas de las cepas WT y Δg en diferentes medios de crecimiento (A) YPD, (B) MM-EtOH y (C) MM-Glucosa. Las células se cultivaron por 48 horas a 28°C.

Análisis de la arquitectura mitocondrial. Como ya se mencionó, se sabe que el dímero de la F_1F_0 -ATP sintasa (V_2) está involucrado en el plegamiento de las crestas mitocondriales. Dentro de los objetivos se planteó observar por microscopía de transmisión electrónica la ultraestructura de las mitocondrias de *U. maydis*. La

microscopía electrónica se realizó en el Instituto de Biotecnología de la UNAM, mediante la técnica LR White.

Las mitocondrias de la cepa WT de *U. maydis* (Figura 32A) así como la Δg (Figura 32B) presentan crestas lamelares con la misma morfología, por lo que la eliminación de la subunidad *g* no modifica la ultraestructura mitocondrial. También podemos sugerir que la eliminación de la subunidad *g* no afecta la formación del dímero. Por otro lado las micrografías mostraron que la cepa Δg presenta mitocondrias más grandes, lo que podría ser respuesta a la modificación genética.

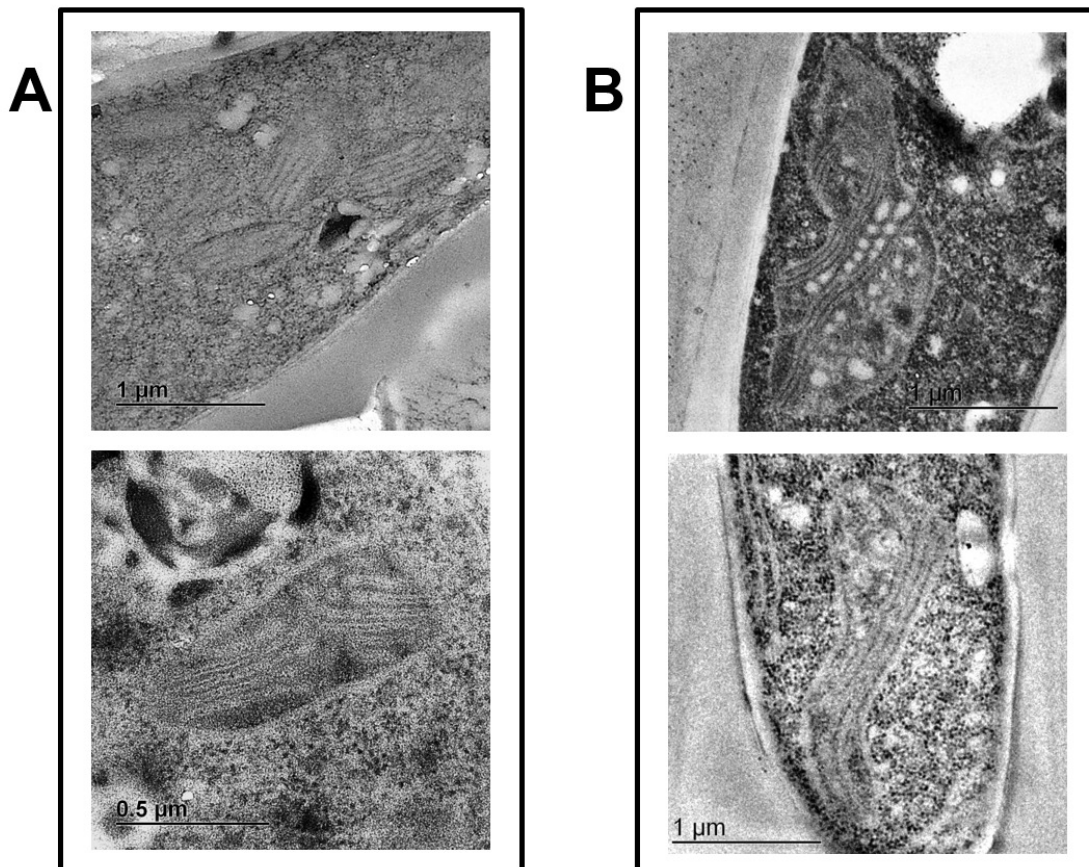


Figura 32. Ultraestructura de las células de *U. maydis*. (A) Imágenes de las mitocondrias de *U. maydis* de la WT y (B) Δg . Ambas cepas muestran crestas de tipo lamelares y sin morfologías anómalas.

Consumo de oxígeno. Las células WT y Δg se cultivaron en diferentes medios de carbono como YPD, MM-EtOH y MM-glucosa, y se tomaron muestras a las 8 horas (fase logarítmica) y a las 24 horas (fase estacionaria) de crecimiento.

Para las células cultivadas en YPD, durante la fase logarítmica de crecimiento se determinó que el consumo de oxígeno por las cepas WT y Δg , fue alrededor de 108 natgO/mg/min y 120 natgO/mg/min respectivamente. Al bloquear el transporte de electrones a nivel del complejo IV con 1 mM de KCN, se eliminó la respiración en las células WT al 100% (Figura 33A); por el contrario, en las células Δg el KCN sólo disminuyó en un 10% la velocidad del consumo de oxígeno (108 natgO/min) y fue totalmente inhibido con 10 μ M de *n*-octil-galato (nOg) (Figura 33B), lo que nos indica la actividad de la oxidasa alterna en las cepas Δg .

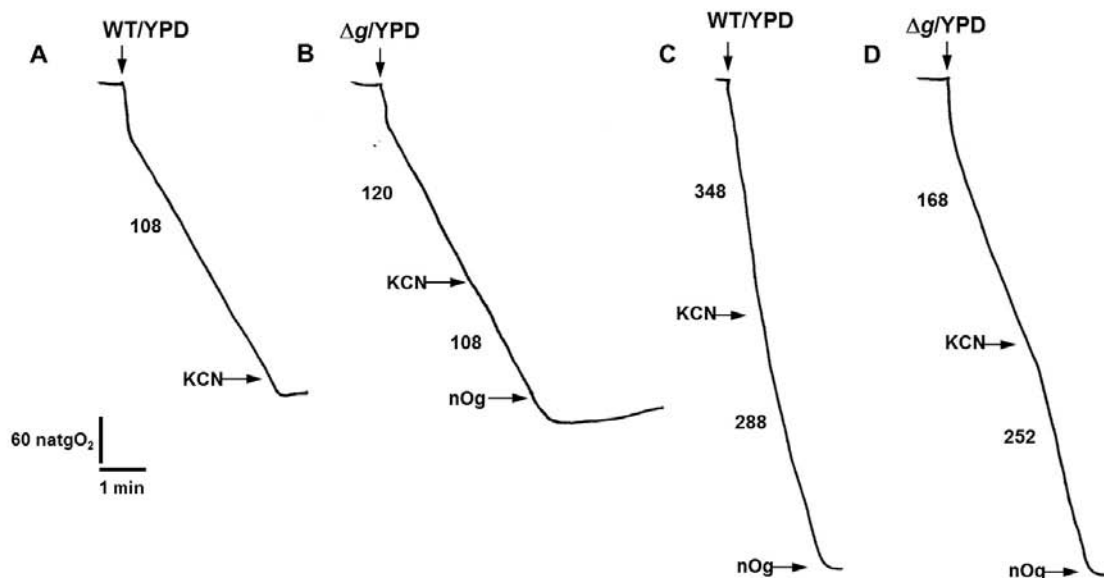


Figura 33. Consumo de oxígeno de las células cultivadas en medio rico YPD. Las células fueron obtenidas de la fase logarítmica de crecimiento WT (A) y Δg (B) y de la fase estacionaria WT (C) y Δg (D) y se incubaron en 10 mM de KH_2PO_4 pH 7.4 y se determinó el consumo de oxígeno con un electrodo tipo Clark como se describió en métodos, donde se señala fue añadido 1 mM KCN o 10 μ M de nOg. Los datos son el promedio de tres repeticiones de cuatro preparaciones independientes.

Por otro lado, en las células cosechadas en la fase estacionaria, el consumo de oxígeno para la WT fue de 348 natgO/mg/min (Figura 33C) y de 168 natgO/mg/min para la Δg (Figura 33D). En ambos casos el KCN no inhibió totalmente la respiración; para el caso de la WT se observó una inhibición parcial

de la velocidad del consumo de oxígeno (288 natgO/mg/min) y para la cepa incluso Δg un aumento de 252 natgO/mg/min, confirmando la actividad de la AOX sensible al nOg en ambas cepas en la fase estacionaria.

En MM-EtOH, el consumo de oxígeno en la fase logarítmica de la WT y de la mutante Δg fue de 72 natgO/mg/min (Figura 34A y B). Al igual que para las células recuperadas del cultivo en YPD, el transporte de electrones fue bloqueado a nivel del complejo IV con 1 mM de KCN, eliminando la respiración en las células de la cepa WT, mientras que en las células Δg el KCN sólo disminuyó la velocidad del consumo de oxígeno a 24 natgO₂/mg/min (66%) y fue totalmente inhibido con 10 μ M de nOg. Lo anterior también sugiere la presencia de la oxidasa alterna en la cepa Δg durante la fase logarítmica. Para las células recuperadas en la fase estacionaria el consumo de oxígeno para la WT fue de 276 natgO/mg/min (Figura 34C) y 324 natgO/mg/min (Figura 34D) para la Δg , esta fue sensible tanto a KCN como a nOg.

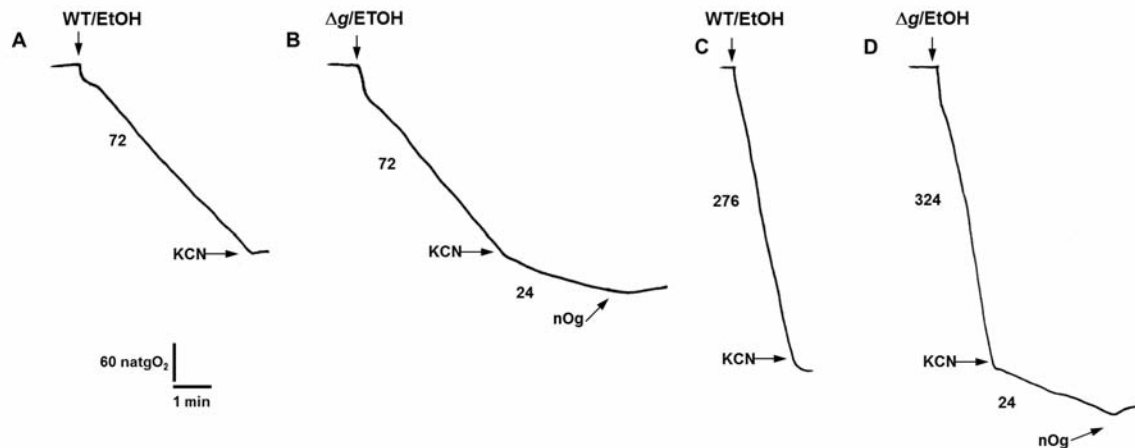


Figura 34. Consumo de oxígeno de las células cultivadas en MM-EtOH. Las células fueron obtenidas de la fase logarítmica de crecimiento de la WT (A) y Δg (B) y de la fase estacionaria de la WT (C) y Δg (D), se incubaron en 10 mM de KH₂PO₄ pH 7.4 y se determinó el consumo de oxígeno con un electrodo tipo Clark como se describió en métodos, donde se señala la añadido 1 mM KCN o 10 μ M de nOg. Los datos son el promedio de tres repeticiones de cuatro preparaciones independientes.

El comportamiento de las células cultivadas en MM-glucosa fue similar a los cultivos anteriores obteniendo un consumo de oxígeno dentro de la fase logarítmica para la WT y Δg de 60 natgO/mg/min (Figura 35A y B). Para las células recuperadas en la fase estacionaria el consumo de oxígeno para la WT y Δg fue de 348

natgO/mg/min (Figura 35C) y 228 natgO/mg/min (Figura 35D) respectivamente, y fue necesario añadir KCN y nOg para inhibir al 100% la respiración.

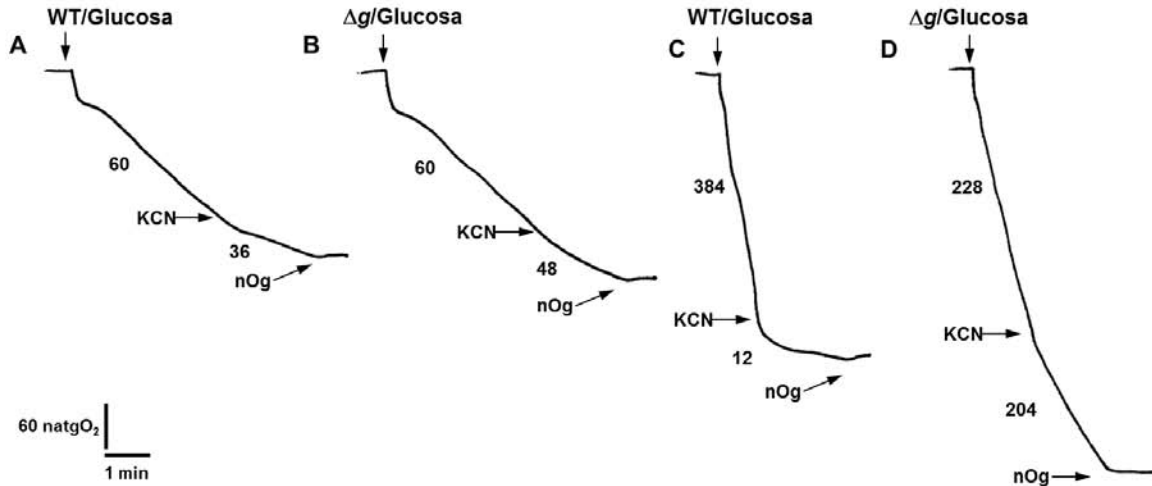


Figura 35. Consumo de oxígeno de las células cultivadas en MM-Glucosa. Las células fueron obtenidas de la fase logarítmica de crecimiento de la WT (A) y Δg (B) y de la fase estacionaria de la WT (C) y Δg (D), se incubaron en 10 mM de KH_2PO_4 pH 7.4 y se determinó el consumo de oxígeno con un electrodo tipo Clark como se describió en métodos, donde se señala 1 mM KCN o 10 μM de nOg fue añadido. Los datos son el promedio de tres repeticiones de cuatro preparaciones independientes.

En las levaduras, el requerimiento de ATP es alto en la fase logarítmica de crecimiento y disminuye cuando las células entran en la fase estacionaria. Como consecuencia, en la fase logarítmica, el consumo de oxígeno debe ser elevado y acoplado a la generación del $\Delta\mu_{\text{H}^+}$ para producir el ATP necesario para la célula. En cambio, durante la fase estacionaria, la forma de mantener un consumo de oxígeno alto sería promoviendo un desacoplamiento controlado.

Tabla 2. Diferencias metabólicas de las cepas WT y Δg .

	WT	Δg
		YPD
Tiempo de duplicación (horas)	2.1 ± 0.5	2.75 ± 0.7
Peso seco (mg/mL)	1.9 ± 0.15	1.51 ± 0.26
Tamaño celular (μm)	18.8 ± 1.8 ^{log} 22.6 ± 3.9 ^{stat}	28.1 ± 1.5 ^{log} 30.1 ± 2.9 ^{stat}
Número de células (1L)	4.12 x 10 ^{9 log}	3.37 x 10 ^{9 log}
Consumo de oxígeno celular (natgO ₂ /mg/min)	108 ^{log} Se inhibe con KCN 348 ^{stat} 288 ^{stat+KCN}	120 ^{log} 108 ^{log+KCN} 168 ^{stat} 252 ^{stat+KCN}
		MM-EtOH
Tiempo de duplicación (horas)	2.7 ± 0.6	3.3 ± 0.7
Peso seco (mg/mL)	0.9 ± 0.07	0.82 ± 0.16
Tamaño celular (μm)	19.9 ± 1.9 ^{log} 26.1 ± 7.2 ^{stat}	29.3 ± 2.7 ^{log} 39.2 ± 10.4 ^{stat}
Número de células (1L)	3.61 x 10 ^{9 log}	2.96 x 10 ^{9 log}
Consumo de oxígeno celular (natgO ₂ /mg/min)	72 ^{log} Se inhibe con KCN 276 ^{stat} Se inhibe con KCN	72 ^{log} 24 ^{log+KCN} 324 ^{stat} 24 ^{stat+KCN}
		MM-Glucosa
Tiempo de duplicación (horas)	3.13 ± 0.2	3.28 ± 0.5
Peso seco (mg/mL)	1.5 ± 0.17	1.39 ± 0.14
Tamaño celular (μm)	26.4 ± 7.96 ^{log} 41.37 ± 5.25 ^{stat}	37.24 ± 12.07 ^{log} 46.25 ± 8.41 ^{stat}
Número de células (1L)	3.53 x 10 ^{9 log}	3.01 x 10 ^{9 log}
Consumo de oxígeno celular (natgO ₂ /mg/min)	60 ^{log} 36 ^{log+KCN} 234 ^{stat} 12 ^{stat+KCN}	60 ^{log} 48 ^{log+KCN} 228 ^{stat} 204 ^{stat+KCN}

Se ha reportado en *U. maydis* que existen dos rutas de transporte de electrones, la vía citocrómica y la vía de los elementos alternos, la cual está constituida por las NADH deshidrogenasas tipo 2 y por la oxidasa alterna (AOX). La AOX es una oxidasa terminal que cataliza la transferencia de electrones del ubiquinol hasta el oxígeno molecular. En contraste con el complejo IV de la vía citocrómica, la AOX no bombea protones y es insensible al cianuro y a la antimicina, pero se inhibe con *n*-octil-galato (nOg) (Juárez *et al.*, 2006). Por consiguiente, al añadir KCN bloqueamos la respiración a nivel del complejo IV pero el consumo de oxígeno no se ve afectado debido a la presencia de la AOX y ésta sólo se inhibe una vez que se agrega nOg. Estudios de nuestro grupo de trabajo indican que la AOX desempeña dos papeles fundamentales en *U. maydis*: 1) forma parte de los mecanismos que previenen la producción de ROS y 2) le permite a la célula adaptarse a condiciones generadas por factores externos que limitan o inhiben la actividad de la vía citocrómica (Juárez *et al.*, 2006).

Determinación del consumo de glucosa. En experimentos alternos se determinó el consumo de glucosa durante el crecimiento de las cepas WT y Δg . En la figura 36 se muestra que la glucosa está en condiciones saturantes (26 mM) y que las levaduras sólo han consumido el 40% (\approx 15 mM) de la glucosa total a las 24 h de crecimiento. Esto podría sugerir que la vía de la degradación de glucosa no incrementa su velocidad para generar más sustratos oxidables que pueda consumir la mitocondria.

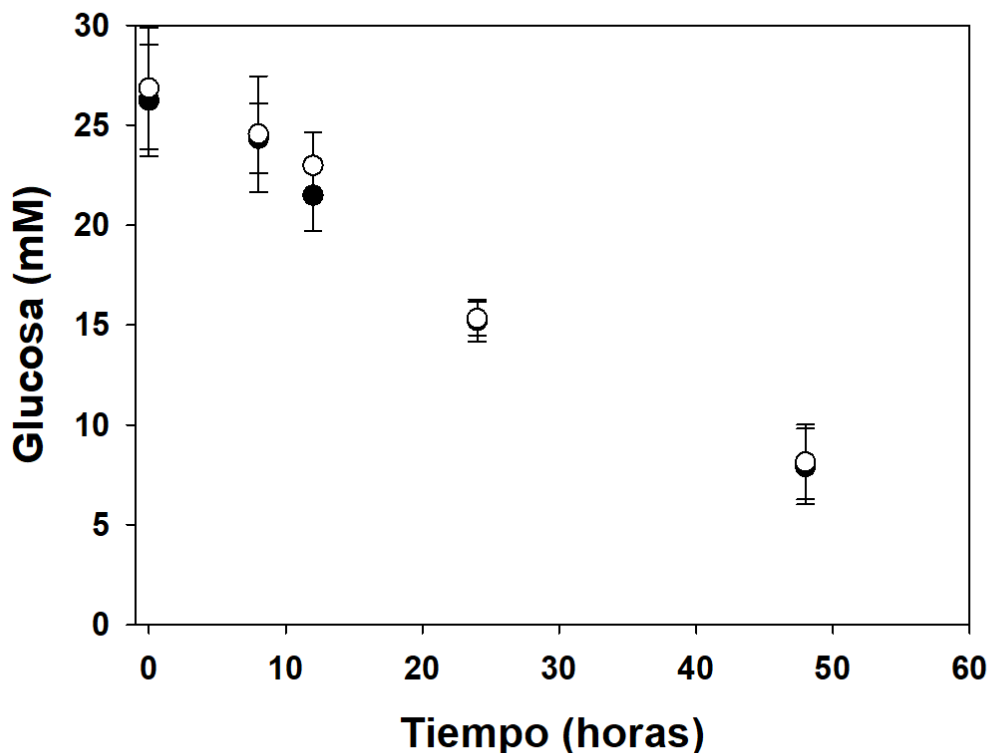


Figura 36. Consumo de glucosa. Las células se cultivaron por 24 h, se inocularon 40u/L en medio YPD. Se incubaron a 28°C en agitación orbital constante a 200rpm. Se tomaron muestras a diferentes tiempos durante el crecimiento de las cepas WT (●) y Δg (○) y se determinó el consumo de glucosa por el método de la glucosa oxidasa a 510 nm. Los datos son el promedio de tres repeticiones de cuatro preparaciones independientes. Las barras de error representan S.D.

Permeabilización de las células para ensayos bioenergéticos. Para determinar la funcionalidad de las células permeabilizadas se determinó el consumo mitocondrial de oxígeno. La figura 37 muestra que la digitonina permeabiliza las células, favoreciendo la salida de los metabolitos y produciendo la disminución de la velocidad del consumo de oxígeno. Posteriormente la adición de succinato estimula la respiración, lo cual indica que este sustrato es utilizado por la mitocondria y acelera el consumo de oxígeno. En estas condiciones experimentales es posible controlar los sustratos y metabolitos que utiliza la mitocondria para el consumo de O_2 . Después de la permeabilización, la velocidad del consumo de oxígeno para la WT es de 32.2 $\text{natgO}_2/\text{mg}/\text{min}$ (Figura 37A) y para la Δg de 50.6 $\text{natgO}_2/\text{mg}/\text{min}$ (Figura 37B).

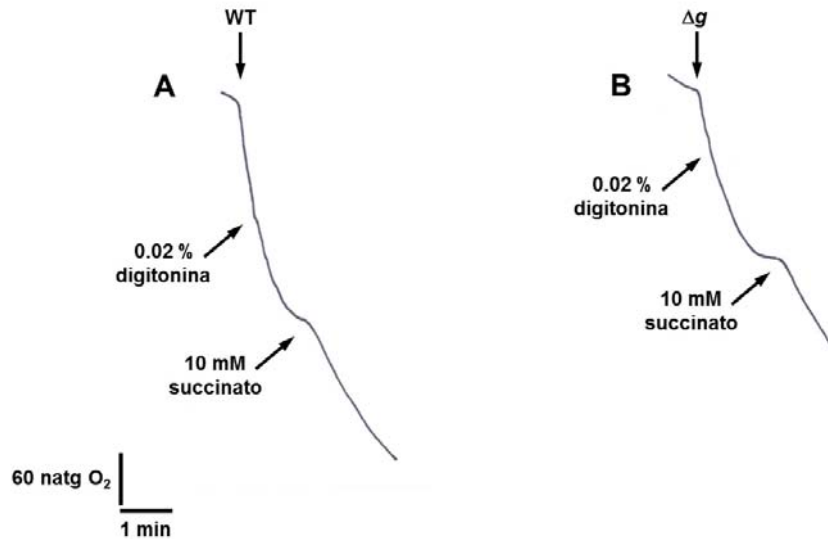


Figura 37. Células permeabilizadas de *U. maydis*. Se permeabilizaron las células WT (A) y Δg (B) con digitonina para realizar los ensayos bioenergéticos. Para el consumo de oxígeno se ocupó como sustrato oxidable 10 mM de succinato. Los datos son el promedio de tres repeticiones de cinco preparaciones independientes.

Determinación del potencial de membrana mitocondrial ($\Delta\Psi_m$). Se determinó el potencial de membrana mitocondrial en las células permeabilizadas y energizadas con succinato (10 mM). A continuación, se adicionó el ADP, el cual es utilizado para la síntesis de ATP acoplada a la despolarización de la membrana interna mitocondrial, lo que se puede interpretar como el estado 3 de la respiración mitocondrial y en presencia de Pi (Figura 38). La adición de CCCP abate el $\Delta\Psi_m$ y confirma la integridad mitocondrial. Se observó que la magnitud del $\Delta\Psi_m$ en ambas cepas es similar (Figura 38), lo que sugiere que la mutante Δg presenta mitocondrias íntegras y acopladas y responden a la estimulación por ADP.

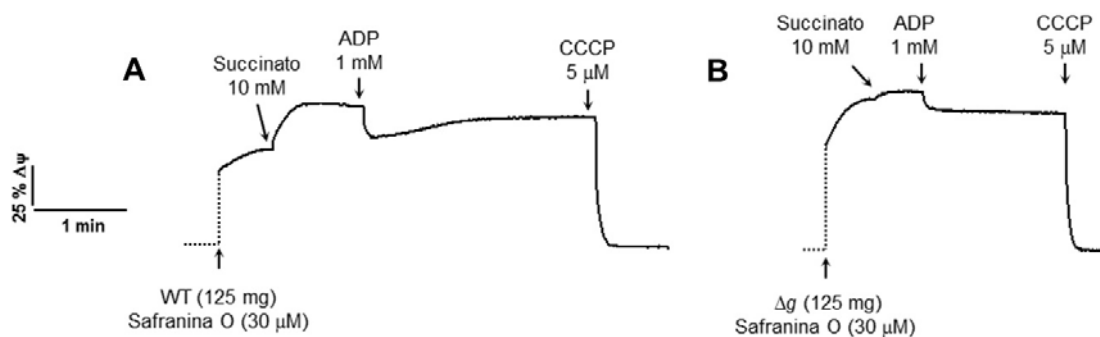


Figura 38. Potencial de membrana ($\Delta\Psi_m$) generado por las células de *U. maydis*. Se emplearon células WT (A) y Δg (B) permeabilizadas con digitonina. Las longitudes de onda para la safranina O son de 533-511 nm. Las células se energizaron con 10 mM de succinato, se despolarizó la membrana con 1 mM ADP y se abatió el potencial con 5 μM de CCCP. Los datos son el promedio de tres repeticiones de cuatro preparaciones independientes.

Cuantificación de la síntesis de ATP. Para la cuantificación de la producción de ATP mitocondrial se utilizaron células permeabilizadas con digitonina. La cuantificación de la síntesis de ATP se realizó por medio de una reacción acoplada siguiendo la reducción del NADP⁺ (Figura 39). Los resultados muestran que la síntesis de ATP en la cepa WT fue de $19.49 \pm 0.84 \mu\text{molas de ATP (g seco}\cdot\text{min}^{-1})$ y para la Δg es de $14.95 \pm 0.57 \mu\text{molas de ATP (g seco}\cdot\text{min}^{-1})$ (Figura 39).

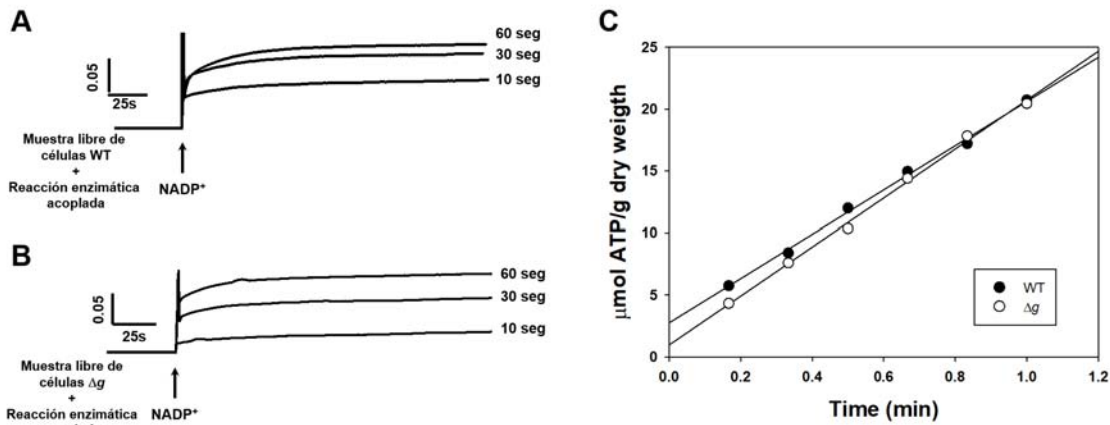


Figura 39. Síntesis de ATP mitocondrial en las células WT y Δg . Cursos temporales para cuantificar la síntesis de ATP mitocondrial en las células de las cepas (A) WT y (B) Δg . (C) El gráfico muestra la producción de ATP contra tiempo por las células permeabilizadas, el cual se determinó mediante un ensayo acoplado a la reducción del NADP⁺. La síntesis de ATP para la cepa WT (●) fue de $19.49 \mu\text{moles de ATP (g}\cdot\text{min}^{-1})$ y para la cepa Δg (○) fue de $14.95 \mu\text{moles de ATP (g}\cdot\text{min}^{-1})$. Los datos son el promedio de tres repeticiones de cuatro preparaciones independientes.

Esto indica que la mutante (Δg) tiene una disminución del 20% en la velocidad de síntesis con respecto a la cepa silvestre, lo que sugiere que el incremento en la acidificación del medio extracelular puede deberse a la aceleración del metabolismo con el fin compensar la baja producción de ATP mitocondrial.

Cuantificación de la producción mitocondrial de peróxido de hidrogeno. La producción de H₂O₂ se realizó cuantificando la fluorescencia de la resorufina e interpolando los datos en una curva estándar de peróxido de hidrógeno. Los resultados muestran que las mitocondrias frescas de la cepa WT produjeron 13.45 pmoles de H₂O₂·mg de proteína mitocondrial, mientras que las de la Δg es de 16.95 pmoles de H₂O₂·mg de proteína mitocondrial en presencia de NADH (Figura 40).

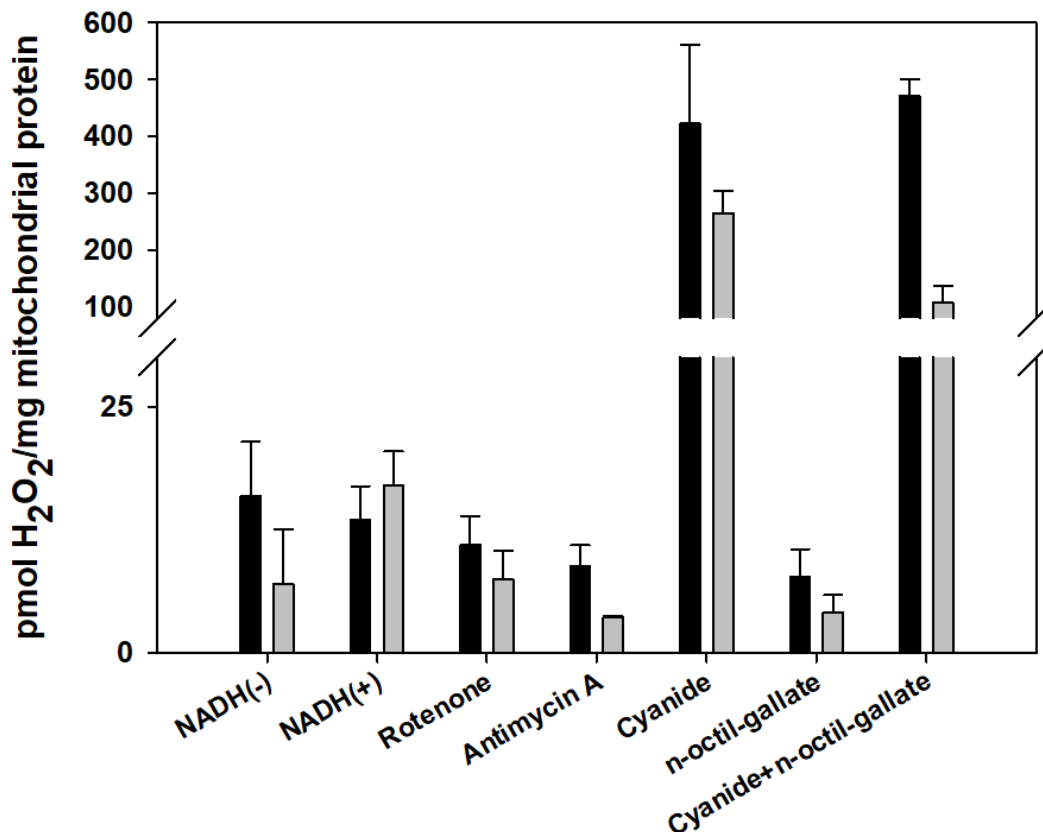


Figura 40. Producción de radicales libres en las mitocondrias de *U. maydis*. En la gráfica se muestra la producción de H₂O₂ en mitocondrias aisladas de la cepa WT (barras negras) y Δg (barras grises) donde se muestra que la cepa Δg tiene una disminución de la cantidad de especies reactivas de oxígeno generadas en comparación con la WT. Los datos son el promedio de tres repeticiones de cuatro preparaciones independientes. Las barras de error representan S.D.

En el ensayo de H₂O₂ se adicionó NADH y los inhibidores clásicos de los complejos respiratorios. Los datos muestran que en presencia de cianuro la cepa WT aumenta 31 veces y la Δg aumentó 15 veces la producción de especies reactivas de oxígeno, quizá a través de los complejos I y III. Por el contrario, cuando usamos el n-octil galato, inhibidor de la AOX, la producción de H₂O₂ disminuyó un 50%, lo que nos sugiere que la toma de los electrones provenientes del ubiquinol por la vía alterna es más lenta en comparación la vía citocrómica.

Solubilización de los supercomplejos y complejos mitocondriales de U. maydis. Los complejos respiratorios de las cepas WT y Δg fueron solubilizados con digitonina, empleando una relación de 0.5, 1.0, 2.0, 3.0 y 5.0 g de digitonina/g de proteína mitocondrial, y se resolvieron en una electroforesis nativa. La ubicación de los complejos y supercomplejos se determinó por la actividad para cada uno de los

complejos respiratorios (Figura 41A-F). La actividad del complejo I en la cepa WT se asoció a los supercomplejos; sin embargo, en la cepa Δg el complejo I se encontró principalmente en forma monomérica.

Es importante recordar que la velocidad de síntesis de ATP en la cepa mutante está disminuida, lo que provocaría la acumulación de los protones en el lado P, aumentando el $\Delta\Psi_m$ y promoviendo el flujo reverso de los electrones en el complejo I, con lo que se estimularía la producción de especies reactivas de oxígeno. En este sentido, el desensamble de los supercomplejos permite la reducción de la poza de quinol y el subsecuente drenado de electrones por la AOX, en un proceso que no involucra el bombeo de protones.

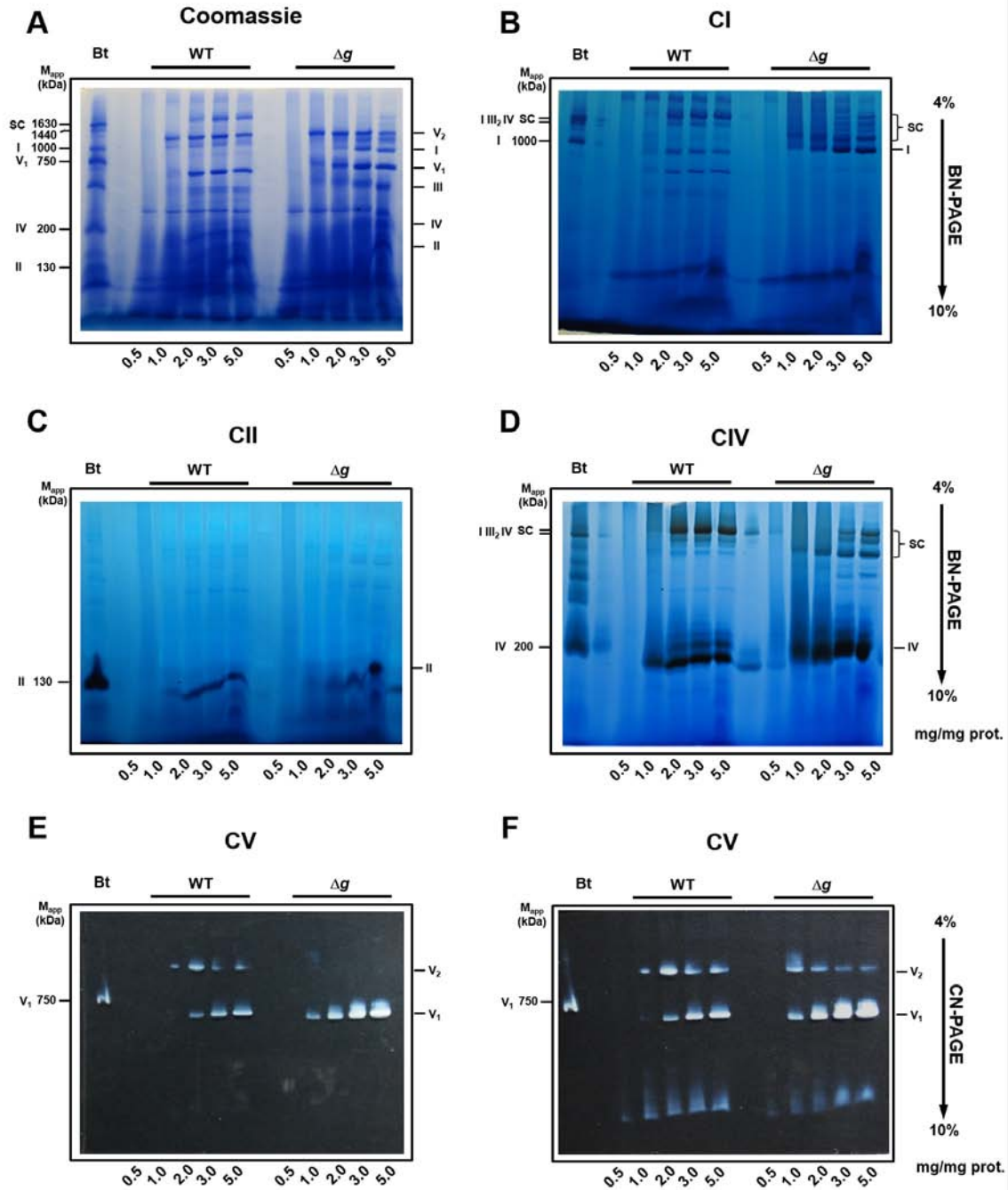


Figura 41. Actividad en gel de los supercomplejos y complejos respiratorios. Los complejos respiratorios solubilizados con digitonina se resolvieron en una BN-PAGE y hrCN-PAGE (para el complejo V) en gel del 4 al 10% de poliacrilamida, usando como estándares los complejos respiratorios de corazón de bovino (Bt). Se hicieron tinciones de actividad en gel para identificar a los complejos respiratorios; **(A)** tinción con Coomassie® R250, **(B)** actividad en gel del complejo I (CI), **(C)** actividad en gel del complejo II (CII), **(D)** actividad en gel del complejo IV (CIV), **(E)** actividad en gel del complejo V (Actividad de ATPasa), **(F)** actividad en gel del complejo V (Actividad de ATPasa) después de 25 horas de incubación y varios cambios del amortiguador de actividad.

Aunado a esto, en lo que se refiere al análisis de la actividad en gel de ATPasa del complejo V mostró la presencia del V_2 y V_1 en las muestras correspondientes a la cepa WT y para el caso de la cepa Δg la actividad de ATPasa solo se asoció con el $V_{1\Delta g}$ durante los primeros 10 min (Figura 41E). No obstante después de 25 horas de incubación y varios cambios de la solución de actividad de ATPasa observó la presencia del $V_{2\Delta g}$ (Figura 41F). Al teñir las proteínas con azul de Coomassie se observó una banda que corresponde al $V_{2\Delta g}$ (Figura 41A), la cual se sometió a una electroforesis en segunda dimensión para comprobar que el $V_{2\Delta g}$ realmente estaba presente aunque en muy baja concentración (Figura 42B). Nuestro grupo de trabajo reportó que el V_{2wt} es estable a los detergentes gracias a la interfase entre los monómeros, por lo tanto, al eliminar la subunidad g , éste pierde la estabilidad y presenta sensibilidad a la digitonina, aun en condiciones bajas del detergente (Figura 42B).

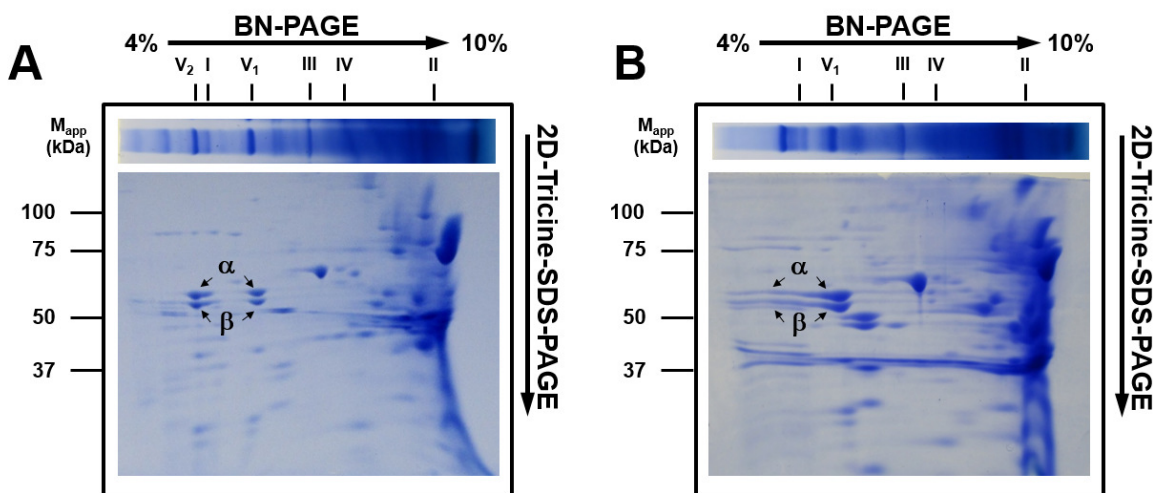


Figura 42. 2D-Tricina-SDS-PAGE. Los complejos respiratorios solubilizados con digitonina se resolvieron en una primera dimensión nativa (BN-PAGE) en gel del 4 al 10% de poliacrilamida. La segunda dimensión se realizó cortando el carril de la primera dimensión nativa y sometándolo a una electroforesis desnaturizante. Las proteínas de los complejos respiratorios se resolvieron en un gel de tricina-SDS-PAGE al 10%. **A)** Identificación de las subunidades α y β en el V_2 y V_1 WT. **B)** Identificación de las subunidades α y β en el V_1 de la cepa Δg .

Aislamiento del dímero y del monómero de la F₁F₀-ATP sintasa. Los oligómeros del complejo V de las cepas WT y Δg fueron aislados en un gradiente continuo de sacarosa y se analizaron en una hrCN-PAGE (Figura 43A y 44A).

El análisis de la actividad en gel de ATPasa del complejo V mostró que el V_{2WT} se localiza en las fracciones del gradiente de sacarosa que tienen una densidad entre 1.14 y 0.99 g/mL, mientras que el V_{1WT} se ubica entre 0.84 y 0.77 g/mL; la mezcla de ambos oligómeros se encontró entre 0.99 y 0.84 g/mL (Figura 43A). Las diferentes fracciones se reúnen en tres lotes independientes, el V_{2wt}, el V_{1wt}, y la mezcla de ambos (V^{2/V1}). Se determinó su concentración de proteína y se almacenaron a -70°C. Por medio de una hrCN-PAGE se realizó el análisis de las muestras concentradas (Figura 43B), con lo que se determinó que los oligómeros mantienen su estructura y actividad de ATPasa y que éstos son las únicas enzimas en esta preparación, que llevan a cabo la hidrólisis del Mg-ATP, además no se observó la presencia del sector F₁ libre. Para corroborar la integridad del complejo V se determinó su sensibilidad a oligomicina (Figura 43C). Las proteínas fueron teñidas con Coomassie, lo que mostró la presencia de otras proteínas distintas al CV (Figura 43D). Debido a la presencia de proteínas contaminantes se realizó la cuantificación del CV en cada preparación para corregir la actividad de ATPasa (ver anexo 10.4 Figura S1).

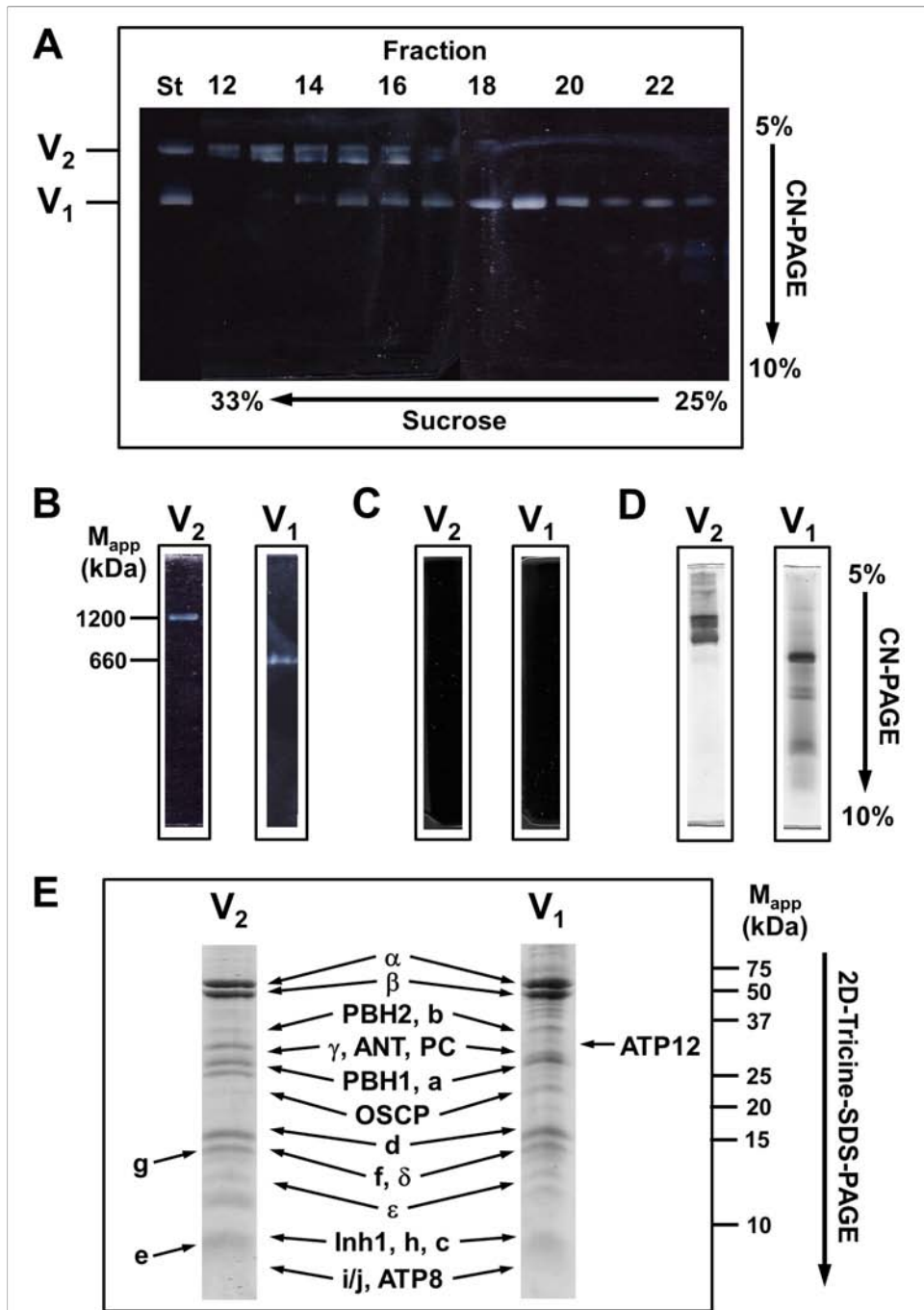


Figura 43. Purificación de los oligómeros de la F_1F_0 -ATP sintasa mitocondrial de la cepa WT. La presencia de los oligómeros de la F_1F_0 -ATP sintasa en el gradiente de sacarosa se determinó en gels hrCN-PAGE (A) La actividad de ATPasa en gel muestra las formas dimerica y monomérica de la ATP sintasa de *U. maydis*. (B) Los oligómeros de la F_1F_0 -ATP sintasa se reunieron y concentraron en filtros de Amicon, el corte de la membrana fue de 100K. El análisis de las muestras concentradas se realizó mediante hrCN-PAGE con lo que se determinó que los oligómeros mantienen su estructura y actividad de ATPasa aún después de almacenarlos a -70°C . (C) Inhibición por oligomicina de la actividad ATPasa en gel de V_2 y V_1 aislado. (D) hrCN-PAGE teñido con azul Coomassie donde se observa al V_2 y V_1 aislados y concentrados sin la presencia de la F_1 libre. (E) La identidad de las subunidades del complejo V se realizó por espectrometría de masas a partir de una electroforesis 2D-Tricine-SDS en gels al 16 % de poliacrilamida. Los oligómeros del complejo V se obtuvieron de una electroforesis BN-PAGE y sus subunidades se resolvieron en una 2D-PAGE. Se muestra la identidad y la masa molecular de cada una de las bandas. PHB1, PHB2 y ANT corresponden a las prohibitinas 1 y 2 y al translocador de adenín nucleótidos respectivamente (En el gradiente de sacarosa 33%=1.1383 g/mL y 25%=.0.7706 g/mL).

El análisis de la actividad de ATPasa en gel de los oligómeros de la cepa Δg , mostró que el $V_{1\Delta g}$ se localiza en las fracciones del gradiente de sacarosa que tienen una densidad entre 0.84 y 0.77 g/mL (Figura 44A). El $V_{1\Delta g}$ aislado (ver materiales y métodos) mantiene su estructura y actividad de ATPasa (Figura 44B) sensible a oligomicina (Figura 44C). La tinción con Coomassie del $V_{1\Delta g}$ (Figura 44D) demostró la presencia de otras proteínas diferentes a la F_1F_0 -ATP sintasa, por lo que nuevamente fue necesario cuantificar la concentración del complejo V para realizar la corrección de la actividad de ATPasa (ver anexo 10.4 Figura S1). Es importante hacer notar que el $V_{2\Delta g}$ es poco estable y que, aunque está presente en el solubilizado con digitonina, no fue posible aislarlo bajo estas condiciones experimentales (gradiente de sacarosa).

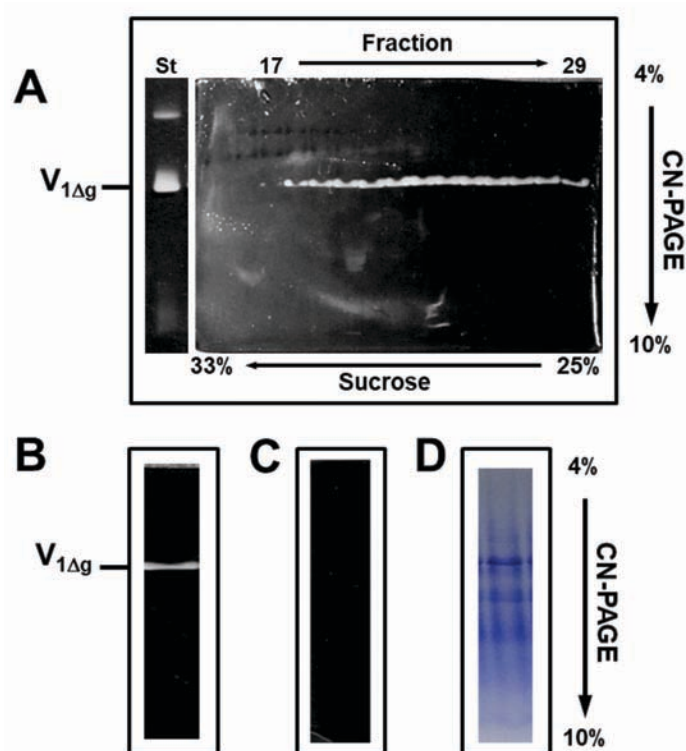


Figura 44. Purificación del monómero de la F_1F_0 -ATP sintasa mitocondrial de la cepa Δg . La presencia de los oligómeros de la F_1F_0 -ATP sintasa en el gradiente de sacarosa se determinó en geles hrCN-PAGE (A) La actividad de ATPasa en gel muestra la actividad del $V_{1\Delta g}$ de la ATP sintasa de *U. maydis*. Los geles se tiñeron con azul Coomassie y las fracciones que contienen al $V_{1\Delta g}$ se reunieron y concentraron en filtros de Amicon, el corte de la membrana fue de 10K. (B) El análisis de las muestras concentradas se realizó mediante hrCN-PAGE con lo que se determinó que el $V_{1\Delta g}$ mantiene su estructura y actividad de ATPasa aún después de almacenado a -70°C . (C) Inhibición por oligomicina de la actividad ATPasa en gel de $V_{1\Delta g}$ aislado. (D) hrCN-PAGE teñido con azul Coomassie® 250 donde se observa al $V_{1\Delta g}$ aislado y concentrado sin la presencia de F_1 libre.

Identificación de las subunidades del dímero y monómero de la F₁F₀-ATP sintasa. Las subunidades del V₂ y del V₁ de la F₁F₀-ATP sintasa se resolvieron mediante su movilidad electroforética en la 2D-Tricina-PAGE (Figura 43E). Las proteínas se tiñeron con azul brillante de Coomassie® R250 y se identificaron mediante espectrometría de masas.

Se identificaron 15 subunidades asociadas al dímero y monómero de la F₁F₀-ATP sintasa de la cepa WT. Así mismo, se puede observar que el dímero muestra a las subunidades *e* y *g*, responsables de la dimerización del complejo V en *S. cerevisiae* (Arnold *et al.*, 1998; Couoh-Cardel *et al.*, 2010). Dentro de este análisis se encontró a la subunidad ATP12, la cual es una chaperona que participa en el ensamblaje de la enzima. También se identificaron a las prohibitinas 1 y 2 (PBH1 y PBH2) que han sido relacionadas con la formación de las crestas mitocondriales. También se identificó al translocador de adenín nucleótidos (ANT) y el transportador de fosfatos (PC) los cuales son muy importantes para la síntesis de ATP. El encontrar el ANT y el PC asociados al V₂ y V₁ de la ATP sintasa sugiere la presencia del sintasoma de ATP (Ko *et al.*, 2003), lo cual abre la posibilidad de estudiar dicho supercomplejo en este organismo (Esparza-Perusquía *et al.*, 2017).

Determinación de los parámetros cinéticos de la F₁F₀-ATP sintasa. La caracterización de la actividad de ATPasa de los oligómeros del complejo V, se determinó mediante la oxidación del NADH en presencia de un sistema regenerador de ATP (ver métodos). La presencia de un sistema regenerador permite eliminar el ADP producido por la actividad de ATPasa, ya que altas concentraciones de este nucleótido pueden inhibir la actividad de ATPasa de la enzima (Fiske *et al.*, 1925; Penefsky, 1974).

A partir de la pendiente de cada registro espectrofotométrico del curso temporal se obtiene la actividad específica, que aumentó conforme incrementó la concentración de Mg-ATP. Los datos obtenidos se ajustaron al modelo cinético propuesto por Michaelis-Menten. Si la velocidad de una reacción se calcula a una

determinada concentración de sustrato $[S] \ll K_m$, la velocidad de la reacción (v) aumenta linealmente con respecto a $[S]$. Sin embargo, cuando la $[S] \gg K_m$, la enzima se satura y alcanza su velocidad máxima (V_{max}), la cual no sobrepasará en ningún caso, independientemente del aumento de $[S]$. La constante de Michaelis (K_m) se define como la afinidad de la enzima por el sustrato, cuando $[S] = K_m$ y $V_{max}/2$ (Segel, 1993).

Asimismo, los cursos temporales del V_{2WT} , V_{1WT} y $V_{1\Delta g}$ mostraron que la actividad es lineal con respecto al tiempo y que aumenta conforme se incrementa la concentración de Mg-ATP (Figura 45A-C). Para corroborar la integridad del complejo V se inhibió con oligomicina (*vide infra*).

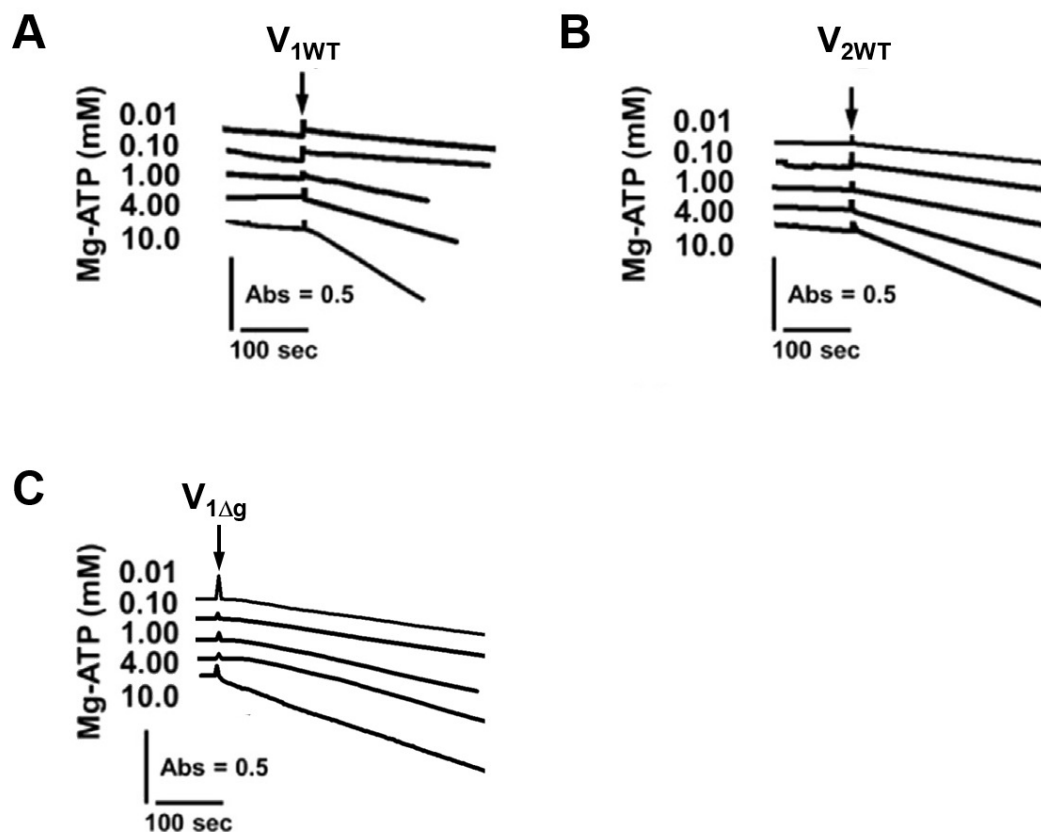


Figura 45. Caracterización cinética de la F_1F_0 -ATP sintasa mitocondrial aislada. La actividad del V_2 , V_1 y $V_{1\Delta g}$ se determinó como se describe en la sección de materiales y métodos. Cursos temporales de la actividad de ATPasa del complejo V a diferentes concentraciones de Mg-ATP. (A) V_{1WT} . (B) V_{2WT} . (C) $V_{1\Delta g}$.

Sin embargo, se ha reportado que la actividad de ATPasa del complejo V se estimula por el detergente *n*-dodecil β -D-maltósido (DDM) (Villavicencio-Queijeiro A, *et al.*, 2009). Por tal motivo, se realizó la titulación de la actividad de ATPasa del V_2 de *U. maydis* con el DDM (Figura 46). Como se puede observar, la actividad de hidrólisis de ATP del V_2 incrementó en presencia del DDM mostrando una AC_{50} de $4 \times 10^{-4}\%$; la máxima estimulación del V_2 de *U. maydis* se alcanza a una concentración del detergente de $5 \times 10^{-3}\%$.

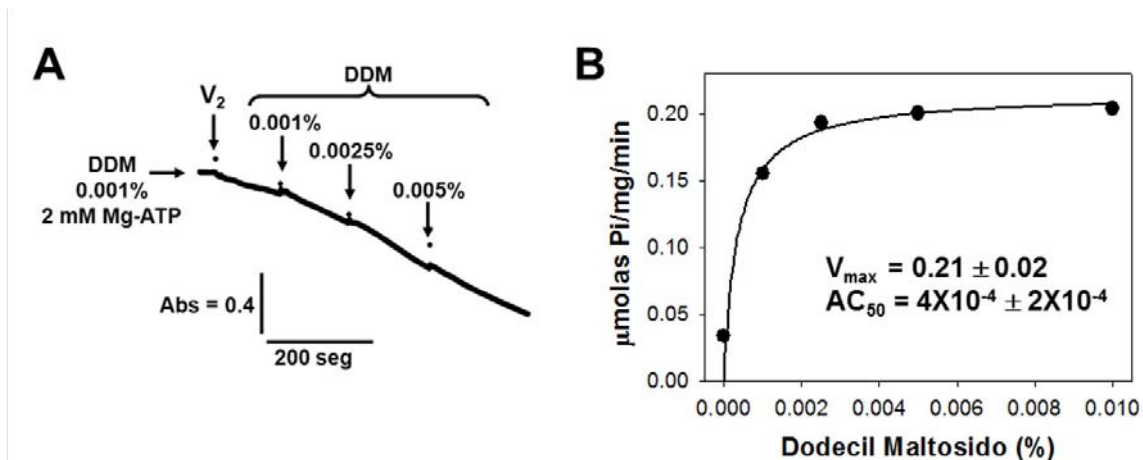


Figura 46. Titulación de la actividad de ATPasa del V_2 con DDM. La actividad de ATPasa del V_2 aislado se estimuló por el DDM (A). A partir de los cursos temporales se calculó una $AC_{50} = 4 \times 10^{-4}\%$. La máxima activación se alcanzó con 0.005% de DDM (B).

Con esta información, se determinó la actividad de ATPasa de V_{2WT} , V_{1WT} y $V_{1\Delta g}$ partir de los cursos temporales en presencia y ausencia de 0.005% de DDM. La figura 47 muestra que la velocidad de ATPasa aumenta en presencia de DDM en cada uno de los oligómeros.

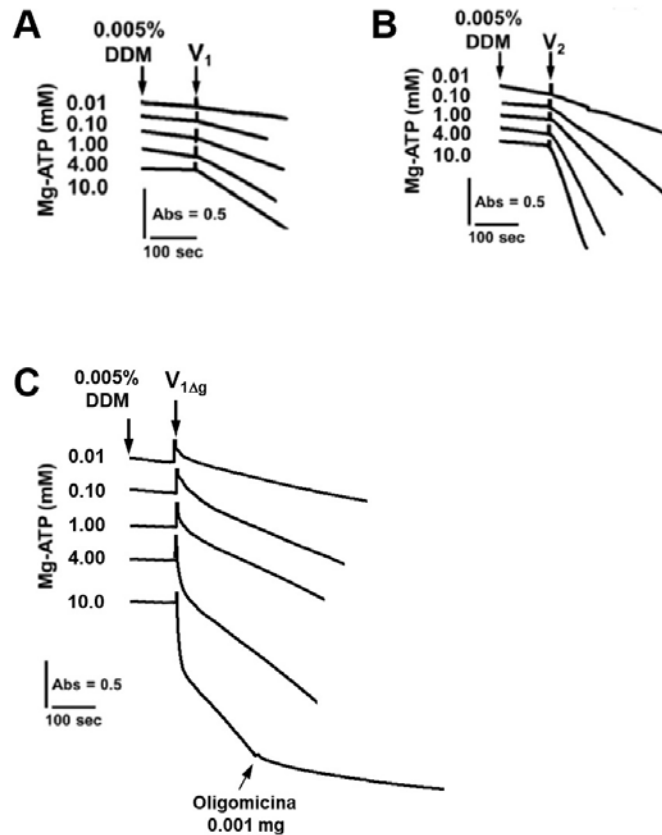


Figura 47. Actividad de la F_1F_0 -ATP sintasa mitocondrial en presencia de DDM. Actividad de ATPasa del V_2 , V_1 y $V_{1\Delta g}$ en presencia de 0.005% de DDM. Donde se indica, se realizó la adición de la muestra. Cursos temporales de la actividad de ATPasa del V_1 (A), V_2 (B) y $V_{1\Delta g}$ (C).

Los cursos temporales mostrados en las Figuras 45 y 47 se ajustaron al modelo de Michaelis-Menten (Figura 48) a partir del cual se determinaron las constantes cinéticas. El V_{1WT} presenta una K_M de $308 \pm 90 \mu\text{M}$ para el Mg-ATP y V_{max} de $0.83 \pm 0.05 \mu\text{mol ATP hidrolizado/mg } F_1F_0\text{-ATP sintasa} \cdot \text{min}^{-1}$ (Figura 48A, círculos negros). Para el caso del V_{2WT} la actividad de ATPasa presenta una K_M de $884 \pm 100 \mu\text{M}$ para el Mg-ATP y V_{max} de $0.54 \pm 0.08 \mu\text{mol ATP hidrolizado/mg } F_1F_0\text{-ATP sintasa} \cdot \text{min}^{-1}$ (Figura 48B, círculos negros). Para el $V_{1\Delta g}$ se determinó una K_M de $155 \pm 0.05 \mu\text{M}$ para el Mg-ATP y V_{max} de $0.58 \pm 0.03 \mu\text{mol ATP hidrolizado/mg } F_1F_0\text{-ATP sintasa} \cdot \text{min}^{-1}$ (Figura 48C, círculos negros).

Por otra parte, analizando los cursos temporales de los oligómeros activados con 0.005% de DMM (Figura 48) observamos que también mostraron un comportamiento cinético que se ajusta al modelo de Michaelis-Menten. El V_{1WT}

activado presenta una K_M de $207 \pm 30 \mu\text{M}$ para el Mg-ATP y una V_{max} de $1.43 \pm 0.04 \mu\text{mol ATP hidrolizado/mg F}_1\text{F}_0\text{-ATP sintasa}\cdot\text{min}^{-1}$ (Figura 48A, círculos blancos). Para el caso del $V_{2\text{WT}}$ activado tiene una actividad de ATPasa con una K_M de $488 \pm 80 \mu\text{M}$ para el Mg-ATP y una V_{max} de $9.60 \pm 0.26 \mu\text{mol ATP hidrolizado/mg F}_1\text{F}_0\text{-ATP sintasa}\cdot\text{min}^{-1}$ (Figura 48B, círculos blancos). El $V_{1\Delta g}$ tiene una K_M de $920 \pm 200 \mu\text{M}$ para el Mg-ATP y una V_{max} de $2.3 \pm 0.15 \mu\text{mol ATP hidrolizado/mg F}_1\text{F}_0\text{-ATP sintasa}\cdot\text{min}^{-1}$ (Figura 48C, círculos blancos).

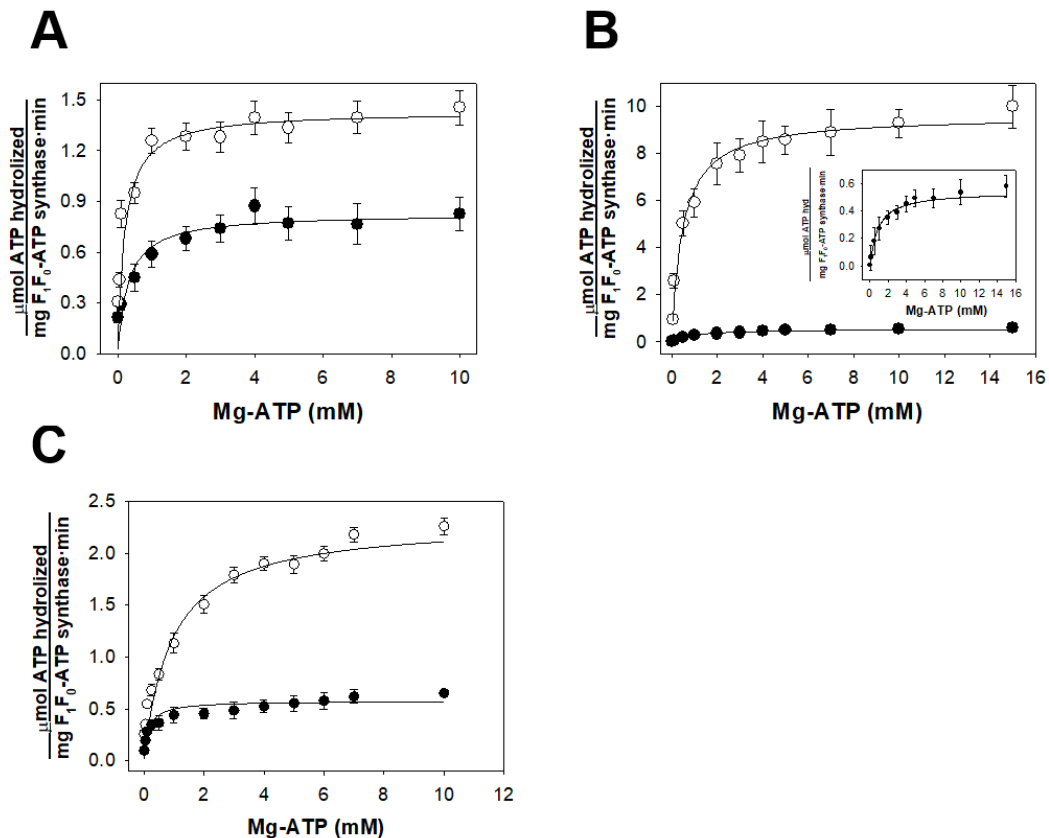


Figura 48. Actividad de ATPasa de los oligómeros de la F_1F_0 -ATP sintasa mitocondrial aislados de las cepas WT y Δg . La hidrólisis de diferentes concentraciones de Mg-ATP por los oligómeros de la F_1F_0 -ATP sintasa aislados se realizó a pH 8.0 y se ajustó a la ecuación de Michaelis-Menten, en presencia (○) o ausencia (●) de 0.005% de DDM. (A) $V_{1\text{WT}}$. (B) $V_{2\text{WT}}$. Para mayor claridad, el recuadro en el panel representa la actividad sin la activación por DDM. (C) $V_{1\Delta g}$. Los datos son el promedio de cuatro réplicas de cinco preparaciones independientes \pm . Las barras de error representan S. D.

La concentración de F_1F_0 -ATP sintasa se determinó mediante un análisis densitométrico de las subunidades α y β . Las proteínas de las muestras $V_{1\text{WT}}$, $V_{2\text{WT}}$ y $V_{1\Delta g}$ se resolvieron en geles de Tricina-SDS-PAGE al 10%, utilizando BSA como estándar. Las proteínas fueron teñidas con azul brillante de Coomassie® R250 (Ver

anexo 10.4, Fig. S1). El análisis de densitometría se realizó con el software MyImage Analysis 2.0 (Thermo Scientific) (ver anexo 10.4 Figura S1).

Efecto de la oligomicina en la actividad de ATPasa del V_1 y V_2 . La oligomicina es un inhibidor específico de la actividad de ATPasa del complejo V que solo actúa cuando se mantiene la interacción del sector F_0 con el F_1 . Debido a que la oligomicina es un inhibidor de asociación lenta pero fuertemente unido, se decidió explorar la velocidad de inhibición de los oligómeros activados por DDM. Se puede observar que el tiempo de inhibición del V_{2WT} , al parecer, es menor que para el V_{1WT} y el $V_{1\Delta g}$ (Figura 49A y D), lo que va acompañado de una mayor sensibilidad del V_{2WT} a la oligomicina (Figura 49B).

La inhibición de V_{1wt} fue superior a 90% a 3.8 μM de oligomicina (Figura 49C, círculos blancos) mientras que para el V_{2wt} (Figura 49C, círculos negros) y el $V_{1\Delta g}$ fue de 1.3 μM (Figura 49E). El análisis de la inhibición de ATPasa por oligomicina mostró que V_{2wt} tenía un $K_i = 24 \pm 3$ nM, la K_i para V_{1WT} fue de 169 ± 10 nM y una $K_i = 52.7 \pm 4.4$ nM para el $V_{1\Delta g}$. Dado que la cantidad de complejo V en ambas preparaciones se cuantificó, fue posible calcular la relación de oligomicina/ F_1F_0 -ATP (Figura 49C y E). La relación fue de 0.85 ± 0.12 para V_{2WT} , de 6 ± 0.43 para V_{1WT} y 5.03 ± 0.57 para el $V_{1\Delta g}$.

En conjunto, nuestros resultados sugieren que los monómeros en el dímero tienen una comunicación interfuncional y que al inhibir a uno de los monómeros se puede alterar la interfase y modificar la K_i para la oligomicina. Cuando se elimina a la subunidad g , el dímero parece ser más sensible a los detergentes. *U. maydis* es un basidiomiceto aerobio estricto que depende principalmente de la fosforilación oxidativa para obtener la energía necesaria para llevar a cabo los procesos metabólicos, si consideramos que la cepa Δg tarda más tiempo en duplicarse y a su vez tiene una síntesis de ATP menor que la cepa WT, podemos suponer que la eliminación de la subunidad g no sólo modifica la interfase de la F_1F_0 -ATP sintasa, sino que también su capacidad catalítica.

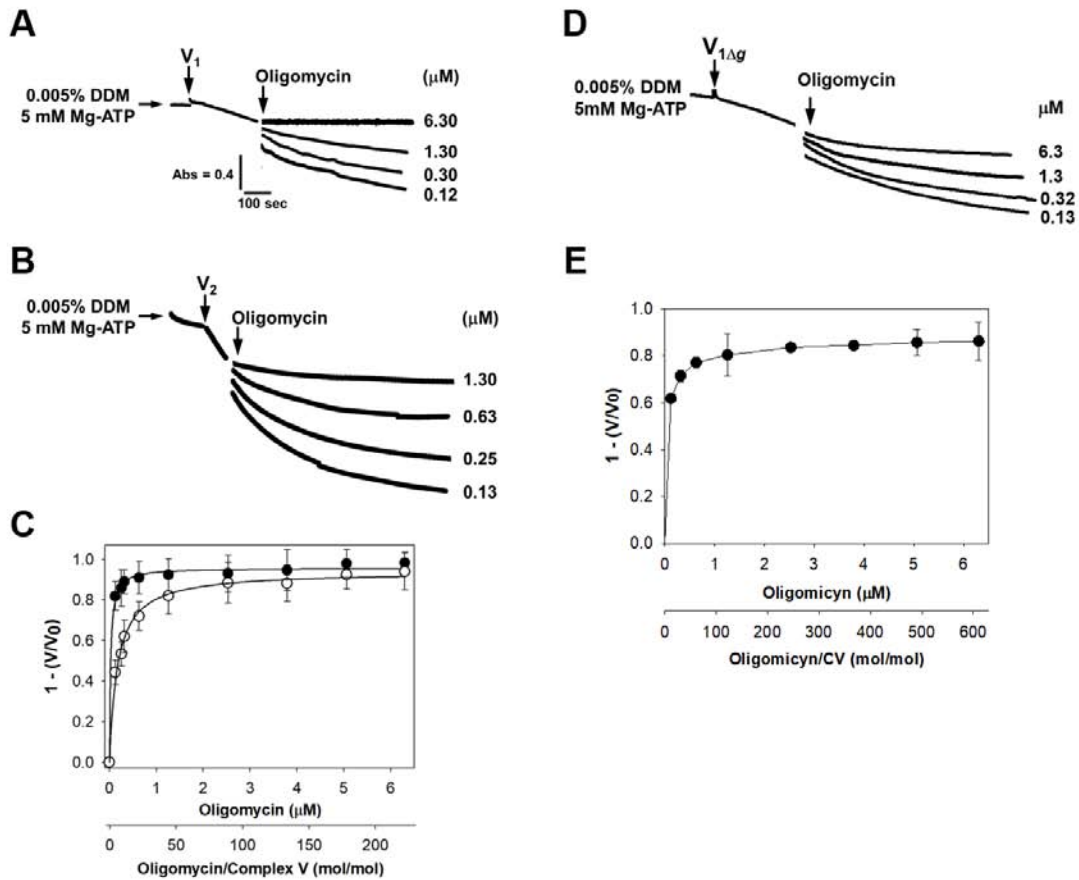


Figura 49. Efecto de la oligomicina sobre la actividad de ATPasa. La actividad del complejo V se determinó en presencia de 0.005% de DDM y 5 mM ATP-Mg. El curso temporal para la oxidación del NADH acoplado a la hidrólisis de ATP se monitoreó durante 25-30 minutos para la máxima inhibición de ATPasa de V_1 (**A**) o V_2 (**B**) y se analizó el registro espectrofotométrico final como se describe en la sección de materiales y métodos. Las flechas indican las adiciones de enzima y oligomicina, a la derecha se muestra la concentración de inhibidor. (**C**) El gráfico muestra $1 - (V/V_0)$ en el intervalo de menor concentración de la oligomicina, para mostrar la sensibilidad diferencial de los oligómeros, la máxima inhibición de V_1 (\circ) o V_2 (\bullet) en función de la concentración de oligomicina. (**D**) El curso temporal para la oxidación del NADH acoplado a la hidrólisis de ATP para la máxima inhibición de ATPasa de $V_{1\Delta g}$. Las flechas indican las adiciones de enzima y oligomicina, a la derecha se muestra la concentración de inhibidor. (**E**) La máxima inhibición de $V_{1\Delta g}$ en función de la concentración de oligomicina. V representa la actividad residual de la inhibición con oligomicina y V_0 representa la actividad ATPasa antes de la adición de oligomicina. Los datos son el promedio de tres repeticiones de cuatro preparaciones independientes. Las barras de error representan S.D.

Termoestabilidad del V_2 y V_1 de la F_1F_0 -ATP sintasa. La termoestabilidad del V_1 y V_2 se realizó incubando a la enzima durante 15 min a diferentes temperaturas en un medio que contenía 30 mM de HEPES, 5% glicerol, pH 8.0. Al término de la incubación se determinó la actividad a 25°C empleando el sistema regenerador de ATP acoplado a la oxidación del NADH (ver materiales y métodos).

La estabilidad térmica del V_2 y V_1 se evaluó determinando la actividad residual de ATPasa. En la figura 50 se puede observar que la actividad residual

(v/v_0) del V_1 y V_2 se mantuvo constante entre los 20 y los 40°C, con un ligero incremento a los 45°C; posteriormente se observó un descenso en la actividad con respecto a la temperatura. En el intervalo de 46 a 59°C ocurre la inactivación de la enzima con un comportamiento que se ajusta a una curva monótonica, de la cual se puede calcular una temperatura de transición aparente (T_m) de aproximadamente 52°C. Esto sugiere que la inactivación del V_1 y V_2 ocurre en un solo paso. Para verificar que funcionalmente el V_1 y V_2 mantienen unidos a los sectores F_1 y F_0 , se determinó la inhibición de la actividad de ATPasa por la oligomicina (2 $\mu\text{g}/\text{mL}$); con esto se demostró que, a cualquier temperatura ensayada, la F_1F_0 -ATP sintasa permanece ensamblada.

Adicionalmente, en el análisis hrCN-PAGE no se observó la liberación de sector F_1 para el V_{1WT} y V_{2WT} en el intervalo de temperaturas evaluadas (Figuras 50B y C). Esto sugiere que la inactivación de V_{2WT} podría ocurrir a través de su disociación en V_1 y finalmente la inactivación de V_{1WT} ; por lo tanto, la interfase monómero-monómero aparentemente no contribuye a la estabilidad de V_{2WT} .

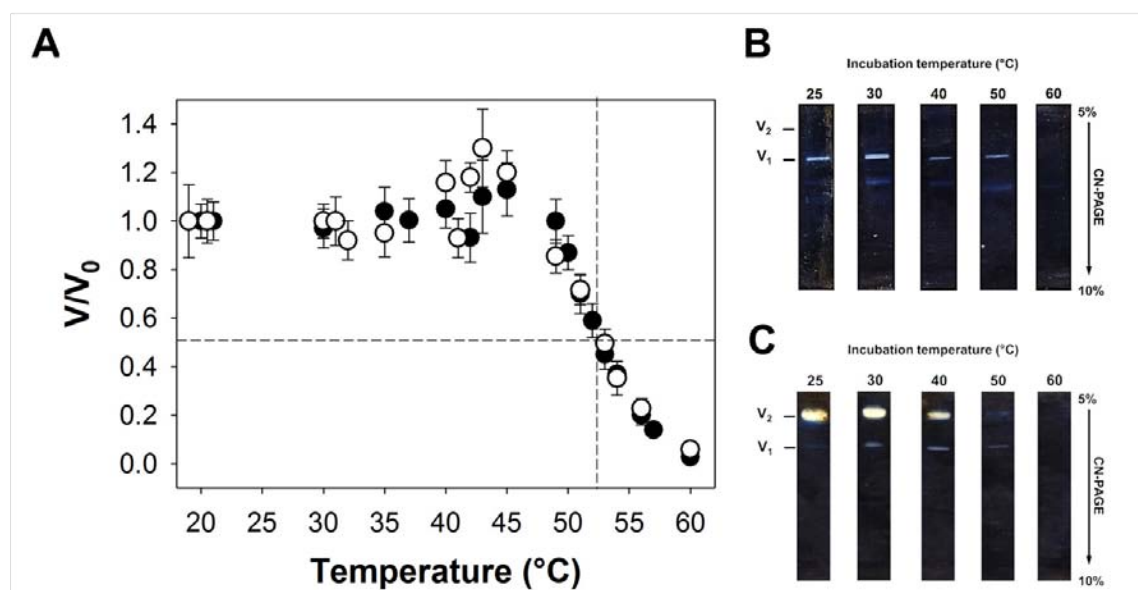


Figura 50. Efecto de la temperatura en la actividad de ATPasa. (A) Curvas de inactivación térmica de V_1 y V_2 . V_1 (○) o V_2 (●) se incubaron durante 15 minutos a las temperaturas indicadas y luego se enfriaron a temperatura ambiente. La actividad residual (V/V_0) se calculó usando V_0 como actividad ATPasa a 25°C antes de calentarse. hrCN-PAGE de V_1 (B) y V_2 (C) se incubaron como se describe en (A). La T_m se calculó en 52.3°C. Los datos son el promedio de tres repeticiones de cuatro preparaciones independientes.



"Networking energies" Odra Noel

Discusión

*"Si haces las cosas bien desde el principio
jamás tendrás problemas" Dr. Armando Gómez-Puyou*

6. DISCUSIÓN

El objetivo del presente trabajo fue caracterizar la actividad y a la estructura de la F₁F₀-ATP sintasa de *U. maydis* cuando se elimina el gen que codifica para la subunidad *g* dimerizante y su repercusión en el estado bioenergético mitocondrial.

El dímero de la F₁F₀-ATP sintasa (V₂) tiene un papel sobresaliente en el plegamiento de la membrana interna mitocondrial para la formación de las crestas. Es importante señalar que en las crestas se localiza la mayor concentración de los complejos y supercomplejos respiratorios, por lo que es ahí donde se realiza principalmente la oxidación de las coenzimas (NADH y FADH₂) y la síntesis de más del 90% del ATP celular. Debido a la estrecha relación que hay entre los V₂, el plegamiento de las crestas y la síntesis de ATP, el estudio del V₂ ha cobrado gran relevancia.

Se ha determinado que cada reino biológico emplea diferentes subunidades para conformar y estabilizar al V₂: la IF₁ en los mamíferos como *Bos taurus*, las subunidades ASA en las algas como *Chlamydomonas reinhartii*, y las subunidades *e* y *g* en los hongos como *Saccharomyces cerevisiae* y *Ustilago maydis*. Esta observación indica claramente que la formación del dímero es un evento de convergencia evolutiva.

Las F₁F₀-ATP sintasas son enzimas altamente conservadas que juegan un papel fundamental tanto en la síntesis del ATP como en el mantenimiento de la arquitectura mitocondrial. Tanto el sector F₁ como el F₀ presentan todas las subunidades conservadas involucradas en la catálisis (Giraud *et al.*, 2002; Wittig *et al.*, 2008; Couoh-Cardel *et al.*, 2010). Debido a la interacción de las diferentes subunidades, hemos clasificado el rearrreglo de las crestas relacionado con dos tipos de asociaciones en la interfase del dímero, un central y otra periférica; la primera constituida por la interacción de las subunidades *a* y *i/j* y la segunda por la interacción de las subunidades *g*, *e* y *k*.

En realidad, se ha descrito que la interfaz monómero-monómero del dímero de levadura y mamífero está constituida por las subunidades *a*, *ij*, *k*, *g* y *e* (Cough-Cardel *et al.*, 2010; Guo *et al.*, 2017). La interfaz se puede dividir en una zona central y una zona periférica. En la zona central, las subunidades *ij* interactúan a través de dos tramos cortos de ~10 residuos; mientras que la interacción entre las subunidades *a* se produce a través de dos hebras que constituyen una estructura plana de cuatro hebras con una superficie hidrófoba y una superficie hidrofílica (Guo *et al.*, 2017).

La zona periférica de la interfaz monómero-monómero está constituida por las subunidades *k* y *e*. Estas subunidades poseen una estructura similar: una hélice α N-terminal con dos dominios, uno transmembrana y uno soluble que se extiende (alrededor de 40 Å para la subunidad *e*) hacia el espacio intermembranal para interactuar con las subunidades equivalentes del otro monómero (Guo *et al.*, 2017). La subunidad *g* se une a la subunidad *e* a través de una sola α hélice transmembranal, probablemente a través del motivo conservado Gly-X-X-X-Gly de las dos proteínas (Bustos *et al.*, 2005). Simultáneamente, el N-terminal de la subunidad *g* interactúa con ~ 50 residuos del N-terminal de la subunidad *b*. Así pues el dominio de la zona periférica de la interfaz monómero-monómero constituido por las subunidades *e*, *g* y *b*, con el apoyo de la subunidad *k*, ayuda a plegar la membrana mitocondrial interna (Baker *et al.*, 2012; Guo *et al.*, 2017).

Para el caso de *S. cerevisiae*, se cree que la oligomerización de la F₁F₀-ATP sintasa puede estar involucrada en la actividad catalítica de la enzima y que de manera indirecta afecta el estado metabólico de las células. Cuando se impide la dimerización de la F₁F₀-ATP sintasa, eliminando genéticamente las subunidades *e* y *g* simultáneamente, las mitocondrias presentan una morfología alterada en las crestas. Así pues, el rearrreglo de las crestas durante la regulación bioenergética de la mitocondria supone el cambio en la proporción dímero/monómero del complejo V (Velours *et al.*, 2009).

Gracias a la estrecha relación que hay entre el V_2 , el plegamiento de las crestas y la síntesis de ATP, se han realizado muchos esfuerzos para determinar que ocurre cuando alguno de estos componentes se altera. Por ejemplo, ¿Qué ocurre con la síntesis de ATP o la arquitectura de las crestas si se pierde el V_2 ? Campanella *et al.*, (2008) haciendo un *knock out* condicional de la subunidad IF_1 en las células HeLa, determinó que al eliminarse el V_2 , se abatía el $\Delta\Psi_m$, la producción de ATP y el número y tamaño de las crestas disminuía. Sin embargo, el papel de la subunidad IF_1 en la formación del V_2 aún es controvertido. Recientemente, se ha creado un ratón *knock out* para la subunidad IF_1 sin que presente alteraciones metabólicas significativas o cambios en la arquitectura mitocondrial (Campanella *et al.*, 2008).

Adicionalmente, la eliminación simultánea de las subunidades dimerizantes *g* y *e* en *S. cerevisiae* induce la pérdida de V_2 y cambios en la morfología de las crestas mitocondriales, presentando estructuras conocidas como aros de cebolla (Velours *et al.*, 2009). Sin embargo, como *S. cerevisiae* es un organismo facultativo, la producción mitocondrial de ATP puede ser suplida por el metabolismo fermentativo, por lo que la participación mitocondrial en la bioenergética de estos mutantes no está clara.

Como *U. maydis* es un basidiomiceto no fermentativo, su metabolismo bioenergético está en manos de las mitocondrias; así, es un buen modelo para determinar la repercusión que tiene la eliminación de la subunidad *g* sobre la formación del V_2 y la síntesis de ATP. Como se demostró en este trabajo, la eliminación de la subunidad *g* no cambia significativamente el metabolismo celular, ya que no se detectaron cambios en el tiempo de duplicación celular, en el consumo de glucosa y en la producción de peso seco. Esto sugiere que la asimilación de carbono y su incorporación en biomasa es similar tanto en la cepa mutante como en la silvestre. Sin embargo, hay que hacer notar que el número de células y el tamaño de las mismas son diferentes entre la cepa WT y la mutante, sin que

tengamos hasta ahora una explicación. No obstante, es claro que la estructura clásica de mitocondrias se conserva en la cepa mutante.

El análisis bioenergético mostró que las mitocondrias de ambas cepas producen un $\Delta\Psi_m$ similar cuando consumen oxígeno por la vía citocrómica clásica utilizando succinato como sustrato (Tabla 2); sin embargo, la cepa Δg mostró una disminución de la síntesis de ATP asociada con la expresión de la AOX desde las primeras etapas del crecimiento. Se ha reportado que condiciones experimentales similares (es decir, $\Delta\Psi_m$ alto, succinato como suministro de electrones para la cadena respiratoria y una disminución de la actividad del complejo V) puede producir el transporte inverso de electrones (RET) en el complejo I y conducir a un aumento en la producción de radicales libres (Robb *et al.*, 2018). En este sentido, la AOX transfiere los electrones de la QH₂ directamente a O₂, sin pasar por el complejo IV y, por lo tanto, actúa como una válvula de seguridad para evitar la reducción excesiva de la poza de quinonas (Robb *et al.*, 2018; El-Khoury *et al.*, 2013; El-Khoury *et al.*, 2014).

Es posible sugerir que la eliminación de la subunidad *g* produce una disminución de la síntesis de ATP debido a que el dímero de la F₁F₀-ATP sintasa fue modificado, lo que resulta en un bajo consumo de $\Delta\Psi_m$, una acumulación de NADH y un aumento de producción de ROS (es decir, a través de RET en el complejo I). En este sentido, la producción de ROS durante la oxidación de succinato se redujo por la expresión de AOX en la cepa Δg . Aunado a esto, la cepa Δg mostró una reducción del 20% en la síntesis de ATP.

Como se ha descrito, la subunidad *g* desempeña un papel importante en la zona periférica de la interfaz monómero-monómero, y su eliminación conduce a que solo la subunidad *e* de un monómero se una a la subunidad *k* del otro monómero; produciendo una interfaz débil. Es importante recordar que la comunicación monómero-monómero es importante para estimular la actividad de ATPasa del V₂ (Esparza-Perusquía *et al.*, 2017); si consideramos que la F₁F₀-ATP sintasa es

termodinámicamente reversible a expensas de consumir o generar el $\Delta\Psi_m$, entonces podemos suponer que la capacidad de síntesis de ATP es mayor por el V_2 que por el V_1 . Esta hipótesis es respaldada por el hecho de que la cepa Δg presenta una baja síntesis de ATP.

Además de la participación de la interfaz monómero-monómero en la membrana interna, se ha propuesto que la subunidad g podría desempeñar un papel importante en la actividad de V_2 (Esparza-Perusquía *et al.*, 2017). La actividad ATPasa de V_{2WT} fue 7 veces mayor que V_{1WT} , además de presentar una alta sensibilidad a la oligomicina (Esparza-Perusquía *et al.*, 2017). Por otro lado pudimos caracterizar el $V_{1\Delta g}$ (Tabla 3), sin embargo no se logró aislar el $V_{2\Delta g}$ ya que este se disocia cuando pasa por el gradiente. Por lo tanto, la eliminación de la subunidad g no compromete la formación del $V_{2\Delta g}$ pero si la estabilidad de éste, así como su resistencia a los detergentes. Aunque se tiene que verificar su capacidad para sintetizar ATP, podemos proponer que la velocidad de consumo del gradiente electroquímico de protones disminuirá y la proporción de complejos respiratorios reducidos aumentará.

Por último, se observó que en la cepa Δg los respirasomas $I_1:(III_2)_{1-2}:(IV)_{1-4}$ son lábiles y los complejos respiratorios se encuentran principalmente como unidades independientes. Se ha reportado que el ensamble de los respirasomas puede limitar la generación de superóxido durante el flujo de electrones y el consumo de oxígeno (Panov *et al.*, 2007; Reyes-Galindo *et al.*, 2019). La inestabilidad de los respirasomas de la cepa Δg nos permite suponer que durante el transporte de electrones aumenta la probabilidad de producir especies reactivas de oxígeno a nivel de los complejos I y III (Panov *et al.*, 2007; Reyes-Galindo *et al.*, 2019). La relación que existe entre la estabilidad del V_2 (y la presencia de la subunidad g) sobre los respirasomas es una hipótesis que debe comprobarse experimentalmente.

Tabla 3. Parámetros cinéticos para la actividad de hidrólisis de ATP para el dímero y el monómero de la F₁F₀-ATP sintasa de *U. maydis*.

	Monómero (V _{1WT}) ^a	Dímero (V _{2WT}) ^a	Monómero (V _{1Δg}) ^a
<i>F₁F₀-ATP sintasa no activada</i>			
V _{max} (μmol ATP hidrolizado/mg F ₁ F ₀ -ATP sintasa·min ⁻¹)	0.83 ± 0.05	0.54 ± 0.08	0.58 ± 0.15
K _m (μM)	308 ± 90	884 ± 100	155 ± 0.047
k _{cat} (s ⁻¹)	8.4 ± 0.06	10.6 ± 0.15	5.86 ± 0.05
k _{cat} /K _m (M ⁻¹ s ⁻¹)	2.7 × 10 ⁴ ± 0.3 × 10 ⁴	1.2 × 10 ⁴ ± 0.1 × 10 ⁴	3.78 × 10 ⁴ ± 0.3 × 10 ⁴
<i>F₁F₀-ATP sintasa activada con DDM</i>			
V _{max} (μmol ATP hidrolizado/mg F ₁ F ₀ -ATP sintasa·min ⁻¹)	1.43 ± 0.04	9.60 ± 0.26	2.3 ± 0.15
K _m (μM)	207 ± 30	488 ± 80	920 ± 200
k _{cat} (s ⁻¹)	14.5 ± 0.03	207.7 ± 0.03	23.26 ± 0.1
k _{cat} /K _m (M ⁻¹ s ⁻¹)	7.0 × 10 ⁴ ± 0.2 × 10 ⁴	4.2 × 10 ⁵ ± 0.2 × 10 ⁴	2.53 × 10 ⁴ ± 0.08 × 10 ⁴
K _i (nM) para la oligomicina	169 ± 10	24 ± 3	52.7 ± 4.4
	160 ± 17 ^b	21 ± 4 ^b	
Relación oligomicina / F ₁ F ₀ -ATP sintasa (mol/mol) para alcanzar el 50% de la inhibición de ATPasa	6.0 ± 0.43	0.85 ± 0.12	5.03 ± 0.57

^a = Los moles de F₁F₀-ATP sintasa en las muestras V₁ y V₂ se determinaron como se describe en la sección de procedimientos, y los parámetros cinéticos se mostraron como mg de F₁F₀-ATP sintasa. ^b = valores K_i calculados por el software DynaFit (ver sección Material y métodos).



"Mitchell's dream" Odra Noel

Science is beautiful: it has truth, it has drama, it is full of wonder.

Conclusiones

7. CONCLUSIONES

- La cepa Δg conserva el fenotipo respiratorio mitocondrial y la capacidad de crecimiento empleando diferentes fuentes de carbono.
- El tiempo de duplicación celular y producción de biomasa fue similar para ambas cepas (WT y Δg) en las tres fuentes de carbono (1% etanol, 1% glucosa y 1% lactato).
- Las mitocondrias de la cepa Δg son más grandes que las de la cepa WT.
- La eliminación de la subunidad *g* no compromete el estado bioenergético de la mitocondria ya que la velocidad de consumo mitocondrial de oxígeno y el potencial de membrana mitocondrial no se afectaron.
- La síntesis de ATP mitocondrial disminuyó un 20% en la cepa Δg .
- En la cepa Δg la AOX se expresa a partir de la fase logarítmica de crecimiento y se mantiene durante la fase estacionaria.
- La presencia de la AOX en la cepa Δg está asociada a una menor producción de especies reactivas de oxígeno.
- La cepa Δg no produce una gran cantidad de especies reactivas de oxígeno comparado con la WT gracias a la presencia de la AOX desde las primeras fases del crecimiento.
- En la cepa Δg los supercomplejos son más sensibles a la digitonina y los complejos respiratorios se encuentran principalmente como supercomplejos menores y unidades independientes.
- La eliminación de la subunidad *g* en *U. maydis* no compromete la dimerización del complejo V pero modifica su estabilidad, a juzgar por su disociación en presencia de bajas concentraciones de digitonina.

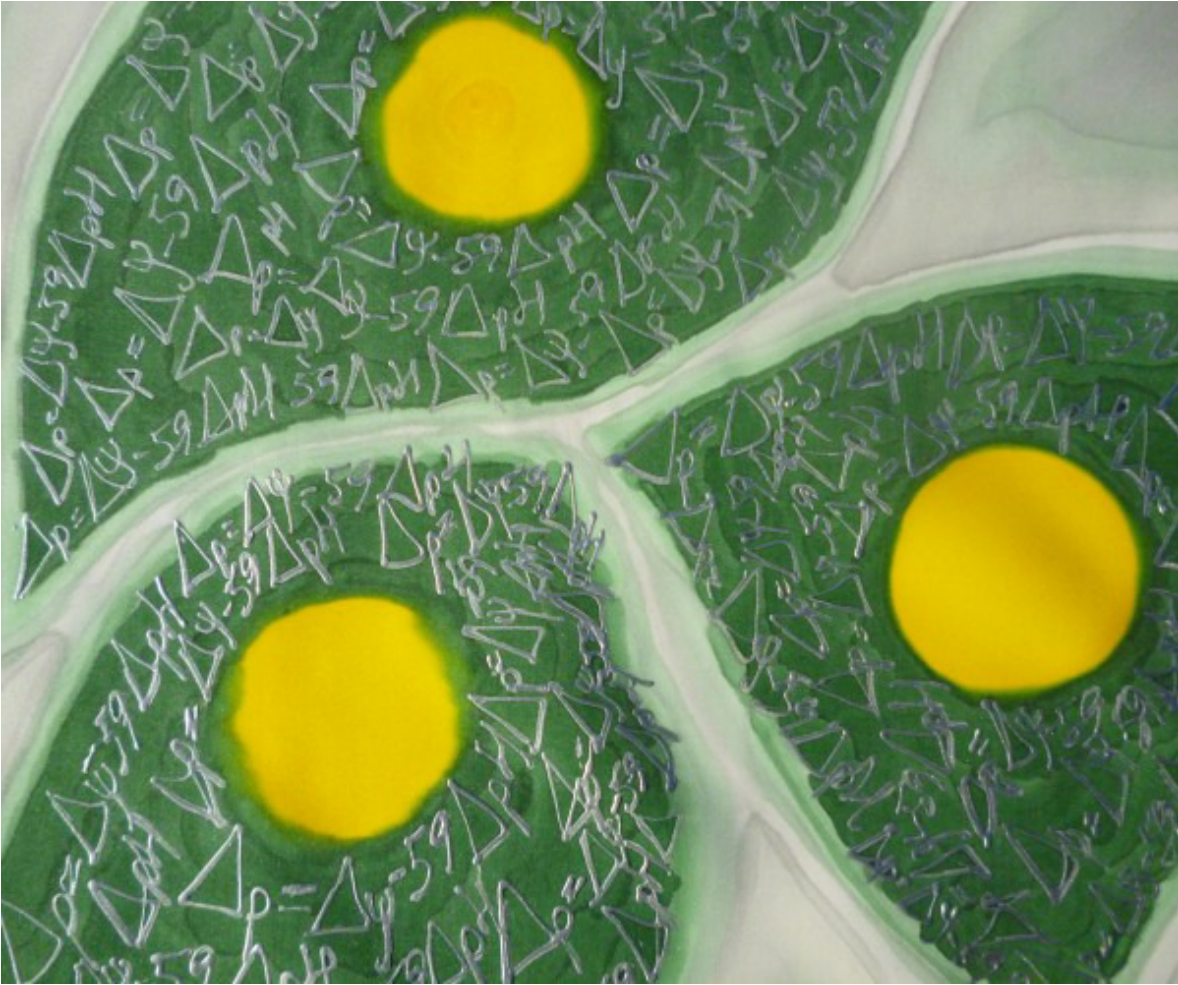


"Mitochondrial dawn" Odra Noel

Perspectivas

8. PERSPECTIVAS

- Construir la mutante Δe y la doble mutante $\Delta e/\Delta g$.
- Realizar experimentos de carbonilación de proteínas como indicador de estrés oxidativo.
- Realizar experimentos de envejecimiento en la cepa Δg .
- Realizar experimentos con diferentes sustratos por ejemplo alimentando el CI con NADH en células permeabilizadas.
- Determinar la formación de crestas mitocondriales de la cepa Δg en ayuno.
- Determinar el potencial de membrana, la respiración y síntesis mitocondrial de ATP en células en ayuno de la cepa Δg .



"Mitchell's equation II" Odra Noel

Referencias Bibliográficas

"Aquí no somos envidiosos" Dr. Antonio Peña

9. REFERENCIAS BIBLIOGRÁFICAS

1. Acín-Pérez, R., Fernández-Silva, P., Peleato, M. L., Pérez-Martos, A. and Enriquez, J. A. (2008) Respiratory active mitochondrial supercomplexes. *Molecular cell*, 32(4):529-39.
2. Abrahams, J. P., Leslie, A. G., Lutter, R. and Walker, J. E. (1994) Structure at 2.8 Å resolution of F₁-ATPase from bovine heart mitochondria. *Nature*, 370(6491):621-8.
3. Adachi, K., Oiwa, K., Nishizaka, T., Furuike, S., Noji, H., Itoh, H., Yoshida, M. and Kinosita, K. Jr. (2007) Coupling of rotation and catalysis in F(1)-ATPase revealed by single-molecule imaging and manipulation. *Cell*, 130:309–321.
4. Affourtit, C., Quinlan, C. L. and Brand. M. D. (2012) Measurement of Proton Leak and Electron Leak in Isolated Mitochondria. *Methods in molecular biology*, 11:165-182.
5. Akerman, K. E. and Wikström, M. K. (1976) Safranin as a probe of the mitochondrial membrane potential. *FEBS Letters*, 68(2):191-7.
6. Alfonzo, M., Kandrach, M. A. and Racker, E. (1981) Isolation, characterization, and reconstitution of a solubilized fraction containing the hydrophobic sector of the mitochondrial proton pump. *Journal of Bioenergetics and Biomembranes*, 13:375-391.
7. Allegretti, M., Klusch, N., Mills, D. J., Vonck, J., Kühlbrandt, W. and Davies, K. M. (2015) Horizontal membrane-intrinsic α -helices in the stator a-subunit of an F-type ATP synthase. *Nature*, 521(7551):237-40.
8. Andrianaivomananjaona, T., Moune-Dimala, M., Herga, S., David, V. and Haraux, F. (2011) How the N-terminal extremity of *Saccharomyces cerevisiae* IF₁ interacts with ATP synthase: a kinetic approach. *Biochimica et Biophysica Acta*, 1807(2):197-204.
9. Arnold, S., Pfeiffer, K., Neupert, W., Stuart, R. A. and Schägger, H. (1998) Yeast mitochondrial F₁F₀-ATP synthase exists as a dimer: identification of three dimer-specific subunits. *The EMBO Journal*, 17:7170-7178.

10. Arselin, G., Vaillier, J., Graves, P. V. and Velours, J. (1996) ATP synthase of yeast mitochondria. Isolation of the subunit h and disruption of the ATP14 gene. *The Journal of Biological Chemistry*, 271:20284-20290.
11. Arselin, G., Vaillier, J., Salin, B., Schaeffer, J., Giraud, M. F., Dautant, A., Brèthes, D. and Velours, J. (2004) The modulation in subunits e and g amounts of yeast ATP synthase modifies mitochondrial cristae morphology. *The Journal of Biological Chemistry*, 279:40392 – 40399.
12. Bisetto, E., Di Pancrazio, F., Simula, M. P., Mavelli, I. and Lippe, G. (2007) Mammalian ATPsynthase monomer versus dimer profiled by blue native PAGE and activity stain. *Electrophoresis*, 28:3178-3185.
13. Bölker, M., Urban, M. and Kahmann, R. (1992) The a mating type locus of *Ustilago maydis* specifies cell signaling components. *Cell*, 68(3):441-50.
14. Bölker, M. *Ustilago maydis* – a valuable model system for the study of fungal dimorphism and virulence (2001) *Microbiology*, 147: 1395- 1401
15. Bonnefoy, N. and Fox, T. D. (2002) Genetic transformation of *Saccharomyces cerevisiae* mitochondria. *Methods and Enzymology*, 350:97-111.
16. Bornhövd, C., Vogel, F., Neupert, W. and Reichert, A. S. (2006) Mitochondrial membrane potential is dependent on the oligomeric state of F₁F₀-ATP synthase supracomplexes. *The Journal of biological chemistry*, 281(20):13990-8.
17. Bottin, A., Kamper, J. and Kahmann, R. (1996) Isolation of a carbon source-regulated gene from *Ustilago maydis*. *Molecular & General Genetics*, 253: 342-352.
18. Boyer, P. D. and Kohlbrenner, W. E. (1981) The present status of the binding change mechanism and its relation to ATP formation by chloroplasts. In: Selman BR, Selman-Peimer S (eds) *Energy coupling in photosynthesis. Elsevier, Amsterdam*, pp 231-240.
19. Boyer, P. D. (2000) Catalytic site forms and controls in ATP synthase catalysis. *Biochimica et Biophysica Acta*, 1458:252-262.

20. Bornhövd, C., Vogel, F., Neupert, W. and Reichert, A. S. (2006) Mitochondrial membrane potential is dependent of the oligomeric state of F₁F₀-ATP synthase supracomplexes. *The Journal of biological chemistry*, 281:13990-13998.
21. Brachmann, A., König, J., Julius, C. and Feldbrügge, M. (2004) A reverse genetic approach for generating gene replacement mutants in *Ustilago maydis*. *Molecular Genetics and Genomic*, 272:261-226.
22. Bravo, C., Minauro-Sanmiguel, F., Morales-Rios, E., Rodríguez-Zabala J. S. and Garcia, J. J. (2004) Overexpression of the inhibitor protein IF(1) in AS-30D hepatoma produces a higher association with mitochondrial F(1)F(0) ATP synthase compared to normal rat liver: functional and cross-linking studies. *Journal of Bioenergetics and Biomembranes*, 36:257-64.
23. Bustos, M. D. and Velours, J. (2005) The modification of the conserved GXXXG motif of the membrane-spanning segment of subunit g destabilizes the supramolecular species of yeast ATP synthase. *The Journal of biological chemistry*, 280(32):29004-10.
24. Buzhynskyy, N., Sens, P., Prima, V., Sturgis, J. N. and Scheuring, S. (2007) Rows of ATP synthase dimers in native mitochondrial inner membranes. *Biophysical Journal*, 93:2870-2876.
25. Cabezón, E., Arechaga, I., Jonathan, P., Butler, G. and Walker, J. E. (2000) Dimerization of bovine F₁-ATPase by binding the inhibitor protein, IF₁. *The Journal of Biological Chemistry*, 275:28353-28355.
26. Cabezón, E., Montgomery, M., G., Leslie, A., G. and Walker, J.E. (2003) The structure of bovine F₁-ATPase in complex with its regulatory protein IF₁. *PNAS*, 10:744-750.
27. Campanella, M., Casswell, E., Chong, S., Farah, Z., Wieckowski, M. R., Abramov, A. Y., Tinker, A. and Duchen, M. R. (2008) Regulation of Mitochondrial Structure and Function by the F₁F₀-ATPase Inhibitor Protein, IF₁. *Cell Metabolism*, 8(1):13-25.
28. Cano-Estrada, A., Vázquez-Acevedo, M., Villavicencio-Queijeiro, A., Figueroa-Martínez, F., Miranda-Astudillo, H., Cordeiro, Y., Mignaco, J. A., Foguel, D., Cardol, P., Lapaille, M., Remacle, C., Wilkens, S. and González-Halphen, D.

- (2010) Subunit-subunit interactions and overall topology of the dimeric mitochondrial ATP synthase of *Polytomella sp.* *Biochimica et Biophysica Acta*, 1797:1439-1448.
29. Cárdenas-Monroy, C. A., Pohlmann, T., Piñón-Zárate, G., Matus-Ortega, G., Guerra, G., Feldbrügge, M. and Pardo, J. P. (2017) The mitochondrial alternative oxidase Aox1 is needed to cope with respiratory stress but dispensable for pathogenic development in *Ustilago maydis*. *PLoS One*, 12(3):e0173389. doi: 10.1371/journal.pone.0173389.
 30. Cardol, P., González-Halphen, D., Reyes-Prieto, A., Baurain, D., Matagne, R. F. and Remacle, C. (2005) The mitochondrial oxidative phosphorylation proteome of *Chlamydomonas reinhardtii* deduced from the Genome Sequencing Project. *Plant Physiology*, 137:447-489.
 31. Cardol, P., Figueroa, F., Remacle, C., Franzén, L. G. and González-Halphen, D. Oxidative phosphorylation: building blocks and related components. David B. Stern (Ed.), *The Chlamydomonas Sourcebook, Organellar and Metabolic Processes*, Volume 2, Elsevier Inc., San Diego (2009), pp. 469-502.
 32. Chance, B. and Williams, G. R. (1957) The respiratory chain and oxidative phosphorylation. *Advances in enzymology and related subjects of biochemistry*, 17:65-134.
 33. Chávez, E., Flores-Herrera, O. y Martínez, F. Capítulo 22, Ciclo de los ácidos tricarbónicos, *Bioquímica de Laguna*, 7ª edición, Laguna, J., Piña, E., Martínez, F., Pardo, J. P. y Riveros, H. (Editores), Manual Moderno, 2013.
 34. Chávez, E., Flores-Herrera, O. y Martínez, F. Capítulo 23, Oxidaciones Biológicas y Bioenergética, *Bioquímica de Laguna*, 7ª edición, Laguna, J., Piña, E., Martínez, F., Pardo, J. P. y Riveros, H. (Editores), Manual Moderno, 2013.
 35. Cogliati, S., Enriquez, J. A. and Scorrano, L. (2016) Mitochondrial Cristae: Where Beauty Meets Functionality. *Trends in biochemical sciences*, 41(3):261-273.
 36. Colina-Tenorio, L., Miranda-Astudillo, H., Cano-Estrada, A., Vázquez-Acevedo, M., Cardol, P., Remacle, C. and González-Halphen, D. (2016)

- Subunit Asa1 spans all the peripheral stalk of the mitochondrial ATP synthase of the chlorophycean alga *Polytomella sp.* *Biochimica et Biophysica Acta*, 1857(4):359-369.
37. Colina-Tenorio, L., Dautant, A., Miranda-Astudillo, H., Giraud, M. F. and González-Halphen, D. (2018) The Peripheral stalk of rotary ATPases. *Frontiers in Physiology*, doi: 10.3389/fphys.2018.01243.
 38. Couoh-Cardel, S., Uribe-Carvajal, S., Wilkens, S. and García-Trejo, J. J. (2010) Structure of dimeric F₁F₀-ATP synthase. *The Journal of biological chemistry*, 285(47):36447-36455.
 39. Cox, G.B., Jans, D. A., Fimmel, A.L., Gibson, F. and Hatch, L. (1984) Hypothesis. The mechanism of ATP synthase. Conformational change by rotation of the beta-subunit. *Biochimica et Biophysica Acta*, 768:201–208.
 40. De los Rios-Castillo, D., Zarco-Zavala, M., Olvera-Sanchez, S., Pardo, J. P., Juarez, O., Martinez, F., Mendoza-Hernandez, G., García-Trejo, J. J. and Flores-Herrera, O. (2011) Atypical cristae morphology of human syncytiotrophoblast mitochondria: role for complex V. *he Journal of biological chemistry*, 286(27):23911-23919.
 41. Devenish, R. J., Prescott, M. and Rodgers, A. J. (2008) The structure and function of mitochondrial F₁F₀-ATP synthases. *International review of cell and molecular biology*, 267:1-58.
 42. Díaz-Ruiz, R., Avéret, N., Araiza, D., Pinson, B., Uribe-Carvajal, S., Devin, A. and Rigoulet, M. (2008) Mitochondrial oxidative phosphorylation is regulated by fructose 1,6-bisphosphate. A possible role in Crabtree effect induction? *The Journal of biological chemistry*, 283(40):26948-26955.
 43. Dienhart, M., Pfeiffer, K., Schagger, H. and Stuart, R. A. (2002) Formation of the yeast F₁F₀-ATP synthase dimeric complex does not require the ATPase inhibitor protein, Inh1. *The Journal of Biological Chemistry*, 277:39289-39295.
 44. Doehlemann, G., Wahl, R., Horst, R. J., Voll, L. M., Usadel, B., Poree, F., Stitt, M., Pons-Kühnemann, J., Sonnewald, U., Kahmann, R. and Kämper, J. (2008) Reprogramming a maize plant: transcriptional and metabolic changes induced

- by the fungal biotroph *Ustilago maydis*. *The Plant journal: for cell and molecular biology*, 56(2):181-195.
45. Dudkina, N. V., Sunderhaus, S., Braun, H. P. and Boekema, E. J. (2006) Characterization of dimeric ATP synthase and cristae membrane ultrastructure from *Saccharomyces* and *Polytomella* mitochondria. *FEBS Letters*, 580:3427-3432.
 46. Duvezin-Caubet, S., Rak, M., Lefebvre-Legendre, L., Tetaud, E., Bonnefoy, N. and di Rago, J. P. (2006) A 'petite-obligate' mutant of *Saccharomyces cerevisiae*: Functional mtDNA is lethal in cells lacking the δ subunit of mitochondrial F₁-ATPase. *The Journal of Biological Chemistry*, 281:16305-16313.
 47. Ebner, E. and Maier, K. L. (1977) A protein inhibitor of mitochondrial adenosine triphosphatase (F₁) from *Saccharomyces cerevisiae*. *The Journal of biological chemistry*, 252(2):671-676.
 48. El-Khoury, R., Dufour, E., Rak, M., Ramanantsoa, N., Grandchamp, N., Csaba, Z., Duvillié, B., Bénit, P., Gallego, J., Gressens, P., Sarkis, C., Jacobs, H. T. and Rustin, P. (2013) Alternative Oxidase Expression in the Mouse Enables Bypassing Cytochrome C Oxidase Blockade and Limits Mitochondrial ROS Overproduction. *PLoS genetics*, 9(1):e1003182.
 49. El-Khoury, R., Kemppainen, K. K., Dufour, E., Szibor, M., Jacobs, H. T. and Rustin, P. (2014) Engineering the Alternative Oxidase Gene to Better Understand and Counteract Mitochondrial Defects: State of the Art and Perspectives. *PLoS genetics*, 171(8):2243-9.
 50. Esparza-Perusquía, M., Olvera-Sánchez, S., Pardo, J. P., Mendoza-Hernández, G., Martínez, F. and Flores-Herrera O. (2017) Structural and kinetics characterization of the F₁F₀-ATP synthase dimer. New repercussion of monomer-monomer contact. *Biochimica et Biophysica Acta -Bioenergetics*. 1858(12):975-981.
 51. Esparza-Perusquía, M., Langner, T., García-Cruz, G., Feldbrügge, M., Zavala, G., Pardo, J. P., Martínez, F. and Flores-Herrera, O. Deletion of subunit g

- affects the stability of the dimeric state of the F₁F₀-ATP synthase and decreases the mitochondrial ATP synthesis. *En preparación*.
52. Estambrook, R. W. (1967) Mitochondrial respiratory control and the polarographic measurement of ADP: O ratios. *Methods and Enzymology*, 10:41-47.
 53. Feinberg, A. P. and Vogelstein, B. (1983) A technique for radiolabeling DNA restriction endonuclease fragments to high specific activity. *Analytical biochemistry*, 132(1):6-13.
 54. Feldbrügge, M., Kämper, J., Steinberg, G. and Kahmann, R. (2004) Regulation of mating and pathogenic development in *Ustilago maydis*. *Current opinion in microbiology*, 7(6):666-672.
 55. Fiske, C. H. and Subbarow, Y. (1925) The Colorimetric Determination Of Phosphorus. *The Journal of Biological Chemistry*, 66:375-400.
 56. Frey, T. G., Renken, C. W. and Perkins, G. A. (2002) Insight into mitochondrial structure and function from electron tomography. *Biochimica et Biophysica Acta*, 1555(1-3):196-203.
 57. Funes, S., Davidson, E., Claros, M. G., van Lis, R., Pérez-Martínez, X., Vázquez-Acevedo, M., King, M. P. and González-Halphen, D. (2002) The typically mitochondrial DNA-encoded ATP6 subunit of F₁F₀-ATPase is encoded by a nuclear gene in *Chlamydomonas reinhaedtii*. *The Journal of Biological Chemistry*, 277:6051-6058.
 58. García, J. J., Morales-Ríos, E., Cortés-Hernández, P. and Rodríguez-Zavala, J. S. (2006) The inhibitor protein (*IF₁*) promotes dimerization of the mitochondrial F₁F₀-ATP synthase. *Biochemistry*, 45:12695-12703.
 59. Gledhill, J. R. and Walker, J. E. (2005) Inhibition sites in F₁-ATPase from bovine heart mitochondria. *The Biochemical journal*, 386(Pt 3):591-598.
 60. Giraud, M. F., Paumard, P., Soubannier, V., Vaillier, J., Arselin, G., Salin, B., Schaeffer, J., Brèthes, D., di Rago, J. P. and Velours, J. (2002) Is there a relationship between the supramolecular organization of the mitochondrial ATP synthase and the formation of cristae? *Biochimica et Biophysica Acta*, 1555:174-180.

61. Guérin, B., Labbe, P. and Somlo, M. (1979). Preparation of yeast mitochondria (*Saccharomyces cerevisiae*) with good P/O and respiratory control ratios. *Methods Enzymology*, 55:149-159.
62. Guerrero-Castillo, S., Cabrera-Orefice, A., Vázquez-Acevedo, M., González-Halphen, D. and Uribe-Carvajal, S. (2012) During the stationary growth phase, *Yarrowia lipolytica* prevents the overproduction of reactive oxygen species by activating an uncoupled mitochondrial respiratory pathway. *Biochimica et Biophysica Acta*, 1817:353–362.
63. Gu, J., Zhang, L., Zong, S., Guo, R., Liu, T., Yi, J., Wang, P., Zhuo, W. and Yang, M. (2019) Cryo-EM structure of the mammalian ATP synthase tetramer bound with inhibitory protein *IF₁*. *Science*, 364(6445):1068-1075.
64. Guo, H., Bueler, S. A. and Rubinstein, J. L. (2017) Atomic model for the dimeric FO region of mitochondrial ATP synthase. *Science*, 358(6365):936-940.
65. Guo, H. and Rubinstein, J. L. (2018) Cryo-EM of ATP Synthases. *Current opinion in structural biology*, 52:71-79.
66. Habersetzer, J., Ziani, W., Larrieu, I., Stines-Chaumeil, C., Giraud, M. F., Brèthes, D., Dautant, A. and Paumard, P. (2013) ATP synthase oligomerization: from the enzyme models to the mitochondrial morphology. *The international journal of biochemistry & cell biology*, 1:99-105.
67. Hackenbrock, C. R., Chazotte, B. and Gupte, S. S. (1986) The random collision model and a critical assessment of diffusion and collision in mitochondrial electron transport. *Journal of Bioenergetics and Biomembranes*, 18:331–368.
68. Herrera, T., Ulloa, M. and Ruiz-Oronoz, M. (1990) El reino de los hongos. *Micología básica y aplicada*. Fondo de la Cultura Económica/IBT-UNAM, Mexico, D.F. pp 294-301.
69. Hirst, J. (2013). Mitochondrial complex I. *Annual review of biochemistry*, 82, 551–575.
70. Horst, R. J., Zeh, C., Saur, A., Sonnewald, S., Sonnewald, U. and Voll, L. M. (2012) The *Ustilago maydis* Nit2 homolog regulates nitrogen utilization and is required for efficient induction of filamentous growth. *Eukaryot Cell*, 11: 368-380.

71. Itoh, H., Takahashi, A., Adachi, K., Noji, H., Yasuda, R., Yoshida, M. and Kinosita, K. (2004) Mechanically driven ATP synthesis by F1-ATPase. *Nature*, 427:465-468.
72. Juárez, O., Guerra, G., Martínez, F. and Pardo, J. P. (2004) The mitochondrial respiratory chain of *Ustilago maydis*. *Biochimica et Biophysica Acta*, 1658(3):244-51.
73. Juárez, O., Guerra, G., Velázquez, I., Flores-Herrera, O., Rivera-Pérez, R. E. and Pardo, J. P. (2006) The physiologic role of alternative oxidase in *Ustilago maydis*. *The FEBS Journal*, 273:4603-4615.
74. Jung, C., Higgins, C. M. and Xu, Z. (2000) Measuring the quantity and activity of mitochondrial electron transport chain complexes in tissues of central nervous system using blue native polyacrylamide gel electrophoresis. *Analytical Biochemistry*, 286:214-223.
75. Junge, W., Lill, H. and Engelbrecht, S. (1997) ATP synthase: an electrochemical transducer with rotatory mechanics. *Trends in biochemical sciences*, 22(11):420-3.
76. Kahmann, R., Basse, C. and Feldbrügge, M. (1999) Fungal-plant signalling in the *Ustilago maydis*-maize pathosystem. *Current opinion in microbiology*, 2(6):647-650.
77. Ko, Y. H., Delannoy, M., Hüllihen, J., Chiu, W. and Pedersen, P. L. (2003) Mitochondrial ATP Synthasome. Cristae-enriched Membranes and a Multiwell Detergent Screening Assay Yield Dispersed Single Complexes Containing the ATP Synthase and Carriers for Pi and ADP/ATP. *The Journal of Biological Chemistry*, 278(14):12305-9.
78. Kühlbrandt, W. (2015) Structure and function of mitochondrial membrane protein complexes. *BMC Biology*, 13(1):89-99.
79. Kühlbrandt, W. and Davies, K. M. (2016) Rotary ATPases: A New Twist to an Ancient Machine. *Trends in biochemical sciences*, 41(1):106-116.
80. Kushner, S. R. (1978) An improved method for transformation of *E. coli* with ColE1 derived plasmids. In *Genetic Engineering*, Boyer H. B. and Nicosia S. (Amsterdam: Elsevier/North-Holland), 17–23.

81. Legros, F., Lombes, A., Frachon, P. and Rojo, M. (2002) Mitochondrial fusion in human cells is efficient, requires the inner membrane potential, and is mediated by mitofusins. *Molecular Biology of the Cell*, 13:4343-4354.
82. Lengeler, J. W. (2000) Metabolic networks: a signal-oriented approach to cellular models. *Biological Chemistry*, 381(9-10):911-920.
83. Letts, J. A. and Sazanov, L. A. (2017) Clarifying the supercomplex: the higher-order organization of the mitochondrial electron transport chain. *Nature structural and molecular biology*, 24(10):800-808
84. Letts, J. A., Fiedorczuk, K., Degliesposti, G., Skehel, M. and Sazanov, L. A. (2019) Structures of respiratory supercomplex I+III₂ reveal functional and conformational crosstalk. *Molecular cell*, 75(6):1131-1146.
85. Levine, R. L., Garland, D., Oliver, C. N., Amici, A., Climent, I., Lenz, A. G., Ahn, B. W., Shaltiel, A. and Stadtman, E. (1990) Determination of carbonyl contents oxidatively modified proteins. *Methods in enzymology*, 186:464-478.
86. Liu, Y. B., Koh, C. M. J. and Ji, L. H. (2011) Bioconversion of crude glycerol to glycolipids in *Ustilago maydis*. *Bioresource Technology*, 102:3927-3933.
87. Lowry, O. H., Rosebrough, N. J., Farr, A. L. and Randall, R. J. (1951) Protein measurement with the Folin phenol reagent. *The Journal of biological chemistry*, 193:265-275.
88. Mahuran, D., Clements, P., Carrella, M. and Strasberg, P. M. (1983) A High Recovery Method for Concentrating Microgram Quantities of Protein from Large Volumes of Solution. *Analytical biochemistry*, 129:513-516.
89. Mannella, C. A. (2000) Introduction: Our changing view of mitochondria. *Journal of Bioenergetics and Biomembranes*, 32:1-4.
90. Mannella, C. A., Pfeiffer, D. R., Bradshaw, P. C., Moraru, I. I., Slepchenko, B., Loew, L. M., Hsieh, C., Buttle, K. and Marko, M. (2001) Topology of the mitochondrial inner membrane: Dynamics and bioenergetic implications. *International Union of Biochemistry and Molecular Biology*, 52:93-100.
91. Mannella C. A. (2006) The relevance of mitochondrial membrane topology to mitochondrial function. *Biochimica et Biophysica Acta*, 1762:140-147.

92. Mannella, C. A., Lederer, W. J. and Jafri, M. S. (2013) The connection between inner membrane topology and mitochondrial function. *International Society for Heart Research*, 62:51-57.
93. Marques, I., Dencher, N.A., Videira, A. and Krause, F. (2007) Supramolecular organization of the respiratory chain in *Neurospora crassa* mitochondria. *American Society for Microbiology*, 6:2391-2405.
94. McArthur, K. and Ryan, M. T. (2020) Resolving mitochondrial cristae: introducing a new model the fold. *The EMBO journal*, 39(14):e105714.
95. McKee, T. and McKee J. R. Capítulo 2, Las células vivas, Bioquímica, Las bases moleculares de la vida, 4ª edición, Mc Graw Hill, 2009.
96. Mendoza-Mendoza, A., Berndt, P., Djamei, A., Weise, C., Linne, U., Marahiel, M., Vranes, M., Kämper, J. and Kahmann, R. (2009) Physical-chemical plant-derived signals induce differentiation in *Ustilago maydis*. *Molecular Microbiology*, 71(4):895-911.
97. Milenkovic, D. Larsson, N. G. (2015) Mic10 Oligomerization Pinches off Mitochondrial Cristae. *Cell Metabolism*, 21(5):660-1.
98. Minauro-Sanmiguel, F., Bravo, C. and García, J. J. (2002) Cross-linking of the endogenous inhibitor protein (IF_1) with rotor (gamma, epsilon) and stator (alpha) subunits of the mitochondrial ATP synthase. *Journal of Bioenergetics and Biomembranes*, 34(6):433-443.
99. Minauro-Sanmiguel, F., Wilkens, S. and García, J. J. (2005) Structure of dimeric mitochondrial ATP synthase: novel F₀ bridging features and the structural basis of mitochondrial cristae biogenesis. *PNAS*, 102:12356-12358.
100. Miranda-Astudillo, H., Cano-Estrada, A., Vázquez-Acevedo, M., Colina-Tenorio, L., Downie-Velasco, A., Cardol, P., Remacle, C., Domínguez-Ramírez, L. and González-Halphen, D. (2014) Interactions of subunits Asa2, Asa4 and Asa7 in the peripheral stalk of the mitochondrial ATP synthase of the chlorophycean alga *Polytomella* sp. *Biochimica et Biophysica Acta - Bioenergetics*, 1837(1):1-13.
101. Mitchell, P. (1961) Coupling of phosphorylation to electron and hydrogen transfer by a chemi-osmotic type of mechanism. *Nature*, 191:155-148.

102. Morales-Ríos, E., De la Rosa-Morales, F., Mendoza-Hernández, G., Rodríguez-Zavala, J. S., Celis, H., Zarco-Zavala, M. and García-Trejo, J. J. (2010) A novel 11-kDa inhibitory subunit in the F1F0 ATP synthase of *Paracoccus denitrificans* and related alpha-proteobacteria. *FASEB journal*, 24(2):599-608.
103. Nicholls, D. G. and Ferguson, S. T. (2013) Bioenergetics 4, *Academic Press*, 207.
104. Orriss, G. L., Leslie, A. G., Braig, K. and Walker, J. E. (1998) Bovine F1-ATPase covalently inhibited with 4-chloro-7-nitrobenzofurazan: the structure provides further support for a rotary catalytic mechanism. *Structure*, 6(7):831-7.
105. Panov, A., Dikalov, S., Shalbuyeva, N., Hemendinger, R., Greenamyre, J. T. and Rosenfeld, J. (2007) Species- and tissue-specific relationships between mitochondrial permeability transition and generation of ROS in brain and liver mitochondria of rats and mice. *Am. J. Physiol. Cell. Physiol.* 292, C708–C718
106. Paumard, P., Vaillier, J., Couлары, B., Schaeffer, J., Soubannier, V., Mueller, D. M., Brèthes, D., Di Rago, J. P. and Velours, J. (2002) The ATP synthase is involved in generating mitochondrial cristae morphology. *The EMBO Journal*, 21:221-230.
107. Penefsky, H. S., Pullman, M. E., Datta, A. and Racker, E. (1960) Partial resolution of the enzymes catalyzing oxidative phosphorylation. II. Purification and properties of soluble dinitrophenol-stimulated adenosine triphosphatase. *The Journal of Biological Chemistry*, 235:3322–3329.
108. Penefsky, H. S. (1974) Mitochondrial and chloroplast ATPases. *The Enzymes*, 10:375-429.
109. Pullman, M. E. and Monroy, G.C. (1963) A naturally occurring inhibitor of mitochondrial adenosine triphosphate. *The Journal of Biological Chemistry*, 238:3762-3769.
110. Rabl, R., Soubannier, V., Scholz, R., Vogel, F., Mendl, N., Vasiljev-Neumeyer, A., Körner, C., Jagasia, R., Keil, T., Baumeister, W., Cyrklaff, M., Neupert, W. and Reichert, A. S. (2009) Formation of cristae and crista junction in

- mitochondria depends on antagonism between Fc_j and su *e/g*. *The Journal of cell biology*, 185:1047-1063.
111. Racker, E. (1963) A mitochondrial factor conferring oligomycin sensitivity on soluble mitochondrial ATPase. *Biochemical and biophysical research communications*, 10:435-439.
 112. Reifschneider, N., Goto, S., Nakamoto, H., Takahashi, R., Sugawa, M., Dencher, N. A. and Krause, F. (2005) Defining the mitochondrial proteomes from five rat organs in a physiologically significant context using 2D blue-native/SDS-PAGE. *Journal of proteome research*, 5:1117-1132.
 113. Reyes-Galindo, M., Suarez, R., Esparza-Perusquía, M., de Lira-Sánchez, J., Pardo, J. P., Martínez, F., and Flores-Herrera O. (2019) Mitochondrial respirasome works as a single unit and the crosstalk between complexes I, III₂ and IV stimulates NADH dehydrogenase activity. *Biochimica et Biophysica Acta -Bioenergetics*. 1860(8):618-627.
 114. Rexroth, S, Tittingdorf, J. M. W. M. Z., Schwassmann, H. J., Krause, F., Seelert, H. and Dencher, N. A. (2004) Dimeric H⁺-ATPsynthase in the chloroplast of *Chlamydomonas reinhardtii*. *Biochimica et Biophysica Acta*, 1658:202-211.
 115. Robb, E. L., Hall, A. R., Prime, T. A., Eaton, S., Szibor, M., Viscomi, C., James, A. M. and Murphy, M. P. (2018) Control of Mitochondrial Superoxide Production by Reverse Electron Transport at Complex I. *The Journal of biological chemistry*, 293(25):9869-9879.
 116. Rogov, A. G., Sukhanova, E. I., Uralskaya, L. A., Aliverdieva, D. A. and Zvyagil'skaya, R. A. (2014) Alternative oxidase: distribution, induction, properties, structure, regulation, and functions. *Biochemistry (Moscow)*, 79(13):1615-34.
 117. Rybicki, E. P. and Purves, M. (1996) Western or enzyme-assisted immunoelectro-blotting (IEB).
 118. Saddar. S and Stuart, R. A. (2005) The yeast F(1)F(0)-ATP synthase: analysis of the molecular organization of subunit g and the importance of a conserved GXXXG motif. *The Journal of biological chemistry*, 280(26):24435-42.

119. Saddar, S., Dienhart, M. K. and Stuart, R. A. (2008) The F₁F₀-ATP synthase complex influences the assembly state of the cytochrome bc₁-cytochrome oxidase supercomplexes and its association with TIM23 machinery. *The Journal of biological chemistry*, 283:6677-6686.
120. Sambrook, J. and D. W. Russell, 2001 *Molecular Cloning: A Laboratory Manual*, Cold Spring Harbor Laboratories, New York.
121. Sánchez-Vásquez, L., Vázquez-Acevedo, M., de la Mora, J., Vega-de Luna, F., Cardol, P., Remacle, C., Dreyfus, G. and González-Halphen, D. (2017) Near-neighbor interactions of the membrane-embedded subunits of the mitochondrial ATP synthase of a chlorophycean alga. *Biochimica et Biophysica Acta*, 1858(7):497-509.
122. Sazanov, L. A. (2015). A giant molecular proton pump: structure and mechanism of respiratory complex I. *Nature reviews. Molecular cell biology*, 16(6):375-88.
123. Schägger, H. and von Jagow, G (1991) Blue native electrophoresis for isolation of membrane protein complexes in enzymatically active form. *Analytical biochemistry*, 199(2):223-231.
124. Schägger, H. (2000) Supercomplexes in the respiratory chains of yeast and mammalian mitochondria. *The EMBO journal*, 19(8):1777-83.
125. Segel, I. H. (1993) *Enzyme kinetics: behavior and analysis of rapid equilibrium and steady-state enzyme systems*. New York: Wiley-Interscience.
126. Song, D. H., Park, J., Philbert, M. A., Sastry, A. M. and Lu, W. (2014) Effects of local pH on the formation and regulation of cristae morphologies. *Physical review. E, Statistical, nonlinear, and soft matter physics*, 90(2):022702.
127. Southern, E. M. (1975) Detection of specific sequences among DNA fragments separated by gel electrophoresis. *Journal of molecular biology*, 98(3):503-517.
128. Strauss, M., Hofhaus, G., Schröder, R. R. and Kühlbrandt, W. (2008) Dimer ribbons of ATP synthase shape the inner mitochondrial membrane. *The EMBO Journal*, 27:1154-1160.

129. Thomas, D., Bron, P., Weimann, T., Dautant, A., Giraud, M.F., Paumard, P., Salin, B., Cavalier, A., Velours, J. and Brèthes, D. (2008) Supramolecular organization of the yeast F₁F₀-ATP synthase. *Biology of the Cell*, 100:591-601.
130. Tomasetig, L., Di Pancrazio, F., Harris, D. A., Mavelli, I., Lippe, G. (2002) Dimerization of F₀F₁ATP synthase from bovine heart is independent from the binding of the inhibitor protein IF₁. *Biochimica Biophysica Acta*, 1556, 133-141.
131. Trautschold, I., Lamprecht, W. and Schweitzer, G. (1995) UV method with hexokinase and glucose-6-phosphate dehydrogenase. *Method of enzymatic analysis*, Bergmeyer, 7:346-357.
132. van Lis, R., Atteia, A., Mendoza-Hernández, G. and González-Halphen, D. (2003) Identification of novel mitochondrial protein components of *Chlamydomonas reinhardtii*. A proteomic approach. *Plant Physiology*, 132:318-330.
133. van Lis, R., Mendoza-Hernández, G., Groth, G. and Atteia, A. (2007) New insights into the unique structure of the F₀F₁-ATP synthase from the chlamydomonad algae *Polytomella sp.* and *Chlamydomonas reinhardtii*. *Plant Physiology*, 144:1190-1199.
134. Vázquez-Acevedo, M., Cardol, P., Cano-Estrada, A., Lapaille, M., Remacle, C. and González-Halphen, D. (2006) The mitochondrial ATP synthase of chlorophycean algae contains eight subunits of unknown origin involved in the formation of an atypical stator-stalk and in the dimerization of the complex. *Journal of bioenergetics and biomembranes*, 38:271-282.
135. Velours, J., Dautant, A., Salin, B., Sagot, I. and Brèthes, D. (2009) Mitochondrial F₁F₀-ATP synthase and organellar internal architecture. *The Internal Journal of Biochemistry and Cell Biology*, 41:1783-1789.
136. Villavicencio-Queijeiro, A., Vázquez-Acevedo, M., Cano-Estrada, A., Zarco-Zavala, M., Tuena de Gómez, M., Mignaco, J. A., Freire, M. M., Scofano, H. M., Foguel, D., Cardol, P., Remacle, C. and González-Halphen, D. (2009) The fully-active and structurally stable form of the mitochondrial ATP synthase of *Polytomella sp.* is dimeric. *Journal of bioenergetics and biomembranes*, 41:1-13.

137. Villavicencio-Queijeiro, A., Pardo, J. P. and González-Halphen, D. (2015) Kinetic and hysteretic behavior of ATP hydrolysis of the highly stable dimeric ATP synthase of *Polytomella* sp. *Archives of biochemistry and biophysics*, 575:30-37.
138. Vollmeister, E., Schipper, K., Baumann, S., Haag, C., Pohlmann, T., Stock, J. and Feldbrügge, M. (2012) Fungal development of the plant pathogen *Ustilago maydis*. *FEMS microbiology reviews*, 36(1):59-77.
139. Vonk, J. and Schäfer, E. (2009) Supramolecular organization of protein complexes in the mitochondrial inner membrane. *Biochimica et Biophysica Acta*, 1793:117-124.
140. Wagner, K., Perschil, I., Fichter, C. D. and van der Laan, M. (2010) Stepwise assembly of dimeric F₁F₀-ATP synthase in mitochondria involves the small F₀-subunits k and i. *Molecular biology of the cell*, 9:1494-1504.
141. Walker, J. E. (1998) ATP Synthesis by Rotary Catalysis (Nobel lecture). *Angewandte Chemie International Edition*, 37:2308-2319.
142. Walker, J. E. and Dickson, V.K. (2006) The peripheral stalk of the mitochondrial ATP synthase. *Biochimica et Biophysica Acta*, 1757:286–296.
143. Waterborg, J. and Matthews, H. (1984) The Lowry method for protein quantitation. *The Protein Protocols Handbook*, DOI: 10.1385/1-59259-169-8:7.
144. Watt, I. N., Montgomery, M. G., Runswick, M. J., Leslie, A. G. and Walker, J. E. (2010) Bioenergetic cost of making an adenosine triphosphate molecule in animal mitochondria. *PNAS*, 107:16823-16827.
145. Weber, J. and Senior, A. E. (2003) ATP synthesis driven by proton transport in F₁F₀-ATP synthase. *FEBS Letters*, 545:61-70.
146. Wittig, I., Braun, H. P. and Schägger, H. (2006) Blue native PAGE. *Nature protocols*, 1(1):418-428.
147. Wittig, I., Karas, M. and Schägger, H. (2007) High resolution clear native electrophoresis for in-gel functional assays and fluorescence studies of membrane protein complexes. *Molecular & cellular proteomics*, 6:1215-1225.

148. Wittig, I., Velours, J., Stuart, R. and Schägger, H. (2008) Characterization of domain interfases in monomeric and dimeric ATP synthase. *Molecular and cellular proteomics*, 5:995-1004.
149. Wittig, I. and Schägger, H. (2008) Structural organization of mitochondrial ATP synthase. *Biochimica et Biophysica Acta*, 1777:592-598.
150. Wittig, I., Meyer, B., Heide, H., Steger, M., Bleier, L., Wumaier, Z., Karas, M. And Schägger, H. (2010) Assembly and oligomerization of human ATP synthase lacking mitochondrial subunits a and A6L. *Biochimica et Biophysica Acta*, 1797:1004-1011.
151. Wurm, C. A. and Jakobs, S. Differential protein distributions define two sub-compartments of the mitochondrial inner membrane in yeast. *FEBS letters*, 580(24):5628-34.
152. Yoshida, M., Muneyuki, E. and Isabori, T. (2001) ATP synthase — a marvellous rotatory engine of the cell. *Nature reviews. Molecular cell biology*, 2:669-677.
153. Zerbetto, E., Vergani, L. and Dabbeni-Sala, F. (1997) Quantification of muscle mitochondrial oxidative phosphorylation enzymes via histochemical staining of blue native polyacrylamide gels. *Electrophoresis*, 18(11):2059-2064.
154. Zick, M., Rabl, R. and Reichert, A.S. (2009) Cristae formation-linking ultrastructure and function of mitochondria. *Biochimica et Biophysica Acta*, 1793:5-19.



"The Classical Organell 1- Mitochondria" Odra Noel

Anexos

10. ANEXOS

10.1. Oligonucleótidos usados para la formación del Knock-out para la transformación de *Ustilago maydis*.

Tabla 4. Oligonucleótidos utilizados para generar el plásmido knock-out y para verificar la cepa mutante Δg .

Gen		Secuencia del oligonucleótido
ATP20 (sub <i>g</i>)	U1	5'- GCGTAGTCGATGTCCTTGG -3'
	U2	5'- ATTTAAAT GCTTCCTTGTATTCGGC -3'
	U3	5'- GGCCATCTAGGCC GATGACCGTATTACCCGAAAGAC -3'
	D1	5'- GGCCTGAGTGGCC ACGCTCGACAATTGAATTCG -3'
	D2	5'- ATTTAAATCTGGC ATGTGCTCACC -3'
	D3	5'- GGCCTGCCGTATCAAGTC -3'
	P1	5'- TCCTCACACCATCCCCTT -3'
	P2	5'- GGGAGCAGCAGCTCGGC -3'
Secuenciar	M13F	5'- GTTTTCCCAGTCACGAC -3'
	M13R	5'- CAGGAAACAGCTATGAC -3'
	MF167	5'- AACTCGCTGGTAGTTACCAC -3'
	MF168	5'- ACTAGATCCGATGATAAGCTG -3'

Las letras en negrita indican el sitio de corte para la enzima *SwaI* o *SfiI*.

10.2. Transformación por biobalística.

La transformación para generar la cepa Δg se realizó como lo reporta Bonnefoy *et al.*, (2002). Se cultiva la cepa WT en 30 mL de medio YPD durante 24 horas a 28°C, se toman 500 μ L del cultivo para inocular 50 mL de YPD y se cultivan durante 24 horas a 28°C en agitación orbital constante.

Las células se centrifugan a 2300 *g* por 5 min y el paquete celular se resuspende en 600 μ L de medio YPD. Las células se extienden en 6 cajas de Petri con YPD-Agar suplementado con higromicina (50 μ g higromicina B/mL de PBS) y se dejan secar por 3 horas a temperatura ambiente en esterilidad.

Preparación de los microproyectiles y precipitación del DNA. Se colocan 50 mg de micropartículas de tungsteno en un tubo de 1.5 mL y se esterilizan incubando por 10 min con metanol al 70% (p/v). Se centrifugan a 13,200 g por 15 min y se elimina cuidadosamente el sobrenadante. Las partículas se lavan con agua estéril y se resuspenden hasta una concentración de 50 mg/mL en 50% (v/v) glicerol y se mantienen en hielo. Posteriormente se mezclan 5 µg del pUMa_1704 con 100 µg de la suspensión de partículas de tungsteno, 4 µL de espermidina 1 M (Cf= 26.66 mM) y 100 µL de CaCl₂ 2.5 M (Cf= 1.66 M). Se agitan en vortex inmediatamente después de la adición de cada reactivo. Se adiciona 20 µL de la suspensión en cada uno de los microproyectiles.

Bombardeo de células. El bombardeo se realiza en un Biolistic Gun (PDS-1000He BioRad) esterilizado con metanol al 70% (v/v) y siguiendo las instrucciones del fabricante. Se bombardean las partículas a 1100 psi, considerando un vacío de 29 a 29.5 pulgadas de mercurio. Una vez realizado el bombardeo, las placas se incuban de 5 a 7 días a 28°C hasta que se observe el crecimiento de las colonias.

10.3. *Solución de Sales.* El buffer 1x de solución de sales está compuesto por 117 mM de KH₂PO₄, 28.2 mM de NaSO₄, 107 mM de KCl, 16.6 mM de MgSO₄, 9 mM de CaCl₂.

10.4. *Elementos traza.* El buffer 1x de elementos traza está compuesto por 0.97 mM de H₃BO₃, 0.7 mM de MnCl₂·4H₂O, 2.9 mM de ZnCl₂, 0.18 mM de NaMoO₄·2H₂O, 0.37 mM de FeCl₃·6H₂O y 1.6 mM CuSO₄·5H₂O, pH 7.0.

10.5. *Cuantificación de la cantidad de F₁F₀-ATP sintasa en las muestras V_{2WT}, V_{1WT} y V_{1Δg}.*

Para cuantificar el contenido de F₁F₀-ATP sintasa presente en las muestras V_{2WT}, V_{1WT} y V_{1Δg} (Figura S1), se resolvieron 10 µg de proteína de cada muestra mediante SDS-Tricina-PAGE y se tiñeron con azul brillante de Coomassie® R250. Se utilizó BSA como estándar en el mismo gel y su concentración se determinó

mediante espectroscopía utilizando su coeficiente de extinción molar ($\epsilon = 6.58 \text{ mM}^{-1} \text{ cm}^{-1}$ para el 1% (p/v) BSA). La intensidad de la tinción con azul de Coomassie® R250 de la curva estándar de BSA fue lineal en el intervalo de concentración de proteína utilizada. El gel fue escaneado y la intensidad de la señal de las subunidades α y β del complejo V fue determinada por el software MyImageAnalysis 2.0 (ThermoScientific). El mol (o la cantidad de moles) de cada subunidad se determinó usando el peso molecular de la proteína madura (<https://www.genome.jp/kegg/kegg2.html>) y la estequiometría reportada para el complejo V de *S. cerevisiae*.

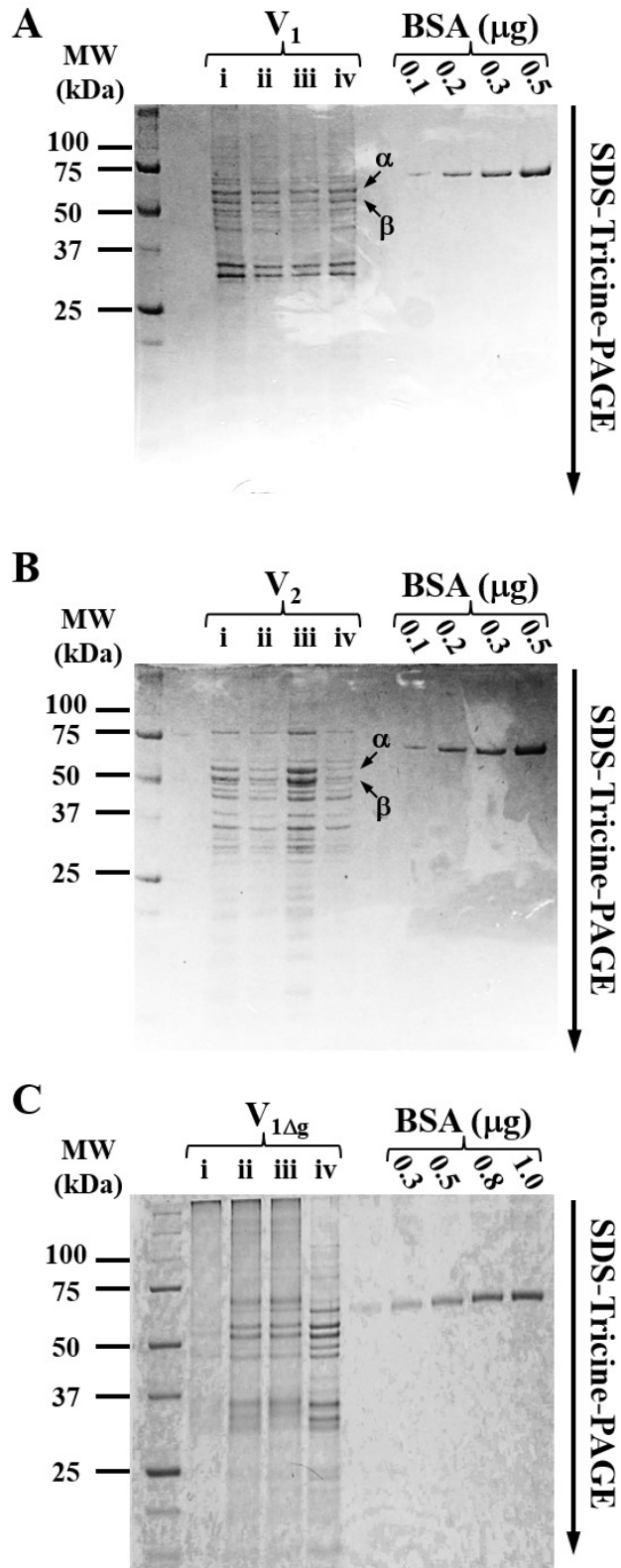


Figura S1. SDS-Tricina-PAGE de V_1 y V_2 . Las proteínas V_1 (A), V_2 (B) y $V_{2\Delta g}$ (C) (10 μg por carril) se resolvieron mediante geles de Tricina-SDS-PAGE y se tiñeron con Coomassie® Blue. La intensidad de la subunidad α y β del complejo V se usó para la cuantificación de la concentración de F_1F_0 -ATP sintasa usando una curva de BSA. i, ii, iii, y iv fueron muestras de V_1 y V_2 , de diferentes preparaciones.

Tabla 5. Cuantificación del contenido de las subunidades α y β del V_{1WT} de la F_1F_0 -ATP sintasa (4 diferentes muestras).

BSA (curva estándar)				
	Señal total			
1.0 μg	5.474	Regresión lineal: $r^2 = 0.979$; $b = 0.185$; $m = 5.04$		
0.5 μg	2.140			
0.3 μg	1.728			
0.1 μg	0.981			
V_1, muestra i				
Subunidad	Señal total	μg	mol	proporción α/β
α	2.210	0.4	7.27×10^{-12}	0.8
β	2.490	0.458	9.08×10^{-12}	
		Promedio ^a = 8.18×10^{-12}		
V_1, muestra ii				
α	1.830	0.326	5.92×10^{-12}	0.8
β	2.110	0.382	7.57×10^{-12}	
		Promedio ^a = 6.75×10^{-12}		
V_1, muestra iii				
α	1.690	0.298	5.41×10^{-12}	0.7
β	2.040	0.368	7.29×10^{-12}	
		Promedio ^a = 6.35×10^{-12}		

Los datos se obtuvieron del análisis de las proteínas teñidas en gel mostradas en la Figura S1 = Dado que α/β tienen una estequiometría 1:1 en la F_1F_0 -ATP sintasa nativa, el valor para α y β se enfocó como el promedio de sus valores independientes.

Tabla 6. Cálculo del contenido de F₁F₀-ATP sintasa en diferentes muestras de V_{1WT} aislados.

Subunidad	MW subunidad madura (Da)	Muestra i			Muestra ii			Muestra iii		
		pmol de subunidad	pmol total	µg ^a	pmol de subunidad	pmol total	µg ^a	pmol de subunidad	pmol total	µg ^a
α (x3)	55047	2.72	8.18	0.450	2.25	6.75	0.372	2.12	6.35	0.350
β (x3)	50465	2.72	8.18	0.412	2.25	6.75	0.341	2.12	6.35	0.320
b (x2)	22281	2.72	5.45	0.121	2.25	4.50	0.100	2.12	4.24	0.010
γ (x1)	33157	2.72	2.72	0.090	2.25	2.25	0.075	2.12	2.12	0.070
a (x1)	27742	2.72	2.72	0.075	2.25	2.25	0.062	2.12	2.12	0.059
OSCP (x1)	21001	2.72	2.72	0.057	2.25	2.25	0.047	2.12	2.12	0.045
d (x1)	15552	2.72	2.72	0.042	2.25	2.25	0.035	2.12	2.12	0.033
f (x1)	7371	2.72	2.72	0.020	2.25	2.25	0.017	2.12	2.12	0.016
δ (x1)	14615	2.72	2.72	0.039	2.25	2.25	0.033	2.12	2.12	0.031
h (x1)	10419	2.72	2.72	0.028	2.25	2.25	0.023	2.12	2.12	0.022
ε (x1)	7538	2.72	2.72	0.021	2.25	2.25	0.017	2.12	2.12	0.016
Inh1 (x1)	7281	2.72	2.72	0.019	2.25	2.25	0.016	2.12	2.12	0.015
c (x12)	7394	2.72	32.6	0.244	2.25	27.0	0.200	2.12	25.4	0.188
i/j (x1)	6454	2.72	2.72	0.018	2.25	2.25	0.015	2.12	2.12	0.014
8 (x1)	5713	2.72	2.72	0.016	2.25	2.25	0.013	2.12	2.12	0.012
g (x0)	17300	—	—	—	—	—	—	—	—	—
e (x0)	9240	—	—	—	—	—	—	—	—	—
Total	606 669		87.8	1.652		69.8	1.366		65.7	1.201

^a = El valor en µg fue calculado como (MW de la subunidad madura) x (moles totales).

Tabla 7. Cuantificación del contenido de las subunidades α y β del V_{2WT} de la F_1F_0 -ATP sintasa (4 diferentes muestras).

BSA (curva estándar)				
	Señal total			
1.0 μg	6.076	Regresión lineal: $r^2 = 0.999$; $b = 0.242$; $m = 5.78$		
0.5 μg	3.038			
0.3 μg	1.930			
0.1 μg	0.909			
V_2, muestra i				
Subunidad	Señal total	μg	mol	Proporción α/β
α	1.569	0.2295	4.169×10^{-12}	0.9
β	1.635	0.2409	4.77×10^{-12}	
		Promedio ^a = 4.47×10^{-12}		
V_2, muestra ii				
α	1.143	0.1558	2.83×10^{-12}	0.8
β	1.320	0.1865	3.7×10^{-12}	
		Promedio ^a = 3.27×10^{-12}		
V_2, muestra iii				
α	2.192	0.337	6.12×10^{-12}	1.4
β	1.524	0.2217	4.39×10^{-12}	
		Promedio ^a = 5.26×10^{-12}		

Los datos se obtuvieron del análisis de las proteínas teñidas en gel mostradas en la Figura S1 = Dado que α/β tienen una estequiometría 1:1 en la F_1F_0 -ATP sintasa nativa, el valor para α y β se enfocó como el promedio de sus valores independientes.

Tabla 8. Cálculo del contenido de F₁F₀-ATP sintasa en diferentes muestras de V_{2WT} aislados.

Subunidad	MW subunidad madura (Da)	Muestra i			Muestra ii			Muestra iii		
		pmol de subunidad	pmol total	µg ^a	pmol de subunidad	pmol total	µg ^a	pmol de subunidad	pmol total	µg ^a
α (x3)	55047	1.49	4.47	0.246	1.09	3.27	0.180	1.75	5.26	0.290
β (x3)	50465	1.49	4.47	0.226	1.09	3.27	0.165	1.75	5.26	0.265
b (x2)	22281	1.49	2.98	0.066	1.09	2.18	0.049	1.75	3.50	0.078
γ (x1)	33157	1.49	1.49	0.049	1.09	1.09	0.036	1.75	1.75	0.058
a (x1)	27742	1.49	1.49	0.041	1.09	1.09	0.030	1.75	1.75	0.049
OSCP (x1)	21001	1.49	1.49	0.031	1.09	1.09	0.023	1.75	1.75	0.037
d (x1)	15552	1.49	1.49	0.023	1.09	1.09	0.017	1.75	1.75	0.027
f (x1)	7371	1.49	1.49	0.011	1.09	1.09	0.008	1.75	1.75	0.013
δ (x1)	14615	1.49	1.49	0.022	1.09	1.09	0.016	1.75	1.75	0.026
h (x1)	10419	1.49	1.49	0.016	1.09	1.09	0.011	1.75	1.75	0.018
ε (x1)	7538	1.49	1.49	0.011	1.09	1.09	0.008	1.75	1.75	0.013
lnh1 (x1)	7281	1.49	1.49	0.011	1.09	1.09	0.008	1.75	1.75	0.013
c (x12)	7394	1.49	17.9	0.132	1.09	13.1	0.097	1.75	21.0	0.155
i/j (x1)	6454	1.49	1.49	0.010	1.09	1.09	0.007	1.75	1.75	0.011
8 (x1)	5713	1.49	1.49	0.009	1.09	1.09	0.006	1.75	1.75	0.010
g (x1)	17300	1.49	1.49	0.026	1.09	1.09	0.019	1.75	1.75	0.030
e (x1)	9240	1.49	1.49	0.014	1.09	1.09	0.010	1.75	1.75	0.016
Total	606 669	25.33	49.2	0.944	18.53	36.0	0.690	29.75	57.8	0.476

^a = El valor en µg fue calculado como (MW de la subunidad madura) x (moles totales).

Tabla 9. Cuantificación del contenido de las subunidades α y β del $V_{1\Delta g}$ de la F_1F_0 -ATP sintasa (4 diferentes muestras).

BSA (curva estándar)				
	Señal total			
1.0 μg	6.076	Regresión lineal: $r^2 = 0.999$; $b = 0.242$; $m = 5.78$		
0.5 μg	3.038			
0.3 μg	1.930			
0.1 μg	0.909			
$V_{1\Delta g}$, muestra i				
Subunidad	Señal total	μg	mol	Proporción α/β
α	1.569	0.4788	8.7×10^{-12}	0.92
β	1.635	0.4788	9.49×10^{-12}	
		Promedio ^a = 9.09×10^{-12}		
$V_{1\Delta g}$, muestra ii				
α	1.143	0.5331	9.68×10^{-12}	0.86
β	1.320	0.571	11.31×10^{-12}	
		Promedio ^a = 10.50×10^{-12}		
$V_{1\Delta g}$, muestra iii				
α	3.990	0.4475	8.13×10^{-12}	0.82
β	3.290	0.4998	9.90×10^{-12}	
		Promedio ^a = 9.02×10^{-12}		
$V_{1\Delta g}$, muestra iv				
α	2.192	0.3615	6.57×10^{-12}	0.85
β	1.524	0.3919	7.77×10^{-12}	
		Promedio ^a = 7.17×10^{-12}		

Los datos se obtuvieron del análisis de las proteínas teñidas en gel mostradas en la Figura S1 = Dado que α/β tienen una estequiometría 1:1 en la F_1F_0 -ATP sintasa nativa, el valor para α y β se enfocó como el promedio de sus valores independientes.

Tabla 10. Cálculo del contenido de F₁F₀-ATP sintasa en diferentes muestras de V₁Δg aislados.

Subunidad	MW subunidad madura (Da)	Muestra i			Muestra ii			Muestra iii			Muestra iv		
		pmol de subunidad	pmol total	μg ^a	pmol de subunidad	pmol total	μg ^a	pmol de subunidad	pmol total	μg ^a	pmol de subunidad	pmol total	μg ^a
α (x3)	55047	3.0310	9.0929	0.5005	3.4999	10.4996	0.5780	3.0056	9.0167	0.4963	3.7887	11.3661	0.6257
β (x3)	50465	3.0310	9.0929	0.4589	3.4999	10.4996	0.5299	3.0056	9.0167	0.4550	3.7887	11.3661	0.5736
b (x2)	22281	3.0310	6.0619	0.1351	3.4999	6.9997	0.1560	3.0056	6.0111	0.1339	3.7887	7.5774	0.1688
γ (x1)	33157	3.0310	3.0310	0.1005	3.4999	3.4999	0.1160	3.0056	3.0056	0.0997	3.7887	3.7887	0.1256
a (x1)	27742	3.0310	3.0310	0.0841	3.4999	3.4999	0.0971	3.0056	3.0056	0.0834	3.7887	3.7887	0.1051
OSCP (x1)	21001	3.0310	3.0310	0.0637	3.4999	3.4999	0.0735	3.0056	3.0056	0.0631	3.7887	3.7887	0.0796
d (x1)	15552	3.0310	3.0310	0.0471	3.4999	3.4999	0.0544	3.0056	3.0056	0.0467	3.7887	3.7887	0.0589
f (x1)	7371	3.0310	3.0310	0.0223	3.4999	3.4999	0.0258	3.0056	3.0056	0.0222	3.7887	3.7887	0.0279
δ (x1)	14615	3.0310	3.0310	0.0443	3.4999	3.4999	0.0512	3.0056	3.0056	0.0439	3.7887	3.7887	0.0554
h (x1)	10419	3.0310	3.0310	0.0316	3.4999	3.4999	0.0365	3.0056	3.0056	0.0313	3.7887	3.7887	0.0395
ε (x1)	7538	3.0310	3.0310	0.0228	3.4999	3.4999	0.0264	3.0056	3.0056	0.0227	3.7887	3.7887	0.0286
Inh1 (x1)	7281	3.0310	3.0310	0.0221	3.4999	3.4999	0.0255	3.0056	3.0056	0.0219	3.7887	3.7887	0.0276
c (x12)	7394	3.0310	36.3716	0.2689	3.4999	41.9984	0.3105	3.0056	36.0666	0.2667	3.7887	45.4643	0.3362
i/j (x1)	6454	3.0310	3.0310	0.0196	3.4999	3.4999	0.0226	3.0056	3.0056	0.0194	3.7887	3.7887	0.0245
8 (x1)	5713	3.0310	3.0310	0.0173	3.4999	3.4999	0.0200	3.0056	3.0056	0.0172	3.7887	3.7887	0.0216
g (x1)	17300	-	-	-	-	-	-	-	-	-	-	-	-
e (x1)	9240	-	-	-	-	-	-	-	-	-	-	-	-
Total	606 669	45.4645	93.9599	1.8388	52.4981	108.4960	2.1233	45.0833	93.1721	1.8234	56.8304	117.4495	2.2985

^a = El valor en μg fue calculado como (MW de la subunidad madura) x (moles totales).

10.6. Cuantificación de la cantidad de F_1F_0 -ATP sintasa en las mitocondrias de las cepas WT y Δg .

La cuantificación del contenido de F_1F_0 -ATP sintasa presente en las WT y Δg (Figura S2), se resolvió como se describió en el punto 10.4 (anexo).

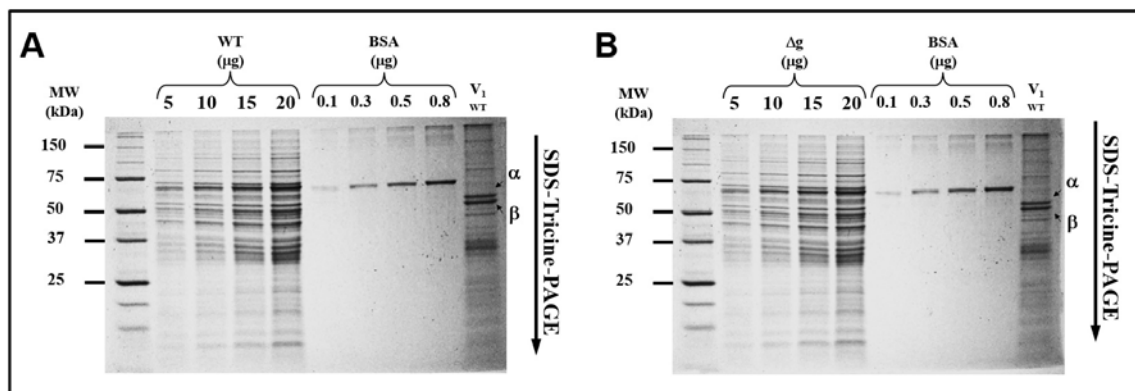


Figura S2. SDS-Tricina-PAGE de las mitocondrias WT y Δg . Las proteínas WT (A) y Δg (B) se resolvieron mediante geles de Tricina-SDS-PAGE y se tiñeron con Coomassie® Blue. La intensidad de la subunidad α y β del complejo V se usó para la cuantificación de la concentración de F_1F_0 -ATP sintasa usando una curva de BSA.

Tabla 11. Cuantificación del contenido de las subunidades α y β de la F_1F_0 -ATP sintasa total en las mitocondrias de la cepa WT.

BSA (curva estándar)				
	Señal total			
0.1 μ g	21588	R = 0.9992; b = 19301.42; m = 20080.02		
0.3 μ g	25186			
0.5 μ g	29812			
0.8 μ g	35980			
WT Muestra i (10μg)				
Subunidad	Señal total	μg	mol	Proporción α/β
α	25443	0.295	5.36	
β	26985	0.369	7.31	0.73
Promedio ^a		6.34		
WT Muestra ii (15μg)				
α	27756	0.406	7.38	0.72
β	30069	0.518	10.26	
Promedio ^a		8.82		
WT Muestra iii (20μg)				
α	32125	0.616	11.19	0.75
β	34952	0.752	14.90	
Promedio ^a		13.05		

Los datos se obtuvieron del análisis de las proteínas teñidas en gel mostradas en la Figura S2 = Dado que α/β tienen una estequiometría 1:1 en la F_1F_0 -ATP sintasa nativa, el valor para α y β se enfocó como el promedio de sus valores independientes.

Tabla 12. Cálculo del contenido de F₁F₀-ATP sintasa total en las mitocondrias de la cepa WT.

Subunidad	MW subunidad madura (Da)	Muestra i			Muestra ii			Muestra iii		
		pmol de subunidad	pmol total	µg ^a	pmol de subunidad	pmol total	µg ^a	pmol de subunidad	pmol total	µg ^a
α (x3)	55047	2.1118	6.3355	0.3488	2.9400	8.8200	0.4855	4.3486	13.0459	0.7181
β (x3)	50465	2.1118	6.3355	0.3197	2.9400	8.8200	0.4451	4.3486	13.0459	0.6584
b (x2)	22281	2.1118	4.2237	0.0941	2.9400	5.8800	0.1310	4.3486	8.6973	0.1938
γ (x1)	33157	2.1118	2.1118	0.0700	2.9400	2.9400	0.0975	4.3486	4.3486	0.1442
a (x1)	27742	2.1118	2.1118	0.0586	2.9400	2.9400	0.0816	4.3486	4.3486	0.1206
OSCP (x1)	21001	2.1118	2.1118	0.0444	2.9400	2.9400	0.0617	4.3486	4.3486	0.0913
d (x1)	15552	2.1118	2.1118	0.0328	2.9400	2.9400	0.0457	4.3486	4.3486	0.0676
f (x1)	7371	2.1118	2.1118	0.0156	2.9400	2.9400	0.0217	4.3486	4.3486	0.0321
δ (x1)	14615	2.1118	2.1118	0.0309	2.9400	2.9400	0.0430	4.3486	4.3486	0.0636
h (x1)	10419	2.1118	2.1118	0.0220	2.9400	2.9400	0.0306	4.3486	4.3486	0.0453
ε (x1)	7538	2.1118	2.1118	0.0159	2.9400	2.9400	0.0222	4.3486	4.3486	0.0328
Inh1 (x1)	7281	2.1118	2.1118	0.0154	2.9400	2.9400	0.0214	4.3486	4.3486	0.0317
c (x12)	7394	2.1118	25.3421	0.1874	2.9400	35.2801	0.2609	4.3486	52.1837	0.3858
i/j (x1)	6454	2.1118	2.1118	0.0136	2.9400	2.9400	0.0190	4.3486	4.3486	0.0281
8 (x1)	5713	2.1118	2.1118	0.0121	2.9400	2.9400	0.0168	4.3486	4.3486	0.0248
g (x1)	17300	2.1118	2.1118	0.0365	2.9400	2.9400	0.0509	4.3486	4.3486	0.0752
e (x1)	9240	2.1118	2.1118	0.0195	2.9400	2.9400	0.0272	4.3486	4.3486	0.0402
Total	606 669	35.9013	69.6908	1.3372	49.9802	97.0203	1.8616	73.9269	143.5052	2.7536

^a = El valor en µg fue calculado como (MW de la subunidad madura) x (moles totales).

Tabla 13. Cuantificación del contenido de las subunidades α y β de la F_1F_0 -ATP sintasa total en las mitocondrias de la cepa Δg .

BSA (curva estándar)				
	Señal total			
0.1 μ g	17219	R = 0.9986; b = 15030.90; m = 21929.1		
0.3 μ g	21331			
0.5 μ g	26471			
0.8 μ g	32382			
Δg Muestra i (10μg)				
Subunidad	Señal total	μg	mol	Proporción α/β
α	19275	0.193	3.51	0.57
β	21845	0.311	6.16	
Promedio ^a		4.83		
Δg Muestra ii (15μg)				
α	23387	0.381	6.92	0.74
β	25443	0.475	9.41	
Promedio ^a		8.17		
Δg Muestra iii (20μg)				
α	26728	0.533	9.68	0.68
β	30840	0.721	14.29	
Promedio ^a		11.98		

Los datos se obtuvieron del análisis de las proteínas teñidas en gel mostradas en la Figura S2 = Dado que α/β tienen una estequiometría 1:1 en la F_1F_0 -ATP sintasa nativa, el valor para α y β se enfocó como el promedio de sus valores independientes.

Tabla 14. Cálculo del contenido de F₁F₀-ATP sintasa total en las mitocondrias de la cepa Δg .

Subunidad	MW subunidad madura (Da)	Muestra i			Muestra ii			Muestra iii		
		pmol de subunidad	pmol total	μg^a	pmol de subunidad	pmol total	μg^a	pmol de subunidad	pmol total	μg^a
α (x3)	55047	1.6115	4.8344	0.2661	2.7223	8.1669	0.4496	3.9950	11.9849	0.6597
β (x3)	50465	1.6115	4.8344	0.2440	2.7223	8.1669	0.4121	3.9950	11.9849	0.6048
b (x2)	22281	1.6115	3.2229	0.0718	2.7223	5.4446	0.1213	3.9950	7.9899	0.1780
γ (x1)	33157	1.6115	1.6115	0.0534	2.7223	2.7223	0.0903	3.9950	3.9950	0.1325
a (x1)	27742	1.6115	1.6115	0.0447	2.7223	2.7223	0.0755	3.9950	3.9950	0.1108
OSCP (x1)	21001	1.6115	1.6115	0.0338	2.7223	2.7223	0.0572	3.9950	3.9950	0.0839
d (x1)	15552	1.6115	1.6115	0.0251	2.7223	2.7223	0.0423	3.9950	3.9950	0.0621
f (x1)	7371	1.6115	1.6115	0.0119	2.7223	2.7223	0.0201	3.9950	3.9950	0.0294
δ (x1)	14615	1.6115	1.6115	0.0236	2.7223	2.7223	0.0398	3.9950	3.9950	0.0584
h (x1)	10419	1.6115	1.6115	0.0168	2.7223	2.7223	0.0284	3.9950	3.9950	0.0416
ϵ (x1)	7538	1.6115	1.6115	0.0121	2.7223	2.7223	0.0205	3.9950	3.9950	0.0301
Inh1 (x1)	7281	1.6115	1.6115	0.0117	2.7223	2.7223	0.0198	3.9950	3.9950	0.0291
c (x12)	7394	1.6115	19.3376	0.1430	2.7223	32.6676	0.2415	3.9950	47.9395	0.3545
i/j (x1)	6454	1.6115	1.6115	0.0104	2.7223	2.7223	0.0176	3.9950	3.9950	0.0258
8 (x1)	5713	1.6115	1.6115	0.0092	2.7223	2.7223	0.0156	3.9950	3.9950	0.0228
g (x1)	17300	1.6115	1.6115	0.0000	2.7223	2.7223	0.0000	3.9950	3.9950	0.0000
e (x1)	9240	1.6115	1.6115	0.0149	2.7223	2.7223	0.0252	3.9950	3.9950	0.0369
Total	606 669	27.3949	53.1783	0.9925	46.2792	89.8360	1.6767	67.9143	131.8337	2.4605

^a = El valor en μg fue calculado como (MW de la subunidad madura) x (moles totales).



"Mitochondrial Oroboros" Odra Noel

Artículos

11. ARTÍCULOS

11.1. Artículo de requisito

- STRUCTURAL AND KINETICS CHARACTERIZATION OF THE F₁F₀-ATP SYNTHASE DIMER. NEW REPERCUSSION OF MONOMER-MONOMER CONTACT (2017) **Mercedes Esparza-Perusquía**, Sofía Olvera-Sánchez, Juan Pablo Pardo, Guillermo Mendoza-Hernández, Federico Martínez, and Oscar Flores-Herrera. *BBA-Bioenergetics*. 1858(12):975-981. doi: 10.1016/j.bbabi.2017.09.002.

11.2. Publicaciones directas.

- DELETION OF SUBUNIT G FROM F₁F₀-ATP SYNTHASE AFFECTS THE STABILITY OF ITS DIMERIC STATE AND THE MITOCHONDRIAL ATP SYNTHESIS. **Esparza-Perusquía M**, Langner T, Feldbrügge M, Pardo JP, Martínez F, and Flores-Herrera O. *En preparación*.
- DELETION OF THE NATURAL INHIBITORY PROTEIN INH1 FROM USTILAGO MAYDIS ATP SYNTHASE DOES NOT INCREASE THE ACTIVITY OF THE DIMERIC STATE OF F₁F₀-ATP SYNTHASE. Romero-Aguilar Lucero*, **Esparza-Perusquía Mercedes***, Langner Thorsten, García Giovanni, Feldbrügge Michael, Pardo Juan Pablo, Martínez Federico, and Flores-Herrera Oscar. *En preparación*.

11.3. Otras publicaciones.

- MITOCHONDRIAL PROTEASES ACT ON STARD3 TO ACTIVATE PROGESTERONE SYNTHESIS IN HUMAN SYNCYTIOTROPHOBLAST (2015) **Mercedes Esparza-Perusquía**, Sofía Olvera-Sánchez, Oscar Flores-Herrera, Héctor Flores-Herrera, Alberto Guevara-Flores, Juan P Pardo, María T Espinosa-García y Federico Martínez. *BBA-General Subjects*. 1850(1):107-117. doi: 10.1016/j.bbagen.2014.10.009.
- MEMBRANE POTENTIAL REGULATES THE MITOCHONDRIAL ATP-DIPHOSPHOHYDROLASE ACTIVITY BUT IT IS NOT INVOLVED IN THE

PROGESTERONE BIOSYNTHESIS IN HUMAN SYNCYTIOTROPHOBLAST CELL (2015) Oscar Flores-Herrera, Sofía Olvera-Sánchez, **Mercedes Esparza-Perusquía**, Juan Pablo Pardo, Juan Luis Rendón, Guillermo Mendoza-Hernández, and Federico Martínez. *BBA-Bioenergetics*. 1847(2):143-52. doi: 10.1016/j.bbabi.2014.10.002.

- MULTIPLE FUNCTIONS OF SYNCYTIOTROPHOBLAST MITOCHONDRIA IN PREGNANCY (2015) Federico Martínez, Sofía Olvera-Sánchez, **Mercedes Esparza-Perusquía**, Erika Gómez-Chang, Oscar Flores-Herrera. *Steroids*, 103:11-22. doi: 10.1016/j.steroids.2015.09.006.
- STREPTOZOTOCIN INDUCED ADAPTIVE MODIFICATION OF THE MITOCHONDRIAL SUPERCOMPLEXES IN LIVER OF WISTAR RATS AND THE PROTECTIVE EFFECT OF *MORINGA OLEIFERA* LAM (2018) Alejandra Sánchez-Muñoz, Mónica A Valdez-Solana, Mara I Campos-Almazán, Oscar Flores-Herrera, **Mercedes Esparza-Perusquía**, Sofía Olvera-Sánchez, Guadalupe García-Arenas, Claudia Avitia-Domínguez, Alfredo Téllez-Valencia and Erick Sierra-Campos. *Biochemistry Research International*. 1-15. ID 5681081. doi:10.1155/2018/5681081.
- CARDIOPROTECTIVE STRATEGIES PRESERVE THE STABILITY OF RESPIRATORY CHAIN SUPERCOMPLEXES AND REDUCE OXIDATIVE STRESS IN REPERFUSED ISCHEMIC HEARTS (2018) Ixchel Ramírez-Camacho, Francisco Correa, Mohammed El-Hafidi, Alejandro Silva-Palacios, Marcos Ostolga-Chavarría, **Mercedes Esparza-Perusquía**, Sofía Olvera-Sánchez, Oscar Flores-Herrera and Cecilia Zazueta. *Free Radical Biology and Medicine*. 129:407-417. doi: 10.1016/j.freeradbiomed.2018.09.047.
- MITOCHONDRIAL RESPIRASOME WORKS AS A SINGLE UNIT AND THE CROSSTALK BETWEEN COMPLEXES I, III₂ AND IV STIMULATES NADH DEHYDROGENASE ACTIVITY (2019) Meztli Reyes-Galindo, Roselia Suarez, **Mercedes Esparza-Perusquía**, Jaime de Lira-Sánchez, Juan Pablo Pardo, Federico Martínez, and Oscar Flores-Herrera. *BBA-Bioenergetics*. 1860(8):618-627. doi: 10.1016/j.bbabi.2019.06.017.

- ASPECTOS GENERALES DEL TRANSPORTE DE COLESTEROL EN LA ESTEROIDOGENESIS DE LA PLACENTA HUMANA (2019) Sofía Olvera-Sánchez, **Mercedes Esparza-Perusquía**, Oscar Flores-Herrera, Viviana A. Urban-Sosa y Federico Martínez. *TIP Revista Especializada en Ciencias Químico-Biológicas*, 22:1-9. DOI: 10.22201/fesz.23958723e.
- STEADY-STATE PERSISTENCE OF RESPIRATORY SYNCYTIAL VIRUS IN A MACROPHAGE-LIKE CELL LINE AND IDENTIFICATION OF NON-SYNONYMOUS MUTATIONS THROUGH SEQUENCING OF THE PERSISTENT VIRAL GENOME. Ximena Ruiz-Gómez, Joel Armando Vázquez-Pérez, Oscar Flores-Herrera, **Mercedes Esparza-Perusquía**, Carlos Santiago-Olivares, Jorge Gaona, Beatriz Gómez, Carmen Méndez, Evelyn Rivera-Toledo. *MDPI-viruses*, Manuscript ID: 842162. Enviado.



Structural and kinetics characterization of the F_1F_0 -ATP synthase dimer. New repercussion of monomer-monomer contact



Mercedes Esparza-Perusquía, Sofía Olvera-Sánchez, Juan Pablo Pardo, Guillermo Mendoza-Hernández, Federico Martínez, Oscar Flores-Herrera*

Departamento de Bioquímica, Facultad de Medicina, Universidad Nacional Autónoma de México, 04510 México City, México

ARTICLE INFO

Keywords:

F_1F_0 -ATP synthase dimer
Supercomplexes
ATPase activity
Ustilago maydis mitochondria

ABSTRACT

Ustilago maydis is an aerobic basidiomycete that fully depends on oxidative phosphorylation for its supply of ATP, pointing to mitochondria as a key player in the energy metabolism of this organism. Mitochondrial F_1F_0 -ATP synthase occurs in supramolecular structures. In this work, we isolated the monomer (640 kDa) and the dimer (1280 kDa) and characterized their subunit composition and kinetics of ATP hydrolysis. Mass spectrometry revealed that dimerizing subunits e and g were present in the dimer but not in the monomer. Analysis of the ATPase activity showed that both oligomers had Michaelis-Menten kinetics, but the dimer was 7 times more active than the monomer, while affinities were similar. The dimer was more sensitive to oligomycin inhibition, with a K_i of 24 nM, while the monomer had a K_i of 169 nM. The results suggest that the interphase between the monomers in the dimer state affects the catalytic efficiency of the enzyme and its sensitivity to inhibitors.

1. Introduction

The F_1F_0 -ATP synthase is the principal source of cellular ATP. The yeast mitochondrial F_1F_0 -ATP synthase is a 600 kDa complex that contains at least 17 distinct subunits [1] organized into a catalytic soluble-component called F_1 , with three catalytic sites, and a membrane-spanning component called F_0 , composed by hydrophobic subunits forming a specific proton channel. F_0 and F_1 are linked by central and peripheral stalks [2]. The enzyme uses the proton electrochemical gradient generated by the respiratory chain to produce ATP from ADP and inorganic phosphate. This enzyme is a nano-motor where the proton translocation through F_0 induces the rotation of a ring of 9–14 hydrophobic c-subunits [3], which drives the rotation of a central stalk inside the catalytic head which results in the synthesis of ATP [4].

The mitochondrial ATP synthase acquires supramolecular structures that have been found in many organisms by native gel electrophoresis, mainly in the dimeric form [5–7] but also in higher molecular forms (*i.e.* tetramers, hexamers) according to the electrophoresis technique used [7–10]. Depending on the detergent used during the extraction and the purification procedures, the isolated complexes were monomers and/or dimers as shown by electron microscopy single particle analysis [11–16], although higher structures such as tetramers have also been reported [16].

Dimers of mitochondrial ATP synthase have been observed *in situ* by

atomic force microscopy [17], transmission electron microscopy [16] and electron cryo-tomography [18]. Higher supramolecular structures (tetramers, hexamers) have been reported both in blue native gel and cross-linking experiments showing that subunits e and g are involved in dimer stabilization [19] and the oligomerization process [7,20–22].

The ATP synthase dimer from *Saccharomyces cerevisiae* adopts a V-like structure with the two F_0 parts linked together [23]. Several F_0 subunits, as e, g, i, k and 8, are essential for dimerization [5,23] and oligomerization [19], but are not involved in the ATPase or ATP synthase activity.

Even though the dimer's structure and its role in cristae architecture have been defined with high precision, only a few attempts have been made to understand the effect of oligomerization on ATPase activity. Because the ATP synthase oligomers remain in the native state, BN-PAGE had been combined with in-gel activity staining to estimate ATPase activity [7,21,24–26]. However, the results are not conclusive due to differences in assay conditions, optimization of the in-gel ATPase assay, and/or ADP accumulation in the assay mixture. Therefore, it is important to study spectrophotometrically the ATPase activity to facilitate the comparison of the specific activities of monomer and dimer of the F_1F_0 -ATP synthase.

In this work, the dimer and monomer of the F_1F_0 -ATP synthase from *Ustilago maydis*, an aerobic basidiomycete, were solubilized with digitonin, a soft detergent, and isolated by sucrose gradient centrifugation.

* Corresponding author at: Departamento de Bioquímica, Facultad de Medicina, Universidad Nacional Autónoma de México, Apdo. Postal 70-159, Coyoacán 04510, México, Cd. Mx., México.

E-mail address: oflores@bq.unam.mx (O. Flores-Herrera).

<http://dx.doi.org/10.1016/j.bbambio.2017.09.002>

Received 11 May 2017; Received in revised form 24 August 2017; Accepted 12 September 2017

Available online 14 September 2017

0005-2728/© 2017 Elsevier B.V. All rights reserved.

It was determined by MS/MS analysis that the dimer showed the subunits e and g as dimerizing components; additionally, the dimer was 7 times more active than the monomer and more sensitive to oligomycin. Thermostability kinetics showed that the dimer dissociates into monomers previous to their inactivation. The apparent T_m was about 52 °C for both oligomeric states. This is the first report on the kinetic characterization of the isolated dimer and monomer of the F_1F_0 -ATP synthase from a single organism, and it shows that these oligomeric states have different catalytic properties besides their subunit composition. In this sense, a new role of the interphase between individual monomers is discussed.

2. Materials and methods

2.1. Cell culture and mitochondria isolation

Ustilago maydis cells (strain FB2) were prepared as previously described [27]. *U. maydis* mitochondria were isolated using the method described by Waterfield and Sisler [28].

2.2. Solubilisation and isolation of dimer and monomer of F_1F_0 -ATP synthase

The dimer (V_2) and monomer (V_1) of F_1F_0 -ATP synthase from *U. maydis* mitochondria (35 mg) were solubilized as described [29–31], by incubation at 4 °C for 30 min with digitonin (detergent/protein ratio of 2:1), and centrifuged at 100,000 g for 30 min at 4 °C. The supernatant was recovered (16 mg protein) and immediately loaded on 24 ml of a continuous sucrose gradient (16–42% sucrose, 15 mM Tris, pH 7.4, 20 mM KCl, and 0.2% digitonin). This mixture was centrifuged at 131,000 g for 18 h at 4 °C. Fractions (0.5 ml) were collected from the bottom of the gradient. Fractions containing V_1 and V_2 were identified by hrCN-PAGE [29], pooled separately and diluted 10 folds with 30 mM HEPES, pH 8.0 and 5% glycerol and concentrated using a Centrifugal Filters Units (100 K, Millipore Amicon Ultra) to a final volume of 100 μ l, and stored at –70 °C until used. The concentration of F_1F_0 -ATP synthase in each V_1 and V_2 sample was determined by a densitometry analysis of Coomassie© Brilliant Blue R-125 stained α - and β -subunits from an SDS-Tricine-PAGE, using Coomassie stained BSA as a standard (see Supplemental material section, Fig. S1). Densitometry analysis was performed with ImageJ software [32].

For hrCN-PAGE, 50 μ g protein (per lane) were applied to 4–10% native-PAGE gels and run at 4 °C, 35 V for 10 h. The molecular weight of complexes and supercomplexes was determined by their electrophoretic mobilities and in-gel catalytic activities, using the complexes of digitonin-solubilized bovine heart mitochondria as standards.

The in-gel activity of complex V was performed as described by Jung [30] in 50 mM glycine (adjusted to pH 8.0 with triethanolamine), 10 mM MgCl₂, 0.15% Pb(ClO₄)₂ and 5 mM ATP. The presence of respiratory complexes and supercomplexes was determined by their in-gel activity, and by MS/MS analysis (see Supplemental material section, Fig. S1).

2D-Tricine-SDS-polyacrylamide gel electrophoresis (2D-SDS-PAGE) was performed according to Schägger [31] on a 16% polyacrylamide gel under denaturing conditions, and proteins were visualized with Coomassie and used for subunit identification by tandem mass spectrometry (LC/ESI-MS/MS) [33]. Database searching and protein identification were performed with the MS/MS spectra data sets using the MASCOT search algorithm (version 1.6b9, Matrix Science, London, U.K., available at <http://www.matrixscience.com>). Mass tolerances of 0.5 Da for the precursor and 0.3 Da for the fragment ion masses were used. Carbamidomethyl-cysteine was the fixed modification, and one missed cleavage for trypsin was allowed. Searches were conducted using the Fungi subset of the NCBI nr database (<http://www.ncbi.nih.gov>). Protein identifications were accepted when at least two MS/MS spectra matched at 95% confidence level ($p < 0.05$).

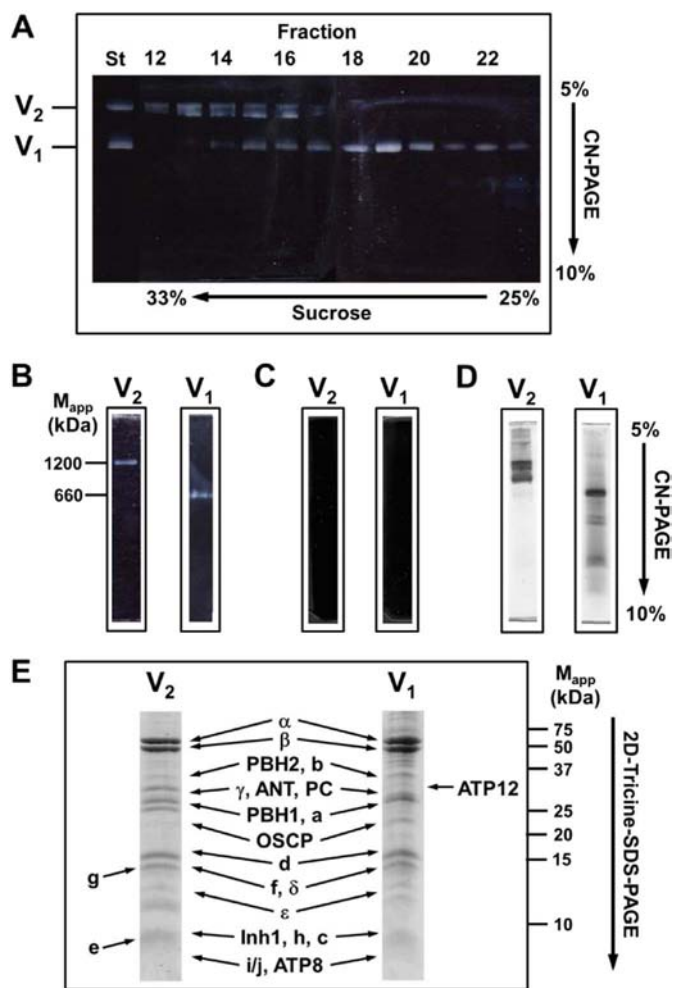


Fig. 1. Isolation, in-gel activity, and subunit composition of the dimer (V_2) and monomer (V_1) of the F_1F_0 -ATP synthase. V_2 and V_1 from *Ustilago maydis* mitochondria were solubilized with digitonin and subsequently isolated by sucrose-gradient ultracentrifugation and their in-gel activity analyzed by hrCN-PAGE (A). Fractions from the bottom [12–13] and the middle [19–22] of the sucrose gradient were used to obtain isolated V_2 and V_1 , respectively (B). Inhibition by oligomycin of the in-gel ATPase activity of isolated V_2 or V_1 (C). Note that no F_1 activity was observed. Coomassie stained of V_1 and V_2 proteins from CN-PAGE (D). The in-gel activity of V_2 and V_1 were excised from CN-PAGE gel and proteins were resolved by 2D-Tricine-SDS-PAGE and subunits identities elucidated by MS/MS (E, and Table 1).

2.3. Measurements of ATP hydrolysis by F_1F_0 -ATP synthase dimer and monomer

ATP hydrolysis by isolated V_1 or V_2 was measured spectrophotometrically at 25 °C using an assay coupled to the oxidation of NADH ($\epsilon_{340nm} = 6.2 \text{ mM}^{-1} \text{ cm}^{-1}$) in an Agilent 8453 UV-visible spectrophotometer (Agilent Technologies, USA). The assay medium contained 50 mM HEPES, pH 8.0, 1 mM MgSO₄, 90 mM KCl; the ATP-regenerating system was 5 mM phosphoenolpyruvate (PEP), 0.2 mM NADH, 50 units/ml of pyruvate kinase (PK), and 30 units/ml of lactate dehydrogenase (LDH). The protein concentration was 10–15 μ g F_1F_0 -ATP synthase/ml, and the ATPase reaction was started by the addition of the enzyme and NADH absorbance was continuously monitored (see Supplemental material section). The time response, checked by ADP additions, was < 1 s. Initial velocities were further obtained from the slope of the linear region in each spectrophotometric recording, and the linear region of the traces was corroborated with the plot of the first-derivative against time (see Supplemental material section). Since a non-specific NADH oxidation was observed prior to the enzyme addition, the actual value of ATPase activity was calculated as the

Table 1
Molecular mass and subunit identity of complex V₁ and V₂ *Ustilago maydis* mitochondria.

V ₂ (1200 kDa)	V ₁ (660 kDa)	Molecular mass (kDa)	Exclusive unique peptides	Unique exclusive spectra/total spectra	Coverage (%)	Access number NCBI
Subunit identity						
α	α	55.05	16	20/41	32	XP_011392137
β	β	50.47	21	39/99	50	XP_011389783
γ	γ	31.16	9	10/18	39	XP_011388164
a	a	27.74	5	6/10	40	Q0H8Y6
b	b	22.28	7	7/9	21	XP_011392148
OSCP	OSCP	21.00	7	8/14	38	XP_011388314
d	d	15.55	3	4/9	41	XP_011392758
δ	δ	14.62	4	4/4	39	XP_011387060
h	h	10.42	5	7/9	43	XP_011388666
ε	ε	7.54	7	9/22	74	XP_011391935
c	c	7.39	7	10/15	62	Q0H8W9
f	f	7.37	3	3/5	32	XP_011388343
Inh1	Inh1	7.28	5	6/11	41	XP_011388667
i/j	i/j	6.45	5	5/9	36	XP_011391953
8	8	5.71	5	6/11	28	Q0H8Y5
g	—	17.3	5	6/14	22	XP_011386964
e	—	9.24	6	8/14	31	XP_011389516
Accessory proteins						
ANT	ANT	33.75	11	12/23	32	XP_011386926
PC	PC	34	12	13/25	30	XP_011388175
PHB2	PBH2	35.56	13	17/75	43	XP_011391320
PHB1	PBH1	29.76	11	15/49	32	XP_011390099

The molecular weight from V₂ and V₁ was determined by BN-PAGE using mitochondrial respiratory complexes from heart bovine as standard. The subunit molecular weight was determined by 2D-Tricine-SDS-PAGE. ANT = adenine nucleotide translocase; PC = phosphate carrier; PHB1 = prohibitin 1; PHB2 = prohibitin 2; ANT = ADP/ATP carrier protein. The identity of each protein was determined by mass spectrometry. The accession number was obtained from NCBI.

subtraction of the slope of this region from the slope that is obtained after adding the enzyme (see Supplemental material section). Oligomycin (3 μM) was added to inhibit ATPase activity and verify F₁F₀-ATP synthase integrity. Only samples with ATPase activity 100% inhibited by oligomycin were used in this study. Data for the hydrolysis of ATP were analyzed by robust, weighted, non-linear regression analysis using the SigmaPlot software (Systat Software, Inc., Version 10.0), and represent the average of three replicates from five independent preparations.

2.4. Thermal inactivation of F₁F₀-ATP synthase dimer and monomer

V₂ or V₁ (500 μg/ml) were suspended in a medium containing 50 mM HEPES, pH 8.0, 1 mM MgSO₄, 90 mM KCl. 250 μl was placed into a glass tube and heated at indicated temperatures for 15 min. The suspension was cooled to room temperature, and a 100 μl aliquot was drawn and immediately assayed at 25 °C for Mg-ATP hydrolysis in the presence of an ATP-regenerating system as described in previously section. Triplicates were performed at each temperature, as well as a control sample which was kept at room temperature for an equal length of time before assay.

2.5. Oligomycin inhibition of F₁F₀-ATP synthase dimer and monomer

Continuous monitoring of ATP hydrolysis by F₁F₀-ATP synthase V₂ or V₁ coupled to NADH oxidation was carried out as described in the previous section. ATP hydrolysis was initiated by Mg-ATP addition; after 2–4 min oligomycin was added and ATPase activity decayed. Because oligomycin is a slow-binding inhibitor the total recording time for maximal ATPase activity inhibition, at different oligomycin concentrations, was about 25–35 min. The spectrophotometric recording was used to calculate the residual activity of ATPase as V(I) / V(0). V(0) is the constant rate of absorbance variation before oligomycin addition in absorbance units per second (proportional to the initial ATPase activity), and V(I) the final rate of absorbance variation after oligomycin addition (proportional to the final ATPase activity). To calculate the K_i the relation between the 1 – (V(I) / V(0)) ratio and the inhibitor

concentration ([I]) were fitted to the following function:

$$1 - V(I)/V(0) = 1 - (v_r + (1 - v_r)/(1 + [I]/K_i)) \quad (1)$$

where v_r is the inhibitor-insensitive fraction of V(0) (always lower than 3%). Initially, it was assumed that the [I] was much higher than the enzyme concentration. Therefore, the total and free concentrations of the [I] could be considered identical and constant during the kinetics of inhibition; however, when the concentration of F₁F₀-ATP synthase was quantified, it was observed a low oligomycin/F₁F₀-ATP synthase ratio when the oligomycin concentration was lower than 1 μM (Fig. 3C). With this information, a new statistical analysis of data was performed with the DynaFit software [34], in which no assumption about a higher concentration of oligomycin over the concentration of the enzyme is required. The K_i values obtained by both methods were similar and were inserted in Table 2. Oligomycin/F₁F₀-ATP synthase ratio was determined from F₁F₀-ATP synthase concentration and the oligomycin used in each spectrophotometric assay.

3. Results

3.1. Isolation of dimeric and monomeric F₁F₀-ATP synthase and subunits identification

Dimeric and monomeric ATP synthase were extracted from *U. maydis* mitochondria with digitonin and isolated by sucrose density gradient centrifugation. The presence of isolated dimeric and monomeric F₁F₀-ATP synthase at the bottom and the middle of the sucrose density gradient, respectively, was confirmed by ATPase activity staining in hrCN-PAGE (Fig. 1A). The V₂ and V₁ samples were pooled independently and concentrated until F₁F₀-ATP synthase content was similar as monitored by Coomassie Blue staining of the α and β subunits (Fig. 1E); their integrity was analyzed by hrCN-PAGE (Fig. 1B). These samples contained oligomycin-sensitive ATPase activity corresponding to V₂ or V₁ without free F₁ sector (Fig. 1C). As expected, the Coomassie® stain (Fig. 1D) showed the presence of supercomplexes (I-III₂-IV) and complex I in the V₂ sample, while individual complexes III₂ and IV were observed in V₁ sample (see Supplemental material section). Therefore,

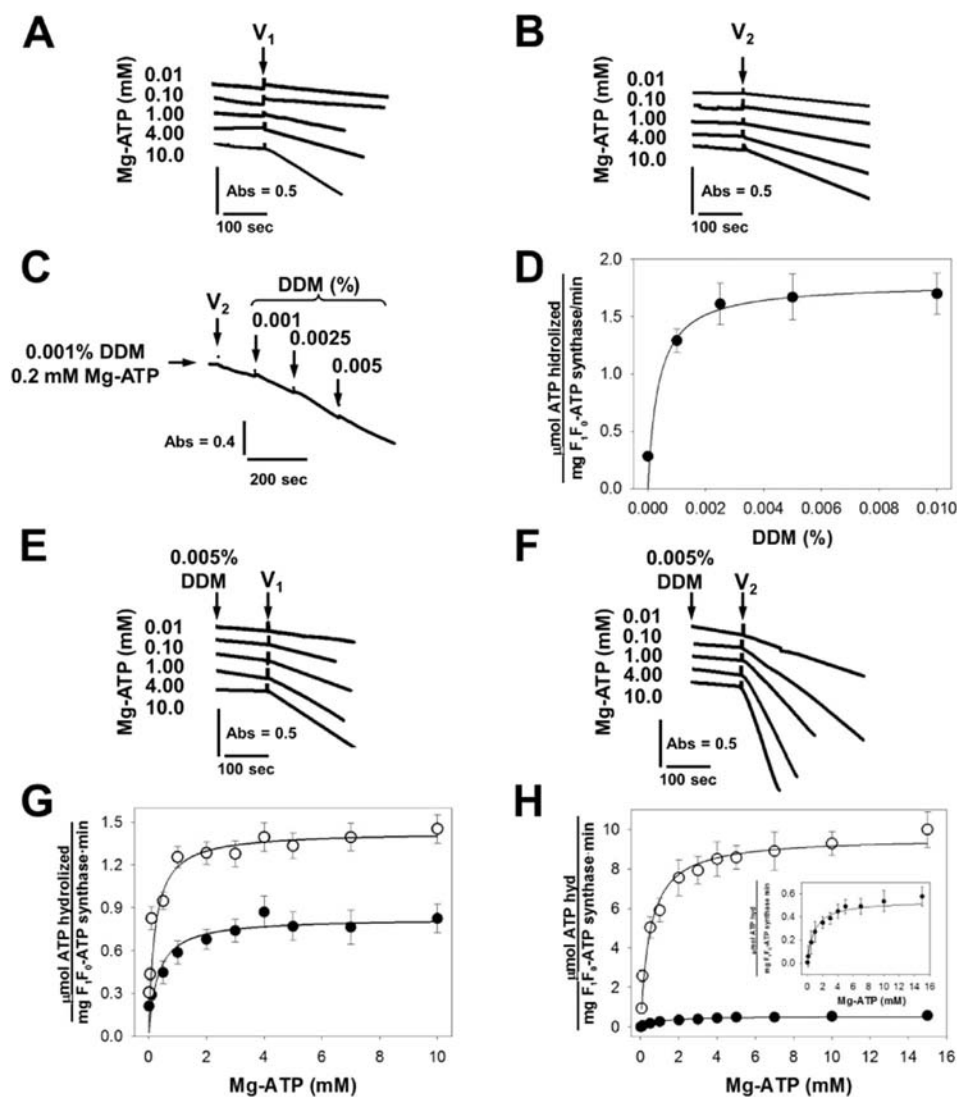


Fig. 2. Kinetic characterization of V_2 and V_1 . Time course of ATP hydrolysis by V_1 (A) and V_2 (B) monitored by NADH absorbance at 340 nm. Stimulation of V_2 activity by different additions of DDM (C); maximal activation was observed at 0.005% DDM (D). ATPase activity of V_1 (E) and V_2 (F) in the presence of 0.005% DDM at different Mg-ATP concentrations. Enzyme or DDM additions indicated by vertical arrows and Mg-ATP concentration at the left side. The dependence of V_1 (G) and V_2 (H) activity on Mg-ATP concentration at pH 8 was fitted to the Michaelis-Menten equation, in the presence (open circles) or absence (closed circles) of DDM. For clarity, inset in panel H represent the activity of V_2 without DDM activation. The data are the average of three replicates from five independent preparations. Error bars represent S.D.

to compare the kinetics of V_1 and V_2 , the concentration of F_1F_0 -ATP synthase was determined in each V_2 and V_1 preparations, and the ATPase activities were corrected by the actual amount of complex V present (see Supplemental material section). The molecular weight calculated for V_1 and V_2 was 660 and 1200 kDa respectively.

The V_2 and V_1 samples were analyzed by MS/MS tandem spectrometry. The monomer showed the complete set of F_1F_0 -ATP synthase subunits (Fig. 1E and Table 1); the dimer showed the supernumerary subunits e and g (Table 1), which have been related to the dimerization process of F_1F_0 -ATP synthase [5–7]. Interestingly, the ADP/ATP translocase (ANT) and phosphate carrier (PC) were joined to both oligomeric states (Fig. 1E), suggesting the presence of the ATP-synthasome. Also, prohibitin 1 (PBH1) and 2 (PBH2) were associated to both oligomers. Then, it was possible to obtain both V_2 and V_1 separated from each other with oligomycin-sensitive ATPase activity.

3.2. Kinetics of ATP hydrolysis by the dimer and monomer of F_1F_0 -ATP synthase

ATPase activity of V_1 and V_2 was dependent on Mg-ATP concentration (Fig. 2A and B) and showed a Michaelis-Menten kinetics for the hydrolysis of ATP. V_{max} value was $0.83 \pm 0.05 \mu\text{mol ATP hydrolyzed}(\text{mg } F_1F_0\text{-ATP synthase-min})^{-1}$ and a $K_m = 308 \pm 90 \mu\text{M}$ for V_1 (Fig. 2G, close circles); while V_2 exhibited a low ATPase activity, with a $V_{max} = 0.54 \pm 0.08 \mu\text{mol ATP hydrolyzed}(\text{mg } F_1F_0\text{-ATP synthase-min})^{-1}$ and a $K_m = 884 \pm 100 \mu\text{M}$ (Fig. 2H inset). It has been reported that ATPase activity of the F_1F_0 -ATP synthase increased in the presence of a nonionic detergent, *i.e.* DDM [35]. Titration curves with increasing concentration of DDM showed a significant increase in the ATPase activity of the V_2 (Fig. 2C and D). Maximal activation was observed at a concentration of 0.005% (w/v) of DDM, and the enzyme was fully sensitive to oligomycin (Figs. 1C and 3). Activation of V_2 by DDM was not due to dissociation of the oligomer, since increasing the detergent concentration to 0.5% in the hrCN-PAGE did not release the monomer (Fig. 1). In the presence of DDM, V_1 showed a V_{max} and K_m values of $1.431 \pm 0.04 \mu\text{mol ATP hydrolyzed}(\text{mg } F_1F_0\text{-ATP synthase-min})^{-1}$ and $207 \pm 30 \mu\text{M}$, respectively (Fig. 2G, open circles). V_2 showed a $V_{max} = 9.604 \pm 0.26 \mu\text{mol ATP hydrolyzed}(\text{mg } F_1F_0\text{-ATP synthase-min})^{-1}$ and a $K_m = 490 \pm 80 \mu\text{M}$ (Fig. 2H, open circles, for comparison the activity of V_2 without DDM activation was included, closed circles). The k_{cat} for DDM activated oligomers were 14.5 and 207.7 s^{-1} for V_1 and V_2 , respectively (Table 2). In this sense, the k_{cat}/K_m values from the V_1 and the V_2 were 7×10^4 and $4.2 \times 10^5 \text{ M}^{-1} \text{ s}^{-1}$, respectively, indicating a higher specificity of V_2 .

ATPase activity of V_1 and V_2 was dependent on Mg-ATP concentration (Fig. 2A and B) and showed a Michaelis-Menten kinetics for the hydrolysis of ATP. V_{max} value was $0.83 \pm 0.05 \mu\text{mol ATP hydrolyzed}(\text{mg } F_1F_0\text{-ATP synthase-min})^{-1}$ and a $K_m = 308 \pm 90 \mu\text{M}$ for V_1 (Fig. 2G, close circles); while V_2 exhibited a low ATPase activity, with a $V_{max} = 0.54 \pm 0.08 \mu\text{mol ATP hydrolyzed}(\text{mg } F_1F_0\text{-ATP synthase-min})^{-1}$ and a $K_m = 884 \pm 100 \mu\text{M}$ (Fig. 2H inset). It has been reported that ATPase activity of the F_1F_0 -ATP synthase increased in the presence of a nonionic detergent, *i.e.* DDM [35]. Titration curves with increasing concentration of DDM showed a significant increase in the ATPase activity of the V_2 (Fig. 2C and D). Maximal activation was observed at a concentration of 0.005% (w/v) of DDM, and the enzyme was fully sensitive to oligomycin (Figs. 1C and 3). Activation of V_2 by DDM was not due to dissociation of the oligomer, since increasing the detergent concentration to 0.5% in the hrCN-PAGE did not release the monomer (Fig. 1). In the presence of DDM, V_1 showed a V_{max} and K_m values of $1.431 \pm 0.04 \mu\text{mol ATP hydrolyzed}(\text{mg } F_1F_0\text{-ATP synthase-min})^{-1}$ and $207 \pm 30 \mu\text{M}$, respectively (Fig. 2G, open circles). V_2 showed a $V_{max} = 9.604 \pm 0.26 \mu\text{mol ATP hydrolyzed}(\text{mg } F_1F_0\text{-ATP synthase-min})^{-1}$ and a $K_m = 490 \pm 80 \mu\text{M}$ (Fig. 2H, open circles, for comparison the activity of V_2 without DDM activation was included, closed circles). The k_{cat} for DDM activated oligomers were 14.5 and 207.7 s^{-1} for V_1 and V_2 , respectively (Table 2). In this sense, the k_{cat}/K_m values from the V_1 and the V_2 were 7×10^4 and $4.2 \times 10^5 \text{ M}^{-1} \text{ s}^{-1}$, respectively, indicating a higher specificity of V_2 .

3.3. Inhibition of V_1 and V_2 F_1F_0 -ATP synthase by oligomycin

Fig. 3 shows typical kinetics of V_1 (A) and V_2 (B) inhibition by oligomycin. The inhibition by oligomycin was time dependent, and the steady state ATPase activity decreased with oligomycin concentration.

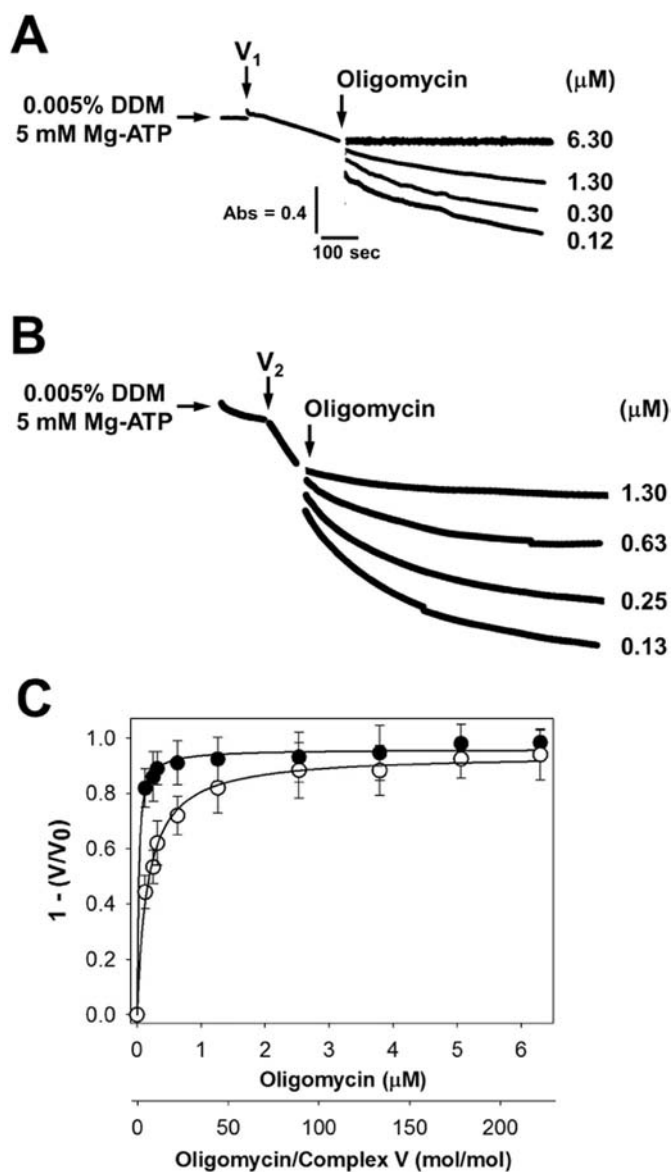


Fig. 3. ATPase inhibition by oligomycin of V_1 and V_2 . Conditions as in Fig. 2E and F except that Mg-ATP concentration was held at 5 mM. Time course of NADH oxidation coupled to ATP hydrolysis was monitored during 25–30 min for maximal ATPase inhibition of V_1 (A) or V_2 (B) and final spectrophotometric recording was analyzed as described in material and methods section. Enzyme or oligomycin additions indicated by vertical arrows and inhibitor concentration at the right side. (C) Maximal extent of inhibition of isolated V_1 (open circles) or V_2 (closed circles) as a function of oligomycin concentration. V_0 was the ATPase activity before oligomycin addition. The data are the average of three replicates from four independent preparations. Error bars represent S.D.

The time course of the inhibition did not follow monoexponential decay. Inhibition of V_1 was over 90% at 3.8 μM (Fig. 3C, open circles) while for V_2 it was at 1.3 μM (Fig. 3C, closed circles). Analysis of ATPase inhibition by oligomycin showed that V_2 had a $K_i = 24 \pm 3$ nM, while the K_i for V_1 was 169 ± 10 nM.

Since the amount of complex V in both preparations was quantified (see Supplemental material), it was possible to calculate the oligomycin/ F_1F_0 -ATP synthase ratio that resulted in 50% of ATPase inhibition (Fig. 3C, bottom offset axis and Table 2). The ratio was 0.85 ± 0.12 for V_2 and 6 ± 0.43 for V_1 . Taken together, our results suggest that the interphase between monomers in the dimer changed the oligomycin sensitivity.

Table 2
Kinetics parameters of ATPase activity of the monomer and the dimer of F_1F_0 -ATP synthase from *Ustilago maydis* mitochondria.

	Monomer (V_1) ^a	Dimer (V_2) ^a
<i>Non-activated F_1F_0-ATP synthase</i>		
V_{\max} ($\mu\text{mol ATP hydrolyzed/mg } F_1F_0\text{-ATP synthase}\cdot\text{min}^{-1}$)	0.83 ± 0.05	0.54 ± 0.08
K_m (μM)	308 ± 90	884 ± 100
k_{cat} (s^{-1})	8.4 ± 0.06	10.6 ± 0.15
k_{cat}/K_m ($\text{M}^{-1}\text{s}^{-1}$)	$2.7 \times 10^4 \pm 0.3$	$1.2 \times 10^4 \pm 0.1$
<i>DDM activated F_1F_0-ATP synthase</i>		
V_{\max} ($\mu\text{mol ATP hydrolyzed/mg } F_1F_0\text{-ATP synthase}\cdot\text{min}^{-1}$)	1.43 ± 0.04	9.60 ± 0.26
K_m (μM)	207 ± 30	488 ± 80
k_{cat} (s^{-1})	14.5 ± 0.03	207.7 ± 0.03
k_{cat}/K_m ($\text{M}^{-1}\text{s}^{-1}$)	$7.0 \times 10^4 \pm 0.2$	$4.2 \times 10^5 \pm 0.2$
K_i (nM) for oligomycin	169 ± 10	24 ± 3
	160 ± 17^b	21 ± 4^b
Ratio oligomycin/ F_1F_0 -ATP synthase (mol/mol) to reach 50% of ATPase inhibition	6.0 ± 0.43	0.85 ± 0.12

^a F_1F_0 -ATP synthase mol in V_1 and V_2 samples was determined as described in procedures section, and kinetics parameters were showed as mg of F_1F_0 -ATP synthase.

^b K_i values calculated by DynaFit software (see Materials and methods section).

3.4. Thermal inactivation of isolated V_1 and V_2 from F_1F_0 -ATP synthase

Thermal stability of V_1 and V_2 was monitored by measuring their residual ATPase activity. Fig. 4A shows typical transition curves for Mg-ATP hydrolysis rate of V_1 and V_2 plotted against the temperature of incubation. The activity (V/V_0) of V_1 and V_2 was not affected by incubation below 40 °C. However, a dramatic reduction in activity occurred for samples preincubated above 40 °C. The midpoint of the irreversible inactivation (T_m) was 52.3 °C. No loss of oligomycin sensitivity for V_1 and V_2 was detected in the range of temperatures tested, and no release of F_1 upon heat denaturation was observed in the hrCN-PAGE analysis (Fig. 4B and C). This suggested that V_2 inactivation might occur through its dissociation into V_1 and finally the inactivation of V_1 ; therefore, the monomer-monomer interphase apparently did not contribute to V_2 stability.

4. Discussion

Subunit composition of the dimer and monomer of mitochondrial complex V have been determined in many organisms, including mammals [15], the colorless alga *Polytomella* sp. [36,37] and *S. cerevisiae* [7,8,38]. Structurally, V_2 and V_1 from the basidiomycete *U. maydis* contains fifteen conserved subunits, while V_2 exhibited the e and g dimerizing subunits (Table 1). Interestingly, the presence of the ANT and the phosphate carrier suggests that the ATP-synthasome could be formed in both ATP-synthase oligomers, highlighting their role in mitochondrial bioenergetics.

Although mitochondrial architecture is closely related to the presence of V_2 [39], studies focused on its kinetic activity are scarce. In the past decade, there have been some efforts to determine the kinetic constants of the dimer [26]. In that report, the activity rate V_2/V_1 was equal to 1; and a slight increase was observed at 37 °C. However, the results were based on in-gel activity analysis of complex V using a long time span. In these conditions, ADP produced by ATPase activity will accumulate in the medium, which in turn would inhibit the enzyme. Additionally, densitometry quantification of the in-gel activity could be inaccurate due to gel oversaturation by calcium phosphate precipitation. Also, this method does not allow the calculation of enzyme affinity nor its inhibition by oligomycin. These drawbacks can be prevented by isolating the dimer. In this sense, Gonzalez-Halphen's group isolated

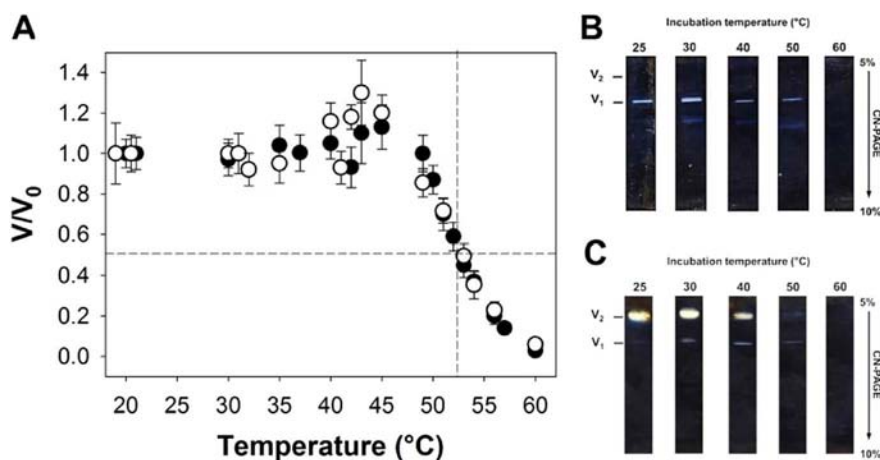


Fig. 4. Thermal inactivation curves of V_1 and V_2 . V_1 (open circles) or V_2 (closed circles) were incubated for 15 min at indicated temperatures and then cooled to room temperature. Activity assay was as described in Fig. 2E and F with 5 mM of Mg-ATP. A) Residual activity (V/V_0) was calculated using V_0 as the ATPase activity at 25 °C before heated. $T_m = 52.3$ °C. BN-PAGE of V_1 (B) and V_2 (C) incubated as described in (A). The data are the average of three replicates from four independent preparations. Error bars represent S.D.

and characterized kinetically a highly stable V_2 from *Polytomella* sp. [35]; however, because the high stability of V_2 , no data about V_1 activity was provided for comparison. In this study, we isolated both the V_2 and V_1 from *U. maydis* to determine their subunit composition by MS/MS, and to study their kinetics by spectrophotometric analysis in the presence of an ATP-regenerating system to eliminate the inhibition by ADP.

Characterization of the ATPase activity of V_2 and V_1 from *U. maydis* showed that the monomer is 1.5 times more active than the dimer; the low ATPase activity of V_2 was also observed in the *Polytomella* sp. dimer of complex V [35]. However, activation by DDM increased 18-fold the activity of V_2 while the affinity was not modified. Activation of V_1 by DDM increased only a 1.7-fold the V_{max} with no change of K_m . Specificity constant (k_{cat}/K_m) was 6 times higher for the V_2 than for V_1 , illustrating the differences between both oligomers again. It is important to mention that no dissociation of V_2 into V_1 or F_1 sector was observed in these experiments (Fig. 1), and ATPase activity was fully inhibited by oligomycin (Fig. 3). Since the CMC of DDM is 120–160 μ M and it was used at 98 μ M in the assay, activation of V_2 by DDM could be attributed to the interaction between the enzyme and the detergent. Interestingly, both oligomers were activated by DDM, and their maximum ATPase activities were achieved.

The activation of V_1 and V_2 by DDM could also be due to the Inh1 release (the regulatory subunit); however, it has been shown in mammalian cells that this subunit is removed from the F_1F_0 -ATP synthase at high pH (i.e. pH = 8.0), promoting full ATPase activity [40]. In this work the ATPase activity of V_1 and V_2 was assayed at pH = 8, but it is important further to explore the effect of pH on the activation of V_1 and V_2 by DDM. An important correction used for the comparison of the activities of V_1 and V_2 was the quantification of the actual concentration of F_1F_0 -ATP synthase in each V_2 and V_1 samples. Thus for the spectrophotometric assay, approximately the same amount of F_1F_0 -ATP synthase was added either in the dimer or monomer state. Therefore, the V_2 activity was much more than the sum of two V_1 activities, even when both enzymes were activated by DDM. These results indicate that the monomer-monomer interphase affected the function of the F_1F_0 -ATP synthase, increasing the V_{max} of the dimer by 7 times and its sensitivity to oligomycin. Importantly, kinetic parameters for DDM-activated V_1 agreed with those reported for the F_1F_0 -ATP synthase from *Escherichia coli* [41] or *Bos taurus* [42–44]; while parameters of V_2 from *U. maydis* resembles those of *Polytomella* sp. dimer [35].

Regarding to the role of the subunit interphase in the enzyme activity, it has been described that intersubunit contacts play a significant role in the catalytic properties of *Escherichia coli* glucosamine-6-P deaminase, particularly in the allosteric equilibrium between the R and T-state [45]. Similarly, in the 3-Deoxy-D-manno-oculosonate-8-P synthase the subunit interphase is important for substrate selectivity and

binding; the mutation of amino acid residues in this region produces a reduction in protein stability [46]. The deletion of the dimerizing subunit g in *U. maydis* doesn't prevent complex V dimerization, but isolated V_2 from the mutant strain showed a large decrease in ATPase activity comparing to the V_2 from WT, and mutant V_2 was not activated by DDM (Esparza-Perusquía, manuscript in preparation). Since subunit g is located at the monomers interphase [23], its deletion may promote a change in the structure of the interphase that affects the ATPase activity. Interestingly, ATPase activity of V_1 was similar in both *U. maydis* strains (Esparza-Perusquía, manuscript in preparation).

Thermal inactivation of V_2 and V_1 showed a $T_m = 52$ °C for both oligomers, and a single inactivation transition was observed. Analysis of the inactivation by hrCN-PAGE showed the dissociation of V_2 into V_1 as an early step in the inactivation; later, V_1 was denatured without the release of an active F_1 , contrary to what has been observed for the *Polytomella* sp. dimer [35]. In this sense, the interaction between monomers didn't increase the stability of the dimer.

Under physiological conditions, the monomer-monomer interface may have two possible roles: 1) a well-supported function of the dimer in the cristae folding, and 2) optimization of V_2 activity and the increase of the specificity constant of the F_1F_0 -ATP synthase. If the cellular requirement of ATP increases and there is an optimal $\Delta\mu_H^+$, V_2 could be activated 7-times in the ATP synthesis direction, compared with the monomer; contrary, if ATP synthesis is not required, V_2 shows a lower ATPase activity than the monomer. In this sense, it would be interesting to study the synthesis of ATP by V_1 and V_2 incorporated into liposomes, but the presence of high detergent concentrations during liposomes preparation process will disturb the monomer-monomer interface.

Transparency document

The [Transparency document](#) associated with this article can be found, in online version.

Acknowledgments

We dedicate this work as a memorial to Dr. Guillermo Mendoza-Hernandez, an exceptional friend and colleague, and coauthor of this paper, who passed away suddenly on July 13, 2012. This work was supported by Dirección General de Asuntos del Personal Académico (DGAPA) (IN214914, IN209614 and IN211715) from Universidad Nacional Autónoma de México (UNAM) and Consejo Nacional de Ciencia y Tecnología (CONACyT) (168025). Mercedes Esparza-Perusquía is a PhD student of the Programa de Doctorado en Ciencias Biológicas (511021118), UNAM and supported by the CONACyT through a doctoral scholarship (254400). The authors thank to the

Posgrado en Ciencias Biológicas, UNAM for the academic support. This manuscript partially fulfils the requirements of MEP to obtain her Ph.D. degree.

Conflict of interest

The authors declare no conflict of interest.

Author contribution

Esparza-Perusquía M and Flores-Herrera O designed and performed principal experiments; Olvera-Sánchez S, technical assistance; Pardo JP and Martínez F analyzed data; Mendoza-Hernández G carried out mass spectrometric analyses, Flores-Herrera O supervised project and wrote the paper with contributions from all authors.

Appendix A. Supplementary data

Supplementary data to this article can be found online at <http://dx.doi.org/10.1016/j.bbabo.2017.09.002>.

References

- J. Velours, G. Arselin, The *Saccharomyces cerevisiae* ATP synthase, *J. Bioenerg. Biomembr.* 4 (2000) 383–390.
- J.E. Walker, V.K. Dickson, The peripheral stalk of the mitochondrial ATP synthase, *Biochim. Biophys. Acta* 1757 (2006) 286–296.
- J. Symersky, V. Pagadala, D. Osowski, A. Krah, T. Meier, J.D. Faraldo-Gómez, D.M. Mueller, Structure of the c10 ring of the yeast mitochondrial ATP synthase in the open conformation, *Nat. Struct. Mol. Biol.* 19 (2012) 485–491.
- R.J. Devenish, M. Prescott, A.J. Rodgers, The structure and function of mitochondrial F₁F₀-ATP synthases, *Int. Rev. Cell Mol. Biol.* 267 (2008) 1–58.
- I. Arnold, K. Pfeiffer, W. Neupert, R.A. Stuart, H. Schägger, Yeast mitochondrial F₁F₀-ATP synthase exists as a dimer: identification of three dimer-specific subunits, *EMBO J.* 17 (1998) 7170–7178.
- H. Eubel, L. Jänsch, H.P. Braun, New insights into the respiratory chain of plant mitochondria. Supercomplexes and a unique composition of complex II, *Plant Physiol.* 133 (2003) 274–286.
- F. Krause, N.H. Reifschneider, S. Goto, N.A. Dencher, Active oligomeric ATP synthases in mammalian mitochondria, *Biochem. Biophys. Res. Commun.* 329 (2005) 583–590.
- P. Paumard, J. Vaillier, B. Coulary, J. Schaeffer, V. Soubannier, D.M. Mueller, D. Brèthes, J.P. di Rago, J. Velours, The ATP synthase is involved in generating mitochondrial cristae morphology, *EMBO J.* 21 (2002) 221–230.
- M.F. Giraud, P. Paumard, V. Soubannier, J. Vaillier, G. Arselin, B. Salin, J. Schaeffer, D. Brèthes, J.P. di Rago, J. Velours, Is there a relationship between the supramolecular organization of the mitochondrial ATP synthase and the formation of cristae? *Biochim. Biophys. Acta* 1555 (2002) 174–180.
- I. Wittig, H. Schägger, Structural organization of mitochondrial ATP synthase, *Biochim. Biophys. Acta* 1777 (2008) 592–598.
- J.L. Rubinstein, J.E. Walker, R. Henderson, Structure of the mitochondrial ATP synthase by electron cryomicroscopy, *EMBO J.* 22 (2003) 6182–6192.
- W.C. Lau, L.A. Baker, J.L. Rubinstein, Cryo-EM structure of the yeast ATP synthase, *J. Mol. Biol.* 382 (2008) 1256–1264.
- N.V. Dudkina, J. Heinemeyer, W. Keegstra, E.J. Boekema, H.P. Braun, Structure of dimeric ATP synthase from mitochondria: an angular association of monomers induces the strong curvature of the inner membrane, *FEBS Lett.* 579 (2005) 5769–5772.
- N.V. Dudkina, S. Sunderhaus, H.P. Braun, E.J. Boekema, Characterization of dimeric ATP synthase and cristae membrane ultrastructure from *Saccharomyces* and *Polytomella* mitochondria, *FEBS Lett.* 580 (2006) 3427–3432.
- F. Minauro-Sanmiguel, S. Wilkens, J.J. García, Structure of dimeric mitochondrial ATP synthase: novel F₀ bridging features and the structural basis of mitochondrial cristae biogenesis, *Proc. Natl. Acad. Sci. U. S. A.* 102 (2005) 12356–12358.
- D. Thomas, P. Bron, T. Weimann, A. Dautant, M.F. Giraud, P. Paumard, B. Salin, A. Cavalier, J. Velours, D. Brèthes, Supramolecular organization of the yeast F₁F₀-ATP synthase, *Biol. Cell.* 100 (2008) 591–601.
- N. Buzhynskyy, P. Sens, V. Prima, J.N. Sturgis, S. Scheuring, Rows of ATP synthase dimers in native mitochondrial inner membranes, *Biophys. J.* 93 (2007) 2870–2876.
- M. Strauss, G. Hofhaus, R.R. Schröder, W. Kühlbrandt, Dimer ribbons of ATP synthase shape the inner mitochondrial membrane, *EMBO J.* 27 (2008) 1154–1160.
- R. Fronzes, T. Weimann, J. Vaillier, J. Velours, D. Brèthes, The peripheral stalk participates in the yeast ATP synthase dimerization independently of e and g subunits, *Biochemistry* 45 (2006) 6715–6723.
- G. Arselin, M.F. Giraud, A. Dautant, J. Vaillier, D. Brèthes, B. Coulary-Salin, J. Schaeffer, J. Velours, The GxxxG motif of the transmembrane domain of subunit e is involved in the dimerization/oligomerization of the yeast ATP synthase complex in the mitochondrial membrane, *Eur. J. Biochem.* 270 (2003) 1875–1884.
- I. Wittig, H. Schägger, Advantages and limitations of clear-native PAGE, *Proteomics* (2005) 4338–4346.
- D.M. Bustos, J. Velours, The modification of the conserved GXXXG motif of the membrane-spanning segment of subunit g destabilizes the supramolecular species of yeast ATP synthase, *J. Biol. Chem.* 280 (2005) 29004–29010.
- S.J. Couch-Cardel, S. Uribe-Carvajal, S. Wilkens, J.J. García-Trejo, Structure of dimeric F₁F₀-ATP synthase, *J. Biol. Chem.* 285 (2010) 36447–36455.
- L. Tomasetig, F. Di Pancrazio, D.A. Harris, I. Mavelli, G. Lippe, Dimerization of F₀F₁-ATP synthase from bovine heart is independent from the binding of the inhibitor protein IF1, *Biochim. Biophys. Acta* 1556 (2002) 133–141.
- E. Zerbetto, L. Vergani, F. Dabbeni-Sala, Quantification of muscle mitochondrial oxidative phosphorylation enzymes via histochemical staining of blue native polyacrylamide gels, *Electrophoresis* 18 (1997) 2059–2064.
- E. Bisetto, F. Di Pancrazio, M.P. Simula, I. Mavelli, G. Lippe, Mammalian ATP synthase monomer versus dimer profiled by blue native PAGE and activity stain, *Electrophoresis* 28 (2007) 3178–3185.
- O. Juárez, G. Guerra, F. Martínez, J.P. Pardo, The mitochondrial respiratory chain of *Ustilago maydis*, *Biochim. Biophys. Acta* 1658 (2004) 244–251.
- W.F. Waterfield, H.D. Sisler, A convenient procedure for rapid release of protoplasts from *Ustilago maydis*, *BioTechniques* 6 (1988) 832–834.
- I. Wittig, M. Karas, H. Schägger, High resolution clear native electrophoresis for integral functional assays and fluorescence studies of membrane protein complexes, *Mol. Cell. Proteomics* 6 (2007) 1215–1225.
- C. Jung, C.M. Higgins, Z. Xu, Measuring the quantity and activity of mitochondrial electron transport chain complexes in tissues of central nervous system using blue native polyacrylamide gel electrophoresis, *Anal. Biochem.* 286 (2000) 214–223.
- H. Schägger, W.A. Cramer, G. von Jagow, Analysis of molecular masses and oligomeric states of protein complexes by blue native electrophoresis and isolation of membrane protein complexes by two-dimensional native electrophoresis, *Anal. Biochem.* 217 (1994) 220–230.
- W.S. Rasband, ImageJ, U.S. National Institutes of Health, Bethesda, Maryland, USA, 1997–2016 <http://imagej.nih.gov/ij/>.
- M. González-Zamorano, G. Mendoza-Hernández, W. Xolalpa, C. Parada, A.J. Vallecillo, F. Bigi, C. Espitia, Mycobacterium tuberculosis glycoproteomics based on ConA-lectin affinity capture of mannoseylated proteins, *J. Proteome Res.* 8 (2009) 721–733.
- P. Kuzmic, DynaFit—a software package for enzymology, *Methods Enzymol.* 467 (2009) 247–280.
- A. Villavencio-Queijeiro, J.P. Pardo, D. González-Halphen, Kinetic and hysteretic behavior of ATP hydrolysis of the highly stable dimeric ATP synthase of *Polytomella* sp, *Arch. Biochem. Biophys.* 575 (2015) 30–37.
- P. Cardol, D. González-Halphen, A. Reyes-Prieto, D. Baurain, R.F. Matagne, C. Remacle, The mitochondrial oxidative phosphorylation proteome of *Chlamydomonas reinhardtii* deduced from the Genome Sequencing, Project, *Plant Physiol.* 137 (2005) 447–459.
- M. Vázquez-Acevedo, P. Cardol, A. Cano-Estrada, M. Lapaille, C. Remacle, D. González-Halphen, The mitochondrial ATP synthase of chlorophycean algae contains eight subunits of unknown origin involved in the formation of an atypical stator-stalk and in the dimerization of the complex, *J. Bioenerg. Biomembr.* 38 (2006) 271–282.
- J. Velours, A. Dautant, B. Salin, I. Sagot, D. Brèthes, Mitochondrial F₁F₀-ATP synthase and organellar internal architecture, *Int. J. Biochem. Cell Biol.* 41 (2009) 1783–1789.
- D. De los Ríos-Castillo, M. Zarco-Zavala, S. Olvera-Sanchez, J.P. Pardo, O. Juárez, F. Martínez, G. Mendoza-Hernández, J.J. García-Trejo, O. Flores-Herrera, Atypical cristae morphology of human syncytiotrophoblast mitochondria: role for complex V, *J. Biol. Chem.* 286 (2011) 23911–23919.
- D.L. Feinstein, E.N. Moudrianakis, Response of the adenosine triphosphatase activity of the soluble latent F1 enzyme from beef heart mitochondria to changes in Mg²⁺ and H⁺ concentrations, *J. Biol. Chem.* 259 (1984) 4230–4236.
- D.L. Foster, M.E. Mosher, M. Futai, R.H. Fillingame, Subunits of the H⁺-ATPase of *Escherichia coli*. Overproduction of an eight-subunit F₁F₀-ATPase following induction of a lambda-transducing phage carrying the unc operon, *J. Biol. Chem.* 255 (1980) 12037–12041.
- P. Swanlung, L. Frigeri, K. Ohlson, L. Ernster, Studies on the activation of purified mitochondrial ATPase by phospholipids, *Biochim. Biophys. Acta* 305 (1973) 519–533.
- F. Zanotti, A. Gnoni, R. Mangiullo, S. Papa, Effect of the ATPase inhibitor protein IF1 on H⁺ translocation in the mitochondrial ATP synthase complex, *Biochem. Biophys. Res. Commun.* 384 (2009) 43–48.
- H.S. Penefsky, Differential effects of adenylyl imidodiphosphate on adenosine triphosphate synthesis and the partial reactions of oxidative phosphorylation, *J. Biol. Chem.* 249 (1974) 3579–3585.
- D.A. Cisnerosa, G.M. Montero-Moran, S. Lara-Gonzalez, M.L. Calcagno, Inversion of the allosteric response of *Escherichia coli* glucosamine-6-P deaminase to N-acetylglucosamine 6-P, by single amino acid replacements, *Arch. Biochem. Biophys.* 421 (2004) 77–84.
- T.M. Allison, F.C. Cochrane, G.B. Jameson, E.J. Parker, Examining the role of intersubunit contacts in catalysis by 3-deoxy-D-manno-oculosonate 8-phosphate synthase, *Biochemistry* 52 (2013) 4676–4686.

Deletion of subunit g affects the stability of the dimeric state of the F₁F₀-ATP synthase and decreases the mitochondrial ATP synthesis.

F₁F₀-ATP synthase complex interactions in vivo can occur in the absence of the dimer specific subunit g

Esparza-Perusquía M^a, Langner T^b, Feldbrügge M^c, Pardo JP^a, Martínez F^a, and Flores-Herrera O^{a1}

^aDepartamento de Bioquímica, Facultad de Medicina, Universidad Nacional Autónoma de México, Apartado Postal 70-159, Coyoacán 04510, México, D. F., México.

^bThe Sainsbury Laboratory, Norwich Research Park, Norwich NR4 7UH, United Kingdom.

^cInstitute for Microbiology, Cluster of Excellence on Plant Sciences, Department of Biology, Heinrich-Heine University Düsseldorf, Düsseldorf, Germany.

To whom correspondence should be addressed: Oscar Flores-Herrera. Departamento de Bioquímica, Facultad de Medicina, Universidad Nacional Autónoma de México, Apdo. Postal 70-159, Coyoacán 04510, México, Cd. Mx., México; Phone: 55-56232510; Fax: 55-56162419; E-mail: oflores@bq.unam.mx

Keywords:

Abstract

F₁F₀-ATP synthase is the transducer of electrochemical proton gradient to ATP and occurs in the inner membrane mitochondria as a monomer and dimer. The dimer shows a higher ATPase activity than monomer, and is involved with the cristae folding. The interface monomer-monomer is constituted by subunits a, i/j, e, g, and k. The role of the subunit g in a respiratory strict organism is unknown. A gene knockout was generated in order to verify subunit g role in the mitochondrial metabolism and cristae architecture of *Ustilago maydis*. Deletion of subunit g does not affect cell growth, glucose consumption, and biomass production. Ultrastructure analyzes showed that mitochondrial size and cristae shape was similar to wild strain. The membrane potential from wild type and mutant had a similar magnitude, but oxygen consumption was higher in mutant strain. ATP synthesis was 20% lower in mutant strain. Additionally, mutant strain expresses the AOX since exponential face of growth, and a lower ROS production was observed. Dimer from mutant strain was unstable during digitonin solubilization avoiding its isolation and kinetics characterization. Isolate monomeric state showed similar kinetics constant to monomer from WT strain. The ATP synthesis decrease and the AOX presence suggests that deletion of subunit g induces a ROS stress.

1. Introduction

The F₁F₀-ATP synthase (Complex V) of mitochondria, chloroplast and eubacteria use the energy of the proton electrochemical gradient for ATP synthesis from ADP and Pi. This enzyme is constituted by a catalytic sector (called F₁), a membrane sector (called F₀) and two connecting stalks (central and peripheral). The F₁ sector is a water-soluble entity composed of subunits α , β , γ , δ , and ϵ . The F₀ sector is embedded in the membrane and is composed by the hydrophobic subunits a, b, c, f, and 8. The central stalk is constituted by γ , δ , and ϵ subunits; while the peripheral stalk by subunits 4, h, d, f, and OSCP. The functional enzyme occurs when F₁ and F₀ sectors are coupled by connecting stalks and the whole complex could be considered as an H⁺-pumping ATP synthase or ATPase (1). The F₁F₀-ATP synthase is a nano-motor which uses the proton translocation through F₀ sector to promote the rotation of the ring of hydrophobic subunit c and the central stalk inside the F₁ sector.

Additionally, regulation of catalytic sector is carried out by the natural inhibitor peptide called IF₁ in mammalian or Inh1 in yeast.

Supernumerary subunits i/j, e, g, and k have been identify associated to F₀ sector (2, 3) and are involved in dimerization of F₁F₀-ATP synthase (3- 8). Dimer of complex V (V₂) folds the inner membrane into mitochondrial cristae (9) and its dissociation in monomer (V₁) is related to loss of cristae architecture. Particularly, deletion of subunits g and e in *Saccharomyces cerevisiae* produces mitochondria with onion-like structures (10, 11). It has been observed that these mutants growth in non-fermentable media (3) suggesting that dimerizing subunits g and e could not be involved in the activity of complex V. Nevertheless, it is widely accepted that the mitochondrial cristae architecture is important to generate the membrane potential ($\Delta\Psi_m$) used for the ATP synthesis. Then, are the mitochondria with onion-like cristae able to synthesize ATP?

In this work deletion of dimerizing subunit g (Δg) was performed in *Ustilago maydis*, a strict aerobic basidiomycete, and the analysis of mitochondrial ultrastructure, membrane potential ($\Delta\Psi_m$), oxygen uptake, ATP synthesis, and H₂O₂ production were performed. Quantification of mitochondrial complex V content was performed in both strains, and the presence of V₂ and V₁ was determined as reported previously by our group (12).

Results show that mutant strain preserves their mitochondrial network and cristae ultrastructure, but have a lower F₁F₀-ATP synthase amount. An unstable dimer of complex V (V_{2 Δg}) was observer over digitonine solubilization of OXPHOS complexes. Kinetics characterization demonstrate that the monomeric state of complex V from WT and Δg strains have similar kinetics parameters. Bioenergetics analysis shows that ATP synthesis decrease in mutant mitochondria while $\Delta\Psi_m$ remains constant. Interestingly, Δg strain expresses the alternative oxidase (AOX) since log-phase of growth. The role of subunit g in the stability and function of V₂ is discussed.

2. Materials and methods

2.1 Standard molecular biology techniques and Δg strain generation

To generate a gene replacement construct, the module of choice is fused to PCR-amplified flanks of about 1 kb using the restriction enzymes *SfiI* and *SwaI* and gene was replaced for the hygR cassette. Oligos RL615_um00975 U2 (atttAAATGCTTCCTTGTATTTCGGC- small letters indicated the restriction site for *SwaI*) and RL616_um00975 U3

(ggccatctAGGCCGATGACCGTATTACCCGAAAGAC- small letters indicated the restriction site for *SfiI*) were used to UF (upstream flank PRC-amplification) and RL617_um00975 D1 (ggcctgagTGGCCACGCTCGACAATTGAATTCG- small letters indicated the restriction site for *SfiI*) and RL618_um00975 D2 (atttAAATCTGGCATGTGCTCACC - small letters indicated the restriction site for *SwaI*).

Strain was constructed by transformation of FB2 strain with linearized plasmid pUMa1704. After transformation the cells were streaked on solid 1% glucose, 1% yeast extract, 0.25% bactopectone, 2% agar, 25 µg Hygromycin. All homologous integration events were verified by Southern blot analysis.

2.2 Cell culture

Cultivation was performed using standard techniques. Growth conditions for *U. maydis* strain and source of antibiotics were described elsewhere (13). The Δg strain was growth at 28°C in complete medium (1% glucose, 1% yeast extract and 0.25% bactopectone) (14). From this solid culture, an inoculum was used to grow cells in 100 ml of YPD (0.5% yeast extract, 0.25% bactopectone, 0.5% glucose) for 20-24 h at 28°C and then transfer 20-30 absorbance units (600 nm) of this suspension to 1 liter of YPD medium, to continue the growth of cells for 8 or 24 h at 28°C in a gyratory shaker at 200 rpm. Aliquots were withdrawn and their absorbance at 600 nm was determinate for cell growth curve evaluation. Alternatively, glucose consumption was evaluated using a kit (Glucose-LQ, Spinreact) following the manufacturer instructions. The strain was preserve at -70°C with 30% glycerol.

2.3 Mitochondrial ultrastructure analyzes

Cell pellets were fixed in 4% paraformaldehyde/2.5% glutaraldehyde for 1 h at room temperature; then they were washed two times (10 min each) in PBS and stained with 1% osmium tetraoxide for 1 h at 4°C, followed by two washes with PBS and water. Total dehydration was made in ethanol (graded 50 – 100%) and propylene oxide. Pellets were embedded in epoxy resin and cut into 70 nm sections. For immunoelectron microscopy, cell pellets were fixed with 4% paraformaldehyde/0.1% glutaraldehyde for 30 min at 4°C. After ethanol dehydration (graded 70 – 100%) pellets without osmication were embedded in LR White. Ultra-thin sections were mounted on nickel grids, blocked with 5% fat free milk in TBST for 15 min and probed with a 1:10 dilution of anti LC3 (Cell Signaling Technology Inc., Danvers, MA, USA) at 4°C, overnight. A 1:10 dilution of colloidal gold-conjugated secondary antibody (GAR Auroprobe, Amersham) was incubated for 2 h at room

temperature. Sections were washed with TBST and PBS, post-fixed with 1% glutaraldehyde in PBS, thoroughly washed and stained with 2% aqueous uranyl acetate. A control without first antibody was included. Electron microscopy was performed at 80 kV on a Zeiss EM900 Transmission Electron Microscope. Images were recorded with a Gatan Dual Vision CCD 300W camera (Gatan, Pleasanton, CA).

2.4 Oxygen consumption measurement

Oxygen uptake was estimated polarographically using a Clark type electrode in 10 mM KH_2PO_4 , pH 7.4, and 1 mg of wet weight of wild type strain or mutant strain cells per ml was added (15). Temperature was set at 30°C. Oxygen consumption was supported by endogenous substrates. Where indicated, 1 mM cyanide (KCN) or 50 μM n-octyl-galate was added to inhibit respiration. Alternatively, the oxygen uptake was assayed using isolated mitochondria in a solution composed by 500 mM sucrose, 20 mM MgCl_2 , 20 mM KH_2PO_4 , 2 mM EGTA, 0.2% BSA, pH 7.4. Maximum activity of complex IV was assayed with 4 mM ascorbate and 6 mM 2,3,5,6-tetramethyl-p-phenyldiamine (TMPD) to reduce the horse heart cytochrome c.

2.5 Cell permeabilization

U. maydis cells (125 mg wet weight/ml) from WT and Δg strains were permeabilized with 0.02% digitonin in 300 mM sorbitol, 10 mM HEPES, 1 mM EGTA, 7 mM MgSO_4 , 150 mM KCl, 10 mM KH_2PO_4 , pH 7.4, at 25°C during 20 min with constant stirring.

2.6 Membrane potential determination

The membrane potential ($\Delta\Psi_m$) of permeabilized *U. maydis* cells (125 mg wet weight/ml) was determined in the medium described for cell permeabilization and supplemented with 10 μM Safranin O. Succinate (10 mM, pH 7.4) was added to $\Delta\Psi_m$ generation (16). Where indicated, 1 mM ADP was added to verify the membrane potential depolarization coupled to oxygen uptake and ATP synthesis stimulation. CCCP (5 μM) was added to abolish the membrane potential. The membrane potential was evaluated in a double beam spectrophotometer (Aminco DW 2000, Olis, Inc.) by using the difference of wavelengths between 533–511 nm. The recording was performed in a 3.0 ml cuvette with constant stirring and the temperature was held at 25°C.

2.7 Mitochondrial ATP synthesis

ATP synthesis was performed at 25°C using permeabilized *U. maydis* cells (125 mg wet weight/ml) in the medium described for cell permeabilization supplemented with 10 mM succinate, 100 µM P¹,P⁵-Di(adenosine-5')pentaphosphate ammonium salt. ATP synthesis was started by the addition of 5 mM ADP and aliquots were withdrawn at different times and mixed with perchloric acid (7% final concentration) for stop the reaction. The samples were spin-out in a refrigerate Eppendorf microfuge at 13,000 rpm during 5 min. Supernatant was recovered and pH adjusted to 7.0 with KOH. To remove the potassium perchlorate the samples were spin-out again, and supernatant recovered and pH adjusted to 7.4. ATP content in each sample was quantify with an assay coupled to the reduction of NADP⁺ ($\epsilon_{340\text{ nm}} = 6.2\text{ mM}^{-1}\cdot\text{cm}^{-1}$). The reaction mixture contained 0.5 mM NADP⁺, 6 units/ml glucose-6-phosphate dehydrogenase, 16 units/ml hexokinase, 10 mM glucose, 5 mM MgCl₂, 10 mM KH₂PO₄, pH 7.5.

2.8 Mitochondria isolation

The method described by Waterfield and Sisler (17) was used with minor modifications. Cells were grown in YPD medium for 24 h, collected by centrifugation (3,800 g for 10 min), washed twice with distilled water, and the pellet suspended with 0.6 M ammonium sulfate (11.25 ml/g wet weight). To produce protoplasts, 1 g of wet weight of *U. maydis* cells suspension were incubated with 0.016 g of *Trichoderma harzianum* lytic enzymes, during 60 min at 30°C. The protoplasts were recovered by centrifugation at 3,800 g for 10 min, and suspended in 0.8 M sucrose, 10 mM Tris, 2 mM EDTA, 3% BSA, and 20 mM KH₂PO₄, pH 7.0; this suspension was centrifuged in similar condition described above to wash out the lytic enzymes. The pelleted protoplasts were suspended in 0.4 M sucrose, 10 mM Tris, 2 mM EDTA, 3% BSA, and 20 mM KH₂PO₄, pH 7.0 (buffer A). PMSF (1 mM) and 25 µl/g wet weight of the protease inhibitors cocktail (fungal and yeast protease inhibitor cocktail, Sigma p8215) were added to the suspension and homogenized 15-20 times in a Teflon potter homogenizer. The homogenization extract was 3-fold diluted with buffer A and centrifuged at 3,800 g for 10 min at 4°C. The supernatant was centrifuged at 17,000 g for 10 min and the mitochondrial pellet suspended in buffer A to a protein concentration of 20-30 mg/ml.

2.9 Solubilisation of OXPHOS complexes

The OXPHOS complexes from *U. maydis* mitochondria were solubilized with digitonin, a very mild detergent, as described (12, 18-20). Briefly, two mg of mitochondrial protein were suspended in 0.2 ml of 50 mM Bis-Tris and 500 mM 6-aminocaproic acid, pH 7.0, supplemented with 10 mM succinate and 10 mM ATP and solubilized with increasing digitonin concentration in a ratio of 0.5, 1, 2, 3, and 5 mg of digitonin per mg of protein. The digitonin was added drop by drop and the

mixtures were incubated for 30 min at 4°C with gentle stirring, and then centrifuged at 100,000 g for 30 min at 4°C. The supercomplexes and complexes were recovered from supernatant and analyzed by blue native PAGE (BN-PAGE) and clear native PAGE high resolution (hrCN-PAGE) as described (18-20).

2.10 *F₁F₀-ATP synthase complexes isolation*

Mitochondrial supercomplexes and complexes from *U. maydis* were solubilized with a digitonin/protein ratio of 2:1 and processed as described by Esparza-Perusquia et. al (2017). Digitonin-solubilized mitochondrial supercomplexes and complexes (16 mg of protein) were loaded on 24 ml of a continuous sucrose gradient (16 – 42% sucrose, 15 mM Tris, pH 7.4, 20 mM KCl, and 0.2% digitonin) and centrifuged at 131,000 g for 16 h at 4°C. Fractions (0.5 ml) were collected from the bottom of the gradient. The presence of V₂ and V₁ in each gradient-fraction was determined by in-gel activity of ATPase from BN-PAGE and hrCN-PAGE. If applicable, the fraction containing each oligomer were pooled separately, and diluted 7 folds with 30 mM HEPES, pH 8.0 and 5% glycerol; then concentrated using a Centrifugal Filters Units (100K, Millipore Amicon Ultra) to a final volume of 100 µl, and stored at -70°C until used. The V_{2Ag} was so unstable and scarce that it was used immediately as gradient-fractionation was done and its presence detected.

The anode buffer for BN-PAGE was 50 mM Bis-Tris/HCl, pH 7.0; the cathode buffer contained 50 mM tricine, 15 mM Bis-Tris, pH 7.0 and the anionic Coomassie dye (0.02%). For hrCN-PAGE the anode buffer contained 25 mM imidazole/HCl, pH 7.0; the cathode buffer was 50 mM Tricine, 7.5 mM imidazole, pH 7.0, 0.01% dodecyl-β-D-maltopyranoside (DDM) and 0.05% deoxycholate (DOC). The gel front was visualized with Ponceau Red (21). The electrophoresis (BN or hrCN) were performed at 4°C and the voltage was set to 35 V for 10 h and stopped when the sharp line of the dye approached the gel front. Molecular weight of the respiratory complexes and supercomplexes was determined by their electrophoretic mobility and in-gel catalytic activity, using the complexes of digitonine-solubilized bovine heart mitochondria as standards.

The concentration of F₁F₀-ATP synthase in each V₁ and V₂ sample was determined by a densitometry analysis of Coomassie© Brilliant Blue R-125 stained α- and β-subunits from an SDS-Tricine-PAGE, using Coomassie stained BSA as a standard (See Supplemental material section, Figure S1). Densitometry analysis was performed with the My Image Software Thermo Fisher Scientific Inc, 2014.

2.11 In-gel catalytic activity assays

The in-gel assays of digitonine-solubilized supercomplexes and complexes from *U. maydis* mitochondria were performed as described by Jung (19) using gel strips loaded with 150 µg of protein. NADH dehydrogenase activity (NADH:methylthiazolyldiphenyl tetrazolium bromide (MTT) oxidoreductase) was assayed in a buffer containing 1.2 mM MTT and 1.0 mM NADH in 10 mM Tris/HCl, pH 7.4, at 20 – 25°C. For succinate dehydrogenase activity (Succinate:MTT oxidoreductase) NADH was replaced by 10 mM succinate, in a buffer of 10 mM K₂HPO₄, pH 7.4, 5 mM EDTA and 0.2 mM phenazine methosulfate (PMS). NADH or succinate dehydrogenase activity was correlated with the development of purple precipitates on the gel. Activity was monitored as purple-staining appears (10 – 20 min) and then the reaction was stopped with fixing solution (50% methanol, 10% acetic acid). The in-gel activity of complex IV was assayed in 50 mM K₂HPO₄, pH 7.2, 4.7 mM 3,3'-diaminobenzidine tetrahydrochloride (DAB) and 16 µM horse heart cytochrome c, during 30 – 40 min of incubation at 20 – 25°C. The activity was observed as a brown precipitate and the reaction was stopped with the fixing solution. Activity of complex V was assayed in 50 mM glycine (adjusted to pH 8.0 with triethanolamine), 10 mM MgCl₂, 0.15% Pb(ClO₄)₂ and 5 mM ATP. ATP hydrolysis correlated with the appearance of a white lead phosphate precipitates. The reaction was stopped using 50% methanol, and subsequently the gel was transferred to water and scanned against a dark background as described previously (18-19).

2.12 2D-Tricine-SDS gel electrophoresis

2D-Tricine-SDS-polyacrylamide gel electrophoresis (2D-SDS-PAGE) was performed according to Schägger (20). Proteins from a native PAGE gel strip loaded with 150 µg of digitonine-solubilized supercomplexes and complexes were separated by 2D-Tricine-SDS-PAGE on a 16% polyacrylamide gel under denaturing conditions. After the run, the proteins were stained with Coomassie© Brilliant Blue R-125.

2.13 Measurements of ATP hydrolysis by F₁F₀-ATP synthase complexes

ATP hydrolysis by F₁F₀-ATP synthase complexes was measured spectrophotometrically in an Agilent 8453 UV-visible spectrophotometer (Agilent Technologies, USA) as described by (12), using an assay coupled to the oxidation of NADH ($\epsilon_{340\text{nm}} = 6.2 \text{ mM}^{-1} \cdot \text{cm}^{-1}$). The assay medium contained 50 mM HEPES, pH 8.0, 1 mM MgSO₄, 90 mM KCl, and the temperature was held at 25°C. The ATP-regenerating system was 5 mM phosphoenolpyruvate (PEP), 1 mM NADH, 50 units/ml pyruvate kinase (PK), and 30 units of lactate dehydrogenase (LDH)/ml. The ATPase

reaction was started by the addition of an equimolar mixture of Mg-ATP complex. The NADH absorbance was continuously monitored and the time response, checked by ADP additions, was less than 1 s. The slope of the linear region of each spectrophotometric recording was used to obtain the initials velocities. The linear region of the traces was corroborated with plotting the first-derivative against time. Since a non-specific NADH oxidation was observed with no enzyme addition, the actual value of ATPase activity was calculated as the subtraction of the slope of this region from the slope that is obtained after adding the enzyme. Oligomycin (3 μ M) was added to inhibit ATPase activity to verify F_1F_0 -ATP synthase integrity. Only samples with ATPase activity 100% inhibited by oligomycin were used in this study.

Data for the ATP hydrolysis were analyzed by robust, weighted, non-linear regression analysis using the SigmaPlot software (Systat Software, Inc., version 10.0), and represent the average of three replicates from seven independent experiments.

2.14 Oligomycin inhibition of F_1F_0 -ATP synthase

Continues monitoring of ATP hydrolysis by F_1F_0 -ATP synthase dimer or monomer coupled to NADH oxidation was carried out as described by Esparza-Perusquia et al (12). ATP hydrolysis was initiated by Mg-ATP addition; after 2-4 min oligomycin was added and ATPase activity decayed. Because oligomycin is a slow-union inhibitor the total recording time for maximal ATPase activity inhibition, at different oligomycin concentrations, was about 25-35 min. The final spectrophotometric recording was fitted to a monoexponential decay of the ATPase activity as described by (12).

2.15 Determination of protein concentration.

Samples were treated with 0.4% deoxycholate and the protein content was determined as described by Lowry et al. [56]. Bovine serum albumin (BSA) was used as standard.

3. RESULTS

*3.1 Deletion of the g subunit from the *Ustilago maydis* genome*

The g subunit gene was deleted by homologous recombination as reported by Brachmann et. al., (13) using a hygromycin resistant gene (Hyg). The correct construction of knock-out plasmid (pUMa1704) was verify by *Sfi*I enzyme restriction activity (Fig. 1A), which produced one band of

1.88 Kb (Hyg gene resistant) and other of 6.37 Kb (the UF-DF vector). The *U. maydis* cells transformed with the plasmid pUMa1704 were selected by hygromycin resistant (Fig. 1B). The deletion of the g subunit gene by the correct insertion of the hygromycin resistant gene was determined by PCR using the UF and DF flanks described in materials and methods section. The presence of the 1.5 and 1.7 amplified confirm the correct insertion of the Hyg-gene (Fig. 1C). Finally, the genomic DNA (gDNA) from WT and Δg mutant strains was processed by the restriction enzyme *NcoI* and the product analyzed by Southern Blot (Fig. 1D). As the Hyg gene has a cutoff point for the *NcoI*, two PCR product were identified from Δg mutant gDNA while only one from WT strain (Fig. 1D). These results showed that g subunit was successfully deleted from *U. maydis* genome and is not present in the Δg strain.

3.1 Growth of Δg mutant strain

The elimination of subunit g from F_1F_0 -ATP synthase in *Ustilago maydis* was obtained as described in methods section, and growth cells characterization of mutant strain included the doubling time, number of cell, glucose consumption, dry weight, and cell length. The doubling time was similar for both strain (2.9 ± 0.7 h and 2.4 ± 0.5 h for mutant and WT, respectively). However, the number of cells was quiet different; mutant strain produce 82% (3.37×10^9 cell·L⁻¹) of the total number of WT cells (4.12×10^9 cell·L⁻¹); however, the mutant cells were 1.5-times longer in the log-phase (28 ± 2 and 19 ± 2 μ m, for the mutant and WT strains, respectively) and 1.3-times in the stationary-phase (30 ± 3 and 23 ± 4 μ m, for the mutant and WT strains, respectively) than WT cells. This indicates that the mutant cells were longer that WT, but its cell production was lower.

In this line of thought, the glucose consumption was similar for both strains in the log-phase (25 ± 3 and 24 ± 2 mmol by mutant and WT strain, respectively) or in the stationary-phase (15 ± 0.7 and 15 ± 0.9 mmol for mutant and WT strain, respectively). Interestingly, both strain reached a similar dry weight at stationary phase of growth (2.0 ± 0.3 and 2.0 ± 0.2 mg/ml, for mutant and WT strain, respectively). This suggested that carbon incorporation in both strains was similar, regardless that the cells in the mutant strain were longer but fewer.

3.2 Mitochondrial ultrastructure and bioenergetics of Δg mutant strain

The mitochondrial cristae from Δg strain showed a tubular and lamellar ultrastructure, similar to WT (Fig. 2). Additionally, the $\Delta\Psi_m$ from Δg mutant was stimulated by succinate in a similar magnitude to WT mitochondria (Fig. 2). Simultaneously, the activity of the NADH:DBQ oxido-

reductase (Complex I) and succinate:DBQ oxido-reductase (Complex II) was determined. WT strain showed a complex I activity of $0.18 \pm 0.06 \mu\text{mol NADH oxidized} \cdot (\text{mg} \cdot \text{min})^{-1}$, while Δg mutant of $0.16 \pm 0.03 \mu\text{mol NADH oxidized} \cdot (\text{mg} \cdot \text{min})^{-1}$. The complex II has an activity of $0.05 \pm 0.01 \mu\text{mol DCPIP reduced} \cdot (\text{mg} \cdot \text{min})^{-1}$ from WT and of $0.04 \pm 0.01 \mu\text{mol DCPIP reduced} \cdot (\text{mg} \cdot \text{min})^{-1}$ from mutant strain.

In this condition the ATP synthesis was $20 \pm 1 \mu\text{mol ATP} \cdot (\text{mg} \cdot \text{min})^{-1}$ and $15 \pm 0.9 \mu\text{mol ATP} \cdot (\text{mg} \cdot \text{min})^{-1}$ for the WT and Δg strains, respectively. This difference (25%) in the ATP synthesis suggested that 1) respiratory oxygen uptake and ATP synthesis could be uncoupled, or 2) the F_1F_0 -ATP synthase activity is decreased. As a first step to explore these hypotheses, mitochondrial oxygen uptake at log- and stationary-phase of growth (*i.e.* 8 and 24 hours, respectively) was determined (Fig. 2).

At 8 hours of growth, the respiration was similar in both strains ($112 \pm 15 \text{ ng atoms O}$ and $130 \pm 17 \text{ ng atoms O}$, for WT and Δg strains, respectively); however, the cyanide inhibits only the WT strain respiration (Fig. 2). Maximum activity of complex IV was stimulated with ascorbate, TMPD, and cytochrome c as described in methods section. Activity of complex IV was higher in WT mitochondria (*i.e.* $1048 \pm 21 \text{ ng atoms O} \cdot (\text{mg} \cdot \text{min})^{-1}$) than in Δg strains mitochondria (*i.e.* $827 \pm 18 \text{ ng atoms O} \cdot (\text{mg} \cdot \text{min})^{-1}$) (Table 1). Total inhibition of oxygen uptake was reached with *n*-octyl-galate addition, indicating the presence of the alternative oxidase (AOX). AOX is a quinol:oxygen oxido-reductase but it is not a proton pump. At stationary state of growth, both strains express the AOX but their activity was sharp different, $124 \pm 23 \text{ ng atoms O} \cdot (\text{mg} \cdot \text{min})^{-1}$ and $262 \pm 4 \text{ ng atoms O} \cdot (\text{mg} \cdot \text{min})^{-1}$ for WT and Δg strains, respectively (Table 1). The decrease of the activity of complex IV (*i.e.* 20%) and the 2-time increase of AOX activity in the Δg strain, suggests that ROS stress could occur in the mutant strain.

The AOX presence has been associated with ROS production prevention. To explore this possibility, the H_2O_2 production was determinate at 8 and 24 hour of growth (Table 1). Succinate or NADH was used as oxidizable substrate and the H_2O_2 production was $470 \pm 80 \text{ nmol H}_2\text{O}_2 \cdot (\text{mg} \cdot \text{min})^{-1}$ and $280 \pm 30 \text{ nmol H}_2\text{O}_2 \cdot (\text{mg} \cdot \text{min})^{-1}$ in WT and Δg strains, respectively; suggesting that in the Δg strain the AOX could avoid ROS production.

Although mitochondrial ultrastructure and $\Delta\Psi_m$ was similar in both strains, the ATP synthesis was affect in the Δg mutant simultaneously to AOX expression since early state of growth. Deletion of

the dimerizing g-subunit from complex V could be involved with the decrease of ATP synthesis, while AOX presence with the stress resistance.

3.3 Supercomplexes and complexes analyzes

The respiratory supercomplexes and complexes from WT and Δg strains were solubilized with different ratio of digitonine/protein and analyzed by BN-PAGE (Fig. 3). The activity of NADH:MTT oxidoreductase from WT strain was associated to supercomplexes of high molecular weight but principally to a main band of 1600 kDa, and in lower proportion to free-complex I (*i.e.* 990 kDa) (Fig. 3B). Activity of succinate:MTT oxidoreductase from complex II was associated with a single band of 130 kDa (Fig. 3C). Free-complex IV activity was located at 200 kDa and supercomplexes also exhibits activity of complex IV (Fig. 3D), similarly to previously reported by our laboratory (22). The in-gel activity of the F_1F_0 -ATP synthase from WT occurs as monomeric (V_1) and dimeric (V_2) state, with 660 and 1200 kDa, respectively (Fig. 3E). It is important to note that amount of V_1 and V_2 from the WT strain was very similar, determined as described in materials and methods section (*vide infra*) (Fig. 3A).

The analysis of supercomplexes and complexes from Δg strain showed that in-gel activity of NADH:MTT oxidoreductase was mainly associated to free-complex I (990 kDa) and supercomplexes of low molecular weight (*i.e.* 1200 – 1300 kDa) (Fig. 3B). Interestingly, monomeric complex II was clearly observed from a ratio digitonine/protein = 3 (Fig. 3C). The complex IV activity was associated to supercomplexes and a free-complex IV (Fig. 3D). The ATPase activity of F_1F_0 -ATP synthase from Δg strain was associated to a single band of 660 kDa, corresponding to the V_1 (Fig. 3E). The activity of the V_2 was observed only after a 24 h of incubation in the in-gel ATPase activity medium (Fig. 3F), indicating that this oligomers showed a very low activity; indeed, in some replicates was not observed at all. A 2D-SDS-PAGE from the BN-PAGE lane showed that the amount of complex V from V_2 was substantially diminished respect to the V_1 (data no shown).

To explore the kinetics of V_2 from Δg strain, many attempts to isolate it were performed (Fig. 4A); however, due that V_2 was very unstable it was impossible to isolate it in sufficient quantity to perform kinetics studies. Interestingly, the total amount of complex V in the mitochondria was $132 \pm 6 \mu\text{g}$ of complex V $\cdot (\text{mg mitochondrial protein})^{-1}$ and $111 \pm 7 \mu\text{g}$ of complex V $\cdot (\text{mg mitochondrial protein})^{-1}$ for WT and Δg , respectively. This suggests that deletion of subunit g decrease only a 16% the F_1F_0 -ATP synthase amount in the Δg mitochondria but V_2 was unstable and dissociate straightaway into single subunits during digitonine solubilization, without V_1 accumulation.

The kinetics characterization of the $V_{1\Delta g}$ was performed and it has had a K_M of 155 ± 47 μM and a V_{max} of 0.58 ± 0.03 $\mu\text{mol hydrolyzed ATP} \cdot (\text{mg F}_1\text{F}_0\text{-ATP synthase} \cdot \text{min})^{-1}$. The k_{cat} was 5.86 ± 0.05 s^{-1} and the k_{cat}/K_M of $3.78 \times 10^4 \pm 0.3 \times 10^4$ ($\text{M}^{-1}\text{s}^{-1}$). The $V_{1\Delta g}$ activated with DDM increases its V_{max} to 2.3 ± 0.2 $\mu\text{mol hydrolyzed ATP} \cdot (\text{mg F}_1\text{F}_0\text{-ATP synthase} \cdot \text{min})^{-1}$ with a K_M value of 920 ± 20 μM . The values for k_{cat} and specificity constant were 23.26 ± 0.1 s^{-1} and $2.53 \times 10^4 \pm 0.08 \times 10^4$, respectively. Additionally, the inhibition of $V_{1\Delta g}$ ATPase activity by oligomycin had a K_i value of 53 ± 4 nM . The kinetics parameters of $V_{1\Delta g}$, its activation by DDM and oligomycin inhibition were similar to $V_{1\text{WT}}$ previously reported (12), suggesting that ATPase activity of $V_{1\Delta g}$ was not modified by deletion of subunit g.

Dimerizing g-subunit deletion doesn't avoid $V_{2\Delta g}$ state of complex V (*i.e.* determined as mitochondrial cristae folding, generation of the $\Delta\Psi_m$, and oxygen uptake) but could deteriorate the interphase monomer-monomer inducing an instable dimeric state, which probably could be related to lower ATP synthesis.

4. DISCUSSION

The role of the dimeric state of F_1F_0 -ATP synthase in the mitochondrial crista folding has been widely accepted (6-9). Actually, it has been described that the interface monomer-monomer of the yeast dimer is constituted by subunits a, i/j, k, g, and e (23). The interface can be divided into a central zone and a peripheral zone. In the central zone, the subunits i/j interact through two short stretches of ~ 10 residues; while interaction between subunits a occurs through two strands that constituted a four stranded planar structure with one hydrophobic surface and one hydrophilic surface (23).

The peripheral zone of the monomer-monomer interface is constituted by subunits k and e. These subunits possess a similar structure: an N-terminal α -helix with two domains, one transmembrane, and one soluble which extent (~ 40 \AA for subunit e) into the intermembrane space to interact between them (23). Subunit g is holding the subunit e through a single transmembrane α -helix, probably via the conserved Gly-X-X-X-Gly motif of the two proteins (24). Simultaneously, the N-terminal α -helix of subunit g interact with the N-terminal ~ 50 residues of subunit b. The domain of the peripheral zone of interface monomer-monomer constituted by subunits e, g, and b with support from subunit k bend the mitochondrial inner membrane (23, 25).

In *Saccharomyces cerevisiae* simultaneous deletion of dimerizing subunits g and e induces the loss of V_2 and the change of mitochondrial cristae morphology into structures called onion rings.

However, as *S. cerevisiae* is a facultative organism, mitochondrial participation in the bioenergetics of these mutants is not clear. As *Ustilago maydis* is a non-fermentative basidiomycete, which bioenergetics metabolism is held by mitochondria, the study of the effect of deletion of dimerizing subunits in mitochondrial bioenergetics could be very illustrative.

Deletion of subunit g in *U. maydis* doesn't change the cellular doubling time, glucose consumption and dry weight production, suggesting a similar carbon uptake and its incorporation into biomass. However, until now, we haven't an explanation about why the cells of Δg strain were longest than WT, and why the total amount of mutant cells was few. Additionally, presence of classic mitochondria structure from mutant strain was conserved.

Bioenergetics analysis showed that mitochondria from both strains used succinate to produce a similar $\Delta\Psi_m$ associated to oxygen uptake by the classic cytochrome chain (Table 1); however, Δg strain showed a decrease of ATP synthesis associated with expression, since early stage of growth, of the AOX. It has been reported that similar experimental conditions (*i.e.* high $\Delta\Psi_m$, succinate as electron supply of respiratory chain, and a decrease of complex V activity) could produce reverse electron transport (RET) at complex I and lead to an increase in superoxide production (26). In this sense, AOX transfers electrons from QH_2 directly to O_2 , bypassing complex IV, and thus act as a safety valve to prevent the excessive reduction of the Q pool (26-28).

It is plausible to hypothesize that deletion of subunit g produce a decrease of the ATP synthesis by the dimer of F_1F_0 -ATP synthase, which results in a low consumption of the $\Delta\Psi_m$, an accumulation of NAD(P)H, and an increase of H_2O_2 production (*i.e.* through RET at complex I). In this sense, H_2O_2 production during succinate oxidation was decreased by AOX expression by Δg strain, similarly as shown previously (26, 29).

Alternatively the role of deletion of subunit g in F_1F_0 -ATP synthase could be analyzed by ATP synthesis. In this sense, the ATP production showed 20% reduction in the mutant strain. As subunit g is involved in the peripheral zone of monomer-monomer interface the conformation of dimer could be preserved but the ATP synthase activity don't. Additionally to the participation of the interface monomer-monomer in folding inner membrane, it has been proposed that it could play an important role in the activity of V_2 , highlighting the role of the dimerizing subunits (12). Indeed, the ATPase activity of $\text{V}_{2\text{WT}}$ was 7 times higher than $\text{V}_{1\text{WT}}$ and exhibits a high sensitivity to oligomycin (12).

In this sense, modification of the interface monomer-monomer could provide evidences about the role of the dimerizing subunit in the activity of the V_2 . Unfortunately, the mutant $V_{2\Delta g}$ was so unstable and scarce to be isolated and characterized as WT dimer was; and only a few determination of its activity showed that it was 8-times lower than mutant $V_{1\Delta g}$. As has been describe above, subunit g play an important role in the peripheral zone of the interface monomer-monomer, and its deletion lead only subunit e from one monomer interacting with subunit k from the other monomer; producing a weak interface. This leak interface monomer-monomer could evoke a low ATP synthesis, contrary to observed in V_{2WT} , which show a high activity compared with V_{1WT} (12).

Acknowledgment

This work was supported by Direccion General de Asuntos del Personal Academico (DGAPA) (IN222617) from Universidad Nacional Autonoma de Mexico (UNAM). ME-P is a PhD student of the Programa de Doctorado en Ciencias Biologicas (511021118) from UNAM and supported by CONACyT through a doctoral scholarship (254400). The authors thank to the Posgrado en Ciencias Biologicas from UNAM for the academic support.

References

- 1) Pedersen PL. (1996) *J. Bioenerg. Biomembr.* 28, 389–395.
- 2) Vaillier J, Arselin G, Graves PV, Camougrand N, Velours J. (1999) *J. Biol. Chem.* 274, 543–548
- 3) Arnold I, Pfeiffer K, Neupert W, Stuart RA, Schaeffger H. (1998) *EMBO J.* 17, 7170–7178
- 4) Rubinstein JL, Walker JE, Henderson R. (2003) *EMBO J.* 22, 6182–92
- 5) Lau WC, Baker LA, Rubinstein JL. (2008) *J Mol Biol.* 382, 1256–64
- 6) Minauro-Sanmiguel F, Wilkens S, García JJ. (2005) *Proc Natl Acad Sci USA.* 102, 12356–8
- 7) Dudkina NV, Heinemeyer J, Keegstra W, Boekema EJ, Braun HP. (2005) *FEBS Lett.* 579, 5769–72
- 8) Thomas D, Bron P, Weimann T, Dautant A, Giraud MF, Paumard P, et al. (2008) *Biol Cell.* 100, 591–601
- 9) Dudkina NV, Sunderhaus S, Braun HP, Boekema EJ. (2006) *FEBS Lett.* 580, 3427–32
- 10) Paumard P, Vaillier J, Couлары B, Schaeffer J, Soubannier V, Mueller DM, et al. (2002) *EMBO J.* 21, 221–30

- 11) Soubannier V, Vaillier J, Paumard P, Couлары B, Schaeffer J, Velours J. (2002) *J Biol Chem.* 277, 10739–45
- 12) Esparza-Perusquía M, Olvera-Sánchez S, Pardo JP, Mendoza-Hernández G, Martínez F, Flores-Herrera O. (2017) *Biochim Biophys Acta Bioenerg.* 1858, 975-981.
- 13) Brachmann A1, König J, Julius C, Feldbrügge M. (2004) *Mol Genet Genomics.* 272, 216-26.
- 14) Holliday R. *Ustilago maydis*. In: King R, editor. *Handbook of Genetics*. New York: Plenum; 1974. p. 575–95
- 15) De los Rios Castillo D, Zarco-Zavala M, Olvera-Sanchez S, Pardo JP, Juarez O, Martinez F, Mendoza-Hernandez G, García-Trejo JJ, Flores-Herrera O. (2011) *J Biol Chem.* 286, 23911-9.
- 16) Flores-Herrera O, Olvera-Sánchez S, Esparza-Perusquía M, Pardo JP, Rendón JL, Mendoza-Hernández G, Martínez F. (2015) *Biochim Biophys Acta.* 1847, 143-152.
- 17) Waterfield WF & Sisler HD (1988) *Biotechniques* 6, 832-834
- 18) Wittig I, Karas M, Schägger H. (2007) *Mol Cell Proteomics.* 6, 1215-25.
- 19) Jung C, Higgins CM, Xu Z. (2000) *Anal Biochem.* 286, 214-223.
- 20) Schägger H, Cramer WA, von Jagow G. (1994) *Anal Biochem.* 217, 220-230.
- 21) Waterfield WF, Sisler HD. (1988) *Biotechniques.* 6, 832-834.
- 22) Reyes-Galindo M, Suarez R, Esparza-Perusquía M, de Lira-Sánchez J, Pardo JP, Martínez F, Flores-Herrera O. (2019) *Biochim Biophys Acta Bioenerg.* 1860, 618-627.
- 23) Guo H, Bueler SA, Rubinstein JL. (2017) *Science.* 358, 936-940.
- 24) Bustos DM, Velours J. (2005) *J. Biol. Chem.* 280, 29004–29010 (2005)
- 25) Baker LA, Watt IN, Runswick MJ, Walker JE, Rubinstein JL. (2012) *Proc. Natl. Acad. Sci. U.S.A.* 109, 11675–11680
- 26) Ellen L. Robb, Andrew R. Hall, Tracy A. Prime, Simon Eaton, Marten Szibor, Carlo Viscomi, Andrew M. James, and Michael P. Murphy. (2018) *J. Biol. Chem.* 293, 9869–9879
- 27) El-Khoury R, Dufour E, Rak M, Ramanantsoa N, Grandchamp N, Csaba Z, Duvillie B, Benit P, Gallego J, Gressens P, Sarkis C, Jacobs HT, Rustin P. (2013) *PLoS Genet.* 9, e1003182
- 28) El-Khoury R, Kemppainen KK, Dufour E, Szibor M, Jacobs HT, Rustin P. (2014) *Br. J. Pharmacol.* 171, 2243–2249
- 29) Szibor M, Dhandapani PK, Dufour E, Holmstrom KM, Zhuang Y, Salwig I, Wittig I, Heidler J, Gizatullina Z, Gainutdinov T, Fuchs H, Gailus-Durner V, de Angelis MH, Nandania J, Velagapudi V, (2017) *Dis. Model. Mech.* 10, 163–171

Table 1. Structural and bioenergetics parameters of the wild type and Δg strains of *Ustilago maydis*.

	WT	Δg
<i>Mitochondrial structure</i>		
Cristae folding	Yes	Yes
<i>Bioenergetics</i>		
Membrane potential generation	Yes	Yes, 100% of WT
<i>Mitochondrial oxygen consumption with succinate (ng at O/mg·min⁻¹)</i>		
cyanide sensitive	397 ± 31	441 ± 12
n-octyl gallate sensitive	112 ± 24	278 ± 18
<i>Maximum mitochondrial oxygen consumption by complex IV or AOX (ng at O/mg·min⁻¹)</i>		
Total	1210 ± 35 ($\Delta p \rightarrow 0$)	1150 ± 20 ($\Delta p \rightarrow 0$)
complex IV in presence of ascorbate and TMPD, cyanide sensitive	1048 ± 21	827 ± 18
AOX in presence of ascorbate and TMPD, n-octyl-gal sensitive	124 ± 23	262 ± 4
<i>Mitochondrial NADH dehydrogenase activity ($\mu\text{mol NADH oxidized/mg}\cdot\text{min}^{-1}$)</i>		
Total	0.21 ± 0.03 ($\Delta p \rightarrow 0$)	0.20 ± 0.02 ($\Delta p \rightarrow 0$)
Rotenone sensitive	0.18 ± 0.06	0.16 ± 0.03
Flavone sensitive	0.04 ± 0.015	0.03 ± 0.010
<i>Succinate dehydrogenase activity ($\mu\text{mol DCPIP reduced/mg}\cdot\text{min}^{-1}$)</i>		
Total	0.05 ± 0.01 ($\Delta p \rightarrow 0$)	0.04 ± 0.01 ($\Delta p \rightarrow 0$)
<i>Mitochondrial F_1F_0-ATP synthase activity ($\mu\text{mol ATP}\cdot(\text{mg}\cdot\text{min})^{-1}$)</i>		
ATP synthesis ($\mu\text{mol ATP}\cdot(\text{mg}\cdot\text{min})^{-1}$)	20 ± 0.9	15 ± 0.9
ATP hydrolysis ($\mu\text{mol ATP}\cdot(\text{mg}\cdot\text{min})^{-1}$)	45 ± 6	31 ± 5

Table 2. Kinetics parameters of the ATPase activity of the monomer of the F₁F₀-ATP synthase from *Ustilago maydis* Δg strain.

	Monomer (V _{1Δg}) ^a
<i>Non-activated F₁F₀-ATP synthase</i>	
V _{max} (μmol ATP hydrolyzed/mg F ₁ F ₀ -ATP synthase·min ⁻¹)	0.58 ± 0.03
K _M (μM)	155 ± 47
k _{cat} (s ⁻¹)	5.86 ± 0.05
k _{cat} /K _M (M ⁻¹ s ⁻¹)	3.78 X 10 ⁴ ± 0.3 X 10 ⁴
<i>DDM activated F₁F₀-ATP synthase</i>	
V _{max} (μmol ATP hydrolyzed/mg F ₁ F ₀ -ATP synthase·min ⁻¹)	2.3 ± 0.2
K _M (μM)	920 ± 20
k _{cat} (s ⁻¹)	23.26 ± 0.1
k _{cat} /K _M (M ⁻¹ s ⁻¹)	2.53 X 10 ⁴ ± 0.08 X 10 ⁴
K _i (nM) for oligomycin	53 ± 4
Ratio oligomycin/F ₁ F ₀ -ATP synthase (mol/mol) to reach 50% of ATPase inhibition	5.03 ± 0.57

^a = F₁F₀-ATP synthase mol in V₁ sample was determined as described in procedures section, and kinetics parameters were showed as mg of F₁F₀-ATP synthase (See Material and methods section).

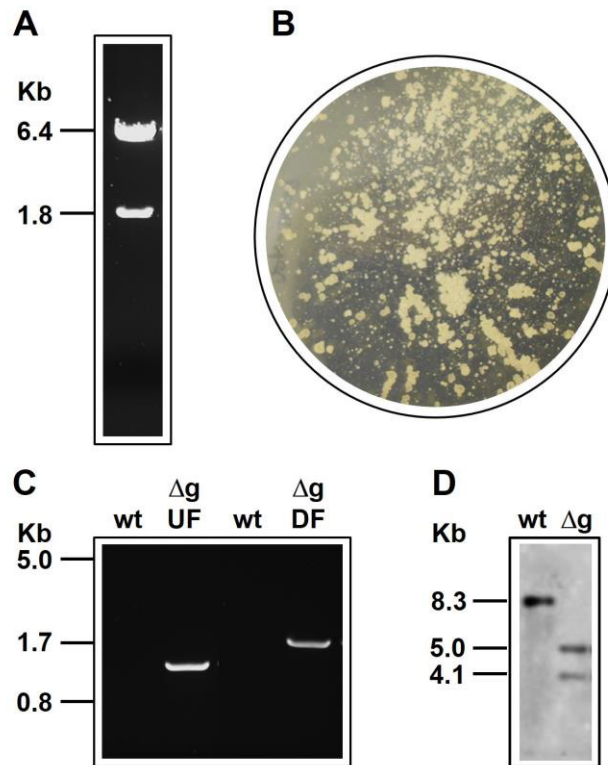
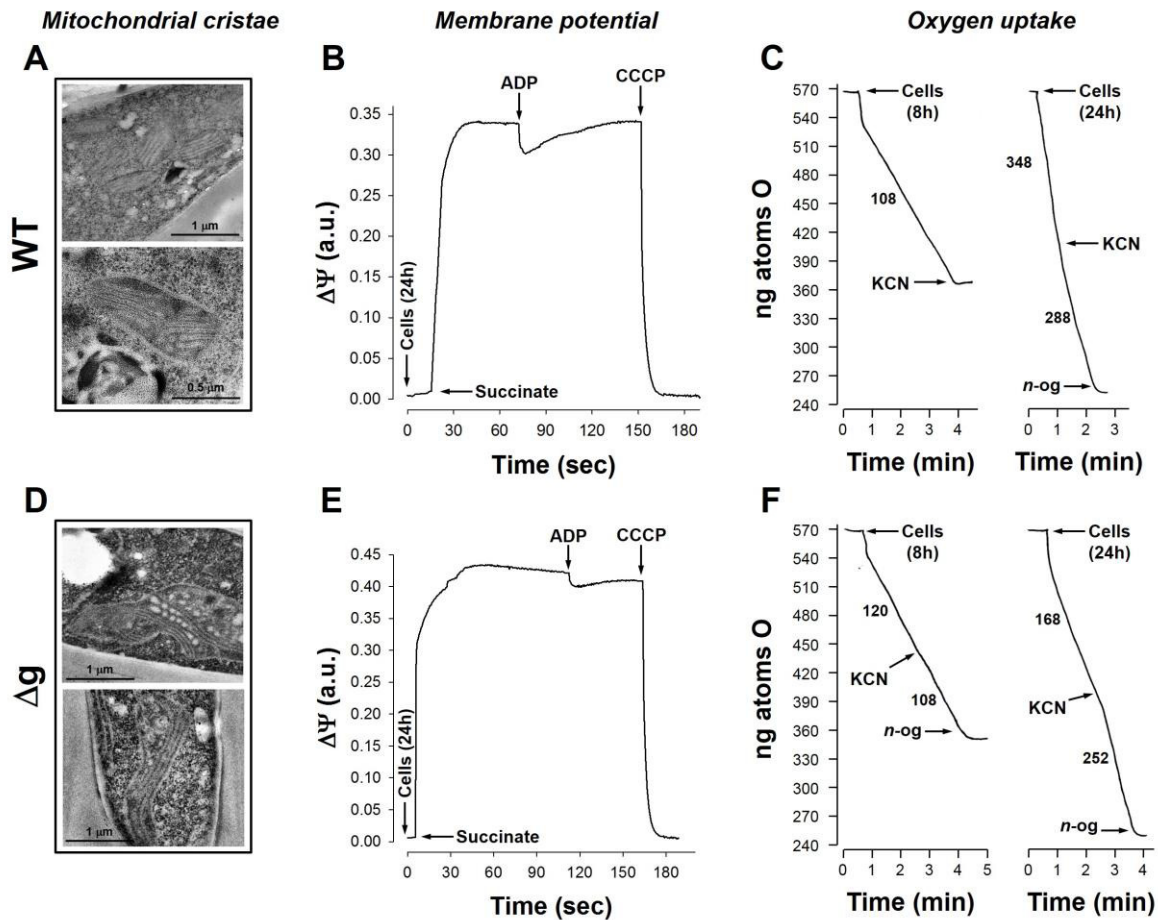


Figure 1. Confirmation of replacement by homologous recombination of subunit g gene by hygromycin resistant gene. A) PCR was used to amplify sequences of DNA that includes the sequences of Inh1 or HygR and the flanking regions on each side of the Inh1 gene. B) Hygromycin resistant phenotype of the Δ Inh1 strain. C) The products were analyzed on 1% agarose gel (see supplementary material for the primers used). The expected lengths of the product from the WT and Δ Inh1 are shown at the right. D) WB analysis of the DNA sequence.



Figures 2. Mitochondrial ultrastructure and bioenergetics analysis of the WT and Δg strains.

The Δg strain display typical mitochondrial morphologies (D) similar to WT (A). Cells were harvested at 24 h and permeabilized with digitonine as described in material and methods section and the generation of $\Delta\Psi_m$ was assayed. The $\Delta\Psi_m$ was measurement with Safranin O. Arrows indicate sequential additions of permeabilized cells from WT (B) or mutant (E) strains. Where showed 10 mM succinate (Succ); ADP (1 mM); CCCP (5-10 μ M). Oxygen uptake by WT cells (C) or Δg cells (F) was inhibited by cyanide (CN) and n-octyl-galate (nOg). Cells were harvested at 8 or 24 h. Where indicated 5 mM CN or 2 mM nOg was added. Numbers below each recording represent the velocity of oxygen consumption. Figure shows representative experiments of at least four different and independent cell culture preparations

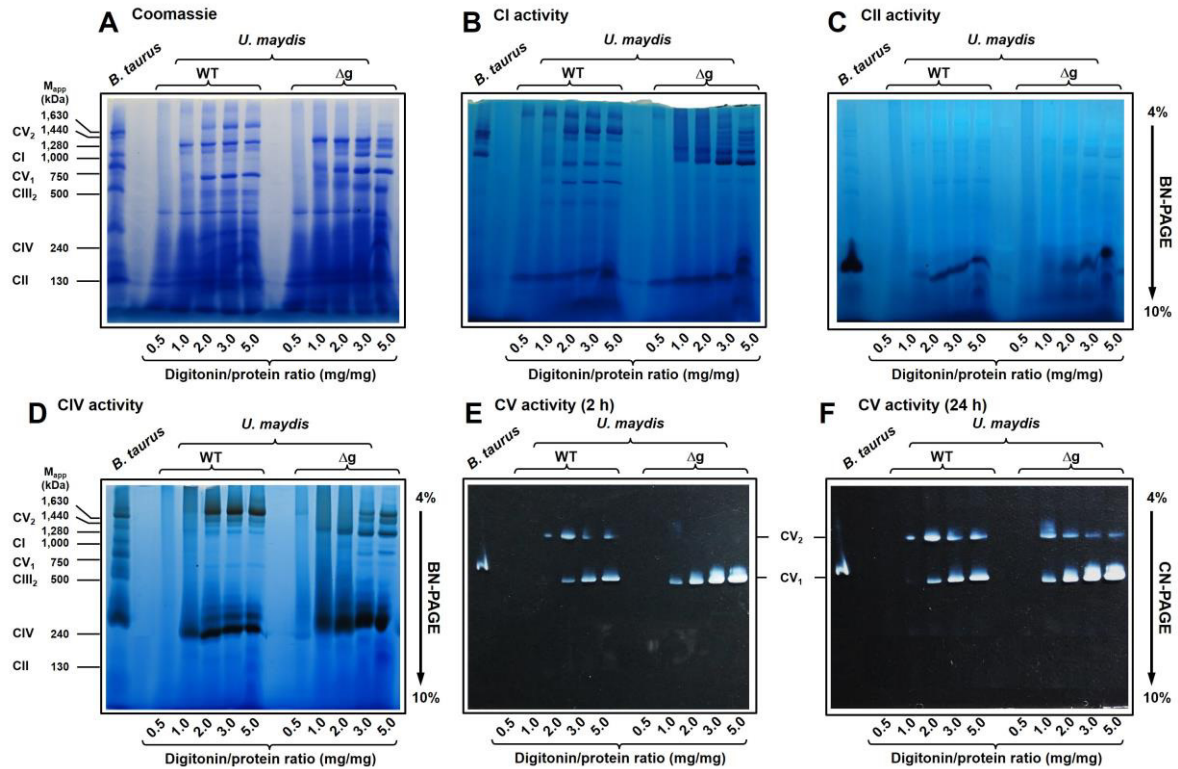


Figure 3. Digitonin Solubilization and in-gel activity of the respiratory complex and supercomplexes from *Ustilago maydis* mitochondria. Mitochondria from WT or Δg strains were isolated as described in the material and method section. Respiratory complex and supercomplexes from WT or Δg mitochondria were solubilized with digitonin and their electrophoretic profile determined in a BN-PAGE. Proteins were stained with brilliant blue Coomassie (A) and the in-gel activities of NADH:MTT oxidoreductase (B), succinate:MTT oxidoreductase (C), cytochrome c oxidase (D) and ATPase (E and F) were assayed. CI = complex I activity; CII = complex II activity; CIV = complex IV activity; CV = complex V activity. In-gel activity of the $V_{2\Delta g}$ and $V_{1\Delta g}$ was incubated from 24 h (F) Respiratory complexes and supercomplexes from bovine heart mitochondria were solubilized with digitonine and used as molecular weight standart.

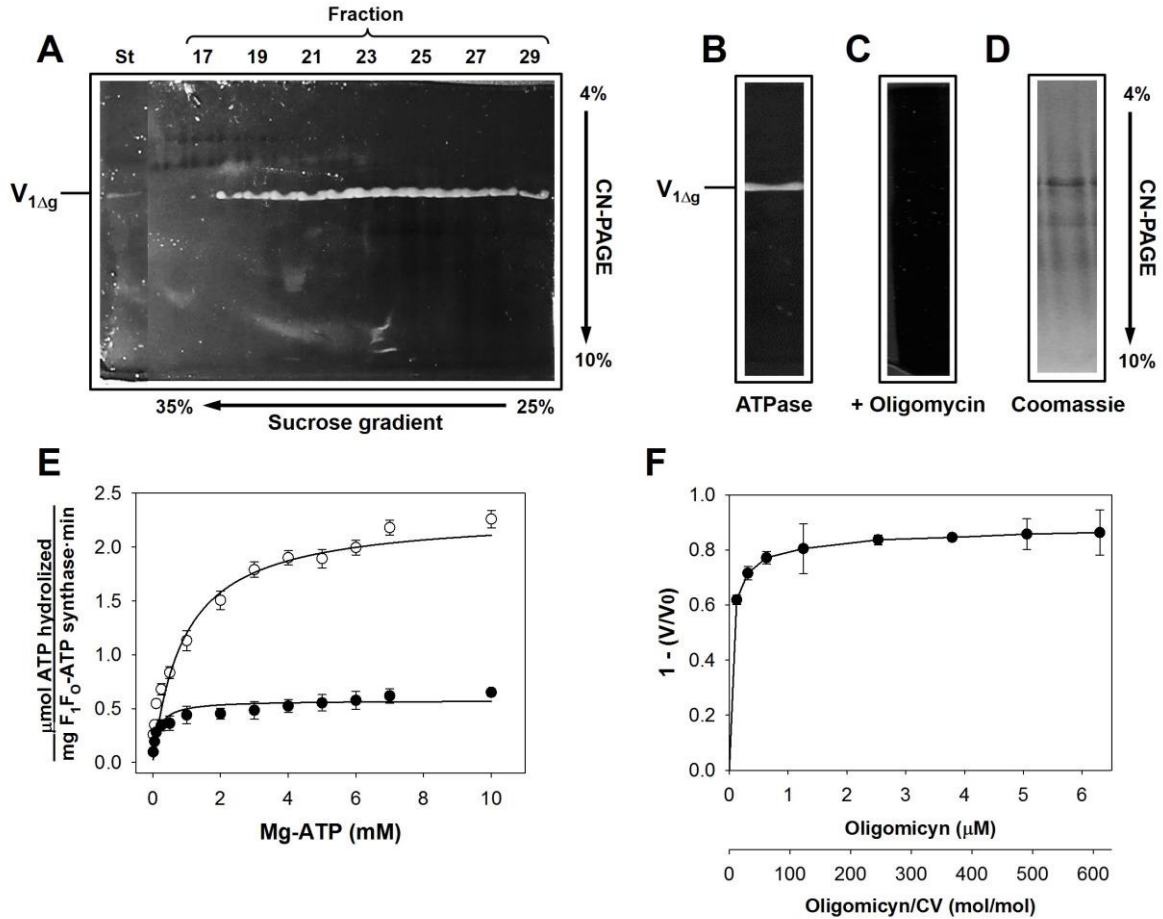


Figure 4. Isolation of V₁ from mutant strain and its kinetics characterization. Mitochondrial supercomplexes were digitonin solubilized and isolated in a sucrose gradient as described in material and methods section. In-gel activity of the ATPase from V₁ was observed from fraction 18 to 29 from sucrose gradient (A). No dimeric state was observed. These fractions were pooled and concentrated, and ATPase activity was observed at monomer position (B). Oligomycin inhibited ATPase in-gel activity (C). Coomassie stained showed a main protein band at the position of monomer and no dimer was observed (D). Kinetics characterization of the monomer with (open circles) or without (close circles) DDM addition (E). Kinetics ATPase inhibition by oligomycin (F).

Deletion of the natural inhibitory protein Inh1 from *Ustilago maydis* does not modify the oligomeric states of the F₁F₀-ATP synthase but increase their ATPase activity

Romero-Aguilar Lucero^{a*}, Esparza-Perusquía Mercedes^{a*}, Langner Thorsten^b, García-Cruz Giovanni^a, Feldbrügge Michael^c, Pardo Juan Pablo^a, Martínez Federico^a, and Flores-Herrera Oscar^{a1}.

^aDepartamento de Bioquímica, Facultad de Medicina, Universidad Nacional Autónoma de México, Apartado Postal 70-159, Coyoacán 04510, México, D. F., México.

^bThe Sainsbury Laboratory, Norwich Research Park, Norwich NR4 7UH, United Kingdom.

^cInstitute for Microbiology, Cluster of Excellence on Plant Sciences, Department of Biology, Heinrich-Heine University Düsseldorf, Düsseldorf, Germany.

To whom correspondence should be addressed: Oscar Flores-Herrera. Departamento de Bioquímica, Facultad de Medicina, Universidad Nacional Autónoma de México, Apdo. Postal 70-159, Coyoacán 04510, México, Cd. Mx., México; Phone: 55-56232510; Fax: 55-56162419; E-mail: oflores@bq.unam.mx

*L. Romero-Aguilar and M. Esparza-Perusquia contributed equally to this paper.

Keywords: dimer of complex V, bioenergetics, ATPase activity, oxidative phosphorylation, Inh1 subunit.

Abstract

Transduction of electrochemical proton gradient to ATP synthesis is performed by F_1F_0 -ATP synthase. The reverse reaction is avoided by regulatory subunit Inh1 in fungi. A gene knockout was generated in order to assign a function to Inh1 in the mitochondrial metabolism and cristae architecture. Deletion of Inh1 protein does not affect cell growth, glucose consumption, and biomass production. Ultrastructure and fluorescence analyzes showed that mitochondrial size and cristae shape, network, and distribution was similar to wild strain. The membrane potential, ATP synthesis, and oxygen consumption from wild type and mutant had a similar magnitude. Kinetics analysis of ATPase activity of complex V in permeabilized mitochondria showed similar values of V_{max} and K_M for both strains, and no effect of pH was observed. Isolated monomer and dimer from mutant mitochondria have a V_{max} values 5-times higher than WT strain suggesting a Inh1 regulatory role; however no effect of pH was observed. ATPase activity of WT oligomers was stimulated several times by dodecyl-maltoside (DDM); however DDM induces an inactive form of the mutant oligomers, probably by dissociation of F_1 sector suggesting a structural role for Inh1. The structural and kinetics role of the Inh1 subunit is discussed.

1 Introduction

The energy stored in the electrochemical proton-motive force (Δp) across the membrane of almost all eubacteria, thylakoids or mitochondria is used by the F_1F_0 -ATP synthase, an energy-transducing enzyme, to ATP synthesis from ADP and inorganic phosphate. F_1F_0 -ATP synthase consist of two interconnected sectors, F_1 and F_0 . F_0 is an integral membrane complex which acts as a proton-driven turbine, spinning the γ subunit that drives sequential conformational changes in the three α/β subunits pairs (principally in the β subunits) from F_1 sector. These sequential conformational changes are related to binding ADP + Pi (β_{DP}), to synthesize tightly bound ATP (β_{TP}), and to release the bond ATP (β_E) to the N-side of the membrane. Then, ATP production occurs in the membrane-extrinsic F_1 domain, by a rotatory mechanism where the γ chain within $\alpha_3\beta_3$ and hydrophobic c ring domains, rotate in one direction with $3/120^\circ$ steps.

The F_1F_0 -ATP synthase could be considered as a reversible ATP-hydrolyzing protons pump whose direction depends on the thermodynamics balance between Δp and free energy for ATP synthesis (ΔG_p).

Under conditions of high Δp and for most energy-conserving membranes, the balance is in favor of ATP synthesis; however, damage to the electron transport chain, increase proton leakage, or severe hypoxia can lower Δp such that the F_1F_0 -ATP synthase reverses and start to hydrolyze ATP over ATP synthesis. To avoid ATP hydrolysis by F_1F_0 -ATP synthase, different strategies have been development: in thylakoids, in the dark, an intermolecular disulfide bond occurs in the γ subunit near the interface with F_0 , and F_1F_0 -ATP synthase relaxes back into an inactive state; in bacteria such as *Escherichia coli* and *Bacillus PS3*, the subunit ϵ confer the unidirectional behavior of F_1F_0 -ATP synthase (i.e. ATP synthesis) by acting like a ratchet. This subunit might take up two different conformations, in one of these the C-terminal domain extends toward the F_1 sector and allows the enzyme only to synthesize ATP. In mitochondria from mammals (i.e. *Bos taurus*) and yeast (i.e. *Saccharomyces cerevisiae*) the ratchet subunit is the IF_1 and $Inh1$, respectively. Interaction of the IF_1 or $Inh1$ at a catalytic interface between α and β subunits and the γ subunit in F_1 is pH dependent, binding under conditions of lowered pH generally associated with a decrease of Δp .

Actually, Hirst's group has been determined that deletion of ζ subunit from *Paracoccus denitrificans* F_1F_0 -ATP synthase does not activate ATP hydrolysis (1), suggesting that ϵ subunit could adopt an inhibitory conformation, similar to observed in *E. coli* enzyme (2, 3), and blocks ATP hydrolysis.

Additionally to the bioenergetics role of the F_1F_0 -ATP synthase, it plays an important role, as a homodimer, in the mitochondrial cristae folding. In yeast subunit g and e maintain the dimer structure. Characterization of the ATPase activity of the F_1F_0 -ATP synthase dimer showed that it was 7-times more active than monomer, was more sensitive to oligomycin inhibition, and its specificity constant was 12-times higher than monomer (4). These features clearly show that dimer and monomer are kinetically different and point out the role of the monomer-monomer interphase.

In mammals the IF_1 was, controversially, implicated in dimerization of the F_1F_0 -ATP synthase. Deletion of IF_1 subunit from mouse F_1F_0 -ATP synthase has no effect on the growth, in both male and female cases (5). There were no changes in the expression levels of subunits α and β of F_1 in the brain, thymus, heart, lung, stomach, liver and testicle. In addition, changes were not found in the crista architecture and in the mitochondrial network (5). Similar results were observed in the zebra fish erythroblasts, *Caenorhabditis elegans*, in the HeLa cells (6), and in *S. cerevisiae*. Although deletion of IF_1 from mitochondria has been performed to assess its role in the dimerization of F_1F_0 -ATP synthase, no studies on dimer ATPase activity have been done.

In this work, the subunit *Inh1* was deleted from the genome of *Ustilago maydis*, a strict respiratory basidiomycete, and F_1F_0 -ATP synthase dimer and monomer were isolated and their activity characterized. We found that deletion of *Inh1* does not activate ATPase activity of the dimer and monomer, but ATP synthesis was lowered in the intact mitochondria. The role of *Inh1* on the ATP synthesis is discussed.

2 Materials and methods

2.1 Molecular biology techniques, strain generation and growth conditions

E. coli top 10 (Life Technologies, Carlsbad, CA, USA) were used for cloning purpose. *U. maydis* strain FB2 (a2b2 genotype ATCC 201384) were described previously by (7). Cell transformation was performed using standard molecular techniques and strain generation methods. Plasmid pCRII-Topo (Invitrogen) was as a cloning vehicles. The plasmid pUMa1737 was constructed by replacing the 468-bp (ATPI gene, UMAG_02361) by hygromycin resistance cassette (HygR). Plasmid for generating deletion mutant Δ *Inh1*-HygR (Δ *Inh1*), resistance cassette is flanked 1161 pb upstream and 925 pb downstream region of *Inh1* gene. Flanking regions were amplified by PRC using RL682/RL683 and RL686/RL687 and UM518 (FB2) wild-type DNA template; then plasmid linearized was inserted into the protoplasts for transformation. All homologous interaction events were verified by Southern blot analysis (7).

The Δ *Inh1*^R strain recovered to CM (0.25% Casaminoacids (Difco), 0.1% Yeast-Extract (Difco), 1.0% vitamin solution from Holliday '74, 6.25% salt solution from Holliday '74, 0.05%

DNA degraded. Free Acid (Sigma, D-3159), 0.15% NH_4NO_3 (Sigma, A9642), pH 7.0 and 2% agar) supplemented with 1% glucose. The cells were resuspended in 100 ml YPD (1% glucose, 1% yeast extract, 0.25% bactopectone), growth for about 24 hr at 28°C, and harvested for make aliquots (1 ml cell in 25% glycerol) and stored at -70°C stock.

2.2 Growth conditions of WT and ΔInh1 strains

The WT (FB2) and ΔInh1 cells were sowed on 2% agar, supplemented with 1% glucose, 1% yeast extract, and 0.25% bactopectone, and growth at 28°C for 72 h. An inoculum was added to 100 ml of YPD (0.5% yeast extract, 0.25% bactopectone, 0.5% glucose) and cultivated during 24 h at 28°C and then, 30 absorbance units (600 nm) of this suspension were transfer to 1 liter of YPD medium, to continue the growth for 24 h at 28°C at 200 rpm.

2.3 Oxygen consumption measurement

Oxygen uptake was determined using a Clark-type electrode (YSI Model 5300). The respiration was started with the addition of 1 mg of cells (dry weight) in 10 mM KH_2PO_4 , pH 7.3 (final volume of 1.5 mL of air-saturated medium; 100% = 660 ng atoms O_2); 1.7 mM potassium cyanide (KCN) was added for the inhibition of cytochromic pathway and 13 μM of n-octyl-gallate (nOg) for alternative oxidase inhibition (8-10).

2.4 Mitochondrial membrane potential ($\Delta\Psi_m$) measurement

The cells were permeabilized with 0.02% digitonin in 300 mM sorbitol, 10 mM HEPES, 1 mM EGTA, 10 mM KH_2PO_4 , 10 mM MgSO_4 , 150 mM KCl, pH 7.4, at 4°C during 20 min with constant stirring. Generation of membrane potential ($\Delta\Psi_m$) was determined using 30 μM safranine-O and initiated with 10 mM succinate, pH 7.4; 5 μM carbonyl cyanide m-chlorophenyl hydrazone (CCCP) was added to collapse $\Delta\Psi_m$. The $\Delta\Psi_m$ was recorded in an AMINCO DW 2000 double beam spectrophotometer (Olis, Inc., Bogart, GA, EUA) at 533 and 511 nm. The final volume was 3.0 ml, at 25°C with constant stirring (11).

2.5 Microscopy Analysis

Cell pellets were fixed with a mixture of 4% paraformaldehyde/2.5% glutaraldehyde for 1 hr at room temperature; then it was washed two times in PBS and stained with 1% osmium tetroxide for 1 hr at 4°C, and washed with PBS. The gradual dehydration was made in ethanol (graded 50–100%) and propylene oxide. Pellets were embedded in epoxy resin and cut into 70 nm sections. For immunoelectron microscopy cell pellets were fixed with 4% paraformaldehyde/0.1%

glutaraldehyde for 30 min at 4°C. After ethanol dehydration (graded 70–100%) pellets without osmication were embedded in LR White. Electron microscopy was performed at 80 kV on a Zeiss EM900 Transmission Electron Microscope. Images were recorded with a Gatan Dual Vision CCD 300W camera (Gatan, Pleasanton, CA).

2.6 Mitotracker staining

Mitochondrial staining was done in cells grown in YPD for 24 h, harvested and washed twice with 0.9% NaCl. Then, they were suspended at a final optical density of 20 unit/L in a previously warmed (28°C) media containing 5% of glucose and 30 nM of MitoTracker® Deep Red FM (Thermo Fisher Scientific). Cells were microscopically examined with a confocal microscope (Zeiss LSM5 Pascal, Carl Zeiss GmbH, Göttingen, Germany) with a water immersion 160x N.A. 1.3 objective.

2.7 Mitochondria isolation

The *U. maydis* mitochondria isolation was performed as described by Juárez et al., (12) with a minor modifications (4). Cells were grown in complete medium (YPD) for 24 h, harvested by centrifugation at 3,800 g for 10 min and washed with distilled water (twice). The cells were resuspended with 12.5 ml of 0.6 M ammonium sulfate, 20 mM KH₂PO₄ pH 5.5, per g wet weight, supplemented with *Trichoderma harzianum* lytic enzyme (0.016 g/g wet weight) and incubated during 60 min at 30°C for protoplast production.

The protoplasts were recovered by centrifugation at 3,800 g for 10 min, suspended in 0.8 M sucrose, 10 mM Tris, 2 mM EDTA, 20 mM KH₂PO₄, and 3% bovine albumin serum fatty acid free, pH 7.0 and centrifuged at 3,800 g for 10 min to wash out the lytic enzymes. The protoplast was resuspended in 0.4 M sucrose, 10 mM Tris, 2 mM EDTA, 20 mM KH₂PO₄, and 3% bovine albumin serum fatty acid free, pH 7.0 (buffer A) and homogenizer in a Teflon potter for 20 times with 1 mM PMSF and 25 µl of the protease inhibitor cocktail (Sigma P8340). The samples were diluted to 130 ml per 16 g wet weight and centrifuged at 3,800 g for 10 min. Finally, the supernatant was centrifuged at 17,000 g for 10 min and mitochondrial fraction was suspended in buffer A.

2.8 Determination of protein concentration

The protein content was determined as described by Lowry et. al., (13) with minor modifications (14). Crystalline bovine serum albumin (BSA) was used as standard and its concentration was determined at 278 nm using a molar extinction coefficient (ϵ) of 6.58 (1%).

2.9 Solubilization of the respiratory complex and supercomplexes

The mitochondrial respiratory complexes and supercomplexes were solubilized with different digitonin:protein (g/g) ratios as described (15-17). Briefly, mitochondrial protein (2 mg) were suspended in 200 μ L of 50 mM Bis-Tris and 500 mM 6-aminocaproic acid, pH 7.0, supplemented with 10 mM succinate and 10 mM ATP (4). The digitonin was added drop by drop until reach the ratio required and the mixture was incubated for 30 min at 4°C with gentle stirring, and then centrifuged at 100,000 g for 30 min at 4°C. The supercomplexes and complexes were recovered from supernatant and analyzed by blue native PAGE (BN-PAGE) and clear native PAGE high resolution (hrCN-PAGE) as described (15-17).

2.10 In-gel catalytic activity assay of respiratory complexes and supercomplexes.

The in-gel activity assays were performed as described by Jung et al., (16) and Wittig et al., (15), using a gel strip loaded with 150 μ g of protein. The NADH dehydrogenase activity of complex I (NADH:methylthiazolyldiphenyl tetrazolium bromide (MTT) oxidoreductase) was assayed in 10 mM Tris/HCl pH 7.4, 1.2 mM MTT, and 1 mM NADH, at 25°C. The succinate dehydrogenase activity (Succinate:MTT oxidoreductase) was assayed in 10 mM K_2HPO_4 , pH 7.4, 5 mM EDTA, 0.2 mM phenazine methosulfate (PMS), and 10 mM succinate. NADH and succinate activity was correlated with the development of purple precipitates on the gel. After purple-staining appear (10 – 20 min) the reaction was stopped with fixing solution (50% methanol, 10% acetic acid). The in-gel activity of complex IV was assayed in 50 mM K_2HPO_4 , pH 7.2, 4.7 mM 3,3'-diaminobenzidine tetrahydrochloride (DAB) and 16 μ M horse heart cytochrome c, during 30 – 40 min of incubation at 25°C. The activity was observed as a brown precipitate and the reaction was stopped with the fixing solution. Activity of complex V was assayed in 50 mM glycine (adjusted to pH 8.0 with triethanolamine), 10 mM $MgCl_2$, 0.15% $Pb(ClO_4)_2$ and 5 mM ATP. ATP hydrolysis correlated with the appearance of a white lead phosphate precipitates. The reaction was stopped using 50% methanol, and subsequently the gel was transferred to water and scanned against a dark background as described previously (4).

2.11 Isolation of submitochondrial particles (SMP).

Mitochondria were diluted 1:1 (vol/vol) in buffer A (see mitochondria isolation section), and sonicated at full power (14 microns with ½ inch diameter tip) in a Soniprep 150 MSE (USA) during 30 sec with 90 sec of rest (5 cycles). Sonication was performed in an ice-cooled bath to hold temperature at 4°C. After sonication the mixture was centrifuged at 17,300 g for 10 min, the supernatant recovered and ultracentrifuged at 100,000 g for 30 min at 4°C. SMP were recovered

from the pellet and resuspended in buffer A (See mitochondrial isolation section) and stored at -17°C until used (18).

2.12 Isolation of dimer and monomer F_1F_0 -ATP synthase

The monomer (V_1) and dimer (V_2) of F_1F_0 -ATP synthase were isolated as reported by (4). The digitonin-solubilized mitochondrial complexes and supercomplexes (16 mg) were loaded on 24 mL of a continuous sucrose gradient (16 - 42%) and ultracentrifuged at 13,000 g during 16 h at 4°C. Fractions (500 μ L) were collected and the presence of the F_1F_0 -ATP synthase oligomers were identified by hrCN-PAGE (15). The fractions with the V_1 or V_2 were pooled separately, diluted in a ratio of 1:5 with 30 mM HEPES, pH 8.0 and 5% glycerol and then concentrated in 100K Millipore Amicon Ultra, the final samples (100 - 200 μ L) were stored at -70°C until use (4).

The concentration of F_1F_0 -ATP synthase in V_{1WT} , V_{2WT} , $V_{1\Delta Inh1}$, and $V_{2\Delta Inh1}$ samples was determined by a densitometry analysis of Coomassie® Brilliant Blue R-125 stained α - (ID XP_011392137) and β - (ID XP_011389783) subunits from an SDS-Tricine-PAGE, using Coomassie stained BSA as a standard. The gel was scanned and the stain-intensity of α - and β -subunits, and BSA was determined by the Image Analysis software version 1.0 (Thermo Fisher Scientific Inc.), and their intensities were measured by peak integration after densitometry analyses (4). The mol of α - and β -subunits were determined using the molecular weight of the mature protein (55.05 and 50.47 kDa, respectively). The amount of F_1F_0 -ATP synthase in V_{1WT} and V_{2WT} samples was $3.3 \pm 0.7 \mu\text{g}/10 \mu\text{g}$ total protein and $2.8 \pm 0.5 \mu\text{g}/10 \mu\text{g}$ total protein, respectively; while in $V_{1\Delta Inh1}$, and $V_{2\Delta Inh1}$ samples was $3.3 \pm 0.7 \mu\text{g}/10 \mu\text{g}$ total protein and $2.8 \pm 0.5 \mu\text{g}/10 \mu\text{g}$ total protein. These amounts of complex V were used to kinetics parameters estimation.

2.13 Measurements of ATP hydrolysis by F_1F_0 -ATP synthase by V_1 or V_2

The ATPase activity was determined spectrophotometrically as described by (4). Briefly, ATP hydrolysis was measured using an assay coupled to NADH oxidation ($\epsilon_{340\text{nm}} = 6.2 \text{ mM}^{-1} \cdot \text{cm}^{-1}$) in an Agilent 8453 UV-visible spectrophotometer (Agilent Technologies, USA). NADH absorbance was continuously monitored and the time response was less than 1 s. The reaction mixture was 1 mM MgSO_4 , 90 mM KCl, 50 units/mL of pyruvate kinase (PK), 30 units/mL of lactate dehydrogenase (LDH), and 5mM of phosphoenol pyruvate (PEP). The pH buffer was HEPES (50 mM) for pH = 8.0 or MES (50 mM) for pH = 6.0. The pH change doesn't modified perceptibly the activity of the coupling enzymes. The reaction was started by F_1F_0 -ATP synthase (10-15 μg) addition and its kinetic analysis of ATPase activity (initial velocity) was carried out using the direct spectrophotometric recording. Initial velocities were further obtained from the slope

of the linear region in each spectrophotometric recording, and the linear region of the traces was corroborated with the plot of the first derivative against time. Data were analyzed by robust, weighted, non-linear regression analysis using the SigmaPlot software (Systat Software, Inc., version 10.0). The data represent the average of five independent experiments. The data were corrected to F_1 - F_0 -ATP synthase content in each V_1 or V_2 samples as described by (4).

2.14 Activity assay of mitochondrial NADH and succinate dehydrogenase and ATPase

Isolated mitochondria were permeabilized with 0.01% Triton X-100 and the reaction mixture was 30 mM KH_2PO_4 , 5 mM $MgCl_2$, 1 mM EGTA, 120 mM KCl, pH 7.4, at 25°C. Spectrophotometric recorder of the NADH:2,6-dimethoxy-1,4-benzoquinone (DBQ) oxidoreductase activity was determined at 340 nm by following the oxidation of NADH. NADH addition was 100 μ M plus 600 μ M of DBQ, and NADH dehydrogenase activity was inhibited by 10 μ M rotenone (19-21) and 50 μ M flavone. Activity of succinate:DCPIP oxidoreductase was stimulated with 10 mM succinate and determined at 600 nm by following the reduction of the artificial electron acceptor 2,6-dichlorophenol-indophenol (DCPIP; 50 μ M; $\epsilon_{DCPIP} = 21 \text{ mM}^{-1}\text{cm}^{-1}$), and was inhibited by 20 mM malonate. ATPase activity in permeabilized mitochondria was performed in 200 mM KCl, 50 mM HEPES pH 8.0 (or MES pH 6.0), 3 mM $MgSO_4$, and using 500 μ g mitochondrial protein/mL. The reaction was initiated by adding different concentrations of Mg-ATP. Aliquots of 0.15 mg of mitochondria were withdrawn at intervals of 30 seconds, placed in 6% of previously cooled trichloroacetic acid. Samples were centrifuged at 10,000 rpm at 4°C, in a tabletop centrifuge. Supernatant was analyzed according to the Fiske & Subbarow, (1925) (22) method with minor modifications (23).

2.15 Structure prediction of Inh1 protein

The Inh1 sequence was obtained from the database of the *U. maydis* genome using the sequence of the bovine IF1. Only one coding sequence was found for the Inh1 protein, UMAG-02361 (XP_011388667). This sequence was analyzed with MITOPROT (<https://ihg.gsf.de/ihg/mitoprot.html>) (24) to eliminate the signal peptide. In order to compare the amino acids sequence of the Inh1 protein against *Saccharomyces cerevisiae* and *Bos taurus* subunits, the sequences of the inhibitor proteins of these organisms were obtained from the protein database UniProtKB (<https://www.uniprot.org/help/uniprotkb>). The mature protein from *U. maydis* consists of 64 amino acids with a molecular weight of 7.3 kDa, while the *S. cerevisiae* protein consists of 36 amino acids (MW of 4.0 kDa), and the *B. taurus* of 65 amino acids (MW of 7.7 kDa). These proteins were aligned with Clustal W (25) and the score of the predicted alignment with T-

coffee (<http://tcoffee.org.cat/>) (26) was 65%. The protein 3D structure was predicted using Modeller 9.2 (<https://salilab.org/modeller/>) (27).

2.16 Statistic analysis

The statistical analysis of data was performed in the GraphPad Prism V.6b (Trial).

3 Results

3.1 Inh1 of *Ustilago maydis* has an alpha-helix type structure

The *S. cerevisiae*, *B. taurus* and *U. maydis* sequence conserve: two lysine residues, two glutamic residues, one arginine-rich and one alanine-rich, as well as five residues of amino acids with similar properties (> 0.5 score) and one residue with similar low properties (< 0.5 score) (Fig. 1). Interestingly, *U. maydis* subunit is the only one which contain tryptophan (1.6%). The 3D structure prediction shows that Inh1 from *U. maydis* has an alpha-helix similar to predicted for *S. cerevisiae* and *B. taurus* (Fig. 1). There is a disordered structure that stands out in the NH₂-terminus which interacts with the F₁ portion of the ATP synthase (Fig. 1). The PYMOL software alignment showed that the alpha helix of IF₁ is larger than Inh1 from *U. maydis* and *S. cerevisiae*; while the *S. cerevisiae* is the smallest one.

Modeling of Inh1 from *U. maydis* using the crystalized structure of *S. cerevisiae* as template shows that both have a disordered NH₂-terminus which could interact with the F₁ sector (Fig. 1), particularly at the α/β interphase. The 3D structure prediction for Inh1 subunit from *U. maydis* allows us to hypothesize that its role as regulatory ATPase activity of the F₁F₀-ATP synthase could be similar to reported in *S. cerevisiae* and bovine (i.e. avoid ATP hydrolysis if $\Delta p \rightarrow 0$). Then, deletion of Inh1 from *U. maydis* genome could promote an increase in the ATPase activity of F₁F₀-ATP synthase.

3.2 Deletion of the Inh1 subunit from the *Ustilago maydis* genome

The Inh1 gene was deleted by homologous recombination as reported by Brachmann et. al., (7) using a hygromycin resistant gene (Hyg). The mutant strain of *U. maydis* with the Inh1 gene deleted (Δ Inh1) was confirmed by PCR analyses using different primers (see supplemental material). The first pair of primer sequences is internal to the Inh1 gene and to the flanking regions on each side of the Inh1 gene, so the WT strain gave a products of length of 1431 and 1227 bp while the Δ Inh1 strain gave no product (Fig. 2A). The other pair of primers have an internal sequence to the Hyg gene and to the flanking regions of the Inh1 gene, so the Δ Inh1 strain gave two products of 2270 and 1988 bp (Fig. 2A) indicating the gene substitution and its correctly

incorporation. Finally, the mutant strain was hygromycin resistant while WT doesn't (Fig. 2B). These results showed that Inh1 subunit was deleted from *U. maydis* genome and is not present in the Δ Inh1 strain.

3.3 Inh1 deletion *doesn't* modified strain growth

In order to determine the possible participation of Inh1 in the *U. maydis* (FB2:a2b2) growth, the Δ Inh1 and the WT strains were cultivated in YPD. The cell duplication time was of 2.4 ± 0.1 and 2.7 ± 0.1 hours for WT and Δ Inh1 strains respectively. Glucose consumption was of 1.62 ± 0.1 $\text{g}\cdot\text{h}^{-1}$ for WT and 1.44 ± 0.1 $\text{g}\cdot\text{h}^{-1}$ for Δ Inh, and no statistically significant difference was found using a non-parametric t-student. The biomass produced at 24 h of cultivating was 1.9 ± 0.2 $\text{g}\cdot\text{L}^{-1}$ and 1.4 ± 0.04 $\text{g}\cdot\text{L}^{-1}$ for WT and Δ Inh1, respectively. Biomass generation matches the glucose consumption. WT strain showed a cell amount of 4.1×10^9 cells $\cdot\text{L}^{-1}$ while Δ Inh1 strain had 3.4×10^9 cells $\cdot\text{L}^{-1}$ at the end of culture. The cellular length was of 23 ± 4 μm for WT while for Δ Inh1 was 28 ± 3 μm at stationary phase of growth. These observations indicate that deletion of Inh1 doesn't modify the growth, time of duplication, and biomass generation by *U. maydis* mutant.

3.4 The Δ Inh1 strain preserves the cristae and the mitochondrial network

ATP-synthase forms dimers in the inner mitochondrial membrane of yeast and mammals folding the inner membrane in cristae; it has been suggested that IF_1 could take part in a dimerization process; however, the role of Inh1 is not conclusive (28-30). To determine whether Inh1 deletion modified mitochondrial cristae, a transmission electron microscopy of the WT and Δ Inh1 strain cells was conducted. Large mitochondria with similar morphology were observed in both strains and no alterations were found in the mitochondrial cristae density in Δ Inh1 strain (Fig. 3A and E); indeed, both mitochondria contain lamellar (and presumably tubular) cristae in an orthodox configuration. The mitochondrial network analysis showed that a tubular mitochondrial network was found across the mutant cell similarly as in WT strain (Fig. 3B and F). Both observations indicated that mitochondrial network and cristae architecture were intact in the Δ Inh1 strain.

3.5 Bioenergetics in WT and Δ Inh1 strains

To verify mitochondrial functions, some bioenergetics parameters from WT and Δ Inh1 strain were determined. For instance, cellular respiration recording showed a similar value for both strains: 348 ng atom $\text{O}\cdot(\text{mg}\cdot\text{min})^{-1}$ for WT (Fig. 3C) and 322 ng atom $\text{O}\cdot(\text{mg}\cdot\text{min})^{-1}$ for Δ Inh1 (Fig. 3G). Cyanide addition reduced respiration to 288 and 225 ng atom $\text{O}\cdot(\text{mg}\cdot\text{min})^{-1}$ for WT and Δ Inh1, respectively. Total inhibition of respiration was observed with cyanide plus n-octyl-gallate addition;

suggesting that alternative oxidase (AOX) was expressed as well as classical electron transport chain complexes.

Mitochondrial membrane potential ($\Delta\Psi_m$) from WT and ΔInh1 strains was determined in digitonin-permeabilized cells in order to allow Safranin O and substrates reach mitochondria. Succinate addition induces $\Delta\Psi_m$ generation in both strains with similar magnitude (Fig. 3D and H), and ADP produces a transitory membrane depolarization (related to ATP synthesis, *vide infra*). CCCP addition increased the proton conductance ($\Delta\Psi_m \rightarrow 0$). These observations showed that mitochondria from both strains are functional. Additionally, the activity of NADH dehydrogenase was 0.22 ± 0.03 and 0.28 ± 0.04 $\mu\text{mol NADH oxidized}\cdot(\text{mg}\cdot\text{min}^{-1})$ for the WT and ΔInh1 strains, respectively. Triton X-100 or CCCP was used to $\Delta p \rightarrow 0$ and the NADH activity was increased to 0.38 ± 0.04 and 0.36 ± 0.02 $\mu\text{mol NADH oxidized}\cdot(\text{mg}\cdot\text{min}^{-1})$ (Table 1). This suggested that complex I and alternative NADH dehydrogenases (i.e. Nde1, Nde2, and Ndi1) were presents in both strains. The succinate dehydrogenase showed an activity of 0.035 ± 0.01 and 0.049 ± 0.01 $\mu\text{mol DCPIP reduced}\cdot(\text{mg}\cdot\text{min}^{-1})$ for WT and mutant strains, respectively. Dissipation of the Δp with Triton X-100 or CCCP reduce the succinate activity to 0.017 ± 0.007 and 0.017 ± 0.006 $\mu\text{mol DCPIP reduced}\cdot(\text{mg}\cdot\text{min}^{-1})$ for the WT and ΔInh1 strains, respectively (Table 1).

ATP synthesis promoted by the Δp is the central role of F_1F_0 -ATP synthase, and elimination of the Inh1 subunit could affect its correct functioning. ATP synthesis was determined using digitonin-permeabilized cells and was stimulated by ADP addition (Fig. 3D and H). The WT and ΔInh1 showed an ATP synthesis very similar (i.e. 18 ± 0.9 $\mu\text{mol}\cdot(\text{g of dry weight}\cdot\text{min})^{-1}$, and 20 ± 0.9 $\mu\text{mol}\cdot(\text{g of dry weight}\cdot\text{min})^{-1}$, respectively); suggesting that Δp promotes the ATP synthesis in the absence of the Inh1 subunit (Table 1). This results indicate that deletion of Inh1 subunit don't affect the principal mitochondrial bioenergetics parameters.

3.6 ATPase activity by mitochondrial F_1F_0 -ATP synthase from the WT and ΔInh1 strains

The Inh1 is the regulatory subunit of ATPase activity of the complex V under unfavorable conditions; generally, a pH increase at the mitochondrial matrix triggers hydrolase activity. The ATPase activity was determined in both strains (WT and ΔInh1) at pH values of 8.0 and 6.0 (Fig. 4) using Triton-X100 to permeabilize mitochondria in order to dissipate the Δp and allow that ATP reach matrix. The activity of the complex V in the mitochondrial membranes was similar for both strains assayed at pH of 8.0 (Fig. 4A), with a V_{max} values of 130 ± 3 nmoles/min·mg mitochondrial protein, and $K_M = 1.5 \pm 0.1$ mM for the ΔInh1 strain, while the value of V_{max} for the WT strain was 125 ± 4 nmoles/min·mg mitochondrial protein and K_M of 1.3 ± 0.1 mM (Table 2). This suggested

that at pH of 8 the Inh1 subunit could be removed from complex V from WT strain and ATPase activity of both strain reach similar values of V_{max} . However, at pH = 6.0 (Fig. 4B) the ATP hydrolysis by complex V from WT strain showed no change in magnitude ($V_{max} = 140 \pm 3$ nmoles/min-mg mitochondrial protein and $K_M = 1.4 \pm 0.1$ mM); moreover, the Δ Inh1 strain showed a slight increase (i.e. the $V_{max} = 190 \pm 7$ nmoles/min-mg mitochondria and $K_M = 1.5 \pm 0.2$ mM) (Table 2). There was no statistically significant difference using a non-parametric t-student, suggesting that deletion of Inh1 subunit has a worthless stimulatory effect on ATPase activity. These results suggested that pH shift could not be involved with the displacement of the regulatory subunit of F_1F_0 -ATP synthase.

3.7 The Δ Inh1 assemble an active F_1F_0 -ATP synthase dimer

Supercomplexes and complexes were efficiently solubilized using a digitonin:protein ratio from 2 to 5, and their activities analyzed by BN-PAGE (Fig. 5). The staining of protein with the Coomassie brilliant blue shows that the complexes and supercomplexes profile was similar in both strains (Fig. 5A). The ATPase activity of the complex V was associated to two main protein bands with a molecular weight of 1200 kDa, which correspond to the V_2 , and 660 kDa which is the V_1 (Fig. 5B), similar to previous report (4). Occasionally, a third ATPase activity band appear with a molecular weight of 1100 kDa, which contained the 17 subunits of the dimeric state of complex V and no kinetics differences has been observed against the dimer of 1200 kDa (4).

The NADH dehydrogenase activity (Fig. 5C) was associated to a protein band of 1000 kDa (individual complex I), and a protein set of different molecular weight (i.e. from 1200 to 1700 kDa) which correspond to the supercomplexes (i.e. I:III₂:IV, vide infra). Interestingly, the presence and activity of the individual complex I was enriched in the Δ Inh1 strain, while supercomplexes were diminished, suggesting that supercomplexes could be rearranged or could be labile to digitonin solubilization. Complex II showed a molecular weight of 130 kDa and no supercomplexes were associated with this activity (Fig. 5D). Finally, the activity of complex IV was distributed into a protein band of 240 kDa and the supercomplexes of higher molecular weight (Fig. 5 E) similar to previous report from our group (31).

To get inside in the effect of Inh1 deletion on the ATPase activity of the F_1F_0 -ATP synthase, its dimeric (V_2) and monomeric (V_1) state from WT (V_{2WT} , V_{1WT}) and Δ Inh1 ($V_{2\Delta$ Inh1}, $V_{1\Delta$ Inh1}) mitochondria were digitonin-solubilized with a ratio 2:1 and isolated as reported previously by our group (4).

3.8 Kinetics characterization of the V_1 and V_2 at different pH values

The monomeric and dimeric states of the F₁F₀-ATP synthase from the WT and Δ Inh1 strains were efficiently isolated (Fig. 6) and their activity was assayed at pH 8.0 and 6.0 using an ATP-regenerating system (4).

The activity of the V_{1WT} assayed at pH = 8.0 (Fig. 6B, open circles) showed a Michaelis-Menten kinetics with a V_{max} of 0.93 ± 0.02 μmol of ATP hydrolyzed·(mg of complex V·min)⁻¹ and a K_M of 1.4 ± 0.1 mM. The V_{2WT} showed a very low activity and affinity (Fig. 6E, open circles), with a V_{max} and K_M values of 0.5 ± 0.01 μmol of ATP hydrolyzed·(mg of complex V·min)⁻¹ and 0.35 ± 0.05 mM, respectively. It has been reported that DDM (0.05%) could stimulate the activity of the V_{1WT} and the V_{2WT} (4). As showed in figure 6E (close circles) the V_{2WT} increase several times its ATPase activity while V_{1WT} have a 1.6-time increase (Fig. 6B, close circles, and Table 3). Interestingly, when pH was shifted to 6.0, the V_{1WT} shows a 3.6-time increase in the V_{max}, with or without DDM addition respect to control conditions (Table 2). For the V_{2WT} there no changes in the kinetics parameters neither in the DDM ATPase activity stimulation were observed (Fig. 6C and F, and Table 3) suggesting that Inh1 role in the ATPase activity regulation couldn't be associated to proton concentration. To verify this hypothesis, the kinetics characterization of V_{1 Δ Inh1} and V_{2 Δ Inh1} was performed.

The ATPase activity of the V_{1 Δ Inh1} assayed at pH = 8.0 (Fig. 6H, open circles) showed a Michaelis-Menten kinetics and was 4.4-times higher than V_{1WT}, showing a V_{max} values of 4.1 ± 0.1 μmoles of ATP hidrolized·(mg of F₁F₀-ATP synthase·min)⁻¹ and a K_M = 1.8 ± 0.2 mM (Table 2). Contrary to observed with the V_{2WT}, the V_{2 Δ Inh1} showed a V_{max} = 3.4 ± 0.16 μmoles·(mg of F₁F₀-ATP synthase·min)⁻¹ and a K_M = 1.4 ± 0.23 mM (Table 2), a similar ATPase activity to V_{1 Δ Inh1} (Fig. 6K, open circles). These results clearly showed that deletion of Inh1 increased the ATPase activity of complex V oligomers but the pH effect was not observed.

Interestingly, the ATPase activation of the V_{1WT} and V_{2WT} by DDM addition doesn't occurs with the V_{1 Δ Inh1} and V_{2 Δ Inh1}; indeed, DDM induces the inhibition of the ATPase activity of the V_{1 Δ Inh1} and V_{2 Δ Inh1} (Fig. 6H and K, close circles, respectively). The shift of pH to 6.0 doesn't modify the activity of the V_{1 Δ Inh1} and V_{2 Δ Inh1} (Table 2), neither DDM inhibition (Fig. 6I and L). These results indicate that pH shift (from 8 to 6) doesn't modify the interaction between the Inh1 subunit and the F₁ sector in the WT strain; but deletion of Inh1 increases the ATPase activity independently of the pH shift. The effect of DDM suggests that Inh1 could play an alternative role as a stabilizer of the F₁F₀-ATP synthase, since its deletion induces the inactivation of the ATPase activity by DDM.

4. Discussion

In healthy respiratory mitochondria the complexes from respiratory chain generate the Δp which drives the F_1F_0 -ATP synthase to synthesize ATP. Under unfavorable conditions where the oxygen or substrate availability is limited such as ischemia, Parkinson's and motor neuron diseases the F_1F_0 -ATP synthase hydrolyzes the ATP (30). Indeed, the ATPase activity of F_1F_0 -ATP synthase increases as well as matrix pH decrease, which is related with the oxygen limitation (32). In these conditions, the inhibitory protein (IF₁ in mammals and Inh1 in fungi) is the responsible to inhibit the ATPase activity; this binds to the soluble F₁ sector, interfering with rotation of the central stalk and the conformational changes in the catalytic α/β interfaces (33). If Δp increases, the inhibitor protein is expelled and ATP synthesis resumes (34). As the Inh1 subunit of *U. maydis* adopts a similar conformation to the IF₁ inhibitor protein of mammalian and Inh1 of *S. cerevisiae* (Fig. 1), a similar regulatory mechanism could be proposed for it during unfavorable conditions.

In this research, deletion of the Inh1 subunit in the eukaryotic model *U. maydis* has no observable effect on the growth of cells, biomass production, glucose consumption, neither on the cristae structure and mitochondrial network (see Fig. 3), nor on the mitochondrial oxygen consumption, membrane potential generation, and complexes I, II, and IV activities (see Table 1). Additionally, the functionality of the F_1F_0 -ATP synthase was corroborated as its ability to synthesize ATP in both WT and Δ Inh1 *U. maydis* cells (Table 1). Additionally, activity of the complexes I, II, and IV was similar (Table 1), however their activity and distribution into individual complexes or supercomplexes was slightly different between WT and Δ Inh1 strains. The amount of individual complex I in the Δ Inh1 was higher than WT, and its activity associated with supercomplexes was lower (Fig. 5). Similarly, single complex IV activity was higher in the WT than Δ Inh1 and its presence into supercomplexes was greater in WT strain. This suggests that supercomplexes with the composition I:III₂:IV (i.e. the respirasome as reported by (31)) is most stable in the WT strain than in the Δ Inh1. Finally, complex II was observed as a single state in both strains; however, its activity was higher in the WT strain. However, new studies must be performed to determine the effect of Inh1 deletion into the composition and amount of the supercomplexes.

The role of the regulatory subunit, Inh1, is to inhibit the ATPase activity of the F_1F_0 -ATP synthase when $\Delta p \rightarrow 0$ and the mitochondrial matrix pH decrease; in this sense, an acidic condition (i.e. pH = 6.0) does not modify ATP hydrolysis in permeabilized mitochondria from WT or Δ Inh1 strains (see Table 2 and Fig. 4), suggesting that deletion of Inh1 subunit was not sufficient to activate ATP hydrolysis (i.e. pH = 8.0).

As the F_1F_0 -ATP synthase in the inner membrane mitochondria occurs principally as a monomer (V_1) and a dimer (V_2), a further analysis of ATPase activity at different pH-values was

performed using the isolated oligomers (see Table 2 and Fig. 6). The ATPase activity of the V_1 from WT was higher than the dimeric state assayed at pH 8.0. Similarly to previous report, both states were stimulated by DDM (0.005%); in this conditions, V_2 showed an increasing of V_{max} by 9-times than V_1 (Fig. 4). Similar effect was observed at pH = 6.0. The oligomers from Δ Inh1 strain showed a slightly higher activity than WT (Fig. 4) at both pHs assayed; however, DDM addition decreased their activity, contrary to observed for the WT (Fig. 4). This result suggests that Inh1 could play a main stabilizing role rather than as a regulatory subunit of F_1F_0 -ATP synthase activity.

Interestingly, activity of isolated oligomers from mutant mitochondria showed V_{max} 3-times higher than WT strain, suggesting that deletion of Inh1 could

Acknowledgment

This work was supported by Direccion General de Asuntos del Personal Academico (DGAPA) (IN222617) from Universidad Nacional Autonoma de Mexico (UNAM). ME-P is a PhD student of the Programa de Doctorado en Ciencias Biologicas (511021118) from UNAM and supported by CONACyT through a doctoral scholarship (254400). The authors thank to the Posgrado en Ciencias Biologicas from UNAM for the academic support and to DGAPA-UNAM for the fellowship provided to Lucero Romero-Aguilar.

Author contributions

OFH: He conceptualized and coordinated the research, suggested experiments, analyzed data, wrote and edited the manuscript and provided funding to support the research. **MF:** He conceptualized and coordinated the mutant construction, revised and edited the manuscript. **LT:** He produced the mutant strain and revised the manuscript. **ME:** She produced the mutant strain, suggested experiments, analyzed the data, performed experiments wrote the original draft and reviewed and edited the manuscript. **LRA:** She performed experiments and analyzed the data. **JPP:** He suggested experiments, analyzed the data, revised and edited the manuscript.

References

- 1) Varghese F, Blaza JN, Jones AJY, Jarman OD, Hirst J. (2018) *Open Biol.* 8: 170206
- 2) Cingolani G, Duncan TM. (2011) *Nat. Struct. Mol. Biol.* 18, 701–707
- 3) Sobti M, Smits C, Wong ASW, Ishmukhametov R, Stock D, Sandin S, Stewart AG. (2016). *eLife.* 5, e21598
- 4) Esparza-Perusquia M, Olvera-Sanchez S, Pardo JP, Mendoza-Hernandez G, Martinez F, Flores-Herrera O. (2017) *Biochimica et biophysica acta Bioenergetics.* 1858, 975-981
- 5) Nakamura J, Fujikawa M, Yoshida M. (2013) *Bioscience reports.* 33

- 6) Sanchez-Cenizo L, Formentini L, Aldea M, Ortega AD, Garcia-Huerta P, Sanchez-Arago M, Cuezva JM. (2010) *J. Biol Chem.* 285, 25308-13
- 7) Brachmann A, König J, Julius C, Feldbrügge M. (2004) *Molecular Genetics and Genomic*, 272:261-226
- 8) Estambrook RW. (1967) *Methods and Enzymology*, 10:41-47
- 9) Guerrero-Castillo S, Cabrera-Orefice A, Vázquez-Acevedo M, González-Halphen D, Uribe-Carvajal S. (2012) *Biochimica et Biophysica Acta*, 1817:353–362
- 10) Affourtit C, Quinlan CL, Brand MD. (2012) *Methods in molecular biology*, 11:165-182
- 11) Flores-Herrera O, Olvera-Sánchez S, Esparza-Perusquía M, Pardo JP, Rendón JL, Mendoza-Hernández G, Martínez F. (2015) *Biochim Biophys Acta.* 1847, 143-152.
- 12) Juárez O, Guerra G, Velázquez I, Flores-Herrera O, Rivera-Pérez RE, Pardo JP. (2006) *FEBS Journal*, 273:4603-4615
- 13) Lowry OH, Rosebrough NJ, Farr AL, Randall RJ. (1951) *J Biol Chem.* 193:265-275
- 14) Mahuran D, Clements P, Carrella M, Strasberg PM. (1983) *Analytical biochemistry*, 129: 513-516
- 15) Wittig I, Karas M, Schägger H. (2007) *Mol Cell Proteomics.* 6, 1215-25.
- 16) Jung C, Higgins CM, Xu Z. (2000) *Anal Biochem.* 286, 214-223.
- 17) Schägger H, Cramer WA, von Jagow G. (1994) *Anal Biochem.* 217, 220-230.
- 18) Harmon HJ. (1982) *Journal of Bioenergetics and Biomembranes.* 14, 377-386
- 19) Nakashima Y, Shinzawa-Itoh K, Watanabe K, Naoki K, Hano N, Yoshikawa S. (2002) *J. Bioenerg. Biomembr.* 34:11-9
- 20) Vinogradov AD, Grivennikova VG. (2005) *Biochemistry (Mosc).* 70:120-127
- 21) Dröse S, Galkin A, Brandt U. (2005) *Biochim. Biophys. Acta.* 1710:87-95
- 22) Fiske CH, Subbarow Y. (1925) *Journal of Biological Chemistry.* 66, 375-400
- 23) Rule CS, Patrick M, Sandkvist M. (2016) *Journal of visualized experiments : JoVE*
- 24) Claros MG, Vincens P. (1996) *European journal of biochemistry.* 241, 779-86
- 25) Larkin MA, Blackshields G, Brown NP, Chenna R, McGettigan PA, McWilliam H, Valentin F, Wallace IM, Wilm A, Lopez R, Thompson JD, Gibson TJ, Higgins DG. (2007) *Bioinformatics.* 23, 2947-8
- 26) Di Tommaso P, Moretti S, Xenarios I, Orobitz M, Montanyola A, Chang JM, Taly JF, Notredame C. (2011) *Nucleic acids research.* 39, W13-7
- 27) Webb B, Sali A. (2014) *Current protocols in bioinformatics.* 47, 5 6 1-32
- 28) Campanella M, Casswell E, Chong S, Farah Z, Wieckowski MR, Abramov AY, Tinker A, Duchon MR. (2008) *Cell metabolism.* 8, 13-25

- 29) Garcia JJ, Morales-Rios E, Cortes-Hernandez P, Rodriguez-Zavala JS. (2006) *Biochemistry*. 45, 12695-703
- 30) Campanella M, Parker N, Tan CH, Hall AM, Duchen MR. (2009) *Trends in biochemical sciences*. 34, 343-50
- 31) Reyes-Galindo M, Suarez R, Esparza-Perusquía M, de Lira-Sánchez J, Pardo JP, Martínez F, Flores-Herrera O. (2019) *Biochim Biophys Acta Bioenerg*. 1860, 618-627.
- 32) Khodjaev E, Komarnitsky FB, Capozza G, Dukhovich VF, Chernyak BV, Papa S. (1990) *FEBS letters*. 272, 145-8
- 33) Garcia JJ, Morales-Rios E, Cortes-Hernandez P, Rodriguez-Zavala JS. (2006) *Biochemistry*. 45, 12695-703
- 34) Scwerzmann K, Pedersen PL. 1981. *Biochemistry* 20, 6305-6311.

Table 1. Structural and bioenergetics parameters of the wild type and Δ Inh1 strains of *Ustilago maydis*.

	WT	Δ Inh1
Presence of mitochondrial network	Yes	Yes
Mitochondrial cristae folding	Yes	Yes
Membrane potential generation	Yes	Yes, 100% of WT
Oxygen consumption (ng at O/mg·min ⁻¹)	348 ± 32	322 ± 35
Oxygen consumption cyanide resistant (ng at O/mg·min ⁻¹)	288 ± 30	225 ± 22
NADH dehydrogenase activity (μ mol NADH oxidized/mg·min ⁻¹)	0.22 ± 0.03 0.38 ± 0.04 (Δ p→0)	0.28 ± 0.04 0.36 ± 0.02 (Δ p→0)
Succinate dehydrogenase activity (μ mol DCPIP reduced/mg·min ⁻¹)	0.035 ± 0.009 0.017 ± 0.007 (Δ p→0)	0.049 ± 0.01 0.017 ± 0.006 (Δ p→0)
ATP synthesis (μ mol ATP·(mg·min) ⁻¹)	18 ± 0.9	20 ± 0.9

Table 2. Kinetics parameters of ATPase activity of the F₁F₀-ATP synthase from WT and Δ Inh1 strains from *Ustilago maydis* mitochondria.

	WT		Δ Inh1	
	pH = 8.0	pH = 6.0	pH = 8.0	pH = 6.0
Permeabilized mitochondria				
V_{\max} (nmol ATP hydrolyzed/mg protein·min ⁻¹)	125 ± 4	136 ± 3	128 ± 3	189 ± 7
K_M (mM)	1.3 ± 0.1	1.4 ± 0.1	1.5 ± 0.1	1.5 ± 0.2
Non-activated monomer (V ₁) ATPase activity				
V_{\max} (μ mol ATP hydrolyzed/mg CV·min ⁻¹)	0.93 ± 0.02	3.4 ± 0.1	4.1 ± 0.11	3.6 ± 0.07
K_M (mM)	1.4 ± 0.1	0.6 ± 0.1	1.8 ± 0.2	1.5 ± 0.1
DDM-activated V ₁ ATPase activity				
V_{\max} (μ mol ATP hydrolyzed/mg CV·min ⁻¹)	1.5 ± 0.02	5.4 ± 0.1	0.12 ± 0.01	0.038 ± 0.003
K_M (mM)	0.8 ± 0.06	0.4 ± 0.05	0.5 ± 0.6	2.2 ± 0.5
Non-activated dimer (V ₂) ATPase activity				
V_{\max} (μ mol ATP hydrolyzed/mg CV·min ⁻¹)	0.5 ± 0.01	0.7 ± 0.03	3.4 ± 0.16	3.3 ± 0.1
K_M (mM)	0.35 ± 0.05	0.31 ± 0.09	1.4 ± 0.23	0.64 ± 0.1
DDM-activated V ₂ ATPase activity				
V_{\max} (μ mol ATP hydrolyzed/mg CV·min ⁻¹)	11 ± 0.3	12.7 ± 0.3	0.0098 ± 0.003	0.02 ± 0.001
K_M (mM)	0.9 ± 0.1	0.35 ± 0.05	0.79 ± 0.1	0.73 ± 0.1

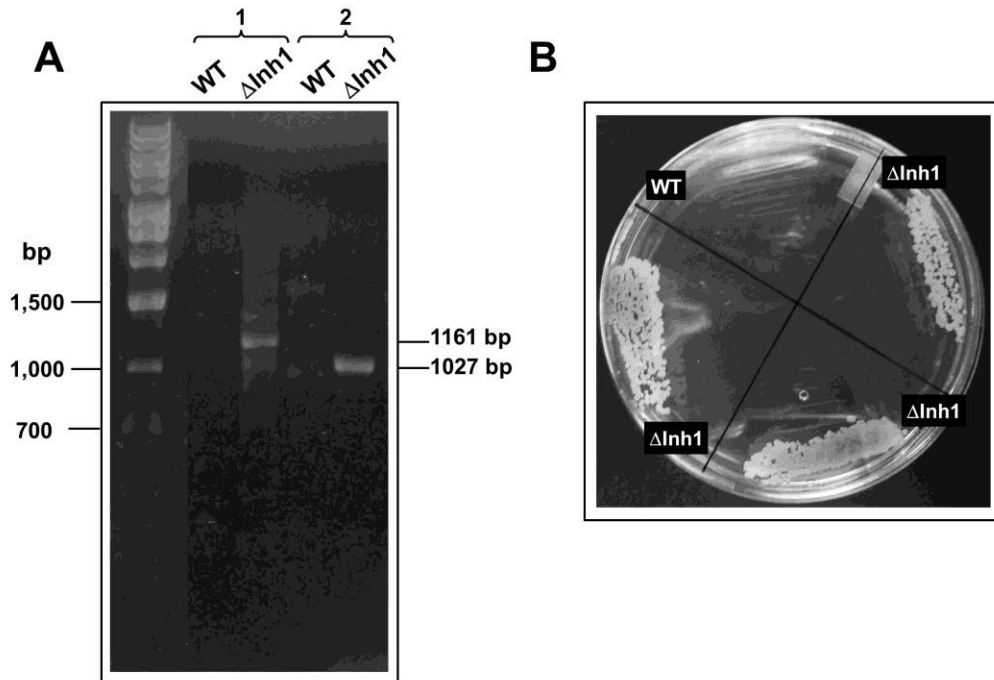


Figure 2. Confirmation of replacement by homologous recombination of *Inh1* gene by hygromicine resistant gene. A) PCR was used to amplify sequences of DNA that includes the sequences of *Inh1* or *HygR* and the flanking regions on each side of the *Inh1* gene. The products were analyzed on 1% agarose gel (see supplementary material for the primers used). The expected lengths of the product from the WT and Δ *Inh1* are shown at the right. B) Hygromicine resistant phenotype of the Δ *Inh1* strain.

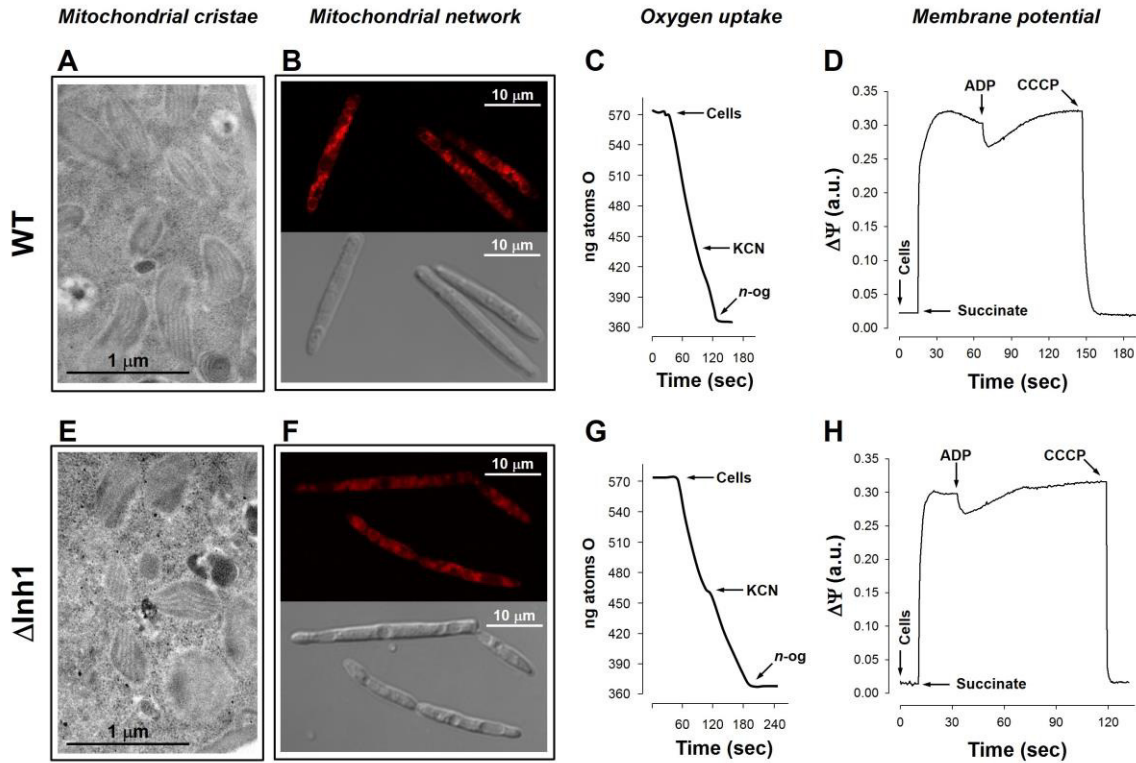


Figure 3. Structural and bioenergetics analysis of the mitochondria from WT and $\Delta Inh1$ strains. WT is showed at the upper panel and $\Delta Inh1$ at the bottom panel. Transmission electron microscopy of the WT (A) and $\Delta Inh1$ (E) shown round shape mitochondria containing lamellar cristae. MitoTracker® Deep Red FM stain and light field microscopy of the mitochondrial network of the WT (B) and $\Delta Inh1$ (F). Oxygen uptake by the WT (C) and $\Delta Inh1$ (G) cells. Where is indicated cells, cyanide (to inhibit the complex IV) or n-octyl-gallate (to inhibit the alternative oxidase) were added. Mitochondrial membrane potential ($\Delta\Psi_m$) of the WT (D) and $\Delta Inh1$ (H) cells was monitoring in presence of safranin-O. Where is indicated cells, succinate (to produce the $\Delta\Psi_m$), ADP (to stimulate ATP synthesis), and CCCP (to increase the proton conductance) were added.

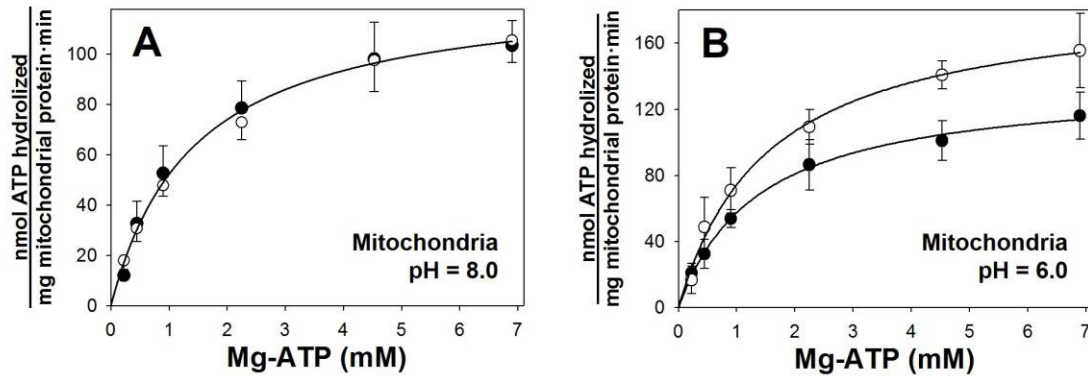


Figure 4. Dependence on ATP concentration of rate of ATP hydrolysis in permeabilized mitochondria. Mitochondria from WT (●) or Δ Inh1 (○) were permeabilized with digitonine and ATPase activity of complex V was assayed at pH = 8.0 (A) or pH = 6.0 (B). Data were adjusted with a Michaelis-Menten equation and were analyzed with the GraphPad software. The results were the average \pm SD of 3 different preparations assayed by triplicates.

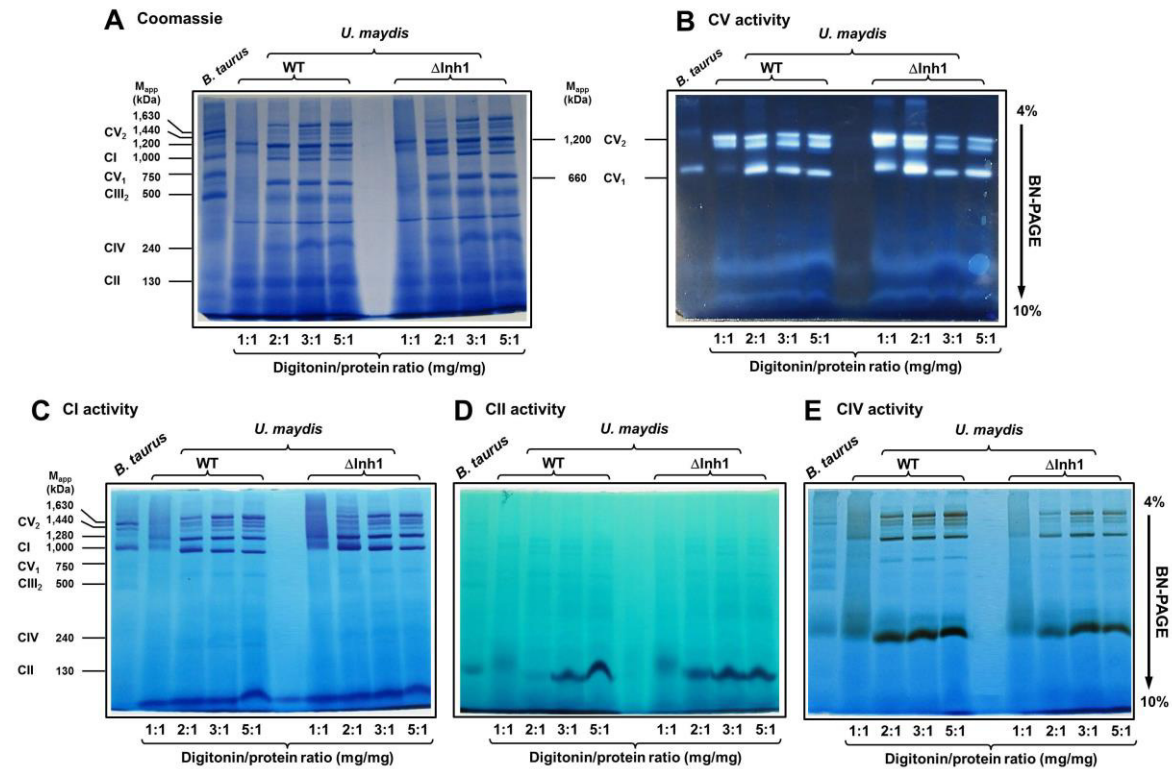


Figure 5. In-gel activity of the mitochondrial OXPHOS complexes and supercomplexes. OXPHOS complex and supercomplexes from *U. maydis* WT and Δ Inh1 strains were solubilized with different digitonin/protein ratio and analyzed by BN-PAGE. A) Coomassie brilliant blue stained native gel. In-gel activities assay of the complexes V (B), I (C), II (D), and IV (E). *Bos taurus* respiratory complex and supercomplexes were solubilized with digitonin (ratio of 2:1) and used as standard. Where indicate CI = complex I, CII = complex II, CIII₂ = dimer of complex III₂, CIV = complex IV, CV₁ = monomeric state of complex V, and CV₂ = dimeric state of complex V.

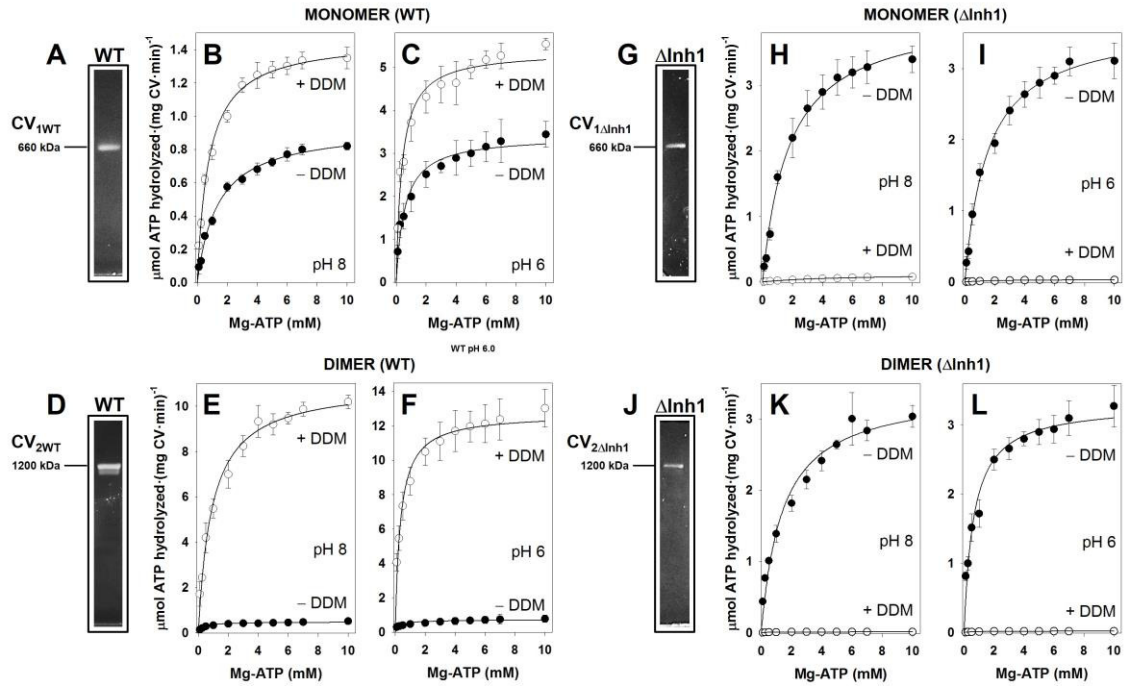
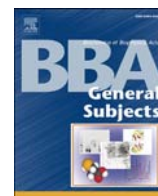


Figure 6. Kinetics characterization of the monomeric and dimeric state of the F_1F_0 -ATP synthase from WT and $\Delta Inh1$ strains. V_1 and V_2 from WT (V_{1WT} and V_{2WT}) and $\Delta Inh1$ ($V_{1\Delta Inh1}$ and $V_{2\Delta Inh1}$) were isolated and its in-gel ATPase activity analyzed (A, D, G, and J, respectively). Kinetics analysis was performed at pH = 8.0 (B, E, H, and K) or pH = 6.0 (C, F, I, and L). Close symbols = +DDM addition (0.005%); open symbols = no DDM added. Data were the average \pm SD of three independent assays from 4 different preparations.



Mitochondrial proteases act on STARD3 to activate progesterone synthesis in human syncytiotrophoblast



Mercedes Esparza-Perusquía^{a,1}, Sofía Olvera-Sánchez^{a,1}, Oscar Flores-Herrera^a, Héctor Flores-Herrera^b, Alberto Guevara-Flores^a, Juan Pablo Pardo^a, María Teresa Espinosa-García^a, Federico Martínez^{a,*}

^a Departamento de Bioquímica, Facultad de Medicina, Universidad Nacional Autónoma de México, Mexico

^b Departamento de Bioquímica y Biología Molecular, Instituto Nacional de Perinatología "Isidro Espinosa de los Reyes", Mexico

ARTICLE INFO

Article history:

Received 20 February 2014

Received in revised form 6 October 2014

Accepted 10 October 2014

Available online 18 October 2014

Keywords:

Human syncytiotrophoblast mitochondria

Progesterone synthesis

STARD3 protein

Mitochondrial metalloprotease

ABSTRACT

Background: STARD1 transports cholesterol into mitochondria of acutely regulated steroidogenic tissue. It has been suggested that STARD3 transports cholesterol in the human placenta, which does not express STARD1. STARD1 is proteolytically activated into a 30-kDa protein. However, the role of proteases in STARD3 modification in the human placenta has not been studied.

Methods: Progesterone determination and Western blot using anti-STARD3 antibodies showed that mitochondrial proteases cleave STARD3 into a 28-kDa fragment that stimulates progesterone synthesis in isolated syncytiotrophoblast mitochondria. Protease inhibitors decrease STARD3 transformation and steroidogenesis.

Results: STARD3 remained tightly bound to isolated syncytiotrophoblast mitochondria. Simultaneous to the increase in progesterone synthesis, STARD3 was proteolytically processed into four proteins, of which a 28-kDa protein was the most abundant. This protein stimulated mitochondrial progesterone production similarly to truncated-STARD3. Maximum levels of protease activity were observed at pH 7.5 and were sensitive to 1,10-phenanthroline, which inhibited steroidogenesis and STARD3 proteolytic cleavage. Addition of 22(R)-hydroxycholesterol increased progesterone synthesis, even in the presence of 1,10-phenanthroline, suggesting that proteolytic products might be involved in mitochondrial cholesterol transport.

Conclusion: Metalloproteases from human placental mitochondria are involved in steroidogenesis through the proteolytic activation of STARD3. 1,10-Phenanthroline inhibits STARD3 proteolytic cleavage. The 28-kDa protein and the amino terminal truncated-STARD3 stimulate steroidogenesis in a comparable rate, suggesting that both proteins share similar properties, probably the START domain that is involved in cholesterol binding.

General significance: Mitochondrial proteases are involved in syncytiotrophoblast-cell steroidogenesis regulation. Understanding STARD3 activation and its role in progesterone synthesis is crucial to getting insight into its action mechanism in healthy and diseased syncytiotrophoblast cells.

© 2014 Elsevier B.V. All rights reserved.

1. Introduction

Mitochondria carry out cellular respiration and ATP synthesis to supply the energy requirements of aerobic cells. Mitochondria are essential for the synthesis of a number of important biological compounds such as lipids, heme, amino acids, nucleotides and steroid hormones. The physiological function and homeostasis of mitochondria entail selective proteolysis in which various specific mitochondrial proteases, including processing peptidases, ATP-dependent proteases, and oligopeptidases are involved [1].

Steroid hormones are synthesized from cholesterol, a substrate for mitochondria of specialized cells of the adrenal cortex, gonads and placenta. The steroidogenic acute regulatory protein (StAR; STARD1) [2–6], a nuclear-encoded mitochondrial protein expressed upon stimulation of steroidogenic tissues by their respective trophic hormones [7–9], promotes cholesterol supply to mitochondria from acutely regulated steroidogenic tissue. It has been suggested that STARD3 (or MLN64), a member of the START domain family, is the protein responsible for transporting cholesterol in the human placenta [10], a steroidogenic tissue which does not show acute regulation of steroidogenesis nor expresses STARD1 [11].

The amino acid sequence of the STARD3 carboxy-terminal region sequence is similar to that of STARD1 [12]. While full-length STARD3 has minimal STARD1-like activity, the 234 amino-terminal residue deletion (N-218 STARD3) results in a protein with substantial STARD1-like activity in transfected cells [10]. Like N-62 STARD1 (a StAR protein with a deletion of 62 amino-acids in its amino-

* Corresponding author at: Departamento de Bioquímica, Facultad de Medicina, Universidad Nacional Autónoma de México, Apdo. Postal 70-159, Coyoacán 04510, México, D. F., México. Tel.: +52 55 56232168; fax: +52 55 56162419.

E-mail address: fedem@bq.unam.mx (F. Martínez).

¹ M. Esparza-Perusquía and S. Olvera-Sánchez contributed equally to this paper.

terminal region), N-218 STARD3 lacks a mitochondrial leader sequence that prevents it from entering the mitochondrion, and apparently exerts its function in the outer mitochondrial membrane. Alpy et al. [13] identified the full-length STARD3 to be associated with late endosomes, which constitute its sole cellular location reported to date.

STARD1 and STARD3 transfer cholesterol from the outer to the inner mitochondrial membrane, where the cholesterol side chain cleavage enzyme, cytochrome P450 (P450_{sc}, CYP11A1; EC 1.14.15.6), converts it to the first product in steroid hormone synthesis: pregnenolone [14–16]. Hypothetical mechanisms suggest that STARD1 activates cholesterol transfer by virtue of its association with a macromolecular complex that consists of outer membrane proteins such as the mitochondrial membrane translocator protein (TSPO), and the TSPO-associated protein PAP7, that bind and lead the regulatory subunit RI- α of the cAMP-dependent protein kinase (PKARI α) towards mitochondria [17]. However, it has been recently described that, in knockout mice with a specific TSPO deletion, gametogenesis, reproduction, histological structure, and steroidogenesis of Leydig cells are not affected. This suggests that the presence of TSPO is not crucial for steroidogenesis [18]. Previous data from our laboratory have also demonstrated that TSPO (earlier named PBR) is absent from the human placenta [19]. In human placenta mitochondria, STARD3 is associated with steroidogenic contact sites and HSP60, resulting in an increase in progesterone synthesis [20,21].

STARD1 is synthesized in the cytosol as a 37-kDa pre-protein carrying an amino terminal targeting sequence that directs its import into mitochondria, where it is proteolytically processed to a mature 30-kDa protein [2,22–24]. Although the important role of STARD1 proteolysis during steroid hormone synthesis by acutely regulated steroidogenic tissue has been described, the role of proteases in the modification of STARD3 in the human placenta has not been studied.

In this work, the participation of mitochondrial proteases in the modification of STARD3 in progesterone synthesis in human syncytiotrophoblast mitochondria was determined. Although the role of STARD3 in the human placenta remains to be elucidated, its proteolysis from a 55-kDa protein into lower molecular weight proteins appears to be essential for placental steroidogenesis.

2. Materials and methods

2.1. Isolation of human syncytiotrophoblast mitochondria

Full term human placentas were collected immediately after normal delivery. Mitochondria were prepared as previously described [25]. Briefly, placental cotyledons were placed in ice-cold 250 mM sucrose, 1 mM EDTA, and 10 mM Tris, pH 7.4. The suspension was homogenized with a Polytron (Brinkmann Instruments, Westbury, NY, USA) at 3000 rev/min for 1 min for two cycles with a one minute interval. The whole process was carried out at 4 °C. The pH of the homogenate was adjusted to pH 7.4 with Tris and centrifuged at 1500 g for 15 min. The supernatant was recovered and centrifuged at 4000 g to obtain a pellet of cytotrophoblast mitochondria (heavy mitochondria). The supernatant was centrifuged again at 16,000 g for 15 min and the pellet containing the syncytiotrophoblast mitochondria (light mitochondria) was suspended in the same solution and centrifuged at 1500 g for 10 min to remove the remaining erythrocytes. Then, the mitochondrial pellet was obtained by centrifugation of the last supernatant at 12,000 g for 10 min. To purify mitochondria of syncytiotrophoblast, the enriched mitochondrial suspension was loaded onto a 35% sucrose solution (25 ml) and centrifuged at 15,000 g for 45 min at 4 °C. The mitochondrial fraction was collected, suspended in 250 mM sucrose, 1 mM EDTA, and 10 mM Tris (pH 7.4) and centrifuged at 16,000 g for 15 min at 4 °C. The resulting mitochondrial pellet was suspended in this buffer and

stored at 4 °C. Protein concentration was measured as reported by Refs. [26,27].

2.2. Mitochondrial oxygen consumption

Oxygen uptake was estimated polarographically using a Clark type electrode in a mixture containing 250 mM sucrose, 10 mM HEPES, pH 7.4, 1 mM EGTA, 1 mM EDTA, 10 mM succinate, 10 mM KH₂PO₄, 5 mM MgCl₂, 0.2% bovine serum albumin and 1 mg/ml of syncytiotrophoblast mitochondrial protein [28]. Temperature was maintained at 37 °C and oxygen consumption was stimulated by the addition of 300–500 nmol ADP (state 3 of respiration). Respiratory control was defined as oxygen uptake rate of state 3/oxygen uptake rate of state 4 (state 4 started when all ADP was converted into ATP, and respiration slowed down) [29].

2.3. Mitochondrial enzyme activity determination

Activities of complex I (NADH:DCPIP oxidoreductase) and complex II (succinate:DCPIP oxidoreductase) were determined spectrophotometrically at 600 nm by following the reduction of the artificial electron acceptor 2,6-dichlorophenol-indophenol (DCPIP; 50 μ M; $\epsilon_{\text{DCPIP}} = 21 \text{ mM}^{-1} \text{ cm}^{-1}$). Mitochondria were permeabilized with 0.01% Triton X-100 and incubated in 30 mM KH₂PO₄, 5 mM MgCl₂, 1 mM EGTA, 120 mM KCl, pH 7.4, and either 500 μ M NADH (complex I) or 2 mM succinate (complex II). Complex II was activated by pre-incubation in the presence of 0.2 mM phenazinemethosulfonate (PMS) for 10 min at 25 °C [30,31]. The protein concentration of syncytiotrophoblast mitochondria was 50 μ g/ml and the reaction was started by the addition of NADH or succinate. ATP synthesis by complex V was measured at 37 °C using an assay coupled to the reduction of NADP⁺ ($\epsilon_{340 \text{ nm}} = 6.2 \text{ mM}^{-1} \text{ cm}^{-1}$). The reaction mixture contained 0.5 mM NADP⁺, 1 mM ADP, 6 units/ml glucose-6-phosphate dehydrogenase, 16 units/ml hexokinase, 10 mM succinate, 100 μ M P¹,P⁵-di(adenosine-5') pentaphosphate-ammonium, 10 mM glucose, 150 mM sucrose, 5 mM MgCl₂, 20 mM Tris/HCl, and 20 mM KH₂PO₄, at pH 7.5. ATP synthesis was started by the addition of syncytiotrophoblast mitochondria (50 μ g/ml). The values reported were obtained by subtracting the rate of ATP synthesis in the presence of oligomycin (5 μ g/mg mitochondrial protein) from the amount of ATP synthesis under control conditions [32].

2.4. Mitochondrial progesterone synthesis

Progesterone synthesis was determined at 37 °C as previously reported [28] in a medium (P4M) containing 120 mM KCl, 10 mM MOPS, 0.5 mM EGTA, 10 mM isocitrate, and 5 mM KH₂PO₄, pH 7.4 in a final volume of 500 μ l with 1 mg/ml of syncytiotrophoblast mitochondrial protein. Where indicated, 25 μ M 22(R)-hydroxycholesterol was added to verify cytochrome P450_{sc}, adrenodoxin, adrenodoxin reductase and 3 β -hydroxysteroid dehydrogenase activities [33]. After incubation, the reaction was stopped with 75 μ l methanol and progesterone was determined using a radioimmunoassay kit (Diagnostic Systems Laboratories, Inc. Webster, Texas, USA), following the manufacturer's instructions. The concentration of progesterone at time zero was subtracted from the amount of progesterone at different times and this net progesterone synthesis was reported. Alternatively, syncytiotrophoblast mitochondria were incubated for 20 min at 37 °C in P4M and centrifuged at 14,000 g in an Eppendorf 5415R refrigerated centrifuge for 15 min at 4 °C. The mitochondrial pellet and the supernatant were separated. The supernatant was concentrated in an Amicon Ultra Centrifugal Filter system (10K) and either processed for SDS-PAGE and Western blot analysis using anti-MLN64 antibodies (*vide infra*) or used to stimulate mitochondrial progesterone synthesis.

2.5. Effect of protease inhibitors in proteolytic STARD3 cleavage and mitochondrial progesterone synthesis

The effect of protease inhibitors in STARD3 cleavage was assessed by incubating mitochondria in PM4 medium with either one of the following: the inhibitor mixture from Sigma (cat. P8215), PMSF (1 mM), EGTA (5 mM), EDTA (5 mM), or 1,10-phenanthroline (9 mM), for 20 min at 37 °C. Afterwards, mitochondrial proteins were processed for SDS-PAGE and Western blot analysis against the STARD3 protein (*vide infra*). To verify the effects of STARD3 on progesterone synthesis, 2 μ M of purified N-218 STARD3 was added to mitochondria incubated in the P4M medium.

2.6. In-gel protease activity assays

SDS-polyacrylamide (8%) gels were co-polymerized with porcine gelatin (1 mg/ml) and loaded with syncytiotrophoblast mitochondria (50 μ g per well) in non-denaturing loading buffer with or without β -mercaptoethanol. Electrophoresis was performed under constant current (10 mA per gel) for 6 h at 4 °C. Gels were washed in 2.5% Triton X-100 for 30 min to eliminate SDS remnants and incubated overnight at 37 °C in an activation buffer (50 mM Tris, pH 7.4, 150 mM NaCl, 20 mM CaCl₂, and 0.02% NaN₃). The buffers used to determine pH-dependence activity were: sodium acetate (from pH 4 to 5.3), MES (from pH 5.3 to 7), Tris (from pH 7 to 8.8) and AMPSO (pH 8.8). Gels were stained with 0.2% Coomassie® brilliant blue R-250 (Sigma). MMP2 and MMP9, constitutively secreted by U937 (ATCC; Rockville, MD) (a promyelocyte cell line) were used as activity standard markers. Protease activity correlated with the unstained band and the densitometric analysis was performed with the Image Analysis software version 1.0 (Thermo Fisher Scientific Inc.). The intensities of activity were measured by peak integration after densitometric analysis.

2.7. SDS gel electrophoresis and Western blot analysis

Syncytiotrophoblast mitochondrial proteins (50 μ g per well) were separated by SDS-PAGE according to Laemmli [34] in a 10% polyacrylamide gel under denaturing conditions. After the run, proteins were stained with either Coomassie® brilliant blue R-250 or silver, using a commercial kit (Bio-Rad) (see Fig. 2D). Alternatively, proteins were electrotransferred to a PVDF membrane (Immobilon P; Millipore, Bedford, MA) in a semi-dry electroblotting system (Bio-Rad) at 25 V for 50 min. Membranes were blocked in 500 mM NaCl, 0.05% Tween-20, and 20 mM Tris-base, pH 7.5 (TTBS buffer), containing 5% blotting grade blocker non-fat dry milk (Bio-Rad). Then, membranes were incubated with anti-MLN64 polyclonal antibodies (1:1000). Immunoreactive bands were visualized with the Enhanced ChemiLuminescence assay (Amersham Life Science, Inc.), according to the manufacturer's instructions, using horseradish peroxidase-conjugated goat antimouse IgG (Pierce) at a dilution ratio of 1:35,000, and densitometric analyses were performed with the Image Analysis software version 1.0 (Thermo Fisher Scientific Inc.). The intensities of proteins were measured by peak integration after densitometric analysis.

The presence of endosome marker proteins, Niemann-Pick type C1 protein (NPC1) and Rab5 was assayed [35,36] by Western blot, as described above. The dilution ratio of either anti-NPC1 or anti-Rab5 antibodies was 1:2000. After being washed, the blots were incubated with the corresponding secondary antibodies. Protein-antibody complexes were visualized as described above.

2.8. Production of the N-218 STARD3 protein

The recombinant N-218 STARD3 protein was produced in BL21 *Escherichia coli* expressing human STARD3-START (amino acids 218–445; N-218 STARD3) [10] as previously described [37]. The expressed protein contained a His₆-tag at the C-terminus. Bacteria

were cultivated in LB medium containing 25 μ g/ml ampicillin. For protein expression, 400 ml of growth medium (with antibiotic) was inoculated with 1 ml of BL21 overnight culture. The culture was incubated at 37 °C with constant shaking until an optical density of 0.5–1.0 at 600 nm was reached. Expression was induced by the addition of 0.5 M isopropyl- β -D-thiogalactopyranoside. After 4.5 h bacteria were pelleted.

The resulting pellet was suspended in ice in 10 ml of the following buffer: 300 mM NaCl, 50 mM NaH₂PO₄, 20 mM Tris-HCl (pH 7.4), and 10 mM β -mercaptoethanol. Bacteria were sonicated in ice (15 pulses of 1 s, three times at maximum output level), using a MSE Soniprep (UK) model 150. The suspension was centrifuged at 4 °C for 30 min at 20,000 g. The supernatant was incubated with 500 μ l of Ni²⁺-nitrilotriacetic acid-agarose matrix (Qiagen, Hilden, Germany). The mixture was incubated with constant rotation at 4 °C overnight. The matrix was placed in a column and washed with 20 ml of the following buffer: 300 mM NaCl, 50 mM NaH₂PO₄ (pH 8.0), and 20 mM imidazole. To avoid aggregation of N-218 MLN64, the elution buffer was supplemented with 40% (w/v) glycerol. The eluted proteins were dialyzed (molecular mass cutoff: 12-kDa; Sigma) against the following buffer: 150 mM NaCl, 50 mM KCl, 50 mM Tris (pH 7.4), 10 mM dithiothreitol, and 40% (w/v) glycerol [37].

2.9. Tandem mass spectrometry (LC/ESI-MS/MS)

The protein band (indicated as 28-kDa in Fig. 2B) was cut off from the Coomassie® brilliant blue R-250-stained SDS-PAGE gels and sent to the Proteomics Core Facility at the University of Arizona, USA, to determine its identity.

Outer mitochondrial membranes were isolated as reported by Uribe et al. [20]. Briefly, 20–25 mg of mitochondrial protein was incubated at 4 °C with 10 mM H₃PO₄ and adjusted to pH 7.3 with Tris base in the presence of protease inhibitor cocktail (Complete, Roche). After incubation, sucrose was added to attain a final concentration of 0.38 M. The resulting mixture was incubated for 20 more minutes at 4 °C and then centrifuged at 12,500 g for 10 min. The supernatant containing the outer mitochondrial membranes was centrifuged at 137,000 g for 1 h to recover the membrane fraction. The resulting mitochondrial outer membrane was incubated in 100 mM ammonium bicarbonate (pH = 7.8) for 30 min, centrifuged at 100,000 g at 4 °C and sent to the Proteomics Core Facility at the University of Arizona, USA.

2.10. Statistical analyses

Statistical analyses (one- and two-way analyses of variance, ANOVA) of the data were performed using Sigma Stat software, version 3.5. When necessary, nonlinear regression of the data to a single exponential decay equation was performed in Sigma Plot software, version 10.0.

2.11. Materials

Analytical grade reagents were purchased from Sigma Chemical Co. (St. Louis, MO, USA), E. Merck (Darmstadt, Germany), and Bio-Rad (Hercules, CA, USA).

3. Results

3.1. Functional state of syncytiotrophoblast mitochondria

To determine the functional integrity of isolated syncytiotrophoblast mitochondria, respiratory rates and respiratory controls were calculated from oxygen uptake traces using succinate as substrate (Table 1). Oxygen uptake in state 3 and state 4 was 135 ± 28 ng atom of oxygen/min · mg protein, and 21 ± 8 ng atom of oxygen/min · mg protein, respectively. The respiratory control value was 6.7 ± 2 while ATP synthesis rate of complex V was 160 ± 12 nmol/min · mg protein. Addition of 2,4-dinitrophenol to energized mitochondria increased the permeability of the

Table 1
Bioenergetics and steroidogenic parameters of syncytiotrophoblast mitochondria.

Complexes activities ^a	
Complex I	113 ± 20 μmol/min·mg
Complex II	14 ± 4 μmol/min·mg
Complex V	160 ± 12 nmol/min·mg
Oxygen uptake	
State 3 ^b	135 ± 28 ng atom of oxygen/min·mg protein
State 4 ^c	21 ± 8 ng atom of oxygen/min·mg protein
Respiratory control ^d	6.7 ± 2
Progesterone synthesis ^e	
Control	30.6 ± 1.3 ng progesterone/min·mg
+22(R)-hydroxycholesterol	85 ± 6.0 ng progesterone/min·mg

^a Specific activities from complexes I and II were measured spectrophotometrically in sonicated mitochondria: complex I, NADH:DCPIP oxidoreductase and complex II, succinate:DCPIP oxidoreductase. Complex II activity was stimulated as described in **Materials and methods** section. Specific complex V activity was determined in intact mitochondria as ATP synthesis. Values shows are the mean ± S.D. (n = 7 independent determinations from different placental tissue).

^b Defined as oxygen consumption stimulated by ADP added in presence of succinate as substrate. Values are the mean ± S.D. (n = 25 independent determinations from different placental tissue).

^c Defined as oxygen consumption reduction due to all ADP added was converted to ATP. Values are the mean ± S.D. (n = 25 independent determinations from different placental tissue).

^d Respiratory control = oxygen uptake rate of state 3/oxygen uptake rate of state 4. Values are the mean ± S.D. (n = 25 independent determinations from different placental tissue).

^e Progesterone synthesis was determined as described in **Materials and methods** section. 22(R)-hydroxycholesterol was used to verify cytochrome P450_{scc}, adrenodoxin, adrenodoxin reductase and 3β-hydroxysteroid dehydrogenase activities [30]. Values here are the mean ± S.D. from eight determinations from eight different placental tissues.

coupling membrane to protons, and induced maximum respiratory rate (205 ± 33 ng atom of oxygen/min·mg protein); no oligomycin-sensitive-ATP synthesis occurred. These data indicate functional coupling of mitochondrial respiration and ATP synthesis in syncytiotrophoblast mitochondrial preparations. Activities of 113 ± 20 μmol/min·mg protein for NADH:DCPIP oxidoreductase (complex I), and 14 ± 4 μmol/min·mg protein for succinate:DCPIP oxidoreductase (complex II) were also assessed (Table 1).

Endosome marker proteins, NPC1 and Rab5 [35,36], were not identified by Western blot in isolated syncytiotrophoblast mitochondria. Taken together, these results indicate the presence of functional mitochondria isolated from syncytiotrophoblast cells, capable of increasing oxygen consumption and of synthesizing ATP upon the addition of ADP.

Human syncytiotrophoblast mitochondria are steroidogenic organelles that synthesize progesterone due to the presence of 3β-hydroxysteroid dehydrogenase in their inner membrane [25,38]. The rate of progesterone synthesis was 30.6 ± 1.3 ng progesterone/min·mg protein and was not modified when exogenous cholesterol was added (data not shown). Furthermore, previously reported data indicated that placental mitochondria have enough cholesterol [39] so addition of exogenous cholesterol is not necessary to stimulate progesterone synthesis. The addition of 22(R)-hydroxycholesterol – a soluble substrate used to verify cytochrome P450_{scc}, adrenodoxin, adrenodoxin reductase and 3β-hydroxysteroid dehydrogenase activities [33], increased steroidogenic activity to 85 ± 6.0 ng progesterone/min·mg protein (Table 1 and Fig. 5A). These results are in agreement with the specialized role of syncytiotrophoblastic tissue [25] and evidence that isolated mitochondria, as used in this work, retain their physiological function.

3.2. Syncytiotrophoblast mitochondrial protease activity

The experiments performed in the present study were designed to assay the role of syncytiotrophoblast mitochondrial proteases in progesterone synthesis. The first approach was to detect the in-gel protease activities and its pH dependence (Fig. 1A). Densitometric analysis of in-gel protease activity showed that it was null at low pH (pH = 4.3),

while an increase was observed starting at pH = 5.3 (Fig. 1A). Since the identity of the proteases in syncytiotrophoblast mitochondria is unknown (but an effort to elucidate it is in progress in our lab), the intensity of each activity band was pooled to obtain the total activity of proteases from each pH value (Fig. 1B). Total protease activity was maximum at pH 7.5 (Fig. 1B) and five different protease activity bands were observed (Fig. 1A). Interestingly, the band with the lowest molecular weight (marked as E) was only detected at pH = 7.5 (Fig. 1A). Mitochondrial protease activity was compared with MMP9 and MMP2 activity constitutively secreted by U937, used as protease activity standards (Fig. 1C). The proteolytic activity was sensitive to 1,10-phenanthroline (Fig. 1D) or β-mercaptoethanol (data not shown), suggesting that syncytiotrophoblast mitochondria contain metalloproteases.

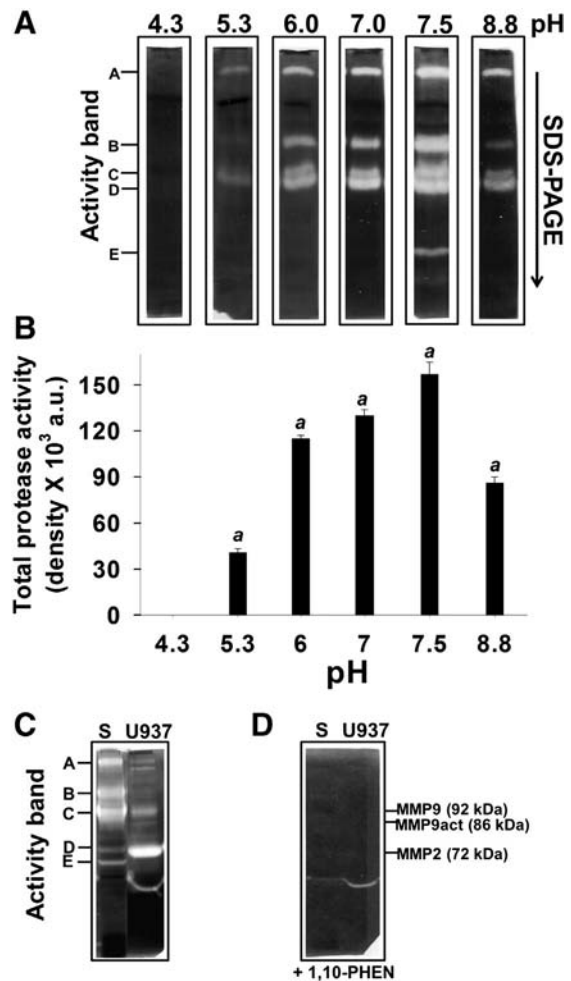


Fig. 1. In-gel protease activity from syncytiotrophoblast mitochondria. A) pH dependence of protease activity. Buffer used: sodium acetate (from pH 4 to 5.3), MES (from pH 5.3 to 7), Tris (from pH 7 to 8.8) and AMPSO (pH 8.8), and continued with the protocol described in the **Syncytiotrophoblast mitochondrial protease activity** section. B) Densitometric analysis from in-gel protease activity shown in A. The density of each band of protease activity was defined as band-intensity/area and the total protease activity shown is the sum of protease activity in each band. A significant increase in the intensity of total protease activity was observed at pH = 7.5, as compared to protease-activity at alkaline or acid pH values. The one-way ANOVA test indicates that these differences are statistically significant (indicated as a) ($p < 0.001$, $n = 4$, from four different placental tissues) (all Pairwise Multiple Comparison Procedures were performed with the Tukey test). Results are presented as the mean ± S.D.; a.u. = arbitrary units. C) Mitochondrial protease activity was determined at pH = 7.4 and compared to MMP2 and MMP9 proteases constitutively secreted by U937 used as protease activity standard (ATCC; Rockville, MD). S means protease activity from syncytiotrophoblast mitochondria. D) Inhibition of protease activity by 1,10-phenanthroline (9 mM) added to protease incubation mixture (+1,10-PHEN). Gels were stained with Coomassie® brilliant blue R-250 and protease activity correlated with the unstained band.

3.3. Syncytiotrophoblast mitochondrial protease and progesterone synthesis

In steroidogenic tissues acutely regulated, STARD1 promotes cholesterol transfer from the outer to the inner mitochondrial membrane. Once in the mitochondrion, steroidogenesis increases and STARD1 is proteolytically cleaved. Since the human placenta expresses STARD3 instead of STARD1 [10,21] we investigated the possible relationship among protease activity, STARD3 proteolytic cleavage, and progesterone synthesis in syncytiotrophoblast mitochondria (Fig. 2). It is important to mention that STARD3 remains tightly bound to isolated syncytiotrophoblast mitochondria (Fig. 2B and [21]), although it was described as an endosome protein [13]. The endosome markers Rab5 and NPC1 were not detected in the syncytiotrophoblast mitochondrial fraction (data not shown), in accordance with previous reports [21].

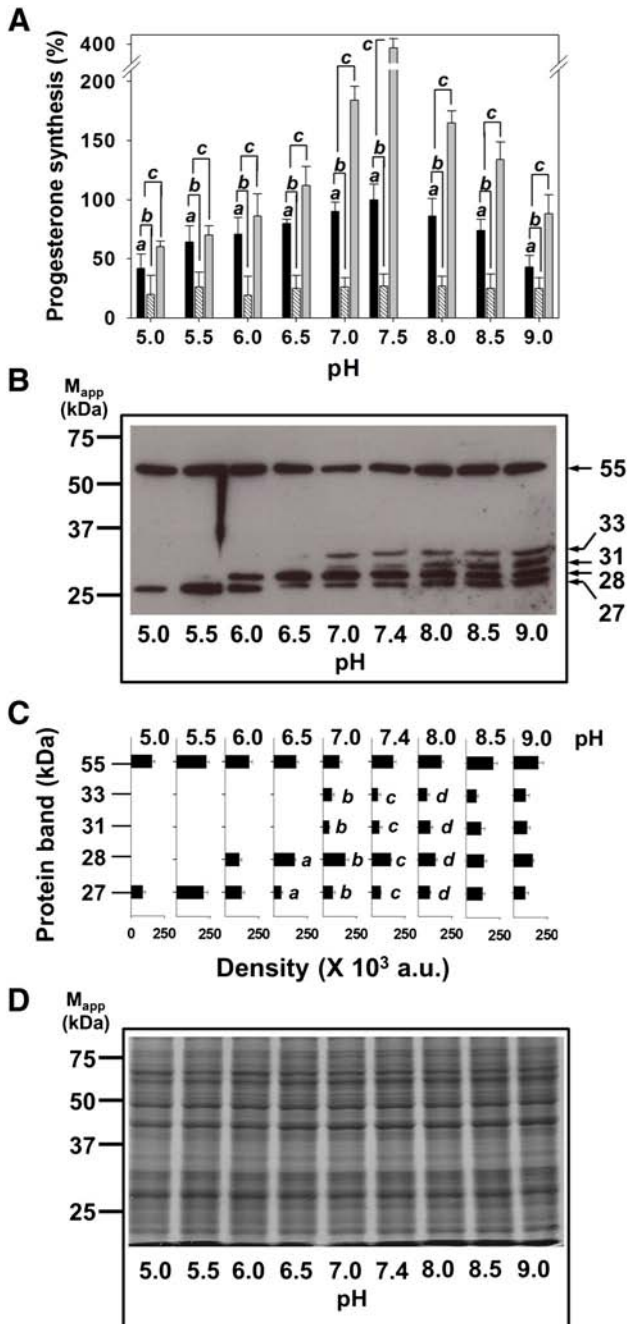


Fig. 2. Proteolytic cleavage of STARD3 and progesterone synthesis in syncytiotrophoblast mitochondria. A) pH dependence of progesterone synthesis in the presence (dashed bars)

Since protease activity was dependent on pH, progesterone synthesis and STARD3 proteolysis were analyzed at different pH values. The synthesis of progesterone increased from pH = 5 to 7.4 (Fig. 2A, black bars), but a decrease was observed at pH = 9. This decrease might be due to the steroidogenic machinery being affected by the alkaline conditions. The effect of pH on cytochrome P450_{sc} and 3 β -hydroxysteroid dehydrogenase activities was verified by the addition of 22(R)-hydroxycholesterol to mitochondria incubated under different pH conditions (Fig. 2A, gray bars). As anticipated, progesterone production was increased by 22(R)-hydroxycholesterol at different pH values, with maximum levels of production detected at pH = 7.4, confirming the inhibitory effect of acid or alkaline pH on cytochrome P450_{sc} and 3 β -hydroxysteroid dehydrogenase. Concomitant with the increase in progesterone synthesis at pH = 7.4, Western blot assays for STARD3 revealed that the 55-kDa protein was proteolytically processed into four proteins released from mitochondria with molecular weights of 27, 28, 31, and 33-kDa (Fig. 2B). Densitometric analysis showed that the relative signal of the STARD3 55-kDa protein was similar at every pH value tested. However, the relative intensity of the proteolytic products increased as pH became alkaline (Fig. 2B and C). The initial proteolytic product was the 27-kDa protein, although the signal of the 28-kDa protein appeared at pH = 6.0. The signal increased and the 28-kDa protein was shown to be the main proteolytic product throughout the pH range tested (Fig. 2C). STARD3 cleavage matched the increase of progesterone synthesis in the physiologic pH range. Although the actual 28-kDa/STARD3 stoichiometry could not be estimated by densitometric analysis, the results are consistent with the hypothesis that STARD3 must be proteolytically processed into a smaller protein that promotes progesterone synthesis in the human placenta [40].

Since Western blot results suggested that STARD3 was processed into a protein belonging to a family of low molecular weight proteins (Fig. 2B), it was important to define its identity. MS/MS analysis of the 28-kDa protein showed that it contains the START-domain sequence (Fig. 3). Moreover, the 28-kDa protein shared 68% of protein identity and 72% of protein similitude to the human STARD3 (Fig. 3). These results confirm the identity of the 28-kDa protein as STARD3, and therefore will be indicated as STARD3-28 kDa from now on. Interestingly, the size of STARD3-28 kDa is approximate to that of the domain of N-218

or absence (black bars) of 9 mM 1,10-phenanthroline. The progesterone synthesis medium described in the Materials and methods section was supplemented with the following buffer: sodium acetate (from pH 4 to 5.3), MES (from pH 5.3 to 7), Tris (from pH 7 to 8.8) and AMPSO (pH 8.8), and the results are expressed as the mean \pm S.D. of at least five separate experiments, with five different placental tissues. The one-way ANOVA analysis of control conditions (black bars) showed a significant increase in progesterone (P4) synthesis at pH = 7.4 when compared to P4 production at lower or higher values of pH (indicated by a). The difference is greater than expected by chance and there is a statistically significant difference ($p \leq 0.001$, $n = 8$) (all Pairwise Multiple Comparison Procedures were performed with the Tukey test). 100% of progesterone synthesis taken at pH 7.4 was considered as the maximum with a value of 30 ± 1.3 ng P4/mg/min. The two way ANOVA analysis showed a statistically significant difference between the treatment groups when 1,10-phenanthroline was present (dashed bars) or absent (black bars) (indicated as b) ($p \leq 0.005$, $n = 16$) (all Pairwise Multiple Comparison Procedures were performed with the Holm-Sidak method). The addition of 22(R)-hydroxycholesterol to mitochondria increased P4 synthesis (gray bars). A two-way ANOVA analysis showed a statistically significant difference between control conditions and 22(R)-hydroxycholesterol addition (indicated as c) ($p \leq 0.001$, $n = 5$) (all Pairwise Multiple Comparison Procedures were performed with the Holm-Sidak method). B) Western blot against STARD3 protein. Mitochondria were incubated in P4M medium as described in the Materials and methods section, and after 20 min of incubation at 37 °C mitochondrial proteins were resolved in SDS-PAGE, and processed for Western blot or stained with Coomassie® brilliant blue R-125 (D). C) Densitometric analysis from Western blot shown in B. The one-way ANOVA of each band intensity at different pH values showed a significant increase in the 28-kDa protein band intensity at pH = 6.5 (indicated by a), 7.0 (indicated by b), 7.4 (indicated by c), and 8.0 (indicated by d), when compared to the other STARD3 proteolytic products (i.e. 27, 31 and 33-kDa proteins) ($p \leq 0.001$, $n = 4$, from four different placental tissues) (all Pairwise Multiple Comparison Procedures were performed with the Tukey test), whereas the 55-kDa protein (STARD3 full length protein) intensity was similar at all pH values tested. The density of each band was defined as band-intensity/area. a.u. = arbitrary units.

STARD3	MSKLPRELTRDLERSLPAVASLGSSLSHSQSLSSHLLPPPEKRRRAISDVRRTFCLFVTFD	60
STARD3-28 kDa	MSKLPRELTRDLERSLPAVASLGSSLSHSQSLSSHLLPPPEKRRRAISDVRRTFCLFVTFD	60

STARD3	LLFISLLWIIELNNTNTGIRKNLEQEI IQYNFKTSFFDFVLAFFRFSGLLGLGYAVLRLRH	120
STARD3-28 kDa	LLFISLLWIIELN-----VLAFFRFSGLLGLGYAVLRLRH	94

STARD3	WW-----VIALLSKG-----AFGYLLPIVSFVLAWLETW---FLDFKVLQPQEAEE	162
STARD3-28 kDa	WWVIAVTTLVSSAFLIVKVI LSELLSKGAFGYLLPIVSFVLAWLETWFLDFKVLQPQEAEE	154
** * : : : * : . * * *****		
STARD3	ER---WYLAAQVAVARGPLLFSGALSEGQFYSPPEFAGSDNESDEEVAGKKSFSQAQER	218
STARD3-28 kDa	ER---WYLAAQVAVARGPLLFSGALSEGQFYSPPEFAGSDNESDEEVAGKKSFSQAQER	210
** *****		
STARD3	<u>EYIRQGKEATAVVDQILAQEENWKFEKNNEYGDTVYTIIEVFPFHGKTFILKTFILPCPAELV</u>	278
STARD3-28 kDa	<u>EYIRQGKEATAVVDQILAQEENWKFEKNNEYGDTVYTIIEVFPFHGKTFILKTFILPCPAELV</u>	270

STARD3	<u>YQEVILQPERMVLWNKTVTACQILQRVEDNTLISYDVSAGAAGGVVSPRDFVNVVRIERR</u>	338
STARD3-28 kDa	<u>YQEVILQPERMVLWNKTVTACQILQRVEDNTLISYDVSAGAAGGVVSPRDFVNVVRIERR</u>	330

STARD3	<u>RDRYLSSGIATSHSAKPPTHK YVRG</u> ENGPGGFIVLKSASNPRVCTFVWILNTDLKG----	394
STARD3-28 kDa	<u>RDRYLSSGIATSHSAKPPTHK YVRG</u> ENGPGGFIVLKSASNPRVCTFVWILNTDLKVGCGW	390

STARD3	----RLPRYLIIHQSLAATMFEFAFHLRQRISELG-----ARA----	427
STARD3-28 kDa	<u>AARAACPGTSSTRASRPCLNLPFTCDSSASASWGPGRDCAPSHPAGQGPVATTSRARKGA</u>	450
* : : . : : * . : . *		
STARD3	-----	
STARD3-28 kDa	<u>SWARTAHMGPGPRLSPSTEPRSAWS</u>	475

Fig. 3. Identification of the 28-kDa protein produced during steroidogenesis from human syncytiotrophoblast mitochondria as STARD3. The MS/MS analysis of the 28-kDa protein produced three peptides whose sequences are indicated in the boxes. The coverage of the 28-kDa protein was 16.3% and its identity was defined as STARD3 protein (ID J3QLM1_HUMAN from UNIPROT KB/TrEMBL). Sequences from whole human placenta STARD3 (indicated as STARD3-28 kDa) and STARD3 (NP_001159410 from NCBI) were aligned and showed an identity of 68% and 72% similitude (Clustal W program). START domain is underlined with a solid line; STARD3-28 kDa sequence is underlined with a dashed line. The arrow indicates the first amino acid in the N218-STARD3 reported by Ref. [40].

STARD3 (Fig. 3) reported by Ref. [40], which might have a role in cholesterol flux from the outer to the inner mitochondrial membrane. However, no mitochondrial targeting presequence was observed.

To verify the participation of proteases in STARD3 cleavage during progesterone synthesis, the effect of 1,10-phenanthroline, a metalloprotease inhibitor, on steroidogenesis was studied (Fig. 4). The time course of progesterone synthesis showed that 1,10-phenanthroline inhibits steroidogenesis (Fig. 4A). Indeed, progesterone synthesis was inhibited by 1,10-phenanthroline depending on its concentration and was totally abolished at 9 mM (Fig. 4B). Additionally, the 1,10-phenanthroline effect on progesterone synthesis at different pH values was explored (Fig. 2A, dashed bars). Once again, the protease inhibitor abolished mitochondrial steroidogenesis at every pH value, suggesting protease participation in progesterone synthesis. Simultaneously, the proteolytic cleavage of STARD3 was abolished by 1,10-phenanthroline (Fig. 4C). Other protease inhibitors like the protease inhibitor cocktail (Sigma), PMSF, EGTA, or EDTA (data not shown) prevented STARD3 cleavage into low molecular weight proteins (Fig. 4C).

3.4. STARD3 cleavage participates in the placental steroidogenesis

Although the relationship between protease activity, STARD3 cleavage, and progesterone synthesis had been demonstrated, it was necessary to determine the potential role of proteolytically-cleaved STARD3. 22(R)-hydroxycholesterol – a cholesterol analog that reaches P450_{sc} independently of the mitochondrial transport system used by cholesterol – was added to syncytiotrophoblast mitochondria to stimulate progesterone

synthesis when the proteolytic cleavage of STARD3 into the STARD3-28 kDa protein was inhibited by 1,10-phenanthroline (Fig. 5A). 22(R)-hydroxycholesterol produced a three-fold increase in progesterone synthesis, even in the presence of 1,10-phenanthroline (Fig. 5A), which inhibited the formation of the STARD3-28 kDa protein (Fig. 4C), suggesting the following implications: 1) P450_{sc} and all the enzymes involved in progesterone synthesis are functional during protease inhibition, and 2) protease activity might be involved in the transport of cholesterol, i.e. the STARD3-28 kDa protein is obtained from STARD3 proteolytic cleavage. When purified the N218-STARD3 protein was added to syncytiotrophoblast mitochondria (Fig. 4C, last lane) and an increase in progesterone synthesis was observed (Fig. 5B). This result suggests that STARD3 proteolysis is an important step in the human placenta progesterone synthesis.

In an attempt to determine the sub-mitochondrial site where the proteolytic cleavage of STARD3 occurs, syncytiotrophoblast mitochondria were centrifuged during progesterone synthesis. The supernatant, where proteins not bound to mitochondria were released, was recovered. This procedure allowed isolating the low molecular weight proteins derived from STARD3 proteolysis (Fig. 6A). It is important to mention that mitochondria showed a respiratory control of 3.2 ± 1.1 after centrifugation, which confirms that the inner membrane remained intact. This suggests that the proteolytic cleavage of STARD3 could take place in the intermembrane space and that proteins are released through the outer membrane as a consequence of centrifugation (Fig. 6A). The subsequent hypothesis is that STARD3 is cleaved in the intermembrane space where its proteolytic products (mainly STARD3-28 kDa) are involved in

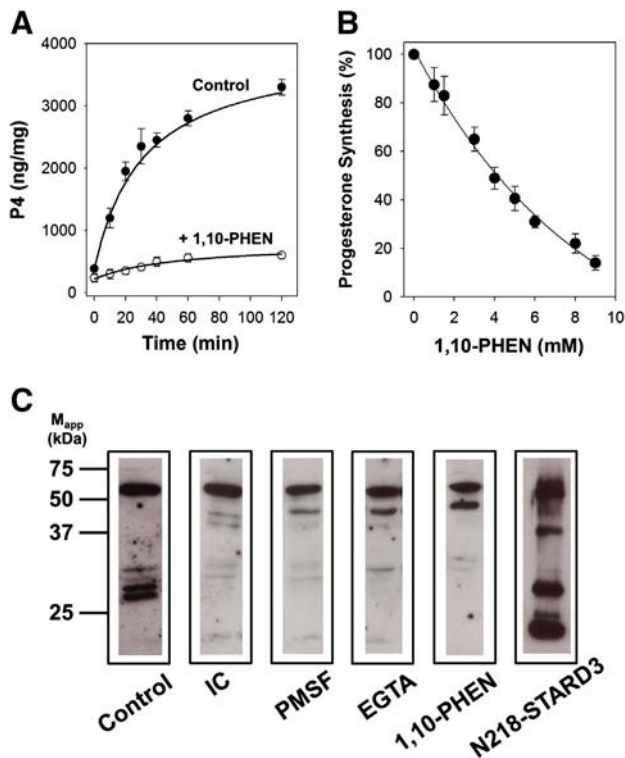


Fig. 4. Effect of 1,10-phenanthroline on mitochondrial progesterone synthesis and STARD3 cleavage. A) Time course of mitochondrial progesterone synthesis in the presence (○) or absence (●) of 9 mM 1,10-phenanthroline. Mitochondria were incubated in P4M medium at 37 °C and at the indicated times, an aliquot was removed and progesterone determined as described in the [Materials and methods](#) section. Results are presented as the mean \pm S.D. of three separate experiments performed with three different placental tissues. B) Inhibition of progesterone synthesis by 1,10-phenanthroline (1,10-PHEN). The inhibition follows an exponential decay and the percentage of inhibition was calculated as the ratio between progesterone synthesis at the indicated 1,10-phenanthroline concentration against control conditions. The data were fitted to the equation $f = y_0 + a \cdot \exp(-b \cdot x)$ using the Sigma Plot software, where $y_0 = -32.6 \pm 7.5$; $a = 143.72 \pm 16.4$; $b = 0.118 \pm 0.025$; $R = 0.9998$. C) Immunodetection of STARD3 protein during mitochondrial progesterone synthesis. Mitochondria were incubated in P4M for 20 min at 37 °C in the presence of an inhibitor cocktail from Sigma (cat. P8215), or PMSF (1 mM), or EGTA (5 mM), or 1,10-phenanthroline (9 mM) and then processed for Western blot analysis. Additionally, purified N-218 STARD3 (85 μ M) was added to mitochondria.

cholesterol efflux between mitochondrial membranes. The high concentration of progesterone bound to a protein fraction that was released from the mitochondria (Fig. 6B, white bars) evidences the interaction of these peptides with steroid molecules. Denaturation of these low molecular weight proteins with cold methanol releases progesterone (Fig. 6B, black bars and Ref. [21]).

To verify the effect of the STARD3–28 kDa protein in progesterone synthesis, mitochondrial protein supernatant was collected and concentrated (as described in the [Materials and methods](#) section) and added to fresh and intact syncytiotrophoblast mitochondria (Fig. 6C, close circles), and progesterone synthesis was determined. Simultaneously, another set of fresh mitochondria was incubated with isolated N-218 STARD3 as control (Fig. 6C, open circles). The addition of the released protein fraction (*i.e.* STARD3–28 kDa protein) to fresh mitochondria induced an increase in progesterone synthesis just as N-218 STARD3 does, suggesting a similar role for both proteins.

4. Discussion

The physiological functions of human syncytiotrophoblast are crucial for the maintenance of pregnancy. Our group is interested in the study of the molecular mechanisms involved in the synthesis of progesterone by the human placenta. The study described here sought to

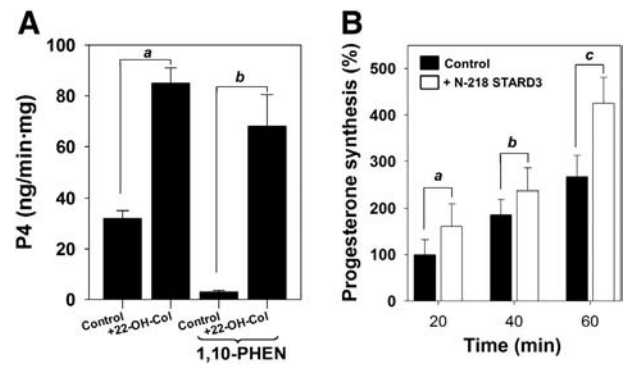


Fig. 5. Effect of 22(R)-hydroxycholesterol and purified N-218 STARD3 protein on progesterone synthesis. A) Syncytiotrophoblast mitochondria were incubated in P4M mixture for progesterone (P4) synthesis and 25 μ M 22(R)-hydroxycholesterol was added. P4 was determined as described in the [Materials and methods](#) section. 1,10-Phenanthroline (1,10-PHEN) concentration was 9 mM. Results are presented as the mean \pm S.D. of five separate experiments performed with five different placental tissues. The one-way ANOVA analysis showed a significant increase of P4 synthesis in the presence of 22(R)-hydroxycholesterol against control conditions (indicated as a) ($p \leq 0.0001$, $n = 4$, from four different placental tissues), or against 1,10-PHEN addition (indicated as b) ($p \leq 0.0001$, $n = 4$, from four different placental tissues) (all Pairwise Multiple Comparison Procedures were performed with the Tukey test). B) Time course of mitochondrial progesterone synthesis with (□) or without (■) N-218 STARD3 protein (85 μ M). N-218 STARD3 protein was overexpressed and purified as described in the [Materials and methods](#) section. Results are presented as the mean \pm S.D. of seven separate experiments performed with seven different placental tissues. The one-way ANOVA analysis showed a statistically significant difference in P4 production, which increased in the presence of N-218 STARD3 protein as compared to control conditions (indicated as a for 20 min; b for 40 min; c for 60 min) ($p \leq 0.001$, $n = 4$, from four different placental tissues) (all Pairwise Multiple Comparison Procedures were performed with the Tukey test).

reveal the role of mitochondrial proteases regarding STARD3 during progesterone synthesis in mitochondria from syncytiotrophoblast cells.

It has been put forward that the STARD3 protein, similarly to STARD1, transfers cholesterol from the outer to the inner mitochondrial membrane [40]. Although the molecular mechanism of STARD1 activity is still unknown, two models have been proposed. In the first one, STARD1 transfers cholesterol during its import into mitochondria. In the matrix, proteases degrade STARD1 to prevent its accumulation and subsequent mitochondrial damage [41–43]. Thus, it has been proposed that STARD1 import into the mitochondrial matrix serves as an off-switch for STARD1 activity. In the second model, mitochondrial import is not required for STARD1 activity, since N-terminally truncated STARD1 proteins retain full activity and it was not imported into mitochondria [4,6,22,44].

Despite the important role of STARD1, some steroidogenic tissues do not express it, as the human placenta. In this regard, elucidating the function of STARD3 is of considerable interest since it might promote steroidogenesis in tissues that do not express STARD1. Because the STARD1 role in steroidogenesis is associated with mitochondrial protease activity, in the present work we determined both, protease activity in syncytiotrophoblast mitochondria and proteolytic activation of STARD3.

Protease activity in syncytiotrophoblast mitochondria was associated with five different bands with an optimal pH = 7.5, and was sensitive to 1,10-phenanthroline, EGTA, EDTA, PMSF and β -mercaptoethanol, which suggests the presence of metalloproteases (Figs. 1, 2B and 4C).

Western blotting of isolated human syncytiotrophoblast mitochondria revealed the presence of apparently full-length (55-kDa) STARD3 and various proteolytic products (27, 28, 31, and 33-kDa) (Fig. 2B). Although STARD3 has been reported to be associated with endosomes [13], STARD3-antibodies recognized a protein of approximately 54 kDa in the isolated syncytiotrophoblast mitochondria, where Rab5 and NPC1 were not detected. This result is in accordance with Ref. [21]. A possible explanation is that some endosomes could still be present in the pellet that comprises isolated mitochondria. Also, this result could indicate a close

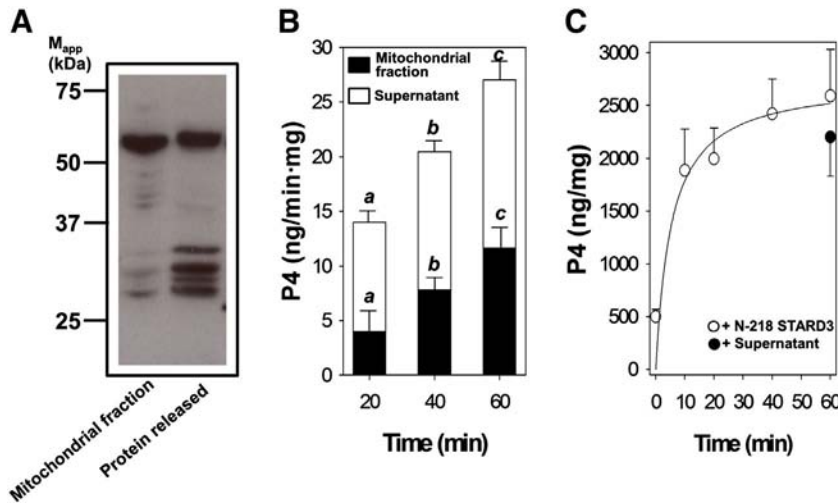


Fig. 6. Release of proteolytically cleaved STARD3 from syncytiotrophoblast mitochondria during progesterone synthesis. Syncytiotrophoblast mitochondria were incubated in P4M medium for 20 min at 37 °C as described in the [Materials and methods](#) section, and then mitochondria were centrifuged and the mitochondrial pellet and supernatant were separated and analyzed by Western blot against STARD3 (A); progesterone content was also determined (B). Where indicated, (■) corresponds to mitochondrial pellet and (□) corresponds to protein released to supernatant. A one-way ANOVA test indicated that the differences in progesterone content between mitochondrial pellet and supernatant are statistically significant (statistical significance indicated as *a* for 20 min; *b* for 40 min; *c* for 60 min) ($p < 0.001$, $n = 7$, from seven different placental tissues) (all Pairwise Multiple Comparison Procedures were performed with the Tukey test). Results are presented as the mean, and error bars indicate S.D. of seven separate experiments. The effect of isolated N-218 STARD3 (○) or mitochondrial supernatant (●) on progesterone synthesis is shown in (C). Protein released from mitochondria during progesterone synthesis was collected, pooled and concentrated in an Amicon Ultra Centrifugal Filter (10K) and added to fresh syncytiotrophoblast mitochondria to determine its effect on progesterone synthesis. Simultaneously, another set of mitochondria were incubated with N-218 STARD3 protein (85 μ M), and progesterone synthesis was determined. No significant differences were observed between protein released from mitochondria and N-218 STARD3 in progesterone synthesis stimulation. The total progesterone content of the mitochondrial supernatant protein was 900 ng of progesterone/mg of protein/60 min, and it was subtracted from the values showed in the graph.

relationship between mitochondria and endosomes during placental steroidogenesis. Nevertheless this hypothesis should be further investigated.

The fact that inner-membrane-impermeable 1,10-phenanthroline, EDTA and EGTA inhibited STARD3 proteolytic cleavage (Fig. 4C)

suggests that metalloproteases could be located in the intermembrane space (IMS), *i.e.* the YME1L, an *i*-AAA protease that exerts its activity on the IMS side of the inner membrane of mitochondria (Fig. 7) [45, 46], or in the cytoplasmic side of the outer membrane. Proteolytic

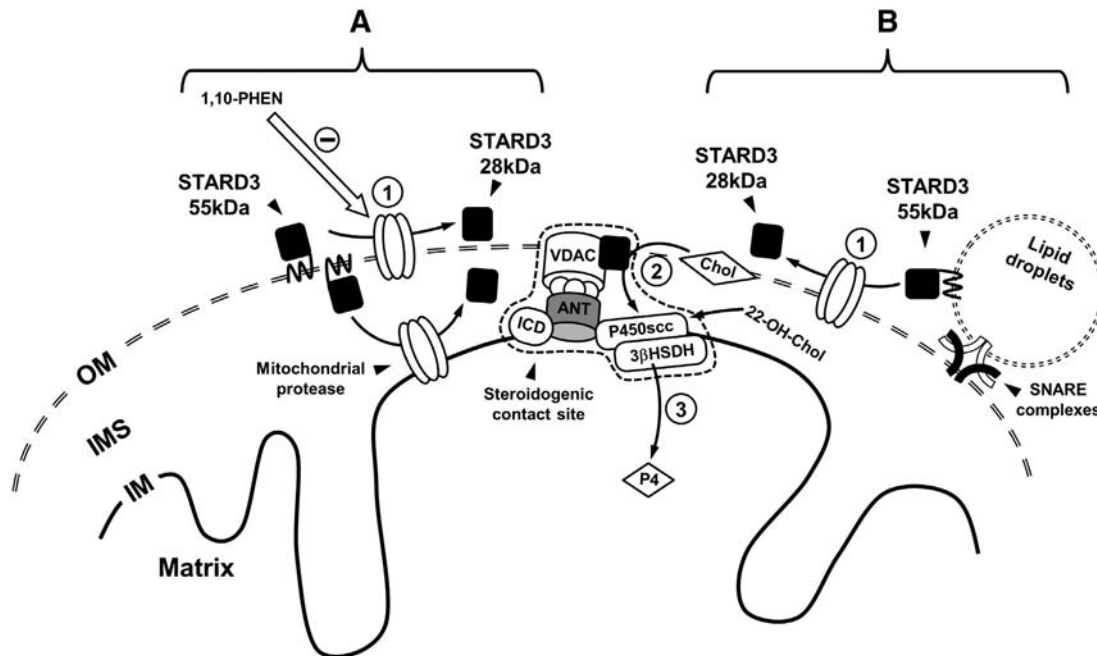


Fig. 7. Model proposed for the role of mitochondrial proteasomes in STARD3 cleavage and progesterone synthesis in human syncytiotrophoblast cells. Protease activities in the activation of MLN64 and the subsequent progesterone synthesis increase have been divided into three steps. Step 1: Proteolytic transformation of STARD3 from a 55-kDa into a 28-kDa protein by a protease that exerts its activity on the IMS side of the inner membrane of mitochondria or at the outer membrane (see text for details). This protease is sensitive to 1,10-phenanthroline, EGTA, or EDTA (shown as an empty arrow). Step 2: The STARD3-28 kDa protein, which has been shown to contain the cholesterol binding domain ([40] and the present work), would increase cholesterol flux from the outer into the inner mitochondrial membrane to reach the cytochrome P450scc machinery and increase progesterone production (Step 3). If protease activity is inhibited and no STARD3-28 kDa protein is produced, 22(R)-hydroxycholesterol might promote progesterone synthesis. STARD3 incorporation to mitochondria could occur without a classical mitochondrial targeting presequence (A) or through the association between mitochondria and lipid droplets *via* the SNARE complex (B). OM = outer mitochondrial membrane; IMS = intermembrane space; IM = inner mitochondrial membrane; steroidogenic contact site = marked with a dashed line; Chol = cholesterol; P450scc = cytochrome P450scc; 3 β HSDH = 3 β -hydroxysteroid dehydrogenase; 22-OH-Chol = 22(R)-hydroxycholesterol.

activation of STARD3 in the intermembrane space or in the outer membrane is also supported by the fact that STARD3 contains no mitochondrial leader sequence and hence does not enter the mitochondrial matrix. Instead its proteolytic products (*i.e.* STARD3-28 kDa protein) could be released from mitochondria by centrifugation without inner membrane damage (Fig. 6A). Although STARD3 lacks a classical mitochondrial targeting presequence, it is tightly joined to syncytiotrophoblast mitochondria and its role in steroidogenesis is demonstrated in the present work. It has been reported that many mitochondrial hydrophobic membrane proteins are synthesized without cleavable extensions [47]. These proteins typically contain several targeting signals that are distributed throughout the length of the protein [48]. This could be the case for STARD3. Once incorporated into mitochondrial membranes, STARD3 might be proteolytically activated and then associated with steroidogenic contact sites to promote cholesterol transport (Fig. 7A). Although this hypothesis needs to be elucidated, STARD3 intermembrane space location is important due to the possible role that has been suggested for the STARD3-28 kDa protein in cholesterol transfer between mitochondrial membranes [40].

Additionally, a model for the incorporation of STARD3 into mitochondria and its activation was put forward, based on the results from mass spectrometric analysis of mitochondrial outer membrane proteins (Fig. 7B). It has been reported that lipid droplets contain constituent proteins of the SNARE complexes [49–53], which include α -SNAP, Syntaxins and VAMP. Human syncytiotrophoblast mitochondria contained SNAP (P54920_SNAAP_HUMAN), Syntaxin-3 (F8W9Y0_STX3_HUMAN), Syntaxin-7 (O15400-2_STX7_HUMAN), Syntaxin-12 (Q86Y82_STX12_HUMAN), Syntaxin-binding Protein-2 (STXBP-2, Q15833_E7EQD5_HUMAN), Syntaxin-binding Protein-3 (STXBP-3, O00186_STXB3_HUMAN), and VAMP-8 proteins (Q9BV40_VAMP8_HUMAN). It has been shown that the SNAP protein promotes interaction between lipid droplets and mitochondria [54], and that steroidogenic cells express SNARE proteins such as Syntaxin-17, SNAP-23, and SNAP-25 [55–59]. These observations strongly suggest that SNARE proteins might mediate cholesterol transport from lipid droplets to steroidogenic mitochondria, most likely by promoting the functional interaction between lipid droplets and mitochondria. In syncytiotrophoblast cells, the STARD3 protein might be incorporated into mitochondria from lipid droplets through SNARE complexes and proteolytically activated by mitochondrial proteases. Once STARD3-28 kDa has been produced, it might then be incorporated to steroidogenic contact sites [20] and promote cholesterol transport for progesterone synthesis (Fig. 7).

Steroidogenic contact sites are multiprotein complexes associated with cholesterol transport and steroidogenesis [20]. Several proteins like HSP60 might be involved, as suggested by Ref. [21]. Although TPSO is a protein apparently essential for several mitochondrial processes, its function does not seem to be crucial to the permeability of the transition pore [60], the steroidogenesis of Leydig cells [18] and the human placenta [19].

Nevertheless, it has been reported that the rate-determining step of placental progesterone synthesis is the electron supply to cytochrome P450_{sc} from adrenodoxin reductase [61,62]. It has been demonstrated that in purified human syncytiotrophoblast mitochondria [63] or in the isolated steroidogenic contact sites [20], the addition of 22(*R*)-hydroxycholesterol increases progesterone synthesis compared with the control condition (*i.e.* mitochondria were incubated with isocitrate as oxidable substrate in a medium that promotes progesterone synthesis; see Refs. [20,21,28,32] and the **Materials and methods** section). This suggests that electron supply to P450_{sc} might not be the limiting-step. The addition of 22(*R*)-hydroxycholesterol, a cholesterol analog that freely reaches cytochrome P450_{sc} [33], rendered three-fold increases in progesterone production, even if proteases were inhibited with 1,10-phenanthroline (Fig. 5A) and no STARD3 proteolytic cleavage occurred (Fig. 4C). This evidences a specific effect of the protease inhibitor, as well as that the proteolytic products of STARD3 might be involved in cholesterol transport.

Mitochondrial metalloprotease activity, relative to alkaline pH; simultaneous proteolytic activation of STARD3; and an increase in progesterone synthesis, were observed (see Figs. 1, 2 and 4). Moreover, the proteolysis of 55-kDa STARD3 into a STARD3-28 kDa protein was associated with the maximal rate of progesterone synthesis observed (Fig. 2). It has been shown that the N-218 STARD3 protein (with similar size to STARD3-28 kDa) has substantial STAR-like activity in transfected cells [10]. In addition, Bose et al. [40] used a total protein homogenate from midterm human placenta to show that the presence of the full-length STARD3 protein and various proteolytic products, among which the 28-kDa peptide was predominant. However, purified syncytiotrophoblast mitochondria were used in this work to demonstrate that mitochondrial metalloproteases could be responsible for the proteolytic transformation of STARD3 into the STARD3-28 kDa protein, which could be involved in cholesterol transfer between mitochondrial membranes. Furthermore, the addition of the protein N-218 STARD3 or the STARD3-proteolytic-products (*i.e.* the STARD3-28 kDa protein which is released from mitochondria while progesterone synthesis occurs) to isolated syncytiotrophoblast mitochondria produced a similar enhancement of steroidogenesis (Fig. 6C), highlighting the role of STARD3 and its proteolytic product, the STARD3-28 kDa protein. Currently, transfection of HEK-293 cells with the whole progesterone synthesis machinery and the N-218 STARD3 protein is being performed in our laboratory to determine if STARD3 cleavage by proteases is the key step in progesterone synthesis. However, with all the results described so far, we propose that STARD3 is processed *in vivo* by metalloproteases from human syncytiotrophoblast mitochondria to the STARD3-28 kDa protein, a product similar to N-218 STARD3 that might promote steroidogenesis in a similar way to that described in the proposed model for the STARD1 protein (Fig. 7).

Although less is known about the roles of mitochondrial proteases in mammalian cells, it has been shown that loss-of-function mutations in human genes encoding mitochondrial proteases are often associated with clinical disorders [64–67]. Therefore, molecular and biochemical characterization of such proteolytic activities is of the utmost importance, as suggested by Ref. [68]. Finally, future research using STARD3 knockout mice [69] will be relevant to determine the specific cellular location of STARD3 and its role in reproduction.

The present study suggests that the STARD3 protein can be used as an authentic natural substrate to explore multiple mitochondrial proteases, to provide new insights into their mode of action in healthy and diseased steroidogenic cells, and to allow understanding of the different ways in which steroids are produced.

Acknowledgements

This work was supported by grants IN211912, IN217609 and IN214914 from Dirección General de Apoyo al Personal Académico de la Universidad Nacional Autónoma de México, and the grant 168025 from Consejo Nacional de Ciencia y Tecnología (CONACYT). Mercedes Esparza-Perusquía is a PhD student of the Biological Science Program of Universidad Nacional Autónoma de México (511021118) and fellow to CONACYT (254400). Héctor Flores-Herrera is a PhD student of the Biomedical Science Program of Universidad Nacional Autónoma de México (513025057). We thank Dr. Jerome Strauss (Virginia Commonwealth University) for the STARD3 (MLN64)-Ab. We also thank Dr. José Luis Pérez-García (Facultad de Medicina, UNAM) and Dra. Elizabeth Rodríguez Salinas for reviewing the correct usage of English in this manuscript and Dr. Esther Urrutia for her support in the statistical analysis of data.

References

- [1] M. Koppen, T. Langer, Protein degradation within mitochondria: versatile activities of AAA proteases and other peptidases, *Crit. Rev. Biochem. Mol. Biol.* 42 (2007) 221–242.

- [2] B.J. Clark, J. Wells, S.R. King, D.M. Stocco, The purification, cloning, and expression of a novel luteinizing hormone-induced mitochondrial protein in MA-10 mouse Leydig tumor cells. Characterization of the steroidogenic acute regulatory protein (StAR), *J. Biol. Chem.* 269 (1994) 28314–28322.
- [3] D. Lin, T. Sugawara, J.F. Strauss III, B.J. Clark, D.M. Stocco, P. Saenger, A. Rogol, W.L. Miller, Role of steroidogenic acute regulatory protein in adrenal and gonadal steroidogenesis, *Science* 267 (1995) 1828–1831.
- [4] C.B. Kallen, J.T. Billheimer, S.A. Summers, S.E. Stayrook, M. Lewis, J.F. Strauss III, Steroidogenic acute regulatory protein (StAR) is a sterol transfer protein, *J. Biol. Chem.* 273 (1998) 26285–26288.
- [5] D.M. Stocco, The steroidogenic acute regulatory (StAR) protein two years later. An update, *Endocrine* 6 (1997) 99–109.
- [6] X. Wang, Z. Liu, S. Eimerl, R. Timberg, A.M. Weiss, J. Orly, D.M. Stocco, Effect of truncated forms of the steroidogenic acute regulatory protein on intramitochondrial cholesterol transfer, *Endocrinology* 139 (1998) 3903–3912.
- [7] D.M. Stocco, B.J. Clark, Regulation of the acute production of steroids in steroidogenic cells, *Endocr. Rev.* 17 (1996) 221–244.
- [8] J. Orly, D.M. Stocco, The role of the steroidogenic acute regulatory (StAR) protein in female reproductive tissues, *Horm. Metab. Res.* 31 (1999) 389–398.
- [9] N. Cherradi, M.F. Rossier, M.B. Vallotton, R. Timberg, I. Friedberg, J. Orly, X.J. Wang, D.M. Stocco, A.M. Capponi, Submitochondrial distribution of three key steroidogenic proteins (steroidogenic acute regulatory protein and cytochrome P450_{sc} and 3 β -hydroxysteroid dehydrogenase isomerase enzymes) upon stimulation by intracellular calcium in adrenal glomerulosa cells, *J. Biol. Chem.* 272 (1997) 7899–7907.
- [10] H. Watari, F. Arakane, C. Moog-Lutz, C.B. Kallen, C. Tomasetto, G.L. Gerton, M.C. Rio, M.E. Baker, J.F. Strauss III, MLN64 contains a domain with homology to the steroidogenic acute regulatory protein (StAR) that stimulates steroidogenesis, *Proc. Natl. Acad. Sci. U. S. A.* 94 (1997) 8462–8467.
- [11] T. Sugawara, J.A. Holt, D. Driscoll, J.F. Strauss III, D. Lin, W.L. Miller, D. Patterson, K.P. Clancy, I.M. Hart, B.J. Clark, D.M. Stocco, Human steroidogenic acute regulatory protein: functional activity in COS-1 cells, tissue-specific expression, and mapping of the structural gene to 8p11.2 and a pseudogene to chromosome 13, *Proc. Natl. Acad. Sci. U. S. A.* 92 (1995) 4778–4782.
- [12] C. Moog-Lutz, C. Tomasetto, C.H. Regnier, C. Wendling, Y. Lutz, D. Muller, M.P. Chenard, P. Basset, M.C. Rio, MLN64 exhibits homology with the steroidogenic acute regulatory protein (StAR) and is over-expressed in human breast carcinomas, *Int. J. Cancer* 71 (1997) 183–191.
- [13] F. Alpy, M.-E. Stoeckel, A. Dierich, J.-M. Escola, C. Wendling, M.-P. Chenardi, M.T. Vanier, J. Gruenberg, C. Tomasetto, M.-C. Rio, The steroidogenic acute regulatory protein homolog MLN64, a late endosomal cholesterol-binding protein, *J. Biol. Chem.* 276 (2001) 4261–4269.
- [14] P.F. Hall, Cytochromes P-450 and the regulation of steroid synthesis, *Steroids* 48 (1986) 131–196.
- [15] E.R. Simpson, M.R. Waterman, Regulation of the synthesis of steroidogenic enzymes in adrenal cortical cells by ACTH, *Annu. Rev. Physiol.* 50 (1988) 427–440.
- [16] W.L. Miller, Mitochondrial specificity of the early steps in steroidogenesis, *J. Steroid Biochem. Mol. Biol.* 55 (1995) 607–616.
- [17] J. Liu, M.B. Rone, V. Papadopoulos, Protein–protein interactions mediate mitochondrial cholesterol transport and steroid biosynthesis, *J. Biol. Chem.* 281 (2006) 38879–38893.
- [18] K. Morohaku, S.H. Pelton, D.J. Daugherty, W.R. Butler, W. Deng, V. Selvaraj, Translocator protein/peripheral benzodiazepine receptor is not required for steroid hormone biosynthesis, *Endocrinology* 155 (2014) 89–97.
- [19] M.G. Maldonado-Mercado, M.T. Espinosa-García, C. Gomez-Concha, J. Monreal-Flores, F. Martínez, Steroidogenesis in BeWo cells: role of protein kinase A and benzodiazepines, *Int. J. Biochem. Cell Biol.* 40 (2008) 901–908.
- [20] A. Uribe, J.F. Strauss III, F. Martínez, Contact sites from human placental mitochondria: characterization and role in progesterone synthesis, *Arch. Biochem. Biophys.* 413 (2003) 172–181.
- [21] S. Olvera-Sanchez, M.T. Espinosa-García, J. Monreal, O. Flores-Herrera, F. Martínez, Mitochondrial heat shock protein participates in placental steroidogenesis, *Placenta* 32 (2011) 222–229.
- [22] F. Arakane, T. Sugawara, H. Nishino, Z. Liu, J.A. Holt, D. Pain, D.M. Stocco, W.L. Miller, J.F. Strauss III, Steroidogenic acute regulatory protein (StAR) retains activity in the absence of its mitochondrial import sequence: implications for the mechanism of StAR action, *Proc. Natl. Acad. Sci. U. S. A.* 93 (1996) 13731–13736.
- [23] S.R. King, T. Ronen-Fuhrmann, R. Timberg, B.J. Clark, J. Orly, D.M. Stocco, Steroid production after in vitro transcription, translation, and mitochondrial processing of protein products of complementary deoxyribonucleic acid for steroidogenic acute regulatory protein, *Endocrinology* 136 (1995) 5165–5176.
- [24] T. Ronen-Fuhrmann, R. Timberg, S.R. King, K.H. Hales, D.B. Hales, D.M. Stocco, J. Orly, Spatio-temporal expression patterns of steroidogenic acute regulatory protein (StAR) during follicular development in the rat ovary, *Endocrinology* 139 (1998) 303–315.
- [25] F. Martínez, M. Kiriakidou, J.F. Strauss III, Structural and functional changes in mitochondria associated with trophoblast differentiation: methods to isolate enriched preparations of syncytiotrophoblast mitochondria, *Endocrinology* 138 (1997) 2172–2183.
- [26] A. Bensaoud, D. Weinstein, Assay of proteins in the presence of interfering materials, *Anal. Biochem.* 70 (1976) 241–250.
- [27] O.H. Lowry, N.J. Rosebrough, A.L. Farr, R.J. Randall, Protein measurement with the Folin phenol reagent, *J. Biol. Chem.* 193 (1951) 265–275.
- [28] O. Flores-Herrera, A. Uribe, C. Garcia-Perez, R. Milan, F. Martínez, 5'-p-Fluorosulfonylbenzoyl adenosine inhibits progesterone synthesis in human placental mitochondria, *Biochim. Biophys. Acta* 1585 (2002) 11–18.
- [29] B. Chance, G.R. Williams, The respiratory chain and oxidative phosphorylation, *Adv. Enzymol.* 17 (1956) 65–134.
- [30] J.C. Fischer, W. Ruitenbeek, J.A. Berden, J.M.F. Trijbels, J.H. Veerkamp, A.M. Stadhouders, R.C.A. Sengers, J.M. Janssen, Differential investigation of the capacity of succinate oxidation in human skeletal muscle, *Clin. Chim. Acta* 153 (1985) 23–36.
- [31] K. Kita, C.R.T. Vibat, S. Meinhardt, J.R. Guest, R.B. Gennis, One-step purification from *Escherichia coli* of complex II (succinate:ubiquinone oxidoreductase) associated with succinate-reducible cytochrome b556, *J. Biol. Chem.* 264 (1989) 2672–2677.
- [32] D. De Los Rios-Castillo, M. Zarco-Zavala, S. Olvera-Sanchez, J.P. Pardo, O. Juarez, F. Martínez, G. Mendoza-Hernandez, J.J. García-Trejo, O. Flores-Herrera, Atypical cristae morphology of human syncytiotrophoblast mitochondria role for complex V, *J. Biol. Chem.* 286 (2011) 23911–23919.
- [33] R.C. Tuckey, Cholesterol side-chain cleavage by mitochondria from the human placenta. Studies using hydroxycholesterols as substrates, *J. Steroid Biochem. Mol. Biol.* 42 (1992) 883–890.
- [34] U.K. Laemmli, Cleavage of structural proteins during the assembly of the heat of bacteriophage T4, *Nature* 227 (1970) 680–685.
- [35] J. Huotari, A. Helenius, Endosome maturation, *EMBO J.* 30 (2011) 3481–3500.
- [36] K. Subramanian, W.E. Balch, NPC1/NPC2 function as a tag team duo to mobilize cholesterol, *Proc. Natl. Acad. Sci. U. S. A.* 105 (2008) 15223–15224.
- [37] J. Reitz, K. Gehrig-Burger, J.F. Strauss III, G. Gimp, Cholesterol interaction with the related steroidogenic acute regulatory lipid-transfer (START) domains of StAR (STARD1) and MLN64 (STARD3), *FEBS J.* 275 (2008) 1790–1802.
- [38] J.L. Thomas, R.P. Myers, R.C. Strickler, Human placental 3 beta-hydroxy-5-ene-steroid dehydrogenase and steroid 5 Δ 4-ene-isomerase: purification from mitochondria and kinetic profiles, biophysical characterization of the purified mitochondrial and microsomal enzymes, *J. Steroid Biochem.* 33 (1989) 209–217.
- [39] J. Navarrete, O. Flores-Herrera, A. Uribe, F. Martínez, Differences in cholesterol incorporation into mitochondria from hepatoma AS-30D and human term placenta, *Placenta* 20 (1999) 285–291.
- [40] H.S. Bose, R.M. Whittall, M.C. Huang, M.A. Baldwin, W.L. Miller, N-218 MLN64, a protein with StAR-like steroidogenic activity, is folded and cleaved similarly to StAR, *Biochemistry* 39 (2000) 11722–11731.
- [41] Z. Granot, R. Geiss-Friedlander, N. Melamed-Book, S. Eimerl, R. Timberg, A.M. Weiss, K.H. Hales, D.B. Hales, D.M. Stocco, J. Orly, Proteolysis of normal and mutated steroidogenic acute regulatory proteins in the mitochondria: the fate of unwanted proteins, *Mol. Endocrinol.* 17 (2003) 2461–2476.
- [42] Z. Granot, E. Silverman, R. Friedlander, N. Melamed-Book, S. Eimerl, R. Timberg, K.H. Hales, D.B. Hales, D.M. Stocco, J. Orly, The life cycle of the steroidogenic acute regulatory (StAR) protein: from transcription through proteolysis, *Endocr. Res.* 28 (2002) 375–386.
- [43] T. Minamikawa, D.A. Williams, D.N. Bowser, P. Nagley, Mitochondrial permeability transition and swelling can occur reversibly without inducing cell death in intact human cells, *Exp. Cell Res.* 246 (1999) 26–37.
- [44] H.S. Bose, V.R. Lingappa, W.L. Miller, Rapid regulation of steroidogenesis by mitochondrial protein import, *Nature* 417 (2002) 87–91.
- [45] K. Leonhard, A. Stiegler, W. Neupert, T. Langer, Chaperone-like activity of the AAA domain of the yeast Yme1 AAA protease, *Nature* 398 (1999) 348–351.
- [46] R.N. Rainey, J.D. Glavin, H.W. Chen, S.W. French, M.A. Teitell, C.M. Koehler, A new function in translocation for the i-AAA protease Yme1: import of polynucleotide phosphorylase into the intermembrane space, *Mol. Cell Biol.* 26 (2006) 8488–8497.
- [47] A. Chacinska, N. Pfanner, C. Meisinger, How mitochondria import hydrophilic and hydrophobic proteins, *Trends Cell Biol.* 12 (2002) 299–303.
- [48] T. Stan, J. Brix, J. Schneider-Mergener, N. Pfanner, W. Neupert, D. Rapaport, Mitochondrial protein import: recognition of internal import signals of BCS1 by the TOM complex, *Mol. Cell Biol.* 23 (2003) 2239–2250.
- [49] J. Hu, Z. Zhang, W.J. Shen, S. Azhar, Cellular cholesterol delivery, intracellular processing and utilization for biosynthesis of steroid hormones, *Nutr. Metab.* 7 (2010) 47–72.
- [50] P. Boström, L. Andersson, M. Rutger, J. Perman, U. Lidberg, B.R. Johansson, J. Fernandez-Rodriguez, J. Ericson, T. Nilsson, J. Borén, S.O. Olofsson, SNARE proteins mediate fusion between cytosolic lipid droplets and are implicated in insulin sensitivity, *Nat. Cell Biol.* 9 (2007) 1286–1293.
- [51] R. Jahn, R.H. Scheller, SNAREs—engines for membrane fusion, *Nat. Rev. Mol. Cell Biol.* 7 (2006) 631–643.
- [52] S. Martens, H.T. McMahon, Mechanisms of membrane fusion: disparate players and common principals, *Nat. Rev. Mol. Cell Biol.* 9 (2009) 543–556.
- [53] T.C. Sühof, J.E. Rothman, Membrane fusion: grappling with SNARE and SM proteins, *Science* 323 (2009) 474–477.
- [54] M.S. Jägerström, S. Polesie, Y. Wickström, B.R. Johansson, H.D. Schroder, K. Højlund, P. Boström, Lipid droplets interact with mitochondria using SNAP23, *Cell Biol. Int.* 33 (2009) 934–940.
- [55] M. Steegmaier, V. Oorschot, J. Klumperman, R.H. Scheller, Syntaxin 17 is abundant in steroidogenic cells and implicated in smooth endoplasmic reticulum membrane dynamics, *Mol. Cell Biol.* 11 (2000) 2719–2731.
- [56] N.J. Grant, R. Hepp, W. Krause, D. Aunis, P. Oehme, K. Langley, Differential expression of SNAP-25 isoforms and SNAP-23 in the adrenal gland, *J. Neurochem.* 72 (1999) 363–372.
- [57] M. Jo, M.C. Gieske, C.E. Payne, S.E. Wheeler-Price, J.B. Gieske, I.V. Ignatius, T.E. Curry, C. Ko, Development and application of a rat ovarian gene expression database, *Endocrinology* 145 (2004) 5384–5396.
- [58] J. Grosse, A. Bulling, C. Brucker, U. Berg, A. Amsterdam, A. Mayerhofer, M. Gratzl, Synaptosome-associated protein of 25 kilodaltons in oocytes and steroid-producing cells of rat and human ovary: molecular analysis and regulation by gonadotropins, *Biol. Reprod.* 63 (2000) 643–650.
- [59] M. Shimada, Y. Yanai, T. Okazaki, Y. Yamashita, V. Sriraman, W.C. Wilson, J.C. Richards, Synaptosomal-associated protein 25 gene expression is hormonally regulated during ovulation and is involved in cytokine/chemokine exocytosis from granulosa cells, *Mol. Endocrinol.* 21 (2007) 2487–2502.

- [60] J. Sileikyte, E. Blachly-Dyson, R. Sewell, A. Carpi, R. Menabò, F. Di Lisa, F. Ricchelli, P. Bernardi, M. Forte, Regulation of the mitochondrial permeability transition pore by the outer membrane does not involve the peripheral benzodiazepine receptor (Translocator Protein of 18 kDa (TSPO)), *J. Biol. Chem.* 289 (2014) 13769–13781.
- [61] R.C. Tuckey, J. Sadleir, The concentration of adrenodoxin reductase limits cytochrome p450_{scc} activity in the human placenta, *Eur. J. Biochem.* 263 (1999) 319–325.
- [62] R.C. Tuckey, A.J. McKinley, M.J. Headlam, Oxidized adrenodoxin acts as a competitive inhibitor of cytochrome P450_{scc} in mitochondria from the human placenta, *Eur. J. Biochem.* 268 (2001) 2338–2343.
- [63] M. Zhang, P. Liu, N.K. Dwyer, L.K. Christenson, T. Fujimoto, F. Martinez, M. Comly, J.A. Hanover, E.J. Blanchette-Mackie, J.F. Strauss III, MLN64 mediates mobilization of lysosomal cholesterol to steroidogenic mitochondria, *J. Biol. Chem.* 277 (2002) 33300–33310.
- [64] N. Wang, S. Gottesman, M.C. Willingham, M.M. Gottesman, M.R. Maurizi, A human mitochondrial ATP-dependent protease that is highly homologous to bacterial LON protease, *Proc. Natl. Acad. Sci. U. S. A.* 90 (1993) 11247–11251.
- [65] O. Hori, F. Ichinoda, T. Tamatani, A. Yamaguchi, N. Sato, K. Ozawa, Y. Kitao, M. Miyazaki, H.P. Harding, D. Ron, M. Tohyama, D.M. Stern, S. Ogawa, Transmission of cell stress from endoplasmic reticulum to mitochondria: enhanced expression of Lon protease, *J. Cell Biol.* 157 (2002) 1151–1160.
- [66] P. Bross, T.J. Corydon, B.S. Andresen, M.M. Jorgensen, L. Bolund, N. Gregersen, Protein misfolding and degradation in genetic diseases, *Hum. Mutat.* 14 (1999) 186–198.
- [67] G. Casari, M. De Fusco, S. Ciarmatori, M. Zeviani, M. Mora, P. Fernandez, G. De Michele, A. Filla, S. Coccozza, R. Marconi, A. Durr, B. Fontaine, A. Ballabio, Spastic paraplegia and OXPHOS impairment caused by mutations in paraplegin, a nuclear-encoded mitochondrial metalloprotease, *Cell* 93 (1998) 973–983.
- [68] L. Issop, M.B. Rone, V. Papadopoulos, Organelle plasticity and interactions in cholesterol transport and steroid biosynthesis, *Mol. Cell. Endocrinol.* 371 (2013) 34–46.
- [69] T. Kishida, I. Kostetskii, Z. Zhang, F. Martinez, P. Liu, S.U. Walkley, N.K. Dwyer, E.J. Blanchette-Mackie, G.L. Radice, J.F. 3er Strauss, Targeted mutation of the MLN64 START domain causes only modest alterations in cellular sterol metabolism, *J. Biol. Chem.* 279 (2004) 19276–19285.



Membrane potential regulates mitochondrial ATP-diphosphohydrolase activity but is not involved in progesterone biosynthesis in human syncytiotrophoblast cells



Oscar Flores-Herrera^{*}, Sofia Olvera-Sánchez, Mercedes Esparza-Perusquía, Juan Pablo Pardo, Juan Luis Rendón, Guillermo Mendoza-Hernández, Federico Martínez

Universidad Nacional Autónoma de México, Facultad de Medicina, Departamento de Bioquímica y Biología Molecular, México City, Mexico

ARTICLE INFO

Article history:

Received 16 May 2014

Received in revised form 17 September 2014

Accepted 7 October 2014

Available online 14 October 2014

Keywords:

ATP-diphosphohydrolase

Placental mitochondria

Mitochondrial bioenergetics

ATP hydrolysis

Progesterone synthesis

ABSTRACT

ATP-diphosphohydrolase is associated with human syncytiotrophoblast mitochondria. The activity of this enzyme is implicated in the stimulation of oxygen uptake and progesterone synthesis. We reported previously that: (1) the detergent-solubilized ATP-diphosphohydrolase has low substrate specificity, and (2) purine and pyrimidine nucleosides, tri- or diphosphates, are fully dephosphorylated in the presence of calcium or magnesium (Flores-Herrera 1999, 2002). In this study we show that ATP-diphosphohydrolase hydrolyzes first the nucleoside triphosphate to nucleoside diphosphate, and then to nucleotide monophosphate, in the case of all tested nucleotides. The activation energies (E_a) for ATP, GTP, UTP, and CTP were 6.06, 4.10, 6.25, and 5.26 kcal/mol, respectively; for ADP, GDP, UDP, and CDP, they were 4.67, 5.42, 5.43, and 6.22 kcal/mol, respectively. The corresponding Arrhenius plots indicated a single rate-limiting step for each hydrolyzed nucleoside, either tri- or diphosphate. In intact mitochondria, the ADP produced by ATP-diphosphohydrolase activity depolarized the membrane potential ($\Delta\Psi_m$) and stimulated oxygen uptake. Mitochondrial respiration showed the state-3/state-4 transition when ATP was added, suggesting that ATP-diphosphohydrolase and the F_1F_0 -ATP synthase work in conjunction to avoid a futile cycle. Substrate selectivity of the ATP-diphosphohydrolase was modified by $\Delta\Psi_m$ (*i.e.* ATP was preferred over GTP when the inner mitochondrial membrane was energized). In contrast, dissipation of $\Delta\Psi_m$ by CCCP produced a loss of substrate specificity and so the ATP-diphosphohydrolase was able to hydrolyze ATP and GTP at the same rate. In intact mitochondria, ATP hydrolysis increased progesterone synthesis as compared with GTP. Although dissipation of $\Delta\Psi_m$ by CCCP decreased progesterone synthesis, NADPH production restores steroidogenesis. Overall, our results suggest a novel physiological role for $\Delta\Psi_m$ in steroidogenesis.

© 2014 Elsevier B.V. All rights reserved.

1. Introduction

One of the main functions of the placenta is the synthesis of progesterone (P4) to maintain pregnancy. Mitochondria from human syncytiotrophoblast cells contain the machinery for steroid synthesis. It consists of an electron transport chain (ETC-P450_{scc}) composed by the cytochrome P450_{scc} (CYP11A1; EC 1.14.15.6) that receives electrons from NADPH + H⁺ through two proteins: adrenodoxine and adrenodoxine reductase. These proteins are located in the inner mitochondrial membrane and transform cholesterol into pregnenolone (P5) [3–5]. An additional enzyme, type II 3 β -hydroxysteroid-dehydrogenase- Δ 4-5 isomerase (3 β HSD) also embedded in the inner

mitochondrial membrane of syncytiotrophoblast cells, transforms pregnenolone into progesterone [4,5].

Mitochondria are best known as the major source of ATP in aerobic cells. Oxidative phosphorylation provides the main source of ATP. This metabolic pathway relies on the activity of two components: the oxidative and the phosphorylation systems. The oxidative system (*i.e.* respiratory chain) couples redox reactions to the production of a proton electrochemical gradient that drives the synthesis of ATP by the phosphorylation system (*i.e.* F_0F_1 -ATP synthase and the ADP/ATP and phosphate carriers). Studies conducted in primary and MA-10 tumor Leydig cells suggest an interrelation between steroidogenesis and oxidative phosphorylation. Steroidogenic mitochondria perform a double role: synthesize ATP and produce hormones. Steroidogenesis is affected when the classic mitochondrial electron-transport chain (ETC), membrane potential ($\Delta\Psi_m$), or ATP synthesis is disrupted [6,7], suggesting a close relationship between both metabolic pathways.

The relative amount of ETC-P450_{scc} and classic ETC components present in cells depends on the type of steroidogenic tissue. In acute-

^{*} Corresponding author at: Departamento de Bioquímica, Facultad de Medicina, Universidad Nacional Autónoma de México, Apdo. Postal 70-159, Coyoacán 04510, México, D. F., Mexico. Tel.: +52 1 55 56232510; fax: +52 1 55 56162419.

E-mail address: oflores@bq.unam.mx (O. Flores-Herrera).

regulated steroidogenic tissues (*i.e.* the adrenal gland and gonads) the content of ETC-P450scc is several times higher than in the classic ETC. In the syncytiotrophoblast, a constitutive steroidogenic tissue, the amounts of both electron transfer chain components is similar [8]. This suggests that the activity of both pathways will generate enough ATP for the cell to function properly and enough P4 to maintain pregnancy. Both processes are equally important for the physiological role of human placenta, and their activity must be tightly regulated.

Human syncytiotrophoblast mitochondria contain accessory enzymes, like the ATP-diphosphohydrolase. This enzyme is tightly bound to mitochondrial membranes and is involved in progesterone synthesis, mainly in cholesterol transport [1]. Studies have related cholesterol transport across the membranes of syncytiotrophoblast mitochondria with the activity of mitochondrial ATP-diphosphohydrolase [1,2]. Probably, ATP-diphosphohydrolase provides the required energy to drive cholesterol transport between mitochondrial membranes in an analogous way to that of the mitochondrial GDPase in the adrenal gland [9]. The underlying molecular mechanism involved remains unknown.

Simultaneously, in the intact and energized mitochondria, the ATP-diphosphohydrolase hydrolyzes ATP to ADP. The latter promotes oxygen uptake and ATP synthesis by the F_1F_0 -ATP synthase [10]. The activities of the ATP-diphosphohydrolase (ATP hydrolysis) and the F_1F_0 -ATP synthase (ATP synthesis) must be coordinated to avoid a futile cycle and energy dissipation.

Nevertheless, the physiological role of the ATP-diphosphohydrolase must be examined in intact syncytiotrophoblast mitochondria. Since ATP-diphosphohydrolase activity is involved in progesterone synthesis [2] and mitochondrial bioenergetics [10], regulatory mechanisms must be involved to keep trophoblast cells alive and functional. In the present work we evaluated the relationship between $\Delta\Psi_m$, ATP-diphosphohydrolase activity, and progesterone synthesis in syncytiotrophoblast mitochondria. Results suggest that ATP-diphosphohydrolase activity is modified by $\Delta\Psi_m$, but an increase in NADPH content and ATP hydrolysis supports progesterone synthesis when $\Delta\Psi_m$ decreases. This study puts forward a novel physiological role for the $\Delta\Psi_m$ in human placenta steroidogenesis.

2. Experimental procedures

2.1. Isolation of human syncytiotrophoblast mitochondria

Full term human placenta was collected immediately after normal delivery at the IMSS Hospital No. 4, approval under the Ethical Committee regulations. Mitochondria were prepared as previously described [3]. Briefly, placental cotyledons were placed in ice-cold 250 mM sucrose and 1 mM EDTA, 10 mM Tris, pH 7.4. The suspension was homogenized by means of a Polytron (Brinkmann Instruments, Westbury, NY, USA), at 3000 rev/min for 1 min for two cycles separated by an interval of 1 min. The whole process was carried out at 4 °C. The pH of the homogenate was adjusted to pH 7.4 with Tris and centrifuged at 1500 g for 15 min. The supernatant was recovered and centrifuged at 4000 g to pellet the cytotrophoblast mitochondria (*i.e.* heavy mitochondria). The supernatant was centrifuged again at 16,000 g for 15 min and the pellet containing the syncytiotrophoblast mitochondria (*i.e.* light mitochondria) was resuspended in the same solution and then centrifuged at 1500 g for 10 min to remove any remaining erythrocytes. Mitochondria were pelleted by centrifugation at 12,000 g for 10 min. The resulting syncytiotrophoblast mitochondria were loaded on a 35% sucrose solution (25 ml) and centrifuged at 15,000 g for 45 min at 4 °C. The mitochondrial fraction was collected, suspended in 250 mM of sucrose, 1 mM of EDTA, and 10 mM of Tris (pH 7.4) and centrifuged at 16,000 g for 15 min at 4 °C; the mitochondrial pellet was suspended in this buffer and stored at 4 °C. Protein concentration was measured as reported by [11,12].

2.2. Mitochondrial oxygen consumption

Oxygen uptake was estimated polarographically using a Clark type electrode in a mixture containing 250 mM of sucrose, 10 mM of HEPES pH 7.4, 1 mM of EGTA, 1 mM of EDTA, 10 mM of succinate, 10 mM of KH_2PO_4 , 5 mM of $MgCl_2$, 0.2% bovine serum albumin and 1 mg/ml of syncytiotrophoblast mitochondrial protein [2]. Temperature was set at 37 °C and oxygen consumption was stimulated by the addition of 300–500 nmol of ATP or ADP (state 3 of respiration). Respiratory control was defined as oxygen uptake rate of state 3/oxygen uptake rate of state 4 (state 4 of respiration started when all ADP was converted to ATP and respiration slowed down) [13]. Where indicated, mitochondria were incubated with 5 μ M carboxyatractyloside (CAT) to inhibit the translocation of adenine nucleotides by blocking the ADP/ATP carrier. Simultaneously, 10 μ M of carbonyl cyanide *m*-chlorophenyl hydrazine (CCCP) was added to depolarize the inner membrane and stimulate maximal oxygen uptake (*vide infra*). At the indicated times (see Figs. 3–5) an aliquot was withdrawn and used to determine the nucleotide concentration by HPLC (*vide infra*).

2.3. Mitochondrial membrane potential ($\Delta\Psi_m$)

The following media was used to determine the $\Delta\Psi_m$ of syncytiotrophoblast mitochondria: 125 mM of KCl; 5 mM of $MgCl_2$; 10 mM of acetate-Tris, pH 7.4; 10 mM of Tris-HCl, pH 7.4; 1 μ M of rotenone; 3.3 mM of H_3PO_4 , pH 7.4; 9.6 mM of Safranin O, and 1 mg of mitochondrial protein/ml. Generation of the membrane potential was initiated by adding 10 mM of succinate-Tris, pH 7.4 [14] to the solution containing syncytiotrophoblast mitochondria. Where indicated, mitochondria were incubated with 5 μ M CAT to inhibit the ADP/ATP carrier, and 10 μ M of CCCP was added to abolish $\Delta\Psi_m$. The membrane potential was evaluated in a double beam spectrophotometer by using the difference of wavelengths between 533 and 511 nm. The final volume was 1.5 ml and was kept at 25 °C.

2.4. Activity determinations of mitochondrial enzymes

Activities of complex I (NADH:DCPIP oxidoreductase) and complex II (succinate:DCPIP oxidoreductase) were determined spectrophotometrically at 600 nm by following the reduction of the artificial electron acceptor 2,6-dichlorophenol-indophenol (DCPIP; 50 μ M; $\epsilon_{DCPIP} = 21 \text{ mM}^{-1} \text{ cm}^{-1}$). Mitochondria were permeabilized with 0.01% Triton X100, incubated in 120 mM of KCl, 5 mM of $MgCl_2$, 1 mM of EGTA, 30 mM of KH_2PO_4 , pH 7.4, and either 500 μ M of NADH (complex I) or 2 mM of succinate (complex II). Complex II was activated by pre-incubation in the presence of 0.2 mM of phenazine methosulfonate (PMS) for 10 min at 25 °C [15,16]. Protein concentration of syncytiotrophoblast mitochondria was 50 μ g/ml and the reaction was started by the addition of NADH or succinate.

Mitochondrial ATP-diphosphohydrolase activity was determined either by nucleotide separation by HPLC (*vide infra*) or by measuring the release of inorganic phosphate (Pi) as described by Flores-Herrera et al. [1], using an ATP-diphosphohydrolase enriched fraction [1], or isolated syncytiotrophoblast mitochondria. Briefly, proteins (50 μ g) were incubated in a final volume of 0.5 ml at 30 °C in 30 mM Tris-HCl (pH 8.5), and the ATP-diphosphohydrolase reaction was started by the addition of the substrate (Mg-nucleotide complex) plus 1 mM of free Mg^{2+} . Aliquots were withdrawn at one minute intervals and used for nucleotide separation by HPLC (*vide infra*), or mixed with the malachite-molybdate-Triton X-100 mixture for Pi determination, as described by Lanzetta et al. [17]. The nucleotides used were ATP, ADP, GTP, GDP, UTP, UDP, CTP, CDP or TTP. The experiments were performed at least four times in duplicate.

2.5. Nucleotide separation by HPLC

Quantification of nucleotides was performed from either mitochondrial oxygen consumption experiments or a fraction enriched with a detergent-solubilized ATP-diphosphohydrolase. At the indicated times aliquots from ATP-diphosphohydrolase nucleotide hydrolysis activity or oxygen uptake determination were withdrawn and mixed with trichloroacetic acid (6% final) to stop the reaction. Nucleotides were separated by anion exchange HPLC on a Hypersil SAX column (120 Å, 5 µm, 250 × 4.6 mm) from Alltech International. The low concentration buffer (A) was 5 mM NH₄H₂PO₄ (pH 2.8) and the high concentration buffer (B) was 750 mM NH₄H₂PO₄ (pH 3.7). The sample was loaded on the column equilibrated with buffer (A). Then, a gradient of buffer (B) (30 min, 0–100%) was used for elution. The flow rate was 1 ml/min and detection was performed at 254 nm [18].

2.6. Mitochondrial progesterone synthesis

Progesterone synthesis was determined at 37 °C as reported previously [2] in 120 mM of KCl, 10 mM of MOPS, 0.5 mM of EGTA, 10 mM of isocitrate, 4 µg of aprotinin/ml, 1 µM of leupeptin, and 5 mM of KH₂PO₄, pH 7.4, in a final volume of 500 µl with 1 mg/ml of syncytiotrophoblast mitochondrial protein. Where indicated, 25 µM 22-(R)-hydroxy-cholesterol was added to verify cytochrome P450_{scc}, adrenodoxin, adrenodoxin reductase, and 3β-hydroxysteroid dehydrogenase activities [19]. After 20 min of incubation the reaction was arrested with 75 µl methanol and progesterone concentration was determined using a radioimmunoassay kit (Diagnostic Systems Laboratories, Inc. Webster, Texas, USA), according to the manufacturer's instructions. The concentration of progesterone at time zero was subtracted from the amount of progesterone quantified at 20 min and the resulting net progesterone synthesis was reported.

2.7. Sample preparation for native electrophoresis

The ATP-diphosphohydrolase from syncytiotrophoblast mitochondria was resolved by native PAGE following the general procedures reported previously [20,21], with minor modifications [22]. Briefly, syncytiotrophoblast (2 mg) mitochondria were suspended in 50 mM Bis-Tris and 500 mM 6-aminocaproic acid, pH 7.0, and solubilized by adding digitonin, at a detergent/protein ratio of 2 (g/g) in a final volume of 200 µl. The mixture was incubated for 30 min at 4 °C and centrifuged at 100,000 g for 30 min at 4 °C. The supernatants were recovered and immediately loaded on a linear polyacrylamide gradient gel (5–10%) for Blue Native PAGE (BN-PAGE) or Clear Native PAGE (CN-PAGE) [21]. The molecular weight of ATP-diphosphohydrolase activity was estimated by using the digitonin-solubilized bovine mitochondrial complexes as standard.

2.8. In-gel catalytic activity assays

The in-gel activity assays were performed as described by [18]. Briefly, gel strips were preincubated in 30 mM Tris-HCl, pH 8.5, 5% glycerol, 15 mM CaCl₂ for 30 min at 37 °C in the presence or absence of the complex V inhibitor oligomycin (5 µg/ml), or 5'-*p*-fluorosulfonylbenzoyl adenosine (FSBA, 1 mM) the ATP-diphosphohydrolase inhibitor. The equilibration solution was discarded and the gel strips were then added to the assay buffer containing 30 mM of Tris-HCl, pH 8.5, 5% glycerol, 15 mM of CaCl₂ and 5 mM of ATP, ADP, GTP or GDP, with or without oligomycin (5 µg/ml) or FSBA (1 mM). After incubation at 37 °C for approximately 2 h, nucleotide hydrolysis correlated with the development of white calcium phosphate precipitates. The reaction was stopped using 50% methanol, and subsequently, the gel was transferred to water and scanned against a dark background as described previously [22].

2.9. Isolation of steroidogenic contact sites

Steroidogenic contact sites were isolated as reported by Uribe et al. [23]. Briefly, 20–25 mg of mitochondrial protein was incubated at 4 °C with 10 mM H₃PO₄, adjusted to pH 7.3 with Tris base in the presence of 10 µg aprotinin/ml, 1 mM phenylmethylsulfonyl fluoride, and 10 µg leupeptin/ml. After incubation, sucrose was added to attain a concentration of 0.38 M. The resulting mixture was incubated for another 20 min at 4 °C and then centrifuged at 12,500 g for 10 min. The pellet containing mitoplasts was recovered and incubated in 1 mM H₃PO₄, adjusted to pH 7.3 with Tris base, for 20 min at 4 °C. Sucrose was added to reach a concentration of 0.31 M and the mixture was incubated for another 20 min at 4 °C and centrifuged at 102,000 g for 1 h. The pellet containing the inner membrane fraction was sonicated four times in an ice bath for five seconds in a MSE Soniprep 150 at maximal output. The fraction containing the inner membranes was layered over a discontinuous sucrose gradient (densities of 1.06 to 1.29 g/ml) and centrifuged at 96,000 g for 20 h at 4 °C. The steroidogenic contact sites were recovered at sucrose densities of 1.20–1.22 g/ml and washed three times with 0.25 M sucrose, 1 mM EDTA, with pH adjusted with Tris base to 7.4, and recovered by centrifugation at 137,000 g for 30 min at 4 °C. Protein content was determined as described above and the obtained samples were stored at –70 °C.

2.10. Tandem mass spectrometry (LC/ESI-MS/MS)

The mitochondrial inner membrane obtained during the isolation of steroidogenic contact sites (see previous section) was incubated in 100 mM ammonium bicarbonate (pH = 7.8) for 30 min and centrifuged at 100 000 ×g at 4 °C. The pellet containing the mitochondrial inner membranes was sent to the Proteomics Core Facility at the University of Arizona, USA.

2.11. Statistical analyses

Statistical analyses (one- and two-way analysis of variance, ANOVA) of the data were performed using Sigma Stat software, version 3.5. When necessary, nonlinear regression of the data to a single exponential decay equation was performed in Sigma Plot software, version 10.0.

2.12. Materials

Analytical grade reagents were purchased from Sigma Chemical Co. (St. Louis, MO, USA), E. Merck (Darmstadt, Germany), and BioRad (Hercules, CA, USA).

3. Results

3.1. Functional state of syncytiotrophoblast mitochondria

We calculated respiratory controls from oxygen uptake traces, using succinate as a substrate, to determine the functional integrity of isolated syncytiotrophoblast mitochondria (Table 1). Oxygen uptakes in state 3 and state 4 were 110 ± 18 ng atom of oxygen/min · mg protein, and 19 ± 6 ng atom of oxygen/min · mg protein, respectively. The value of the respiratory control was 5.5 ± 1.2. Adding CCCP to energized mitochondria increased the permeability of the membrane to protons and induced maximum respiration rate (200 ± 35 n atom g of oxygen/min · mg protein) and dissipation of ΔΨ_m (Fig. 4 later in the paper), inhibiting oligomycin-sensitive-ATP synthesis. These data indicated functional coupling of respiration and ATP synthesis in syncytiotrophoblast mitochondria. In addition, activities of 110 ± 27 µmol/min · mg protein for the NADH:DCPIP oxidoreductase (complex I), and 7 ± 1.5 µmol/min · mg protein for the succinate:DCPIP oxidoreductase (complex II) were obtained (Table 1). These results indicated the presence of functional mitochondria that retained

Table 1
Bioenergetics and steroidogenic parameters of syncytiotrophoblast mitochondria.

<i>Oxygen uptake</i>	
State 3 ^a	110 ± 18 ng atom of oxygen/min · mg protein
State 4 ^b	19 ± 6 ng atom of oxygen/min · mg protein
Respiratory control ^c	5.5 ± 1.2
<i>Complexes activities^d</i>	
Complex I	110 ± 27 μmol/min · mg
Complex II	7 ± 1.5 μmol/min · mg
<i>Progesterone synthesis^e</i>	
Control	143 ± 1.5 ng progesterone/min · mg
+ 22(R)-hydroxy-cholesterol	606 ± 52 ng progesterone/min · mg

^a Defined as oxygen consumption stimulated by ADP added in presence of succinate as substrate. Values are the mean ± S.D. (n = 20 independent determinations from different placental tissue).

^b Defined as oxygen consumption reduction because all ADP added was converted to ATP. Values are the mean ± S.D. (n = 20 independent determinations from different placental tissue).

^c Respiratory control = oxygen uptake rate of state 3/oxygen uptake rate of state 4. Values are the mean ± S.D. (n = 20 independent determinations from different placental tissue).

^d Specific activities from complexes I and II were measured spectrophotometrically in sonicated mitochondria: complex I, NADH:DCPIP oxide reductase; and complex II, succinate:DCPIP oxide reductase. Complex II activity was stimulated as described in the [Experimental procedures](#) section. Values shows are the mean ± S.D. (n = 9 independent determinations from different placental tissue).

^e Progesterone synthesis was determined as described in the [Experimental procedures](#) section. The 22(R)-hydroxy-cholesterol was used to verify cytochrome P450_{sc}, adrenodoxin, adrenodoxin reductase and 3β-hydroxysteroid dehydrogenase activities [19]. Values here are the mean ± S.D. from four determinations, from four different placental tissues.

the ability to increase the consumption of oxygen and the synthesis of ATP upon the addition of ADP.

Human placental mitochondria are steroidogenic organelles that synthesize progesterone, due to the presence of the type II 3-β-hydroxy steroid dehydrogenase in their inner membrane [3–5]. We determined steroidogenic activity of syncytiotrophoblast mitochondria to verify their physiological function. As observed in [Table 1](#) synthesis of progesterone by syncytiotrophoblast mitochondria was 143 ± 12 ng progesterone/min · mg protein ([Fig. 6](#) later in the paper), reaching a maximum of 606 ± 52 ng progesterone/min · mg protein in the presence of 22-(R)-hydroxy-cholesterol, which is a soluble substrate used to verify cytochrome P450_{sc}, adrenodoxin, adrenodoxin reductase and 3β-hydroxysteroid dehydrogenase activities [19]. These results agree with the specialized role of syncytiotrophoblast tissue [3] and support the functional integrity of the isolated syncytiotrophoblast mitochondria used in this work.

3.2. Nucleotide hydrolysis by mitochondrial ATP-diphosphohydrolase

We designed the experiments in the present work to investigate the possible involvement of $\Delta\Psi_m$ in mitochondrial ATP-diphosphohydrolase activity and progesterone synthesis in human syncytiotrophoblast cells. We first obtained a detergent-solubilized ATP-diphosphohydrolase fraction to determine their nucleotide hydrolysis activity [1]. We monitored the time course of nucleotide hydrolysis by HPLC ([Figs. 1](#) and [1S](#)). Hydrolysis of nucleoside diphosphates (NDP) by mitochondrial ATP-diphosphohydrolase was associated with the accumulation of the corresponding nucleoside monophosphate (NMP), whether a purine or pyrimidine nucleotide was involved ([Figs. 1A](#) and [2S](#)). A transient accumulation of NDP was observed when a nucleoside triphosphate (NTP) was hydrolyzed. NDP were dephosphorylated to NMP ([Figs. 1B](#) and [2S](#)). Since this hydrolyzing activity is exerted by the mitochondrial ATP-diphosphohydrolase, it can be inhibited by 5'-p-fluorosulfonyl benzoyl adenosine [1]. The kinetics of ATP-diphosphohydrolase was similar regardless of the substrate of choice ([Figs. 1](#) and [2S](#)), confirming its low substrate specificity [1]. Additionally, we determined the activation energy (E_a) for the

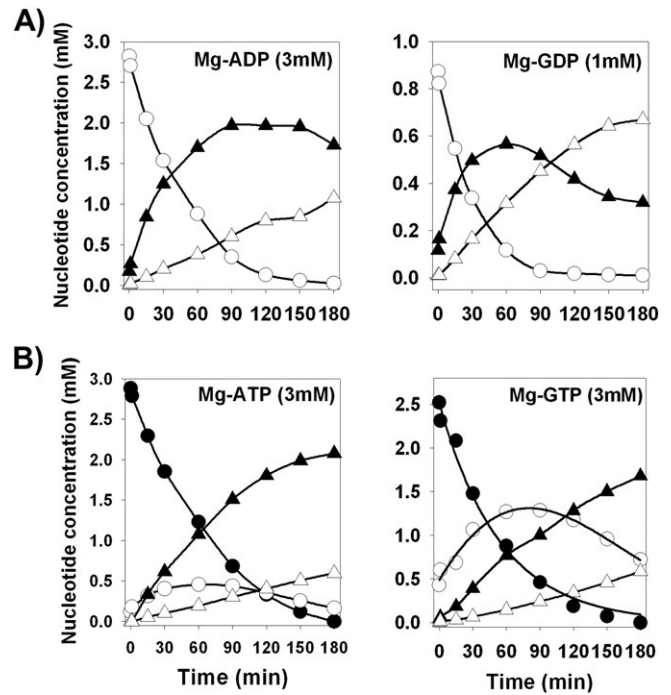


Fig. 1. Nucleotide hydrolysis of isolated syncytiotrophoblast mitochondrial ATP-diphosphohydrolase. ATP-diphosphohydrolase from syncytiotrophoblast mitochondria was isolated and its hydrolytic nucleotide activity was determined as described in the [Experimental procedures](#) section. Nucleotide concentration was quantified at different times by HPLC. A) Hydrolysis of Mg-ADP (3 mM) or Mg-GDP (1 mM) by mitochondrial ATP-diphosphohydrolase: (○) = nucleoside diphosphate (NDP); (▲) = nucleoside monophosphate (NMP); (Δ) = nucleoside. B) Hydrolysis of Mg-ATP (3 mM) or Mg-GTP (3 mM) by mitochondrial ATP-diphosphohydrolase: (●) = nucleoside triphosphate (NTP); (○) = NDP; (▲) = NMP; (Δ) = nucleoside. The figure shows representative experiments.

solubilized ATP-diphosphohydrolase activity by measuring the reaction rate constant (V_{max}) at different temperatures and by plotting $\ln(V_{max})$ versus $1/T$ ([Fig. 3S](#)). Data were adjusted to the integrated form of the Arrhenius equation: $E_a = ((RT_2T_1) / (T_2 - T_1)) \cdot \ln(V_{max})$. The Arrhenius plot was linear in the temperature range spanning 10–55 °C ([Fig. 3S](#)), suggesting a single rate-limiting step. A sudden drop in the Arrhenius plot at low $1/T$ (high temperature, 60–70 °C) indicated protein denaturation ([Fig. 3S](#)). The E_a values for nucleoside triphosphates such as ATP, GTP, UTP, and CTP were 6.06, 4.10, 6.25, and 5.26 kcal/mol, respectively. For ADP, GDP, UDP, and CDP the E_a values were 4.67, 5.42, 5.43, and 6.22 kcal/mol, respectively. These results suggest that solubilized ATP-diphosphohydrolase had a similar rate-limiting step for either tri- or diphosphates nucleoside hydrolysis.

3.3. BN-PAGE analysis

To support the hypothesis that a single enzyme hydrolyzes ATP, ADP, GTP, or GDP, we conducted blue native PAGE of syncytiotrophoblast mitochondria ([Fig. 2](#)). Since the calcium–nucleotide complex can be used as a substrate by the mitochondrial ATP-diphosphohydrolase, but not by the F_1F_0 -ATP synthase, the in-gel activity was determined in the presence of $CaCl_2$ with ATP, ADP, GTP or GDP as substrate, in the absence or presence of oligomycin (not shown). Phosphohydrolytic activity produced a single band of calcium phosphate precipitate ([Fig. 2](#)), which displayed no oligomycin inhibition but identical electrophoretic mobility with an apparent molecular weight of 167 kDa. FSBA inhibited ATP-diphosphohydrolase activity with any of the tested substrates ([Fig. 2](#)). Results indicated that solubilized ATP-diphosphohydrolase from syncytiotrophoblast mitochondria was the only enzyme capable of hydrolyzing calcium–nucleotide complexes. These results confirmed the wide spectrum of substrates

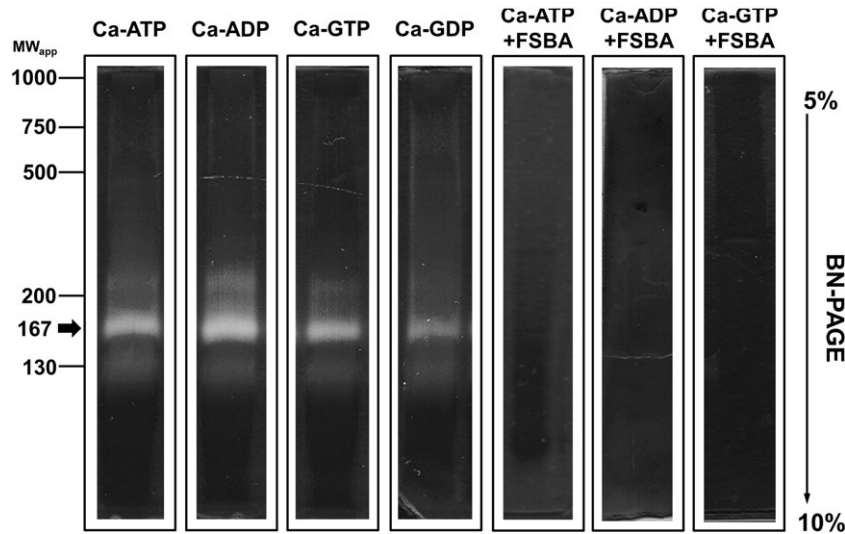


Fig. 2. In-gel activity of digitonin-solubilized mitochondrial ATP-diphosphohydrolase from syncytiotrophoblast in native gels. Mitochondria were solubilized using digitonin (2 g/g of protein), and ATP-diphosphohydrolase was separated by BN-PAGE. Native-PAGE was performed in linear polyacrylamide gradient gels from 5 to 10% as described in the [Experimental procedures](#) section. Electrophoresis was conducted at 30 V for 12 h at 4 °C. In the spots containing ATP-diphosphohydrolase activity, white precipitates of calcium phosphate appeared within 2 h after the addition of Ca-ATP, Ca-ADP, Ca-GTP or Ca-GDP complex. The presence of 1 mM of FSBA inhibited ATP hydrolysis while oligomycin (5 µg/mg) did not modify the hydrolytic activity (data not shown). The molecular weight of ATP-diphosphohydrolase activity was estimated by using the digitonin-solubilized bovine mitochondrial complexes as standard. The figure shows representative experiments from four different mitochondrial preparations.

that ATP-diphosphohydrolase exhibits. In the second approach, we analyzed the ATP-diphosphohydrolase activity associated to intact mitochondria undergoing oxygen uptake or progesterone synthesis. The tandem mass spectrometry (LC/ESI-MS/MS) analysis showed the isoform 2 of the ATP-diphosphohydrolase (P49961-2|ENTP1_HUMAN), which belong to the ectonucleoside triphosphate diphosphohydrolase group, with a molecular weight of 59 kDa. The hydropathy analysis

displayed four transmembrane segments (see Fig. 4S). However, no mitochondrial targeting presequence was observed.

3.4. ATP hydrolysis by ATP-diphosphohydrolase stimulates mitochondrial respiration and depolarizes the inner membrane

To evaluate the ATP-diphosphohydrolase activity during mitochondrial oxygen uptake, the time course of the hydrolysis of nucleotides was analyzed by HPLC (Fig. 3). Syncytiotrophoblast mitochondria were energized by succinate, and oxygen uptake was stimulated by ATP (Fig. 3A). Results show that ATP-diphosphohydrolase hydrolyzed ATP and produced ADP (Fig. 3B), which in turn was translocated into the mitochondrial matrix, where it was transformed to ATP by the F_1F_0 -ATP synthase at the expense of the proton electrochemical gradient ($\Delta\mu_{H^+}$). Simultaneously, the inner membrane was depolarized (Fig. 3C). This series of events is defined as state 3 of mitochondrial respiration [13], and continues until the ATP-diphosphohydrolase hydrolyses ATP to ADP and ADP to AMP. In this situation $\Delta\Psi_m$ increased (Fig. 3C) and mitochondrial respiration decreased to a minimum, a condition that is known as state 4 of mitochondrial respiration [13] (Fig. 3). A new cycle of mitochondrial oxygen uptake stimulation, depolarization of $\Delta\Psi_m$, ATP synthesis and ATP-diphosphohydrolase activity was observed when ADP was added (Fig. 3). It is crucial to highlight that ATP-diphosphohydrolase activity is closely related to an increase in mitochondrial respiration and inner membrane depolarization in the presence of ATP. Additionally, syncytiotrophoblast mitochondria contain a phosphatase [1] that is responsible for adenosine production from AMP. However, inhibiting it with phenylalanine or sodium molybdate [1] did not modify the results described (data not shown).

3.5. Substrate selectivity and catalytic rate by ATP-diphosphohydrolase during mitochondrial respiration

We added a different nucleoside triphosphate to support the notion that the ATP-diphosphohydrolase activity could be modified by mitochondrial bioenergetics during oxygen uptake (Fig. 4). After the transition from state 3 to 4 of mitochondrial respiration, addition of GTP did not stimulate oxygen uptake (Fig. 4A), nor depolarized the inner membrane (Fig. 4B). Although GTP was hydrolyzed by ATP-

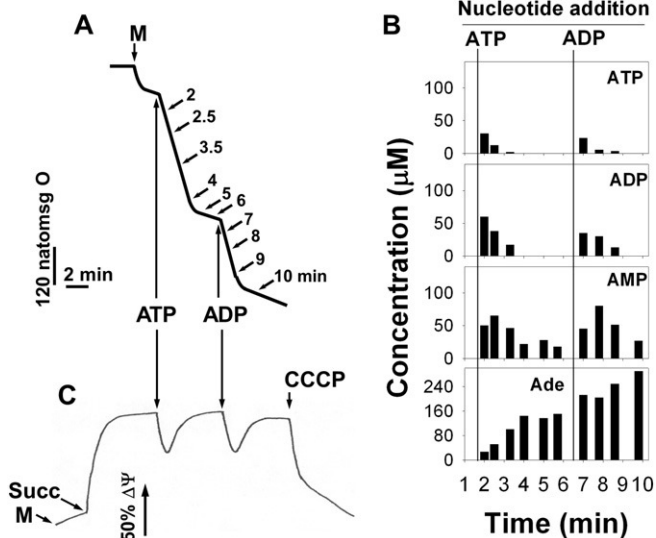


Fig. 3. Mitochondrial ATP-diphosphohydrolase induces mitochondrial oxygen consumption and $\Delta\Psi_m$ depolarization. Syncytiotrophoblast mitochondria were isolated as described in the [Experimental procedures](#) section. A) Mitochondria were incubated in oxygen uptake medium at 37 °C and mitochondrial respiration was stimulated by ATP or ADP addition. Arrows indicate sequential additions of (M) mitochondria (1 mg/ml); ATP (130 µM); or ADP (130 µM). Simultaneous to mitochondrial oxygen uptake recording, an aliquot was withdrawn at the indicated time (bold arrows) and used to quantify nucleotide concentration by HPLC (B). Concentrations of ATP, ADP, AMP or Adenosine (Ade) at different times after addition of ATP or ADP during the time course of oxygen uptake showed in (A). C) $\Delta\Psi_m$ measurement with Safranine O as described in the [Experimental procedures](#) section. Arrows indicate sequential additions of mitochondria (M); 10 mM succinate (Succ); ATP (130 µM); ADP (130 µM); CCCP (10 µM). In all cases curves show representative experiments of at least four different mitochondrial preparations.

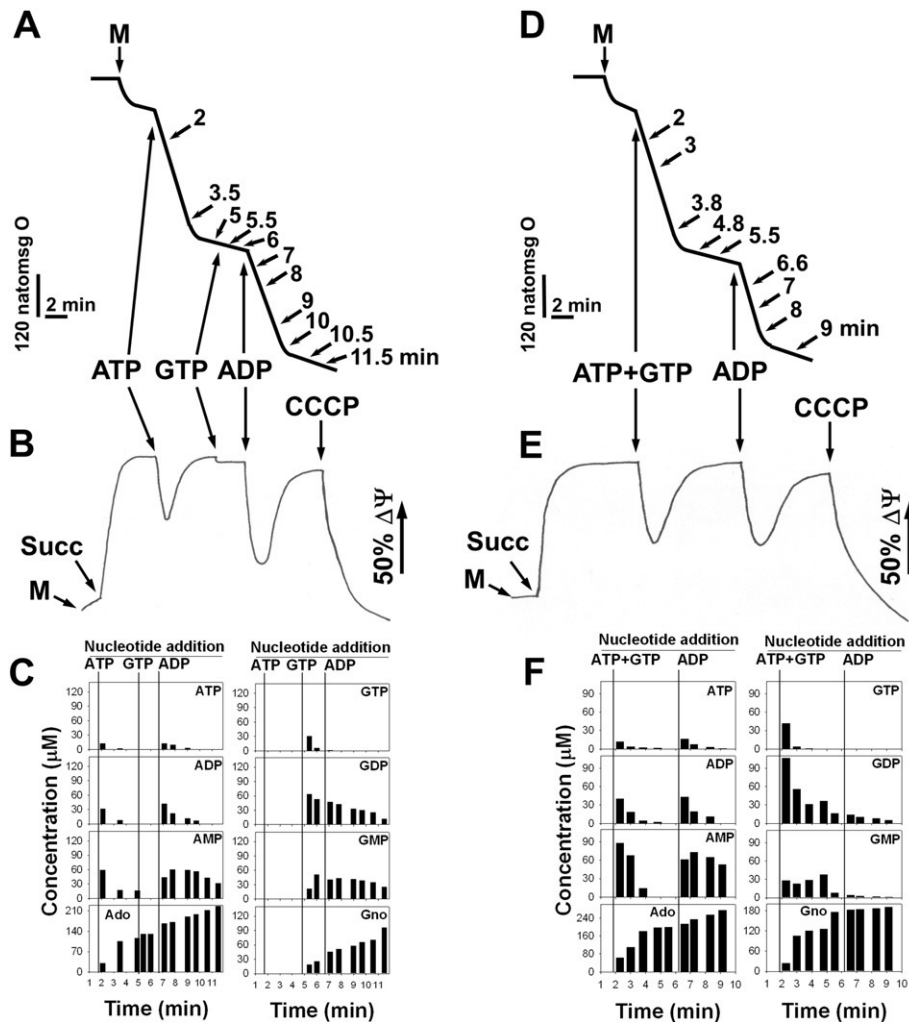


Fig. 4. Mitochondrial ATP-diphosphohydrolase selectively hydrolyzes ATP in energized and coupled mitochondria. **A**) Mitochondria were incubated in oxygen uptake medium at 37 °C and mitochondrial respiration was stimulated by ATP or ADP addition. The arrows indicate sequential additions of (M) mitochondria (1 mg/ml); ATP (130 μM); GTP (130 μM); or ADP (130 μM). During mitochondrial oxygen uptake an aliquot was withdrawn at the indicated time (bold arrows) and used to quantify nucleotide concentration by HPLC. **B**) $\Delta\Psi_m$ measurement with Safranin O as described in Fig. 3. Arrows indicate the sequential additions of mitochondria (M); 10 mM succinate (Succ); ATP (130 μM); GTP (130 μM); ADP (130 μM); CCCP (10 μM). **C**) Concentrations of ATP, ADP, AMP, Ade, GTP, GDP, GMP, or guanosine (Gno) after addition of ATP, GTP or ADP during oxygen uptake. **D**) Mitochondria were incubated in oxygen uptake medium and a mixture of ATP (130 μM) and GTP (130 μM) was added to stimulate respiration. Oxygen uptake (**D**), $\Delta\Psi_m$ measurement (**E**) and nucleotide concentration (**F**) were determined as described in the Experimental procedures section. Arrows indicate sequential additions of mitochondria (M); 10 mM succinate (Succ); a mixture of ATP + GTP (130 μM each one); ADP (130 μM); CCCP (10 μM). In all cases curves show representative experiments of at least four different and independent mitochondrial preparations.

diphosphohydrolase ($855 \pm 137 \mu\text{mol}/\text{mg}\cdot\text{min}$), its catalytic rate was lower than that observed with ATP ($1910 \pm 265 \mu\text{mol}/\text{mg}\cdot\text{min}$) (Figs. 4C and 6B). Indeed, addition of ADP, in the presence of GDP produced from GTP hydrolysis, induced oxygen consumption and decreased $\Delta\Psi_m$, while the rate of GDP hydrolysis was very small (Fig. 4C). This result contrasts with the one of the detergent-solubilized ATP-diphosphohydrolase, which displays a similar hydrolysis rate for ATP, ADP, GTP, and GDP (Fig. 1).

To examine substrate selectivity of the mitochondrial ATP-diphosphohydrolase, we added simultaneously ATP and GTP (Fig. 4D). The enzyme consistently hydrolyzed ATP instead of GTP (Fig. 4E), and the produced ADP induced oxygen consumption and membrane depolarization (Fig. 4D and E, respectively).

3.6. $\Delta\Psi_m$ determines ATP-diphosphohydrolase substrate selectivity and catalytic rate

$\Delta\Psi_m$ is a central component of mitochondrial metabolism that provides the driving force for oxidative phosphorylation, for the import of proteins and metabolites, and for regulating the activity of membrane proteins like the adenine nucleotide translocase (ANT) [24–26].

We examined the effect of the mitochondrial protonophore and respiration uncoupler CCCP on $\Delta\Psi_m$ to assess whether the ATP-diphosphohydrolase substrate selectivity was mediated by $\Delta\Psi_m$ (Fig. 5). Syncytiotrophoblast mitochondria were incubated with CAT to inhibit the adenine nucleotide translocase and avoid ATP internalization into the mitochondrial matrix in the presence of CCCP (see the Experimental procedures section). When CCCP was added to mitochondria, oxygen uptake was stimulated and $\Delta\Psi_m$ collapsed (Fig. 5A and B, respectively). Further addition of ATP did not modify oxygen consumption nor $\Delta\Psi_m$. Importantly, ATP-diphosphohydrolase activity was lower ($812 \pm 30 \mu\text{mol}/\text{mg}\cdot\text{min}$) when compared to control conditions, (*i.e.* in the absence of CCCP). Also, a transient accumulation of ADP was observed (Figs. 5C and 6B).

In identical experimental conditions, GTP addition to CCCP-uncoupled mitochondria rendered a lower rate of GTP hydrolysis ($642 \pm 37 \mu\text{mol}/\text{mg}\cdot\text{min}$), and a transient accumulation of GDP (Figs. 5D–F and 6B), similar to the results obtained with ATP. To compare ATP and GTP hydrolysis in CCCP-uncoupled mitochondria, both nucleotides were added at the same time (Fig. 5G–I). The ATP-diphosphohydrolase catalyzed simultaneously the hydrolysis of both nucleotides and displayed similar velocities (Fig. 5I), without any

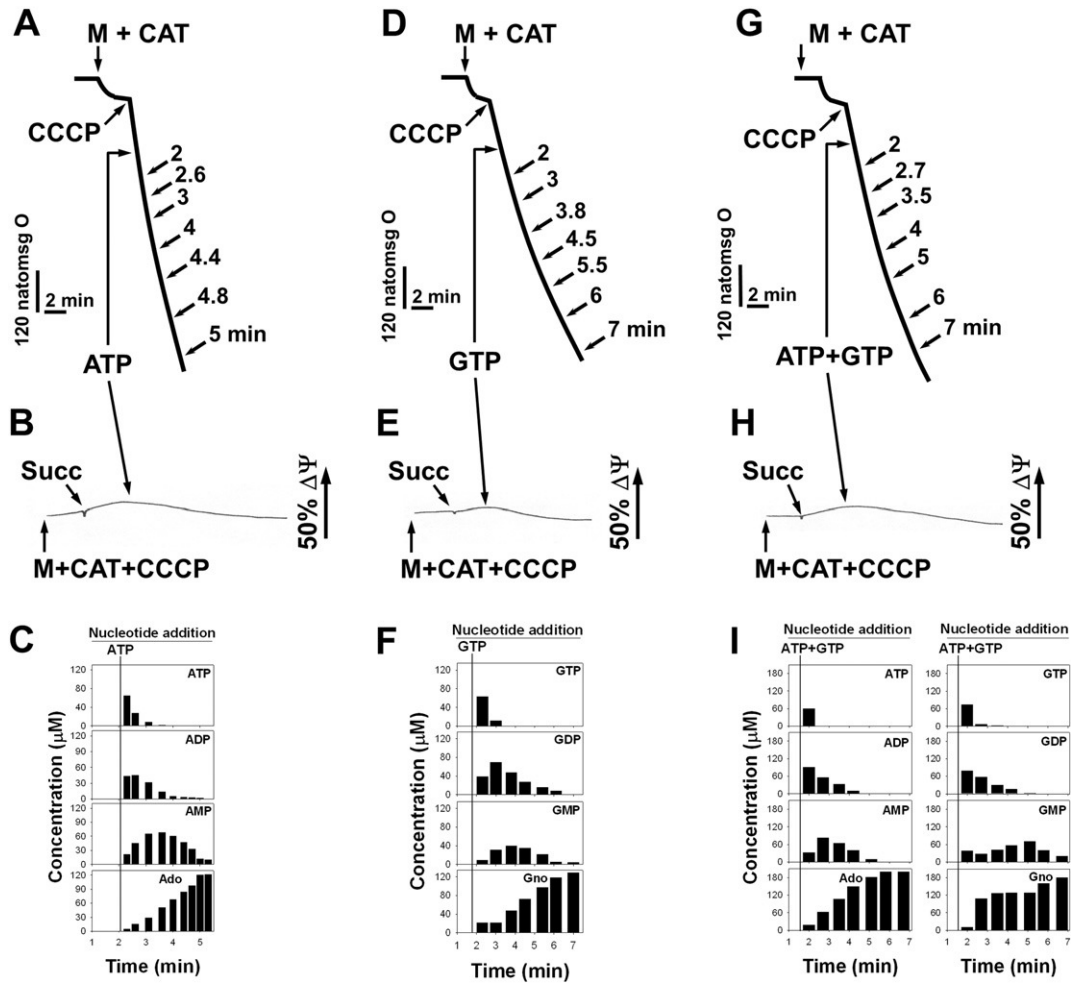


Fig. 5. $\Delta\Psi_m$ regulates syncytiotrophoblast mitochondrial ATP-diphosphohydrolase substrate selectively. Mitochondria were incubated in oxygen uptake medium (described in the [Experimental procedures](#) section) plus 5 μM carboxyatractyloside (CAT) to inhibit the translocation of adenine nucleotides by blocking the ADP/ATP carrier. CCCP (10 μM) was added to collapse $\Delta\Psi_m$ and obtain the maximum oxygen uptake rate. After CCCP, the addition of 130 μM ATP (A), 130 μM GTP (D) or an ATP + GTP mixture (130 μM each one, G) was performed. Mitochondria were incubated with CAT (5 μM), CCCP (10 μM), and 10 mM of succinate (Succ), and then 130 μM of ATP (B), 130 μM of GTP (E), or an ATP + GTP mixture (130 μM of each, H) was added. At the times indicated in the oxygen uptake recording, an aliquot was withdrawn to quantify the nucleotide concentration by HPLC when ATP (C), GTP (F), or ATP + GTP (I) were added. The figure shows representative experiments of at least four different and independent mitochondrial preparations.

selectivity for ATP as observed in [Fig. 4](#). This observation suggests that substrate selectivity of ATP-diphosphohydrolase (*i.e.* ATP versus GTP preference) is regulated by $\Delta\Psi_m$.

3.7. Progesterone synthesis by syncytiotrophoblast mitochondria

In intact syncytiotrophoblast mitochondria, ATP, ADP, GTP, and GDP hydrolysis by the ATP-diphosphohydrolase has been associated with progesterone synthesis, particularly with cholesterol flux between mitochondrial membranes [2]. As ATP-diphosphohydrolase inhibition with FSBA decreased progesterone production [2] we explored the control of $\Delta\Psi_m$ on progesterone synthesis ([Fig. 6A](#)). Syncytiotrophoblast mitochondria were incubated as described in the [Experimental procedures](#) section in the presence of isocitrate to maintain a high NADPH/NADP⁺ ratio to supply energy to P450_{scc} [27]. Under these conditions mitochondrial progesterone (P4) synthesis was 143 ± 12 ng P4/min·mg protein; it increased to 391 ± 10 ng P4/min·mg protein when ATP was added, and to 606 ± 52 ng P4/min·mg protein if 22-(R)-hydroxy cholesterol was present ([Fig. 6A](#)). The concomitant addition of ATP and 22-(R)-hydroxy cholesterol augmented progesterone production to 594 ± 82 ng P4/min·mg protein. This increase in progesterone synthesis was observed even in the presence of CCCP (427 ± 15 and 536 ±

12 ng/mg·min respectively) ([Fig. 6A](#)). The addition of ADP, GTP, or GDP slightly increased progesterone synthesis (340 ± 82; 206 ± 17, and 173 ± 19 ng P4/min·mg protein, respectively). However, when mitochondria were incubated without isocitrate, with the consequent suppression of NADPH synthesis, progesterone production decreased even in the presence of ATP, ADP, GTP or GDP (100 ± 10; 75 ± 12; 53 ± 9, and 44 ± 11 ng/mg·min, respectively) ([Fig. 6A](#)). ATP-diphosphohydrolase activity was evaluated simultaneously for progesterone synthesis ([Fig. 6B](#)). In the presence of $\Delta\Psi_m$ adenine nucleosides, tri- and diphosphates were preferentially hydrolyzed over guanosine nucleotides, *i.e.* GTP or GDP ([Fig. 6B](#), black bars). In the presence of CCCP (which collapsed the $\Delta\Psi_m$), ATP-diphosphohydrolase activity was similar with all nucleotides tested (ATP, ADP, GTP, and GDP) ([Fig. 6B](#), white bars). Although CAT was added prior to $\Delta\Psi_m$ dissipation with CCCP, it did not have any significant effect on ATP-diphosphohydrolase activity ([Fig. 6B](#), gray bars).

This suggested that $\Delta\Psi_m$ might be involved in cholesterol flow by regulating ATP-diphosphohydrolase activity, but for progesterone synthesis the NADPH/NADP⁺ ratio is important. To verify this possibility, we used the mitochondrial steroidogenic contact sites [23] from human placenta as an alternative experimental approach.

These contact sites can synthesize progesterone [23] since they contain the whole steroidogenic machinery, including the cytochrome

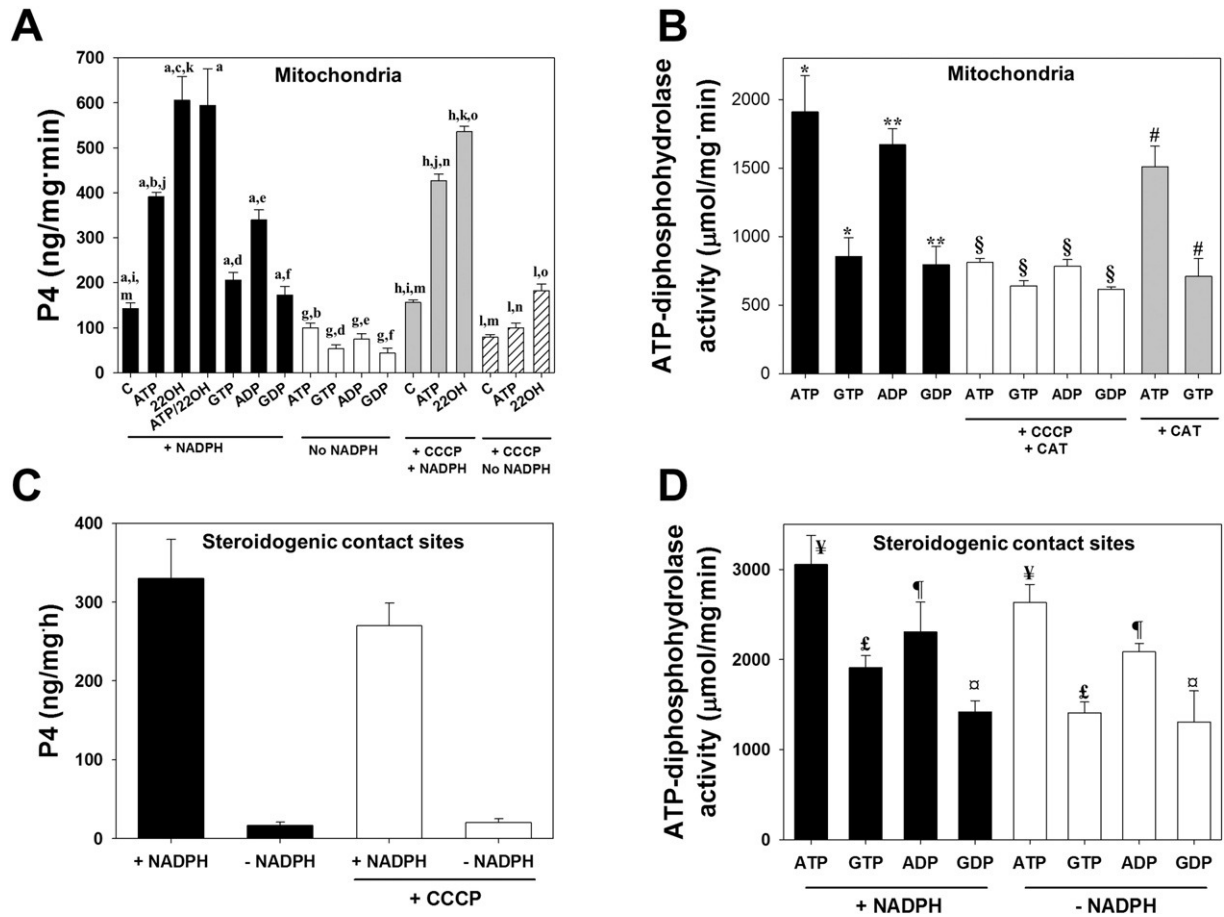


Fig. 6. Steroidogenesis and nucleotide hydrolysis in syncytiotrophoblast mitochondria or steroidogenic contact sites. A) Progesterone synthesis by intact mitochondria. Mitochondria were incubated in the presence (black bars) or absence (white bars) of isocitrate to maintain NADPH production (see text for details). ATP (1 mM), GTP (1 mM), ADP (1 mM), GDP (1 mM) or 22-hydroxy cholesterol (22OH, 25 μM) was added to stimulate progesterone synthesis. Alternatively, CCCP (10 μM) was added in the presence (gray bars) or absence (dashed bars) of isocitrate. The results are the mean ± S.D. of n = 4 different and independent mitochondrial preparations. B) ATP-diphosphohydrolase activity in intact mitochondria incubated in the presence (white bars) or absence (black bars) of CCCP. Results are the mean ± S.D. with n = 4. C) Progesterone production by steroidogenic contact sites in the presence (+NADPH) or absence (-NADPH) of 2 mM of NADPH. CCCP was added (white bars) to test its effect on progesterone synthesis. Results are the mean ± S.D. with n = 3. D) ATP-diphosphohydrolase activity by steroidogenic contact sites in the presence (+NADPH, black bars) or absence (-NADPH, white bars) of 2 mM NADPH. Results are the mean ± S.D. with n = 3. The one-way ANOVA analysis showed a statistically significant difference ($p \leq 0.001$) between different groups of data marked with: a, g, h, i, *, and **. The difference is greater than it would be expected by chance (all pairwise multiple comparison procedures were performed with the Tukey test). The comparison marked with § shows no significant difference ($p \leq 0.001$). The two way ANOVA analysis showed a statistically significant difference ($p \leq 0.005$) between groups marked with: b, c, d, e, f, i, j, k, m, n, o, ¥, £, ¥, and ¶ (all pairwise multiple comparison procedures were performed with the Holm-Sidak method).

P450scc, the 3-β-hydroxy-steroid dehydrogenase, the adrenodoxin and adrenodoxin reductase, the ATP-diphosphohydrolase [23], and a NADP-dependent isocitrate dehydrogenase [27]. It is important to mention that these contact sites do not generate $\Delta\Psi_m$, so that the participation of this parameter was excluded. Contact sites were isolated as described in the **Experimental procedures** section, incubated in either the absence or presence of isocitrate to stimulate NADPH production, with or without CCCP, and the amount of progesterone synthesis was determined (Fig. 6C). NADPH is the substrate of the adrenodoxin reductase that supports cytochrome P450scc activity, and isocitrate dehydrogenase activity regenerates NADPH [27]. Progesterone synthesis reached a value of 330 ± 50 ng/mg·h in the presence of NADPH production, while in the absence of NADPH there was no progesterone synthesis (Fig. 6C, black bars). CCCP had no effect on progesterone synthesis in the presence of NADPH (Fig. 6C, white bars). ATP-diphosphohydrolase activity associated with the contact sites was unaffected by the presence or absence of NADPH (Fig. 6D).

4. Discussion

Human placenta is essential to maintain pregnancy. Mitochondria of syncytiotrophoblast cells, besides generating ATP, synthesize

progesterone using cholesterol as a substrate [3]. Therefore, syncytiotrophoblast mitochondria must reconcile ATP synthesis with hormone production.

Isolated syncytiotrophoblast mitochondria retain their ability to couple oxygen uptake to ATP synthesis as well as their capacity to synthesize progesterone (Table 1). The specific hormone(s) or substance(s) that modulate P4 synthesis and ATP production during pregnancy are currently unknown [3,28]. The most striking observation of this work shows that the ATP-diphosphohydrolase, an accessory enzyme involved in cholesterol flux between outer and inner syncytiotrophoblast mitochondrial membranes [1,2], might be regulated by $\Delta\Psi_m$.

Kinetic characterization of the detergent-solubilized ATP-diphosphohydrolase from mitochondria showed that this enzyme had low substrate selectivity (Figs. 1 and 2). It was capable of hydrolyzing purine or pyrimidine, tri or diphosphate nucleotides with similar affinities [1]. Its activation energy showed values between 4 and 6 kcal/mol with a single rate-limiting step during catalysis.

In sharp contrast, ATP-diphosphohydrolase is regulated by $\Delta\Psi_m$ in energized mitochondria. If mitochondria were energized (*i.e.* with succinate), the ATP-diphosphohydrolase preferentially hydrolyzed ATP, even if other substrates such as GTP, were present (Fig. 4), and

promoted mitochondrial oxygen uptake coupled to ATP synthesis (Fig. 3). In energized mitochondria from all organisms tested, ADP but not ATP increased the respiration rate. This is controlled by the adenine nucleotide translocase (ANT), which does not recognize outer mitochondrial ATP if $\Delta\Psi_m$ is generated by ETC. This is a key control mechanism that prevents a futile-cycle and energy waste as heat.

In syncytiotrophoblast mitochondria energized with succinate, ATP addition induced oxygen uptake through the ATP-diphosphohydrolase activity, which hydrolyzed ATP to ADP and inorganic phosphate (Fig. 3 and [1,10]). The activities of the ATP-diphosphohydrolase (ATP hydrolysis) and F_1F_0 -ATP synthase (ATP synthesis) do not produce permanent oxygen uptake stimulation ([10] and the present study) as has been observed with the brain hexokinase associated with the outer mitochondrial membrane [29].

This observation is consistent with the proposed role for this enzyme [2]; it was suggested that the ATP-diphosphohydrolase could perform sequential hydrolysis of ATP to ADP, and ADP to AMP and simultaneously stimulate cholesterol transport between mitochondrial membranes for progesterone synthesis [2] (Fig. 7). Although cholesterol transfer during steroidogenesis in the adrenals glands occurs through a macromolecular complex that consists of outer membrane proteins such as the mitochondrial membrane translocator protein (TSPO), and the TSPO-associated protein PAP7 that bind and lead the regulatory subunit RI- α of the cAMP-dependent protein kinase (PKAR1 α) towards mitochondria [30], the TSPO protein in human syncytiotrophoblast mitochondria remains unidentified [31]. A potential candidate exists. A multiprotein complex, the steroidogenic contact sites, has been associated with cholesterol transport and steroidogenesis in human syncytiotrophoblast mitochondria [23]. These contact sites contain proteins such as HSP60 [32], ANT, VDAC, cytochrome P450_{sc}, adrenodoxin reductase, adrenodoxin, NADP-dependent isocitrate dehydrogenase, 3- β -hydroxysteroid dehydrogenase, STARD3 protein and ATP-diphosphohydrolase [3,23].

The molecular weight of the ATP-diphosphohydrolase calculated from native-gel was 163 kDa, in contrast with the 59 kDa determined

from tandem mass spectrometry. The reported molecular weight from SDS-PAGE, radiation-inactivation or gel filtration goes from 64 to 70 kDa [33–35]. The molecular weights in native conditions can be explained by one of the following hypotheses: A) that the native state of mitochondrial ATP-diphosphohydrolase is a homo-oligomer (*i.e.* a dimer or trimer), as has been reported for other organisms [36,37], or B) that ATP-diphosphohydrolase interacts with other mitochondrial membrane protein(s) (*i.e.* steroidogenic contact site proteins). We can hypothesize that $\Delta\Psi_m$ regulates ATP-diphosphohydrolase activity through the close interactions between proteins from contact sites. Although ATP-diphosphohydrolase lacks a classic mitochondrial targeting presequence, it has been reported that many mitochondrial hydrophobic membrane proteins are synthesized without cleavable extensions [38]. These proteins typically contain several targeting signals that are distributed over the entire length of the protein [39]. However, this hypothesis needs to be elucidated.

Even though $\Delta\Psi_m$ reflects efficient mitochondrial oxygen consumption and ATP synthesis, it is not crucial for progesterone synthesis in syncytiotrophoblast cells. When intact mitochondria were incubated in the presence of CCCP to collapse $\Delta\Psi_m$, and isocitrate to maintain NADPH, cholesterol was efficiently transformed into progesterone (Fig. 6A). Although in the presence of CCCP ATP-diphosphohydrolase did not show substrate selectivity and its activity was decreased, ATP hydrolysis in the presence or absence of CCCP increased cholesterol transport and its transformation into progesterone, in the presence of NADPH. This suggested that the remaining activity of the ATP-diphosphohydrolase (around 50%) fully supports the synthesis of progesterone.

As $\Delta\Psi_m$, respiration and ATP synthesis are solid indicators of functional mitochondria, they are believed to be crucial for Leydig cell steroidogenesis [6,7]. However, using steroidogenic contact sites from syncytiotrophoblast mitochondria in this study allowed us to focus on the role of ATP (ATP-diphosphohydrolase activity) and NADPH (NADP-dependent isocitrate dehydrogenase activity) in the synthesis of progesterone; it is important to mention that steroidogenic contact sites do not generate $\Delta\Psi_m$, but transform cholesterol into progesterone (Fig. 6C). With this experimental approach, we were able to establish that progesterone synthesis is sensitive to the presence of NADPH and nucleotide hydrolysis but insensitive to $\Delta\Psi_m$ (the present study and [23]).

In syncytiotrophoblast cells $\Delta\Psi_m$ regulates the specificity of ATP-diphosphohydrolase allowing most of the ATP available to be used for cholesterol transport during progesterone synthesis (Fig. 7), leaving GTP, GDP and other nucleotides available for other important metabolic reactions (*i.e.* proteins synthesis). However, in some pathological events such as preeclampsia, calcium accumulation in mitochondria of trophoblast cells may collapse $\Delta\Psi_m$ and interfere with ATP synthesis. In an attempt to sustain progesterone synthesis, ATP-diphosphohydrolase may use any nucleotide available (*i.e.* GTP), to maintain the required cholesterol flux for progesterone synthesis.

Supplementary data to this article can be found online at <http://dx.doi.org/10.1016/j.bbbaio.2014.10.002>.

Acknowledgements

We dedicate this work as a memorial to Dr. Guillermo Mendoza-Hernandez, an exceptional friend and colleague, and coauthor of this paper, who passed away suddenly on July 13, 2012. This work was partially supported by research grants IN214914 (OFH), IN209614 (JPP) and IN211912 (FM) from Dirección General de Asuntos del Personal Académico (DGAPA) from Universidad Nacional Autónoma de México (UNAM), as well as Grant 168025 from CONACYT (FM). Mercedes Esparza-Perusquía is a Ph.D. student of the Biological Science Program of Universidad Nacional Autónoma de México (511021118) and fellow of CONACYT (254400).

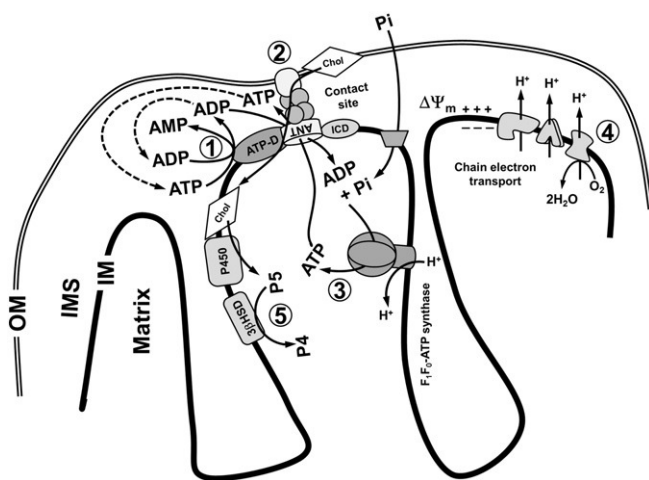
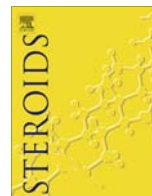


Fig. 7. Model for the regulation of mitochondrial ATP-diphosphohydrolase by $\Delta\Psi_m$ in syncytiotrophoblast cells. $\Delta\Psi_m$ induces ATP hydrolysis by ATP-diphosphohydrolase (1) during cholesterol transport (2) at the contact sites. ADP can be hydrolyzed to AMP by ATP-diphosphohydrolase (1) or can enter the mitochondrial matrix for ATP synthesis by F_1F_0 -ATP synthase (3), stimulating oxygen uptake and the proton pump by CTE (4). Cholesterol is transformed into pregnenolone (P5) by cytochrome P450_{sc} and then into progesterone (P4) by 3- β -hydroxysteroid dehydrogenase (5). Steroidogenic contact sites are constituted by different proteins including adenine nucleotide translocase (ANT), ATP-diphosphohydrolase (ATP-D), NADP-dependent isocitrate dehydrogenase (ICD), cytochrome P450_{sc} (P450) and 3- β -hydroxysteroid dehydrogenase (3 β HSD). OM = outer mitochondrial membrane; IM = inner mitochondrial membrane; IMS = inter membrane space; Chol = cholesterol.

References

- [1] O. Flores-Herrera, A. Uribe, J.P. Pardo, J.L. Rendon, F. Martinez, A novel ATPdiphosphohydrolase from human term placental mitochondria, *Placenta* 20 (1999) 475–484.
- [2] O. Flores-Herrera, A. Uribe, C. Garcia-Perez, R. Milan, F. Martinez, 5'-*p*-Fluorosulfonylbenzoyl adenosine inhibits progesterone synthesis in human placental mitochondria, *Biochim. Biophys. Acta* 1585 (2002) 11–18.
- [3] F. Martinez, M. Kiriakidou, J.F. Strauss III, Structural and functional changes in mitochondria associated with trophoblast differentiation: methods to isolate enriched preparations of syncytiotrophoblast mitochondria, *Endocrinology* 138 (1997) 2172–2183.
- [4] N. Cherradi, G. Defaye, E.M. Chambaz, Characterization of the 3 betahydroxysteroid dehydrogenase activity associated with bovine adrenocortical mitochondria, *Endocrinology* 134 (1994) 1358–1364.
- [5] C. Brand, N. Cherradi, G. Defaye, A. Chinn, E.M. Chambaz, J.J. Feige, S. Bailly, Transforming growth factor beta1 decreases cholesterol supply to mitochondria via repression of steroidogenic acute regulatory protein expression, *J. Biol. Chem.* 273 (1998) 6410–6416.
- [6] J.A. Allen, T. Shankara, P. Janus, S. Buck, T. Diemer, K.H. Hales, D.B. Hales, Energized, polarized, and actively respiring mitochondria are required for acute Leydig cell steroidogenesis, *Endocrinology* 147 (2006) 3924–3935.
- [7] A.S. Midzak, H. Chen, M.A. Aon, V. Papadopoulos, B.R. Zirkin, ATP synthesis, mitochondrial function, and steroid biosynthesis in rodent primary and tumor Leydig cells, *Biol. Rep.* 84 (2011) 976–985.
- [8] F. Martinez, R. Milan, O. Flores-Herrera, S. Olvera-Sanchez, E. Gomez-Chang, M.T. Espinosa-Garcia, The role of mitochondria in syncytiotrophoblast cells: bioenergetics and steroidogenesis Chapter 19 in: J. Zheng (Ed.), *Recent Advances in: Research on the Human Placenta*, Croatia, 2012, pp. 397–428.
- [9] X. Xu, T. Xu, D.G. Robertson, J.D. Lamberth, GTP stimulates pregnenolone generation in isolated rat adrenal mitochondria, *J. Mol. Biol.* 264 (1989) 17674–17680.
- [10] F. Martinez, M.T. Espinosa-Garcia, O. Flores-Herrera, J.P. Pardo, Respiratory control induced by ATP in human term placental mitochondria, *Placenta* 14 (1993) 321–331.
- [11] A. Bensadoun, D. Weinstein, Assay of proteins in the presence of interfering materials, *Anal. Biochem.* 70 (1976) 241–250.
- [12] O.H. Lowry, N.J. Rosebrough, A.L. Farr, R.J. Randall, Protein measurement with the Folin phenol reagent, *J. Biol. Chem.* 193 (1951) 265–275.
- [13] B. Chance, G.R. Williams, The respiratory chain and oxidative phosphorylation, *Adv. Enzymol.* 17 (1956) 65–134.
- [14] F. Martinez, J.P. Pardo, O. Flores-Herrera, M.T. Espinosa-Garcia, The effect of osmolarity on human placental mitochondria function, *Int. J. Biochem. Cell Biol.* 27 (1995) 795–803.
- [15] J.C. Fischer, W. Ruitenbeek, J.A. Berden, J.M.F. Trijbels, J.H. Veerkamp, A.M. Stadhouders, R.C.A. Sengers, J.M. Janssen, Differential investigation of the capacity of succinate oxidation in human skeletal muscle, *Clin. Chim. Acta* 153 (1985) 23–36.
- [16] K. Kita, C.R.T. Vibat, S. Meinhardt, J.R. Guest, R.B. Gennis, One-step purification from *Escherichia coli* of complex II (succinate:ubiquinoneoxidoreductase) associated with succinate-reducible cytochrome b556, *J. Biol. Chem.* 264 (1989) 2672–2677.
- [17] P.A. Lanzetta, L.J. Alvarez, P.S. Reinach, O.A. Candia, An improved assay for nanomole amounts of inorganic phosphate, *Anal. Biochem.* 100 (1979) 95–97.
- [18] A. Guevara-Flores, S. Olvera-Sanchez, C. Gómez-Concha, O. Juárez, M. Esparza-Perusquia, J.P. Pardo, G. Mendoza-Hernández, F. Martinez, O. Flores-Herrera, 5'-*p*-Fluorosulfonyl benzoyl adenosine inhibits an ecto-ATP-diphosphohydrolase in the tegument surface of *Taenia crassiceps* cysticerci, *Mol. Biochem. Parasitol.* 162 (2008) 123–133.
- [19] R.C. Tuckey, Cholesterol side-chain cleavage by mitochondria from the human placenta. Studies using hydroxycholesterols as substrates, *J. Steroid Biochem. Mol. Biol.* 42 (1992) 883–890.
- [20] H. Schagger, W.A. Cramer, G. von Jagow, Analysis of molecular masses and oligomeric states of protein complexes by blue native electrophoresis and isolation of membrane protein complexes by two-dimensional native electrophoresis, *Anal. Biochem.* 217 (1994) 220–230.
- [21] I. Wittig, H. Schagger, Electrophoretic methods to isolate protein complexes from mitochondria, *Methods Cell Biol.* 80 (2007) 723–741.
- [22] D. de Los Rios-Castillo, M. Zarco-Zavala, S. Olvera-Sanchez, J.P. Pardo, O. Juárez, F. Martinez, G. Mendoza-Hernandez, J.J. García-Trejo, O. Flores-Herrera, Atypical cristae morphology of human syncytiotrophoblast mitochondria. Role for complex V, *J. Biol. Chem.* 286 (2011) 23911–23919.
- [23] A. Uribe, J.F. Strauss III, F. Martinez, Contact sites from human placental mitochondria: characterization and role in progesterone synthesis, *Arch. Biochem. Biophys.* 413 (2003) 172–181.
- [24] B. Kadenbach, R. Ramzan, L. Wen, S. Vogt, New extension of the Mitchell Theory for oxidative phosphorylation in mitochondria of living organisms, *Biochim. Biophys. Acta* 1800 (2010) 205–212.
- [25] G. Daum, J.E. Vance, Import of lipids into mitochondria, *Prog. Lipid Res.* 36 (1997) 103–130.
- [26] D. Mokranjac, W. Neupert, Energetics of protein translocation into mitochondria, *Biochim. Biophys. Acta* 1777 (2008) 758–762.
- [27] C. Garcia-Perez, J.P. Pardo, F. Martinez, Ca(2+) modulates respiratory and steroidogenic activities of human term placental mitochondria, *Arch. Biochem. Biophys.* 405 (2002) 104–111.
- [28] J.F. Strauss III, F. Martinez, M. Kiriakidou, Placental steroid hormone synthesis: unique features and unanswered questions, *Biol. Reprod.* 54 (1996) 303–311.
- [29] W.S. da-Silva, A. Gómez-Puyou, M.T. de Gómez-Puyou, R. Moreno-Sanchez, F.G. de Felice, L. de Meis, M.F. Oliveira, A. Galina, Mitochondrial bound hexokinase activity as a preventive antioxidant defense: steady-state ADP formation as a regulatory mechanism of membrane potential and reactive oxygen species generation in mitochondria, *J. Biol. Chem.* 279 (2004) 39846–39855.
- [30] J. Liu, M.B. Rone, V. Papadopoulos, Protein-protein interactions mediate mitochondrial cholesterol transport and steroid biosynthesis, *J. Biol. Chem.* 281 (2006) 38879–38893.
- [31] M.G. Maldonado-Mercado, M.T. Espinosa-Garcia, C. Gomez-Concha, J. Monreal-Flores, F. Martinez, Steroidogenesis in BeWo cells: role of protein kinase A and benzodiazepines, *Int. J. Biochem. Cell Biol.* 40 (2008) 901–908.
- [32] S. Olvera-Sanchez, M.T. Espinosa-Garcia, J. Monreal, O. Flores-Herrera, F. Martinez, Mitochondrial heat shock protein participates in placental steroidogenesis, *Placenta* 32 (2011) 222–229.
- [33] M.A. Valenzuela, A.M. Kettlun, S. Sandoval, L. García, M. Mancilla, G. Neckelmann, L. Chayet, A. Alvarez, F. Cuevas, L. Collados, V. Espinosa, A. Traverso-Cori, I. Bravo, C.G. Acevedo, E. Aranda, Comparison of the biochemical properties, regulation and function of ATP-diphosphohydrolase from human placenta and rat kidney, *Braz. J. Med. Biol. Res.* 29 (1996) 589–597.
- [34] A. Biederbick, C. Kosan, J. Kunz, H.P. Elsässer, First apyrase splice variants have different enzymatic properties, *J. Biol. Chem.* 275 (2000) 19018–19024.
- [35] A.M. Kettlun, A. Alvarez, R. Quintar, M.A. Valenzuela, L. Collados, E. Aranda, A. Banda, L. Chayet, M. Chiong, M. Mancilla, Human placental ATP-diphosphohydrolase: biochemical characterization, regulation and function, *Int. J. Biochem.* 26 (1994) 437–448.
- [36] E. Faudry, J.M. Santana, C. Ebel, T. Vernet, A.R. Teixeira, Salivary apyrases of *Triatoma infestans* are assembled into homo-oligomers, *Biochem. J.* 396 (2006) 509–515.
- [37] B.U. Failer, A. Aschrafi, G. Schmalzing, H. Zimmermann, Determination of native oligomeric state and substrate specificity of rat NTPDase1 and NTPDase2 after heterologous expression in *Xenopus* oocytes, *Eur. J. Biochem.* 270 (2003) 1802–1809.
- [38] A. Chacinska, N. Pfanner, C. Meisinger, How mitochondria import hydrophilic and hydrophobic proteins, *Trends Cell Biol.* 12 (2002) 299–303.
- [39] T. Stan, J. Brix, J. Schneider-Mergener, N. Pfanner, W. Neupert, D. Rapaport, Mitochondrial protein import: recognition of internal import signals of BCS1 by the TOM complex, *Mol. Cel. Biol.* 23 (2003) 2239–2250.



Review

Multiple functions of syncytiotrophoblast mitochondria



Federico Martinez*, Sofia Olvera-Sanchez, Mercedes Esparza-Perusquia, Erika Gomez-Chang, Oscar Flores-Herrera

Departamento de Bioquímica, Facultad de Medicina, Universidad Nacional Autónoma de México, Apdo. Postal 70-159, Coyoacan 04510, México, D.F., Mexico

ARTICLE INFO

Article history:

Received 2 February 2015
Received in revised form 16 September 2015
Accepted 27 September 2015
Available online 3 October 2015

Keywords:

Syncytiotrophoblast mitochondria
MLN64
Mitochondrial kinases
Mitochondrial structure
Protein phosphorylation
Cholesterol transport

ABSTRACT

The human placenta plays a central role in pregnancy, and the syncytiotrophoblast cells are the main components of the placenta that support the relationship between the mother and fetus, in apart through the production of progesterone. In this review, the metabolic processes performed by syncytiotrophoblast mitochondria associated with placental steroidogenesis are described. The metabolism of cholesterol, specifically how this steroid hormone precursor reaches the mitochondria, and its transformation into progesterone are reviewed. The role of nucleotides in steroidogenesis, as well as the mechanisms associated with signal transduction through protein phosphorylation and dephosphorylation of proteins is discussed. Finally, topics that require further research are identified, including the need for new techniques to study the syncytiotrophoblast in situ using non-invasive methods.

© 2015 Elsevier Inc. All rights reserved.

Contents

1. General aspects	11
2. Cholesterol synthesis in the human placenta	12
3. Lipoprotein receptors for cholesterol supply to placenta	12
4. Involvement of organelle-mitochondria interactions in intracellular lipid flux	13
5. StAR in adrenal glands and gonads	14
6. MLN64 in human placenta	14
7. Mitochondrial contact sites associated with steroidogenesis	15
8. Steroidogenic contact sites in human syncytiotrophoblast mitochondria	15
9. Architecture and physiological characteristics of syncytiotrophoblast mitochondria	16
10. Role of $\Delta\psi_m$ in placental steroidogenesis: regulation of mitochondrial ATP-diphosphohydrolase	17
11. Placental signal transduction machinery	17
12. cAMP-mediated signal transduction cascade in progesterone synthesis	18
13. Conclusion and perspectives	19
Acknowledgements	19
References	19

1. General aspects

The human placenta plays a major role during pregnancy. Through progesterone synthesis, it establishes central communication mechanisms between mother and fetus. Proges-

terone is essential for blastocyst implantation, extracellular matrix remodeling, and promoting trophoblast migration. The human placenta safeguards the fetus and contributes to its maturation [1].

The human placenta undertakes metabolic processes related to hormone synthesis as well as transport of nutrients, gases and

* Corresponding author.

E-mail address: fedem@bq.unam.mx (F. Martinez).

disposal of waste products. In this context, the placenta exhibits functions that can be compared to those of the pituitary gland, ovaries, intestines, lungs, and kidneys.

During human placentation, cell fusion of mononuclear cytotrophoblast cells occurs to produce a multinucleated cellular layer named syncytiotrophoblast, which forms an interface between the maternal and fetal circulation [2], and is also the site of progesterone synthesis [3,4]. Approximately, two weeks after conception, the villus structures appear containing cytotrophoblasts and syncytiotrophoblast. The syncytiotrophoblast is maintained during pregnancy by continuous fusion of cytotrophoblasts.

Cytotrophoblast differentiation into syncytiotrophoblast is accompanied by changes in cell morphology, mitochondrial cristae remodeling, and the acquisition of the steroidogenic machinery. The steroidogenic machinery of syncytiotrophoblast cells consists of an electron transport chain (ETC-P450_{scc}) composed of cytochrome P450_{scc} (CYP11A1), which receives electrons from NADPH + H⁺ through adrenodoxin and adrenodoxin reductase. These proteins are located in the inner mitochondrial membrane and transform cholesterol into pregnenolone [5–7]. An additional enzyme, the 3 β -hydroxysteroid-dehydrogenase- Δ^{4-5} isomerase type I (3 β HSDI), also embedded in the inner mitochondrial membrane of syncytiotrophoblast cells [6], transforms pregnenolone into progesterone [5,7].

The human placenta is a transient tissue exclusively present during pregnancy. Its multiple functions must be strictly regulated to ensure the successful completion of pregnancy, and hence, from an evolutionary perspective, the maintenance of the human race. It has been suggested that the placenta functions under autonomous control through autocrine, paracrine, or intracrine signals which render it independent from other tissues and organs.

It has been demonstrated that human placental explants resist non-physiological physical conditions (*i.e.*, hypotonic media or temperatures higher than 45 °C) unlike other tissues, and that trophoblasts can synthesize progesterone under stress conditions [8]. These data suggest that the human placenta has self-preserving mechanisms that are independent of external stimuli and serve as physiological, metabolic, and functional control strategies to protect the fetus [8].

The regulation of the human placenta and how it modifies maternal functions, remain to be elucidated. Recently, an editorial comment was issued about how little attention is given to placental studies. It focused on the lack of non-invasive methods to treat illnesses of both the mother and the fetus, which could prove life-saving or allow *in utero* treatment to prevent birth defects [9].

The human placenta produces high levels of progesterone from the cholesterol provided by the mother, a steroid hormone synthesized by syncytiotrophoblast mitochondria that regulates the immunological processes that prevent fetal rejection. The absence or a significant decrease in progesterone levels, regardless of its etiology, results in the lack of communication between mother and fetus, and usually in spontaneous abortion or miscarriage. Hence, a central role of human placental steroidogenesis is to maintain the pregnancy. However, pregnancies where the fetus has a CYP11A1 mutation can end in a viable neonate despite very low progesterone levels [10,11].

It has been suggested that intracellular cholesterol transport takes place through a strictly regulated mechanism performed by multi-protein complexes [12]. Biological membranes and some cellular processes require specific concentrations of this sterol, since slight modifications in its concentration may produce significant functional alterations. The lipid composition of membranes contributes to the cellular distribution of cholesterol. For instance, the concentration of cholesterol in the endoplasmic reticulum of mammalian cells is low, 5 mol% of phospholipids. In contrast, in the Golgi apparatus, the concentration is ≥ 30 mol% [12]. However,

the largest concentrations of cholesterol in a cell are found in the plasma membrane, which has been reported to contain up to 60% of the sterol [12]. The different cholesterol concentrations found among cellular compartments suggest the existence of systems that distribute cholesterol to the required sites, as is the case of steroidogenic mitochondria [13]. Cholesterol transport pathways involve vesicles and specific proteins. There are proteins that control the synthesis of lipids, those that function as inducers or modulators of gene expression, and the ones that transport lipids themselves. Regardless of the mechanism, it is essential to know what determines the movement of cholesterol, because the concentration of cholesterol in membranes can modify their biological functions as well as that of associated proteins. When pregnenolone is synthesized, particularly in the placenta, cholesterol transport toward the mitochondria is vectorial, efficient, and in adequate concentration to elicit a response according to cellular needs without disturbing other cell functions.

Among sterol carrier proteins involved in the intracellular flux of cholesterol in steroidogenic tissues, the START family of proteins are most relevant [14], particularly the STar (STARD1) and MLN64 (STARD3) proteins, which play a central role in cholesterol movement between mitochondrial membranes supplying substrate for hormones synthesis. The START proteins are associated, either with multiprotein complexes belonging to vesicles, or with specific organelles (*i.e.*, mitochondria). This allows for the efficient and targeted distribution of cholesterol.

Diverse contact sites between organelles have been described (see *Organelles and mitochondria interaction for intracellular lipid flux* section). These consist of transporters, enzymes and anchor proteins, among others, that generate protein membrane domains [15]. Among the different types of contact sites that have been described are the Mitochondria Associated Membrane (MAMs) between the endoplasmic reticulum and mitochondria, which contribute to the control of metabolism. However, although the mitochondria play a pivotal role in steroidogenic tissues [16], it should be noted that mitochondria also participate in other cellular processes [17], such as ATP production, intracrine signaling [18], apoptosis, innate immunity, autophagy, or the stress response [19], suggesting that mitochondria by themselves, or associated with other structures, are important to maintaining cellular functions. This is a topic that requires a further investigation in the human placenta.

2. Cholesterol synthesis in the human placenta

Distinct from other steroidogenic tissues, such as adrenal glands [20], the human placenta does not produce significant amounts of cholesterol *de novo*. Studies using acetate-¹⁴C have shown that this precursor is not the main substrate for the sterol synthesis pathway in human placenta [21–24]. However, cholesterol is needed for the substantial placental progesterone synthesis during pregnancy. In this sense, cholesterol production by human placenta is not sufficient to support steroidogenesis. The modest amount of cholesterol synthesized by the placenta could be used to satisfy its own requirements such as the structural needs, *i.e.*, to maintain the plasma membrane morphology and function. In the syncytiotrophoblast, the cholesterol needed for progesterone synthesis comes from LDL [25,26], which are internalized through receptors mediated by endocytosis [27].

3. Lipoprotein receptors for cholesterol supply to placenta

The trophoblast cells have different types of receptors; one of these is for LDL [28]. Also, HDL receptors have been described on trophoblast cells [29], in BeWo cells line [30], and numerous steroidogenic tissues (Fig. 1). Unlike LDL, HDL are not processed

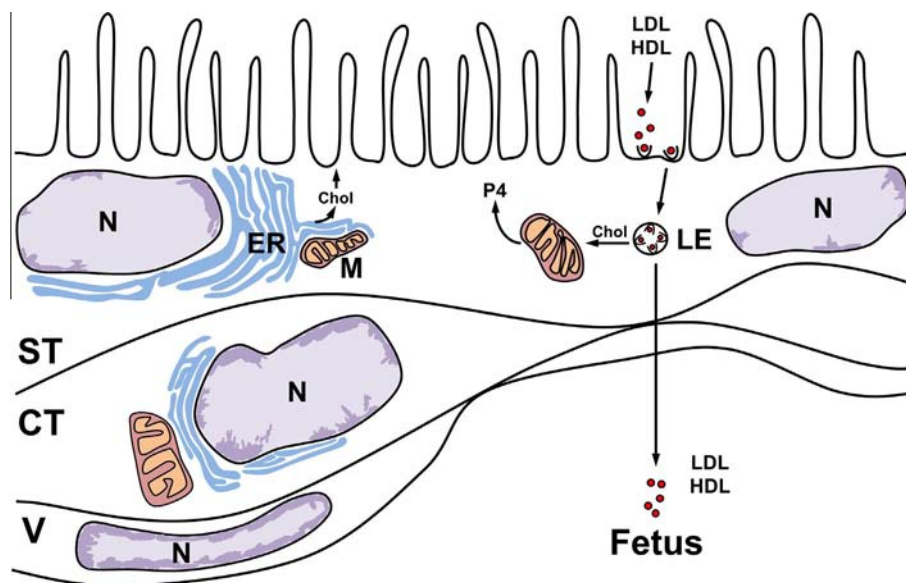


Fig. 1. Cholesterol uptake by syncytiotrophoblast and its route through the placenta. Cholesterol is transported by endocytosis via specific receptors for HDL or VLDL and is distributed by endosomes to mitochondria and into the fetal bloodstream. Mitochondria transform cholesterol into progesterone to maintain pregnancy. Syncytiotrophoblast has a low capacity of cholesterol synthesis, which is probably used for membrane microvilli structure. ST = syncytiotrophoblast cell; CT = cytotrophoblast cell; V = vascular endothelium; N = nuclei; LE = late endosome; M = mitochondria; ER = endoplasmic reticulum; P4 = progesterone; Chol = cholesterol; LDL = low density lipoproteins; HDL = high density lipoproteins.

through the lysosomal degradation pathway [31], suggesting that placenta can obtain cholesterol from different pathways.

Progesterone synthesis presumably depends on the capacity of the cells to bind LDL and thus supply mitochondria with cholesterol. The concentration of LDL receptors is regulated by the presence of LDL. In dispersed trophoblast culture cells incubated with LDL-¹²⁵I for long periods of time, uptake and degradation of LDL decreased by 90%. These results suggest that trophoblast cells regulate the number of LDL receptors expressed in the plasma membrane. This effect was observed when trophoblast cells were incubated in the presence of HDL [32]. Recent data suggest that the placenta uses both LDL and HDL as a source of cholesterol for progesterone synthesis [33], which secures a constant cholesterol input for steroidogenesis, even under conditions that may alter cholesterol concentration, safeguarding pregnancy. However, in abetalipoproteinemia, progesterone levels during pregnancy are reduced indicating that HDL cholesterol cannot compensate for diminished LDL levels [34].

Although it is beyond the scope of this review, it is important to mention that the human placenta also transports cholesterol to the fetal bloodstream (Fig. 1). The fetus requires cholesterol for cell growth and development. The following references address this issue [35,36] and highlight the diverse array of proteins that is required [37–40].

4. Involvement of organelle-mitochondria interactions in intracellular lipid flux

Mitochondrial Inner Membrane Organizing System (MINOS) and Mitochondria Associated Membrane (MAMs) have been put forward as potential types of unions between membranes of diverse organelles. Diverse types of unions are associated with transport mechanisms, vesicle mediated transport, and protein mediated translocation. MAMs are multiprotein structures whose existence was identified by cosedimentation of the endoplasmic reticulum and mitochondria. MAMs participate in lipid exchange [41], highlighting their role in the endoplasmic reticulum and

mitochondria contact sites [42–48]. Membrane Contact Sites (MCS) result from the proximity between two membranes (<20–30 nm). Proteins associate transiently and undertake a specific function without the fusion of membranes [15]. It has been suggested that MCS and MAMs participate in the association between lipid droplets and endosomes, where perilipin and SNARE elements potentially play a crucial role [42,44,45]. The cytoskeleton is also important since colchicine decreases steroidogenesis [49–52]. Particularly for steroidogenic tissues, these observations provide a basis for an integrated model of cholesterol flux from endoplasmic reticulum, late endosomes or lipid droplets, to mitochondria, which could represent an initial step in steroidogenesis [53–55]. However, lipid composition of mitochondrial membranes is precisely controlled.

Horvath and Daum [56] describe the reasons why mitochondria are unique organelles regarding lipid transport. Firstly, they possess a double bilayer. Although they are closely positioned, each layer maintains its structural and functional properties. Secondly, each layer and its subcompartments perform specific biochemical functions.

The mitochondrial membranes have a particular lipid composition. High concentrations of cholesterol accumulate in the outer membrane but not in the inner membrane [58].

In the presence of a BSA-cholesterol complex, human placental mitochondria increased progesterone synthesis, but not when mitochondria were treated with trypsin [57]. Similar results were observed under different experimental conditions, showing that mitochondria treated with trypsin were unable to accumulate cholesterol in the presence of the BSA-cholesterol complex, suggesting that proteins are involved in the incorporation of cholesterol into the human placental mitochondria [58]. Therefore, successful cholesterol transport, its transformation into pregnenolone in acutely regulated steroidogenic tissues, or progesterone in the case of the human placenta (a “chronically” regulated tissue), requires multiple systems that include: proteins like StAR and MLN64; late endosomes; lipid droplets; the cytoskeleton; MAMs, MINOS, MCS; and contact sites between mitochondrial membranes (see below).

5. StAR in adrenal glands and gonads

As it has been mentioned, once cholesterol has been incorporated into the cell (*i.e.*, late endosomes, or lipid droplets), it is directed through a precise and effective transport system to mitochondria, where pregnenolone is synthesized [59] (Fig. 2). This transport system may be mediated by vesicles or sterol carrier proteins; in steroidogenic tissues both systems operate simultaneously.

The sterol carrier proteins called START have been broadly studied in steroidogenic tissues. From this family, the StAR is the most important protein in the cholesterol transfer system in mitochondria from adrenal glands and gonads [60]; mutations in the STARD1 gene cause Congenital Lipoid Adrenal Hyperplasia [61]. Several studies analyzed its genetic regulation [62], function and its role in steroidogenesis [16,63,64]. The transcription of the STARD1 gene increases significantly in response to adrenocorticotrophic and luteinizing hormones, and phosphorylation of StAR

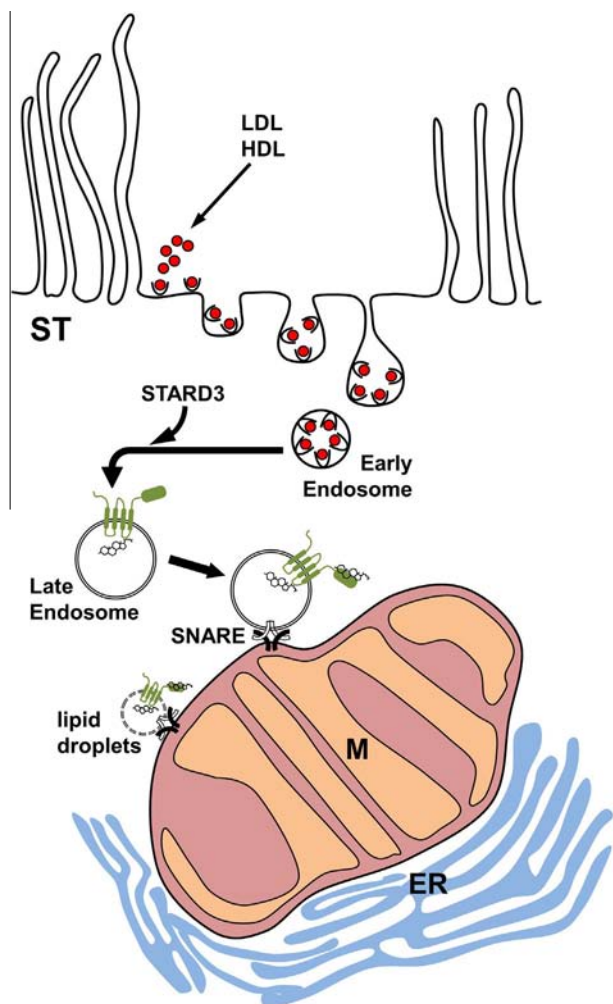


Fig. 2. Flux of cholesterol to syncytiotrophoblast mitochondria. Cholesterol is incorporated by endocytosis. Early endosomes initiate cholesterol transport to mitochondria to stimulate steroid hormone synthesis. Incorporation of STARD3 into early endosomes promotes its maturation into late endosomes. STARD3 facilitates transport of late endosomal cholesterol to mitochondria. STARD3 is a member of the START domain superfamily that possesses cholesterol binding and transport activity. Lipid droplets are an alternative route to cholesterol flux to mitochondria. Late endosomes and lipid droplets might anchor to mitochondria through SNARE complexes. ST = syncytiotrophoblast; LDL = low density lipoproteins; HDL = high density lipoproteins; M = mitochondria; ER = endoplasmic reticulum; SNARE = S-NARE complexes.

stimulates cholesterol transport and steroidogenesis [65,66]. The StAR protein does not need to enter into the mitochondria to promote cholesterol transfer since a truncated StAR protein (StAR-N62) lacking the mitochondrial targeting sequence is able to drive cholesterol transport, although it is not incorporated into the mitochondria [67].

Interaction between cholesterol and StAR under acidic conditions induces a conformational change from the native structure to the molten globule state [68], suggesting that this dynamic state is involved in intramitochondrial sterol transfer [68]. Although these studies were performed *in vitro*, the mitochondrial conditions, particularly the acidic conditions of the intermembrane space could support this hypothesis. The mechanism of action of StAR remains unknown. However, it has been suggested that it mediates cholesterol transport from the outer to the inner mitochondrial membrane. This process regulates steroidogenesis by controlling the conversion rate of cholesterol into pregnenolone by cytochrome P450sc.

While acutely regulated steroidogenic tissues display a high, but transitory flux of cholesterol to mitochondria, the amount of cholesterol in mitochondrial membranes is low [56], suggesting a fast transformation of the sterol into pregnenolone. In contrast, the constant flow of cholesterol from cytosol to syncytiotrophoblast outer mitochondrial membrane impacts the mitochondrial sterol content, which reaches a value of 13.5 μg of cholesterol/mg mitochondrial protein [58], five times higher than reported for other types of mitochondria and close to the value observed in the plasma membrane. The constant transport of cholesterol to syncytiotrophoblast mitochondria allows the increased production of progesterone during pregnancy [59], *i.e.*, in the last trimester of pregnancy, the human placenta can produce about 250–500 mg of progesterone daily [65,69]. Once located in the outer mitochondrial membrane, cholesterol must continue its transit to the inner mitochondrial membrane, reach cytochrome P450sc, and be transformed into pregnenolone. This step needs a sterol carrier protein, MLN64.

6. MLN64 in human placenta

Similar to the gonads and adrenal glands, in human syncytiotrophoblast there must be a sterol carrier protein involved in mitochondrial cholesterol transport. Although StAR is the main protein associated with mitochondrial cholesterol flux in different acutely regulated steroidogenic tissues, it is not expressed in the human placenta [61]. In the last decade a new member of the START family, named MLN64, was identified in syncytiotrophoblast cells [70]. MLN64 was initially described as an endosomal membrane protein in a metastatic lymphatic nodule, and contains the START domain for cholesterol binding [71]. Since the syncytiotrophoblast does not express StAR, MLN64 was considered to be the main intracellular protein involved in cholesterol transport in this tissue [56].

Alpy and Tomasetto [64] reported that although StAR and MLN64 contain a START domain, they also have different features that determine their intracellular location and structure. MLN64 is an endosomal protein with four transmembrane segments in its amino terminal end (named the MENTAL domain). Its subcellular localization is relevant because late endosomes and lysosomes contain 50% of total cellular cholesterol, and they might play a role in the distribution of cholesterol in the cell [72]. Also, van der Kant et al. [72] showed that there are two types of late endosomes, one that contains the protein ORP1L and transports oxysterols; and another with MLN64 and ABCA3 (an ATP dependent transport protein that translocate substrates, including lipids). Hence, they suggested that MLN64 could be involved in cholesterol flux from late

endosomes to mitochondria. It has also been noted that amino acid residues M307 and N311 are essential for cholesterol binding to MLN64 [60,73,74]. We have demonstrated that MLN64 is incorporated into syncytiotrophoblast mitochondria and proteolytically activated by a mitochondrial protease to stimulate steroidogenesis [75]. The proteolytic product (*i.e.*, MLN64-28 kDa protein) is associated with steroidogenic contact sites (see below), probably to facilitate cholesterol transport between mitochondrial membranes.

Charman et al. [73] transformed CHO cells into steroidogenic cells by transfecting them with a vector encoding a fusion protein with the complete electron transport chain of P450_{scc} (F2-plasmid). Although the expression of MLN64 was depleted by 80–90% with siRNA, progesterone synthesis was inhibited only by 30%, suggesting that MLN64 is not the only protein responsible for cholesterol transport for steroidogenesis [73]. Kishida et al. [76] demonstrated that in embryonic fibroblasts, lacking StAR, and obtained from MLN64 mutant mice, transfection with F2 plasmid resulted in reduced but not absent transformation of endogenous cholesterol into steroid hormones compared to wild-type embryonic fibroblasts. This suggests that the MLN64 START domain is not necessarily the only protein participating in sterol metabolism. This is relevant for human placental steroidogenesis, since it expresses MLN64 and lacks the StAR protein.

In this way, we have determined that HSP60 protein shares epitopes with the START domain of MLN64. Both proteins co-immunoprecipitated, and HSP60 labeled with fluorescein maleimide inhibited progesterone synthesis [77]. This observation suggests that HSP60 could participate in steroidogenesis in addition to MLN64. At present, we are conducting experiments to elucidate the role of HSP60 in this process.

The presence of multiple proteins and steps during progesterone synthesis in adrenal glands, gonads and placenta, supports the hypothesis, that at least in part, the limiting step in the regulation of steroidogenesis is cholesterol transport from the outer to the inner mitochondrial membrane. In this sense, the contact sites between mitochondrial membranes which contains multiple proteins, such as MLN64 and HSP60, could play a major role for cholesterol transfer to P450_{scc} [78,79].

The interaction between StAR with a mitochondrial membrane multiprotein complex has been proposed to affect cholesterol transport. These complexes could be the transduceosome complex, which consists of membrane and cytoplasmic proteins [80]; or the steroidogenic metabolon, composed of mitochondrial membrane proteins [80,81]. In human placenta, MLN64 interacts with the steroidogenic contact sites [75] (see below).

7. Mitochondrial contact sites associated with steroidogenesis

Mitochondrial contact sites are domains where inner and outer membranes are in close proximity, allowing exchange between them. Contact sites are established and maintained in durable or transient states by different proteins and enzymes. Hackenbrock [82] noted that mitochondria exhibit different types of contact sites: multiprotein complexes that perform various mitochondrial functions. Their assembly takes place through a dynamic process that requires the association of specific proteins and enzymes. According to their protein composition, contact sites may participate in multiple mitochondrial processes, including protein import or progesterone synthesis.

Proteins that are found in mitochondrial contact sites also participate in other processes, including oxidative phosphorylation (adenine nucleotide translocase –ANT–, VDAC, creatine kinase, and hexokinase [83,84]; or apoptosis (ANT, VDAC, cyclophilin D, and hexokinase II). The outer membrane contains proteins that

are able to interact with actin and establish ATP-dependent junctions, and antiapoptotic proteins of the Bcl-2 family that, when overexpressed, block apoptosis [85–87]. Another example is the permeability transition pore [88], a multiprotein complex that forms non-selective pores in the inner membrane and is associated with structural components as the ANT, cyclophilin D and VDAC. TP50 has been identified in association with the outer membrane pore; creatine kinase with the intermembrane space; and hexokinase II with VDAC in the outer membrane, and with the proteins Bax/Bcl-2 [55,87].

It has been suggested that in steroidogenesis by the adrenal glands and gonads, the contact sites are constituted by various proteins such as voltage-dependent anion channel (VDAC) [89,90], the σ -1 receptor [91], an ATPase-ATD3 [92], TP50, ANT, IP3R (ER-resident inositol triphosphate receptor), Mfn1 and Mfn2 (mitofusine 1 y 2), among others [55,93]. Outer membranal proteins (*i.e.*, VDAC1 and TP50) associated with inner membranal proteins (*i.e.*, ATPase-ATAD3a) constitute the core of a complex that regulates mitochondrial cholesterol import in adrenal glands and gonads [51,94]. Recent data indicate that although ANT is part of the contact sites, apparently, it is not essential for cholesterol transport [94]. The association between the proteins Tom22, Tim23, Tim 50, and 3 β HSD2 has been shown to affect steroidogenesis [95,96]. Alternatively, some elements of this complex could interact with the endoplasmic reticulum, lipid droplets or late endosomes [16,80,97,98].

8. Steroidogenic contact sites in human syncytiotrophoblast mitochondria

Mitochondrial contact sites in syncytiotrophoblast have been isolated and their composition determined [99]. They have been proposed to be the conduit for cholesterol flux from the outer to the inner membrane. In the human syncytiotrophoblast, it has been proposed that cholesterol flux is accomplished through a series of steps that involve various intracellular organelles associated with lipid droplets [75] and proteins from contact sites like HSP60 [77], ATP-diphosphohydrolase [100,101], and MLN64 [75]. ATP-diphosphohydrolase activity supplies energy for cholesterol flux during progesterone synthesis (see below). HSP60 is a mitochondrial chaperone that has been associated with MLN64 in progesterone production [77].

Other proteins or enzymes that are associated with placental steroidogenic contact sites are VDAC, ANT, ETC-P450_{scc}, 3 β HSD1, NADP-dependent isocitrate dehydrogenase [102], and the catalytic subunit of PKA [103]. The steroidogenic machinery reported in adrenal glands includes TP50 [16]. Although in human term placental explants specific ligands for peripheral benzodiazepine binding sites (PBzS) caused an increase of progesterone and estradiol-17 β secretion [104], and it has been also reported that maternal obesity during pregnancy negatively regulates mitochondrial TP50, which impairs mitochondrial steroidogenesis [105], the role and localization of TP50 remains to be clarified. In fact, the effect of ligands of PBzS on steroidogenesis was observed only in intact placental explants (where plasma membrane, cytosol and the whole signal transduction machinery were present) [104], and the identification of TP50 in mitochondria was performed on frozen placental tissue where the intactness of cellular and mitochondrial architecture is not assured [105]. We isolated highly purified syncytiotrophoblast mitochondria from fresh placentas [6]. These syncytiotrophoblast mitochondria retain their steroidogenic and bioenergetics functions, and the TP50 protein was not present, nor did ligands of PBzS have any effect on steroidogenesis [106]. Similarly, in isolated mitochondria from BeWo cells, TP50 protein was absent [77,106].

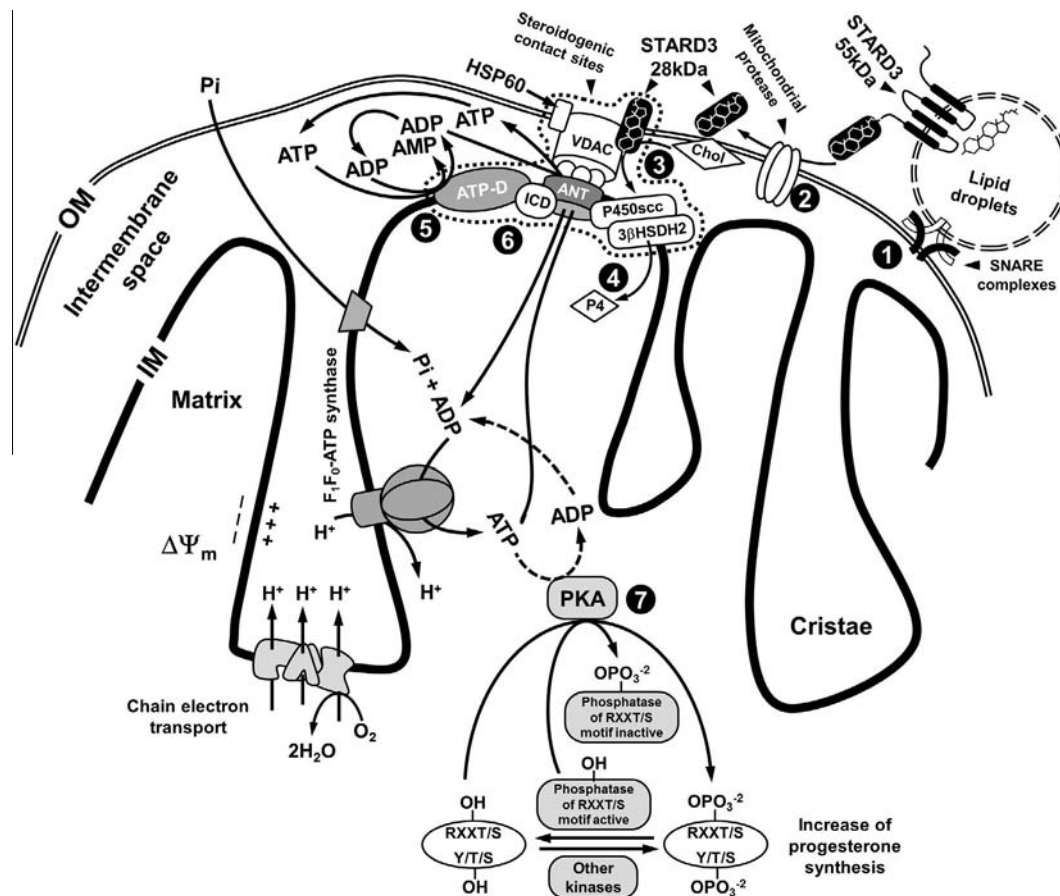


Fig. 3. Model proposed for progesterone synthesis in human syncytiotrophoblast mitochondria. Progesterone synthesis has been divided into seven steps. (1) Anchoring of lipid droplets or late endosomes to mitochondria via SNARE complexes. STARD3 is attached to lipid droplets or late endosomes. (2) Proteolytic transformation of STARD3 from a 55-kDa into a 28-kDa protein by a metalloprotease that exerts its activity on the cytosolic side of the outer membrane of mitochondria. This metalloprotease is sensitive to 1,10-phenanthroline, EGTA, or EDTA. (3) The STARD3–28 kDa protein, which contains the cholesterol binding domain (START), is associated with steroidogenic contact sites, and increases cholesterol flux from the outer into the inner mitochondrial membrane, where it reaches the machinery of cytochrome P450scc and increases progesterone production (step 4). If protease activity is inhibited and no STARD3–28 kDa protein is produced, no progesterone synthesis occurs. (5) $\Delta\psi_m$ induces ATP hydrolysis by ATP-diphosphohydrolase during cholesterol transport throughout the steroidogenic contact sites. ADP can be hydrolyzed to AMP by ATP-diphosphohydrolase or can enter the mitochondrial matrix for ATP synthesis by F_1F_0 -ATP synthase, stimulating oxygen uptake and the proton pump by the ETC. (6) NADP-dependent isocitrate dehydrogenase produces NADPH to supply energy to the ETC associated to P450scc constituted by adrenodoxin and adrenodoxin reductase. (7) PKA activity stimulates progesterone synthesis. Several syncytiotrophoblast mitochondrial proteins are suitable substrates for PKA and perhaps for other kinases. PKA maintains a major pool of inactive phosphorylated phosphatases, leaving few active phosphatases that remove the phosphate from the amino acids that belong to RRXT/S motifs. PKA inhibition by H89 produced a decrease in progesterone synthesis. Steroidogenic contact sites, marked with a dashed line, are constituted by different proteins including adenine nucleotide translocase (ANT); voltage dependent anionic channel (VDAC); ATP-diphosphohydrolase (ATP-D), NADP-dependent isocitrate dehydrogenase (ICD), cytochrome P450scc (P450scc) and type II 3β -hydroxysteroid dehydrogenase (3β HSD2). RRXT/S-specific motifs recognized by PKA; Y/T/S-tyrosine, threonine and serine residues; OM = outer mitochondrial membrane; IM = inner mitochondrial membrane; Chol = cholesterol.

Steroidogenic mitochondrial contact sites from syncytiotrophoblast contain cholesterol and the complete machinery for progesterone synthesis: STARD3, which promotes cholesterol flux; ETC-P450scc, which transforms cholesterol into pregnenolone; 3β HSD1, which transforms pregnenolone into progesterone; and NADP-isocitrate dehydrogenase, which supplies the energy for ETC-P450scc activity (Fig. 3). Thus, the contact sites synthesize progesterone [99,102]. Interestingly, in isolated mitochondrial contact sites, $\Delta\psi_m$ was not produced, and therefore, its role in steroidogenesis must be re-assessed, leaving NADPH and ATP as the principal energy sources [99].

In addition to the description of proteins from steroidogenic contact sites, we have discovered the presence of diverse SNARE elements associated with mitochondrial outer membranes [75], and put forward a model for MLN64 in human placenta mitochondria [75] in which lipid droplets containing SNARE protein complexes [74,107–110] (i.e., α -SNAP, syntaxin 3, 7 y 12, syntaxin-Binding Protein-2, syntaxin-Binding Protein-3, and VAMP-8) probably participate in cholesterol transport. It has been

demonstrated that SNAP promotes interactions between lipid droplets and mitochondria [111] and that steroidogenic cells express syntaxin-17, SNAP-23 and SNAP-25 [112–116]. These observations suggest that SNARE proteins could participate in cholesterol transport by promoting functional interactions among lipid droplets, the endoplasmic reticulum, endosomes and mitochondria. In syncytiotrophoblast cells, MLN64 could be incorporated into mitochondria through these complexes and then be activated by mitochondrial proteases [75], favoring its uptake into mitochondria (i.e., contact sites) [46,79], and promoting cholesterol transport [77,102].

9. Architecture and physiological characteristics of syncytiotrophoblast mitochondria

As it has been mentioned earlier, differentiation of the syncytiotrophoblast involves mitochondrial cristae remodeling. This mitochondrial remodeling involves turning large round

mitochondria with lamellar cristae with an orthodox configuration from cytotrophoblasts, into small irregular structure exhibiting protuberances in the outer and inner membranes, a condensed matrix, and cristae composed of vesicular regions connected by narrow tubules observed in syncytiotrophoblast [6,59,99,117]. We have demonstrated that the acquisition of steroidogenic activity in syncytiotrophoblast mitochondria involves changes in F_1F_0 -ATP synthase dimerization [117]. The F_1F_0 -ATP synthase is present as a native functional dimer assembled into long rows of oligomers in the mitochondrial membrane [118]. This constitutive self-association promotes membrane curvature and the formation of the classical mitochondrial cristae ultrastructure [118–121]. The dimeric structure of F_1F_0 -ATP synthase was solved by transmission electron microscope [119–125]. This supercomplex had a critical role in maintaining a high transmembranal potential that ensures optimal conditions for efficient ATP synthesis [126].

Syncytiotrophoblast mitochondria contain low levels of dimeric complex V, in contrast to cytotrophoblast mitochondria, which have standard cristae morphology and a higher content of the ATP synthase dimer [117]. The proportion of F_1F_0 -ATP synthase dimer that can be extracted from mitochondria was assessed through Blue Native-PAGE and WB analysis. It was demonstrated that cytotrophoblast cells contain a higher dimer/monomer ratio than syncytiotrophoblast cells [117], and that the ATP synthase supercomplex is the consequence of a higher relative amount of IF_1 in the cytotrophoblasts [117].

Syncytiotrophoblast mitochondria exhibit the same morphology (*i.e.*, tubular, vesicular or tubulovesicular cristae [117]) like those of other steroidogenic tissues such as Leydig cells [127]. In contrast, electron microscopic tomography studies of liver [128,129], neuronal [130,131], brown adipose tissue [132], fungi [133,134], rods and cones [135] mitochondria show typical lamellar cristae architecture.

It has been suggested that cristae morphology has a direct impact on ATP production in Leydig cells, since the narrow gap between lamellae prevents the correct distribution of the F_1 subunit of ATP synthase [127]. Allen et al. [136] have shown that mitochondrial membrane potential ($\Delta\psi_m$), mitochondrial ATP synthesis, and mitochondrial respiration are required to support Leydig cell steroidogenesis [136]. In contrast, the rate of ATP synthesis in isolated human cytotrophoblast and syncytiotrophoblast mitochondria is similar (151 ± 16 nmol/mg/min and 153 ± 13 nmol/mg/min, respectively), while progesterone synthesis is ten times higher in syncytiotrophoblast than cytotrophoblast mitochondria (35.7 ± 0.90 ng of progesterone/mg/min and 3.6 ± 1.34 ng of progesterone/mg/min, respectively) [117]. This suggests that in human syncytiotrophoblast, ATP and progesterone synthesis are quite important to cell physiology. In this sense, the relative amount of ETC-P450scc and classic electron transport chain (ETC) components is different in each steroidogenic tissue. In acutely regulated steroidogenic tissues (*i.e.*, the adrenal glands and gonads) the content of ETC-P450scc is several times higher than classic ETC elements, suggesting that these cells have a quick response to the external signal to activate steroidogenesis. In contrast, in syncytiotrophoblast the amount of both electron transfer chain components is similar [59], indicating that this cell, with its unique mitochondrial architecture, has parity between steroidogenesis and the bioenergetics metabolism.

We have assembled a general model for steroidogenic metabolism for human syncytiotrophoblast [59,99] (Fig. 3). It has been suggested that the size reduction of mitochondria and the structural changes of their cristae may improve the steroidogenic activity of syncytiotrophoblast cells [6]. If translocation of cholesterol to cytochrome P450scc is the rate-limiting step in steroidogenesis, a larger surface to volume ratio might improve the movement of cholesterol to the inner membrane where cytochrome P450scc is

located. A non-orthodox structure may also play a crucial role in maintaining progesterone synthesis [117,137].

10. Role of $\Delta\psi_m$ in placental steroidogenesis: regulation of mitochondrial ATP-diphosphohydrolase

Human syncytiotrophoblast mitochondria contain proteins and enzymes that participate in steroidogenic metabolism, *i.e.*, an ATP-diphosphohydrolase (P49961-2|ENTP1_HUMAN) in the inner membrane [99], which is involved in progesterone synthesis, mainly in cholesterol transport [100,101]. ATP-diphosphohydrolase might provide the required energy to drive cholesterol transport between the mitochondrial membranes in a similar way to mitochondrial GTPase in the adrenal glands [138]. Detergent solubilized ATP-diphosphohydrolase catalyzes the hydrolysis of tri- (ATP, GTP, UTP, and CTP), and di-phosphonucleosides (ADP, GDP, UDP, and CDP) in a Mg^{2+} -, Ca^{2+} -, or Mn^{2+} -dependent manner with a single rate-limiting step for each hydrolyzed nucleoside [99]. However, in the intact and energized mitochondria, ATP-diphosphohydrolase hydrolyzes mainly ATP [99]. The resulting ADP promotes oxygen uptake and ATP synthesis by F_1F_0 -ATP synthase [99,139]. The activities of ATP-diphosphohydrolase (ATP hydrolysis) and F_1F_0 -ATP synthase (ATP synthesis) are strongly coordinated to avoid a futile cycle and energy dissipation.

Mitochondrial inner membrane potential ($\Delta\psi_m$) is a central component of mitochondrial metabolism. It provides the driving force for oxidative phosphorylation, for protein or metabolites import, and to regulate the activity of membrane proteins like the ANT [11,140,141]. We have demonstrated that, in syncytiotrophoblast mitochondria, $\Delta\psi_m$ regulates ATP-diphosphohydrolase activity [99], particularly its substrate selectivity (*i.e.*, ATP versus GTP preference). Also, ATP-diphosphohydrolase has been associated with cholesterol transport between mitochondrial membranes during progesterone synthesis [101]. Dissipation of $\Delta\psi_m$ by CCCP (carbonyl cyanide *m*-chlorophenyl-hydrazone) induces ATP-diphosphohydrolase to hydrolyze ATP as well as GTP. Under these conditions, when $\Delta\psi_m$ decreased, NADPH production by mitochondrial isocitrate dehydrogenase and ATP hydrolysis by ATP-diphosphohydrolase were essential for progesterone synthesis [99]. Studies with mitochondrial steroidogenic contact sites allow the assessment of the role and impact of the ETC function, the electrochemical proton gradient, oxygen consumption, and ATP synthesis on progesterone synthesis [99].

11. Placental signal transduction machinery

Steroid hormones have important functions in mammalian physiology and metabolic regulation through signaling cascades. Protein phosphorylation is the most common regulatory mechanism of protein function in cells. These have been widely studied in steroidogenic tissues like the adrenal glands and gonads, whose regulation is associated with changes in cAMP concentrations [142].

The human placenta is dynamically regulated by a wide range of intrinsic and extrinsic factors mediated by several signal transduction pathways. The proteins that constitute signaling cascades have been associated with different events, including: myometrial relaxation [143], maintenance of uterine quiescence during pregnancy [144], myometrium adrenoreceptor coupling to adenylate cyclases (AC) [145], AC isoform expression in human myometrium during pregnancy [146], and high intracellular cAMP levels associated with syncytium formation in human placental tissue [147].

Signaling cascades are perfectly orchestrated and are pivotal in pregnancy. Studying the function and composition of signaling systems is crucial to understanding cellular processes and the

interaction between the placenta, the mother and the fetus. Protein kinases control cell signaling pathways, which consist of sequential steps, initiated by different stimuli that result in the phosphorylation of serine, threonine or tyrosine residues. It is important to study the subcellular locations of the different phosphodiesterase (PDE) families, adenylate cyclases (AC), phosphatases (PP), and kinases associated with protein post-translational modification. The effect of these enzymes on the regulation of intracellular concentrations of second messengers and on cellular processes is an important subject of study [142,148].

Although mitochondria contain proteins associated with the cell signaling machinery and their own pool of second messengers, the kinetics, targets and effectors remain unknown. Moreover, how proteins can be phosphorylated in the mitochondrial matrix is yet to be elucidated [149]. Second messengers (*i.e.*, cAMP and cGMP) regulate several cellular functions. PDEs (PDE 1–11) regulate intracellular levels of cyclic nucleotides, determining the balance between their production and degradation, which leads to the rapid turnoff of the cAMP signal. cAMP cannot permeate the inner mitochondrial membrane, however, a soluble adenylate cyclase (sAC) activated by bicarbonate anion has been described [150,151]. The cellular expression and location of specific PDEs is determined by the local concentration of cyclic nucleotide and the phosphorylation/dephosphorylation mechanism [152]. Acin-Perez et al. [150] have described a mitochondrial signaling cascade where PDE is involved in the phosphorylation/dephosphorylation mechanism, and interacts with sAC, PKA and a cAMP mitochondrial microdomain. cAMP is synthesized by the transmembrane (tmAC) or sAC. The latter is located in the nucleus, mitochondria, microtubules, and centrioles. This variable location suggests that cAMP microdomains exist and are generated in response to extracellular or intrinsic signals regulated by PDEs [153,154]. It has been demonstrated that cytosolic sAC can generate second messengers at the site of the complex of A-kinase anchoring proteins (AKAPs)-cAMP-dependent protein kinases is located, removing the membrane-proximal limitation of cAMP generation [155].

Bernatchez et al. [156] demonstrated the differential expression of several adenylyl cyclase isoforms in trophoblast cells from human placenta, according to the stage of differentiation (*i.e.*, cytotrophoblast and syncytiotrophoblast). AC isoforms are subdivided into four groups according to the activating or inhibiting involved mechanism: group 1 is stimulated by calcium and calmodulin (I, III and VIII ACs), group 2 is activated by G-protein and protein kinase C (PKC) (II, IV and VII ACs), group 3 is inhibited by low concentrations of calcium (V and VI ACs), and group 4 is inhibited by phosphatase calcineurin (AC IX) [157–159]. ACs exert an important function during differentiation of trophoblast cells, depending on external factors such as PKC phosphorylation, calcium/calmodulin concentrations, or the binding of agonists that stimulate cytotrophoblast cells to differentiate into syncytiotrophoblast. However, the complete signaling pathways, the proteins involved, and upstream activators and downstream effectors, have not been elucidated.

Protein kinases play a key role in multiple cellular processes. Akt 1/2/3 (or PKB α / β / γ) is a serine/threonine-specific kinase whose activity is to modulate some cellular functions through phosphorylation of several substrates. Akt1 deficient mice exhibit structural anomalies in the placenta, suggesting fetal growth failure [160]. Another protein kinase that has been identified and expressed abundantly in the human placenta is ERK1/2. ERK2 transgenic mice exhibit defects in trophoblast morphogenesis and development, which induces damage in the vascularization of the fetal labyrinthine layer [161]. The ERK1/2 cascade is associated with the 11 β -HSD2 [162], which is negatively regulated, suggesting an important regulation point for the function of the human placenta and fetal development [163].

MAPK pathways are involved in morphological and functional differentiation of villous trophoblast, and have been implicated in oxidative injury where JNK/p38 and ERK pathways have an important effect. These data suggest an underlying equilibrium in the oxidative functions that help maintain pregnancy by preventing abortion, and preeclampsia due to oxidative stress [164–166].

Since the system of phosphorylation/dephosphorylation of proteins is an important regulatory mechanism in many cellular processes, the identification of tyrosine and serine/threonine phosphatases is essential. PP2C phosphatase has been described as a negative modulator of MAPK cascades, mainly p38 and JNK, dephosphorylating and inactivating at different levels of the signaling pathway [167]. Nevertheless, Daoud's group [168] demonstrated that ERK1/2 and p38 expression in human trophoblast cells is crucial to mediate the initiation of trophoblast differentiation. Other proteins are probably implicated in this process and control trophoblast differentiation and processes that depend on signaling cascades [168]. The identification and subcellular distribution of these signaling proteins is essential to prevent damage to the fetus, to develop selective and effective pharmacological methodologies to reduce the incidence of preterm labor and of complications associated with preterm deliveries attributed to progesterone synthesis.

It has been hypothesized that several cellular processes are related to alkaline phosphatases. The placenta expresses an alkaline phosphatase named placental alkaline phosphatase (PLAP). It has been described in early and full-term placentae, associated with insulin-like growth factor (IGF) regulation through dephosphorylation of the IGF binding protein-1 (IGFBP-1) in the maternal-fetal interface. Therefore, abnormal regulation of these pathways could lead to complications in fetal growth and pregnancy [169,170].

The orientation and location of enzymatic systems associated with progesterone synthesis as well as protein phosphorylation/dephosphorylation, cholesterol transport between mitochondrial membranes, and cholesterol processing by cytochrome P450_{sc} is important to understand mitochondrial function in placental tissue, including steroidogenesis. It has been proposed that steroidogenesis is a constitutive process of the human placenta, apparently without a regulatory control mechanism. However, the presence of PKA tightly bound to syncytiotrophoblast mitochondria suggests that a hormonal control mechanism is present [171].

12. cAMP-mediated signal transduction cascade in progesterone synthesis

The most studied transduction pathway in steroidogenic tissues is the one mediated by cAMP-PKA. In Leydig tumor cell line, basal steroidogenesis, independent of cAMP, is lower than 1% compared to the activation through cAMP-PKA dependent pathways induced by LH/hCG [171], however, in isolated primary Leydig cells normally comprises 10–25% of maximally stimulated steroidogenesis [172]; a similar situation is seen in isolated adrenocortical cells [173,174].

The human placenta is considered to be an autonomous/constitutively active tissue due to the absence of short term fluctuations in maternal progesterone. However, human placental steroidogenesis can be regulated by the luteinizing (LH) and human chorionic gonadotropin (hCG) hormones. hCG is known to bind and activate the G-protein coupled to the luteinizing hormone/hCG receptor, activating the cAMP/PKA pathway, which triggers events related to progesterone synthesis, decidualization and trophoblast differentiation [175]. The role of other key hormones that modulate cAMP levels and the participation of other signal transduction pathways independent of cAMP/PKA

are still unknown. Insulin, insulin-like growth factor 1, calcitriol, phorbol esters, epidermal growth factor, oestrogens and cytokines (IL-1 and TNF α) have been implicated in the stimulation of progesterone synthesis independent of PKA [176–180].

Primary cultures of trophoblast cells, choriocarcinoma derived cell lines and mitochondria isolated from syncytiotrophoblast, have been extensively employed as models of placental functions [6,106,181–183]. In these models steroidogenesis has been assessed through the use of activators of the PKA signaling cascade. In BeWo cells, it was observed that progesterone synthesis increases in the presence of the cAMP analog, 8-Br-cAMP. In the presence of H89, a kinase inhibitor widely used to block PKA activity, progesterone synthesis decreases from 70% to 90%, besides increasing phosphorylation of mitochondrial proteins [106].

In order to facilitate phosphorylation of the target substrate, several phosphorylation/dephosphorylation systems have a specific cell distribution that allows kinases to associate with specific organelles. This spatial and temporal modulation of signaling cascades can be achieved by the presence of AKAPs, which tether PKA to precise intracellular sites, such as mitochondria [184,185]. A PKA and a phosphotyrosine phosphate D1 (PTPD1) have been reported to be tightly associated with mitochondria isolated from human placenta through AKAP-121. The activity of this kinase is sensitive to H89 and the specific PKA inhibitor, PKI. The reported sub-localization of PKA and AKAP-121 in syncytiotrophoblast is mitochondrial contact sites [186], which are known to participate in progesterone synthesis [102]. Additionally, phosphorylation of proteins in the steroidogenic contact sites was blocked by H89, suggesting that contact sites contain potential PKA substrates. In the same study, it was observed that progesterone synthesis is either inhibited or abolished, depending on the H89 concentration. Also, phosphorylation of intact mitochondrial proteins increases in the presence of this inhibitor, suggesting the participation of other kinases and phosphatases modulated by PKA [187]. The presence of the PKA α catalytic (C α) subunit has also been detected in the cytoplasm, nucleus and mitochondria of placental cells; PKA C α subunit is located predominantly in the outer mitochondrial membrane [103].

We have assessed the overall contribution of PKA in progesterone synthesis and protein phosphorylation in syncytiotrophoblast mitochondria. We observed by submitochondrial fractionation that the PKA C α subunit is located in the outer, the inner and the soluble fraction. The C α subunit of the inner membrane has the highest activity. The β II regulatory (R β II) subunit was identified as the main isoform of PKA distributed in both the outer and inner membranes. This is relevant since the specificity in PKA signaling can be ensured by a differential expression of the R subunits, which have different roles in cell homeostasis.

Additionally, the identification of PKA associated with the membrane fraction of placental mitochondria suggests that it could make the signal transduction pathway involved in steroidogenesis more efficient. However, PKA is tightly associated with the mitochondrial membrane fraction, and dissociation of its subunits cannot be induced by holoenzyme activators, such as db-cAMP, as in the classical model of PKA activation. Furthermore, incubation of mitochondria in the presence or absence of cAMP or db-cAMP neither modified progesterone synthesis, nor protein phosphorylation [103]. These data suggest that the human placenta contains a constitutively active PKA as part of a complex signaling cascade where other kinases and phosphatases may be participating to modulate the dynamic phosphorylation and dephosphorylation of mitochondrial proteins to synthesize progesterone during pregnancy.

13. Conclusion and perspectives

The human placenta plays a central role during pregnancy because it carries out multiple metabolic functions similar to those performed by the pituitary, ovaries, bowels, liver, and kidneys. The placenta plays an important role in the transport of nutrients, oxygen, and waste products from the fetal metabolism; additionally, the placenta synthesizes multiple hormones, progesterone being among the most important because it establishes and maintains the maternal fetal interface required to assure normal pregnancy.

Although an effort has been made to understand the metabolism of the human placenta, our knowledge of the function of this organ is still not complete. In the future, it will be important to know how placental cells handle cholesterol distribution for its own metabolic needs in the trophoblast cells, and for the fetus. Also, the participation of mitochondria in the distribution of energy to synthesize ATP and/or progesterone should be studied. Finally, the signal transduction with the central participation of mitochondria to control cellular processes will be important to elucidate, since this information will inform how the trophoblast maintains the relationship between the mother and fetus leading to maintenance of pregnancy to term. Then, a further research should be oriented to new methods, including the need for new techniques to study the syncytiotrophoblast in situ using non-invasive methods.

Acknowledgements

This work was partially supported by Grants IN211912, IN211715 and IN214914 from Dirección General de Asuntos del Personal Académico (DGAPA) from the Universidad Nacional Autónoma de México and Grant 168025 from CONACYT, México. The authors thanks Dr. Jerome F. Strauss III of Virginia Commonwealth University School of Medicine, for his valuable suggestions and the critical review of the manuscript.

References

- [1] M. Halasz, J. Szekeres-Bartho, The role of progesterone in implantation and trophoblast invasion, *J. Reprod. Immunol.* 97 (1) (2013) 43–50.
- [2] K. Benirschke, P. Kaufmann, *Pathology of the Human Placenta*, Springer-Verlag, New-York, 2000, p. 22–70.
- [3] B. Eaton, S. Contractor, in: C.W. Redman, I.L. Sargent, P.M. Starkey (Eds.), *In vitro Assessment of Trophoblast Receptors and Placental Transport Mechanisms*, Blackwell Scientific Publication, London, 1993, pp. 471–503.
- [4] H. Kliman, J. Nestler, E. Sermasi, J. Sanger, J. Strauss III, Purification, characterization, and in vitro differentiation of cytotrophoblasts from human term placenta, *Endocrinology* 118 (1986) 1567–1582.
- [5] N. Cherradi, G. Defaye, E.M. Chambaz, Characterization of the 3 beta-hydroxysteroid dehydrogenase activity associated with bovine adrenocortical mitochondria, *Endocrinology* 134 (3) (1994) 1358–1364.
- [6] F. Martinez, M. Kiriakidou, J.F. Strauss III, Structural and functional changes in mitochondria associated with trophoblast differentiation: methods to isolate enriched preparations of syncytiotrophoblast mitochondria, *Endocrinology* 138 (5) (1997) 2172–2183.
- [7] C. Brand, N. Cherradi, G. Defaye, A. Chinn, E.M. Chambaz, J.J. Feige, et al., Transforming growth factor beta1 decreases cholesterol supply to mitochondria via repression of steroidogenic acute regulatory protein expression, *J. Biol. Chem.* 273 (11) (1998) 6410–6416.
- [8] S. Paul, B.L. Jaikhan, G.P. Talwar, Isolation and functional maintenance in culture of syncytiotrophoblasts from human placenta, *Indian J. Exp. Biol.* 16 (12) (1978) 1226–1235.
- [9] J. Kaiser, Gearing up for a closer look at the human placenta, *Science* 344 (6188) (2014) 1073.
- [10] C.J. Kim, Congenital lipid adrenal hyperplasia, *Ann. Pediatr. Endocrinol. Metab.* 19 (2014) 179–183.
- [11] D.W. Nebert, K. Wikvall, W.L. Miller, Human cytochromes P450 in health and disease, *Philos. Trans. R. Soc. B* 368 (2013) 20120431.
- [12] B.J. Clark, The mammalian START domain protein family in lipid transport in health and disease, *J. Endocrinol.* 212 (2012) 257–275.
- [13] C. Daum, J.E. Vance, Import of lipids into mitochondria, *Prog. Lipid Res.* 36 (2–3) (1997) 103–130.


- [14] R.E. Soccio, J.L. Breslow, StAR-related lipid transfer (START) proteins: mediators of intracellular lipid metabolism, *J. Biol. Chem.* 278 (25) (2003) 22183–22186.
- [15] S.C.J. Helle, G. Kanfer, K. Kolar, A. Lang, A.H. Michel, B. Kornmann, Organization and function of membrane contact sites, *Biochim. Biophys. Acta* 1833 (2013) 2526–2541.
- [16] V. Papadopoulos, W.L. Miller, Role of mitochondria in steroidogenesis, *Best Pract. Res. Clin. Endocrinol. Metab.* 26 (6) (2012) 771–790.
- [17] S.W. Tait, D.R. Green, Mitochondria and cell signalling, *J. Cell Sci.* 125 (2012) 807–815.
- [18] A. Carlucci, L. Lignitto, A. Feliciello, Control of mitochondria dynamics and oxidative metabolism by cAMP, AKAPs and the proteasome, *Trends Cell Biol.* 18 (12) (2008) 604–613.
- [19] L. Galluzzi, O. Kepp, G. Kroemer, Mitochondria: master regulators of danger signaling, *Nat. Rev. Mol. Cell Biol.* 13 (12) (2012) 780–788.
- [20] J.T. Gwynne, J.F. Strauss 3rd., The role of lipoproteins in steroidogenesis and cholesterol metabolism in steroidogenic glands, *Endocr. Rev.* 3 (3) (1982) 299–329.
- [21] L. Zelewski, C.A. Villee, The biosynthesis of squalene, lanosterol, and cholesterol by minced human placenta, *Biochemistry* 5 (6) (1966) 1805–1814.
- [22] H. van Leusden, C.A. Villee, The de novo synthesis of sterols and steroids—from acetate by preparations of human term placenta, *Steroids* 6 (1965) 31–45.
- [23] R.S. Mathur, D.F. Archer, N. Wiqvist, E. Diczfalusy, Quantitative assessment of the de novo sterol and steroid synthesis in the human foeto-and secretion of cholesterol and cholesterol sulphate, *Acta Endocrinol. (Copenh)* 65 (4) (1970) 663–674.
- [24] H.A. van Leusden, C. Thomas, G. Telegdy, E. Diczfalusy, Lack of squalene and lanosterol synthesis by the perfused human placenta at term, *J. Steroid Biochem.* 4 (4) (1973) 349–354.
- [25] C.A. Winkel, J.M. Snyder, P.C. MacDonald, E.R. Simpson, Regulation of cholesterol and progesterone synthesis in human placental cells in culture by serum lipoproteins, *Endocrinology* 106 (4) (1980) 1054–1060.
- [26] C.A. Winkel, P.C. MacDonald, P.G. Hemsell, E.R. Simpson, Regulation of cholesterol metabolism by human trophoblastic cells in primary culture, *Endocrinology* 109 (4) (1981) 1084–1090.
- [27] N.M. Gude, C.T. Roberts, B. Kalionis, R.G. King, Growth and function of the normal human placenta, *Thromb. Res.* 114 (5–6) (2004) 397–407.
- [28] M. Furuhashi, H. Seo, S. Mizutani, O. Narita, Y. Tomoda, N. Matsui, Expression of low density lipoprotein receptor gene in human placenta during pregnancy, *Mol. Endocrinol.* 3 (8) (1989) 1252–1256.
- [29] C. Wadsack, A. Hammer, S. Levak-Frank, G. Desoye, K.F. Kozarsky, B. Hirschmugl, et al., Selective cholesteryl ester uptake from high density lipoprotein by human first trimester and term villous trophoblast cells, *Placenta* 24 (2–3) (2003) 131–143.
- [30] T.A. Pagler, S. Golsabahi, M. Doringier, S. Rhode, G.J. Schutz, M. Pavelka, et al., A Chinese hamster ovarian cell line imports cholesterol by high-density lipoprotein degradation, *J. Biol. Chem.* 281 (50) (2006) 38159–38171.
- [31] C. Röhr, H. Stangl, HDL endocytosis and resecretion, *Biochim. Biophys. Acta* 1831 (11) (2013) 1626–1633.
- [32] C.A. Winkel, P.C. MacDonald, E.R. Simpson, The role of receptor-mediated low-density lipoprotein uptake and degradation in the regulation of progesterone biosynthesis and cholesterol metabolism by human trophoblasts, *Placenta Suppl.* 3 (1981) 133–143.
- [33] J.T. Sanderson, Placental and fetal steroidogenesis, in: J. Lafond, C. Vaillancourt (Eds.), *Human Embryogenesis: Methods and Protocols*, vol. 550, Tennessee: Humana Press, a part of Springer Science + Business Media, 2009, pp. 127–136.
- [34] R. Zamel, R. Khan, R.L. Pollex, R.A. Hegele, Abetalipoproteinemia: two case reports and literature review, *Orphanet J. Rare Dis.* 8 (3) (2008) 19.
- [35] L.A. Woollett, Review: transport of maternal cholesterol to the fetal circulation, *Placenta* 32 (Suppl. 2) (2011) S218–S221.
- [36] J. Bhattacharjee, F. Ietta, R. Romagnoli, N. Bechi, I. Caniggia, L. Paulesu, ABC transporters in human placenta and their role in maternal-fetal cholesterol transfer: ABCA1 candidate target, in: Jing Zheng (Ed.), *Recent Advances in Research on the Human Placenta*, In Tech, Croatia, 2012, pp. 336–354.
- [37] T. Plösch, E.M.E. van Straten, F. Kuipers, Cholesterol transport by the placenta: placental liver X receptor activity as a modulator of fetal cholesterol metabolism?, *Placenta* 28 (7) (2007) 604–610.
- [38] M.E. Baardman, W.S. Kerstjens-Frederikse, R.M.F. Berger, M.K. Bakker, R.M.W. Hofstra, T. Plösch, The role of maternal-fetal cholesterol transport in early fetal life: current insights, *Biol. Reprod.* 88 (1) (2013) 24 (1–9).
- [39] C.D. Klaassen, L.M. Aleksunes, Xenobiotic, bile acid, and cholesterol transporters: function and regulation, *Pharmacol. Rev.* 62 (1) (2010) 1–96.
- [40] G. Desoye, M. Gauster, C. Wadsack, Placental transport in pregnancy pathologies, *Am. J. Clin. Nutr.* 94 (Suppl. 6) (2011) 1896S–1902S.
- [41] B. Kornmann, The molecular hug between the ER and the mitochondria, *Curr. Opin. Cell Biol.* 25 (4) (2013) 443–448.
- [42] A. Toulmay, W.A. Prinz, Lipid transfer and signaling at organelle contact sites: the tip of the iceberg, *Curr. Opin. Cell Biol.* 23 (4) (2011) 458–463.
- [43] M. Fujimoto, T. Hayashi, T.P. Su, The role of cholesterol in the association of endoplasmic reticulum membranes with mitochondria, *Biochem. Biophys. Res. Commun.* 417 (1) (2012) 635–639.
- [44] V.K. Khora, W.J. Shena, F.B. Kraemer, Lipid droplet metabolism, *Curr. Opin. Clin. Nutr. Metab. Care* 16 (6) (2013) 632–637.
- [45] M. Scharwey, T. Tatsuta, T. Langer, Mitochondrial lipid transport at a glance, *J. Cell Sci.* 126 (Pt 23) (2013) 5317–5323.
- [46] L. Issop, M.B. Rone, V. Papadopoulos, Organelle plasticity and interactions in cholesterol transport and steroid biosynthesis, *Mol. Cell. Endocrinol.* 371 (1–2) (2013) 34–46.
- [47] F.B. Kraemer, V.K. Khor, W.J. Shen, S. Azhar, Cholesterol ester droplets and steroidogenesis, *Mol. Cell. Endocrinol.* 371 (1–2) (2013) 15–19.
- [48] T. Tatsuta, M. Scharwey, T. Langer, Mitochondrial lipid trafficking, *Trends Cell Biol.* 24 (1) (2014) 44–52.
- [49] P.F. Hall, G. Almahbobi, The role of the cytoskeleton in the regulation of steroidogenesis, *J. Steroid Biochem. Mol. Biol.* 43 (8) (1992) 769–777.
- [50] M.B. Sewer, D. Li, Regulation of steroid hormone biosynthesis by the cytoskeleton, *Lipids* 43 (12) (2008) 1109–1115.
- [51] G. Almahbobi, L.J. Williams, P.F. Hall, Attachment of mitochondria to intermediate filaments in adrenal cells: relevance to the regulation of steroid synthesis, *Exp. Cell Res.* 200 (1992) 361–369.
- [52] G. Almahbobi, L.J. Williams, P.F. Hall, Attachment of steroidogenic lipid droplets to intermediate filaments in adrenal cells, *J. Cell Sci.* 101 (1992) 383–393.
- [53] F. Alpy, A. Rousseau, Y. Schwab, F. Legueux, I. Stoll, C. Wendling, et al., STARD3/STARD3NL and VAP make a novel molecular tether between late endosomes and the ER, *J. Cell Sci.* 126 (Pt 23) (2013) 5500–5512.
- [54] R.C. Tuckey, H.S. Bose, I. Czerwionka, W.L. Miller, Molten globule structure and steroidogenic activity of N-218 MLN64 in human placental mitochondria, *Endocrinology* 145 (4) (2004) 1700–1707.
- [55] L.A. Martin, B.E. Kennedy, B. Karten, Mitochondrial cholesterol: mechanisms of import and effects on mitochondrial function, *J. Bioenerg. Biomembr.* (2014), <http://dx.doi.org/10.1007/s10863-014-9592-6>.
- [56] S.E. Horvath, G. Daum, Lipids of mitochondria, *Prog. Lipid Res.* 52 (4) (2013) 590–614.
- [57] M.T. Espinosa-Garcia, J.F. Strauss 3rd, F. Martinez, A trypsin-sensitive protein is required for utilization of exogenous cholesterol for pregnenolone synthesis by placental mitochondria, *Placenta* 21 (2000) 654–660.
- [58] J. Navarrete, O. Flores-Herrera, A. Uribe, F. Martínez, Differences in cholesterol incorporation into mitochondria from hepatoma AS-30D and human term placenta, *Placenta* 20 (4) (1999) 285–291.
- [59] F. Martinez, R. Milan, O. Flores-Herrera, S. Olvera-Sanchez, E. Gomez-Chang, M.T. Espinosa-Garcia, Espinosa-Garcia, The role of mitochondria in syncytiotrophoblast cells: bioenergetics and steroidogenesis, in: J. Zheng (Ed.), *Recent Advances in Research on the Human Placenta*, In Tech, Croatia, 2012, pp. 397–428.
- [60] R.C. Tuckey, M.J. Headlam, H.S. Bose, W.L. Miller, Transfer of cholesterol between phospholipid vesicles mediated by the steroidogenic acute regulatory protein (StAR), *J. Biol. Chem.* 277 (49) (2002) 47123–47128.
- [61] D. Lin, T. Sugawara, J.F. Strauss 3rd, B.J. Clark, D.M. Stocco, P. Saenger, A. Rogol, W.L. Miller, Role of steroidogenic acute regulatory protein in adrenal and gonadal steroidogenesis, *Science* 267 (5205) (1995) 1828–1831.
- [62] P.R. Manna, M.T. Dyson, D.M. Stocco, Regulation of the steroidogenic acute regulatory protein gene expression: present and future perspectives, *Mol. Hum. Reprod.* 15 (6) (2009) 321–333.
- [63] H.A. LaVoie, S.R. King, Transcriptional regulation of steroidogenic genes: STARD1, CYP11A1 and HSD3B, *Exp. Biol. Med.* (Maywood). 234 (8) (2009) 880–907.
- [64] F. Alpy, C. Tomasetto, START ships lipids across interorganelle space, *Biochimie* 96 (2014) 85–95.
- [65] F. Arakane, S.R. King, Y. Du, C.B. Kallen, L.P. Walsh, H. Watari, et al., Phosphorylation of steroidogenic acute regulatory protein (StAR) modulates its steroidogenic activity, *J. Biol. Chem.* 272 (51) (1997) 32656–32662.
- [66] G. Sasaki, M. Zubair, T. Ishii, T. Mitsui, T. Hasegawa, R.J. Auchus, The contribution of serine 194 phosphorylation to steroidogenic acute regulatory protein function, *Mol. Endocrinol.* 28 (7) (2014) 1088–1096.
- [67] F. Arakane, C.B. Kallen, H. Watari, J.A. Foster, N.B. Sepuri, D. Pain, et al., The mechanism of action of steroidogenic acute regulatory protein (StAR). StAR acts on the outside of mitochondria to stimulate steroidogenesis, *J. Biol. Chem.* 273 (26) (1998) 16339–16345.
- [68] M. Rajapaksha, J. Kaur, M. Bose, R.M. Whittall, H.S. Bose, Cholesterol-mediated conformational changes in the steroidogenic acute regulatory protein are essential for steroidogenesis, *Biochemistry* 52 (41) (2013) 7242–7253.
- [69] E.R. Simpson, P.C. MacDonald, *Endocrine physiology of the placenta*, *Annu. Rev. Physiol.* 43 (1981) 163–188.
- [70] H.S. Bose, R.M. Whittall, M.C. Huang, M.A. Baldwin, W.L. Miller, N-218MLN64, a protein with StAR-like steroidogenic activity, is folded and cleaved similarly to StAR, *Biochemistry* 39 (2000) 11722–11731.
- [71] C. Tomasetto, C. Regnier, C. Moog-Lutz, M.G. Mattei, M.P. Chenard, R. Lidereau, et al., Identification of four novel human genes amplified and overexpressed in breast carcinoma and localized to the q11–q21.3 region of chromosome 17, *Genomics* 28 (3) (1995) 367–376.
- [72] R. van der Kant, I. Zondervan, L. Janssen, J. Neefjes, Cholesterol-binding molecules MLN64 and ORP1L mark distinct late endosomes with transporters ABCA3 and NPC1, *J. Lipid Res.* 54 (8) (2013) 2153–2165.
- [73] M. Charman, B.E. Kennedy, N. Osborne, B. Karten, MLN64 mediates egress of cholesterol from endosomes to mitochondria in the absence of functional Niemann-Pick Type C1 protein, *J. Lipid Res.* 51 (5) (2010) 1023–1034.
- [74] J. Hu, Z. Zhang, W.J. Shen, S. Azhar, Cellular cholesterol delivery, intracellular processing and utilization for biosynthesis of steroid hormones, *Nutr. Metab. (Lond)* 7 (2010) 47.

- [75] M. Esparza-Perusquía, S. Olvera-Sánchez, O. Flores-Herrera, H. Flores-Herrera, A. Guevara-Flores, J.P. Pardo, et al., Mitochondrial proteases act on STARD3 to activate progesterone synthesis in human syncytiotrophoblast, *Biochim. Biophys. Acta* 1850 (1) (2015) 107–117.
- [76] T. Kishida, I. Kostetskii, Z. Zhang, F. Martinez, P. Liu, S.U. Walkley, et al., Targeted mutation of the MLN64 START domain causes only modest alterations in cellular sterol metabolism, *J. Biol. Chem.* 279 (18) (2004) 19276–19285.
- [77] S. Olvera-Sanchez, M.T. Espinosa-García, J. Monreal, O. Flores-Herrera, F. Martinez, Mitochondrial heat shock protein participates in placental steroidogenesis, *Placenta* 32 (3) (2011) 222–229.
- [78] J.F. Strauss 3rd, T. Kishida, L.K. Christenson, T. Fujimoto, H. Hiroi, StAR domain proteins and the intracellular trafficking of cholesterol in steroidogenic cells, *Mol. Cell. Endocrinol.* 202 (1) (2003) 59–65.
- [79] W.L. Miller, H.S. Bose, Early steps in steroidogenesis: intracellular cholesterol trafficking, *J. Lipid Res.* 52 (12) (2011) 2111–2135.
- [80] J. Fan, V. Papadopoulos, Evolutionary origin of the mitochondrial cholesterol transport machinery reveals a universal mechanism of steroid hormone biosynthesis in animals, *PLoS ONE* 8 (10) (2013) e76701.
- [81] A.T. Slominski, T.K. Kim, J. Chen, M.N. Nguyen, W. Li, C.R. Yates, et al., Cytochrome P450_{sc}-dependent metabolism of 7-dehydrocholesterol in placenta and epidermal keratinocytes, *Int. J. Biochem. Cell Biol.* 44 (2012) 2003–2018.
- [82] C.R. Hackenbrock, Chemical and physical fixation of isolated mitochondria in low-energy and high-energy states, *Proc. Natl. Acad. Sci. U.S.A.* 61 (2) (1968) 598–605.
- [83] V. Adams, W. Bosch, J. Schelege, T. Wallimann, D. Brdiczka, Further characterization of contact sites from mitochondria of different tissues: topology of peripheral kinases, *Biochim. Biophys. Acta* 981 (2) (1993) 213–225.
- [84] D. Brdiczka, Contact sites between mitochondrial envelope membranes. Structure and function in energy- and protein-transfer, *Biochim. Biophys. Acta* 1071 (3) (1991) 291–312.
- [85] J.M. Adams, S. Cory, Life-or-death decisions by the Bcl-2 protein family, *Trends Biochem. Sci.* 26 (1) (2001) 61–66.
- [86] N. Zamzami, G. Kroemer, The mitochondrion in apoptosis: how Pandora's Box opens, *Nat. Rev. Mol. Cell Biol.* 2 (1) (2001) 67–71.
- [87] D.F. Suen, K.L. Norris, R.J. Youle, Mitochondrial dynamics and apoptosis, *Genes Dev.* 22 (12) (2008) 1577–1590.
- [88] A. Rasola, P. Bernardi, The mitochondrial permeability transition pore and its adaptive responses in tumor cells, *Cell Calcium* 56 (6) (2014) 437–445.
- [89] M. Bose, R.M. Whittal, W.L. Miller, H.S. Bose, Steroidogenic activity of StAR requires contact with mitochondrial VDAC1 and phosphoglycerate carrier protein, *J. Biol. Chem.* 283 (14) (2008) 8837–8845.
- [90] M. Prasad, J. Kaur, K.J. Pawlak, M. Bose, R.M. Whittal, H.S. Bose, Mitochondria associated ER-Membrane (MAM) regulates steroidogenic activity via StAR-VDAC2 interaction, *J. Biol. Chem.* 290 (5) (2015) 2604–2616.
- [91] K.S. Marriott, M. Prasad, V. Thapliyal, H.S. Bose, Σ -1 receptor at the mitochondrial-associated endoplasmic reticulum membrane is responsible for mitochondrial metabolic regulation, *J. Pharmacol. Exp. Ther.* 343 (3) (2012) 578–586.
- [92] L. Issop, J. Fan, S. Lee, M.B. Rone, K. Basu, J. Mui, et al., Mitochondria-associated membrane formation in hormone-stimulated Leydig cell steroidogenesis: role of ATAD3, *Endocrinology* 1 (1) (2015) 334–345.
- [93] C. Giatzakis, A. Batarseh, L. Dettin, V. Papadopoulos, The role of Ets transcription factors in the basal transcription of the translocator protein (18 kDa), *Biochemistry* 46 (16) (2007) 4763–4774.
- [94] M.B. Rone, A.S. Midzak, L. Issop, G. Rammouz, S. Jagannathan, J. Fan, et al., Identification of a dynamic mitochondrial protein complex driving cholesterol import, trafficking and metabolism to steroid hormones, *Mol. Endocrinol.* 26 (11) (2012) 1868–1882.
- [95] J. Nicholas, N.J. Hoogenraad, L.A. Ward, M.T. Ryan, Import and assembly of proteins into mitochondria of mammalian cells, *Biochim. Biophys. Acta* 1592 (1) (2002) 97–105.
- [96] J. Kevin, K.J. Pawlak, M. Prasad, J.L. Thomas, R.M. Whittal, H.S. Bose, Inner mitochondrial translocase Tim50 interacts with 3 β -hydroxysteroid dehydrogenase type 2 to regulate adrenal and gonadal steroidogenesis, *J. Biol. Chem.* 286 (45) (2011) 39130–39140.
- [97] M. Beller, K. Thiel, P.J. Thul, H. Jäckle, Lipid droplets: a dynamic organelle moves into focus, *FEBS Lett.* 584 (11) (2010) 2176–2182.
- [98] H. Yang, A. Galea, V. Sytnyk, M. Crossley, Controlling the size of lipid droplets: lipid and protein factors, *Curr. Opin. Cell Biol.* 24 (4) (2012) 509–516.
- [99] O. Flores-Herrera, S. Olvera-Sánchez, M. Esparza-Perusquía, J.P. Pardo, J.L. Rendón, et al., Membrane potential regulates mitochondrial ATP-diphosphohydrolase activity but is not involved in progesterone biosynthesis in human syncytiotrophoblast cells, *Biochim. Biophys. Acta* 1847 (2) (2015) 143–152.
- [100] O. Flores-Herrera, A. Uribe, J.P. Pardo, J.L. Rendón, F. Martínez, A novel ATP-diphosphohydrolase from human term placental mitochondria, *Placenta* 20 (5–6) (1999) 475–484.
- [101] O. Flores-Herrera, A. Uribe, C. García-Perez, R. Milan, F. Martínez, 5'-p-fluorosulfonylbenzoyl adenosine inhibits progesterone synthesis in human placental mitochondria, *Biochim. Biophys. Acta* 1585 (1) (2002) 11–18.
- [102] A. Uribe, J.F. Strauss 3rd, F. Martínez, Contact sites from human placental mitochondria: characterization and role in progesterone synthesis, *Arch. Biochem. Biophys.* 413 (2) (2003) 172–181.
- [103] E. Gomez-Chang, M.T. Espinosa-García, S. Olvera-Sanchez, O. Flores-Herrera, F. Martinez, PKA tightly bound to human placental mitochondria participates in steroidogenesis and is not modified by cAMP, *Placenta* 35 (9) (2014) 748–762.
- [104] E.R. Barnea, F. Fares, M. Gavish, Modulatory action of benzodiazepines on human term placental steroidogenesis in vitro, *Mol. Cell. Endocrinol.* 64 (2) (1989) 155–159.
- [105] L. Lassance et al., Obesity-induced down-regulation of the mitochondrial translocator protein (TSPO) impairs placental steroid production, *J. Clin. Endocrinol. Metab.* 100 (2015) E11–E18.
- [106] M.G. Maldonado-Mercado, M.T. Espinosa-García, C. Gómez-Concha, J. Monreal-Flores, F. Martinez, Steroidogenesis in BeWo cells: role of protein kinase A and benzodiazepines, *Int. J. Biochem. Cell Biol.* 40 (5) (2008) 901–908.
- [107] R. Jahn, R.H. Scheller, SNAREs—engines for membrane fusion, *Nat. Rev. Mol. Cell Biol.* 7 (9) (2006) 631–643.
- [108] P. Boström, L. Andersson, M. Rutberg, J. Perman, U. Lidberg, B.R. Johansson, et al., SNARE proteins mediate fusion between cytosolic lipid droplets and are implicated in insulin sensitivity, *Nat. Cell Biol.* 9 (11) (2007) 1286–1293.
- [109] S. Martens, H.T. McMahon, Mechanisms of membrane fusion: disparate players and common principals, *Nat. Rev. Mol. Cell Biol.* 9 (7) (2009) 543–556.
- [110] T.C. Sühof, J.E. Rothman, Membrane fusion: grappling with SNARE and SM proteins, *Science* 323 (5913) (2009) 474–477.
- [111] M.S. Jägerström, S. Polesie, Y. Wickström, B.R. Johansson, H.D. Schroder, K. Højlund, et al., Lipid droplets interact with mitochondria using SNAP23, *Cell Biol. Int.* 33 (9) (2009) 934–940.
- [112] N.J. Grant, R. Hepp, W. Krause, D. Aunis, P. Oehme, K. Langley, Differential expression of SNAP-25 isoforms and SNAP-23 in the adrenal gland, *J. Neurochem.* 72 (1) (1999) 363–372.
- [113] M. Steegmaier, V. Oorschot, J. Klumperman, R.H. Scheller, Syntaxin 17 is abundant in steroidogenic cells and implicated in smooth endoplasmic reticulum membrane dynamics, *Mol. Biol. Cell* 11 (8) (2000) 2719–2731.
- [114] J. Grosse, A. Bulling, C. Brucker, U. Berg, A. Amsterdam, A. Mayerhofer, et al., Synaptosome-associated protein of 25 kilodaltons in oocytes and steroid-producing cells of rat and human ovary: molecular analysis and regulation by gonadotropins, *Biol. Reprod.* 63 (2) (2000) 643–650.
- [115] M. Jo, M.C. Gieske, C.E. Payne, S.E. Wheeler-Price, J.B. Gieske, I.V. Ignatius, et al., Development and application of a rat ovarian gene expression database, *Endocrinology* 145 (11) (2004) 5384–5396.
- [116] M. Shimada, Y. Yanai, T. Okazaki, Y. Yamashita, V. Sriraman, W.C. Wilson, et al., Snaptosom-associated protein 25 gene expression is hormonally regulated during ovulation and is involved in cytokine/chemokine exocytosis from granulosa cells, *Mol. Endocrinol.* 21 (10) (2007) 2487–2502.
- [117] D. De los Rios Castillo, M. Zarco-Zavala, S. Olvera-Sanchez, J.P. Pardo, O. Juarez, F. Martinez, et al., Atypical cristae morphology of human syncytiotrophoblast mitochondria: role for complex V, *J. Biol. Chem.* 286 (27) (2011) 23911–23919.
- [118] M. Strauss, G. Hofhaus, R.R. Schröder, W. Kühlbrandt, Dimer ribbons of ATP synthase shape the inner mitochondrial membrane, *EMBO J.* 27 (7) (2008) 1154–1160.
- [119] R.D. Allen, C.C. Schroeder, A.K. Fok, An investigation of mitochondrial inner membranes by rapid-freeze deep-etch techniques, *J. Cell Biol.* 108 (6) (1989) 2233–2240.
- [120] R.D. Allen, Membrane tubulation and proton pumps, *Protoplasma* 189 (1995) 1–8.
- [121] P. Paumard, J. Vaillier, B. Couly, J. Schaeffer, V. Soubannier, D.M. Mueller, et al., The ATP synthase is involved in generating mitochondrial cristae morphology, *EMBO J.* 21 (3) (2002) 221–230.
- [122] H. Yao, R.A. Stuart, S. Cai, D.S. Sem, Structural characterization of the transmembrane domain from subunit e of yeast F1Fo-ATP synthase: a helical GXXXG motif located just under the micelle surface, *Biochemistry* 47 (7) (2008) 1910–1917.
- [123] J. Velours, A. Dautant, I. Sagot, D. Brethes, Mitochondrial F1Fo-ATP synthase and organellar internal architecture, *Int. J. Biochem. Cell Biol.* 41 (10) (2009) 1783–1789.
- [124] K.M. Davies, M. Strauss, B. Daum, J.H. Kief, H.D. Osiewicz, A. Rycovska, et al., Macromolecular organization of ATP synthase and complex I in whole mitochondria, *Proc. Natl. Acad. Sci. U.S.A.* 108 (34) (2011) 14121–14126.
- [125] F. Minauro-Sanmiguel, S. Wilkens, J.J. Garcia, Structure of dimeric mitochondrial ATP synthase: novel F0 bridging features and the structural basis of mitochondrial cristae biogenesis, *Proc. Natl. Acad. Sci. U.S.A.* 102 (35) (2005) 12356–12358.
- [126] C. Bornhövd, F. Vogel, W. Neupert, A.S. Reichert, Mitochondrial membrane potential is dependent on the oligomeric state of F1Fo-ATP synthase supracomplexes, *J. Biol. Chem.* 281 (20) (2006) 13990–13998.
- [127] F.P. Prince, Lamellar and tubular associations of the mitochondrial cristae: unique forms of the cristae present in steroid-producing cells, *Mitochondrion* 1 (4) (2002) 381–389.
- [128] C.A. Mannella, M. Marko, P. Penczek, D. Barnard, J. Frank, The internal compartmentation of rat-liver mitochondria: tomographic study using the high-voltage transmission electron microscope, *Microsc. Res. Tech.* 27 (4) (1994) 278–283.
- [129] C.A. Mannella, Minireview: on the structure and gating mechanism of the mitochondrial channel, VDAC, *J. Bioenerg. Biomembr.* 29 (6) (1997) 525–531.

- [130] G.A. Perkins, C.W. Renken, J.Y. Song, T.G. Frey, S.J. Young, S. Lamont, et al., Electron tomography of large, multicomponent biological structures, *J. Struct. Biol.* 120 (3) (1997) 219–227.
- [131] G.A. Perkins, C.W. Renken, T.G. Frey, M.H. Ellisman, Membrane architecture of mitochondria in neurons of the central nervous system, *J. Neurosci. Res.* 66 (5) (2001) 857–865.
- [132] G.A. Perkins, J.Y. Song, L. Tarsa, T.J. Deerinck, M.H. Ellisman, T.G. Frey, Electron tomography of mitochondria from brown adipocytes reveals crista junctions, *J. Bioenerg. Biomembr.* 30 (5) (1998) 431–442.
- [133] D. Nicastro, A.S. Frangakis, D. Typke, W. Baumeister, Cryo-electron tomography of neurospora mitochondria, *J. Struct. Biol.* 129 (1) (2000) 48–56.
- [134] G.A. Perkins, C.W. Renken, I.J. van der Klei, M.H. Ellisman, W. Neupert, T.G. Frey, Electron tomography of mitochondria after the arrest of protein import associated with Tom19 depletion, *Eur. J. Cell Biol.* 80 (2) (2001) 139–150.
- [135] G.A. Perkins, M.H. Ellisman, D.A. Fox, Three-dimensional analysis of mouse rod and cone mitochondrial cristae architecture: bioenergetic and functional implications, *Mol. Vis.* 9 (2003) 60–73.
- [136] J.A. Allen, T. Shankara, P. Janus, S. Buck, T. Diemer, K.H. Hales, D.B. Hales, Energized, polarized, and actively respiring mitochondria are required for acute Leydig cell steroidogenesis, *Endocrinology* 147 (8) (2006) 3924–3935.
- [137] W.L. Miller, Steroid hormone biosynthesis and actions in the materno-feto-placental unit, *Clin. Perinatol.* 25 (4) (1998) 799–817.
- [138] X. Xu, T. Xu, D.G. Robertson, J.D. Lamberth, GTP stimulates pregnenolone generation in isolated rat adrenal mitochondria, *J. Mol. Biol.* 264 (30) (1989) 17674–17680.
- [139] F. Martínez, T. Espinosa-García, O. Flores-Herrera, J.P. Pardo, Respiratory control induced by ATP in human term placental mitochondria, *Placenta* 14 (3) (1993) 321–331.
- [140] B. Kadenbach, R. Ramzan, L. Wen, S. Vogt, New extension of the Mitchell Theory for oxidative phosphorylation in mitochondria of living organisms, *Biochim. Biophys. Acta* 1800 (3) (2010) 205–212.
- [141] D. Mokranjac, W. Neupert, Energetics of protein translocation into mitochondria, *Biochim. Biophys. Acta* 1777 (7–8) (2008) 758–762.
- [142] V.C. Manganiello, T. Murata, M. Taira, P. Belfrage, E. Degerman, Diversity in cyclic nucleotide phosphodiesterase isoenzyme families, *Arch. Biochem. Biophys.* 322 (1) (1995) 1–13.
- [143] J. Senior, K. Marshall, R. Sangha, G.S. Baxter, J.K. Clayton, *in vitro* characterization of prostanoid EP-receptors in the nonpregnant human myometrium, *Br. J. Pharmacol.* 102 (3) (1991) 747–753.
- [144] M.L. Casey, J. Smith, G. Alasbrook, P.C. MacDonald, Activation of adenylyl cyclase in human myometrial smooth muscle cells by neuropeptides, *J. Clin. Endocrinol. Metab.* 82 (9) (1997) 3087–3092.
- [145] M.H. Litime, G. Pointis, M. Breuille, D. Cabrol, F. Ferre, Disappearance of β -adrenergic response of human myometrial adenylyl cyclase at the end of pregnancy, *J. Clin. Endocrinol. Metab.* 69 (1) (1989) 1–6.
- [146] S.A. Price, I. Pochun, S. Phaneuf, Lopez Bernal A. Adenylyl cyclase isoforms in pregnant and non-pregnant human myometrium, *J. Endocrinol.* 164 (1) (2000) 21–30.
- [147] L. Kao, G.O. Babalola, G.S. Kopf, C. Coutifaris, J.F. Strauss III, Differentiation of human trophoblasts: structure–function relationships, in: P.K.C. Leung, A.J. W. Hsueh, H.G. Friesen (Eds.), *Molecular Basis of Reproductive Endocrinology*, Springer-Verlag, New York, 1993, pp. 159–170.
- [148] M. Conti, G. Nemos, C. Sette, E. Vicini, Recent progress in understanding the hormonal regulation of phosphodiesterases, *Endocr. Rev.* 16 (3) (1995) 370–389.
- [149] K. Lefkimiatis, D. Leranni, A.M. Hofer, The inner and outer compartments of mitochondria are sites of distinct cAMP/PKA signaling dynamics, *J. Cell Biol.* 202 (3) (2013) 453–462.
- [150] R. Acin-Perez, E. Salazar, M. Kamenetsky, J. Buck, L.R. Levin, G. Manfredi, Cyclic AMP produced inside mitochondria regulates oxidative phosphorylation, *Cell Metab.* 9 (3) (2009) 265–276.
- [151] R. Acin-Perez, D.L. Gatti, Y. Bai, G. Manfredi, Protein phosphorylation and prevention of cytochrome oxidase inhibition by ATP: coupled mechanisms of energy metabolism regulation, *Cell Metab.* 13 (6) (2011) 712–719.
- [152] K. Omori, J. Kotera, Overview of PDEs and their regulation, *Circ. Res.* 100 (3) (2007) 309–327.
- [153] J.H. Zippin, Y. Chen, P. Nahirney, M. Kamenetsky, M.S. Wuttke, D.A. Fischman, et al., Compartmentalization of bicarbonate-sensitive adenylyl cyclase in distinct signaling microdomains, *FASEB J.* 17 (1) (2003) 82–84.
- [154] D.H. Miles, M. Graeme, Tailoring cAMP-signalling responses through isoform multiplicity, *Trends Biochem. Sci.* 22 (6) (1997) 217–224.
- [155] J. Buck, M.L. Sinclair, L. Schapal, M.J. Cann, L.R. Levin, Cytosolic adenylyl cyclase defines a unique signaling molecule in mammals, *Proc. Natl. Acad. Sci. U.S.A.* 96 (1) (1999) 79–84.
- [156] R. Bernatchez, L. Belkacemi, E. Rassart, G. Daoud, L. Simoneau, J. Lafond, Differential expression of membrane and soluble adenylyl cyclase isoforms in cytotrophoblast cells and syncytiotrophoblasts of human placenta, *Placenta* 24 (6) (2003) 648–657.
- [157] R. Taussig, A.G. Gilman, Mammalian membrane-bound adenylyl cyclases, *J. Biol. Chem.* 270 (1) (1995) 1–4.
- [158] J. Hanoune, Y. Pouille, E. Tzavara, T. Shen, L. Lipskaya, N. Miyamoto, et al., Adenylyl cyclases: structure, regulation and function in an enzyme superfamily, *Mol. Cell. Endocrinol.* 128 (1–2) (1997) 179–194.
- [159] F.A. Antoni, S.M. Smith, J. Simpson, R. Rosie, G. Fink, J.M. Paterson, Calcium control of adenylyl cyclase: the calcineurin connection, *Adv. Second Messenger Phosphoprotein Res.* 32 (1998) 153–172.
- [160] Z.Z. Yang, O. Tschopp, M. Hemmings-Mieszczak, J. Feng, D. Brodbeck, E. Perentes, B.A. Hemmings, Protein kinase B α /Akt1 regulates placental development and fetal growth, *J. Biol. Chem.* 278 (34) (2003) 32124–32131.
- [161] N. Hatano, Y. Mori, M. Oh-hora, A. Kosugi, T. Fujikawa, N. Nakai, et al., Essential role for ERK2 mitogen-activated protein kinase in placental development, *Genes Cells* 8 (11) (2003) 847–856.
- [162] Z. Krozowski, J.A. Maguire, A.N. Stein-Oakley, J. Dowling, R.E. Smith, R.K. Andrews, Immunohistochemical localization of the 11 β -hydroxysteroid dehydrogenase type II enzyme in human kidney and placenta, *J. Clin. Endocrinol. Metab.* 80 (7) (1995) 2203–2209.
- [163] H. Guan, K. Sun, K. Yang, The ERK1/2 signaling pathway regulates 11 β -hydroxysteroid dehydrogenase type 2 expression in human trophoblast cells through a transcriptional mechanism, *Biol. Reprod.* 89 (4) (2013) 1–7.
- [164] L. Poston, M.T. Rajmakers, Trophoblast oxidative stress, antioxidants and pregnancy outcome – a review, *Placenta* 25 (Suppl. A) (2004) S72–S78.
- [165] C. Vaillancourt, D. Lanoix, F. Le Bellego, G. Daoud, J. Lafond, Involvement of MAPK signalling in human villous trophoblast differentiation, *Mini Rev. Med. Chem.* 9 (8) (2009) 962–973.
- [166] C. Runchel, A. Matsuzawa, H. Ichijo, Mitogen-activated protein kinases in mammalian oxidative stress responses, *Antioxid. Redox Signal.* 15 (1) (2011) 205–218.
- [167] M. Takekawa, T. Maeda, H. Saito, Protein phosphatase 2 α inhibits the human stress-responsive p38 and JNK MAPK pathways, *EMBO J.* 17 (16) (1998) 4744–4752.
- [168] G. Daoud, M. Amyot, E. Rassart, A. Masse, L. Simoneau, J. Lafond, ERK1/2 and p38 regulate trophoblasts differentiation in human term placenta, *J. Physiol.* 566 (Pt 2) (2005) 409–423.
- [169] T. Sakiyama, J.C. Robinson, J.Y. Chou, Characterization of alkaline phosphatases from first trimester placentas, *J. Biol. Chem.* 254 (3) (1979) 935–938.
- [170] A.L. Solomon, K.W. Siddals, P.N. Baker, J.M. Gibson, J.D. Aplin, M. Westwood, Placental alkaline phosphatase de-phosphorylates insulin-like growth factor (IGF)-binding protein-1, *Placenta* 35 (7) (2014) 520–522.
- [171] D.M. Stocco, X. Wang, Y. Jo, P.R. Manna, Multiple signaling pathways regulating steroidogenesis and steroidogenic acute regulatory protein expression: more complicated than we thought, *Mol. Endocrinol.* 19 (11) (2005) 2647–2659.
- [172] H. Chen, M.P. Hardy, I. Huhtaniemi, B.R. Zirkin, Age-related decreased Leydig cell testosterone production in the Brown Norway rat, *J. Androl.* 15 (6) (1994) 551–557.
- [173] R.V. Carsia, G.J. Macdonald, S. Malamed, Steroid control of steroidogenesis in isolated adrenocortical cells: molecular and species specificity, *Steroids* 41 (6) (1983) 741–755.
- [174] M.J. DiBartolomeis, C.R. Jefcoate, Characterization of the acute stimulation of steroidogenesis in primary bovine adrenal cortical cell cultures, *J. Biol. Chem.* 259 (16) (1984) 10159–10167.
- [175] M.S. Weedon-Fekjær, K. Taskén, Review: spatiotemporal dynamics of hCG/cAMP signaling and regulation of placental function, *Placenta* 33 (2012) S87–S91.
- [176] O. Ritvos, Modulation of steroidogenesis in choriocarcinoma cells by cholera toxin, phorbol ester, epidermal growth factor and insulin-like growth factor I, *Mol. Cell. Endocrinol.* 59 (1–2) (1988) 125–133.
- [177] B.B. Feinberg, D.J. Anderson, M.A. Steller, V. Fulop, R.S. Berkowitz, J.A. Hill, Cytokine regulation of trophoblast steroidogenesis, *J. Clin. Endocrinol. Metab.* 78 (3) (1994) 586–591.
- [178] Y.G. Shanker, A.J. Rao, Regulation of progesterone biosynthesis in the human placenta by estradiol 17 beta and progesterone, *Biochem. Mol. Biol. Int.* 43 (3) (1997) 591–599.
- [179] R.C. Tuckey, Progesterone synthesis by the human placenta, *Placenta* 26 (4) (2005) 273–281.
- [180] D. Barrera, E. Avila, G. Hernández, A. Halhali, B. Biruete, F. Larrea, et al., Estradiol and progesterone synthesis in human placenta is stimulated by calcitriol, *J. Steroid Biochem. Mol. Biol.* 103 (3–5) (2007) 529–532.
- [181] G.E. Ringler, J.F. Strauss 3rd., *In vitro* systems for the study of human placental endocrine function, *Endocr. Rev.* 11 (1) (1990) 105–123.
- [182] L. Lin, B. Xu, N.S. Rote, The cellular mechanism by which the human endogenous retrovirus ERV-3 env gene affects proliferation and differentiation in a human placental trophoblast model, *BeWo*, *Placenta* 21 (1) (2000) 73–78.
- [183] C. Wadsack, A. Hrzenjak, A. Hammer, B. Hirschnagl, S. Levak-Frank, G. Desoye, et al., Trophoblast-like human choriocarcinoma cells serve as a suitable *in vitro* model for selective cholesterol ester uptake from high density lipoproteins, *Eur. J. Biochem.* 270 (3) (2003) 451–462.
- [184] A. Felicello, M.E. Gottesman, E.V. Avvedimento, The biological functions of A-kinase anchor proteins, *J. Mol. Biol.* 308 (2) (2001) 99–114.
- [185] C.K. Means, B. Lygren, L.K. Langeberg, A. Jain, R.E. Dixon, A.L. Vega, et al., An entirely specific type I A-kinase anchoring protein that can sequester two molecules of protein kinase A at mitochondria, *Proc. Natl. Acad. Sci. U.S.A.* 108 (48) (2011) E1227–35.
- [186] C. Gomez-Concha, O. Flores-Herrera, S. Olvera-Sanchez, M.T. Espinosa-García, F. Martínez, Progesterone synthesis by human placental mitochondria is sensitive to PKA inhibition by H89, *Int. J. Biochem. Cell Biol.* 43 (6) (2011) 1402–1411.
- [187] M.P. Ma, M. Thomson, Protein kinase A subunit α catalytic and A kinase anchoring protein 79 in human placental mitochondria, *Open Biochem. J.* 6 (2012) 23–30.

Research Article

Streptozotocin-Induced Adaptive Modification of Mitochondrial Supercomplexes in Liver of Wistar Rats and the Protective Effect of *Moringa oleifera* Lam

María Alejandra Sánchez-Muñoz,¹ Mónica Andrea Valdez-Solana,¹
Mara Ibeth Campos-Almazán,² Óscar Flores-Herrera,³ Mercedes Esparza-Perusquía,³
Sofía Olvera-Sánchez,³ Guadalupe García-Arenas,² Claudia Avitia-Domínguez,²
Alfredo Téllez-Valencia,² and Erick Sierra-Campos ¹

¹Facultad de Ciencias Químicas, Universidad Juárez del Estado de Durango Campus, Gómez Palacio, DGO, Mexico

²Facultad de Medicina y Nutrición, Universidad Juárez del Estado de Durango Campus, Gómez Palacio, DGO, Mexico

³Departamento de Bioquímica, Facultad de Medicina, Universidad Nacional Autónoma de México, Mexico City, Mexico

Correspondence should be addressed to Erick Sierra-Campos; ericksier@gmail.com

Received 15 November 2017; Accepted 28 December 2017

Academic Editor: Saad Tayyab

Copyright © 2018 María Alejandra Sánchez-Muñoz et al. This is an open access article distributed under the Creative Commons Attribution License, which permits unrestricted use, distribution, and reproduction in any medium, provided the original work is properly cited.

The increasing prevalence of diabetes continues to be a major health issue worldwide. Alteration of mitochondrial electron transport chain is a recognized hallmark of the diabetic-associated decline in liver bioenergetics; however, the molecular events involved are only poorly understood. *Moringa oleifera* is used for the treatment of diabetes. However, its role on mitochondrial functionality is not yet established. This study was aimed to evaluate the effect of *M. oleifera* extract on supercomplex formation, ATPase activity, ROS production, GSH levels, lipid peroxidation, and protein carbonylation. The levels of lipid peroxidation and protein carbonylation were increased in a diabetic group. However, the levels were decreased in *M. oleifera*-treated diabetic rats. Analysis of in-gel activity showed an increase in all complex activities in the diabetic group, but spectrophotometric determinations of complex II and IV activities were unaffected in this treatment. However, we found an oxygen consumption abolition through complex I-III-IV pathway in the diabetic group treated with *Moringa*. While respiration with succinate feeding into complex II-III-IV was increased in the diabetic group. These findings suggest that hyperglycemia modifies oxygen consumption, supercomplexes formation, and increases ROS marker levels in mitochondria from the liver of STZ-diabetic rats, whereas *M. oleifera* may have a protective role against some alterations.

1. Introduction

Mitochondria, which are mainly composed by proteins and lipids, are considered the most complex and the most important organelles of eukaryotic cells. They not only play a leading role in the energy metabolism, but also closely involve in many cellular processes [1]. Moreover, mitochondria are highly dynamic organelles that continuously divide and fuse as well as move within the cell [2]. In addition, it is now well established that the individual respiratory complexes can be organized into supercomplexes,

but the composition and abundance of these may vary among organisms and tissues depending on the metabolic and physiological conditions [3–5] as well as on the lipid content of the mitochondrial inner membrane [6, 7]. However, mitochondria are a source of reactive oxygen species (ROS) which are involved in many pathological scenarios [8] and often play an essential role in physiological cell death mechanisms [9].

Mitochondrial dysfunction has recently been identified as a common metabolic defect associated with diabetes, obesity, and its metabolic complications [10, 11]. Previous

studies have demonstrated that chronic diabetes induced by streptozotocin (STZ) provoked significant alterations in hepatic mitochondrial function which were restored to normality with insulin treatment [12] or with mifepristone (RU 38486) treatment [13]. In addition, it has been postulated that STZ-induced cytotoxicity in HepG2 cells is mediated, at least in part, by the increase in ROS and reactive nitrogen species (RNS) production, oxidative stress, and mitochondrial dysfunction [14]. Moreover, diverse studies suggest that mitochondrial oxidative function was compromised in diabetic and prediabetic humans as evidenced by reduced levels of fatty acid oxidation, insulin-stimulated ATP synthesis, and expression of genes involved in oxidative phosphorylation (OXPHOS) [15–17]. With respect to OXPHOS, activity was suggested that mitochondrial diabetes may also affect the complex V [18], and it is interesting to mention that, in diabetic patients' muscle, blue native gel electrophoresis revealed a striking decrease in complex I, III, and IV containing supercomplexes [19]. In addition, impairment of pyruvate dehydrogenase complex on the citric acid cycle and glucokinase activity during diabetes has been reported [19, 20]. These findings can be associated with an increased in ROS production and a decrease in cellular reduced glutathione (GSH) content in STZ-induced diabetic rats [21] and diabetic patients [22].

Moringa oleifera is commonly used in folk medicine as an antidiabetic agent via its antioxidant property. Yet, its biological activity is not limited to the antioxidant capacity. In fact, other important biological activities such as hypolipidaemic, antiatherosclerotic, and anticarcinogenic activities of *M. oleifera* leaves and seeds have been reported [23–26]. However, phenolic compounds found in *M. oleifera*, especially flavonoids, possess both antioxidant and prooxidant properties depending on concentration used. The latter which is exhibited at higher concentrations of phenolic compounds such as quercetin, galangin, taxifolin, catechin, and prenylated flavonoid have been shown to affect mitochondrial energetic processes (see supplementary materials (available here)) [27, 28]. In addition, it has been shown that mitochondria are a plausible main target of flavonoids mediating preventive actions against stress and mitochondrial dysfunction-associated pathologies [29]. Recent evidence indicates that *M. oleifera* aqueous leaf extract presents anticancerous effect on A549 cancer cells by affecting mitochondrial membrane potential and ATP levels [30]. More recently, Khan et al. [31] showed that aqueous extract of *M. oleifera* leaf protects pancreas against ROS-mediated damage by enhancing cellular antioxidant defenses and minimizing hyperglycemia in STZ-induced diabetes, which might be due to the glucose uptake enhancement in skeletal muscle, insulin secretion stimulation, and alpha-amylase and alpha-glucosidase inhibition. Thus, the favorable roles of *M. oleifera* in glucose metabolism and antioxidant system led us to investigate the effects of *M. oleifera* on diabetes-induced mitochondrial changes in liver. The aim of this study was to investigate the protecting effect of *M. oleifera* extract upon STZ-induced mitochondrial dysfunction. To assess the degree of injury of the STZ, both respiratory and enzyme activity parameters were

evaluated and compared with the changes in the *M. oleifera*-treated group.

2. Materials and Methods

2.1. Preparation of the Extract. The extract was prepared using 23 g of dry-ground sample and 260 mL of 80% methanolic aqueous solution by successive maceration. The mixture was shaken in a magnetic grid at room temperature for 24 h and then filtered through Whatman filter paper number 1. The final extract was concentrated on a rotary evaporator, placed in a deep freezer for 24 h and lyophilized to obtain a powdered extract that was kept at -80°C .

2.2. Ethics Statement. All experiments were performed in compliance with the guideline for the welfare of experimental animals by the National Institutes of Health and in accordance with the guidelines of Institutional Animal Care. This study was approved by the Institutional Animal Ethics Committee at the Faculty of Health Science, UJED.

2.3. Diabetic Model and Treatment. Streptozotocin (STZ) was dissolved in a citrate buffer (0.1 M, pH 4.5) and intraperitoneally injected (55 mg/kg) to induce diabetes in rats. Rats injected only with citrate buffer served as control. Type 1 diabetes was confirmed evaluating fasting plasma glucose levels after 5 days of induction; the inclusion criteria to establish diabetes were 200 mg/dL of fasting plasma glucose. Rats were divided in control (C group), diabetic (D group), and *M. oleifera*-treated diabetic (M group) groups. M group was daily administered with a 200 mg/kg dose of extract by gavage during 3 weeks, and remaining groups were administered with water as vehicle.

2.4. Isolation and Purification of Mitochondria. The rat liver was collected immediately after euthanasia and homogenized in 100 mL of a buffer containing 20 mM Tris-HCl, 200 mM mannitol, 50 mM sucrose, 1 mM EDTA, 1 mM PMSF, 1 protease inhibitor tablet, and 0.1% bovine serum albumin (BSA) (pH 7.4; buffer A). Cellular and nuclear fractions were removed in the pellet by centrifuging at 3,500 rpm for 10 min at 4°C . Mitochondria were obtained by centrifuging the supernatant for 10 min at 11,000 rpm. Then, mitochondria were washed and resuspended in buffer A without BSA and centrifuged at 11,000 rpm for 10 min. Mitochondria were loaded on a Percoll gradient 15, 23, and 40% in buffer A without BSA and centrifuged for 35 min at 25,000 rpm at 4°C [32].

2.5. Oxygen Consumption. Oxygen uptake was estimated polarographically using a Clark-type electrode in a 1.5 ml water-jacketed chamber at 37°C . The mixture contained 250 mM sucrose, 20 mM HEPES, 50 mM K_2HPO_4 , 10 mM H_3PO_4 , 10 mM MgCl_2 , and 1 mM EGTA, 0.1% BSA (pH 7.4) [33]. Oxygen consumption was stimulated by the addition of 0.1 mM NADH or 10 mM succinate (in the presence of $2\ \mu\text{M}$ rotenone). Otherwise, artificial substrates such as

ascorbate/TMPD (10 mM and 100 μ M, respectively, in the presence of 2 μ M antimycin) were used for complex IV activity, and malonate and KCN were added to inhibit complex IV and complex II (10 mM and 5 mM, respectively).

2.6. NADH Dehydrogenase and Succinate Dehydrogenase Activities. Activities of complex I (NADH:DCPIP oxidoreductase) and complex II (succinate:DCPIP oxidoreductase) were determined spectrophotometrically at 600 nm by following the reduction of the artificial electron acceptor 2,6-dichlorophenol-indophenol (DCPIP; 50 μ M; $\epsilon_{\text{DCPIP}} = 21 \text{ mM}^{-1} \cdot \text{cm}^{-1}$). Mitochondria were permeabilized with 0.03% zwittergent and incubated in 10 mM KH_2PO_4 , 5 mM MgCl_2 , 1 mM EGTA, and 120 mM KCl (pH 7.4), either with 0.2 mM NADH (complex I) or 2 mM succinate (complex II), plus 0.2 mM methosulfate phenazine (PMS). Mitochondria protein concentration was 1 mg/ml, and the reaction was started by the addition of NADH or succinate [34].

2.7. ATP Synthase Assay. ATP hydrolysis of complex V was measured spectrophotometrically at 25°C using a coupled assay to the oxidation of NADH ($\epsilon_{340 \text{ nm}} = 6.22 \text{ mM}^{-1} \cdot \text{cm}^{-1}$). The assay contained 100 μ g mitochondrial protein, 10 mM HEPES (pH 8.0), 100 mM NaN_3 , 100 μ M NO_4Na , 90 mM KCl, 3 mM MgSO_4 ; the ATP regenerating system consisted of 5 mM phosphoenolpyruvate, 2 mM ATP, 0.03% zwittergent, 50 units/mL pyruvate kinase, and 30 units/mL lactate dehydrogenase. The ATPase reaction was started by the addition of 0.1 mM NADH. Oligomycin (6 μ g/mL) was added to inhibit ATPase activity and verify F1F0-ATP synthase integrity; mitochondria were incubated with oligomycin for 30 min [35].

2.8. Native Electrophoresis. Respiratory complexes and supercomplexes were resolved by native PAGE as reported previously [36]. Purified liver mitochondria (1 mg) were suspended in 50 mM Bis-Tris and 500 mM 6-aminocaproic acid (pH 7.0) and solubilized by adding digitonin (detergent : protein ratio of 1 : 5). The mixtures were incubated for 30 min at 4°C and centrifuged at 100,000 g for 30 min. The supernatants were recovered and immediately loaded on a linear gradient polyacrylamide gradient gels (4–10%) for Blue Native PAGE (BN-PAGE) or Clear Native PAGE high resolution (hrCN-PAGE).

For BN-PAGE, the anode buffer contained 50 mM Bis-Tris/HCl (pH 7.0); the cathode buffer contained 50 mM tricine and 15 mM Bis-Tris (pH 7.0), and Coomassie (0.02%). For the hrCN-PAGE, the anode buffer contained 25 mM imidazole/HCl (pH 7.0); while the cathode buffer contained 50 mM tricine, 7.5 mM imidazole, 0.01% β dodecyl D-maltoside, and 0.05% sodium deoxycholate (pH 7.0), supplemented with Ponceau S red [37]. Gels were run at 4°C and 35 V for 16 h. The molecular weights of the respiratory complexes or supercomplexes were estimated by using digitonin bovine heart mitochondrial complexes as standard: single complex: I = 1,000 kDa, V = 750 kDa, III₂ = 500 kDa,

IV = 230 kDa, II = 130 kDa; supercomplexes: I-III-IV₁₋₄ = 1500–2100 kDa, V₂ = 1500 kDa.

2.9. Complex and Supercomplexes In-Gel Activities. The in-gel activity assays were performed as Wittig and Schagger [38] for complex I activity (NADH:methylthiazolyl-diphenyl tetrazolium bromide reductase), complex II activity (succinate:methylthiazolyl-diphenyl tetrazolium bromide reductase), and complex IV activity (cytochrome *c*:diaminobenzidine reductase). In all cases, the assays were performed at 20–25°C and stopped with 50% methanol and 10% acetic acid, after 10–25 min.

The in-gel activity of complex V was performed in 50 mM glycine (adjusted to pH 8.0 with triethanolamine), 10 mM MgCl_2 , 0.15% $\text{Pb}(\text{ClO}_4)_2$, and 5 mM ATP. ATP hydrolysis was correlated with the development of white lead phosphate precipitates. The reaction was stopped using 50% methanol, and subsequently, the gel was transferred to water and scanned against a dark background as described previously [39].

2.10. SDS-Gel Electrophoresis and Western Blot Analysis. Liver mitochondrial proteins (20 μ g per well) were separated by SDS-PAGE according to Laemmli [40] in a 10% polyacrylamide gel under denaturing conditions. Proteins were then transferred from gel to PVDF membrane (Immobilon P; Millipore, Bedford, MA) in a semidry electroblotting system (Bio-Rad) at 25 V for 50 min. Membranes were blocked in 500 mM NaCl, 0.05% Tween-20, and 20 mM Tris-base (pH 7.5) (TTBS buffer), containing 5% blotting grade blocker nonfat dry milk. Then, membranes were incubated with antitotal OXPHOS antibody cocktail (at 1/500 dilution). Immunoreactive bands were visualized by enhanced chemiluminescence (Amersham Life Science, Inc.), according to the manufacturer's instructions, using horseradish peroxidase-conjugated antimouse IgG (at 1/10,000 dilution), and densitometric analyses were performed with the software Image Studio Lite version 5.2 (LI-COR Biosciences).

2.11. Protein Determination. The protein levels were estimated by the method described by Lowry et al. using BSA as standard [41].

2.12. Mitochondrial Glutathione Reductase Activity. Glutathione reductase enzymatic activity was recorded by NADPH consumption. Briefly, 50 μ g of purified mitochondria was placed in a phosphate buffer (50 mM, pH 7.0) containing 1 mM GSH and 0.1 M NADPH. NADPH reduction was measured at 340 nm ($\epsilon_{\text{NADPH}} = 6.22 \text{ M}^{-1} \cdot \text{cm}^{-1}$).

2.13. Measurement of Glutathione Concentration by HPLC-UV. To quantify GSH and GSSG concentrations, a standard curve of oxidized and reduced glutathione was used as described by Yilmaz et al. [42]. Mitochondrial samples were centrifuged at 500 rpm for 10 min and filtered to be injected

onto a Kromasil ETERNITY C18 column (4.6 × 150 mm). Mobile phase containing 10 mM of monobasic sodium phosphate and 2% methanol (pH 3.0) was used at a flow rate of 1 mL/min in isocratic run. GSH and GSSG eluted from the column were detected at 210 nm.

2.14. Lipid Peroxidation Assay. Mitochondrial lipid peroxidation was estimated by the thiobarbituric acid reactive substances (TBARS) method consisting of TBA-TCA-HCl reaction as described by Buege and Aust [43]. Samples were boiled at 95°C for 60 min, followed by a cooling and centrifugation steps at 12,000 rpm for 10 min at 4°C. The pink product absorbance (formed when the MDA reacts with TBA) was spectrophotometrically recorded at 532 nm ($\epsilon_{\text{MDA}} = 1.56 \times 10^5 \text{ M}^{-1} \cdot \text{cm}^{-1}$). MDA-TBA adduct peak was calibrated with tert-butyl hydroperoxide simultaneously processed as samples.

2.15. Mitochondrial H₂O₂ Measurement. H₂O₂ emission was determined by the fluorogenic indicator Amplex Red (Invitrogen) oxidation in presence of horseradish peroxidase as described by Starkov [44]. Fluorescence was recorded in a spectrofluorometer (LS 55 PerkinElmer Life Sciences) with excitation and emission wavelengths of 555 and 581, respectively. Briefly, 300 µg of purified mitochondria was added to 1 mL incubation buffer containing 125 mM KCl, 20 mM Hepes, 0.2 mM EGTA, 2 mM KH₂PO₄, 2% BSA, 1 µM Amplex Red, and 4 U horseradish peroxidase (pH 7.2). H₂O₂ production was initiated after addition of 5 mM pyruvate, 2.5 mM malate, and 10 mM succinate as substrates and 1 µM rotenone, 0.2 µM antimycin A, and 5 mM malonate as inhibitors.

2.16. Measurement of Protein Carbonylation. Determination of carbonyl content was followed as Levine et al. [45]. The oxidative damage to proteins was determined by carbonyl groups based on their reaction with 2,4-dinitrophenylhydrazine (DNPH) to form hydrazones. Briefly, 0.5 mg of mitochondria was incubated with 20 mM DNPH solution for 1 h; then proteins were precipitated with 20% (w/v) of trichloroacetic acid and redissolved in DNPH. In brief, the proteins were precipitated by the addition of 20% (w/v) of trichloroacetate; protein pellet was washed three times with ethanol : ethyl acetate (1 : 1) and resuspended in 1 mL of 6 M guanidine. The absorbance was recorded at 370 nm ($\epsilon_{\text{Hydrazone}} = 22 \times 10^3 \text{ M}^{-1} \cdot \text{cm}^{-1}$).

2.17. Measurement of HO-1 Activity. Fresh livers were placed in prechilled Dounce homogenizer, and cold homogenization buffer containing 100 mM potassium phosphate buffer (pH 7.4), 2 mM MgCl₂, 250 mM sucrose, and a protease inhibitor cocktail (10 µg/mL leupeptin, 10 µg/mL trypsin inhibitor, 2 µg/mL aprotinin, and 1 mM PMSF) was added. The homogenate was centrifuged at 10,000 g for 30 min at 4°C, followed by the supernatant centrifugation at 100,000 g for 60 min at 4°C, to obtain the microsomal fraction as a pellet. HO-1 activity was spectrophotometrically measured

as described previously [46]. The microsomal fraction (50 µL) was added to the reaction mixture (500 µL) containing 0.8 mM NADPH, 2 mM glucose-6-phosphate, 0.2 unit of glucose-6-phosphate dehydrogenase, 20 µM hemin, 100 mM potassium phosphate buffer (pH 7.4), and 2 mg of rat liver cytosol as a source of biliverdin reductase. The mixture was incubated at 37°C for 60 min in dark, and samples were left in an ice bath for at least 2 min to stop the reaction. Bilirubin product was determined by calculation from difference in optical density (OD) at 464 nm and 530 nm (OD₄₆₄ - OD₅₃₀ nm) of the sample. HO activity is expressed as pmol/min/mg protein.

2.18. Data Analysis. The obtained data are represented as mean ± standard deviation of three independent determinations, using the Sigma Plot software version 11.0. Differences between means were obtained by analysis of variance (ANOVA) and multiple comparison tests. *P* values < 0.05 were considered as significant.

3. Results and Discussion

The effectiveness of *M. oleifera* extract in alleviating diabetes was assessed in the STZ-induced diabetic model in Wistar rats. In response to STZ, rats showed increased water uptake, increased urine production, increased blood glucose levels, and reduced weight gain (D group = 229 ± 9.05 mg/dL and 156 ± 12 g), which were unaltered in the control group (C group = 78 ± 5.5 mg/dL and 187 ± 18 g), while M group significantly alleviated all parameters of diabetes (86 ± 4.2 mg/dl and 194 ± 8 g). These results suggest that *M. oleifera* leaf may be a potential agent in the treatment of type 1 diabetes and are agreed with the observations that suggest the beneficial effects of *Moringa oleifera* supplementation on diabetes [47, 48]. Hence, these results led us to investigate the valuable effects of the leaf extract on STZ-induced mitochondrial changes, in liver, evaluating STZ injury on both, respiratory and enzyme activities from respiratory chain and some of the antioxidant system comparing them with those from *M. oleifera* treatment.

3.1. *M. oleifera* Attenuates Oxidant Stress and the Decrease in the Glutathione System in Liver Mitochondria. Diabetic cells and tissues have the capacity to invoke adaptive mechanisms that evolved to defend against oxidative stress [49]. One putative mechanism is a defense system that would protect against ROS into mitochondria. These include the superoxide conversion to hydrogen peroxide (H₂O₂) by manganese superoxide dismutase (SOD) and scavenging H₂O₂ by catalase, glutathione peroxidase (GPx), or peroxiredoxin III [50]. Reduced glutathione (GSH) scavenges H₂O₂ via GPx, ubiquitously expressed both in the mitochondria matrix and intermembrane space [51]. In turn, the reduction of oxidized glutathione (GSSG) to GSH is catalyzed by glutathione reductase (GR), which requires NADPH. Thus, increased ROS removal results in increased NADPH turnover. Also, GSH can also be used in conjugation reactions to protect mitochondria enzymes from various toxins, for

TABLE 1: GSH and GSSG levels by HPLC-DAD and GR enzymatic activity in liver mitochondria from different groups.

Group	GSH ($\mu\text{mol}/\text{mg}$ protein)	GSSG ($\mu\text{mol}/\text{mg}$ protein)	GSH/GSSG ratio	Total GSH ($\mu\text{mol}/\text{mg}$ protein)	GR (U/min)
C	174.1 \pm 35.1	4.8 \pm 3.4	36.2 \pm 0.19	178.8 \pm 5.7	267.2 \pm 11.7
D	50.4 \pm 1*	49.8 \pm 1.1*	1 \pm 0.08*	100.2 \pm 1.3*	236 \pm 14.5
M	169 \pm 1.2**	54.7 \pm 2.2**	3 \pm 0.05**	223.7 \pm 2.9**	366.7 \pm 23.8**

C = control; D = diabetic; M = diabetic plus *Moringa*. *Significant difference versus control ($P < 0.05$). **Significant difference versus control and diabetic ($P < 0.05$).

TABLE 2: Levels of MDA and carbonyl groups in liver mitochondria from different treatments.

Group	MDA (nmol/mg prot)	Carbonyl groups (nmol/mg)	HO-1 (pmol/min/mg)
C	0.4317 \pm 0.009	3.7232 \pm 0.57	40.9 \pm 4.9
D	0.5028 \pm 0.06	12.738 \pm 0.28 [#]	85.7 \pm 2.1*
M	0.3851 \pm 0.02*	4.2645 \pm 0.98	105.2 \pm 3.4* [#]

C = control; D = diabetic; M = diabetic plus *Moringa*. *Significant difference versus diabetic ($P < 0.05$). [#]Significant difference versus control ($P < 0.05$).

example, by-products in lipid peroxidation such as 4-hydroxynonenal (HNE) [52].

To assess the influence of STZ injection on redox state, mitochondrial GSH levels and GR of liver were examined. A single dose of STZ caused a significant decrease in GSH and total GSH contents of diabetic rats (Table 1). Basal levels of total GSH were 178.8 \pm 5.7 $\mu\text{mol}/\text{mg}$ of protein in control mitochondria, whereas total GSH levels in isolated mitochondria from STZ-treated rats (D group) were significantly decreased by 70% compared with control (100.2 \pm 1.3 $\mu\text{mol}/\text{mg}$ of protein). In contrast, *M. oleifera* treatment prevented a STZ-mediated decrease in GSH levels (M group = 223.7 \pm 2.9 $\mu\text{mol}/\text{mg}$ of protein), which correspond to an increase of 25% compared with C group. It is worth to mention that M group rats showed a significant increase in values of GSH, total GSH (2 times), and GSH/GSSG ratio ($P < 0.05$) compared with D group. However, the M group ratio was 12 times reduced with respect to C group (Table 1). One possible explanation for this phenomenon may be the inactivation of mitochondrial GR activity. However, as observed in Table 1, STZ administration did not alter the GR activity in liver mitochondria when compared with control rats. However, M group samples significantly increased GR activity when compared with values of D and C groups (Table 1). Hence, these results show that GR inactivation is not the main mechanism of GSSG accumulation into the mitochondria.

The oxidative stress implications in diabetes pathogenesis are suggested to be produced not only by ROS generation but also by a nonenzymatic protein glycation, autooxidation of glucose, impairment of antioxidant enzymes, and peroxides formation. Therefore, GSH level decline is associated with oxidative damage to macromolecules, such as lipids and proteins. ROS-mediated lipid peroxidation is a crucial factor in the development of diabetic liver complications. In addition, GSH depletion induces heme oxygenase-1 (HO-1), a key microsomal enzyme in heme degradation to carbon monoxide (CO), iron (Fe^{2+}), and biliverdin; this latter being converted into bilirubin by the cytosolic biliverdin reductase [53, 54]. Moreover, some observations suggest the cytoprotective mechanism of HO-1 against oxidative stress

involving an increase in mitochondrial carrier levels and antiapoptotic proteins as well as in cytochrome *c* oxidase activity [55].

In order to evaluate this possibility, we measure carbonyls concentration, lipoperoxidation, and HO-1 activity. As observed in Table 2, C group showed the lowest levels of carbonylation and MDA. In contrast, STZ treatment increased lipid peroxidation and protein carbonyl content (Table 2). Besides, M group showed a significant decrease in lipoperoxidation in liver mitochondria ($P < 0.05$) when compared with D group. The carbonylation level in mitochondria of M group was significantly lower and showed significant difference when compared with D group (Table 2). In contrast, *M. oleifera* extract administration did not prevent the HO-1 induction provoked by STZ, where its enzymatic activity remained significantly higher. Our results clearly demonstrated that *M. oleifera* significantly suppressed both lipoperoxidation and protein carbonylation. However, *M. oleifera* did not lower the HO-1 activity, and little is known about the molecular mechanisms responsible for its activation, which requires further investigation.

It has been reported that *M. oleifera* exhibits bifunctional antioxidant properties related to its ability to react directly with ROS and to induce antioxidant enzymes expression such as superoxide dismutase, catalase, glutathione reductase, and glutathione peroxidase [56–58]. We confirmed previous data and showed that *Moringa* not only decreased lipoperoxidation and protein carbonylation levels in rat livers but also increased HO-1 activity, parameters associated with a cytoprotective mechanism against oxidative stress [59].

3.2. *Effects of STZ and M. oleifera on Oxygen Consumption.* Although many previous studies have reported pharmacological properties of *M. oleifera*, particularly as antioxidant and antidiabetic properties that may provide benefits for diabetic patients [25, 60, 61], there are no reports that show *M. oleifera* extract effect on mitochondria functionality. To determine the changes of mitochondrial respiration in STZ-induced diabetic rats and *M. oleifera*

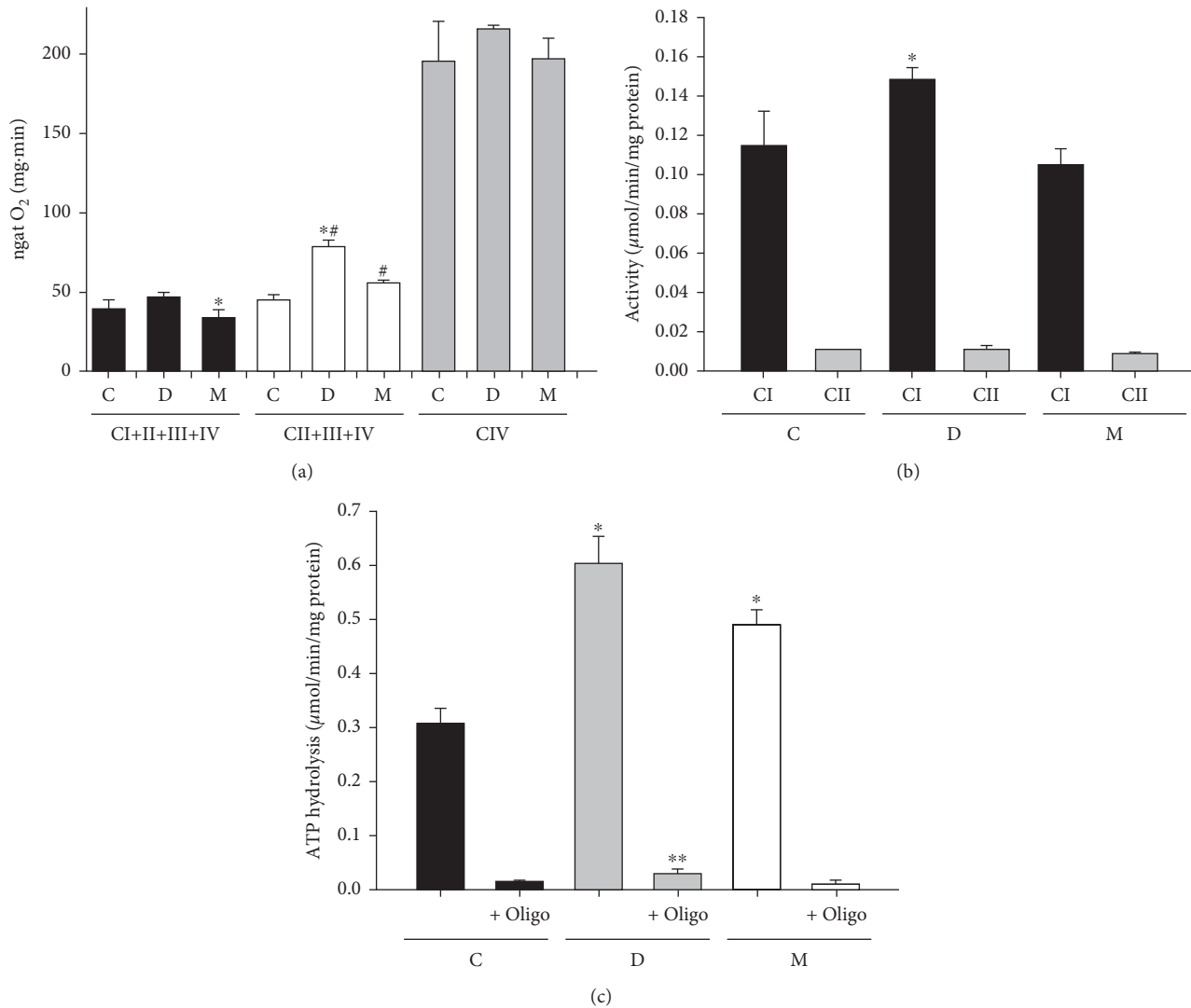


FIGURE 1: *Moringa oleifera* effect on mitochondrial respiratory chain. (a) Oxygen consumption (* $P < 0.05$ versus D; # $P < 0.05$ versus C); (b) enzymatic activity of complex I and II (* $P < 0.05$ versus C and M); (c) F₁/F₀ ATPase activity (* $P < 0.05$ versus C and M; ** $P < 0.05$ versus M + oligo) from liver mitochondria. C: control; D: diabetic; M: *Moringa*-treated diabetic groups.

protective effect, we measured the mitochondrial respiratory chain using Clark-type oxygen electrode and determined enzymatic activity of each complex by spectrophotometric methods.

Figure 1(a) shows the respiratory activity of all groups in presence of complex I, II, and IV substrates. The combination of pyruvate+malate indirectly investigates the monocarboxylate and dicarboxylate transporters and the pyruvate dehydrogenase activities. The substrate combination produces NADH which donates electrons to complex I. In D group, the state 4 respiration with pyruvate + malate was not affected. However, *Moringa* treatment resulted in 15% decrease in the state 4 respiration. By contrast, succinate donates electrons to FAD⁺ in complex II and yields significantly high respiration state 4 rates in both D and M groups compared with C group. Otherwise, in diabetic rats, state 4 respiration with succinate increased by 80% compared with control rats. The observed change in the diabetic

animals was rectified by *Moringa* treatment (Figure 1(a)). Additionally, functional analysis of complex IV (cytochrome *c* oxidase) maximal activity was assayed with ascorbate (Asc) and N,N,N',N'-tetramethyl-p-phenylenediamine (TMPD), which is an artificial redox mediator that assists the electron transfer from ascorbate to cytochrome *c*. Complex IV respiration was calculated as the portion sensitive to cyanide potassium (KCN), a specific inhibitor of cytochrome *c* oxidase (Figure 1(a)), revealing no differences among all experimental groups.

Additionally, we measured the specific activities of respiratory chain complexes in liver mitochondria. Spectrophotometric analysis showed a significant increase in complex I and ATPase activities in D group (Figure 1(c)), while *Moringa* treatment was effectively reversing this alteration nearly to control values. Complex II showed no significant change in mitochondrial fraction of D group (Figure 1(b)). These data show that individual activities of

mitochondrial electron transport chain (ETC) enzymes were not negatively modified in diabetic treatment. In addition, the respiratory properties of D and M groups have approximately 1.5–2 times succinate-respiratory rates compared with that of C group. Therefore, our results suggest that respiratory complex activities were not decreased in liver mitochondria in STZ-induced diabetic rats. These findings, which may appear, at first glance, contradictory, may be interpreted in terms of higher ETC efficiency, thus, avoiding energy losses by electron leakage in response to change in physiological functions and body energy requirements; ETC undergoes some modifications either during pathology development or disease [62]. In addition, several studies concerning STZ-treated rats have been performed with animals of different strains and different amounts of STZ [63, 64]. In addition, in isolated hepatocytes, increasing glucose concentration does not increase $\Delta\mu_{H^+}$, mitochondrial respiratory rate, or cytosolic NADH/NAD⁺ ratio; instead, most of glucose excess is converted to glycogen [65]. In fact, some authors have recently suggested that mitochondria overstimulation is a probable risk factor for insulin resistance, while moderate mitochondrial dysfunction may actually be protective under certain conditions, suggesting the mitochondrial modulation as a prospective therapy for metabolic diseases [66]. For this reason, it is important that future research clarifies the true energy functional state of isolated mitochondria from diabetic animals [67].

3.3. Modulation of Mitochondrial Complexes by STZ. As mitochondrial content can substantially impact on respiratory capacity, protein components of individual respiratory complexes were quantified. To test whether hyperglycemia and *M. oleifera* extract altered the composition of the ETC, we analyzed the expression level of nuclear-encoded mitochondrial complex I subunit NDUFB8, complex II subunit SDHB, complex III UQCRC2, complex IV MTCO1, and complex V ATP5A of each group. Interestingly, in diabetic rats, the NDUFB8 subunit resulted in an increase of complex I expression, while complex II and III were unaltered (Figure 2). These data which resulted in increased expression of NDUFB8 and MTCO1 support the suggestion that increased activity of mitochondrial respiratory chain could result from a proteome alteration leading to modulation of expression/activity of a range of mitochondrial components. More importantly, an upregulation of hepatic CI-NDUFB8 and CIV-MTCO1 was found in diabetic rats, consistent with changes in-gel activity of these complexes. Thus, it is plausible that increased NDUFB8 and MTCO1 contents observed in the STZ group, resulting from diabetes mellitus type 1, may account, in part, for the mitochondrial morphological changes observed, which could have downstream effects on mitochondrial functionality leading to hepatic dysfunction.

3.4. Loss of Redox State Does Not Destabilize Mitochondrial Supercomplexes. It is now widely accepted that mitochondrial respiratory chain is organized with stable and functional entities called supercomplexes (SC) [68]. SC consist of

various ratios of copies of individual complexes (I, III, IV, and V) to form stable, supramolecular structures; for instance, CI forms a supercomplex with CIII₂ and CIV (known as the respirasome), as well as with CIII₂ alone (SC I + III₂). CIII₂ forms a supercomplex with CIV (SC III₂ + IV), and CV forms dimers (CV₂). In addition, another recent advance is that the discovery of respiratory megacomplex (MC I₂III₂IV₂) represents the highest-order assembly of respiratory complexes [69], and it allows mitochondria to respond to energy requiring conditions and to minimize ROS generation during electron transfer reactions [70], as well as the sequestering of vulnerable sites of mitochondrial complexes from oxidative damage as a protective mechanism that prevents tight interactions between the individual complexes [71].

It is fairly well established in rectus abdominis muscle of diabetic obese patients. BN-PAGE revealed a striking decrease in complex I, III, and IV containing mitochondrial SC [72]. According to these results, Lenaz and Genova [71] suggest that oxidative stress acts primarily by disassembling supercomplex associations thereby establishing a vicious circle of oxidative stress and energy failure, ultimately leading to cell damage and disease.

It is interesting to mention that there are diverse specific regulatory proteins for the supramolecular organization of individual complexes that include CIV [73], respiratory SC factors 1 and 2 (Rcf1 and 2) [74], protein Cox interacting (Coi) [75], and COX7a2L [76]. These proteins down-regulation can impair the formation of SC; for instance, some studies show that diverse pathologies decrease CIV subunit levels affecting stoichiometry and assembly of SC [77, 78]. In addition, diabetes induces mitochondrial genome damage by an increased free radical production depleting antioxidant status [79]. Moreover, other structural components as cardiolipin have been shown to be crucial for functionality and SC formation and might be involved in the pathophysiology of diabetes [80]. Thus, the impact of complex IV failure and other enzymes may cause an energy crisis due to a lower ATP synthesis and an increased ROS production.

Figure 3(a) shows the Coomassie blue staining of the gels for all treatments and the colorimetric enzymatic staining of NADH, Succinate, COX, and ATPase complexes after detergent extraction and BN-PAGE or hrCN-PAGE (only for CV). Figure 3(b) clearly indicates that the major form of supercomplexes is present in all samples. In contrast, the amount of free complex I and IV were decreased in D group, and these values did not change in mitochondria isolated from M group. Otherwise, the in-gel activity of complex II was significantly lower in C group compared with those in the D and M groups. In addition, the brown bands indicate the presence of complex IV in all groups and its increase in D group (Figure 3(d)). On the other hand, in-gel ATP hydrolysis/lead phosphate precipitation assay revealed bands representing the F₁F₀ monomer and F₁F₀ dimer bands in Figures 3(e) and 3(f) showing the same functional patterns as the in-solution assays, indicating the level of intrinsic activity driven by complex V. In support, we have shown by comparing the in-gel enzyme activities that the ATPase

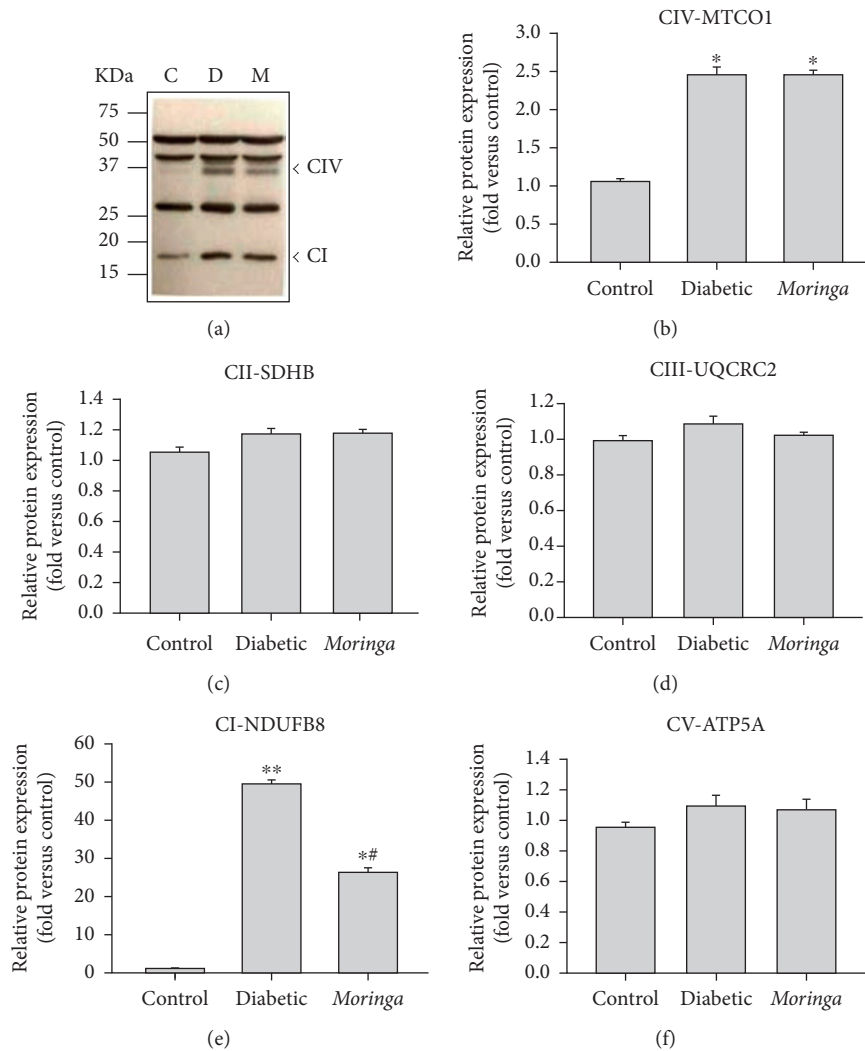


FIGURE 2: Characterization of OXPHOS proteins expressed in liver mitochondria during diabetes. (a) OXPHOS cocktail specificity demonstrated by a Western blot from liver-isolated mitochondria of diabetic rats and treated with *Moringa* extract. Relative expression of (b) MTCO1 subunit of CIV, (c) SDHB subunit of CII, (d) UQCRC2 subunit of CIII, (e) NDUFB8 subunit of CI, and (f) ATP5A subunit of CV was performed by densitometric analysis from gel. Molecular mass standards are shown on the left panel of the gel. C: control; D: diabetic; M: *Moringa*-treated group. Data are shown as mean band density normalized relative to UQCRC2. Significant differences are represented by * $P < 0.05$ versus C; # $P < 0.05$ versus D.

activity of the F_1F_0 -ATP synthase is specifically and significantly increased in D group when compared with C group.

Our results are concerned with the changes in the amount of CIV subunits; for example, Cox6b1 is involved in the regulation of mitochondrial function by promoting SC formation, suggesting its antiaging effects of calorie restriction [81]. In addition, heart failure in dogs induced by coronary microembolism resulted in loss of complex IV containing SC of the electron transport chain [77, 78]. Similarly, in RAW 264.7 macrophages, knockdown of either subunit cytochrome *c* oxidase (CcO) Vb or CcO IV resulted in a significant decrease in CcO containing supercomplexes [78]. Liver mitochondria from ethanol-treated rat also showed a lower level of supercomplexes with a concomitant loss of CcO protein [82]. Therefore, complex IV has been

shown to be necessary for maintaining the stability of complex I in SC, as shown in mouse fibroblast cell lines, where a reduced expression of subunit IVi1 or nonsense mutation in subunit I not only resulted in lower CcO content but also caused significant reduction in complex I [83]. Structural defects in complex III also affected the amount of complex I, whereas chemical inhibition did not. Patients with defects in cytochrome *b* not only lose complex III but also show decreased amounts of complex I, while maintaining a normal enzymatic activity [84]. Conversely, the disruption of complex I function caused by nonsense mutations in NDUFS4, a subunit of this large multimeric complex, led to the partial loss of complex III activity in skin fibroblast cultures obtained from Leigh-like patients [85, 86]. However, defects in the complex I subunit ND5 did not cause a loss of complex III in the I-III supercomplex [87].

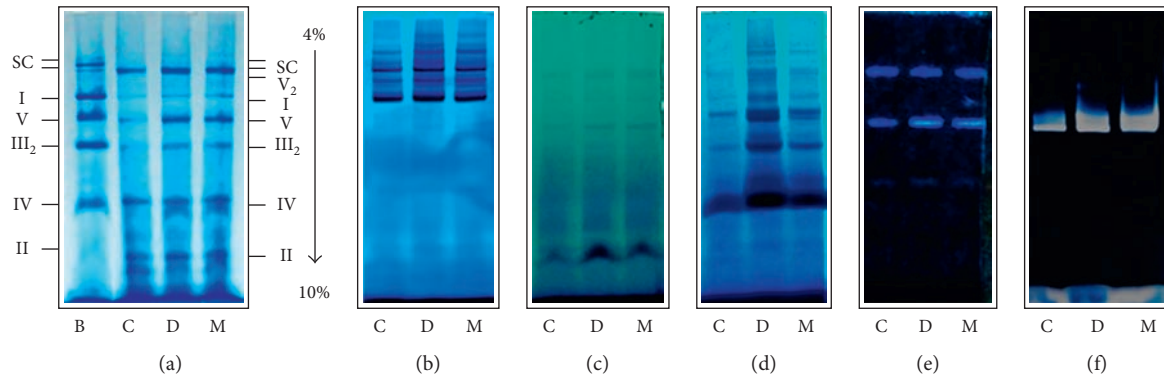


FIGURE 3: Electrophoretic representative pattern of liver mitochondrial solubilized of the different groups (5 g de digitonin/g protein). (a) Blue native polyacrylamide gel electrophoresis (BN-PAGE) stained with Coomassie blue; (b) complex I in-gel activity; (c) complex II in-gel activity; (d) complex IV in-gel activity; (e) complex IV in-gel activity; (f) high resolution clear native polyacrylamide gel electrophoresis (hrCN-PAGE) of complex V. B: bovine heart solubilized mitochondria (positive control); C: control; D: diabetic; M: *Moringa*-treated diabetic groups.

3.5. H_2O_2 Production by Liver Mitochondria Oxidizing Complex I and Complex II Substrates. Several studies have reported that ROS overproduction by mitochondrial ETC is responsible for hyperglycemia-induced oxidative stress and the pathogenesis of diabetic complications [88, 89]; however, it is not clear whether mitochondria of diabetic origin really generate ROS independently of the surrounding diabetic milieu. Herlein et al. [90] showed that the gastrocnemius, heart, and liver mitochondria of STZ-diabetic rats were not irrevocably altered to produce superoxide excess either by complex I or complex III. Moreover, gastrocnemius and heart mitochondria demonstrated an increased respiratory coupling, instead of a decrement. In addition, mitochondria of insulin-deficient diabetic rats did show signs of ROS overproduction. Thus, the detailed molecular mechanism and sites of ROS generation during diabetes are controversial.

In isolated mitochondria, the rate of mitochondrial ROS generation is directly governed by membrane potential ($\Delta\Psi_m$) and pH gradient across the inner membrane, favored only by a state 4 condition [91]. Hence, H_2O_2 production rate was measured in liver mitochondria using fluorescent dye Amplex Red and pyruvate plus malate or succinate, as complex I-III and II-III linked substrates, respectively, and the results are shown in Figure 4. Data presented in Figure 4 (a) show that the major source of ROS is complex I for liver mitochondria of C group, using pyruvate plus malate as substrate, reflecting the generation of superoxide anion. In contrast, with M group-isolated mitochondria oxidizing succinate in state 4 produced 6 times more ROS compared with other treatments (C and D groups) (Figure 4(b)). Therefore, the mitochondrial ROS production rates varied dramatically among the three experimental groups in response to addition of respiratory inhibitors.

At the level of ROS formation, all groups have the same basal formation using malate plus pyruvate or succinate, but the addition of respiratory inhibitors had a varied effect on ROS production in the different groups. In case of the C group, the addition of rotenone and antimycin stimulated

ROS production by using pyruvate and malate (Figure 4(a)). However, in both D group and M group, the addition of rotenone has no effect, while antimycin caused only a slight increase in ROS formation (Figure 4(a)). Nevertheless, with succinate, inhibitors have a different pattern. In the C group, the addition of rotenone causes no effect on ROS production, and antimycin favors its increase; but in this case, malonate has no effect (Figure 4(b)). However, in the diabetic group, antimycin has a greater effect on ROS production than control, and malonate adversely affects ROS formation (Figure 4(b)).

Finally, M group sensitivity to individual training inhibitors was unaltered in case of rotenone and malonate, but adding antimycin in this treatment favored ROS production (Figure 4(b)). Thus, measurements of ROS with Amplex Red cannot be used for sites of ROS generation from liver mitochondria treated with STZ and/or *M. oleifera*. This situation could be attributable to experimental conditions because complex I (rotenone), complex II (malonate), and complex III (antimycin A) inhibitors have been commonly used. However, the final concentration being used is not stationary, causing experimental errors that are different from one method to other. In addition, it is necessary to use other respiratory inhibitors, as stigmatellin and myxothiazol. No obstant, this does not deny other possible explanations that can affect ROS production as differences in the stoichiometry-activity ratios of the respiratory complexes [92], the susceptibility to proton pump slip at complex IV [93], or other mechanisms.

Damage to complex I, the most vulnerable ETC complex, increases ROS production, leading to a vicious circle of further mitochondrial dysfunction. It is important to note that complex I injury has a stronger impact on mitochondrial function compared with the damage to other complexes because mitochondria possess smaller amounts of complex I than other ETC complexes [94]. Superoxide production by complex I is much higher during reverse electron transport from succinate to NAD^+ [95]. In addition, it was found that defective complex I produces more ROS

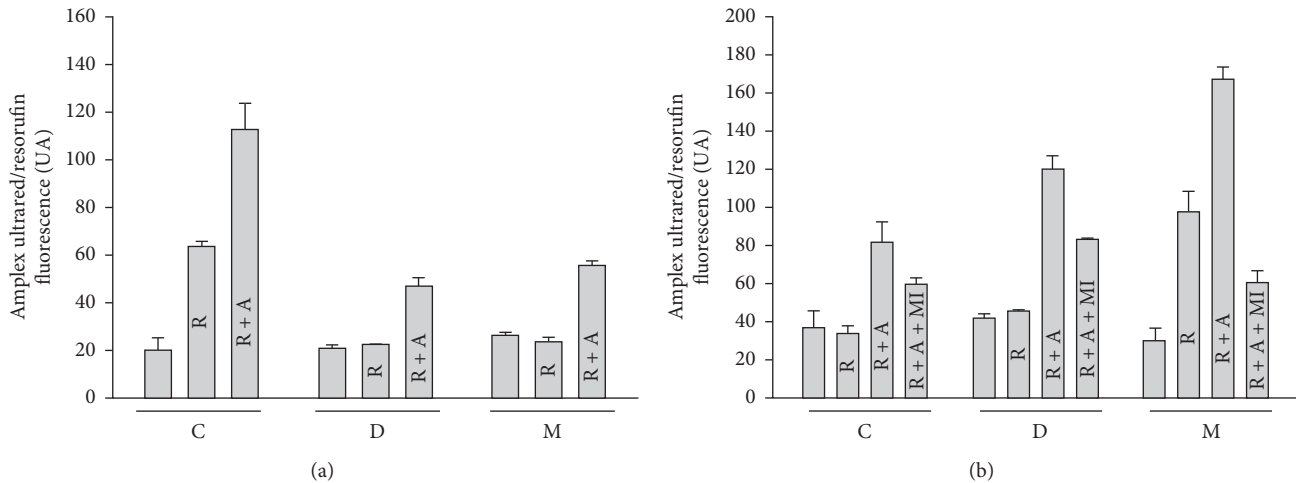


FIGURE 4: H_2O_2 production by mitochondrial respiratory chain measured by Amplex Red (UA) in liver mitochondria from different treatments (C: control; D: diabetic; M: *Moringa*-treated diabetic groups) oxidizing (a) pyruvate plus malate or (b) succinate as substrates and the effects of respiratory chain inhibitors (R: rotenone; A: antimycin A; MI: malonate). Mitochondria were studied during state 4 respiration. To correct for the increase in background fluorescence of the Amplex Red/HRP detection system overtime, fluorescence was monitored for a period of ten minutes. This background was subtracted from resorufin trace. Data are means \pm SEM ($n = 5$).

[96], suggesting that structural modifications of the enzyme may play a crucial role in ROS production process. Recently, it was reported that pancreatic mitochondrial complex I showed aberrant hyperactivity in type 1 and 2 STZ-diabetic mice and rat and in cultured β cells [97]. Further experiments focusing on STZ-induced diabetes in rats revealed that complex I's hyperactivity could be attenuated by metformin. Interestingly, in this study, no changes were reported in complex I activity in brain, liver, and heart by BN-PAGE [97]. However, the reason why complex I activity did not exhibit detectable increases in these tissues is unknown.

Our results in Figure 1(b) show that complex I activity was significantly higher in diabetes than in healthy individuals. This increased activity was apparently contributed by an increased NDUFB8 subunit protein content as shown in Figure 2(e). Moreover, the complex I hyperactivity also imposed pressure in complex IV (Figures 2(b) and 3(d)). These findings suggest that these elevated activities could be attributed for ROS production, given that higher ETC activity can also increase mitochondrial ROS generation [98, 99]. However, our results on specific sites of ROS generation along with ETC are controversial (Figure 4). This may explain why in some tissues seem that inhibition of electron transfer at complex I (by rotenone) may generate an increase in radical formation, whereas, in others, rotenone will reduce radical generation by preventing passage of electron further into the distal part of the chain. However, the basis for such a difference is obscure and presumed to be related to $\Delta\Psi_m$ changes and radicals leakage across the membranes [100].

Polyphenols have been traditionally viewed as antioxidants; however, increasing evidence has emerged supporting the ability of certain polyphenols to exert numerous ROS-scavenging independent actions. Then all these natural compounds modulate mitochondrial functions by inhibiting

organelle enzymes or metabolic pathways, by altering the production of ROS and modulating the activity of transcription factors which regulate the expression of mitochondrial proteins [101]. Thus, some particular polyphenols are now recognized as molecules capable of modulate pathways that define mitochondrial biogenesis (i.e., inducing sirtuins), mitochondrial membrane potential (i.e., mitochondrial permeability transition pore opening and uncoupling effects), mitochondrial electron transport chain and ATP synthesis (i.e., modulating complex I to V activity), intramitochondrial oxidative status (i.e., inhibiting/inducing ROS formation/removal enzymes), and ultimately mitochondrial-triggered cell death (modulating intrinsic apoptosis) (review in [102]). Thus, some studies have indicated that mitochondria may be the target organelle of phenolic compounds [103, 104]. Recently, it was reported that galangin (natural flavonoid) could maintain liver mitochondrial function in diabetic rats through oxidative stress reduction and both antioxidant enzymes and respiratory complexes activities enhancement [79]. Therefore, the likely role of mitochondrial ROS in diabetes has led to efforts for developing effective antioxidant compounds targeted to mitochondria.

This study was designed to investigate the protective effect of *M. oleifera* on liver bioenergetics and to elucidate its potential mechanism. *M. oleifera* resulted in a well-preserved mitochondrial redox potential, significantly by elevating heme oxygenase-1 and decreasing ROS formation and lipoperoxidation. These observations indicated that STZ-induced mitochondrial oxidative damage was remarkably attenuated. Thus, to our knowledge, we have shown for the first time that *M. oleifera* extract modulates mitochondrial respiratory activity, an effect that may account for some of the protective properties of phytochemicals. These effects may be of physiological significance since it seems that some phytochemicals are concentrated into mitochondria. The

results also support a pharmacological use of *M. oleifera* extract in drug to reduce mitochondrial damage in vivo. However, the details about mechanism of action require further investigation.

4. Conclusions

We provide experimental evidence indicating that *M. oleifera* extract targeting mitochondria can be used therapeutically to alleviate diabetes. Therefore, it will be important to identify regulatory proteins involved in the adjustment of respiratory chain complex organization/activity in response to altered redox state. In liver, the alteration of mitochondrial enzymatic activities and oxidative stress induced by STZ suggested of a compensatory response. In addition, *M. oleifera* extract upregulated mitochondrial genes linked with respiratory chain. Our data show an increased mitochondrial function and activity/expression of respiratory complexes in liver of STZ-diabetic rats, which can be normalized by *M. oleifera* at levels that do not markedly alter the consequences of hyperglycemia.

Conflicts of Interest

The authors declare no conflicts of interest.

Authors' Contributions

Erick Sierra-Campos, Mónica Andrea Valdez-Solana, and Óscar Flores-Herrera contributed to conceptualization, literature review, and writing the original draft. María Alejandra Sánchez-Muñoz, Mara Ibeth Campos-Almazán, and Guadalupe García-Arenas conducted the animal studies and performed the experiments. Erick Sierra-Campos, María Alejandra Sánchez-Muñoz, Mercedes Esparza-Perusquía, Sofía Olvera-Sánchez, and Óscar Flores-Herrera analyzed the data. Óscar Flores-Herrera, Alfredo Téllez-Valencia, Claudia Avitia-Domínguez, and Mónica Andrea Valdez-Solana contributed reagents/material/analysis tools. María Alejandra Sánchez-Muñoz and Erick Sierra-Campos wrote the paper. All authors read and approved the final manuscript.

Acknowledgments

The authors would like to express their sincere gratitude to the Consejo Nacional de Ciencia y Tecnología (Conacyt, México) for financial support to Erick Sierra-Campos (Grant 268184). The authors thank Héctor Vázquez-Meza for providing technical assistance. María Alejandra Sánchez Muñoz is also grateful to Conacyt, México, for the financial support for her Masters studies (Grant 601630). The authors are also grateful to the Mexican *Moringa oleifera* producers (Akuanandi) for providing all samples for this study.

Supplementary Materials

Figure S1: Possible mitochondrial processes that are modulated by *Moringa oleifera* extract. It is now well established that the individual mitochondrial respiratory complexes can

be organized into supercomplexes, but the composition and abundance of these may vary among organisms and tissues depending on the metabolic and physiological conditions. Alteration of mitochondrial electron transport chain is a recognized hallmark of the diabetic-associated decline in liver bioenergetics; however, the molecular events involved are only poorly understood. *Moringa oleifera* is used for the treatment of diabetes. However, its role on mitochondrial functionality is not yet established. This study was aimed to evaluate the effect of *M. oleifera* extract on supercomplex formation, ATPase activity, ROS production, GSH levels, lipid peroxidation, and protein carbonylation. The levels of lipid peroxidation and protein carbonylation were increased in the diabetic group. However, the levels were decreased in *M. oleifera*-treated diabetic rats. Analysis of in-gel activity showed an increase in all complexes activities in the diabetic group, but spectrophotometric determinations of complex II and IV activities were unaffected in this treatment. However, we found an oxygen consumption abolition through complex I-III-IV pathway in the diabetic group treated with *Moringa*. Respiration with succinate feeding into complex II-III-IV was increased in the diabetic group. We have shown for the first time that *M. oleifera* extract modulates mitochondrial respiratory activity, an effect that may account for some of the protective properties of phytochemicals. These effects may be of physiological significance since it seems that some phytochemicals are concentrated into mitochondria. The results also support a pharmacological use of *M. oleifera* extract in drug to reduce mitochondrial damage in vivo. (*Supplementary Materials*)

References

- [1] L. D. Osellame, T. S. Blacker, and M. R. Duchon, "Cellular and molecular mechanisms of mitochondrial function," *Best Practice & Research Clinical Endocrinology & Metabolism*, vol. 26, no. 6, pp. 711-723, 2012.
- [2] D. C. Chan, "Mitochondria: dynamic organelles in disease, aging, and development," *Cell*, vol. 125, no. 7, pp. 1241-1252, 2006.
- [3] C. Greggio, P. Jha, S. S. Kulkarni et al., "Enhanced respiratory chain supercomplex formation in response to exercise in human skeletal muscle," *Cell Metabolism*, vol. 25, no. 2, pp. 301-311, 2017.
- [4] S. J. Ramírez-Aguilar, M. Keuthe, M. Rocha et al., "The composition of plant mitochondrial supercomplexes changes with oxygen availability," *Journal of Biological Chemistry*, vol. 286, no. 50, pp. 43045-43053, 2011.
- [5] A. O. Helbig, M. J. L. de Groot, R. A. van Gestel et al., "A three-way proteomics strategy allows differential analysis of yeast mitochondrial membrane protein complexes under anaerobic and aerobic conditions," *Proteomics*, vol. 9, no. 20, pp. 4787-4798, 2009.
- [6] L. Böttinger, S. E. Horvath, T. Kleinschroth et al., "Phosphatidylethanolamine and cardiolipin differentially affect the stability of mitochondrial respiratory chain supercomplexes," *Journal of Molecular Biology*, vol. 423, no. 5, pp. 677-686, 2012.
- [7] J. E. Vance and G. Tasseva, "Formation and function of phosphatidylserine and phosphatidylethanolamine in mammalian cells," *Biochimica et Biophysica Acta (BBA)*-

- Molecular and Cell Biology of Lipids*, vol. 1831, no. 3, pp. 543–554, 2013.
- [8] A. Görlach, E. Y. Dimova, A. Petry et al., “Reactive oxygen species, nutrition, hypoxia and diseases: problems solved?,” *Redox Biology*, vol. 6, pp. 372–385, 2015.
- [9] M. P. Murphy and R. A. J. Smith, “Targeting antioxidants to mitochondria by conjugation to lipophilic cations,” *Annual Review of Pharmacology and Toxicology*, vol. 47, pp. 629–656, 2007.
- [10] B. B. Lowell and G. I. Shulman, “Mitochondrial dysfunction and type 2 diabetes,” *Science*, vol. 307, no. 5708, pp. 384–387, 2005.
- [11] K. Morino, K. F. Petersen, and G. I. Shulman, “Molecular mechanisms of insulin resistance in humans and their potential links with mitochondrial dysfunction,” *Diabetes*, vol. 55, no. 2, pp. S9–S15, 2006.
- [12] J. A. Brignone, C. M. C. de Brignone, R. R. Rodriguez, B. N. Badano, and A. O. M. Stoppani, “Modified oscillation behavior and decreased D-3-hydroxybutyrate dehydrogenase activity in diabetic rat liver mitochondria,” *Archives of Biochemistry and Biophysics*, vol. 214, no. 2, pp. 581–588, 1982.
- [13] J. A. Brignone, C. M. C. de Brignone, C. R. Ricci, I. R. de Mignone, M. C. Susemihl, and R. R. Rodríguez, “Favourable, significant effect of the dose-dependent treatment with RU 38486 (RU) on the alterations of the hepatic mitochondrial function of diabetic rats,” *Diabetes Research and Clinical Practice*, vol. 32, no. 3, pp. 141–148, 1996.
- [14] H. Raza and A. John, “Implications of altered glutathione metabolism in aspirin-induced oxidative stress and mitochondrial dysfunction in HepG2 cells,” *PLoS One*, vol. 7, no. 4, article e36325, 2012.
- [15] G. K. Bandyopadhyay, G. Y. Joseph, J. Ofrecio, and J. M. Olefsky, “Increased malonyl-CoA levels in muscle from obese and type 2 diabetic subjects lead to decreased fatty acid oxidation and increased lipogenesis; thiazolidinedione treatment reverses these defects,” *Diabetes*, vol. 55, no. 8, pp. 2277–2285, 2006.
- [16] J. G. Duncan, “Mitochondrial dysfunction in diabetic cardiomyopathy,” *Biochimica et Biophysica Acta (BBA)-Molecular Cell Research*, vol. 1813, no. 7, pp. 1351–1359, 2011.
- [17] L. Rato, A. I. Duarte, G. D. Tomás et al., “Pre-diabetes alters testicular PGC1- α /SIRT3 axis modulating mitochondrial bioenergetics and oxidative stress,” *Biochimica et Biophysica Acta (BBA)-Bioenergetics*, vol. 1837, no. 3, pp. 335–344, 2014.
- [18] W. C. Parks and R. L. Drake, “Insulin mediates the stimulation of pyruvate kinase by a dual mechanism,” *Biochemical Journal*, vol. 208, no. 2, pp. 333–337, 1982.
- [19] G. Antoun, F. McMurray, A. B. Thrush et al., “Erratum to: Impaired mitochondrial oxidative phosphorylation and supercomplex assembly in rectus abdominis muscle of diabetic obese individuals,” *Diabetologia*, vol. 59, no. 2, pp. 396–397, 2016.
- [20] C. D. Berdanier, H. B. Everts, C. Hermoyian, and C. E. Mathews, “Role of vitamin A in mitochondrial gene expression,” *Diabetes Research and Clinical Practice*, vol. 54, no. 2, pp. S11–S27, 2001.
- [21] D. Loven, H. Schedl, H. Wilson et al., “Effect of insulin and oral glutathione on glutathione levels and superoxide dismutase activities in organs of rats with streptozocin-induced diabetes,” *Diabetes*, vol. 35, no. 5, pp. 503–507, 1986.
- [22] P. S. Samiec, C. Drews-Botsch, E. W. Flagg et al., “Glutathione in human plasma: decline in association with aging, age-related macular degeneration, and diabetes,” *Free Radical Biology and Medicine*, vol. 24, no. 5, pp. 699–704, 1998.
- [23] A. Abd El Latif, B. E. S. El Bialy, H. D. Mahboub, and M. A. Abd Eldaim, “*Moringa oleifera* leaf extract ameliorates alloxan-induced diabetes in rats by regeneration of β cells and reduction of pyruvate carboxylase expression,” *Biochemistry and Cell Biology*, vol. 92, no. 5, pp. 413–419, 2014.
- [24] S. Sreelatha and P. R. Padma, “Antioxidant activity and total phenolic content of *Moringa oleifera* leaves in two stages of maturity,” *Plant Foods for Human Nutrition*, vol. 64, no. 4, pp. 303–311, 2009.
- [25] P. Chumark, P. Khunawat, Y. Sanvarinda et al., “The *in vitro* and *ex vivo* antioxidant properties, hypolipidaemic and antiatherosclerotic activities of water extract of *Moringa oleifera* Lam. leaves,” *Journal of Ethnopharmacology*, vol. 116, no. 3, pp. 439–446, 2008.
- [26] A. L. Al-Malki and H. A. El Rabey, “The antidiabetic effect of low doses of *Moringa oleifera* Lam. seeds on streptozotocin induced diabetes and diabetic nephropathy in male rats,” *BioMed Research International*, vol. 2015, Article ID 381040, 13 pages, 2015.
- [27] D. J. Dorta, A. A. Pigoso, F. E. Mingatto et al., “The interaction of flavonoids with mitochondria: effects on energetic processes,” *Chemico-Biological Interactions*, vol. 152, no. 2-3, pp. 67–78, 2005.
- [28] I. Elingold, M. P. Isollabella, M. B. Casanova et al., “Mitochondrial toxicity and antioxidant activity of a prenylated flavonoid isolated from *Dalea elegans*,” *Chemico-Biological Interactions*, vol. 171, no. 3, pp. 294–305, 2008.
- [29] R. Lagoa, I. Graziani, C. Lopez-Sanchez, V. Garcia-Martinez, and C. Gutierrez-Merino, “Complex I and cytochrome *c* are molecular targets of flavonoids that inhibit hydrogen peroxide production by mitochondria,” *Biochimica et Biophysica Acta (BBA)-Bioenergetics*, vol. 1807, no. 12, pp. 1562–1572, 2011.
- [30] N. Madi, M. Dany, S. Abdoun, and J. Usta, “*Moringa oleifera*’s nutritious aqueous leaf extract has anticancerous effects by compromising mitochondrial viability in an ROS-dependent manner,” *Journal of the American College of Nutrition*, vol. 35, no. 7, pp. 604–613, 2016.
- [31] W. Khan, R. Parveen, K. Chester, S. Parveen, and S. Ahmad, “Hypoglycemic potential of aqueous extract of *Moringa oleifera* leaf and *in vivo* GC-MS metabolomics,” *Frontiers in Pharmacology*, vol. 8, p. 577, 2017.
- [32] R. Hovius, H. Lambrechts, K. Nicolay, and B. de Kruijff, “Improved methods to isolate and subfractionate rat liver mitochondria. Lipid composition of the inner and outer membrane,” *Biochimica et Biophysica Acta (BBA)-Biomembranes*, vol. 1021, no. 2, pp. 217–226, 1990.
- [33] E. Sierra-Campos, I. Velazquez, D. Matuz-Mares, A. Villavicencio-Queijeiro, and J. P. Pardo, “Functional properties of the *Ustilago maydis* alternative oxidase under oxidative stress conditions,” *Mitochondrion*, vol. 9, no. 2, pp. 96–102, 2009.
- [34] D. D. L. R. Castillo, M. Zarco-Zavala, S. Olvera-Sanchez et al., “Atypical cristae morphology of human syncytiotrophoblast mitochondria role for complex V,” *Journal of Biological Chemistry*, vol. 286, no. 27, pp. 23911–23919, 2011.
- [35] M. Esparza-Perusquia, S. Olvera-Sánchez, J. P. Pardo, G. Mendoza-Hernández, F. Martínez, and O. Flores-Herrera, “Structural and kinetics characterization of the F₁F₀-ATP synthase dimer. New repercussion of monomer-monomer contact,” *Biochimica et Biophysica Acta (BBA)-Bioenergetics*, vol. 1858, no. 12, pp. 975–981, 2017.

- [36] H. Schägger and G. von Jagow, "Blue native electrophoresis for isolation of membrane protein complexes in enzymatically active form," *Analytical Biochemistry*, vol. 199, no. 2, pp. 223–231, 1991.
- [37] I. Wittig, M. Karas, and H. Schägger, "High resolution clear native electrophoresis for in-gel functional assays and fluorescence studies of membrane protein complexes," *Molecular & Cellular Proteomics*, vol. 6, no. 7, pp. 1215–1225, 2007.
- [38] I. Wittig and H. Schägger, "Electrophoretic methods to isolate protein complexes from mitochondria," *Methods in Cell Biology*, vol. 80, pp. 723–741, 2007.
- [39] S. J. Couch-Cardel, S. Uribe-Carvajal, S. Wilkens, and J. J. García-Trejo, "Structure of dimeric F₁F₀-ATP synthase," *Journal of Biological Chemistry*, vol. 285, no. 47, pp. 36447–36455, 2010.
- [40] U. K. Laemmli, "Cleavage of structural proteins during the assembly of the head of bacteriophage T4," *Nature*, vol. 227, no. 5259, pp. 680–685, 1970.
- [41] O. H. Lowry, N. J. Rosebrough, A. L. Farr, and R. J. Randall, "Protein measurement with the Folin phenol reagent," *Journal of Biological Chemistry*, vol. 193, no. 1, pp. 265–275, 1951.
- [42] O. Yilmaz, S. Keser, M. Tuzcu et al., "A practical HPLC method to measure reduced (GSH) and oxidized (GSSG) glutathione concentrations in animal tissues," *Journal of Animal and Veterinary Advances*, vol. 8, no. 2, pp. 343–347, 2009.
- [43] J. A. Buege and S. D. Aust, "[30] Microsomal lipid peroxidation," *Methods in Enzymology*, vol. 52, pp. 302–310, 1978.
- [44] A. A. Starkov, "Measurement of mitochondrial ROS production," *Methods in Molecular Biology*, vol. 648, pp. 245–255, 2010.
- [45] R. L. Levine, D. Garland, C. N. Oliver et al., "[49] Determination of carbonyl content in oxidatively modified proteins," *Methods in Enzymology*, vol. 186, pp. 464–478, 1990.
- [46] P. Naughton, R. Foresti, S. K. Bains, M. Hoque, C. J. Green, and R. Motterlini, "Induction of heme oxygenase 1 by nitrosative stress. A role for nitroxyl anion," *Journal of Biological Chemistry*, vol. 277, no. 43, pp. 40666–40674, 2002.
- [47] P. Kiranmayi and B. Babitha, "Effect of *Moringa oleifera* Leaf powder on blood glucose levels in type II diabetes mellitus patients," *Vegetos-An International Journal of Plant Research*, vol. 24, no. 2, pp. 114–116, 2011.
- [48] P. Anthanont, N. Lumlerdkij, P. Akarasereenont, S. Vannasaeng, and A. Sriwijitkamol, "*Moringa oleifera* leaf increases insulin secretion after single dose administration: a preliminary study in healthy subjects," *Journal of the Medical Association of Thailand*, vol. 99, no. 3, pp. 308–313, 2016.
- [49] A. C. Maritim, R. A. Sanders, and J. B. Watkins III, "Effects of α -lipoic acid on biomarkers of oxidative stress in streptozotocin-induced diabetic rats," *Journal of Nutritional Biochemistry*, vol. 14, no. 5, pp. 288–294, 2003.
- [50] A. C. Maritim, R. A. Sanders, and J. B. Watkins III, "Diabetes, oxidative stress, and antioxidants: a review," *Journal of Biochemical and Molecular Toxicology*, vol. 17, no. 1, pp. 24–38, 2003.
- [51] A. B. Egorova, Y. A. Uspenskaya, and V. P. Nefedov, "NAD and glutathione modulate sensitivity of bone marrow cells to oxidative stress," *Bulletin of Experimental Biology and Medicine*, vol. 132, no. 1, pp. 637–640, 2001.
- [52] W. Völkel, R. Alvarez-Sánchez, I. Weick, A. Mallya, W. Dekanta, and A. Pähler, "Glutathione conjugates of 4-hydroxy-2 (E)-nonenal as biomarkers of hepatic oxidative stress-induced lipid peroxidation in rats," *Free Radical Biology and Medicine*, vol. 38, no. 11, pp. 1526–1536, 2005.
- [53] R. Tenhunen, H. S. Marver, and R. Schmid, "The enzymatic conversion of heme to bilirubin by microsomal heme oxygenase," *Proceedings of the National Academy of Sciences*, vol. 61, no. 2, pp. 748–755, 1968.
- [54] R. K. Kutty and M. D. Maines, "Purification and characterization of biliverdin reductase from rat liver," *Journal of Biological Chemistry*, vol. 256, no. 8, pp. 3956–3962, 1981.
- [55] M. A. Di Noia, S. Van Driesche, F. Palmieri et al., "Heme oxygenase-1 enhances renal mitochondrial transport carriers and cytochrome c oxidase activity in experimental diabetes," *Journal of Biological Chemistry*, vol. 281, no. 23, pp. 15687–15693, 2006.
- [56] D. Jaiswal, P. K. Rai, S. Mehta et al., "Role of *Moringa oleifera* in regulation of diabetes-induced oxidative stress," *Asian Pacific Journal of Tropical Medicine*, vol. 6, no. 6, pp. 426–432, 2013.
- [57] R. Gupta, M. Mathur, V. K. Bajaj et al., "Evaluation of antidiabetic and antioxidant activity of *Moringa oleifera* in experimental diabetes," *Journal of Diabetes*, vol. 4, no. 2, pp. 164–171, 2012.
- [58] A. F. Santos, A. C. Argolo, P. M. Paiva, and L. C. Coelho, "Antioxidant activity of *Moringa oleifera* tissue extracts," *Phytotherapy Research*, vol. 26, no. 9, pp. 1366–1370, 2012.
- [59] C. S. T. Origassa and N. O. S. Câmara, "Cytoprotective role of heme oxygenase-1 and heme degradation derived end products in liver injury," *World Journal of Hepatology*, vol. 5, no. 10, p. 541, 2013.
- [60] D. Jaiswal, P. K. Rai, A. Kumar, S. Mehta, and G. Watal, "Effect of *Moringa oleifera* Lam. leaves aqueous extract therapy on hyperglycemic rats," *Journal of Ethnopharmacology*, vol. 123, no. 3, pp. 392–396, 2009.
- [61] S. Adisakwattana and B. Chanathong, "Alpha-glucosidase inhibitory activity and lipid-lowering mechanisms of *Moringa oleifera* leaf extract," *European Review for Medical and Pharmacological Sciences*, vol. 15, no. 7, pp. 803–808, 2011.
- [62] F. M. Ferreira, C. M. Palmeira, R. Seica, A. J. Moreno, and M. S. Santos, "Diabetes and mitochondrial bioenergetics: alterations with age," *Journal of Biochemical and Molecular Toxicology*, vol. 17, no. 4, pp. 214–222, 2003.
- [63] S. Ardestani, D. L. Deskins, and P. P. Young, "Membrane TNF-alpha-activated programmed necrosis is mediated by Ceramide-induced reactive oxygen species," *Journal of Molecular Signaling*, vol. 8, p. 12, 2013.
- [64] D.-D. Zhao, N. Yu, X.-K. Li et al., "Antidiabetic and anti-oxidative effect of Jiang Tang Xiao Ke granule in high-fat diet and low-dose streptozotocin induced diabetic rats," *Evidence-Based Complementary and Alternative Medicine*, vol. 2014, Article ID 475192, 8 pages, 2014.
- [65] E. K. Ainscow and M. D. Brand, "Top-down control analysis of ATP turnover, glycolysis and oxidative phosphorylation in rat hepatocytes," *FEBS Journal*, vol. 263, no. 3, pp. 671–685, 1999.
- [66] C. Desler, T. L. Hansen, J. B. Frederiksen, M. L. Marcker, K. K. Singh, and L. J. Rasmussen, "Is there a link between mitochondrial reserve respiratory capacity and aging?," *Journal of Aging Research*, vol. 2012, Article ID 192503, 9 pages, 2012.
- [67] D. A. Rendon, K. Kotedia, S. F. Afshar et al., "Mapping radiation injury and recovery in bone marrow using ¹⁸F-FLT

- PET/CT and USPIO MRI in a rat model,” *Journal of Nuclear Medicine*, vol. 57, no. 2, pp. 266–271, 2016.
- [68] T. Lobo-Jarne and C. Ugalde, “Respiratory chain super-complexes: structures, function and biogenesis,” *Seminars in Cell & Developmental Biology*, 2017, in press.
- [69] R. Guo, S. Zong, M. Wu, J. Gu, and M. Yang, “Architecture of human mitochondrial respiratory megacomplex I₂III₂IV₂,” *Cell*, vol. 170, no. 6, pp. 1247–1257, 2017.
- [70] D. R. Winge, “Sealing the mitochondrial respirasome,” *Molecular and Cellular Biology*, vol. 32, no. 14, pp. 2647–2652, 2012.
- [71] G. Lenaz and M. L. Genova, “Supramolecular organisation of the mitochondrial respiratory chain: a new challenge for the mechanism and control of oxidative phosphorylation,” *Advances in Experimental Medicine and Biology*, vol. 748, pp. 107–144, 2012.
- [72] G. Antoun, F. McMurray, A. B. Thrush et al., “Impaired mitochondrial oxidative phosphorylation and supercomplex assembly in rectus abdominis muscle of diabetic obese individuals,” *Diabetologia*, vol. 58, no. 12, pp. 2861–2866, 2015.
- [73] C. Oswald, U. Krause-Buchholz, and G. Rödel, “Knockdown of human COX17 affects assembly and supramolecular organization of cytochrome *c* oxidase,” *Journal of Molecular Biology*, vol. 389, no. 3, pp. 470–479, 2009.
- [74] C. R. Lundin, C. von Ballmoos, M. Ott, P. Ädelrotha, and P. Brzezinski, “Regulatory role of the respiratory super-complex factors in *Saccharomyces cerevisiae*,” *Proceedings of the National Academy of Sciences of the United States of America*, vol. 113, no. 31, pp. E4476–E4485, 2016.
- [75] R. K. Singhal, C. Kruse, J. Heidler et al., “Coil is a novel assembly factor of the yeast complex III–complex IV supercomplex,” *Molecular Biology of the Cell*, vol. 28, no. 20, pp. 2609–2622, 2017.
- [76] R. Pérez-Pérez, T. Lobo-Jarne, D. Milenkovic et al., “COX7A2L is a mitochondrial complex III binding protein that stabilizes the III₂ + IV supercomplex without affecting respirasome formation,” *Cell Reports*, vol. 16, no. 9, pp. 2387–2398, 2016.
- [77] M. G. Rosca, E. J. Vazquez, J. Kerner et al., “Cardiac mitochondria in heart failure: decrease in respirasomes and oxidative phosphorylation,” *Cardiovascular Research*, vol. 80, no. 1, pp. 30–39, 2008.
- [78] D. Galati, S. Srinivasan, H. Raza et al., “Role of nuclear-encoded subunit Vb in the assembly and stability of cytochrome *c* oxidase complex: implications in mitochondrial dysfunction and ROS production,” *Biochemical Journal*, vol. 420, no. 3, pp. 439–449, 2009.
- [79] A. A. Aloud, C. Veeramani, C. Govindasamy, M. A. Alsaif, A. S. El Newehy, and K. S. Al-Numair, “Galangin, a dietary flavonoid, improves antioxidant status and reduces hyperglycemia-mediated oxidative stress in streptozotocin-induced diabetic rats,” *Redox Report*, vol. 22, no. 6, pp. 290–300, 2017.
- [80] V. B. Ritov, E. V. Menshikova, K. Azuma et al., “Deficiency of electron transport chain in human skeletal muscle mitochondria in type 2 diabetes mellitus and obesity,” *American Journal of Physiology-Endocrinology and Metabolism*, vol. 298, no. 1, pp. E49–E58, 2010.
- [81] S.-E. Kim, R. Mori, T. Komatsu et al., “Upregulation of cytochrome *c* oxidase subunit 6b1 (Cox6b1) and formation of mitochondrial supercomplexes: implication of Cox6b1 in the effect of calorie restriction,” *Age*, vol. 37, no. 3, p. 45, 2015.
- [82] S. Bansal, M. Siddarth, D. Chawla, B. D. Banerjee, S. V. Madhu, and A. K. Tripathi, “Advanced glycation end products enhance reactive oxygen and nitrogen species generation in neutrophils in vitro,” *Molecular and Cellular Biochemistry*, vol. 361, no. 1-2, pp. 289–296, 2012.
- [83] Y. Li, J.-S. Park, J.-H. Deng, and Y. Bai, “Cytochrome *c* oxidase subunit IV is essential for assembly and respiratory function of the enzyme complex,” *Journal of Bioenergetics and Biomembranes*, vol. 38, no. 5-6, pp. 283–291, 2006.
- [84] H. Schägger, R. de Coo, M. F. Bauer, S. Hofmann, C. Godinot, and U. Brandt, “Significance of respirasomes for the assembly/stability of human respiratory chain complex I,” *Journal of Biological Chemistry*, vol. 279, no. 35, pp. 36349–36353, 2004.
- [85] S. Budde, L. van den Heuvel, R. Smeets et al., “Clinical heterogeneity in patients with mutations in the NDUFS4 gene of mitochondrial complex I,” *Journal of Inherited Metabolic Disease*, vol. 26, no. 8, pp. 813–815, 2003.
- [86] S. Scacco, V. Petruzzella, S. Budde et al., “Pathological mutations of the human NDUFS4 gene of the 18-kDa (AQDQ) subunit of complex I affect the expression of the protein and the assembly and function of the complex,” *Journal of Biological Chemistry*, vol. 278, no. 45, pp. 44161–44167, 2003.
- [87] P. Cardol, L. Boutaffala, S. Memmi, B. Devreese, R. F. Matagnea, and C. Remaclea, “In *Chlamydomonas*, the loss of ND5 subunit prevents the assembly of whole mitochondrial complex I and leads to the formation of a low abundant 700 kDa subcomplex,” *Biochimica et Biophysica Acta (BBA)-Bioenergetics*, vol. 1777, no. 4, pp. 388–396, 2008.
- [88] M. Brownlee, “The pathobiology of diabetic complications,” *Diabetes*, vol. 54, no. 6, pp. 1615–1625, 2005.
- [89] M. R. Duchen, “Roles of mitochondria in health and disease,” *Diabetes*, vol. 53, no. 1, pp. S96–S102, 2004.
- [90] J. A. Herlein, B. D. Fink, Y. O’Malley, and W. I. Sivitz, “Superoxide and respiratory coupling in mitochondria of insulin-deficient diabetic rats,” *Endocrinology*, vol. 150, no. 1, pp. 46–55, 2008.
- [91] M. D. Brand, C. Affourtit, T. C. Esteves et al., “Mitochondrial superoxide: production, biological effects, and activation of uncoupling proteins,” *Free Radical Biology and Medicine*, vol. 37, no. 6, pp. 755–767, 2004.
- [92] L. K. Kwong and R. S. Sohal, “Substrate and site specificity of hydrogen peroxide generation in mouse mitochondria,” *Archives of Biochemistry and Biophysics*, vol. 350, no. 1, pp. 118–126, 1998.
- [93] B. Kadenbach, “Intrinsic and extrinsic uncoupling of oxidative phosphorylation,” *Biochimica et Biophysica Acta (BBA)-Bioenergetics*, vol. 1604, no. 2, pp. 77–94, 2003.
- [94] A. Musatov and N. C. Robinson, “Susceptibility of mitochondrial electron-transport complexes to oxidative damage. Focus on cytochrome *c* oxidase,” *Free Radical Research*, vol. 46, no. 11, pp. 1313–1326, 2012.
- [95] A. J. Lambert and M. D. Brand, “Inhibitors of the quinone-binding site allow rapid superoxide production from mitochondrial NADH: ubiquinone oxidoreductase (complex I),” *Journal of Biological Chemistry*, vol. 279, no. 38, pp. 39414–39420, 2004.
- [96] S. Raha and B. H. Robinson, “Mitochondria, oxygen free radicals, disease and ageing,” *Trends in Biochemical Sciences*, vol. 25, no. 10, pp. 502–508, 2000.
- [97] J. Wu, X. Luo, N. Thangthaeng et al., “Pancreatic mitochondrial complex I exhibits aberrant hyperactivity in diabetes,” *Biochemistry and Biophysics Reports*, vol. 11, pp. 119–129, 2017.

- [98] H. Raza, S. K. Prabu, A. John, and N. G. Avadhani, "Impaired mitochondrial respiratory functions and oxidative stress in streptozotocin-induced diabetic rats," *International Journal of Molecular Sciences*, vol. 12, no. 5, pp. 3133–3147, 2011.
- [99] J. Škrha Jr., M. Kalousová, J. Švarcová et al., "Relationship of soluble RAGE and RAGE ligands HMGB1 and EN-RAGE to endothelial dysfunction in type 1 and type 2 diabetes mellitus," *Experimental and Clinical Endocrinology & Diabetes*, vol. 120, no. 5, pp. 277–281, 2012.
- [100] O. Demin, H. Westerhoff, and B. Kholodenko, "Mathematical modelling of superoxide generation with the bcl complex of mitochondria," *Biochemistry. Biokhimiia*, vol. 63, no. 6, pp. 634–649, 1998.
- [101] L. Gibellini, E. Bianchini, S. De Biasi, M. Nasi, A. Cossarizza, and M. Pinti, "Natural compounds modulating mitochondrial functions," *Evidence-Based Complementary and Alternative Medicine*, vol. 2015, Article ID 527209, 13 pages, 2015.
- [102] C. Sandoval-Acuña, J. Ferreira, and H. Speisky, "Polyphenols and mitochondria: an update on their increasingly emerging ROS-scavenging independent actions," *Archives of Biochemistry and Biophysics*, vol. 559, pp. 75–90, 2014.
- [103] L. Raudone, D. Burdulis, R. Raudonis et al., "Effect of Perilla Frutescens extracts and rosmarinic acid on rat heart mitochondrial functions," *Acta Poloniae Pharmaceutica*, vol. 73, no. 1, pp. 135–145, 2016.
- [104] G. B. Melo, R. L. Silva, V. A. Melo et al., "Effect of the aqueous extract of *Hyptis pectinata* on liver mitochondrial respiration," *Phytomedicine*, vol. 12, no. 5, pp. 359–362, 2005.

Composition Comments

1. We have rephrased the sentence “In addition, impairment ... has been reported” for grammatical correctness and clarity. Please confirm that this is your intended meaning.
2. Note that citation for Supplementary materials section has been added here. Please confirm.
3. Please confirm the journal title for References [44] and [71].

Author(s) Name(s)

It is very important to confirm the author(s) last and first names in order to be displayed correctly on our website as well as in the indexing databases:

Author 1

Given Names: María
Last Name: Alejandra Sánchez-Muñoz

Author 2

Given Names: Mónica Andrea
Last Name: Valdez-Solana

Author 3

Given Names: Mara Ibeth
Last Name: Campos-Almazán

Author 4

Given Names: Óscar
Last Name: Flores-Herrera

Author 5

Given Names: Mercedes
Last Name: Esparza-Perusquía

Author 6

Given Names: Sofia
Last Name: Olvera-Sánchez

Author 7

Given Names: Guadalupe
Last Name: García-Arenas

Author 8

Given Names: Claudia
Last Name: Avitia-Domínguez

Author 9

Given Names: Alfredo
Last Name: Téllez-Valencia

Author 10

Given Names: Erick
Last Name: Sierra-Campos

It is also very important for each author to provide an ORCID (Open Researcher and Contributor ID). ORCID aims to solve the name ambiguity problem in scholarly communications by creating a registry of persistent unique identifiers for individual researchers.

To register an ORCID, please go to the Account Update page (<http://mts.hindawi.com/update/>) in our Manuscript Tracking System and after you have logged in click on the ORCID link at the top of the page. This link will take you to the ORCID website where you will be able to create an account for yourself. Once you have done so, your new ORCID will be saved in our Manuscript Tracking System automatically.



Original article

Cardioprotective strategies preserve the stability of respiratory chain supercomplexes and reduce oxidative stress in reperfused ischemic hearts



I. Ramírez-Camacho^a, F. Correa^a, M. El Hafidi^a, A. Silva-Palacios^a, M. Ostolga-Chavarría^a, M. Esparza-Perusquía^b, S. Olvera-Sánchez^b, O. Flores-Herrera^b, C. Zazueta^{a,*}

^a Departamento de Biomedicina Cardiovascular, Instituto Nacional de Cardiología. I. Ch., 14080 Mexico, D.F., Mexico

^b Departamento de Bioquímica, Facultad de Medicina, Universidad Nacional Autónoma de México, 04510 Mexico, D.F., Mexico

ARTICLE INFO

Keywords:

Mitochondrial respiratory chain
Supercomplexes
Reactive oxygen species
N-acetylcysteine
Postconditioning

ABSTRACT

Electron leakage from dysfunctional respiratory chain and consequent superoxide formation leads to mitochondrial and cell injury during ischemia and reperfusion (IR). In this work we evaluate if the supramolecular assembly of the respiratory complexes into supercomplexes (SCs) is associated with preserved energy efficiency and diminished oxidative stress in post-ischemic hearts treated with the antioxidant N-acetylcysteine (NAC) and the cardioprotective maneuver of Postconditioning (PostC). Hemodynamic variables, infarct size, oxidative stress markers, oxygen consumption and the activity/stability of SCs were compared between groups. We found that mitochondrial oxygen consumption and the activity of respiratory complexes are preserved in mitochondria from reperfused hearts treated with both NAC and PostC. Both treatments contribute to recover the activity of individual complexes. NAC reduced oxidative stress and maintained SCs assemblies containing Complex I, Complex III, Complex IV and the adapter protein SCAFI more effectively than PostC. On the other hand, the activities of CI, CIII and CIV associated to SCs assemblies were preserved by this maneuver, suggesting that the activation of other cardioprotective mechanisms besides oxidative stress contention might participate in maintaining the activity of the mitochondrial respiratory complexes in such superstructures.

We conclude that both the monomeric and the SCs assembly of the respiratory chain contribute to the in vivo functionality of the mitochondria. However, although the ROS-induced damage and the consequent increased production of ROS affect the assembly of SCs, other levels of regulation as those induced by PostC, might participate in maintaining the activity of the respiratory complexes in such superstructures.

1. Introduction

The organization of the respiratory chain complexes has been represented into different models: the fluid state one, in which individual entities and mobile electron carriers diffuse freely in the mitochondrial inner membrane interacting through random collisions [1]; the solid state model, in which the respiratory complexes are arranged into compact conglomerates known as supercomplexes (SCs) or respirasomes [2] and the currently accepted pattern that integrates both types of organization, known as the plasticity model [3]. The controversy on the possible artifacts that mild detergents cause on respiratory complexes' association, has been tempered by experimental evidences that

include the identification of SCs in mitochondria from many organisms [4,5]; the demonstration that almost all Complex I is bound to Complex III in the absence of detergents [5,6] and that the purified SCs are stable and catalytically active [7].

Mitochondrial respiratory complexes are the main source of reactive oxygen species (ROS) production and in consequence, particularly sensitive to their effects. Superoxide anion ($O_2^{\cdot -}$) is produced after one-electron reduction of O_2 in two sites of Complex I: at flavin in the NADH-oxidizing site (site I_F) and in the ubiquinone-reducing site (site I_Q) [8], as well as in the outer quinol-binding site of mitochondrial complex III (site III_{QO}) [9]. The proposal that the structural organization of the respiratory complexes into supramolecular arrangements

Abbreviations: ROS, reactive oxygen species; O_2 , oxygen; $O_2^{\cdot -}$, Superoxide anion; IR, ischemia and reperfusion; SC's, supercomplexes; SCAFI, supercomplex assembly factor I; NAC, N-acetylcysteine; PostC, postconditioning; H_2O_2 , Hydrogen peroxide; NADH, Nicotinamide adenine dinucleotide; HR, Heart rate; LVDP, Left ventricular developed pressure; TTC, Triphenyltetrazolium Chloride

* Correspondence to: Departamento de Biomedicina Cardiovascular Instituto Nacional de Cardiología, Ignacio Chávez, Juan Badiano No. 1. Colonia Sección XVI, Mexico, D.F. 14080, Mexico.

E-mail address: ana.zazueta@cardiologia.org.mx (C. Zazueta).

<https://doi.org/10.1016/j.freeradbiomed.2018.09.047>

Received 6 April 2018; Received in revised form 20 September 2018; Accepted 30 September 2018

Available online 11 October 2018

0891-5849/ © 2018 Elsevier Inc. All rights reserved.

decreases electron leakage and controls ROS production [10] is supported by reports showing that disruption of the association between Complex I and Complex III with dodecyl maltoside augments ROS generation in vitro [11] and that low levels of the III₂IV₂ supercomplex is associated with increased ROS production in yeast mitochondria [12].

It has been established that ROS generated in Complexes I and III contribute to myocardial damage during ischemia and reperfusion (IR) [13–15], but few studies have addressed that their arrangement into SCs might be related with diminution in oxidative stress and with cardioprotection in reperfused hearts. What is known is that the increase of the cytochrome-c-oxidase subunit VIb in SCs, concurs with left ventricular pressure recovery in IR hearts subjected to preconditioning [16] and, that isoflurane-conferred protection in ischemic injury is partially related with the stabilization of oligomers from complexes III/IV [17]. In this work we evaluated the effect of the antioxidant N-acetylcysteine (NAC) and of the mechanical manoeuvre of Post-conditioning (PostC) on the functional properties of the mitochondrial respiratory chain and stability of SCs in mitochondria from IR hearts, to provide further evidences on the causative link between ROS production, energy deficiency and decrease in mitochondrial respirasome formation.

2. Material and methods

This investigation was approved by the Ethics Committee of the National Institute of Cardiology, “Ignacio Chávez” (INC-13806). The experimental protocols followed the guidelines of Norma Oficial Mexicana for the use and care of laboratory animals (NOM-062-ZOO-1999) and for disposal of biological residues (NOM-087-SEMAR-NAT-SSA1-2002).

2.1. Experimental design

Male Wistar rats (300–350 g) were anaesthetized by injecting intraperitoneally a single dose of sodium pentobarbital (60 mg/kg i.p) plus sodium heparin and complete lack of pain response was assessed by determining pedal withdrawal reflex. Hearts were perfused retrogradely in a Langendorff heart perfusion system via the aorta at a constant flow rate of 13 mL/min with Krebs-Henseleit solution (118 mM NaCl, 4.75 mM KCl, 1.18 mM KH₂PO₄, 1.18 mM MgSO₄·7H₂O, 2.5 mM CaCl₂, 25 mM NaHCO₃, 5 mM glucose and 0.1 mM sodium octanoate, pH 7.4), which was continuously bubbled with 95% O₂ and 5% CO₂ at 37 °C. Cardiac performance was measured at left ventricular end-diastolic pressure (LVEDP) of 10 mmHg using a latex balloon inserted into the left ventricle and connected to a pressure transducer. Throughout the experiment, left ventricular developed pressure (LVDP) was recorded using the software LabChart8-Pro v8.1.5 from ADInstruments. Heart rate (HR) expressed as beat number × min⁻¹ was obtained from the left ventricular pressure waveform.

Hearts were perfused for 20 min to reach a steady state and then subjected to the different protocols. The experimental groups were: 1) Control, hearts continuously perfused for additional 90 min 2) IR, hearts subjected to global ischemia for 30 min by turning off the pumping system and then to 60 min of reperfusion. 3) IR+NAC hearts, that were subjected to 30 min of ischemia and that during the first 10 min of reperfusion received 0.25 mM of NAC in the Krebs-Henseleit Buffer and 4) IR+PostC, hearts subjected to 30 min of ischemia, to postconditioning (5 cycles of 30 s reperfusion and 30 s ischemia) and to 60 min of reperfusion (Fig. 1A).

2.2. Infarct size

Infarct size was evaluated by staining with triphenyltetrazolium chloride (TTC). At the end of the experiments the hearts to be used for infarct size calculations were frozen at -20 °C. Heart slices of ~3 mm

were obtained and immersed in 1% TTC solution in phosphate buffer (8.8 mM Na₂HPO₄, 1.8 mM NaH₂PO₄, pH 7.4) for 10 min at 37 °C. Digital images of heart slices were analyzed using the ImageJ® 1.48 software (NIH, MD, USA). Infarct size was expressed as percentage of total heart area [18].

2.3. Mitochondrial isolation

Fresh cardiac tissue from the different groups was placed in cold buffer solution containing 250 mM sucrose, 10 mM HEPES, and 1 mM ethylenediaminetetraacetic acid, pH 7.4. The hearts were minced and incubated for 10 min with the same buffer plus subtilisin A (2 mg/g of tissue) in an ice bath. Then the tissue was washed, suspended in the same buffer without the enzyme and homogenized. Mitochondria were obtained by differential centrifugation as previously described [19].

2.4. ROS production and oxidative stress markers in mitochondria

Hydrogen peroxide production was evaluated as an indicator of ROS generation. Mitochondria (0.250 mg/mL) were incubated in reaction buffer containing 100 mM sucrose, 75 mM KCl, 5 mM Tris, 3 mM MgCl₂, 10 μM EGTA, and 1 mM KH₂PO₄, pH 7.4, plus 0.1 μM dihydrodichlorofluorescein (DCF) and 1 U/mL horseradish peroxidase. Mitochondria were energized with malate/glutamate (5:3 mM) or with succinate (10 mM). Antimycin A (AA; 5 μM) or rotenone (1 μM) were used to enhance ROS production. DCF oxidation was monitored at λ_{ex} = 475 nm (4-nm slit) and λ_{em} = 525 nm (4-nm slit) in a Perkin-Elmer LS50B spectrofluorometer at 30 °C. The slopes of the traces obtained after substrate and/or inhibitor addition were compared against a standard curve of H₂O₂ generated by adding known amounts of H₂O₂ to the buffer containing DCF, horseradish peroxidase and mitochondria as previously described [20].

Malondialdehyde (MDA) was measured as lipoperoxidation marker according with Guerrero-Beltrán et al. [21]. Briefly, 1 mg of mitochondrial protein was added to a medium containing 1-methyl-2-phenylindole. The reaction was started by adding 37% HCl and incubated for 40 min at 45 °C. Then the samples were centrifuged at 3000 g for 5 min and the optical density of the supernatant was measured. The method is based on the formation of a stable chromophore with a maximal intensity of absorbance at 586 nm. Results are expressed in nmol of MDA per milligram of protein.

Reduced glutathione (GSH) was evaluated fluorometrically as described by Galván-Arzate et al. [22]. Briefly, fresh mitochondria (15 μg) were derivatized with 100 μL of o-phthalaldehyde (OPA, 1 mg/mL) and incubated for 20 min at room temperature in 2-mL final volume. Fluorescence was measured at λ_{ex} = 350 nm and λ_{em} = 420 nm in a LS50B Luminescence Spectrophotometer (Perkin Elmer, Waltham, MA). Twin samples were used in parallel to evaluate oxidized glutathione (GSSG). Mitochondria were incubated for 30 min with 100 μL of 40 mM N-ethylmaleimide (NEM) to prevent that glutathione free SH group reacts with OPA. Then, the samples were mixed with 4.3 mL of 0.1 N NaOH (pH 12) to allow GSSG reduction. Finally an aliquot was withdrawn, incubated with 50 μg of OPA for 20 min and fluorescence was measured [23]. Results were normalized per mg protein and expressed as GSH/GSSG ratio.

We also measured protein oxidation with the OxyBlot™ protein oxidation detection kit (Merck-Millipore, Darmstadt, Germany). Briefly, two aliquots of each mitochondrial sample (20–40 μg) were transferred to Eppendorf tubes and denatured by adding a final concentration of 10% SDS. One aliquot was derivatized to 2,4-dinitrophenylhydrazine (DNP) with 2,4-dinitrophenylhydrazine (DNPH), while the aliquot used as the negative control was incubated with the same volume of control solution. Then, samples were neutralized and separated by SDS-PAGE, transferred to PDVF membranes and incubated with rabbit anti-DNP antibodies (1:150 dilution) in PBS-Tween containing 1% bovine serum albumin. Horseradish peroxidase-conjugated secondary antibodies

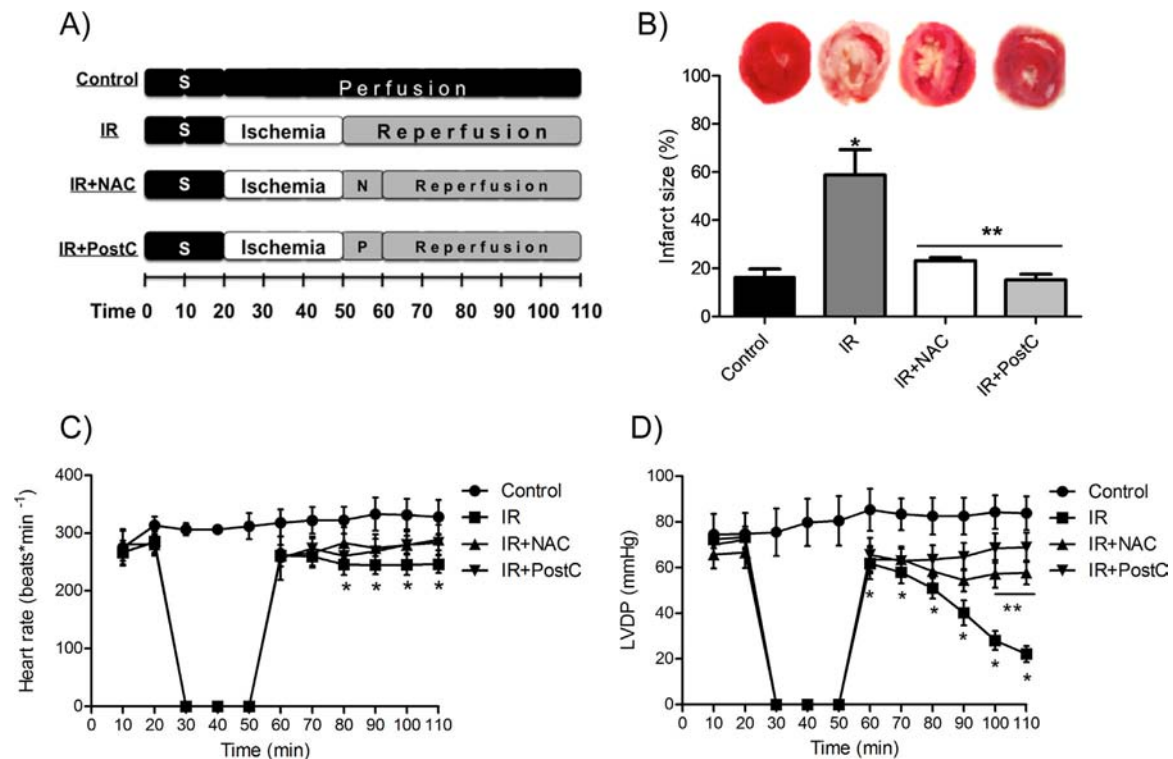


Fig. 1. A) Schematic representation of the experimental protocols in the isolated heart model. All hearts were stabilized during 20 min. Control hearts were continuously perfused during 110 min; IR hearts were subjected to 30 min of global ischemia and 60 min of reperfusion; IR + NAC hearts received 0.25 mM NAC during the first 10 min of reperfusion and IR + PostC hearts were subjected to 5 cycles of 30 s reperfusion and 30 s ischemia and then, to 60 min of reperfusion; B) infarct size; C) heart rate (beats*min⁻¹) and D) left ventricular developed pressure (LVDP). Data are means \pm SD of at least six different experiments. *P < 0.05 vs. Control and **P < 0.05 vs. IR.

(1:300 dilution) and a chemiluminescent reagent were used for signal detection.

2.5. Mitochondrial oxygen consumption

Mitochondrial oxygen consumption was determined using a Clark-type oxygen electrode (Yellow Springs Instruments, Yellow Springs, OH, USA). The experiments were carried out in 1.5 mL of basic medium, containing 125 mM KCl, 10 mM HEPES and 3 mM Pi, pH 7.3. State 4 respiration was evaluated in the presence of 5 mM sodium glutamate and 5 mM sodium malate. State 3 respiration was stimulated by adding 200 μ M adenosine diphosphate (ADP). Respiratory rates are expressed as ng-atoms oxygen/min/mg protein (ngAO/min/mg). Respiratory control ratio (RCR) was calculated as the ratio between the State 3 and State 4 rates. Phosphorylation efficiency (ADP/O ratio) was calculated from the added amount of ADP and total amount of oxygen consumed during state 3. Uncoupled respiration was observed after incubating with 1 μ M of CCCP (Carbonyl cyanide m-chlorophenyl hydrazine).

2.6. Mitochondria solubilization

Separation of electron transport chain complexes was performed using BN-PAGE according to the protocol described by Schäfer et al. [24]. Mitochondrial proteins were solubilized with digitonin using a detergent to protein ratio of 2:1 (mg:mg) in 200 μ L of 3 \times -buffer containing 150 mM BIS-TRIS, 1.5 mM aminocaproic acid, pH 7. After incubating during 30 min, the samples were centrifuged at 18,000 g for 2 h and supernatants were recovered. All procedures were performed at 4 $^{\circ}$ C.

2.7. Blue native polyacrylamide gel electrophoresis (BN-PAGE) and in-gel activity assays

Blue-Native (BN) 3.5–10% gradient gels were loaded with 100 μ g of mitochondrial protein in the presence of Coomassie blue G-250 dye and were run overnight at 30 V in cold. The anode buffer contained 50 mM BIS-TRIS, pH 7.0 and the cathode buffer 50 mM tricine, 15 mM BIS-TRIS/HCl plus 0.002% Coomassie blue G-250. At the end of the electrophoresis, some gels were further stained with Coomassie blue. Other gels were used to measure the enzymatic activities of each mitochondrial respiratory complex as follows: NADH dehydrogenase activity of Complex I (CI) was evaluated by formazan production, after incubating the gels in 10 mM TRIS, 1 mg/mL (w/v) of 4-nitro blue tetrazolium chloride and 0.14 mM NADH, pH 7.0. Succinate dehydrogenase activity of Complex II (CII) was visualized as purple bands in the presence of 80 mM succinate, 2 mg/mL (w/v) of 4-nitro blue tetrazolium chloride and 4.5 mM EDTA, pH 7.0. Complex III (CIII) activity was determined with 0.2 mM TMPD (N,N,N',N'-tetramethyl-p-phenylenediamine) in 70% methanol, 100 mM sodium acetate and 100 μ M H₂O₂, pH 7.0. Cytochrome c oxidase activity of Complex IV (CIV) was visualized by precipitation of 3,3-diaminobenzidine oxides in a buffer containing 50 mM sodium phosphate, 0.5 mg/mL of 3,3-diaminobenzidine-tetrahydrochloride, 0.5 mg/mL cytochrome c, 20 units/mL catalase, and 75 mg/mL sucrose, pH 7.0. Finally, ATPase activity (CV) was detected in a medium containing 30 mg of lead II perchlorate trihydrate, 30 mM Tris-Glycerol, 5 mM ATP and 15 mM CaCl₂ in 20 mL until maximal signal of the lead phosphate band was obtained [25]. The developed bands were analyzed by densitometry using the Image J program from the National Institutes of Health.

2.8. Activity of the respiratory chain complexes

The enzymatic function of the mitochondrial respiratory complexes was also measured spectrophotometrically as described by Spinazzi et al. [26]. Complex I activity was evaluated in 1 mL of 10 mM TRIS buffer pH 7.4, supplemented with 100 μ M NADH and mitochondrial protein (50 μ g). The reaction was started by adding 0.95 μ M 2,6-dichloroindophenol (DCPIP) as terminal electron acceptor. Reduction of DCPIP was followed at 600 nm during 3 min in the presence or absence of 1 μ M rotenone ($\epsilon = 21 \text{ mM}^{-1} \text{ cm}^{-1}$). Specific activity is expressed as nmol/min/mg. Complex II activity was determined incubating 40 μ g of mitochondrial protein in 0.5 M potassium phosphate buffer (pH 7.5) supplemented with 20 mM succinate and 150 μ L of DCPIP 0.015% (w/v). Final volume was adjusted to 1 mL with distilled water. Reduction of DCPIP was followed at 600 nm during 3 min ($\epsilon = 21 \text{ mM}^{-1} \text{ cm}^{-1}$). Specific activity is expressed as nmol succinate_{ox}/min/mg, due that 1 mol of DCPIP is reduced as 1 mol of succinate is oxidized. Complex III was measured as follows: 40 μ g of mitochondrial protein was incubated in 1 mL of potassium phosphate buffer 0.5 M (pH 7.5) plus 1 mM EDTA, 0.5 mM KCN and 50 μ M of oxidized cytochrome c at 30 °C for 15 min. Cytochrome c reduction was initiated by adding 50 μ M of decylubiquinol (DBH₂) in the presence or absence of 10 μ g of antimycin A. The increase in absorbance was followed for 1–2 min at 550 nm ($\epsilon = 18.5 \text{ mM}^{-1} \text{ cm}^{-1}$). Specific complex III activity is the antimycin A-sensitive-activity. Complex IV was evaluated after adding 40 μ g of mitochondrial protein to 1 mL of 50 mM potassium phosphate buffer, (pH 7.0) containing 50 μ M of reduced cytochrome c, with or without 0.5 mM KCN. Decrease in absorbance was immediately registered at 550 nm ($\epsilon = 18.5 \text{ mM}^{-1} \text{ cm}^{-1}$). Complex IV activity is expressed as first order rate constant k ($\text{min}^{-1} \times \text{mg protein}^{-1}$). Oligomycin-sensitive ATPase activity (CV) was evaluated by measuring ATP hydrolysis by a coupled enzymatic assay using lactate dehydrogenase and pyruvate kinase [27]. Forty μ g of mitochondrial protein were incubated in 200 μ L of a medium containing 50 mM Tris-HCl, pH 8.0, 5 mg/mL BSA, 20 mM MgCl₂, 50 mM KCl, 15 μ M CCCP, 5 μ M AA, 10 mM phosphoenolpyruvate (PEP), 2.5 mM ATP, 4U lactate dehydrogenase, 4U pyruvate kinase and 1 mM NADH during 5 min at 37 °C. The reaction was continuously recorded at 340 nm during 3 min, then 3 μ M oligomycin was added and measured for additional 3 min. Hydrolysis NADH concentration was calculated by using an extinction coefficient of 6220 $\text{M}^{-1} \text{ cm}^{-1}$. As the hydrolysis of 1 mol ATP produces the oxidation of 1 mol NADH through this coupling system, the activity is expressed as nmol ATP/mg protein/min.

2.9. Immunodetection in first dimension (1-D) and second dimension (2-D) native gels

BN gels were incubated in 20 mL of a solution containing 0.192 M glycine, 0.025 M TRIS plus 1% SDS during 60 min under constant agitation and transferred onto polyvinylidene difluoride membranes (PVDF) for 50 min at 25 V. Then, the membranes were blocked with 5% defat milk in TBS-T and incubated overnight with anti-NADH dehydrogenase subunit Ndufs4 (ab55540, Abcam, Cambridge, MA, USA; 1:1000); anti-ubiquinol cytochrome c reductase core protein UQCRCF1 (ab14746, Abcam, Cambridge, MA, USA; 1:1000); anti-cytochrome c oxidase subunit II (sc-514489, Santa Cruz Biotechnology, USA; 1:1000) and anti-COX7A2L subunit (Proteintech, Rosemont, IL, USA, 1:1000). Secondary antibodies were used at 1:25,000 dilution. The signals were visualized with C-Digit blot scanner and analyzed by ImageJ (NIH).

2.10. Statistical analysis

Data were analyzed using one or two-way ANOVA followed by Tukey's post-hoc test with the graph Pad PRISM 5.03 software; $P < 0.05$ was considered statistically significant.

3. Results

3.1. N-acetylcysteine and postconditioning maintain cardiac function and reduce infarct size in reperfused hearts

NAC and PostC reduced infarct size to 26% and 18% respectively, in comparison with almost 59% of cell death observed in IR hearts ($P < 0.05$) (Fig. 1B). Heart rate and left-ventricular developed pressure (LVDP) were maintained in Control hearts during 110 min of constant perfusion, while those parameters decreased from the first minutes and until the end of reperfusion in IR hearts. LVDP in the IR group was more affected than heart rate. Both NAC and PostC prevented almost completely from heart dysfunction at the end of reperfusion, being more evident cardiac pressure recovery (Fig. 1C and Fig. 1D).

3.2. Cardioprotection conferred by N-acetylcysteine and postconditioning is related with decreased H₂O₂ content and reduction of oxidative stress

Succinate oxidation in the presence of both Antimycin A (AA) and rotenone (Rot) augmented hydrogen peroxide levels in IR mitochondria in comparison with Control mitochondria (10 ± 3.5 and 10.1 ± 1.3 pmol H₂O₂/min/mg vs. 4.7 ± 1.7 and 1.8 ± 2.3 pmol H₂O₂/min/mg respectively). Both NAC and PostC, diminished hydrogen peroxide at different extent, although PostC showed higher efficiency even without inhibitors. On the other hand, mitochondria from IR hearts energized with glutamate/malate showed higher rate of hydrogen peroxide generation than Control mitochondria, that further increase in the presence of AA, confirming the participation of Complex III in ROS production. Again, both treatments diminished ROS production in comparison with IR mitochondria. Also, the combination of glutamate/malate plus rotenone enhanced H₂O₂ production in IR mitochondria as compared with the Control group (Fig. 2). Lipid peroxidation and protein carbonylation increased in mitochondria from the IR group in correlation with decreased redox state (GSH/GSSG) as compared to the Control group ($P < 0.05$) (Fig. 3). NAC reduced MDA levels by 51% (1.3 ± 0.5 vs. 2.7 ± 0.8 nmol MDA/mg protein in IR mitochondria) ($P < 0.05$) and PostC to 1.65 ± 0.2 nmol MDA/mg protein (48%) (Fig. 3A). GSH/GSSG increased significantly in IR+PostC in comparison with IR mitochondria ($P < 0.05$; Fig. 3B); whereas protein oxidation diminished in both IR+NAC and IR+PostC groups (Fig. 3C).

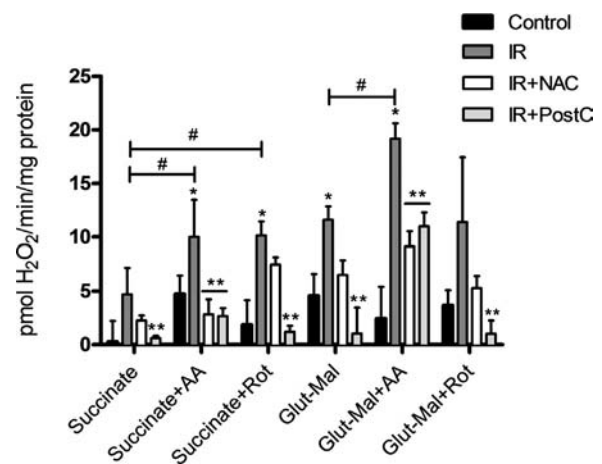


Fig. 2. Effect of NAC and PostC on the rate of hydrogen peroxide production in mitochondria from reperfused hearts. H₂O₂ content was determined by following HRP-catalyzed dichlorofluorescein (DCF) oxidation in mitochondria plus succinate or glutamate/malate in the presence of Antimycin A and/or rotenone. Data are means \pm SD of at least three independent experiments per group. * $P < 0.05$ vs. Control and ** $P < 0.05$ vs. IR. # $P < 0.05$ vs. mitochondria without inhibitors.

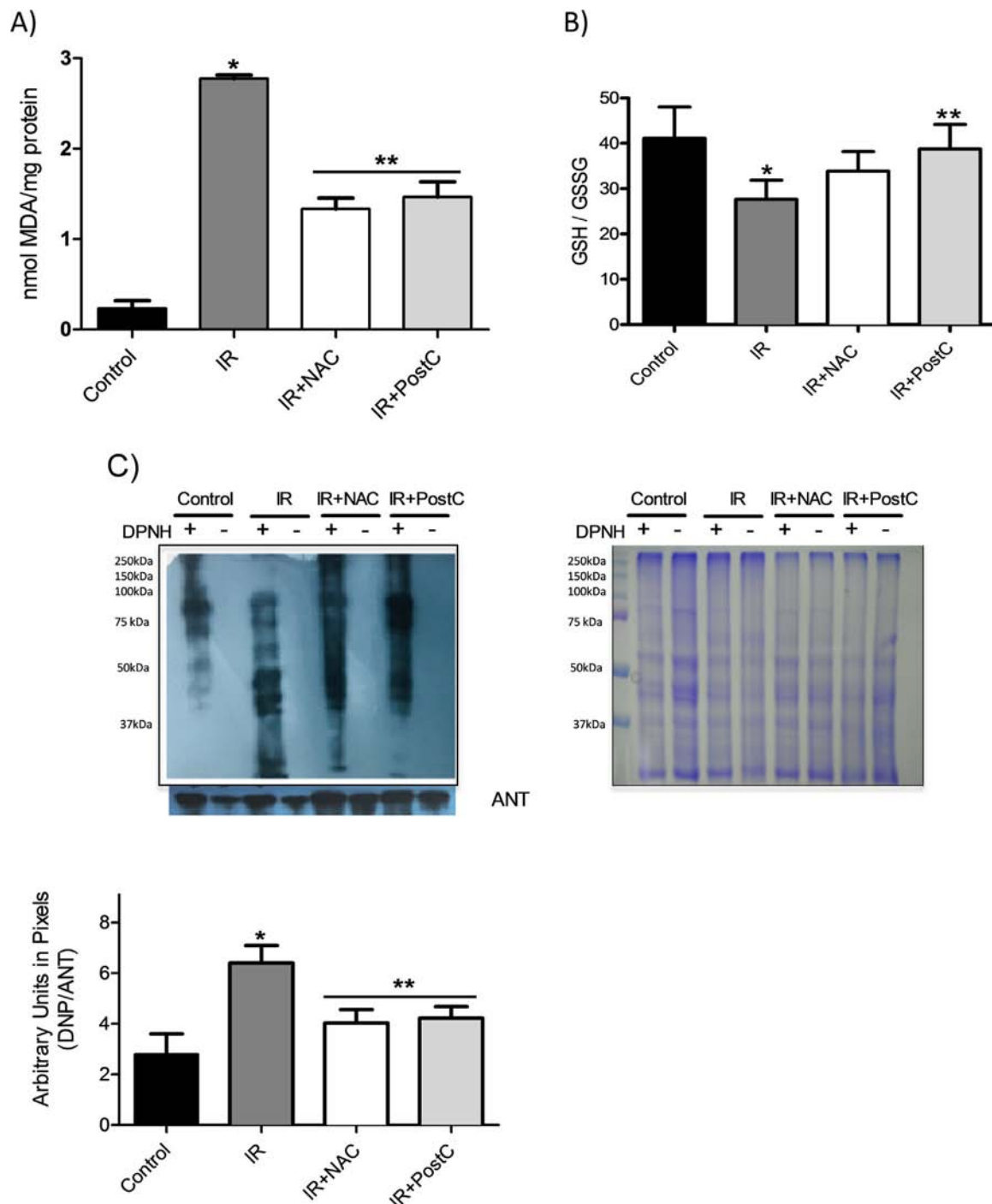


Fig. 3. Oxidative stress markers in isolated mitochondria from reperfused heart treated with NAC and subjected to PostC. A) Malondialdehyde (MDA) levels; B) GSH/GSSG and C) Representative immunoblot of carbonylated proteins and densitometric ratio between total protein carbonylation (DNP) and adenine nucleotide translocator (ANT) content. It is also shown a Coomassie blue staining of the gel. Data are representative of at least five different experiments per group. Data are means \pm SD. *P < 0.05 vs. Control and **P < 0.05 vs. IR.

3.3. Mitochondrial function is preserved by diminishing oxidative stress in reperfused hearts

The association between oxidative stress and oxidative phosphorylation (OXPHOS) was evaluated in isolated mitochondria by performing oxygen consumption experiments. No changes were observed in basal oxygen consumption (State 4) with NADH-linked substrates between Control, IR and IR+NAC mitochondria (Fig. 4A), whereas ADP-stimulated respiration (State 3) diminished in the IR group and was recovered in both IR+NAC and IR+PostC mitochondria. RCR, the

single most useful general measure of mitochondrial function, diminished from 2.89 ± 0.43 to 1.6 ± 0.19 (Control vs. IR mitochondria; P < 0.05) and increased significantly in mitochondria from hearts subjected to both treatments (Fig. 4B). ADP/O, which represents the maximum number of ATP molecules made as an electron pair passes down the respiratory chain from substrate to oxygen, followed a similar pattern, but was only preserved with NAC treatment (P < 0.05). ADP-stimulated (State 3) and uncoupled respiration diminished in the IR group suggesting inhibition of substrate oxidation (Fig. 4C).

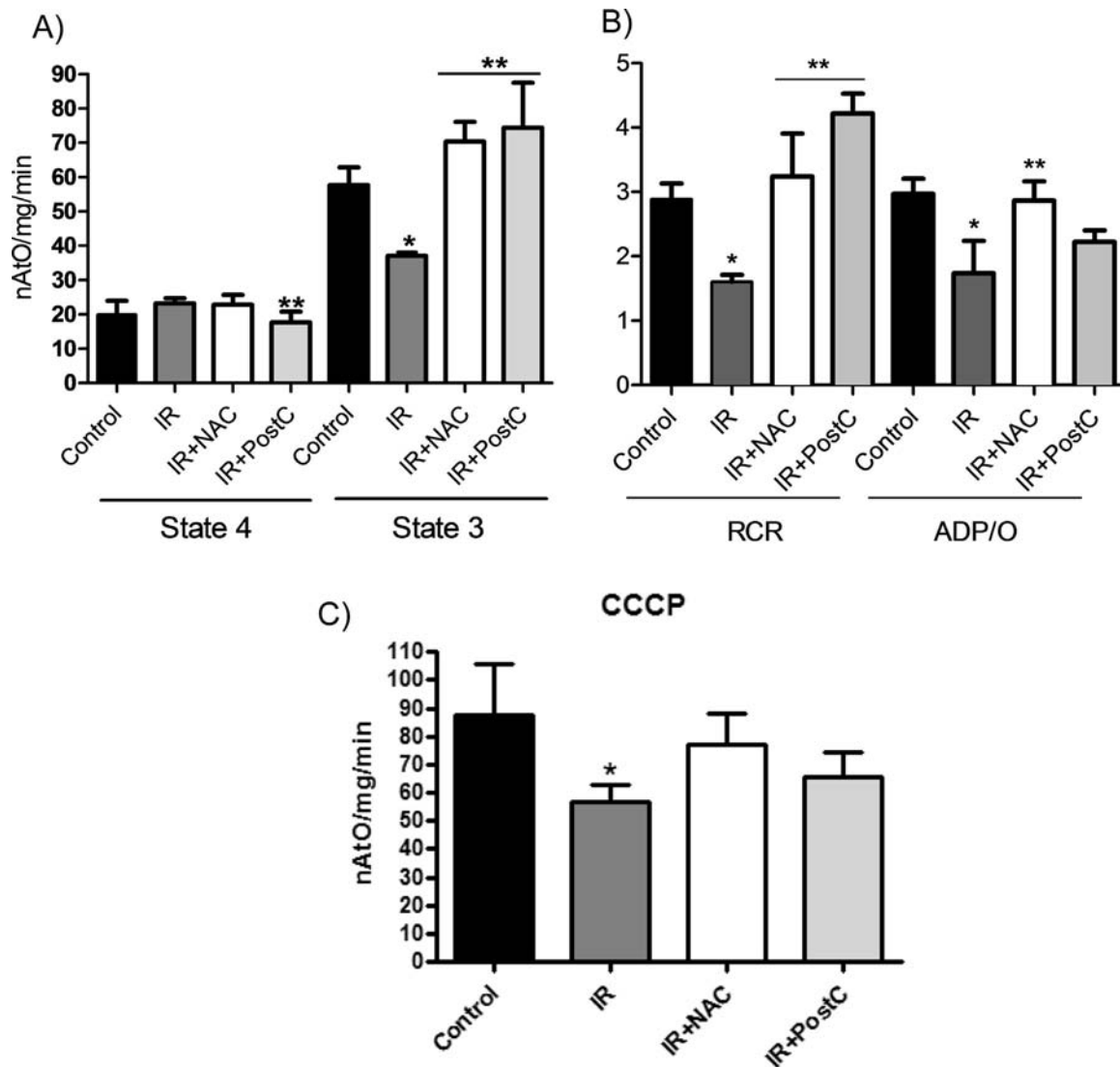


Fig. 4. Oxygen consumption in isolated mitochondria with glutamate plus malate. A) State 4 respiration and State 3 respiration; B) Respiratory Control Rate (RCR) and ADP/O; C) uncoupled respiration. Data are means of at least three different experiments \pm SD. * $P < 0.05$ vs. Control and ** $P < 0.05$ vs. IR.

3.4. Enzymatic activities of the respiratory chain complexes from reperfused hearts treated with N-acetylcysteine and postconditioning

The activity of CI diminished 59% in IR mitochondria when compared with that of Control mitochondria. IR+NAC and IR+PostC groups recovered CI activity, but the difference was significant only in the last one (Fig. 5A). The activities of CII (Fig. 5B) and CIII (Fig. 5C) were also affected by IR, although the counteracting effect of NAC was more evident in CII, than in CIII activity. Conversely, PostC increased CIII activity to higher values than NAC and even than in Control (Fig. 5C). Despite the lack of significant differences, IR mitochondria showed a slight decrease in CIV activity in comparison with mitochondria from the other groups (Fig. 5D). CV activity was fully recovered in both IR+NAC and in IR+PostC mitochondria as compared with IR mitochondria (Fig. 5E).

3.5. Detection of respiratory complex activities in blue native gels

The relative contribution of the monomeric and SCs forms on the total activity of the respiratory chain complexes and the effect of ROS-reducing treatments in mitochondria from IR hearts were evaluated in BN gels. SCs assemblies in which the activities of the three complexes were detected and the additional bands that contained higher mass

complexes than its corresponding monomers were included in the SCs analysis (Fig. 6). To identify putative productive SCs, we performed a careful alignment of the activity gels and label the group of bands in which Complex I, Complex III and Complex IV comigrate. As Complex III assay might render unspecific staining, we correlate the activity bands with the spots obtained after immunodetection with Anti-Complex III subunit UQCRC1 in a two-dimension SDS gel. To further corroborate the identity of the respiratory complexes and its associations in our preparations, a comparison was made with the electrophoretic pattern of bovine heart mitochondria (Supplementary material).

Complex I in situ activity associated to the monomeric form diminished in IR mitochondria and was maintained in the IR+PostC group ($P < 0.05$); this treatment also maintained the activity of CI in SCs at the levels observed in Control mitochondria ($P < 0.05$; Fig. 6A and D). CIII₂ activity diminished in IR mitochondria and was fully recovered in both IR+NAC and IR+PostC groups ($P < 0.05$); whereas the activity associated to SCs increased only in mitochondria from PostC hearts as compared with IR mitochondria ($P < 0.05$; Fig. 6B and D). CIV activity decreased in the monomer and in SCs from IR mitochondria as compared with the other groups. The activity associated to the monomer and to SCs increased significantly only in mitochondria from PostC hearts ($P < 0.05$; Fig. 6C and D).

Although Complex II and Complex V did not contribute to SCs

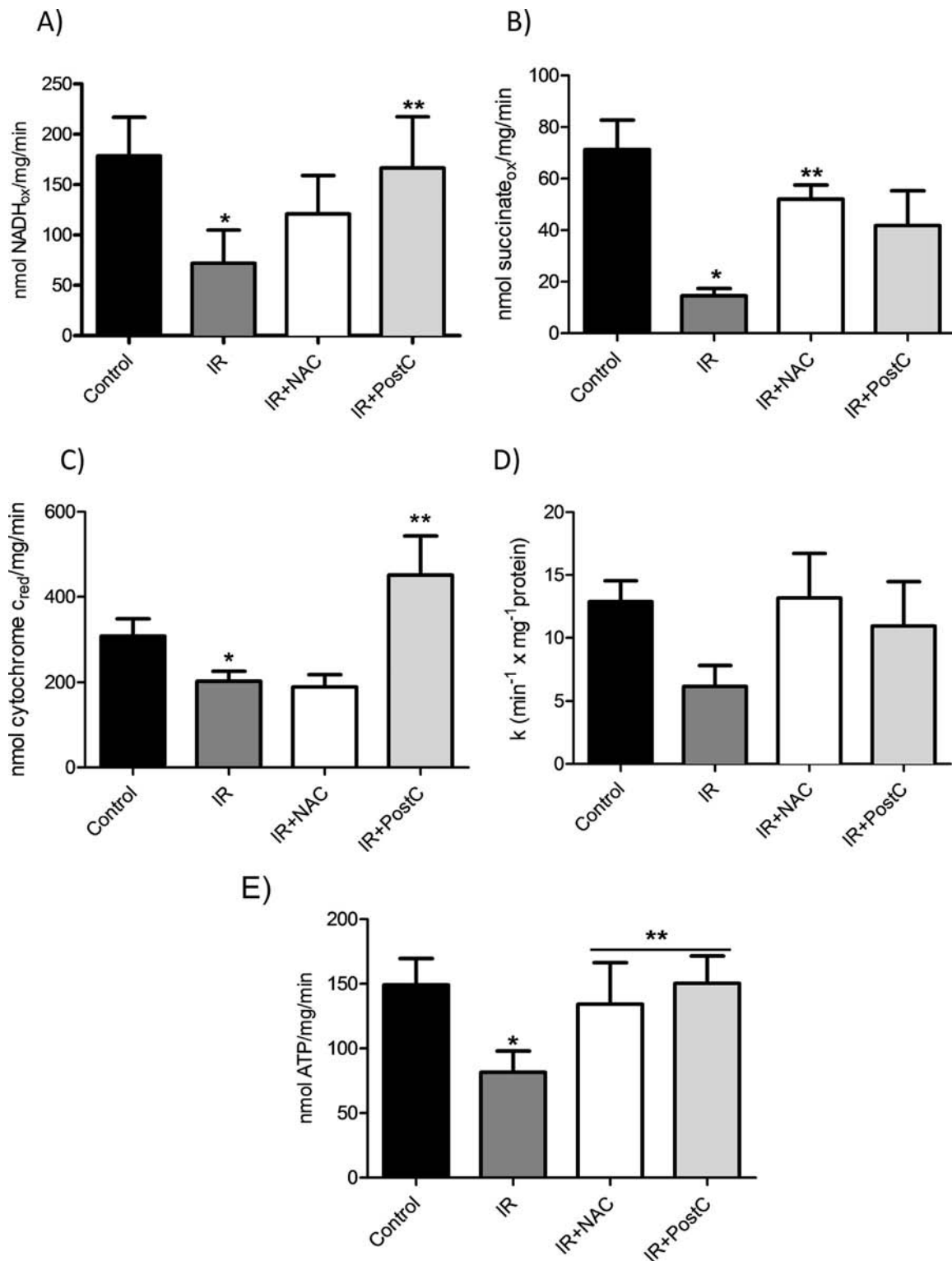


Fig. 5. Spectrophotometric analysis of the respiratory complexes activities in isolated mitochondria. A) Activity of Complex I; B) Complex II; C) Complex III; D) Complex IV and E) Complex V. Values are the means \pm SD of at least four different experiments. * $P < 0.05$ vs. Control and ** $P < 0.05$ vs. IR.

assemblies, their activities were also evaluated. No changes in Complex II activity were detected in any of the experimental groups (Fig. 7A), neither in the activity of the dimeric and monomeric forms of Complex V (Fig. 7B).

3.6. Relative content of respiratory complexes in supercomplex assemblies in reperfused hearts treated with N-acetylcysteine and subjected to postconditioning

We also examined whether IR and ROS-reducing treatments affect respiratory complexes content in SCs by performing (1D-BN) PAGE and subsequent immunoblotting. A I+III₂+IV_n complex was identified in

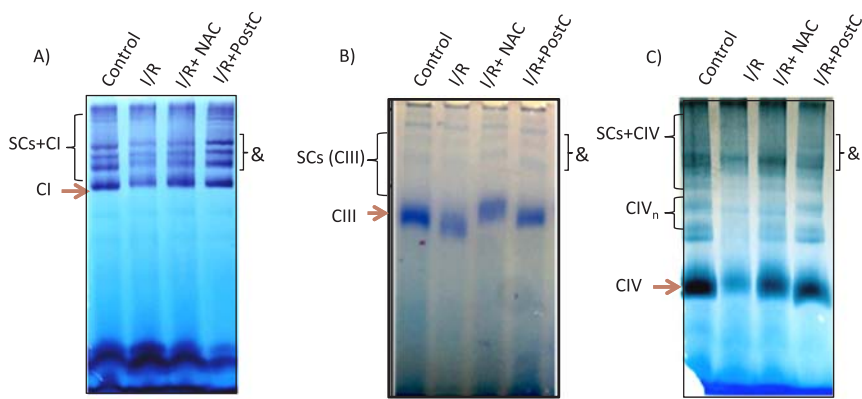


Fig. 6. In gel activities of the respiratory chain complexes (I, III and IV) in BN-gels. Representative images of at least three different experiments of the in-gel activities of respiratory complexes in blue native gels. Gels were prepared and loaded with solubilized mitochondria. Parallel running was performed to optimize the comparison between the activities and location of the different respiratory complexes and SCs. The symbol (&) groups the bands in which activities for Complex I, III and IV were observed. The bands labeled as CIV_n represent possible oligomeric forms of cytochrome c oxidase. A) Complex I activity; B) Complex III activity; C) Complex IV activity and D) densitometric analysis of the activity associated to monomeric (Complex) and SCs forms. Values are the means ± SD of at least three different experiments. *P < 0.05 vs. Control and **P < 0.05 vs. IR.

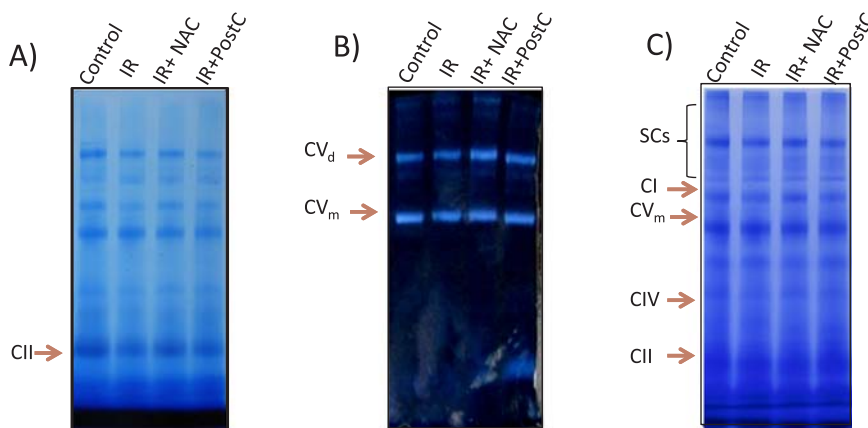
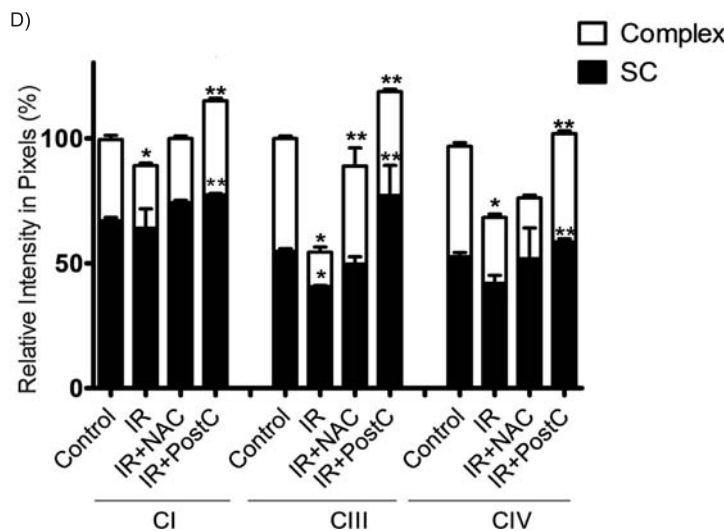


Fig. 7. In gel activities of the respiratory chain complexes (II and V) in BN-gels and Coomassie blue staining. Representative images of at least three different experiments of the in-gel activities of respiratory complexes in blue native gels. Gels were prepared, loaded with solubilized mitochondria and run in parallel to optimize the comparison between the activities and location of the different respiratory complexes and SCs. A) Complex II; B) Complex V (CV_d = CV dimer; CV_m = CV monomer); C) Coomassie blue staining.

mitochondria from the Control group, which also contained the adapter protein SCAFI (Supercomplex assembly factor I). The relative content of the subunits NDUFS4 (Complex I), UQCRF51 (Complex III), COX IV (Complex IV) and COX7A2L (SCAFI) clearly diminished in mitochondria from the IR group and were preserved differentially in the IR + NAC and in the IR + PostC groups (Fig. 8).

4. Discussion

In this work we show that oxidative stress contention promotes heart performance, decreases infarct size, preserves mitochondrial function and maintains the assembly/activities of both SCs and the

individual complexes of the respiratory chain.

These results reinforce the well known paradigm that mitochondria are both producers and ROS targets and incorporate SCs stability as a main factor in mitochondrial function.

The association between SCs' assembly and lower ROS generation has been observed in different conditions. Fibroblasts exposed to respiratory chain complex inhibitors increased ROS in correlation with SCs levels diminution [28], the knockdown of Complex I subunit NDUFS1 decreases the integration of complex I into SCs and augments ROS levels in neurons [29]; whereas age-related changes in SCs architecture modify ROS production [30]. Such association might be the consequence of a more efficient electron transfer in SCs than in

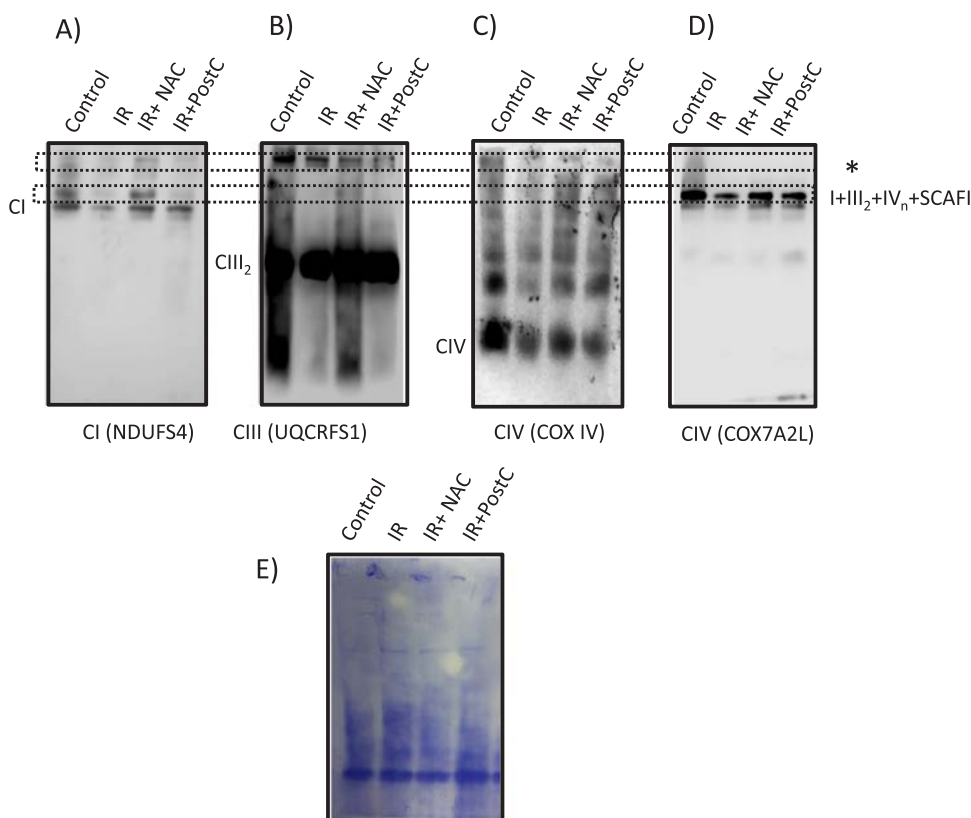


Fig. 8. Immunodetection of SCs assemblies in mitochondria from reperfused hearts treated with NAC and subjected to PostC. Representative western blot images of at least three different protein experiments in which mitochondrial proteins were separated in 1D blue native gels. The same membrane was stripped and confronted to all the antibodies. A) Complex I was detected with anti-NADH dehydrogenase subunit NDUFS4; B) Complex III with anti-Ubiquinol cytochrome C reductase core protein UQCRCF1; C) Complex IV with anti-cytochrome c Oxidase subunit IV; D) SCAFI with anti-COX7A2L supercomplex III-IV subunit; E) Coomassie blue staining of the PVDF membrane used in this set of experiments used as control load. * SCs in which SCAFI was not detected.

individual complexes [31], as the distances between binding sites of coenzyme Q at complexes I-III and of cytochrome c at complexes III-IV in these supramolecular arrangements are shorter [32] than the diffusion lengths calculated by random collision mechanisms for individual complexes [33].

The site of ROS production is still a non-resolved issue. It is generally accepted that during succinate oxidation, ROS are produced to some extent by complex III [34] but mainly through reverse electron transport (RET) to complex I [35]. Indeed, Chouchani et al. [36] reported that succinate is accumulated during ischemia and that is metabolized in parallel with ROS production from Complex I by RET during early reperfusion in vivo. Although it was tempting to speculate that the observed diminution in succinate dehydrogenase activity (Fig. 5B) could drive succinate accumulation, our results show that H_2O_2 production was not sensitive to rotenone, therefore RET is not the main mechanism of ROS production in our experimental setting. In this sense, it was reported that the damage to complex I during ischemia/reperfusion might induce the loss of protein-protein interaction between this complex and complex III, enhancing ROS production by complex III [37]. This scenario might explain our observation of complex III diminution in SCs in association with increased ROS production.

Our finding that individual Complex I and Complex III activities and those associated to SCs assemblies are higher in mitochondria from the PostC group than in the NAC group, might reflect the activation of protective mechanisms independent of those related with oxidative stress contention. PostC modulates the activity of several protein kinases associated with cardioprotection [38]. Results from our group and others show that activation of extracellular signal-regulated kinases 1/2 (ERK1/2) correlates with increased levels of phosphorylated proteins in mitochondria from PostC hearts [39], and that this maneuver increases cGMP levels preventing the opening of the mitochondrial permeability transition pore (mPTP) during the early stage of reperfusion [40]. Phosphate groups attached to residues of subunits IVa and IVb from Complex IV has been detected in mitochondria isolated from pre-conditioned hearts, suggesting a possible role of phosphorylation in

the stability of these proteins [16], that might be extended to SCs.

In this work not only the activity, but the immunoreactivity of some of complexes in both its individual and SCs forms was compromised during IR. Loss of integrity of particular complex subunits after oxidative injury might account for these results, as it has been reported that ischemia diminishes the amount of detectable NDUFA9 subunit from Complex I in both native and denaturing conditions in association with cardiolipin oxidation [41].

We found that COX7A2L was mainly present in I+III₂+IV_n and in much lower extent in free complex IV. This protein was detected in superstructures composed of III₂+IV and I+III₂+IV_n, but not in free complexes III and IV [42]; whereas more recently, Perez-Perez et al. [43] reported that COX7A2L is not exclusively associated with SCs, but it also co-migrates with CIII₂, free complex IV and with different SCs containing complex III. This authors propose that although COX7A2L stabilizes SCs III₂+IV, has not role on respirasome formation. Further controversy on the possible relevance of COX7A2L was added by Boekema et al. [44], which sustain that point mutations within genes encoding subunits of one oxidative phosphorylation complex affect the stability of other complexes.

The idea that dissociation of SCs has pathophysiological implications was first suggested by Lenaz and Genova [45]. Their speculation that ROS reduce electron channeling, lowers electron transfer and/or proton translocation, eliciting further ROS production, fits with the vicious circle of oxidative stress and energetic decline observed in reperfusion damage. However, changes in SCs' assembly has rendered polemic results in the framework of cardiovascular diseases. While Wong et al. [16] reported that SCs levels were similar in mitochondria isolated from IR and from preconditioned hearts; the cardioprotective effect of isoflurane was related, at least in part with maintenance of Complex III and Complex IV activities in SCs [17]. On the other hand, SCs disassembly was observed after long-time (60 min) reperfusion and prevented by inhibiting the permeability transition pore [46], whereas lower levels of supercomplex I+III₂+IV₁ were detected without changes in the individual activities of the respiratory chain complexes

in a canine heart failure model [47]. Here, we find that oxidative stress diminution preserves mitochondrial function and that cardioprotection is related with maintenance of the activity and content of Complex I, Complex III and Complex IV in supramolecular assemblies.

5. Conclusion

We conclude that both the monomeric forms and the SCs of the respiratory chain contribute to the in vivo functionality of the mitochondria. However, although the ROS-induced damage and the consequent production of ROS affect the assembly of SCs, other levels of regulation as those induced by PostC, might participate in maintaining the activity of the mitochondrial respiratory complexes in such superstructures.

Acknowledgments

Jazmín Ixchel Ramírez Camacho is a doctoral student from Programa de Doctorado en Ciencias Biomédicas, Universidad Nacional Autónoma de México (UNAM) and received fellowship 581606 from Consejo Nacional de Ciencia y Tecnología (CONACYT). This work was partially supported by Grant 283363 to CZ from CONACYT, Mexico and Instituto Nacional de Cardiología, I. Ch. and PAPIIT IN222617 to OFH from the Universidad Nacional Autónoma de México.

Appendix A. Supplementary material

Supplementary data associated with this article can be found in the online version at [doi:10.1016/j.freeradbiomed.2018.09.047](https://doi.org/10.1016/j.freeradbiomed.2018.09.047).

References

- C.R. Hackenbrock, B. Chazotte, S.S. Gupte, The random collision model and a critical assessment of diffusion and collision in mitochondrial electron transport, *J. Bioenerg. Biomembr.* 18 (1986) 331–368, <https://doi.org/10.1007/BF00743010>.
- H. Schägger, K. Pfeiffer, Supercomplexes in the respiratory chains of yeast and mammalian mitochondria, *EMBO J.* 19 (2000) 1777–1783, <https://doi.org/10.1093/emboj/19.8.1777>.
- R. Acín-Pérez, J.A. Enríquez, The function of the respiratory supercomplexes: the plasticity model, *Biochim. Biophys. Acta* 1837 (2014) 444–450, <https://doi.org/10.1016/j.bbabi.2013.12.009>.
- L. Robles-Martínez, M.G. Guerra-Sánchez, O. Flores-Herrera, A.N. Hernández-Lauzardo, M.G. Velázquez-Del Valle, J.P. Pardo, The mitochondrial respiratory chain of *Rizopus stolonifer* (Ehrenb.:fr.) Vuill, *Arch. Microbiol.* 195 (2013) 51–61, <https://doi.org/10.1007/s00203-012-0845-7>.
- H. Schägger, K. Pfeiffer, The ratio of oxidative phosphorylation complexes I-V in bovine heart mitochondria and the composition of respiratory chain supercomplexes, *J. Biol. Chem.* 276 (2001) 37861–37867, <https://doi.org/10.1074/jbc.M106474200>.
- G. Lenaz, G. Tioli, A.I. Falasca, M.L. Genova, Complex I function in mitochondrial supercomplexes, *Biochim. Biophys. Acta* 2016 (1857) 991–1000, <https://doi.org/10.1016/j.bbabi.2016.01.013>.
- R. Acín-Pérez, P. Fernández, M.L. Peleato, A. Pérez-Martos, J.A. Enríquez, Respiratory active mitochondrial supercomplexes, *Mol. Cell. Biol.* 32 (2008) 529–539, <https://doi.org/10.1016/j.molcel.2008.10.021>.
- J.R. Treberg, C.L. Quinlan, M.D. Brand, Evidence for two sites of superoxide production by mitochondrial NADH-ubiquinone oxidoreductase (complex I), *J. Biol. Chem.* 286 (2011) 27103–27110, <https://doi.org/10.1074/jbc.M111.252502>.
- M.P. Murphy, How mitochondria produce reactive oxygen species, *Biochem. J.* 417 (2009) 1–13, <https://doi.org/10.1042/BJ20081386>.
- G. Lenaz, A. Baracca, G. Barbero, C. Bergamini, M.E. Dalmonte, M. Del Sole, M. Faccioli, A. Falasca, R. Fato, M.L. Genova, G. Sgarbi, G. Solaini, Mitochondrial respiratory chain super-complex I-III in physiology and pathology, *Biochim. Biophys. Acta* 1797 (2010) 633–640, <https://doi.org/10.1016/j.bbabi.2010.01.025>.
- E. Maranzana, G. Barbero, A.I. Falasca, G. Lenaz, M.L. Genova, Mitochondrial respiratory supercomplex association limits production of reactive oxygen species from complex I, *Antioxid. Redox Signal.* 19 (2013) 1469–1480, <https://doi.org/10.1089/ars.2012.4845>.
- M. Vukotic, S. Oeljeklaus, S. Wiese, F.N. Vögtle, C. Meisinger, H.E. Meyer, A.D.M. Katschinski, D.C. Jans, S. Jakobs, B. Warscheid, P. Rehling, M. Deckers, Rcf1 mediates cytochrome oxidase assembly and respirasome formation, revealing heterogeneity of the enzyme complex, *Cell Metab.* 15 (2012) 336–347, <https://doi.org/10.1016/j.cmet.2012.01.016>.
- R. Ferrari, C. Ceconi, S. Curello, A. Cargnoni, E. Pasini, F. De Giulii, A. Albertini, Role of oxygen free radicals in ischemic and reperfused myocardium, *Am. J. Clin. Nutr.* 53 (1991) 215S–222S.
- F. Arreguín, N. García, S. Hernández-Reséndiz, M. Buelna-Chontal, F. Correa, V. Olín-Sandoval, O.N. Medina-Campos, J. Pedraza-Chaverri, C. Zazueta, Attenuation of oxidant damage in the postconditioned heart involves non-enzymatic response and partial catalytic protection, *Exp. Physiol.* 97 (2012) 1119–1130, <https://doi.org/10.1113/expphysiol.2012.065763>.
- G. Paradies, G. Petrosillo, M. Pistolesse, N. Di Venosa, A. Federici, F.M. Ruggiero, Decrease in mitochondrial complex I activity in ischemic/reperfused rat heart: involvement of reactive oxygen species and cardiolipin, *Circ. Res.* 94 (2004) 53–59, <https://doi.org/10.1161/01.RES.0000109416.566608.64>.
- R. Wong, A.M. Aponte, C. Steenberg, E. Murphy, Cardioprotection leads to novel changes in the mitochondrial proteome, *Am. J. Physiol. Heart Circ. Physiol.* 298 (2010) H75–H91, <https://doi.org/10.1152/ajpheart.00515.2009>.
- C. Lotz, J. Zhang, C. Fang, D. Liem, P. Ping, Isoflurane protects the myocardium against ischemic injury via the preservation of mitochondrial respiration and its supramolecular organization, *Anesth. Analg.* 120 (2015) 265–274, <https://doi.org/10.1213/ANE.0000000000000494>.
- F. Correa, M. Buelna-Chontal, V. Chagoya, G. García-Rivas, R.M. Viguera, J. Pedraza-Chaverri, W.R. García-Niño, R. Hernández-Pando, J.C. León-Contreras, C. Zazueta, Inhibition of the nitric oxide/cyclic guanosine monophosphate pathway limited the cardioprotective effect of post-conditioning in hearts with apical myocardial infarction, *Eur. J. Pharmacol.* 765 (2015) 472–481, <https://doi.org/10.1016/j.ejphar.2015.09.018>.
- E. Parra, D. Cruz, G. García, C. Zazueta, F. Correa, N. García, E. Chávez, Myocardial protective effect of octylguanidine against the damage induced by ischemia reperfusion in rat heart, *Mol. Cell. Biochem.* 269 (2005) 19–26, <https://doi.org/10.1007/s11010-005-2989-0>.
- A. Ruiz-Ramírez, M. Chávez-Salgado, J.A. Peñeda-Flores, E. Zapata, F. Masso, M. El-Hafidi, High-sucrose diet increases ROS generation, FFA accumulation, UCP2 level, and proton leak in liver mitochondria, *Am. J. Physiol. Endocrinol. Metab.* 301 (2011) E1198–E1207, <https://doi.org/10.1152/ajpendo.00631.2010>.
- C.E. Guerrero-Beltrán, M. Calderón-Oliver, E. Tapia, O.N. Medina-Campos, D.J. Sánchez-González, C.M. Martínez-Martínez, K.M. Ortiz-Vega, M. Franco, J. Pedraza-Chaverri, Sulforaphane protects against cisplatin-induced nephrotoxicity, *Toxicol. Lett.* 192 (2010) 278–285, <https://doi.org/10.1016/j.toxlet.2009.11.007>.
- S. Galván-Arzate, J. Pedraza-Chaverri, O.N. Medina-Campos, P.D. Maldonado, B. Vázquez-Román, C. Ríos, A. Santamaría, Delayed effects of thallium in the rat brain: regional changes in lipid peroxidation and behavioral markers, but moderate alterations in antioxidants, after a single administration, *Food Chem. Toxicol.* 43 (2005) 1037–1045, <https://doi.org/10.1016/j.fct.2005.02.006>.
- P.J. Hissin, R. Hilf, A fluorometric method for determination of oxidized and reduced glutathione in tissues, *Anal. Biochem.* 74 (1976) 214–226, [https://doi.org/10.1016/0160-5402\(84\)90059-7](https://doi.org/10.1016/0160-5402(84)90059-7).
- E. Schäfer, H. Seelert, N.H. Reifschneider, F. Krause, N.A. Dencher, J. Vonck, Architecture of active mammalian respiratory chain supercomplexes, *J. Biol. Chem.* 281 (2006) 15370–15375, <https://doi.org/10.1074/jbc.M513525200>.
- C. Jung, C.M. Higgins, Z. Xu, Measuring the quantity and activity of mitochondrial electron transport chain complexes in tissues of central nervous system using blue native polyacrylamide gel electrophoresis, *Anal. Biochem.* 286 (2000) 214–223, <https://doi.org/10.1006/abio.2000.4813>.
- M. Spinazzi, A. Casarin, V. Pertegato, L. Salviati, C. Angelini, Assessment of mitochondrial respiratory chain enzymatic activities on tissues and cultured cells, *Nat. Protoc.* 7 (2012) 1235–1246, <https://doi.org/10.1038/nprot.2012.058>.
- A. Barrientos, In vivo and in organelle assessment of oxphos activities, *Methods* 26 (2002) 307–316, [https://doi.org/10.1016/S1046-2023\(02\)00036-1](https://doi.org/10.1016/S1046-2023(02)00036-1).
- F. Diaz, J.A. Enríquez, C.T. Morales, Cells lacking Rieske iron-sulfur protein have a reactive oxygen species-associated decrease in respiratory complexes I and IV, *Mol. Cell. Biol.* 32 (2012) 415–429, <https://doi.org/10.1128/MCB.06051-11>.
- I. López-Fabuel, J. Le Douce, A. Logan, A.M. James, G. Bonvento, M.P. Murphy, A. Almeida, J.P. Bolaños, Complex I assembly into supercomplexes determines differential mitochondrial ROS production in neurons and astrocytes, *Proc. Natl. Acad. Sci. USA* 113 (2016) 13063–13068, <https://doi.org/10.1073/pnas.1613701113>.
- N.A. Dencher, M. Frenzel, N.H. Reifschneider, M. Sugawa, F. Krause, Proteome alterations in rat mitochondria caused by aging, *Ann. N. Y. Acad. Sci.* 1100 (2007) 291–298, <https://doi.org/10.1196/annals.1395.030>.
- A. Panov, S. Dikalov, N. Shalbuyeva, R. Hemendinger, J.T. Greenamyre, J. Rosenfeld, Species- and tissue-specific relationships between mitochondrial permeability transition and generation of ROS in brain and liver mitochondria of rats and mice, *Am. J. Physiol. Cell Physiol.* 292 (2007) C708–C718, <https://doi.org/10.1152/ajpcell.00202.2006>.
- T. Althoff, D.J. Mills, J.L. Popot, W. Kühlbrandt, Arrangement of electron transport chain components in bovine mitochondrial supercomplex I1III2IV1, *EMBO J.* 30 (2011) 4652–4664, <https://doi.org/10.1038/emboj.2011.324>.
- B. Chazotte, C.R. Hackenbrock, The multicollisional, obstructed, long-range diffusional nature of mitochondrial electron transport, *J. Biol. Chem.* 263 (1988) 14359–14367, <https://doi.org/10.1038/nature19794>.
- Q. Chen, Q. E.J. Vazquez, S. Moghaddas, C.L. Hoppel, E.J. Lesnfsky, Production of reactive oxygen species by mitochondria: central role of complex III, *J. Biol. Chem.* 278 (2003) 36027–36031.
- L.K. Kwong, R.S. Sohal, Substrate and site specificity of hydrogen peroxide generation in mouse mitochondria, *Arch. Biochem. Biophys.* 350 (1998) 118–126.
- E.T. Chouchani, V.R. Pell, E. Gaude, D. Aksejntijević, S.Y. Sundier, E.L. Robb, A. Logan, S.M. Nadtochiy, E.N.J. Ord, A.C. Smith, F. Eyassu, R. Shirley, C.H. Hu, A.J. Dare, A.M. James, S. Rogatti, R.C. Hartley, S. Eaton, A.S.H. Costa, P.D. Brookes,

- S.M. Davidson, M.R. Duchon, K. Saeb-Parsy, M.J. Shattock, A.J. Robinson, L.M. Work, C. Frezza, T. Krieg, M.P. Murphy, Ischaemic accumulation of succinate controls reperfusion injury through mitochondrial ROS, *Nature* 515 (2014) 431–435, <https://doi.org/10.1038/nature13909>.
- [37] H.L. Lee, C.L. Chen, S.T. Yeh, J.L. Zweier, Y.R. Chen, Biphasic modulation of the mitochondrial electron transport chain in myocardial ischemia and reperfusion, *Am. J. Physiol. Heart Circ. Physiol.* 302 (2012) H1410–H1422, <https://doi.org/10.1152/ajpheart.00731.2011>.
- [38] M. Ovize, G.F. Baxter, F. Di Lisa, P. Ferdinandy, D. Garcia-Dorado, D.J. Hausenloy, G. Heusch, J. Vinten-Johansen, D.M. Yellon, R. Schulz, working Group of cellular biology of heart of European Society of Cardiology. postconditioning and protection from reperfusion injury: where do we stand? Position paper from the working group of cellular biology of the heart of the European Society of Cardiology, *Cardiovasc. Res.* 87 (2010) 406–423, <https://doi.org/10.1093/cvr/cvq129>.
- [39] S. Hernández-Reséndiz, C. Zazueta, PHO-ERK1/2 interaction with mitochondria regulates the permeability transition pore in cardioprotective signaling, *Life Sci.* 108 (2014) 13–21, <https://doi.org/10.1016/j.lfs.2014.04.037>.
- [40] M. Fujita, H. Asanuma, A. Hirata, M. Wakeno, H. Takahama, H. Sasaki, J. Kim, S. Takashima, O. Tsukamoto, T. Minamino, Y. Shinozaki, H. Tomoike, M. Hori, M. Kitakaze, Prolonged transient acidosis during early reperfusion contributes to the cardioprotective effects of postconditioning, *Am. J. Physiol.* 29 (2007) H2004–H2008, <https://doi.org/10.1152/ajpheart.01051.2006>.
- [41] A.K. Gardichela, D.F. Stowe, W.E. Antholine, M. Yang, A.K. Camara, Damage to mitochondrial complex I during cardiac ischemia reperfusion injury is reduced indirectly by anti-anginal drug ranolazine, *Biochim. Biophys. Acta* 2012 (1817) 419–429, <https://doi.org/10.1016/j.bbabi.2011.11.021>.
- [42] E. Lapuente-Brun, R. Moreno-Loshuetos, R. Acín-Pérez, A. Latorre-Pellicer, C. Colás, E. Balsa, E. Perales-Clemente, P.M. Quirós, E. Calvo, M.A. Rodríguez-Hernández, P. Navas, R. Cruz, A. Carracedo, C. López-Otín, A. Pérez-Martos, P. Fernández-Silva, E. Fernández-Vizarrá, J.A. Enríquez, Supercomplex assembly determines electron flux in the mitochondrial electron transport chain, *Science* 340 (2013) 1567–1570, <https://doi.org/10.1126/science.1230381>.
- [43] R. Perez-Perez, T. Lobo-Jarne, D. Milenkovic, A. Mourier, A. Bratic, A. Garcia-Bartolome, E. Fernández-Vizarrá, S. Cadenas, A. Delmiro, I. García-Consuegra, J. Arenas, M.A. Martín, N.G. Larsson, C. Ugalde, COX7A2L is a mitochondrial complex III binding protein that stabilizes the III2 + IV supercomplex without affecting respirasome formation, *Cell Rep.* 16 (2016) 2387–2398, <https://doi.org/10.1016/j.celrep.2016.07.081>.
- [44] E.J. Boekema, H.P. Braun, Supramolecular structure of the mitochondrial oxidative phosphorylation system, *J. Biol. Chem.* 282 (2007) 1–4, <https://doi.org/10.1074/jbc.R600031200>.
- [45] G. Lenaz, M.L. Genova, Kinetics of integrated electron transfer in the mitochondrial respiratory chain: random collisions vs. solid state electron channeling, *Am. J. Physiol. Cell Physiol.* 292 (2007) C1221–C1239, <https://doi.org/10.1152/ajpcell.00263.2006>.
- [46] S. Jang, T.S. Lewis, C. Powers, Z. Khuchua, C.P. Baines, P. Wipf, S. Javadov, Elucidating mitochondrial electron transport chain supercomplexes in the heart During ischemia-reperfusion, *Antioxid. Redox Signal.* 27 (2017) 57–69, <https://doi.org/10.1089/ars.2016.6635>.
- [47] M.G. Rosca, E.J. Vazquez, J. Kerner, W. Parland, M.P. Chandler, W. Stanley, H.N. Sabbah, C.L. Hoppel, Cardiac mitochondria in heart failure: decrease in respirasomes and oxidative phosphorylation, *Cardiovasc. Res.* 80 (2008) 30–39, <https://doi.org/10.1093/cvr/cvn184>.



Mitochondrial respirasome works as a single unit and the cross-talk between complexes I, III₂ and IV stimulates NADH dehydrogenase activity



Reyes-Galindo Meztli¹, Suarez Roselia¹, Esparza-Perusquía Mercedes, de Lira-Sánchez Jaime, Pardo J. Pablo, Martínez Federico, Flores-Herrera Oscar*

Departamento de Bioquímica, Facultad de Medicina, Universidad Nacional Autónoma de México, 04510 México City, México

ARTICLE INFO

Keywords:

Respirasome
Mitochondrial supercomplexes
Complex I activity
Ustilago maydis mitochondria
ROS production

ABSTRACT

Ustilago maydis is an aerobic basidiomycete that depends on oxidative phosphorylation for its ATP supply, pointing to the mitochondrion as a key player in its energy metabolism. Mitochondrial respiratory complexes I, III₂, and IV occur in supramolecular structures named respirasome. In this work, we characterized the subunit composition and the kinetics of NADH:Q oxidoreductase activity of the digitonine-solubilized respirasome (1600 kDa) and the free-complex I (990 kDa). In the presence of 2,6-dimethoxy-1,4-benzoquinone (DBQ) and cytochrome c, both the respirasome NADH:O₂ and the NADH:DBQ oxidoreductase activities were inhibited by rotenone, antimycin A or cyanide. A value of 2.4 for the NADH oxidized/oxygen reduced ratio was determined for the respirasome activity, while ROS production was less than 0.001% of the oxygen consumption rate. Analysis of the NADH:DBQ oxidoreductase activity showed that respirasome was 3-times more active and showed higher affinity than free-complex I. The results suggest that the contacts between complexes I, III₂ and IV in the respirasome increase the catalytic efficiency of complex I and regulate its activity to prevent ROS production.

1. Introduction

The proton electrochemical potential, $\Delta\mu_{H^+}$, across energy transducing membranes is the basis of the chemiosmotic hypothesis for energy coupling [1–3]. In mitochondria this electrochemical potential is used for heat production, ion and substrate transport, ATP/ADP exchange, and especially ATP synthesis [4]. The proton translocation across inner mitochondrial membrane occurs through three protein complexes termed NADH:coenzyme Q oxidoreductase (complex I), coenzyme Q:cytochrome c oxidoreductase (complex III₂, which is a functional dimer), and cytochrome c oxidase (complex IV); additionally, the succinate:coenzyme Q oxidoreductase (complex II), that belongs to the electron transport chain, doesn't translocate protons but produce ubiquinol which is a mobile lipid electron carrier [4].

Three models have been proposed to explain the organization of the electron transport chain complexes: 1) “Random collision model”, proposed by Hackenbrock et al. [5] in which individual respiratory complexes in the inner membrane diffuse freely, and electron transfer is based on random collisions between complexes and two small electron carriers, coenzyme Q and cytochrome c; 2) “Solid state model”, in

which complexes are attached in supra-structures called super-complexes [6], which have been founded in mitochondria from mammals, plants, fungi, and bacteria; and 3) “Plasticity model”, which involves both previous models [7].

Supercomplexes have a wide distribution in the natural kingdoms, from bacteria to plants and animals. In *Paracoccus denitrificans* the supercomplexes III₂:IV₁ [8] and I₁:III₂:IV₁ have been reported [9]; while in *Saccharomyces cerevisiae* complex III₂ could be attached to one (III₂:IV₁) or two (III₂:IV₂) monomers of complex IV [10,11]. In *Neurospora crassa* supercomplexes are composed of complexes I, III₂, and IV in different proportions [12]. Supercomplex I₁:III₂ is the most abundant in potato (*Solanum tuberosum*), bean (*Phaseolus vulgaris*), barley (*Hordeum vulgare*), and *Arabidopsis thaliana* [13–15]. Bovine heart mitochondrial supercomplexes described are I₁:III₂:IV₁, I₁III₂, and III₂IV₁ [16]. If complexes I, III₂ and IV are present in the supercomplex and NADH oxidation and oxygen reduction occur, they are called respirasome [10].

Actually, the architecture of respirasomes from porcine (*Sus scrofa*) heart mitochondria [17] and ovine (*Ovis aries*) heart mitochondria [18] has been determined by cryo-electron microscopy with a resolution of

* Corresponding author at: Departamento de Bioquímica, Facultad de Medicina, Universidad Nacional Autónoma de México, Apdo. Postal 70-159, Coyoacán, 04510 México, Cd. Mx., México.

E-mail address: oflores@bq.unam.mx (O. Flores-Herrera).

¹ M. Reyes-Galindo and R. Suarez contributed equally to this paper.

<https://doi.org/10.1016/j.bbabio.2019.06.017>

Received 1 November 2018; Received in revised form 20 June 2019; Accepted 22 June 2019

Available online 25 June 2019

0005-2728/ © 2019 Elsevier B.V. All rights reserved.

5.4 Å and 5.8 Å, respectively.

Initially, respirasomes were associated with electron channeling from NADH to oxygen and the enhancement of electron flow between complexes [5,19]; however this hypothesis has been challenged by new structural and functional evidence [17,18,20]. Currently, the accepted role is related to structural stabilization of complex I [6,21], and prevention of oxygen radicals production [7,21–28]. However, the precise role of supercomplexes remains to be defined.

In this work, digitonin-solubilized respirasomes from *Ustilago maydis* mitochondria were isolated and their subunit composition and activity were characterized. *U. maydis* is an aerobic basidiomycete which infects the corn and teocinte plants in a biotrophic way [29]. In the laboratory the non-pathogenic yeast form of *U. maydis* is easily maintained in standard growth conditions [30]. *U. maydis* contains the four classic mitochondrial respiratory complexes and depends on the oxidative phosphorylation for the supply of ATP [31]. Supercomplexes isolated from *U. maydis* contained complexes I, III₂ and IV, as well as coenzyme Q and cytochrome *c*. NADH oxidation supported oxygen uptake and was sensitive to KCN, antimycin A or rotenone. Additionally, complex I activity from respirasome was inhibited by antimycin A or KCN, even upon the addition of coenzyme Q and cytochrome *c*, suggesting a tight functional interaction between complexes. Kinetic characterization of NADH:Q oxidoreductase activity showed that respirasome was 3-times more active than free-complex I, suggesting a stimulatory effect of the contacts between complexes in the respirasome.

2. Materials and methods

2.1. Cell culture and mitochondria isolation

U. maydis cells (strain FB2) were prepared as previously described [31]. *U. maydis* mitochondria were isolated using the method described by Waterfield and Sisler [32]. For details see Supplemental material.

2.2. Solubilization of respiratory supercomplexes

The respiratory supercomplexes and complexes were solubilized from *U. maydis* mitochondria using digitonin (a very-mild detergent) as described by [33–35], with minor modifications [36]. Briefly, *U. maydis* mitochondria (10 mg/ml) were suspended in 3.5 ml of 50 mM Bis-Tris and 500 mM 6-aminocaproic acid, pH 7.0 and 140 μl digitonin (50% stock) were added to reach a detergent/protein ratio of 2:1. Digitonin was added drop by drop while the mixture was gently stirred in an ice bath and then incubated in this condition during 30 min. The mixture was centrifuged at 100,000g for 30 min at 4 °C and supernatant containing the supercomplexes and individual complexes was recovered and immediately loaded into a sucrose gradient (16–42%) for supercomplexes isolation (*vide infra*).

2.3. Respirasome isolation

Mitochondrial digitonin extract (16 mg protein) was loaded on 24 ml of a continuous sucrose gradient (16–42% sucrose, 15 mM Tris, pH 7.4, 20 mM KCl and 0.2% digitonin) and centrifuged at 131,000g for 16 h at 4 °C [36]. Afterward, 500 μl fractions were collected from the bottom of the gradient. Fractions containing respirasomes were identified by BN-PAGE (*vide infra*). These respirasomes samples were pooled and diluted 7-fold with 30 mM HEPES, pH 8.0 and 5% glycerol; then were concentrated using a Centrifugal Filters Units (100K, Millipore Amicon Utra) to a final volume of 100 μl, and stored at –70 °C until used.

2.4. Blue Native-PAGE and in-gel catalytic activity assays

Samples from the sucrose gradient and the later supercomplexes

fraction were loaded on a linear polyacrylamide gradient gel (4–10%) for Blue Native PAGE (BN-PAGE) [35]. The BN-PAGE buffers were 50 mM Bis-Tris/HCl, pH 7.0 for the anode electrode, and 50 mM tricine, 15 mM Bis-Tris, pH 7.0 and the anionic Coomassie© Brilliant Blue R-125 dye (0.02%) for the cathode electrode [35]. The voltage was set to 35 V for 10 h at 4 °C and the run was stopped when the sharp line of the dye approached the gel front. Molecular weight of the respiratory complexes and supercomplexes was determined by their electrophoretic mobility and in-gel catalytic activity, using the complexes of digitonine-solubilized bovine heart mitochondria as standards.

The in-gel assays were performed as described by Jung [34] using gel loaded with isolated digitonine-solubilized supercomplexes from *U. maydis* mitochondria. NADH dehydrogenase activity (NADH:methylthiazolylidiphenyl tetrazolium bromide (MTT) oxidoreductase) was assayed at 20–25 °C in a buffer containing 1.2 mM MTT and 1.0 mM NADH in 10 mM Tris/HCl, pH 7.4. For succinate dehydrogenase activity (Succinate:MTT oxidoreductase) NADH was replaced by 10 mM succinate, 0.2 mM phenazine methosulfate (PMS), 5 mM EDTA in 10 mM K₂HPO₄, pH 7.4. NADH or succinate dehydrogenase activity was correlated with the development of purple precipitates on the gel. When activity-staining appear (10–20 min) the reaction was stopped with fixing solution (50% methanol, 10% acetic acid). To assay the activity of complex IV the gel was incubated in 50 mM K₂HPO₄, pH 7.2, 4.7 mM 3,3'-diaminobenzidine tetrahydrochloride (DAB) and 16 μM horse heart cytochrome *c*. After 30–40 min of incubation at 20–25 °C, the activity was observed as a brown precipitate and the reaction was stopped with the fixing solution. Activity of complex V was assayed in 50 mM glycine (adjusted to pH 8.0 with triethanolamine), 10 mM MgCl₂, 0.15% Pb (ClO₄)₂ and 5 mM ATP. ATP hydrolysis correlated with the development of white lead phosphate precipitates. The reaction was stopped using 50% methanol, and subsequently the gel was transferred to water and scanned against a dark background as described previously [36,37].

2.5. Kinetic characterization of NADH dehydrogenase activity from respirasomes and free-complex

Activity of complex I (NADH:2,6-dimethoxy-1,4-benzoquinone (DBQ) oxidoreductase activity) from respirasomes or free-complex I was determined spectrophotometrically at 340 nm by following the oxidation of NADH ($\epsilon_{\text{NADH}} = 6.22 \text{ mM}^{-1} \text{ cm}^{-1}$) in an Agilent 8453 UV-visible spectrophotometer (Agilent Technologies, USA). Activity of isolated respirasomes or free-complex I was performed in a reaction mixture containing 120 mM KCl, 5 mM MgCl₂, 1 mM EGTA, 30 mM KH₂PO₄, pH 7.4, at 25 °C. Where indicated, isolated respirasomes or free-complex I, were added to the buffer described above plus 10 μM of horse heart cytochrome *c* [38], 10–1000 μM of DBQ and 10–150 μM NADH to start the reaction. Where indicated, rotenone (1–10 μM) [39–41], antimycin A (0.1–1 μM) [42–44], or cyanide (1–3 mM) [45,46] were added. Addition of cyanide increased the pH to 7.8, but the activity of complex I and the respirasome was the same at pH 7.4 and pH 7.8 (data not shown). To explore the effect of phospholipids on the activity of free-complex I and respirasomes, the protocol reported by [47] was followed using asolectin or lecithin.

Protein concentration of respirasome or free-complex I was 50 μg/ml and the reaction was started by the addition of NADH. NADH absorbance was continuously monitored and the time response was less than 1 s. Kinetic analysis of changes in NADH dehydrogenase activity (initial velocity) was carried out using the direct spectrophotometric recording. Initial velocities were further obtained from the slope of the linear region in each spectrophotometric recording, and the linear region of the traces was corroborated with the plot of the first derivative against time. Data were analyzed by robust, weighted, non-linear regression analysis using the SigmaPlot software (Systat Software, Inc., version 10.0). The data represent the average of eight independent experiments. Rotenone was added to inhibit NADH:DBQ

Table 1Subunit identity and molecular mass of *Ustilago maydis* mitochondrial respirasomes. The identity of each subunit was determined by LC/ESI-MS/MS.

Subunit identity	MW mature protein (kDa)	Exclusive unique peptides	Unique exclusive spectra/total spectra	Coverage (%)	ID (Scaffold-NCBI)	ID (KEGG/PENDANT)
Complex I						
NUAM	77.2	33	51/103	53	Q4P4Z1	UMAG_10695
NUBM	51.6	18	20/32	31	Q4PGP5	UMAG_11170
NUCM	48.2	17	27/47	45	Q4P4N9	UMAG_11162
NUGM	28.3	8	13/18	21	Q4PDY2	UMAG_11896
NUHM	24.3	7	8/15	32	Q4PGX9	UMAG_00634
NUKM	20.5	5	9/18	26	Q4P1W1	UMAG_11038
NUFM	13.4	5	7/15	51	Q4P7I2	UMAG_11517
NB4M	15.0	3	4/4	31	Q4PBS6	UMAG_02437
NUPM	17.2	4	6/8	44		UMAG_05598
NUEM	35.1	17	23/40	57	Q4PHN2	UMAG_00381
N7BM	14.1	5	6/11	41	Q4P6C6	UMAG_10847
NI2M	10.1	4	5/8	38	Q4P2N8	UMAG_05625
NUYM	17.2	6	10/16	34	Q4PHA1	UMAG_00512
NUJM	14.1	4	4/7	55	Q4PAH0	UMAG_11495
NUXM	20.9	5	8/11	46	Q4P5K7	UMAG_10989
NUZM	22.2	5	8/21	40	Q4P0U1	UMAG_12039
NB6M	10.7	5	6/14	52	Q4PF02	UMAG_01311
Complex III ₂						
QCR2	43.2	17	27/49	56	Q4PEI5	UMAG_01478
Cyt1	30.4	10	15/29	36	Q4P5I2	UMAG_11534
QCR7	10.5	8	11/14	70	Q4P6M6	UMAG_04237
RIP1	26.5	6	9/22	21	Q4P7T8	UMAG_10507
Complex IV						
Cox2	28.6	5	8/14	30	Q0H8Y7	Q0H8Y7
Cox4	12.8	3	4/9	41	Q4P511	UMAG_04802
Cox5A	16.8	7	10/20	46	Q4P348	UMAG_05465
Cytochrome c						
	11.9	3	4/7	39	XP_011389077	UMAG_02708

The identity of each protein was determined by mass spectrometry. The subunit molecular weight of the mature protein was determined by 2D-Tricine-SDS-PAGE and corroborated with the molecular weight obtained from *U. maydis* genome analysis (Biomax informatics ag; http://pedant.helmholtz-muenchen.de/pedant3htmlview/pedant3view?Method=analysis&Db=p3_t237631_Ust_maydi_v2GB).

oxidoreductase activity of complex I; samples used in this work were 100% inhibited by rotenone, confirming that complex I was the only NADH dehydrogenase present in both samples. The concentration of complex I in respirasome and free-complex I samples was determined by a densitometry analysis of Coomassie© Brilliant Blue R-125 stained NUAM 77 kDa-subunits (ID Scaffold-NCBI Q4P4Z1; ID KEGG/PENDANT UMAG_10695, Table 1) from an SDS-Tricine-PAGE, using Coomassie stained BSA as a standard (see Supplemental material section). The gel was scanned and the stain-intensity of NUAM subunit and BSA was determined by the Image Analysis software version 1.0 (Thermo Fisher Scientific Inc.). The intensities of NUAM subunit and BSA were measured by peak integration after densitometry analyses. The mol of NUAM subunit was determined using the molecular weight of the mature protein (Table 1). The amount of complex I in respirasomes and free-complex I samples was $3.3 \pm 0.7 \mu\text{g}/10 \mu\text{g}$ total protein and $2.8 \pm 0.5 \mu\text{g}/10 \mu\text{g}$ total protein, respectively; these amounts of complex I in respirasomes and free-complex I were used to kinetics parameters estimation.

2.6. Oxygen consumption by mitochondrial respirasomes

Oxygen consumption by isolated respirasomes was determined using a type Clark electrode in the buffer described above at 30 °C. Mixture reaction was supplemented with 10 μM horse heart cytochrome c, 70 μM DBQ and 20–100 μM NADH. Maximum activity of complex IV from respirasomes was assayed with 4 mM ascorbate and 6 mM 2,3,5,6-tetramethyl-*p*-phenyldiamine (TMPD) to reduce the horse heart cytochrome c. Where indicated, rotenone (10 μM), antimycin A (1 μM), or cyanide (3 mM) were added.

2.7. Quantification of hydrogen peroxide produced by respirasomes

Quantification of hydrogen peroxide was performed with Amplex® Red hydrogen peroxide assay kit (Invitrogen, Molecular Probes, USA), following the manufacturer instructions. Experimental conditions used were similar to those described in Section 2.5 (*vide supra*). Superoxide dismutase (50 U/ml) was added to the reaction mixture to accelerate the production of hydrogen peroxide from the superoxide anion.

2.8. Tandem mass spectrometry (LC/ESI-MS/MS)

Protein identification of isolated supercomplexes was determined by mass spectrometry performed by the Arizona Proteomics Consortium (Cancer Center and by the BIO5 Institute of the University of Arizona). Samples were prepared following the specifications of the Proteomics Core Laboratory. Scaffold program (version Scaffold_4.8.9, Proteome Software Inc., Portland, OR) was used to validate MS/MS based peptide and protein identifications. Peptide identifications were accepted if they could be established at greater than 95.0% probability by the Scaffold Local FDR algorithm. Protein identifications were accepted if they could be established at greater than 99.0% probability and contained at least 2 identified peptides. Protein probabilities were assigned by the Protein Prophet algorithm [48]. Proteins that contained similar peptides and could not be differentiated based on MS/MS analysis alone were grouped to satisfy the principles of parsimony. Proteins sharing significant peptide evidence were grouped into clusters. Proteins were annotated with GO terms from NCBI (downloaded Apr 24, 2018) [49].

2.9. Determination of protein concentration

Samples were treated with 0.4% deoxycholate and the protein content was determined as described by Lowry et al. [50]. Bovine

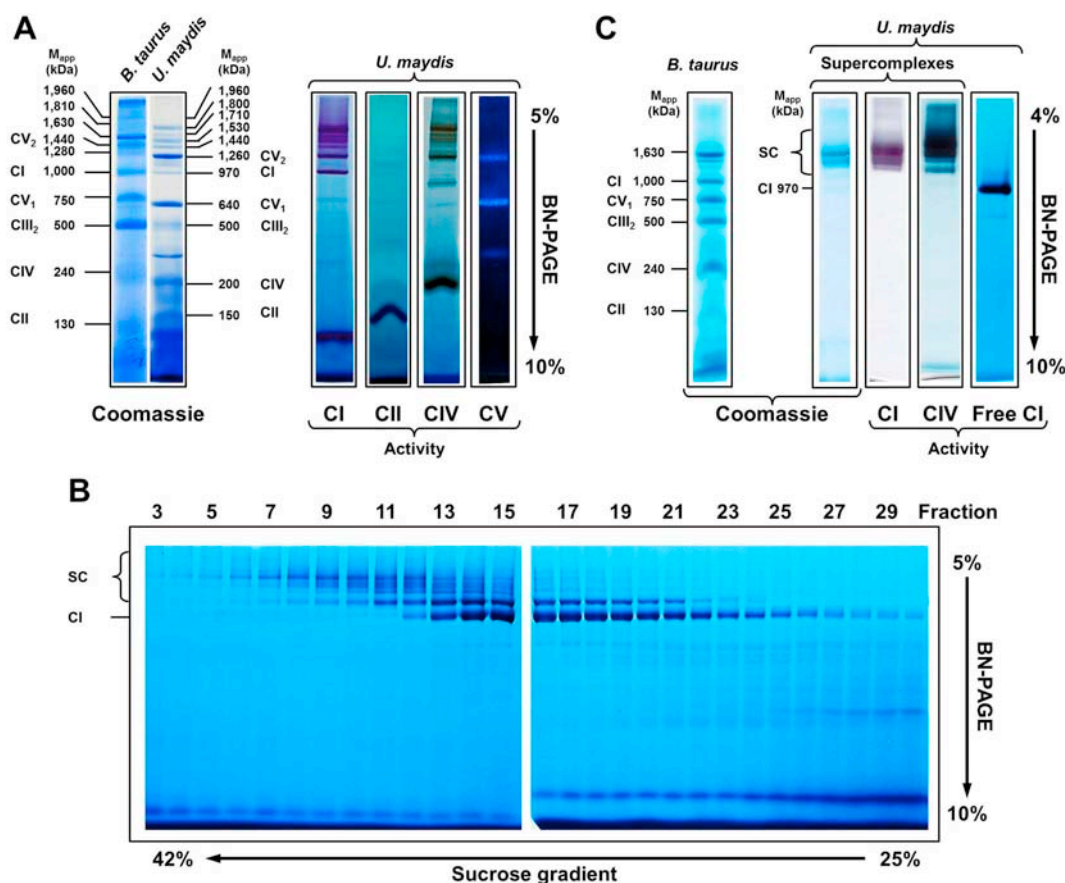


Fig. 1. Isolation and in-gel activity of the respirasome. Respiratory complex and supercomplexes from *U. maydis* mitochondria were solubilized with digitonin (A). Left panel shows the Coomassie-stained native gel strips; CI, CII, CIV, and CV corresponding to in-gel activities assay of complexes I, II, IV, and V, respectively. Respirasome was isolated by sucrose-gradient ultracentrifugation and its in-gel NADH dehydrogenase activity analyzed by BN-PAGE (B). Fractions from the bottom [3–11] and the top [25–30] of the sucrose gradient were used to obtain isolated the respirasome and free-complex I, respectively (C). Where is showed *Bos taurus* respiratory complex and supercomplexes were solubilized with digitonin and used as standard. *U. maydis* respirasome sample was used to subunits identification by MS/MS (Table 1).

serum albumin (BSA) was used as standard.

2.10. Materials

Analytical grade reagents were purchased from Sigma Chemical Co. (St. Louis, MO, USA), E. Merck (Darmstadt, Germany), and BioRad (Hercules, CA, USA). Strain FB2 of *U. maydis* was obtained from the American Type Cell Collection (Manassas, VA, USA).

3. Results

3.1. Composition of isolated respirasomes

Respiratory complexes and supercomplexes from *U. maydis* mitochondria were efficiently solubilized with digitonin preserving their activity (Fig. 1A). In gel-activity of individual complex I, II, IV and V was associated with a protein band of a molecular mass of 960, 150, 240 and 640 kDa, respectively; additionally, ATPase activity of complex V was associated with a single protein band of 1260 kDa, which has been reported as the dimer of F₁F₀-ATP synthase [36]. Activities of complexes I and IV were associated with several bands with molecular masses from 1400 to 1900 kDa (Fig. 1A). MS/MS analysis confirmed the presence of complex III₂ in these supercomplexes.

Digitonin-solubilized respirasomes from *U. maydis* were isolated by sucrose density gradient centrifugation (Fig. 1B). NADH:MTT oxidoreductase activity from complex I was distributed from fraction 3 to 30; however, fractions 3–11 contained exclusively the respirasome, and this

pattern was highly reproducible (Fig. 1B). Free-complex I was recovered from fractions 25–30. The fractions containing respirasomes and free-complex I were pooled separately and concentrated as described in the Materials and methods section and their purity, in terms of NADH dehydrogenase activity, was analyzed by BN-PAGE (Fig. 1C). For the respirasomes, activities of complex I and IV were associated with a main protein band of 1600 kDa, using bovine mitochondrial respiratory complexes solubilized with digitonin as standard (Fig. 1C). No activity of monomeric complex I and IV, or complex III₂ stained with Coomassie was observed, demonstrating that supercomplexes were isolated without contamination by individual complexes. Free-complex I activity was located around 970 kDa as a single band (Fig. 1C, right lane).

Although activities of complexes I and IV were observed in the upper zone of the gel (Fig. 1B), suggesting a broad spectrum of supercomplexes stoichiometries, a main protein band of 1630 kDa was observed in the gel stained with Coomassie (Fig. 1C). Using the molecular weight obtained from *U. maydis* genome database (Biomax informatics ag; http://pedant.helmholtz-muenchen.de/pedant3htmlview/pedant3view?Method=analysis&Db=p3_t237631_Ust_maydi_v2GB) for complex I (900 kDa), dimer of complex III₂ (473 kDa), and complex IV (203 kDa), we hypothesize that the minimum and most probable stoichiometry of this 1630 kDa supercomplex is I₁:(III₂):IV₁. Seventeen subunits for complex I, 4 subunits for complex III₂, and 3 for complex IV were identified by MS/MS analysis of isolated respirasomes (Table 1), confirming their composition. Additionally, cytochrome c was detected in the respirasome

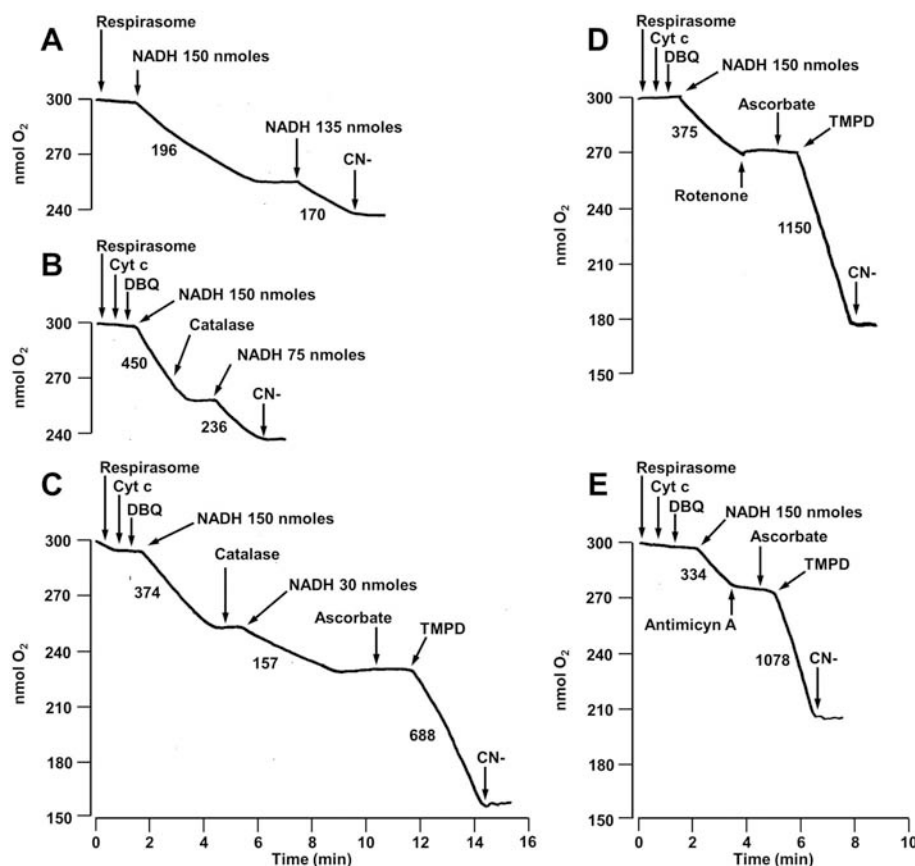


Fig. 2. Oxygen consumption by isolated *Ustilago maydis* respirasome. (A) Electron flux into respirasome was started by 150 nmol of NADH addition in 120 mM KCl, 5 mM MgCl₂, 1 mM EGTA, 30 mM KH₂PO₄, pH 7.4, at 30 °C. (B) Mobile electron carriers stimulate respirasome oxygen uptake (i.e. 65 μM DBQ and 60 μg cytochrome *c*/ml). Maximum activity of complex IV was reached by ascorbate (4 mM) and TMPD (6 mM) addition (C). Where is showed 15 μM rotenone (D), 3 μM antimycin A (E) or 3 mM cyanide (A–E) were added to inhibit respiration through complexes I, III₂ or IV, respectively. Catalase = 2000–4000 Units. Numbers below each recording represent the velocity of oxygen consumption = nmol O₂/mg of CI·min. Different NADH concentrations were added to assay the respirasomes response and the oxygen reduction mean ± S.D. was: 133 ± 17 nmol O₂ reduced/mg of CI·min with 30 nmol of NADH added (n = 6); 266 ± 30 nmol O₂ reduced/mg of CI·min with 75 nmol of NADH added (n = 6); and 397 ± 81 nmol O₂ reduced/mg of CI·min with 150 nmol of NADH added (n = 10). The x-axis scale showed at bottom of C and E is the same for the upper recording (A, B and D). Results were obtained from 7 different preparations.

sample (Table 1). Complex I amount was determined as described in Materials and methods section and Supplementary material.

3.2. Oxygen consumption by respirasomes

Surprisingly, isolated respirasomes reduced oxygen in the presence of NADH (133 ± 17 nmol O₂ reduced·(mg of CI·min)⁻¹), suggesting that they contain, in addition to functional respiratory complexes I, III₂ and IV, the mobile elements, coenzyme Q and cytochrome *c*, allowing the electron flux from NADH to oxygen (Fig. 2A). If mobile electron carriers (i.e. 60 μg cytochrome *c*/ml and 65 μM DBQ) were added to the reaction mixture, oxygen consumption increased (397 ± 41 nmol O₂ reduced·(mg of CI·min)⁻¹; Fig. 2B–E), suggesting that these could be used as substrates by isolated respirasomes. Once NADH has been oxidized, oxygen uptake decreases (Fig. 2A–C), and a new NADH addition promoted respiration again. Although oxygen uptake was supported by NADH oxidation, the maximum complex IV activity was reached with ascorbate and TMPD addition (992 ± 203 nmol O₂ reduced·(mg of CI·min)⁻¹; Fig. 2C–E), indicating that flux control could belong to complexes I or III₂. Oxygen reduction by respirasome in the presence of NADH, cytochrome *c* and DBQ was inhibited by rotenone (Fig. 2D), antimycin A (Fig. 2E), or cyanide (Fig. 2A–E). The total inhibition of electron flux by these specific inhibitors discards the presence of rotenone-insensitive alternative NADH dehydrogenases (i.e. Nde1, Nde2, or Ndi1) or cyanide-resistant alternative oxidase [31] in isolated respirasomes. Additionally, MS/MS analysis confirms the absence of these alternative respiratory elements in the *U. maydis* respirasome. The absence of hydrogen peroxide (H₂O₂) as a result of electron leak during NADH oxidation was demonstrated by the addition of catalase (Fig. 2A and B). Alternatively, H₂O₂ production by respirasomes, assayed with the Amplex Red probe, was of 240 ± 4 pmol of H₂O₂·(mg of CI·min)⁻¹ in the presence of 150 nmol of NADH to assess the maximum rate of oxygen consumption; Cyanide addition

increased ROS production to 550 ± 10 pmol of H₂O₂·(mg of CI·min)⁻¹, and 484 ± 24 pmol of H₂O₂·(mg of CI·min)⁻¹ in the absence or presence of superoxide dismutase, respectively. These values represent 0.001% of the maximum rate of oxygen consumption supported by NADH.

Since H₂O₂ production was negligible (i.e. less than 0.001%) during maximum oxygen consumption by respirasome, one question is arising, the NADH:DBQ oxidoreductase activity of complex I occur even if electron flow in complex III₂ and IV in supercomplexes is interrupted by antimycin A or cyanide? To answer this question, NADH:DBQ oxidoreductase activity by respirasomes was monitored in the presence of inhibitors of complex I, III₂ or IV.

3.3. NADH oxidation by respirasome

Oxidation of NADH by respirasomes was recorded spectrophotometrically at 340 nm in the presence of cytochrome *c* and DBQ (Fig. 3). NADH dehydrogenase activity of respirasomes was inhibited by rotenone (Fig. 3A) demonstrating that this activity belongs exclusively to complex I and alternative NADH dehydrogenases were absent. Interestingly, reduction of DBQ by complex I was stopped when complex III₂ and complex IV were inhibited by antimycin A or cyanide, respectively, even in the presence of an excess of coenzyme Q and cytochrome *c* (Fig. 3B and C). Inhibition of the NADH:DBQ oxidoreductase activity occurs even if inhibitor (i.e. Antimycin A or cyanide) was added before NADH (Fig. 3B and C). This observation indicates that activity of complex I is tightly coordinated with the activities of complexes III₂ and IV in the respirasome (Fig. 2). Antimycin A and cyanide have no effect on free-complex I activity (Fig. 3E and F). Remarkably, the ratio between NADH oxidation (i.e. 959 ± 197 nmol NADH oxidize/mg of CI·min; see Fig. 3) and oxygen reduction (i.e. 397 ± 81 nmol O₂ reduced/mg of CI·min, see Fig. 2) by respirasomes was 2.42 ± 0.3 , very close to the theoretical value of 2 for the electron

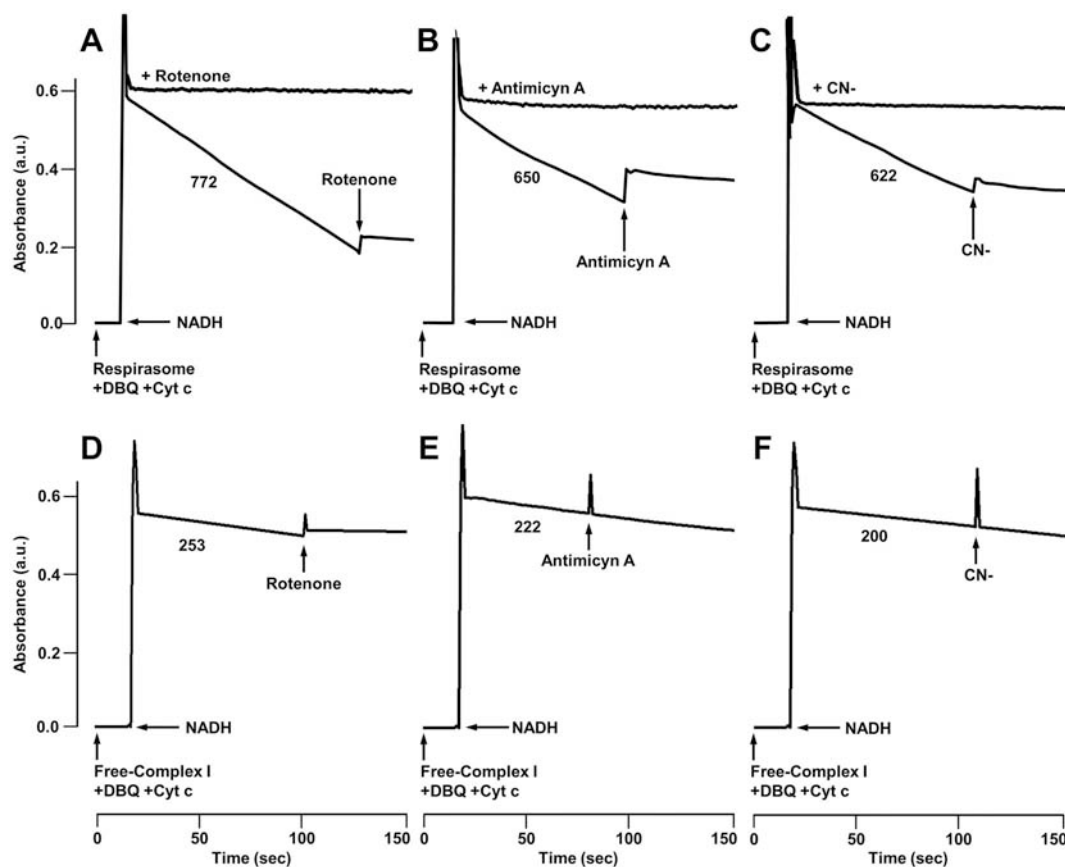


Fig. 3. Effect of rotenone, antimycin A and cyanide on NADH:DBQ oxidoreductase activity of respirasome. Respirasomes were incubated in the buffer described in Fig. 2. NADH oxidation was monitored by NADH absorbance at 340 nm. Where is indicated respirasome, DBQ (65 μ M), cytochrome c (60 μ g/ml), NADH (150 nmol), and (A) rotenone (15 μ M), (B) antimycin A (5 μ g/ml), or (C) cyanide (3 mM), were added. Addition of inhibitor before NADH is showed as +Rotenone (A), +Antimycin A (B), or +CN⁻ (C). Activity of free-complex I was assayed in similar conditions in the presence of rotenone (D), antimycin A (E) or cyanide (F). The number below each recording represents the velocity of NADH oxidation. The mean \pm S.D. value of NADH:DBQ oxidoreductase activity for respirasome in this experimental condition was 959 ± 197 nmol NADH oxidize/mg of CI \cdot min ($n = 9$). Results were obtained from 7 different preparations.

flux from NADH to oxygen through respiratory complexes I-III₂-IV.

Oxygen uptake stimulation by the addition of DBQ and cytochrome c (Fig. 2A and B) suggests that mobile electron carriers were taken from the medium, and their microdiffusion between complexes could play an important role in electron flux. Interestingly, inhibition of complexes III₂ or IV stops the NADH:DBQ oxidoreductase activity of the respirasome (Fig. 3), suggesting that protein-protein contacts between complexes I, III₂ and IV could play an important role in the regulation of respirasome activity. In this sense, we have previously characterized the role of protein-protein interactions in the activity of the complex V dimer [36]. Then, the characterization of NADH dehydrogenase activity in respirasomes and free-complex I could be helpful to elucidate the role of the interactions between complexes in the respirasomes.

3.4. NADH dehydrogenase activity from complex I versus NADH dehydrogenase activity from respirasome

As a first step, activity of NADH:DBQ oxidoreductase from respirasome and free-complex I was determined following the change in absorbance at 340 nm.

Activity of NADH:DBQ oxidoreductase by respirasome (Fig. 4A and B) or free-complex I (Fig. 4C and D) increased as the NADH or DBQ concentrations were raised. The data were fitted to the Michaelis-Menten equation. Respirasome showed a $V_{\max} = 3340 \pm 150$ nmol NADH oxidized \cdot (mg of CI \cdot min)⁻¹, a $K_{M-NADH} = 19 \pm 4$ μ M and a $K_{M-DBQ} = 76 \pm 15$ μ M. In contrast, free-complex I showed a V_{\max} value of 1000 ± 80 nmol NADH oxidized \cdot (mg of CI \cdot min)⁻¹, a K_{M-}

$K_{M-NADH} = 50 \pm 11$ μ M and a $K_{M-DBQ} = 103 \pm 30$ μ M (Table 2). It has been reported that phospholipid reconstitution could increase the activity of DDM-isolated complex I from *Yarrowia lipolytica* [47]; however, this effect was not observed in the free-complex I or respirasome from *U. maydis* (see Suppl material). The Lineweaver-Burk plot for free-complex I as well as complex I from respirasome was consistent with a random Bi Bi mechanism, which predicts a ternary complex (i.e. NADH-CI-DBQ).

The k_{cat} values for free-complex I and respirasome were 15 ± 1 s⁻¹ and 49 ± 2 s⁻¹, respectively (Table 2), confirming that respirasome is 3-times more active than free-complex I. Additionally, the $k_{\text{cat}}/K_{M-NADH}$ values of free-complex I and respirasome were $2.9 \times 10^5 \pm 0.2 \times 10^5$ and $2.6 \times 10^6 \pm 0.6 \times 10^6$ M⁻¹s⁻¹, respectively; while the k_{cat}/K_{M-DBQ} values were $1.4 \times 10^5 \pm 0.3 \times 10^5$ and $6.5 \times 10^5 \pm 1.3 \times 10^5$ M⁻¹s⁻¹ for free-complex I and respirasome, respectively (Table 2), indicating a higher specificity of respirasome for NADH and DBQ. These results indicate that incorporation of complex I into respirasomes and the interaction between complexes I, III₂ and IV, has a stimulatory effect on the activity and affinity of complex I.

3.5. Proteins associated to respirasomes

The MS/MS analysis of isolated respirasomes showed five proteins related with the organization of mitochondrial architecture: Prohibitins 1 (UMAG_11092) and 2 (UMAG_05030); Fcj1 (UMAG_00635), Rcf2 (UMAG_03929) and the mitochondrial inner membrane organizing system protein 1 (UMAG_10488). All these proteins showed

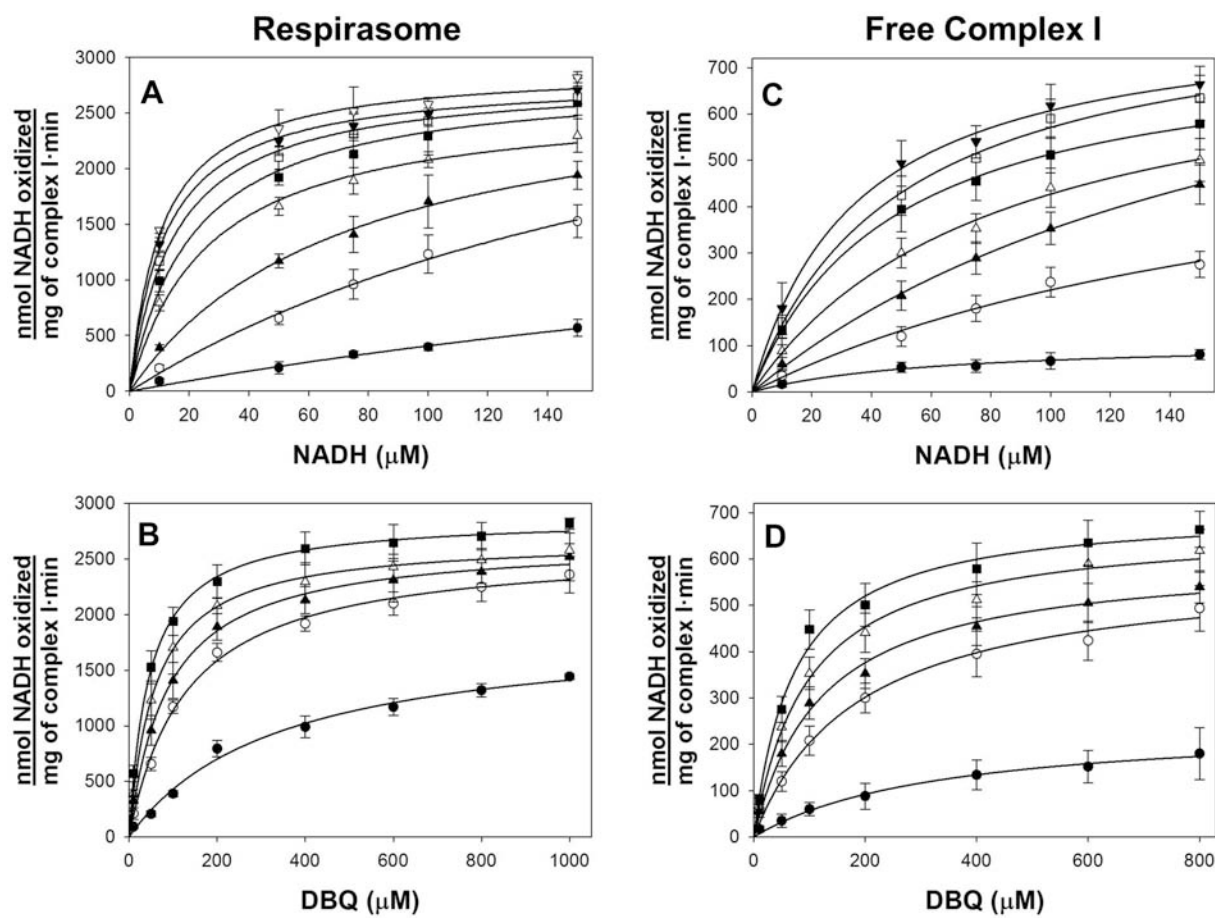


Fig. 4. Kinetic characterization of NADH:DBQ activity from respirasome and free-complex I. The dependence of respirasome (A) and free-complex I (C) activity on NADH at different fixed concentrations of DBQ, and dependence of respirasome (B) and free-complex I (D) activity on DBQ at different fixed NADH concentrations, were fitted to the Michaelis-Menten equation. In (A) and (C) the fixed concentration of DBQ was (●) = 10; (○) = 50; (▲) = 100; (△) = 200; (■) = 400; (□) = 600; (▼) = 800; and (∇) = 1000 μM . In (B) and (D) the fixed concentration of NADH was (●) = 10; (○) = 50; (▲) = 75; (△) = 100; and (■) = 150 μM . The data are the average of four replicates from five independent preparations. The activity was corrected by complex I amount in each preparation of respirasomes and free-complex I as described in [Materials and methods](#) section. Error bars represent S.D.

Table 2

Kinetics parameters of NADH:DBQ oxidoreductase activity of the respirasome and the free-complex I from *Ustilago maydis* mitochondria.

	Free-complex I ^a	Respirasome ^a
V_{max} (nmol NADH oxidized/ mg complex I min ⁻¹)	1000 ± 80	3340 ± 150
k_{cat} (s ⁻¹)	15 ± 1	49 ± 2
		NADH
K_{M} (μM)	50 ± 11	19 ± 4
$k_{\text{cat}}/K_{\text{M}}$ (M ⁻¹ s ⁻¹)	$2.9 \times 10^5 \pm 0.2 \times 10^5$	$2.6 \times 10^6 \pm 0.6 \times 10^6$
		DBQ
K_{M} (μM)	103 ± 30	76 ± 15
$k_{\text{cat}}/K_{\text{M}}$ (M ⁻¹ s ⁻¹)	$1.4 \times 10^5 \pm 0.3 \times 10^5$	$6.5 \times 10^5 \pm 1.3 \times 10^5$

^a Complex I mol in free-Complex I and respirasome samples was determined as described in [Materials and methods](#) section, and kinetics parameters were showed as mg of Complex I.

transmembrane domains but only prohibitin 2 and Rcf2 presented a glycine zipper motif in the transmembrane domains. It has been suggested that proteins with transmembrane glycine zippers play a structural role as glue between the membrane proteins [51]. Finally, three proteins with the pentatricopeptide repeat domain (PPR domain: UMAG_06347 and UMAG_11282; PET127: UMAG_02275) were associated with the respirasome sample.

4. Discussion

Mitochondrial respiratory complex I, III₂ and IV are membrane proton-pumps that transform the energy of NADH into the proton electrochemical gradient ($\Delta\mu_{\text{H}^+}$) across the inner membrane. The free energy stored in the $\Delta\mu_{\text{H}^+}$ is utilized for ATP synthesis. Actually, stable interactions between the respiratory complexes have been determined, and these new structures are named supercomplexes. Although composition and stoichiometry of supercomplexes are diverse, if complexes I, III₂ and IV are present, the electron flow could occur from NADH to oxygen (*i.e.* a respirasome). The respirasome has been described in mitochondria from different eukaryotes such as bovine [16], *Neurospora crassa* [12], and prokaryotes as the α -proteobacteria *Paracoccus denitrificans* [9].

In this work the *U. maydis* respirasome was efficiently solubilized with digitonine and isolated as a highly stable unit (Fig. 1). Composition of *U. maydis* respirasome was assessed by MS/MS analysis (Table 1), in-gel activity (*i.e.* complex I and IV), and NADH:O₂ oxidoreductase activity (*i.e.* electron flux from NADH to oxygen). The minimal stoichiometry of the respirasome was I₁III₂IV₁ with an apparent molecular mass of 1630 kDa (Fig. 1).

Oxygen consumption supported by NADH oxidation strongly indicates that cytochrome *c* and coenzyme Q were present in isolated *U. maydis* respirasome (Fig. 2A), similar to that described for the respirasome obtained from bovine heart mitochondria [52]. This could be

possible because the binding of cytochrome *c* to complex III₂ is strong [53,54], and coenzyme Q was embedded in the lipid annulus of the respirasome. However, incorporation of fresh cytochrome *c* and DBQ into isolated respirasomes increased the electron flow from NADH to oxygen, suggesting that the respirasome can take the quinone and cytochrome *c* from the medium.

Recent experimental evidences support that substrate channeling inside the respirasome doesn't occur. Electron microscopy showed that each monomer in complex III dimer (III₂) contains two Q binding sites (Q_P and Q_N), which are located on opposite sides of the dimer. The activity of complex III₂ involves oxidation of QH₂ and reduction of cytochrome *c*, in a process called the Q-cycle. QH₂ binds at the Q_P site and its electrons are transferred, one to cytochrome *c* in the intermembrane space via the Rieske protein, and the other to a Q bound at the Q_N site, generating a semiquinone (Q·). A new QH₂ binds at the Q_P site and a second cytochrome *c* is reduced, and the Q· bound at the Q_N site is fully reduced to QH₂, which is released into the ubiquinone pool. Kinetic analysis has demonstrated the alternating activity of each monomer [55].

The cryo-electron microscopy analysis of the respirasome shows that the Q binding site of one monomer of complex III₂ is facing the Q site of complex I but separated by ~10 nm (~100 Å), while the other monomer is facing complex IV [18]. Also, these studies showed that there were no proteins involved in substrate channeling between the Q sites of complex I and complex III₂ [18].

Indeed, a time-resolved kinetic study of the respiratory chain in submitochondrial particles or mitochondrial membranes showed that Q exists as a single, common pool which is exchanged freely between respiratory complexes, including supercomplexes [56]. An elegant approach to test the electron channeling in the respirasome was provided by Fedor and Hirst [20], who hypothesized that in the presence of electron channeling between complexes I and III₂, the respiratory activity supported by NADH should be insensitive to enzymes that take the QH₂ from the quinone pool. Using a cyanide-insensitive, non-electrogenic quinol oxidase (AOX), they probed that adding AOX to bovine submitochondrial particles the NADH oxidation rate increases and becomes cyanide insensitive. They concluded that channeling doesn't occur because quinol produced by complex I is released into the quinone pool and oxidized by AOX [20].

However, a recent report shows that in the inner mitochondrial membrane complex I is heterogeneously distributed [57]. In bovine heart about 44% of complex I occurs as a single copy (I₁); 16% as I₁III₂ supercomplexes, and 40% as I₁III₂IV₁₋₂ respirasome [57]. In *Yarrowia lipolytica* the arrangements of complex I founded were: complex I by itself (40%); supercomplexes I₁:III₂ (13%); and I₁III₂IV₁₋₂ (47%) [57].

In this sense, the kinetic behavior of complex I in the different supercomplexes found in the membrane is not necessarily the same. An approach to determine the properties of respirasome is to isolate it. Interestingly, although the NADH:O₂ oxidoreductase activity of *U. maydis* respirasome was sensitive to classical respiratory inhibitors (Fig. 2), inhibition of complexes III₂ or IV prevented NADH oxidation (Fig. 3) in the presence of an excess of DBQ and cytochrome *c*. Particularly, inhibition of NADH:DBQ oxidoreductase activity by antimycin A or cyanide strongly supports the idea that interactions between complex I and complexes III₂ and IV might regulate the activity of complex I, and therefore the respirasome activity. In line with this hypothesis, inhibition of NADH:O₂ oxidoreductase activity in the respirasome with antimycin A or cyanide does not induce H₂O₂ or superoxide production, as confirmed by catalase addition (Fig. 2) or Amplex Red assay in the presence or absence of superoxide dismutase. Since complex IV doesn't use the product of complex I, and its active site is ~20 nm away from complex I Q site [18], the cross-talk (*i.e.* complex-complex contacts) between complexes IV and I is a working hypothesis to explain that inhibition of complex IV induces the inhibition of complex I.

It has been described that intersubunit contacts play a significant role in the catalytic properties of many enzymes. Particularly, in the 3-deoxy-*d*-manno-octulosonate-8-P synthase the subunit interphase is important for substrate selectivity and binding [58]; and in the glucosamine-6-P deaminase from *Escherichia coli* the contacts between the subunits modify the allosteric equilibrium between the R and T-state [59]. In *U. maydis* the contacts between monomers in the dimer of F₁F₀-ATP synthase increase the ATPase activity and decrease the IC₅₀ for oligomycin [36].

In the respirasome, interactions between complex IV and complex I involve subunit 7A of complex IV and either ND5 or the 39-kDa subunit of complex I. Additionally, complexes IV and III₂ interact through subunits *cox* 7A and *cox* 8B and regions of subunits QCR9, QCR8 of complexes IV and III₂, respectively [57].

To explore the effect of complex-complex contacts in the respirasome, we decided to determine NADH:DBQ oxidoreductase activity of complex I in two states, free as well as incorporated in the respirasome. Free-complex I from *U. maydis* showed a V_{max} of 1000 ± 80 nmol NADH oxidized·(mg of complex I·min)⁻¹; similar values (420–840 nmol NADH·(mg·min)⁻¹) have been reported for *Yarrowia lipolytica* [44,60]. However, kinetic analysis showed that the activity of *U. maydis* respirasomal complex I was 3-time higher than that of the individual complex I (V_{max} = 3340 ± 150 nmol NADH oxidized·(mg of complex I·min)⁻¹), and the affinity for NADH and DBQ was also higher. These observations indicate that incorporation of complex I in supercomplexes (*i.e.* respirasome) increased their catalytic (k_{cat}) and the specificity (k_{cat}/K_M) constants, illustrating the possible role of the tight interactions between complexes I, III₂ and IV. In contrast with our results, the group of Shinzawa-Itoh described that the supercomplexes isolated from bovine heart mitochondria showed an NADH:Q₁ oxidoreductase activity of 700–1120 nmol NADH·(mg of SC·min)⁻¹ in the presence of 150 μM NADH, 37 μM Q₁, 200 μM cytochrome *c* and 2 mM KCN [61]. The activity of *U. maydis* respirasome was 3-time higher than the activity of bovine supercomplexes, and under similar concentrations of NADH, coenzyme Q, and cytochrome *c* the *U. maydis* respirasome showed only 30% of its V_{max} (Fig. 4). It's important to note that KCN was present in the mixture assay of the bovine supercomplexes activity [61], while KCN had a different effect on *U. maydis* respirasome.

An important difference between bovine and *U. maydis* respirasomes is the dependence of complex I activity on active complexes III₂ and IV. Here we showed that NADH:DBQ oxidoreductase activity of complex I was depended on active complex III₂ and IV, even in the presence of an excess of DBQ and cytochrome *c*; moreover, inhibition of complex IV abolished complex I activity (Fig. 3). Bovine respirasome showed similar behavior only if coenzyme Q concentration was limiting, suggesting that activities of complex III₂ and IV were important to remove the products [61]. Under this condition electron leak at mammalian complex I or contribution to QH₂ pool would be probable [61]. Additionally, complex-complex contacts in *U. maydis* respirasome promotes NADH:DBQ activity, while in bovine respirasome this stimulating effect was not observed.

To explain the effect of cyanide or antimycin A on the activity of complex I in respirasome, we hypothesized that the respirasome in *U. maydis* is “tighter”, and the interactions between the complexes promoted a conformational change in complex I (*i.e.* formation of deactive status of complex I). Studies on the deactive state of complex I, which is formed during ischemia, showed that an unstructured region in the loop of ND3 prevents coenzyme Q binding [62]. Actually, this deactive state is considered a regulatory mechanism of complex I to minimize ischemia-reperfusion injury [63]. Thus, although a deactive state of complex I in *U. maydis* must be determined experimentally, in the respirasome the cyanide inhibition of complex IV could recreate the ischemia condition, promoting the “deactive state” of complex I and preventing NADH oxidation and coenzyme Q reduction.

Regarding the identity of proteins associated whit the *U. maydis*

respirasomes sample, prohibitins 1 and 2 [64,65] and Rcf2 [66,67] have an important role in the formation and stabilization of supercomplexes. Although Fcj1 has a role in the formation of the mitochondrial crista [68], it has not been reported a role of this protein in respirasome formation.

The common features of the pentatricopeptide repeat domain proteins and Pet127 detected in the respirasome sample are the mitochondrial localization and mRNA binding during the synthesis of proteins in mitochondria. Although deletion of some members of these proteins results in a complete loss of mitochondrial respiratory capacity [69,70], their precise role in the *U. maydis* respirasome should be experimentally determined.

Under physiological conditions, the interaction between complexes I-III₂-IV in the respirasome may have two possible roles: 1) stimulate the NADH:DBQ oxidoreductase activity of complex I, and 2) provide a mechanism of regulation of complex I, stabilizing its deactive/active status to prevent ROS production. If cellular ATP decreases, individual mitochondrial respiratory complexes could associate into respirasomes to improve the electron flux, the proton pumping and generate the $\Delta\mu_{H^+}$ needed for ATP synthesis. Contrary, if there is not a cellular demand for ATP (or an ischemic state) complex I can be in a deactive state to decrease NADH consumption and cytochrome *c* reduction, and then drop the electron flux reducing the ROS production.

Author contribution

Reyes-Galindo M, Suarez R and Flores-Herrera O designed and performed principal experiments; Esparza-Perusquía M, respirasomes isolation and technical assistance; de Lira-Sánchez J, ROS production analysis and technical assistance; Pardo JP and Martínez F analyzed data; Flores-Herrera O supervised project and wrote the paper with contributions from all authors.

Transparency document

The [Transparency document](#) associated with this article can be found, in online version.

Declaration of Competing Interest

The authors declare no conflict of interest.

Acknowledgments

We dedicate this work as a memorial to Professor PhD. Edmundo Chávez-Cossío, an exceptional friend and colleague, who passed away suddenly on December 24, 2018. This work was supported by Dirección General de Asuntos del Personal Académico (DGAPA) (IN222617, IN222117 and IN211715) from Universidad Nacional Autónoma de México (UNAM) and Consejo Nacional de Ciencia y Tecnología (CONACyT) (168025 and 254904). MR-G is a student of Facultad de Medicina (309210120) from UNAM and fellowship from Programa de Apoyo y Fomento a la Investigación Estudiantil (AFINES); RS is a student of Ingeniería Bioquímica (11120199) from Instituto Tecnológico de Morelia, México; ME-P is a PhD student of the Programa de Doctorado en Ciencias Biológicas (511021118) from UNAM and supported by the CONACyT through a doctoral scholarship (254400). JdL-S is a PhD student of the Programa de Doctorado en Ciencias Biomédicas (518024299) from UNAM and supported by the CONACyT through a doctoral scholarship (666472). The authors thank to the Posgrado en Ciencias Biológicas and Ciencias Biomédicas from UNAM for the academic support.

Appendix A. Supplementary data

Supplementary data to this article can be found online at <https://>

doi.org/10.1016/j.bbabi.2019.06.017.

References

- [1] P. Mitchell, Coupling of photophosphorylation to electron and hydrogen transfer by a chemiosmotic type of mechanism, *Nature*. 191 (1961) 144–148.
- [2] P. Mitchell, *Chemiosmotic Coupling and Energy Transduction*, Glynn Research, LTD., Bodmin, Cornwall, U.K, 1968, pp. 1–111.
- [3] P. Mitchell, Chemiosmotic coupling in oxidative and phosphosynthetic phosphorylation, *Biochim. Biophys. Acta* 1807 (2011) 1507–1538.
- [4] D.G. Nicholls, S.J. Ferguson, *Bioenergetics 4*. London, Academic Press, 2013.
- [5] C.R. Hackenbrock, B. Chazotte, S.S. Gupte, The random collision model and a critical assessment of diffusion and collision in mitochondrial electron transport, *J. Bioenerg. Biomembr.* 18 (1986) 331–368.
- [6] J. Vonck, E. Schäfer, Supramolecular organization of protein complexes in the mitochondrial inner membrane, *Biochim. Biophys. Acta* 1793 (2009) 117–124.
- [7] R. Acín-Pérez, J.A. Enriquez, The function of the respiratory supercomplexes: the plasticity model, *Biochim. Biophys. Acta* 1837 (2014) 444–450.
- [8] E.A. Berry, B.L. Trumpower, Isolation of ubiquinol oxidase from *Paracoccus denitrificans* and resolution into cytochrome bc1 and cytochrome c-a₃ complexes, *J. Biol. Chem.* 260 (1985) 2458–2467.
- [9] A. Stroh, O. Anderka, K. Pfeiffer, T. Yagi, M. Finel, B. Ludwig, H. Schagger, Assembly of respiratory complexes I, III, and IV into NADH oxidase supercomplex stabilizes complex I in *Paracoccus denitrificans*, *J. Biol. Chem.* 279 (2004) 5000–5007.
- [10] H. Schagger, K. Pfeiffer, Supercomplexes in the respiratory chains of yeast and mammalian mitochondria, *EMBO J.* 19 (2000) 1777–1783.
- [11] R.A. Stuart, Supercomplex organization of the oxidative phosphorylation enzymes in yeast mitochondria, *J. Bioenerg. Biomembr.* 40 (2008) 411–417.
- [12] I. Marques, N.A. Dencher, A. Videira, F. Krause, Supramolecular organization of the respiratory chain in *Neurospora crassa* mitochondria, *Eukaryot. Cell* 6 (2007) 2391–2405.
- [13] H. Eubel, L. Jänsch, H.P. Braun, New insights into the respiratory chain of plant mitochondria. Supercomplexes and a unique composition of complex II, *Plant Physiol.* 133 (2003) 274–286.
- [14] H. Eubel, J. Heinemeyer, H.P. Braun, Identification and characterization of respirasomes in potato mitochondria, *Plant Physiol.* 134 (2004) 1450–1459.
- [15] N.V. Dudkina, J. Heinemeyer, S. Sunderhaus, E.J. Boekema, H.P. Braun, Respiratory chain supercomplexes in the plant mitochondrial membrane, *Trends Plant Sci.* 11 (2006) 232–240.
- [16] H. Schagger, K. Pfeiffer, The ratio of oxidative phosphorylation complexes I–V in bovine heart mitochondria and the composition of respiratory chain supercomplexes, *J. Biol. Chem.* 276 (2001) 37861–37867.
- [17] G. Jinke, W. Meng, G. Runyu, Y. Kaige, L. Jianlin, G. Ning, Y. Maojun, The architecture of the mammalian respirasome, *Nature*. 537 (2016) 639–643.
- [18] J.A. Letts, K. Fiedorczuk, L.A. Sazanov, The architecture of respiratory supercomplexes, *Nature*. 537 (2016) 644–648.
- [19] M.L. Genova, A. Baracca, A. Biondi, G. Casalena, M. Faccioli, A.I. Falasca, G. Formiggini, G. Sgarbi, G. Solaini, G. Lenaz, Is supercomplex organization of the respiratory chain required for optimal electron transfer activity? *Biochim. Biophys. Acta* 1777 (2008) 740–746.
- [20] J.G. Fedor, J. Hirst, Mitochondrial supercomplexes do not enhance catalysis by quinone channeling, *Cell Metab.* 28 (2018) 525–531.
- [21] R. Acín-Pérez, M.P. Bayona-Bafaluy, P. Fernandez-Silva, R. Moreno-Loshuertos, A. Perez-Martos, C. Bruno, C.T. Morales, J.A. Enriquez, Respiratory complex III is required to maintain complex I in mammalian mitochondria, *Mol. Cell* 13 (2004) 805–815.
- [22] F. Diaz, H. Fukui, S. Garcia, C.T. Moraes, Cytochrome c oxidase is required for the assembly/stability of respiratory complex I in mouse fibroblasts, *Mol. Cell. Biol.* 26 (2006) 4872–4881.
- [23] Y.C. Chen, E.B. Taylor, N. Dephoure, J.M. Heo, A. Tonhato, I. Papandreou, N. Nath, N.C. Denko, S.P. Gygi, J. Rutter, Identification of a protein mediating respiratory supercomplex stability, *Cell Metab.* 15 (2012) 348–360.
- [24] E. Maranzana, G. Barbero, A.I. Falasca, G. Lenaz, M.L. Genova, Mitochondrial respiratory supercomplex association limits production of reactive oxygen species from complex I, *Antioxid. Redox Signal.* 19 (2013) 1469–1480.
- [25] E. Lapuente-Brun, R. Moreno-Loshuertos, R. Acín-Pérez, A. Latorre-Pellicer, C. Colás, E. Balsa, E. Perales-Clemente, P.M. Quirós, E. Calvo, M.A. Rodríguez-Hernández, P. Navas, R. Cruz, Á. Carracedo, C. López-Otín, A. Pérez-Martos, P. Fernández-Silva, E. Fernández-Vizarra, J.A. Enriquez, Supercomplex assembly determines electron flux in the mitochondrial electron transport chain, *Science*. 340 (2013) 1567–1570.
- [26] K. Ikeda, S. Shiba, K. Horie-Inoue, K. Shimokata, S. Inoue, A stabilizing factor for mitochondrial respiratory supercomplex assembly regulates energy metabolism in muscle, *Nat. Commun.* 4 (2013) 2147–2156.
- [27] M.L. Genova, G. Lenaz, Functional role of mitochondrial respiratory supercomplexes, *Biochim. Biophys. Acta* 1837 (2014) 427–443.
- [28] Y. Chaban, E.J. Boekema, N.V. Dudkina, Structures of mitochondrial oxidative phosphorylation supercomplexes and mechanisms for their stabilization, *Biochim. Biophys. Acta* 1837 (2014) 418–426.
- [29] M.P. McCann, K.M. Snetselaar, A genome-based analysis of amino acid metabolism in the biotrophic plant pathogen *Ustilago maydis*, *Fungal Genet. Biol.* 45 (Suppl. 1) (2008) S77–S87.
- [30] J. Ruiz-Herrera, C.G. León, L. Guevara-Olvera, A. Cárabez-Trejo, A yeast-mycelial dimorphism of haploid and diploid strains of *Ustilago maydis* in liquid culture,

- Microbiology. 1421 (1995) 695–703.
- [31] O. Juárez, G. Guerra, F. Martínez, J.P. Pardo, The mitochondrial respiratory chain of *Ustilago maydis*, *Biochim. Biophys. Acta* 1658 (2004) 244–251.
- [32] W.F. Waterfield, H.D. Sisler, A convenient procedure for rapid release of protoplasts from *Ustilago maydis*, *Biotechniques*. 6 (1988) 832–834.
- [33] H. Schagger, W.A. Cramer, G. von Jagow, Analysis of molecular masses and oligomeric states of protein complexes by blue native electrophoresis and isolation of membrane protein complexes by two-dimensional native electrophoresis, *Anal. Biochem.* 217 (1994) 220–230.
- [34] C. Jung, C.M. Higgins, Z. Xu, Measuring the quantity and activity of mitochondrial electron transport chain complexes in tissues of central nervous system using blue native polyacrylamide gel electrophoresis, *Anal. Biochem.* 286 (2000) 214–223.
- [35] I. Wittig, M. Karas, H. Schagger, High resolution clear native electrophoresis for in-gel functional assays and fluorescence studies of membrane protein complexes, *Mol. Cell. Proteomics* 6 (2007) 1215–1225.
- [36] M. Esparza-Perusquia, S. Olvera-Sanchez, J.P. Pardo, G. Mendoza-Hernandez, F. Martinez, O. Flores-Herrera, Structural and kinetics characterization of the F₁F₀-ATP synthase dimer. New repercussion of monomer-monomer contact, *Biochim. Biophys. Acta Bioenerg.* 1858 (2017) 975–981.
- [37] D. De los Ríos-Castillo, M. Zarco-Zavala, S. Olvera-Sanchez, J.P. Pardo, O. Juarez, F. Martinez, G. Mendoza-Hernandez, J.J. García-Trejo, O. Flores-Herrera, Atypical cristae morphology of human syncytiotrophoblast mitochondria: role for complex V, *J. Biol. Chem.* 286 (2011) 23911–23919.
- [38] K.M.C. Sinjorgo, T.B.M. Hakvoort, I. Durak, J.W. Draijer, J.K.P. Post, A.O. Muijsers, Human cytochrome c oxidase isoenzymes from heart and skeletal muscle: purification and properties, *Biochim. Biophys. Acta* 850 (1987) 144–150.
- [39] Y. Nakashima, K. Shinzawa-Itoh, K. Watanabe, K. Naoki, N. Hano, S. Yoshikawa, Steady-state kinetics of NADH:coenzyme Q oxidoreductase isolated from bovine heart mitochondria, *J. Bioenerg. Biomembr.* 34 (2002) 11–19.
- [40] A.D. Vinogradov, V.G. Grivennikova, Generation of superoxide-radical by the NADH:ubiquinone oxidoreductase of heart mitochondria, *Biochemistry (Mosc)* 70 (2005) 120–127.
- [41] S. Dröse, A. Galkin, U. Brandt, Proton pumping by complex I (NADH:ubiquinone oxidoreductase) from *Yarrowia lipolytica* reconstituted into proteoliposomes, *Biochim. Biophys. Acta* 1710 (2005) 87–95.
- [42] M. Candela, E. Zaccherini, D. Zannoni, Respiratory electron transport and light-induced energy transduction in membranes from the aerobic photosynthetic bacterium *Roseobacter denitrificans*, *Arch. Microbiol.* 175 (2001) 168–177.
- [43] A. Galkin, U. Brandt, Superoxide radical formation by pure complex I (NADH:ubiquinone oxidoreductase) from *Yarrowia lipolytica*, *J. Biol. Chem.* 280 (2005) 30129–30135.
- [44] F.A. Rotsaert, M.G. Ding, B.L. Trumpower, Differential efficacy of inhibition of mitochondrial and bacterial cytochrome bc₁ complexes by center N inhibitors antimycin, ilicicolin H and funiculosin, *Biochim. Biophys. Acta* 1777 (2008) 211–219.
- [45] D. Guo, T. Nguyen, M. Oghi, H. Tawfik, G. Ma, Q. Yu, R.W. Caldwell, J.A. Johnson, Protein kinase C-epsilon coimmunoprecipitates with cytochrome oxidase subunit IV and is associated with improved cytochrome-c oxidase activity and cardioprotection, *Am. J. Physiol. Heart Circ. Physiol.* 293 (2007) H2219–H2230.
- [46] T. Sugio, M. Fujii, Y. Ninomiya, T. Kanao, A. Negishi, F. Takeuchi, Reduction of Hg²⁺ with reduced mammalian cytochrome c by cytochrome c oxidase purified from a mercury-resistant *Acidithiobacillus ferrooxidans* strain, MON-1, *Biosci. Biotechnol. Biochem.* 72 (2008) 1756–1763.
- [47] S. Dröse, K. Zwicker, U. Brandt, Full recovery of the NADH:ubiquinone activity of complex I (NADH:ubiquinone oxidoreductase) from *Yarrowia lipolytica* by the addition of phospholipids, *Biochim. Biophys. Acta* 1156 (2002) 65–72.
- [48] A.I. Nesvizhskii, A. Keller, E. Kolker, R. Aebersold, A statistical model for identifying proteins by tandem mass spectrometry, *Anal. Chem.* 75 (2003) 4646–4658.
- [49] M. Ashburner, C.A. Ball, J.A. Blake, D. Botstein, H. Butler, J.M. Cherry, A.P. Davis, K. Dolinski, S.S. Dwight, J.T. Eppig, M.A. Harris, D.P. Hill, L. Issel-Tarver, A. Kasarskis, S. Lewis, J.C. Matese, J.E. Richardson, M. Ringwald, G.M. Rubin, G. Sherlock, Gene ontology: tool for the unification of biology. The Gene Ontology Consortium, *Nat. Genet.* 25 (2000) 25–29.
- [50] O.H. Lowry, N.J. Rosebrough, A.L. Rarr, R.J. Randall, Protein measurement with the Folin-phenol reagent, *J. Biol. Chem.* 193 (1951) 265–275.
- [51] S. Kim, T.-J. Jeon, A. Oberai, D. Yang, J.J. Schmidt, J.U. Bowie, Transmembrane glycine zippers: physiological and pathological roles in membrane proteins, *Proc. Natl. Acad. Sci. U. S. A.* 102 (2005) 14278–14283.
- [52] T. Althoff, D.J. Mills, J.-L. Popot, W. Kühlbrandt, Arrangement of electron transport chain components in bovine mitochondrial supercomplex I₁III₂IV₁, *EMBO J.* 30 (2011) 4652–4664.
- [53] J. Heinemeyer, H.-P. Braun, E.J. Boekema, R. Kouril, A structural model of the cytochrome c reductase/oxidase supercomplex from yeast mitochondria, *J. Biol. Chem.* 282 (2007) 12240–12248.
- [54] A. Nyola, C. Hunte, A structural analysis of the transient interaction between the cytochrome bc₁ complex and its substrate cytochrome c, *Biochem. Soc. Trans.* 36 (2008) 981–985.
- [55] M. Castellani, R. Covian, T. Kleinschroth, O. Anderka, B. Ludwig, B.L. Trumpower, Direct demonstration of half-of-the-sites reactivity in the dimeric cytochrome bc₁ complex. Enzyme with one inactive monomer is fully active but unable to activate the second ubiquinol oxidation site in response to ligand binding at the ubiquinone reduction site, *J. Biol. Chem.* 285 (2010) 502–510.
- [56] J.N. Blaza, R. Serreli, A.J.Y. Jones, K. Mohammed, J. Hirst, Kinetic evidence against partitioning of the ubiquinone pool and the catalytic relevance of respiratory-chain supercomplexes, *Proc. Natl. Acad. Sci. U. S. A.* 111 (2014) 15735–15740.
- [57] K.M. Davies, T.B. Bluma, W. Kühlbrandt, Conserved in situ arrangement of complex I and III₂ in mitochondrial respiratory chain supercomplexes of mammals, yeast, and plants, *Proc. Natl. Acad. Sci. U. S. A.* 115 (2018) 3024–3029.
- [58] T.M. Allison, F.C. Cochrane, G.B. Jameson, E.J. Parker, Examining the role of intersubunit contacts in catalysis by 3-deoxy-d-manno-octulosonate 8-phosphate synthase, *Biochemistry*. 52 (2013) 4676–4686.
- [59] D.A. Cisnerosa, G.M. Montero-Moran, S. Lara-Gonzalez, M.L. Calcagno, Inversion of the allosteric response of *Escherichia coli* glucosamine-6-P deaminase to N-acetylglucosamine 6-P, by single amino acid replacements, *Arch. Biochem. Biophys.* 421 (2004) 77–84.
- [60] A. Waletko, K. Zwicker, A. Abdrakmanova, V. Zickermann, U. Brandt, S. Kersch, Histidine 129 in the 75-kDa subunit of mitochondrial complex I from *Yarrowia lipolytica* is not a ligand for [Fe4S4] cluster N5 but is required for catalytic activity, *J. Biol. Chem.* 280 (2005) 5622–5625.
- [61] K. Shinzawa-Itoh, H. Shimomura, S. Yanagisawa, S. Shimada, R. Takahashi, M. Oosaki, T. Ogura, T. Tsukihara, Purification of active respiratory supercomplex from bovine heart mitochondria enables functional studies, *J. Biol. Chem.* 291 (2016) 4178–4184.
- [62] J.N. Blaza, K.R. Vinothkumar, J. Hirst, Structure of the deactive state of mammalian respiratory complex I, *Structure*. 26 (2018) 312–319.
- [63] E.T. Chouchani, V.R. Pell, E. Gaude, D. Akse, S.Y. Sundier, E.L. Robb, A. Logan, S.M. Nadtochiy, E.N.J. Ord, A.C. Smith, et al., Ischaemic accumulation of succinate controls reperfusion injury through mitochondrial ROS, *Nature*. 515 (2014) 431–435.
- [64] L.G. Nijtmans, S.M. Artal, L.A. Grivell, P.J. Coates, The mitochondrial PHB complex: roles in mitochondrial respiratory complex assembly, ageing and degenerative disease, *Cell. Mol. Life Sci.* 59 (2002) 143–155.
- [65] C. Jian, F. Xu, T. Hou, T. Sun, J. Li, H. Cheng, X. Wang, Deficiency of PHB complex impairs respiratory supercomplex formation and activates mitochondrial flashes, *J. Cell Sci.* 130 (2017) 2620–2630.
- [66] V. Strogolova, A. Furness, M. Robb-McGrath, J. Garlich, R.A. Stuart, Rcf1 and Rcf2, members of the hypoxia-induced gene 1 protein family, are critical components of the mitochondrial cytochrome bc₁-cytochrome c oxidase supercomplex, *Mol. Cell. Biol.* 32 (2012) 1363–1373.
- [67] M. Vukotic, S. Oeljeklaus, S. Wiese, F.N. Vogtle, C. Meisinger, H.E. Meyer, A. Ziesenis, D.M. Katschinski, D.C. Jans, S. Jakobs, B. Warscheid, P. Rehling, M. Deckers, Rcf1 mediates cytochrome oxidase assembly and respirasome formation, revealing heterogeneity of the enzyme complex, *Cell Metab.* 15 (2012) 336–347.
- [68] R. Rab, V. Soubannier, R. Scholz, F. Vogel, N. Mendl, A. Vasiljev-Neumeyer, C. Körner, R. Jagasia, T. Keil, W. Baumeister, M. Cyrklaff, W. Neupert, A.S. Reichert, Formation of cristae and crista junctions in mitochondria depends on antagonism between Fcjl1 and Su e/g, *J. Cell Biol.* 185 (2009) 1047–1063.
- [69] O. Puchta, M. Lubas, K.A. Lipinski, J. Piatkowski, M.M.P. Golik, DMR1 (CCM1/YGR150C) of *Saccharomyces cerevisiae* encodes an RNA-binding protein from the pentatricopeptide repeat family required for the maintenance of the mitochondrial 15S ribosomal RNA, *Genetics*. 184 (2010) 959–973.
- [70] J.P. Mayorga, Y. Camacho-Villasana, M. Shingú-Vázquez, R. García-Villegas, A. Zamudio-Ochoa, A.E. García-Guerrero, G. Hernández, X. Pérez-Martínez, A novel function of Pet54 in regulation of cox1 synthesis in *Saccharomyces cerevisiae* mitochondria, *J. Biol. Chem.* 291 (2016) 9343–9355.

© 2019 Universidad Nacional Autónoma de México, Facultad de Estudios Superiores Zaragoza.

Este es un artículo Open Access bajo la licencia CC BY-NC-ND (<http://creativecommons.org/licenses/by-nc-nd/4.0/>).

TIP Revista Especializada en Ciencias Químico-Biológicas, 22: 1-9, 2019.

DOI: [10.22201/fesz.23958723e](https://doi.org/10.22201/fesz.23958723e).

Aspectos generales del transporte de colesterol en la esteroidogénesis de la placenta humana

Sofía Olvera-Sánchez, Mercedes Esparza-Perusquía,
Oscar Flores-Herrera, Viviana A. Urban-Sosa y Federico Martínez*

Departamento de Bioquímica, Facultad de Medicina, Universidad Nacional Autónoma de México, Alcaldía de Coyoacán, 04510, Ciudad de México, México. E-mail: *fedem@bq.unam.mx

RESUMEN

La placenta humana requiere de colesterol para sintetizar la progesterona que mantiene la relación entre el feto y la madre, lo que le permite concluir de manera exitosa el embarazo. La placenta incorpora el colesterol principalmente a través de las lipoproteínas de baja densidad (LDL) que se obtienen del torrente circulatorio materno por un mecanismo de endocitosis. A los endosomas que se generan en este proceso se les unen varias proteínas conformando los endosomas tardíos, que degradan las LDL y liberan el colesterol a las mitocondrias del sincitiotrofoblasto que lo transforman en pregnenolona y posteriormente en progesterona. Las proteínas de fusión de membranas denominados complejos SNARE participan en la liberación del colesterol en sitios de contacto específicos en donde se localizan las proteínas mitocondriales responsables de la esteroidogénesis.

Palabras Clave: placenta humana, receptores de lipoproteínas, mitocondrias, transporte de colesterol, esteroidogénesis, sitios de contacto.

General aspects of cholesterol transport in the steroidogenesis of the human placenta

ABSTRACT

The human placenta requires cholesterol to synthesize the progesterone that maintains the relationship between the fetus and the mother, which allows it to successfully conclude pregnancy. The placenta incorporates cholesterol through the LDL obtained from the maternal blood stream by a mechanism of endocytosis. Endosomes formed by this process degrade the LDL, bind several proteins forming the late endosomes and releasing the cholesterol to syncytiotrophoblast mitochondria to transform it into pregnenolone and then, into progesterone. The soluble attachment proteins denominated SNARE participates in the transport of cholesterol in specific contact sites where the mitochondrial proteins responsible for steroidogenesis are located.

Key Words: human placenta, lipoprotein receptors, mitochondria, cholesterol transport, steroidogenesis, contact sites.

INTRODUCCIÓN

La placenta humana tiene un papel primordial al establecer mecanismos de comunicación entre el feto y la madre durante el embarazo. En este proceso, la progesterona adquiere un papel central al favorecer la implantación del blastocisto, la remodelación de la matriz extracelular y la promoción de la migración del trofoblasto (Halasz & Szekeres-Bartho, 2013). Además, la síntesis de progesterona se incrementa conforme avanza el embarazo (Morel *et al.*, 2016). Estas funciones garantizan que el producto alcance la madurez que le permita vivir fuera del vientre materno (Burton & Fowden, 2015; Vaughan & Fowden, 2016; Ashary, Tiwari & Modi, 2018).

La placenta es un órgano excepcional capaz de realizar de manera simultánea las funciones de diferentes tejidos, por ejemplo: sintetiza hormonas como las glándulas endocrinas, realiza el intercambio gaseoso como en los pulmones y filtra metabolitos como en los riñones, entre otras funciones (Chatuphonprasert, Jarukamjorn & Ellinger, 2018). A pesar del papel que desempeña la placenta, hasta el momento no se conocen con certeza los mecanismos maternos o fetales que la controlan, aunque se han sugerido posibles señales autocrinas, paracrinas o intracrinas. El linaje celular funcional de la placenta es el trofoblasto, que se divide en cito y sinciotrofoblasto, este último es responsable del transporte de nutrientes y desechos al estar en contacto con las lagunas maternas y al mismo tiempo, el responsable del metabolismo esteroideogénico (en este artículo se considera la esteroideogénesis como la transformación del colesterol en progesterona). Si bien no se conocen varios aspectos del control del metabolismo placentario, lo que sí es claro es que la placenta humana tiene un papel central en las funciones del embarazo (Byrns, 2014), para mantener la relación materno-fetal al sintetizar cantidades elevadas de progesterona, una hormona esteroide que se produce en las mitocondrias del sinciotrofoblasto y que regula, entre otras funciones, los procesos inmunológicos que evitan que el producto sea rechazado, ya que la carencia o disminución de progesterona podría provocar un aborto (Holland *et al.*, 2017a).

Se ha demostrado que los explantes de la placenta humana (pequeños fragmentos que contienen a las células del trofoblasto), son resistentes a condiciones físicas no fisiológicas que un tejido “normal” no podría soportar. Por ejemplo, luego de la incubación en un medio hipotónico o a temperaturas superiores a los 45°C, los explantes realizan todas sus funciones metabólicas, incluyendo la síntesis de progesterona, de manera similar a los explantes que no fueron expuestos a estos tratamientos. Los resultados muestran que la placenta humana contiene mecanismos de autopreservación y como estrategia fisiológica, un control metabólico y funcional independiente a los estímulos externos que desarrolló como

una forma para proteger al producto (Paul, Jailkhani & Talwar, 1978, Paul, Gupta, Jailkhani & Talwar, 1980). En este sentido, se ha reportado que las mitocondrias de la placenta se adaptan de acuerdo con el avance del embarazo (Holland *et al.*, 2017b). Por otro lado, aunque existen abundantes evidencias del metabolismo energético, aún falta mucho por conocer del funcionamiento de la placenta en el ser humano (Kaiser, 2014; Bianco-Miotto *et al.*, 2016).

RECEPTORES A LIPOPROTEÍNAS

Para la síntesis de progesterona es necesario el colesterol; sin embargo, debido a que la placenta no tiene la maquinaria para sintetizar las cantidades de colesterol que se requieren para la producción diaria de progesterona (van Leusden & Vिलlee, 1965; Zelewski & Vилlee 1966), éste es proporcionado por las lipoproteínas maternas a través de los receptores específicos del sinciotrofoblasto. En las células del trofoblasto se ha descrito la presencia de varios tipos de receptores para las lipoproteínas, como el de las lipoproteínas de baja densidad (LDL) que son los que se expresan de manera principal (Winkel, Snyder, MacDonald & Simpson, 1980; Furuhashi *et al.*, 1989; Chatuphonprasert *et al.*, 2018). Las lipoproteínas de alta densidad (HDL) se han identificado en las células del trofoblasto (Wadsack *et al.*, 2003), en las células BeWo (Pagler *et al.*, 2006) y en varios tejidos esteroideogénicos. Sin embargo, a diferencia de las LDL, las HDL se procesan por una vía diferente a la lisosomal (Sanderson, 2009).

Debido a que la síntesis de progesterona está sujeta a la capacidad de incorporar el colesterol de las LDL (Figura 1), se determinó que la concentración de los receptores para las lipoproteínas está regulada por la presencia de las mismas LDL. En células aisladas del trofoblasto y mantenidas en cultivo, la incubación con LDL¹²⁵ por tiempos largos, disminuyó cerca del 90% la captación y degradación de las LDL, lo que sugiere que las células del trofoblasto pueden regular el número de receptores de las LDL en la membrana plasmática. Este efecto no se observó cuando las células se incubaron en presencia de HDL (Winkel, MacDonald & Simpson, 1981). Sin embargo, datos recientes sugieren que la placenta usa tanto las LDL como las HDL para obtener el colesterol necesario para la síntesis de progesterona (Sanderson, 2009). La capacidad de la placenta de emplear ambas lipoproteínas asegura que el aporte de colesterol sea constante para mantener la esteroideogénesis, aun en condiciones que puedan afectar la concentración de cualquiera de éstas, asegurando así que el embarazo no esté en riesgo.

El aporte del colesterol materno no se usa tan solo para la producción de progesterona, ya que también se requiere para satisfacer las necesidades del desarrollo del feto en crecimiento (Woollett, 2011; Bartels & O'Donoghue, 2011; Bhattacharjee *et al.*, 2012; Baardman *et al.*, 2013).

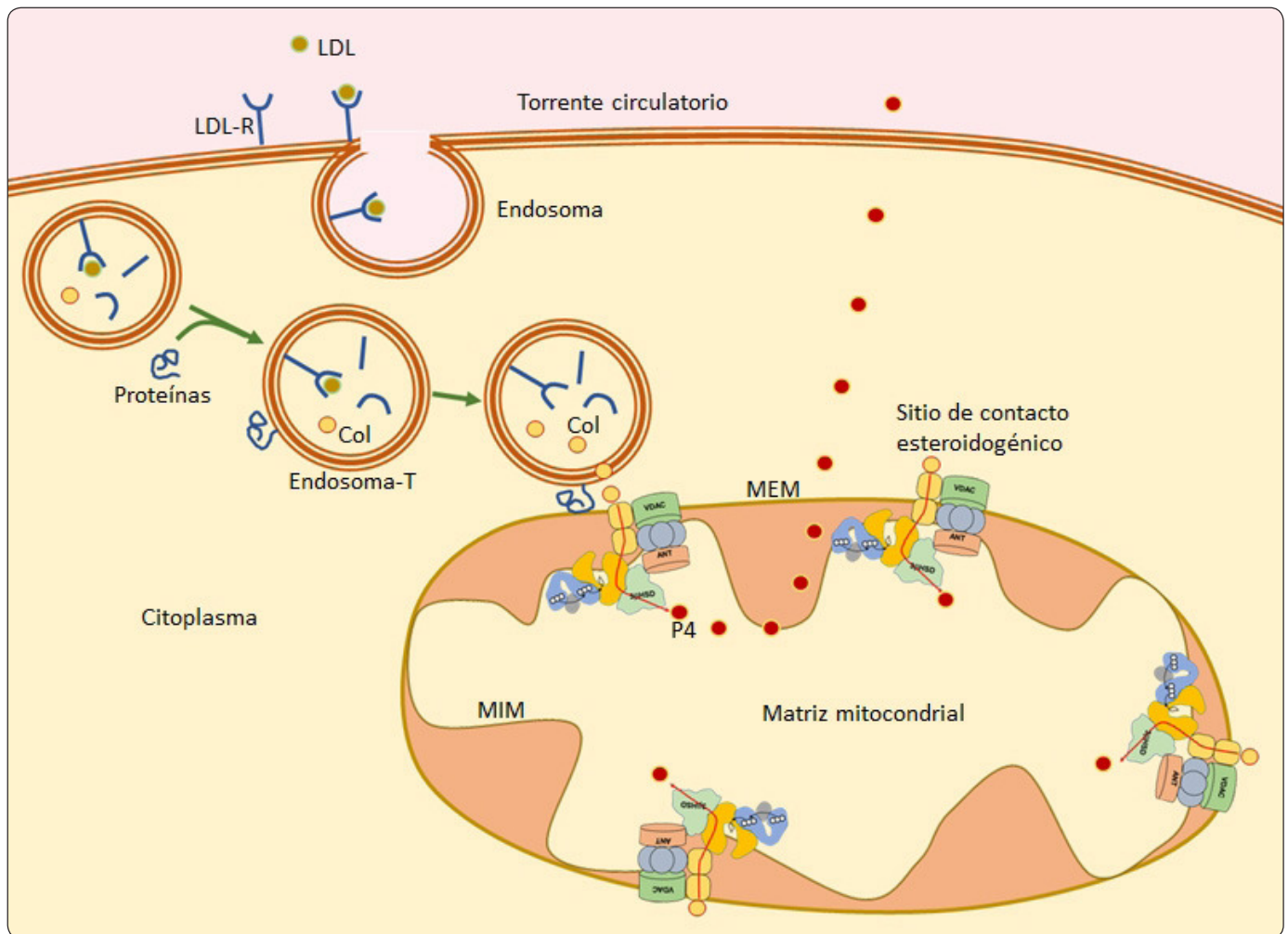


Figura 1. Esquema de transporte del colesterol en el torrente circulatorio materno a las mitocondrias de las células de la placenta humana. Las LDL maternas se asocian a los receptores de las LDL (LDL-R) que son endocitadas conformando el endosoma, en donde el colesterol se libera de las LDL. Posteriormente, se asocian proteínas para constituir el endosoma tardío (Endosoma-T) que permite su asociación a la membrana externa mitocondrial (MEM), en donde se encuentran los sitios de contacto esteroidogénicos. En estos sitios se realiza el transporte de colesterol que ingresa a la membrana interna en donde se localiza la cadena del citocromo P450 para su transformación en pregnenolona (P5) y posteriormente a progesterona (P4). Una vez sintetizada la P4, ésta se libera al torrente circulatorio para mantener la relación materno-fetal. Figura elaborada por los autores.

TEJIDOS ESTEROIDOGÉNICOS Y TRANSPORTE MITOCONDRIAL DEL COLESTEROL

Aunque el colesterol es una molécula hidrofóbica que las células requieren para varias funciones, su concentración es altamente regulada, ya que los cambios en las concentraciones pueden ser fatales para la viabilidad celular; como en el caso de la estabilidad de las membranas. Se ha descrito que, en las células de los mamíferos, la presencia de colesterol en el retículo endoplásmico es baja, pues su concentración corresponde al 5% de los fosfolípidos; sin embargo, en el aparato de Golgi su concentración es mayor al 30% (Mesmin, Antony & Drin, 2013). La mayoría del colesterol se localiza en la membrana plasmática, con un 60% del total del estero-

celular. Las diferencias en la concentración del colesterol en las membranas sugieren la existencia de un mecanismo de regulación celular mediado por al menos dos vías de transporte: vesículas y proteínas específicas (Flis & Daum, 2013).

En los tejidos esteroidogénicos, el transporte de colesterol al citocromo P450cc mitocondrial es relevante, ya que cuando se estimula la síntesis de pregnenolona, la primera hormona esteroide que se genera por la actividad de la cadena acoplada al P450cc, el transporte de colesterol hacia la mitocondria deber ser vectorial, eficiente y en la concentración necesaria para dar respuesta a las necesidades celulares y sin alterar sus funciones (Chien, Rosal & Chung, 2017).

Dentro de las vías de transporte del colesterol celular, se ha descrito una familia de proteínas denominadas STARD, con capacidad de unir al colesterol y participar en su distribución intracelular (Alpy *et al.*, 2013). Estas proteínas se asocian a complejos multiproteicos específicos que aseguran la precisa distribución del estero. Aunado a esto, se han descrito asociaciones entre las membranas de los diferentes organelos celulares (ver más adelante), conformados por transportadores, enzimas y proteínas de andamiaje (Mesmin, Antonny & Drin, 2013), formando microdominios entre las membranas denominados sitios de contacto (Poderoso *et al.*, 2013; Soffientini & Graham, 2016).

Se han descrito varios tipos de sitios de contacto, por ejemplo, las membranas asociadas a las mitocondrias (mitochondria-associated ER membrane, MAMs), que son un microdominio de asociación entre el retículo endoplásmico (RE) y las mitocondrias. Es importante destacar que la mitocondria tiene un papel relevante en el proceso esteroideogénico, ya que es ahí en donde reside la transformación del colesterol en pregnenolona (Papadopoulos & Miller, 2012), además de participar en otros procesos (Tait & Green, 2012), como la síntesis de ATP, señalización intracrina, la apoptosis, la inmunidad innata, la autofagia o la respuesta al estrés (Galluzzi, Kepp & Kroemer, 2012). Este tipo de microdominios se ha sugerido que contribuye al transporte de diferentes lípidos entre las membranas celulares.

En la esteroideogénesis, parecen conjuntarse un sistema mediado por vesículas y otro por proteínas. Dentro del sistema proteico, se ha descrito a la STARD1 como la principal proteína que participa en la esteroideogénesis de gónadas y glándulas suprarrenales. Se ha demostrado que la STARD1 transfiere colesterol eficientemente a la mitocondria (Tuckey, Headlam, Bose & Miller, 2002) y que su interacción con el colesterol induce un cambio conformacional de su estructura nativa a glóbulo fundido ('moltenglobule'), que se ha sugerido como un estado dinámico que permite la transferencia del estero (Rajapaksha, Kaur, Bose, Whittal & Bose, 2013). En la interacción de la STARD1 con la mitocondria durante el transporte del colesterol se han reportado complejos multiproteicos formados por un grupo de diversas proteínas entre las que se encuentran la VDAC (Bose, Whittal, Miller & Bose, 2008; Prasad *et al.*, 2015), el receptor σ -1 (Marriott, Prasad, Thapliyal & Bose, 2012) y la ATPasa ATAD3 (Issop *et al.*, 2015), por mencionar algunas. En este sentido, los complejos multiproteicos a su vez pueden interaccionar con elementos proteicos del retículo endoplásmico, con gotas lipídicas o endosomas tardíos (Beller, Thiel, Thul & Jäckle, 2010; Yang, Galea, Sytnyk & Crossley, 2012).

Aunque hay un gran flujo de colesterol en los tejidos esteroideogénicos de regulación aguda, en las mitocondrias la cantidad de colesterol es baja (Horvath & Daum, 2013);

sin embargo, en las mitocondrias de la placenta humana los niveles de colesterol son altos, semejantes incluso a los de la membrana plasmática (Navarrete, Flores-Herrera, Uribe & Martínez, 1999). Esto adquiere relevancia, ya que hasta el momento no se han descrito moduladores de la esteroideogénesis placentaria; sin embargo, esta característica habla de un transporte permanente de colesterol que permite mantener una producción de progesterona de manera sostenida durante el embarazo.

Una vez que el colesterol ha sido transportado a la membrana externa mitocondrial, éste debe continuar su tránsito hasta la membrana interna donde se encuentra el citocromo P450_{scc} para ser transformado en pregnenolona (Martínez & Strauss, 1997). Esto sugiere que un paso limitante en la esteroideogénesis podría ser la transferencia de colesterol de la membrana externa a la interna mitocondrial. Se ha reportado que para el transporte de colesterol entre las membranas mitocondriales se requiere de los sitios de contacto (Strauss, Kishida, Christenson, Fujimoto & Hiroi, 2003; Miller & Bose, 2011).

No obstante que la STARD1 es la principal proteína asociada al flujo de colesterol hacia la mitocondria y descrita para diferentes tejidos esteroideogénicos de regulación aguda, la placenta humana no la expresa (Miller, 2013). Sin embargo, la placenta sintetiza entre 250 y 500 mg de progesterona al día durante el último trimestre del embarazo (Simpson & MacDonald, 1981; LaVoie & King, 2009); esto implica un flujo continuo de colesterol hacia la mitocondria. En la última década se identificó en las células del sincitiotrofoblasto a la proteína STARD3 (Watari *et al.*, 1997), descrita originalmente en un tumor de mama, la cual presenta el dominio START de unión al colesterol característico de esta familia de proteínas.

La STARD3 es una proteína endosomal con 4 segmentos transmembranales en su extremo amino terminal (dominio MENTAL). Alpy & Tomasetto (2014), reportaron que, aunque la STARD1 y STARD3 presentan un dominio START y comparten ciertas propiedades bioquímicas, también son diferentes en varios aspectos, que van desde su localización hasta su estructura (van der Kant, Zondervan, Janssen & Neeffjes, 2013) demostraron que los endosomas tardíos y los lisosomas contienen la mitad del colesterol celular y que de ellos depende su distribución. También observaron que hay dos tipos de endosomas tardíos, uno presenta a la proteína ORP1L que transporta oxisteroles y otro contiene a la STARD3 y a la ABCA3 (una proteína transportadora que usa ATP para la translocación de sustratos, incluyendo lípidos), (van der Kant, Zondervan, Janssen & Neeffjes, 2013). Esto les permitió sugerir que la STARD3 facilita el flujo de colesterol de los endosomas tardíos a la mitocondria, constituyendo un tipo de transporte vesicular. De igual manera, se ha descrito que la STARD3 requiere de los aminoácidos M307 y N311

para unir al colesterol (van der Kant, Zondervan, Janssen & Neefjes, 2013). Asimismo, construyeron el knock-out del gen que codifica para la STARD3 y observaron que no se eliminó de manera total la síntesis de progesterona, sugiriendo que el transporte de colesterol mediado por la STARD3 no es el único camino que emplea la placenta humana para mantener la esteroidogénesis (van der Kant, Zondervan, Janssen & Neefjes, 2013). En el laboratorio, hemos determinado que la proteína HSP60 comparte epítopes con la STARD3 y que su presencia induce el incremento en la síntesis de progesterona de las mitocondrias del sincitiotrofoblasto (Olvera-Sánchez, Espinosa-García, Monreal, Flores-Herrera & Martínez, 2011). Recientemente se determinó que la HSP60 participa junto con la MLN64 en el transporte de colesterol para llevar a cabo la esteroidogénesis en la placenta humana (Monreal-Flores, Espinosa-García, García-Regalado, Arechavaleta-Velasco & Martínez, 2017).

Se han descrito complejos multiproteicos responsables de conducir el colesterol hasta el P450_{scc}, entre los que se encuentra el transduceosoma, compuesto de diversas proteínas membranales y citoplasmáticas y el metabolón esteroidogénico descrito como un conjunto de proteínas de las membranas mitocondriales (Fan & Papadopoulos, 2013). Al respecto, se reportó que la STARD3 es capaz de generar puntos de contacto entre el RE y los endosomas, como un paso previo al transporte de colesterol a las mitocondrias (Alpy *et al.*, 2013) y un mecanismo particular para la esteroidogénesis de la placenta humana (Tuckey, Bose, Czerwionka & Miller, 2004; Martin, Kennedy & Karten, 2014).

En su conjunto, la información muestra que de manera general el transporte de colesterol para la esteroidogénesis requiere de múltiples sistemas que involucran proteínas como la STARD1 y la STARD3, los endosomas tardíos, las gotas lipídicas, el citoesqueleto y los elementos MAMs, MINOS (mitochondrial inner membrane organizing system) y MCSs (mitochondrial contact sites), así como los sitios de contacto entre las membranas mitocondriales para realizar con éxito el flujo de colesterol y su transformación en pregnenolona en los tejidos esteroidogénicos de regulación aguda y en progesterona en el caso de la placenta humana, un tejido de regulación crónica.

SITIOS DE CONTACTO ENTRE LAS MEMBRANAS MITOCONDRIALES

Hackenbrock & Miller (1975), describieron por primera vez que las mitocondrias poseen diferentes tipos de sitios de contacto y que son complejos multienzimáticos que realizan diferentes funciones mitocondriales. Su formación se lleva a cabo mediante un proceso dinámico que requiere de la asociación de proteínas y enzimas específicas.

Para la fosforilación oxidativa se ha descrito la asociación de varias proteínas, entre las cuales están el acarreador de

los adenín-nucleótidos (ANT), la porina o el canal aniónico dependiente del voltaje (VDAC), la creatina cinasa y la hexocinasa, entre otros (Adams, Bosch, Schelege, Wallimann & Brdiczka, 1989; Papadopoulos, 1993). En la apoptosis, se asocian proteínas como el ANT, la VDAC, la ciclofilina D y la hexocinasa II. Además, la membrana externa posee proteínas que pueden establecer, junto con la actina, uniones dependientes de ATP y proteínas antiapoptóticas de la familia Bcl-2, cuya sobreexpresión tiene como consecuencia el bloqueo de la apoptosis (Adams & Cory, 2001; Suen, Norris & Youle, 2008). Otro ejemplo es el poro de la transición de la permeabilidad (Rasola & Bernardi, 2014), que es un complejo multiproteico que forma poros no selectivos en la membrana interna y que tiene los siguientes componentes estructurales: el ANT, la ciclofilina D, y el VDAC. Adicionalmente, se ha identificado al translocador de proteínas (TPSO, antes conocido como el receptor periférico a benzodiazepinas) unido al poro en la membrana externa, la creatina cinasa en el espacio intermembranal y la hexocinasa II ligadas a la VDAC en la cara citosólica de la membrana externa, así como las proteínas Bax/Bcl-2 (Zanzami & Kroemer, 2001).

Finalmente se ha sugerido que para la esteroidogénesis en las glándulas suprarrenales y gónadas existe un punto de contacto específico, compuesto de un octámero de la creatina cinasa (CK), el VDAC, la TPSO y el ANT, además del IP3R (ER-resident inositol triphosphate receptor), la Mfn2 y la Mfn1 (mitofusina 1 y 2), entre otras (Martin, Kennedy & Karten, 2014). La asociación de las proteínas de la membrana externa como VDAC1 y TPSO con las proteínas de la familia de las ATPasas (ATAD3a) en la membrana interna, forman el núcleo de un complejo que regula la importación del colesterol mitocondrial (Issop *et al.*, 2015). Datos recientes sugieren que la TPSO, aunque forma parte del sitio de contacto, no es indispensable para el transporte del colesterol (Tu *et al.*, 2014; Morohaku *et al.*, 2014). Adicionalmente, se ha descrito que la asociación entre las proteínas Tom22, Tim23, Tim 50, y la β HSD2 puede repercutir en la esteroidogénesis (Pawlak, Prasad, Thomas, Whittal & Bose, 2011; Rajapaksha *et al.*, 2016).

Nuestro grupo de trabajo sugirió un modelo para la participación de la STARD3 en las mitocondrias de la placenta humana (Esparza-Perusquía *et al.*, 2015) donde se propone que las gotas lipídicas contienen proteínas constituyentes de los complejos de fusión de membranas denominados SNARE (soluble N-ethylmaleimide-sensitive factor attachment protein receptor), entre las que incluyen las α -SNAP, syntaxina 3, 7 y 12, syntaxina-Binding Protein-2, syntaxina-Binding Protein-3, y VAMP-8, que podrían estar participando en el transporte del colesterol en las mitocondrias de la placenta humana. Se ha demostrado que la proteína SNAP promueve la interacción entre las gotas de lípidos y las mitocondrias, y que en las células esteroidogénicas las

SNARE se expresan como Syntaxina-17, SNAP-23 y SNAP-25 (Grant *et al.*, 1999; Steegmaier, Oorschot, Klumperman & Scheller, 2000; Jägerström *et al.*, 2009). Estas observaciones sugieren que las proteínas SNARE podrían contribuir en el mecanismo de transporte del colesterol a las mitocondrias esteroidogénicas, muy probablemente mediante la promoción de la interacción funcional entre las gotas de lípidos, el retículo endoplásmico, los endosomas y las mitocondrias. En las células del sincitiotrofoblasto, la proteína STARD3 puede ser incorporada en las mitocondrias a través de estos complejos y ser transformada a su forma activa por proteasas mitocondriales (Esparza-Perusquía *et al.*, 2015), favoreciendo su incorporación o participación en los sitios de contacto (Uribe, Strauss & Martínez, 2003; Miller & Bose 2011) y promover el transporte del colesterol para la síntesis de la progesterona (Strauss, Kishida, Christenson, Fujimoto & Hiroi, 2003).

AGRADECIMIENTOS

Parte de este trabajo fue apoyado por el programa PAPIIT de la UNAM con los proyectos IN211912, IN211715, IN215518 y IN222617 y del proyecto 168025 de CONACYT.

REFERENCIAS

- Adams, J.M. & Cory, S. (2001). Life-or-death decisions by the Bcl-2 protein family. *Trends Biochem. Sci.*, **26**, 61-66. DOI: 10.1016/S0968-0004(00)01740-0.
- Adams, V., Bosch, W., Schelege, J., Wallimann, T. & Brdiczka, D. (1989). Further characterization of contact sites from mitochondria of different tissues: topology of peripheral kinases. *Biochim. Biophys. Acta*, **981(2)**, 213-225. DOI: 10.1016/0005-2736(89)90031-X.
- Alpy, F. & Tomasetto, C. (2014). START ships lipids across interorganelle space. *Biochimie*, **96**, 85-95. DOI: 10.1016/j.biochi.2013.09.015.
- Alpy, F., Rousseau, A., Schwab, Y., Legueux, F., Stoll, I., Wendling, C., Spiegelhalter, C., Kessler, P., Mathelin, C., Rio, M.C., Levine, T.P. & Tomasetto, C. (2013). STARD3 or STARD3NL and VAP form a novel molecular tether between late endosomes and the ER. *J. Cell Sci.*, **126**, 5500-5512. DOI: 10.1242/jcs.139295.
- Ashary, N., Tiwari, A. & Modi, D. (2018). Embryo Implantation: Warin times of love. *Endocrinology*, **159**, 1188-1198. DOI: 10.1210/en.2017-03082.
- Baardman, M.E., Kerstjens-Frederikse, W.S., Berger, R.M.F., Bakker, M.K., Hofstra, R.M.W. & Plösch, T. (2013). The role of maternal-fetal cholesterol transport in early fetal life: current insights. *Biol. Reprod.*, **88(24)**, 1-9. DOI: 10.1095/biolreprod.112.102442.
- Bartels, A. & O'Donoghue, K. (2011). Cholesterol in pregnancy: a review of knowns and unknowns. *Obstet. Med.*, **4**, 147-151. DOI: 10.1258/om.2011.110003.
- Beller, M., Thiel, K., Thul, P.J. & Jäckle, H. (2010). Lipid droplets: A dynamic organelle moves into focus. *FEBS Lett*, **584**, 2176-82. DOI: 10.1016/j.febslet.2010.03.022.
- Bhattacharjee, J., Ietta, F., Romagnoli, R., Bechi, N., Caniggia, I. & Paulesu, L. (2012). *ABC transporters in human placenta and their role in maternal-fetal cholesterol transfer: ABCA1 candidate target*. En Jing Zheng (Ed.). *Recent Advances in Research on the Human Placenta* (pp. 336-354). London: IntechOpen. ISBN 978-953-51-0194-9 DOI: 10.5772/12111.
- Bianco-Miotto, T., Blundell, C., Buckberry, S., Chamley, L., Chong, S., Cottrell, E., Dawson, P., Hanna, C., Holland, O., Lewis, R.M., Moritz, K., Myatt, L., Perkins, A.V., Powell, T., Saffery, R., Sferruzzi-Perri, A., Sibley, C., Simmons, D. & O'Tierney-Ginn, P.F. (2016). IFPA meeting 2015 workshop report I: Placental mitochondrial function, transport systems and epigenetics. *Placenta*, **48**, Suppl. 1, Trophoblast Res., 30, S3-S6. DOI: 10.1016/j.placenta.2015.11.014.
- Bose, M., Whittal, R.M., Miller, W.L. & Bose, H.S. (2008). Steroidogenic activity of StAR requires contact with mitochondrial VDAC1 and phosphate carrier protein. *J. Biol. Chem.*, **283**, 8837-8845. DOI: 10.1074/jbc.M709221200.
- Burton, G.J. & Fowden, A.L. (2015). The placenta: a multifaceted, transient organ. *Phil. Trans. R. Soc. B*, **370**: 20140066. DOI: 10.1098/rstb.2014.0066.
- Byrns, M.C. (2014). Regulation of progesterone signaling during pregnancy: Implications for the use of progestins for the prevention of preterm birth. *J. Steroid Biochem. & Mol. Biol.*, **139**, 173-181. DOI: 10.1016/j.jsbmb.2013.01.015.
- Chatuphonprasert, W., Jarukamjorn, K. & Ellinger, I. (2018). Physiology and pathophysiology of steroid biosynthesis, transport and metabolism in the human placenta. *Front. Pharmacol.*, **9**, 1027. DOI: 10.3389/fphar.2018.01027.
- Chien, Y., Rosal, K. & Chung, B. (2017). Function of CYP11A1 in the mitochondria. *Mol. Cell Endocrinol.*, **441**, 55-61. DOI: 10.1016/j.mce.2016.10.030.
- Esparza-Perusquía, M., Olvera-Sánchez, S., Flores-Herrera, O., Flores-Herrera, H., Guevara-Flores, A., Pardo, J.P., Espinosa-García, M.T. & Martínez, F. (2015). Mitochondrial proteases act on STARD3 to activate progesterone synthesis in human syncytiotrophoblast. *Biochim. Biophys. Acta*, **1850(1)**, 107-117. DOI: 10.1016/j.bbagen.2014.10.009.
- Fan, J. & Papadopoulos, V. (2013). Evolutionary origin of the mitochondrial cholesterol transport machinery reveals a universal mechanism of steroid hormone biosynthesis in animals. *PLoS ONE*, **8**, e76701. DOI:10.1371/journal.pone.0076701.
- Flis, V.V. & Daum, G. (2013). Lipid transport between the endoplasmic reticulum and mitochondria. *Cold Spring Harb Perspect Biol.*, **5(6)**, pii: a013235. DOI: 10.1101/cshperspect.a013235.

- Furuhashi, M., Seo, H., Mizutani, S., Narita, O., Tomoda, Y. & Matsui, N. (1989). Expression of low density lipoprotein receptor gene in human placenta during pregnancy. *Mol. Endocrinol.*, **3**, 1252-6. DOI: 10.1210/mend-3-8-1252.
- Galluzzi, L., Kepp, O. & Kroemer, G. (2012). Mitochondria: master regulators of danger signalling. *Nat. Rev. Moll. Cell Biol.*, **13**, 780-788. DOI: 10.1038/nrm3479. *
- Grant, N.J., Hepp, R., Krause, W., Aunis, D., Oehme, P. & Langley, K. (1999). Differential expression of SNAP-25 isoforms and SNAP-23 in the adrenal gland. *J. Neurochem.*, **72(1)**, 363-372. DOI: 10.1046/j.1471-4159.1999.0720363.x.
- Hackenbrock, C.R. & Miller, K.J. (1975). The distribution of anionic sites on the surfaces of mitochondrial membranes. Visual probing with polycationic ferritin. *J. Cell. Biol.*, **65(3)**, 615-630. DOI: 10.1083/jcb.65.3.615.
- Halasz, M. & Szekeres-Bartho, J. (2013). The role of progesterone in implantation and trophoblast invasion. *J.Reprod. Immunol.*, **97**, 43– 50. DOI: 10.1016/j.jri.2012.10.011.
- Holland, O., Nitert, M.D., Gallo, L.A., Vejzovic, M., Fisher, J.J. & Perkins A.V. (2017a). Placental mitochondrial function and structure in gestational Disorders. *Placenta*, **54**, 2-9. DOI: 10.1016/j.placenta.2016.12.012.
- Holland, O.J., Hickey, A.J.J., Alvsaker, A., Moran, S., Hedges, C., Chamley, L.W. & Perkins, A.V. (2017b). Changes in mitochondrial respiration in the human placenta over gestation. *Placenta*, **57**, 102-112. DOI: 10.1016/j.placenta.2017.06.011.
- Horvath, S.E. & Daum, G. (2013). Lipids of mitochondria. *Prog. Lipid Res.*, **52**, 590-614. DOI: 10.1016/j.plipres.2013.07.002.
- Issop, L., Fan, J., Lee, S., Rone, M.B., Basu, K., Mui, J. & Papadopoulos, V. (2015). Mitochondria-associated membrane formation in hormone-stimulated Leydig cell steroidogenesis: Role of ATAD3. *Endocrinology*, **1**: 334-345. DOI: 10.1210/en.2014-1503.
- Jägerström, M.S., Polesie, S., Wickström, Y., Johansson, B.R., Schroder, H.D., Højlund, K. & Boström, P. (2009). Lipid droplets interact with mitochondria using SNAP23. *Cell Biol Int.*, **33(9)**, 934-940. DOI: 10.1016/j.cellbi.2009.06.011.
- Kaiser, J. (2014). Gearing up for a closer look at the human placenta. *Science*, **344(6188)**, 1073. DOI: 10.1126/science.344.6188.1073.
- LaVoie, H.A. & King, S.R. (2009). Transcriptional regulation of steroidogenic genes: STARD1, CYP11A1 and HSD3B. *Exp. Biol. Med. (Maywood)*, **234**, 880-907. DOI: 10.3181/0903-MR-97.
- Marriott, K.S., Prasad, M., Thapliyal, V. & Bose, H.S. (2012). σ -1 Receptor at the mitochondrial-associated endoplasmic reticulum membrane is responsible for mitochondrial metabolic regulation. *J. Pharmacol. Exp. Ther.*, **343**, 578-586. DOI: 10.1124/jpet.112.198168.
- Martin, L.A., Kennedy, B.E. & Karten, B. (2014). Mitochondrial cholesterol: mechanisms of import and effects on mitochondrial function. *J. Bioenerg. Biomembr.*, **48(2)**, 137-151. DOI: 10.1007/s10863-014-9592-6.
- Martínez, F. & Strauss, J.F. 3rd (1997). Regulation of mitochondrial cholesterol metabolism. *Subcell. Biochem.*, **28**, 205-234. PMID: 9090296.
- Mesmin, B., Antonny, B. & Drin, G. (2013). Insights into the mechanisms of sterol transport between organelles. *Cell. Mol. Life Sci.*, **70**, 3405–3421. DOI: 10.1007/s00018-012-1247-3.
- Miller, W.L. & Bose, H.S. (2011). Early steps in steroidogenesis: intracellular cholesterol trafficking. *J. Lipid Res.*, **52**, 2111-2135. DOI: 10.1194/jlr.R016675.
- Miller, W.L. (2013). Steroid hormone synthesis in mitochondria. *Mol. Cell Endocrinol.*, **379**, 62-73. DOI: 10.1016/j.mce.2013.04.014.
- Monreal-Flores, J., Espinosa-García, M.T., García-Regalado, A., Arechavaleta-Velasco, F. & Martínez, F. (2017). The heat shock protein 60 promotes progesterone synthesis in mitochondria of JEG-3 cells. *Reprod. Biol.*, **17**, 154-161. DOI: 10.1016/j.repbio.2017.04.001.
- Morel, Y., Roucher, F., Plotton, I., Goursaud, C., Tardy, V. & Mallet, D. (2016). Evolution of steroids during pregnancy: Maternal, placental and fetal synthesis. *Ann. Endocrinol. (Paris)*, **77(2)**, 82-89. DOI: 10.1016/j.ando.2016.04.023. 2016.
- Morohaku, K., Pelton, S.H., Daugherty, D.J., Butler, W.R., Deng, W. & Selvaraj, V. (2014). Translocator protein/peripheral benzodiazepine receptor is not required for steroid hormone biosynthesis. *Endocrinology*, **155(1)**, 89–97. DOI: 10.1210/en.2013-1556.
- Navarrete, J., Flores-Herrera, O., Uribe, A. & Martínez, F. (1999). Differences in cholesterol incorporation into mitochondria from hepatoma AS-30D and human term placenta. *Placenta*, **20(4)**, 285-291. DOI: 10.1053/plac.1998.0374.
- Olvera-Sánchez, S., Espinosa-García, M.T., Monreal, J., Flores-Herrera, O. & Martínez, F. (2011). Mitochondrial heat shock protein participates in placental steroidogenesis. *Placenta*, **32**, 222-229. DOI: 10.1016/j.placenta.2010.12.018.
- Pagler, T.A., Golsabahi, S., Doring, M., Rhode, S., Schutz, G.J., Pavelka, M., Wadsack, C., Gauster, M., Lohninger, A., Laggner, H., Strobl, W. & Stangl, H. (2006). A Chinese hamster ovarian cell line imports cholesterol by high density lipoprotein degradation. *J. Biol. Chem.*, **281**, 38159-38171. DOI: 10.1074/jbc.M603334200
- Papadopoulos, V. & Miller, W.L. (2012). Role of mitochondria in steroidogenesis. *Best Pract. Res. Clin. Endocrinol. Metab.*, **26(6)**, 771-790. DOI: 10.1016/j.beem.2012.05.002.
- Papadopoulos, V. (1993). Peripheral-type benzodiazepine/diazepam binding inhibitor receptor: biological role in

- steroidogenic cell function. *Endocr.Rev.*, **14**, 222-240. DOI: 10.1210/edrv-14-2-222.
- Paul, S., Gupta, P.D., Jaikhan, B.L. & Talwar, G.P. (1980). Resistance of human syncytiotrophoblast to hypotonic and thermal stress. *J. Reprod.Fertil.*, **58(1)**, 183-187. PMID: 7359476.
- Paul, S., Jaikhan, B.L. & Talwar, G.P. (1978). Isolation and functional maintenance in culture of syncytiotrophoblasts from human placenta. *Indian J. Exp. Biol.*, **16**, 1226-1235. PMID: 750412.
- Pawlak, K.J., Prasad, M., Thomas, J.L., Whittal, R.M. & Bose, H.S. (2011). Inner mitochondrial translocase Tim50 interacts with 3β -hydroxysteroid dehydrogenase type 2 to regulate adrenal and gonadal steroidogenesis. *J. Biol.Chem.*, **286(45)**, 39130-39140. DOI: 10.1074/jbc.M111.290031.
- Poderoso, C., Duarte, A., Cooke, M., Orlando, U., Gottifredi, V., Solano, A.R. Lemos, J.R. & Podestá, E.J. (2013). The spatial and temporal regulation of the hormonal signal. Role of mitochondria in the formation of a protein complex required for the activation of cholesterol transport and steroids synthesis. *Mol. Cell. Endocrinol.*, **371**, 26-33. DOI: 10.1016/j.mce.2012.12.024.
- Prasad, M., Kaur, J., Pawlak, K.J., Bose, M., Whittal, R.M. & Bose, H.S. (2015). Mitochondria associated ER-Membrane (MAM) regulates steroidogenic activity via StAR-VDAC2 interaction. *J. Biol. Chem.*, **290**, 2604-2616. DOI: 10.1074/jbc.M114.605808.
- Rajapaksha, M., Kaur, J., Bose, M., Whittal, R.M. & Bose, H.S. (2013). Cholesterol-mediated conformational changes in the steroidogenic acute regulatory protein are essential for steroidogenesis. *Biochemistry*, **52**, 7242-7253. DOI: 10.1021/bi401125v.
- Rajapaksha, M., Kaur, J., Prasad, M., Pawlak, K.J., Marshall, B., Perry, E.W., Whittal, R.M. & Bose, H.S. (2016). An outer mitochondrial translocase, Tom22, is crucial for inner mitochondrial steroidogenic regulation in adrenal and gonadal tissues. *Mol. Cell Biol.*, **36(6)**, 1032-1047. DOI: 10.1128/MB.01107-15;
- Rasola, A. & Bernardi, P. (2014). The mitochondrial permeability transition pore and its adaptive responses in tumor cells. *Cell Calcium*, **56(6)**, 437-445. DOI: 10.1016/j.ceca.2014.10.003.
- Sanderson, J.T. (2009). *Placental and Fetal Steroidogenesis Human*. En: Lafond, J. & Vaillancourt, C. (Ed.). *Embryogenesis: Methods and Protocols*. (pp. 127-136) Nueva York:HumanaPress. DOI 10.1007/978-1-60327-009-0 7.
- Simpson, E.R. & MacDonald, P.C. (1981). Endocrine physiology of the placenta. *Annu. Rev. Physiol.*, **43**, 163-188. DOI: 10.1146/annurev.ph.43.030181.001115
- Soffientini, U. & Graham, A. (2016). Intracellular cholesterol transport proteins: roles in health and disease. *Clin. Sci.*, **130**, 1843-1859 DOI: 10.1042/CS20160339
- Steggmaier, M., Oorschot, V., Klumperman, J. & Scheller, R.H. (2000). Syntaxin 17 is abundant in steroidogenic cells and implicated in smooth endoplasmic reticulum membrane dynamics. *Mol. Biol. Cell*, **11(8)**, 2719-2731. DOI: 10.1091/mbc.11.8.2719.
- Strauss, J.F.3rd, Kishida, T., Christenson, L.K., Fujimoto, T. & Hiroi, H. (2003). StAR domain proteins and the intracellular trafficking of cholesterol in steroidogenic cells. *Mol. Cell, Endocrinol.*, **202**, 59-65. DOI: 10.1016/S0303-7207(03)00063-7.
- Suen, D.F., Norris, K.L. & Youle, R.J. (2008). Mitochondrial dynamics and apoptosis. *Genes Dev.*, **22**, 1577-1590. DOI: 10.1101/gad.1658508.
- Tait, S.W. & Green, D.R. (2012). Mitochondria and cell signalling. *J. Cell Sci.*, **125**, 807-815. DOI: 10.1242/jcs.099234.
- Tu, L.N., Morohaku, K., Manna, P.R., Pelton, S.H., Butler, W.R., Stocco, D.M. & Selvaraj, V. (2014). Peripheral benzodiazepine receptor/translocator protein global knock-out mice are viable with no effects on steroid hormone biosynthesis. *J. Biol. Chem.*, **289**, 40, 27444-27454. DOI: 10.1074/jbc.M114.578286.
- Tuckey, R.C., Headlam, M.J, Bose, H.S. & Miller, W.L. (2002). Transfer of cholesterol between phospholipid vesicles mediated by the steroidogenic acute regulatory protein (StAR). *J. Biol. Chem.*, **277**, 47123-28. DOI: 10.1074/jbc.M206965200.
- Tuckey, R.C., Bose, H.S., Czerwionka, I. & Miller, W.L. (2004). Molten globule structure and steroidogenic activity of N-218 MLN64 in human placental mitochondria. *Endocrinology*, **145**, 1700-1707. DOI: 10.1210/en.2003-1034.
- Uribe, A. Strauss, J.F. 3rd & Martínez, F. (2003). Contact sites from human placental mitochondria: characterization and role in progesterone synthesis. *Arch. Biochem. Biophys.*, **413(2)**, 172-181. DOI: 10.1016/S0003-9861(03)00097-3.
- van der Kant, R., Zondervan, I., Janssen, L. & Neefjes, J. (2013). Cholesterol-binding molecules MLN64 and ORP1L mark distinct late endosomes with transporters ABCA3 and NPC1. *J. Lipid Res.*, **54**, 2153-2165. DOI: 10.1194/jlr.M037325
- van Leusden, H. & Vilee, C.A. (1965). The de novo synthesis of sterols and steroids -from acetate by preparations of human term placenta. *Steroids*, **6**, 31-45. DOI: 10.1016/0039-128X(65)90031-0.
- Vaughan, O.R. & Fowden, A.L. (2016). Placental metabolism: substrate requirements and the response to stress. *Reprod. Dom. Anim.*, **51 (Suppl. 2)**, 25-35. DOI: 10.1111/rda.12797.
- Wadsack, C., Hammer, A., Levak-Frank, S., Desoye, G., Kozarsky, K.F., Hirschmugl, B., Sattler, W. & Malle, E. (2003). Selective cholesteryl ester uptake from high density lipoprotein by human first trimester and term

- villous trophoblast cells. *Placenta*, **24**, 31-43. DOI: 10.1053/plac.2002.0912.
- Watari, H., Arakane, F., Moog-Lutz, C., Kallen, C.B., Tomasetto, C., Gerton, G.L., Rio, M.C., Baker, M.E. & Strauss, J.F. 3rd. (1997). MLN64 contains a domain with homology to the steroidogenic acute regulatory protein (StAR) that stimulates steroidogenesis. *Proc. Natl. Acad. Sci. USA*, **94(16)**, 8462-8467doi.org/10.1073/pnas.94.16.8462
- Winkel, C.A., MacDonald, P.C. & Simpson, E.R. (1981). The role of receptor-mediated low-density lipoprotein uptake and degradation in the regulation of progesterone biosynthesis and cholesterol metabolism by human trophoblasts. *Placenta*, (**Suppl. 3**), 133-143. PMID: 6306642.
- Winkel, C.A., Snyder, J.M., MacDonald, P.C. & Simpson, E.R. (1980). Regulation of cholesterol and progesterone synthesis in human placental cells in culture by serum lipoproteins. *Endocrinology*, **106**, 1054-1060. DOI: 10.1210/endo-106-4-1054.
- Woollett, L.A. (2011). Transport of maternal cholesterol to the fetal circulation. *Placenta*, **32 (Suppl. 2)**, S218-21. DOI: 10.1016/j.placenta.2011.01.011.
- Yang, H., Galea, A., Sytnyk, V. & Crossley, M. (2012). Controlling the size of lipid droplets: lipid and protein factors. *Curr. Opin. Cell Biol.*, **24**, 509-516. DOI: 10.1016/j.ceb.2012.05.012.
- Zelewski, L. & Vिलее, C.A. (1966). The biosynthesis of squalene, lanosterol, and cholesterol by minced human placenta. *Biochemistry*, **5**, 1805-1814. PMID: 5963423.
- Zamzami, N. & Kroemer, G. (2001). The mitochondrion in apoptosis: how Pandora's Box opens. *Nat. Rev. Mol. Cell Biol.*, **2(1)**, 67-71. DOI: 10.1038/35048073

1 Article

2 **Steady-state persistence of respiratory syncytial virus**
3 **in a macrophage-like cell line and identification of**
4 **non-synonymous mutations through sequencing of**
5 **the persistent viral genome**

6 **Ximena Ruiz-Gómez¹, Joel Armando Vázquez-Pérez², Oscar Flores-Herrera³, Mercedes**
7 **Esparza-Perusquía³, Carlos Santiago-Olivares¹, Jorge Gaona⁵, Beatriz Gómez¹, Carmen Méndez⁴,**
8 **Evelyn Rivera-Toledo^{1,*}**

9 ¹ Departamento de Microbiología y Parasitología, Facultad de Medicina, Universidad Nacional Autónoma
10 de México, Ciudad Universitaria, Coyoacán 04510, Mexico City, Mexico; menaxrg@hotmail.com (XRG);
11 carlosantigolivares@yahoo.com.mx (CASO); bgomez2017@gmail.com (BG); evelyn.rivera@unam.mx
12 (ERT)

13 ² Instituto Nacional de Enfermedades Respiratorias Ismael Cosío Villegas, Mexico City, Mexico;
14 joevazpe@gmail.com

15 ³ Departamento de Bioquímica, Facultad de Medicina, Universidad Nacional Autónoma de México, Ciudad
16 Universitaria, Coyoacán 04510, Mexico City, Mexico; oflores@bq.unam.mx (OFH); mesparza@bq.unam.mx
17 (MEP)

18 ⁴ Departamento de Embriología y Genética, Facultad de Medicina, Universidad Nacional Autónoma de
19 México, Ciudad Universitaria, Coyoacán 04510, Mexico City, Mexico; mendzmc@unam.mx

20 ⁵ Departamento de Microbiología y Patología, Centro Universitario de Ciencias de la Salud, Universidad de
21 Guadalajara, Guadalajara, Jalisco, Mexico; jgaber2007@gmail.com

22
23

24 * Correspondence: evelyn.rivera@unam.mx (ERT); Tel.: +52 5556232467

25 Received: date; Accepted: date; Published: date

26 **Abstract:** Persistent viral infection in cell cultures have been categorized at least as in
27 “carrier-state”, where there exists a low proportion of cells infected by a lytic virus, and as in
28 “steady-state”, where most of cells are infected, but in absence of cytophatic effect. Here, we
29 showed that human respiratory syncytial virus (hRSV) maintained a steady-state persistence in
30 the macrophage-like cell line P388D1 after 120 passages, since the viral genome was detected in all
31 of the cells analyzed by fluorescence *in situ* hybridization, whereas only defective viruses were
32 identified by sucrose gradients and titration assay. Interestingly, up to 8.0±7.0% of the cells
33 harboring the hRSV genome revealed undetectable expression of the viral nucleoprotein N;
34 however, when this cell population was sorted by flow cytometry and independently cultured,
35 hRSV protein expression was induced at detectable levels since the first post-sorting passage,
36 supporting that sorted cells harbored the viral genome. Finally, sequencing of the persistent hRSV
37 genome obtained from virus particles collected from cell-culture supernatants, allowed
38 assembling of a complete genome sequence that displayed 38 nonsynonymous mutations
39 distributed in ten of the eleven viral proteins. Eight of the 38 nonsynonymous mutations have
40 been previously characterized and they were related to alterations in viral assembly or budding,
41 membrane fusion and evasion of the antiviral response.

42 **Keywords:** Respiratory syncytial virus; viral persistence; steady-state persistence; defective
43 viruses; viral genome sequencing.

44

45 1. Introduction

46 Persistent infection is a relevant strategy for many viruses to be long-term maintained within a host
47 population, since silent viral transmission may be allowed from healthy carriers, although viral
48 persistence could also lead to life-threatening chronic diseases. Human respiratory syncytial virus
49 (hRSV) is an enveloped *Orthopneumovirus* from the *Pneumoviridae* family, with genome encoded in a
50 non-segmented negative strand RNA with approximately 15,200 nucleotides of size and tropism for
51 epithelial cells and macrophages of the respiratory tract [1–3]. The hRSV genome consists of ten
52 genes, NS1-NS2-N-P-M-SH-G-F-M2-L, encoding eleven proteins, since the M2 gene has two
53 overlapping open reading frames expressing M2-1 and M2-2 [4]. Eight RSV proteins are structural,
54 whereas the NS1, NS2 and M2-2 are non-structural proteins with relevant roles in immune evasion
55 and regulation of genome transcription/replication, respectively [5–7].

56 Globally, hRSV is the main etiological agent of severe acute lower respiratory infection (ALRI) in
57 children under five years and it was estimated in 2015 a total of 33.1 million of RSV-ALRI, with 3.2
58 million of hospital admissions and 59,600 in-hospital deaths; of relevance, forty-five percent of
59 hospitalizations occurred in infants younger than six months [8]. RSV-ALRI early in life has been
60 associated to respiratory diseases such as wheezing and asthma-like symptoms in later childhood
61 [9–13], which is highly prevented by Palivizumab prophylaxis in children without a family history
62 of atopy, suggesting that RSV predisposes to long-term airway hyperreactivity in an
63 atopy-independent mechanism [13,14]. It has been proposed that hRSV persistence in the
64 respiratory tract may be at least one mechanism associated to recurrent asthma-like symptoms [15].
65 Experimental models in rats, mice and guinea pigs have shown that hRSV persists *in vivo*,
66 according to long-standing detection of viral antigens, recovery of viral RNA and isolation of
67 infectious virus in pulmonary tissue [16–19]. Evidence of hRSV persistence in humans is limited,
68 but some studies have reported viral RNA in respiratory and non-respiratory tissues of
69 asymptomatic children and adults [20–23], as well as in respiratory secretions of
70 immunocompromised patients [24]. Cell lines as *in vitro* models are useful tools to evaluate
71 mechanisms and potential target cells for virus persistence; in such a way, epithelial cells, dendritic
72 cells and macrophages have been persistently infected by hRSV [25–27].

73 Persistent viral infection in cell cultures has been classified in at least two types: carrier-state and
74 steady-state. In the former, only a small proportion of cells are productively infected, functioning as
75 a permanent source of virus that is delivered to the extracellular medium to be transmitted
76 horizontally to the constantly growing uninfected cell population. In steady-state persistence, most
77 cells are infected and both, virus and cell multiplication, are maintained without cell destruction
78 [28,29].

79 We have studied persistence of hRSV in the macrophage-like cell line P388D1 for over 120 passages
80 and our observations indicate hRSV alters cell survival, IFN-I response and nitric oxide production
81 to persist [30–32]. Most of our persistently hRSV-infected macrophage-like cultures are constituted
82 by >90% of cells expressing viral proteins [31,32]; however, we have also identified some cultures
83 with ≤70% of hRSV positive cells after storage in liquid nitrogen, suggesting it could be associated
84 to a carrier-state. Herein, we report that hRSV established no a carrier-state, but a steady-state
85 persistence in the P388D1 cell line, since viral genomic RNA was detected in all of the cells analyzed
86 by fluorescence *in situ* hybridization, whereas only defective viruses were identified through viral
87 titration and sucrose gradients. Additionally, genomic RNA was isolated from virus particles

88 collected from cell-culture supernatants and sequenced to determine changes experienced in the
89 hRSV genome after several passages.

90 2. Materials and Methods

91 2.1. Cell lines and virus

92 Persistently RSV infected macrophage cultures (MΦP) were obtained and characterized in our
93 laboratory from surviving cells after acute infection of the mouse macrophage-like cell line P388D1
94 at multiplicity of infection of 1 (m.o.i. of 1), with the wild type hRSV Long strain (VR-26, ATCC), as
95 previously described [25]. Viral persistence was constantly monitored (every two or three weeks)
96 through expression of three structural proteins by direct immunofluorescence (section 2.2). MΦP
97 cultures showed non-cytopathic effects and have been subcultured or passaged for over 120 times
98 in RPMI-1640 culture medium (Gibco), supplemented with 5% fetal bovine serum (Biowest), 1%
99 penicillin-streptomycin (Invitro) and 1 μM 2-mercaptoethanol (Sigma). This work was performed
100 with passages 120–150. The original P388D1 cell line was used as a non-infected control (MΦN) and
101 was maintained under similar culture conditions as MΦP. The human epithelial cell line HEp-2 and
102 the monkey kidney epithelial cell line Vero E6 were cultured in Dulbecco's Modified Eagle Medium
103 (DMEM; Gibco), supplemented with 5% fetal bovine serum, 10 nM HEPES (Sigma) and 1%
104 penicillin-streptomycin. HEp-2 cells were acutely infected at m.o.i. of 0.5 with the RSV Long strain
105 for 72 h to compare buoyant density of viruses produced under this condition and buoyant density
106 of viruses in MΦP cultures (see section 2.5).

107 Infectious hRSV from MΦP cultures were quantified in HEp-2 and Vero E6 cells through a limiting
108 dilution method, with viral titers expressed as the 50% tissues culture infectious dose per ml
109 (TCID₅₀/ml).

110

111 2.2. Direct immunofluorescence

112 Percentage of persistently RSV infected cells in MΦP cultures was evaluated by direct
113 immunofluorescence. MΦP were fixed with 4% p-formaldehyde on ice and permeabilized with
114 0.3% saponine at room temperature (15 min each step). After blocking non-specific binding sites (30
115 min) with blocking solution (5% neonate bovine serum (Bioexport) in PBS), a mix of FITC-labeled
116 monoclonal antibodies against three hRSV structural proteins was added by using the IMAGEN
117 Respiratory syncytial virus kit (anti-hRSV-FITC; Oxoid), diluted 1:10 in blocking solution. MΦN
118 were stained under the same protocol to confirm binding specificity of the FITC-labeled anti-hRSV
119 antibody (internal negative control). Percentage of FITC⁺ cells (hRSV-protein⁺ cells) was determined
120 by flow cytometry in a FACS Calibur (BD Biosciences). Unstained MΦP or MΦN were used as
121 negative controls, to determine background fluorescence.

122

123 2.3. Cell sorting

124 FITC⁻ and FITC⁺ cells were isolated from MΦP cultures with ≤70% of hRSV-protein⁺ cells (passages
125 120, 123 and 126) in a FACS Aria II cell sorter (BD Biosciences), after staining with the
126 anti-hRSV-FITC, although cells were not permeabilized. Each subset was defined in a fluorescence
127 histogram and extreme opposed regions, corresponding to FITC⁻ and FITC⁺ populations were
128 selected for sorting. Recovered cells were independently cultured in supplemented RPMI during
129 four to five days before the first, post-sorting passage. Immunofluorescence to determine

130 percentage of hRSV-protein⁺ cells in consecutive post-sorting passages was performed in fixed and
131 permeabilized cells (as described in section 2.2).

132

133 2.4. Fluorescence *in situ* hybridization and indirect immunofluorescence

134 Fluorescence *in situ* hybridization (FISH) for hRSV genomic RNA (hRSV-gRNA) in MΦP cultures
135 was performed with a pool of 29 single stranded DNA probes (20 nucleotides), detecting targeted
136 positions from 1140 to 2285, encompassing the nucleoprotein N gene (GenBank: AY911262.1). Each
137 probe was labeled with the red fluorophore Quasar 570 (Biosearch Technologies). MΦP and MΦN
138 were plated onto coverslips (2.5×10⁵) in 48-well plates and incubated overnight to allow adherence.
139 Cells were washed with PBS and fixed with 4% p-formaldehyde (10 min) and then permeabilized in
140 0.3% saponine (15 min). Permeabilized cells were treated with wash buffer containing 10%
141 formamide and 2× saline sodium citrate (2× SSC; 0.3 M NaCl and 0.03 M sodium citrate, pH 7.4).
142 Heat denaturalized DNA from salmon testes (Sigma), was added at 0.5 mg/ml in hybridization
143 buffer (wash buffer plus 5% Ficoll 400) for 2 h at 37°C. After washing twice, specific DNA probes
144 were added at 4 nM in hybridization buffer overnight at 37°C under constant agitation. Two
145 stringency washes were performed to eliminate unbound probes (30 min each). Indirect
146 immunofluorescence was performed immediately with the anti-N primary antibody (sc-58001;
147 Santa Cruz Biotechnology), dilution 1:100 in 3% neonate bovine serum in PBS (30 min), followed by
148 a FITC-labeled secondary antibody 1:100 (sc-2010; Santa Cruz Biotechnology). Nuclear staining was
149 performed with 0.8 µg/ml Hoechst 33342 (Invitrogen). Cover slides were mounted with 6 µl of
150 mounting fluid (Oxoid). Fluorescence imaging acquisition was performed in a microscope Leica Las
151 X (Leica). Auto-fluorescence of unstained cells was a reference to set the threshold for positive
152 staining of probes and antibodies.

153 Percent of hRSV-protein⁺ cells by confocal microscopy was calculated by counting cells expressing
154 the N protein in at least three different microscopic fields, from three independent experiments and
155 compared to percentages obtained from immunofluorescence analyzed through flow cytometry.

156

157 2.5. Sucrose gradients and buoyant density

158 Virus buoyant density was determined by analysis of viral pellets through sucrose gradients.
159 Supernatants from MΦP cultures or acutely infected HEp-2 cells (72 h post infection) were collected
160 and centrifuged at 59,000×g, 4°C (2.5 h) in a SW45 Ti rotor. Pellets were resuspended in 10 mM
161 Tris-HCl pH 7.5, loaded in a lineal sucrose gradient (20–60%) and centrifuged at 59,000×g, 4°C (2.5
162 h) in a SW28 rotor. Gradients were fractionated from bottom to top in 0.5 ml and optical density at
163 280 nm (O.D. 280 nm) was determined by spectrophotometry, whereas refraction units were
164 determined with a hand-held refractometer (Atago). Buoyant density (ρ) was calculated as
165 $\rho_{20^{\circ}\text{C}}=2.7329\eta - 2.6425$, where η =refraction units [25].

166

167 2.6. Virus genome sequencing

168 Viral genome sequence was obtained from RNA extracted from viral pellets enriched through
169 centrifugation of supernatants collected along five passages from MΦP cultures sorted as FITC⁻ and
170 FITC⁺ (10–15 post-sorting passages), at 59,000×g, 4°C (2.5 h). Viral pellets were resuspended in 10
171 mM Tris-HCl pH 7.5 (90 µl) and treated with 5 U DNase I (Invitrogen) at 37°C (30 min) and 100
172 µg/ml RNase A (Invitrogen) at 37°C (15 min). After nucleases treatment, RNA was immediately
173 extracted with the QIAmp Viral RNA kit (Qiagen), according to the manufacturer's instructions.

174 Depleted RNA was directly fragmented by using the Illumina TruSeq Stranded mRNA Sample
 175 Preparation Kit (Illumina) and two libraries, (Persistent_hRSV_F⁻ and Persistent_hRSV_F⁺), were
 176 constructed according to the manufacturer's instructions.

177 Five millions reads per sample were obtained and RSV genomes were assembled *de novo* using
 178 Spades (v.3.12.0.); contigs were mapped against the VR-26 strain of the hRSV (GenBank accession
 179 no. AY911262.1). Best alignment was for hRSV with 98.8% of coverage for each sample, with depth
 180 of 769× and 552× for Persistent_hRSV_F⁻ and Persistent_hRSV_F⁺, respectively; genome sequences
 181 are available at the National Center for Biotechnology Information (GenBank accession no.
 182 MT492012 and MT492011).

183 2.7. Statistical analysis

184 Mean±standard deviation from three independent experiments was determined by using GraphPad
 185 Prism software.

186

187 3. Results

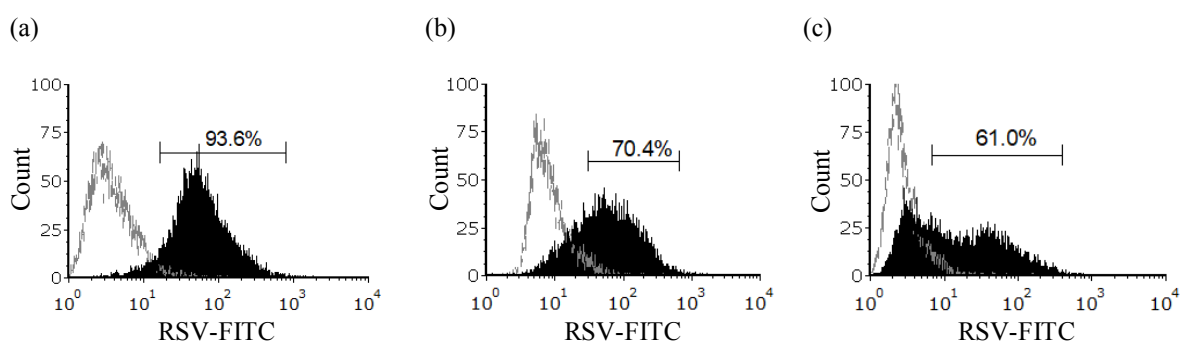
188 3.1. Detection of the hRSV genome in MΦP cultures through fluorescence in situ hybridization

189

190 The MΦP cultures have been previously studied to determine alterations in the biology of the host
 191 cell, associated to maintenance of hRSV persistent infection [30–32]. Our previous reports were
 192 performed in cultures of MΦP with >90% of hRSV-protein⁺ cells, according to direct
 193 immunofluorescence with anti-hRSV-FITC antibodies and analysis by flow cytometry (Figure 1).
 194 However, we also observed few MΦP cultures with ≤70% cells expressing viral proteins after
 195 storage in liquid nitrogen (Figure 1); this type of cultures were of interest in this work to study
 196 whether MΦP cultures were carrier- or steady-state.

197

198



199

200

201

202 **Figure 1.** Persistently hRSV infected macrophages (MΦP) were analyzed by direct immunofluorescence
 203 and flow cytometry to determine percentage of cells expressing viral proteins. Three different MΦP cultures
 204 were identified with high a) or intermediate b), c) percentage of cells expressing hRSV proteins after one week
 205 of their independent thawing from liquid nitrogen.

206

207 First, we evaluated the amount of cells harboring the hRSV-gRNA through FISH and confocal
208 microscopy by using DNA probes directed against the whole hRSV N gene, along with analysis of
209 N protein expression by indirect immunofluorescence (Figure 2a). This assay was performed with
210 MΦP cultures displaying less than 82% cells expressing viral proteins, according to flow cytometry
211 (Table 1). Interestingly, confocal microscopy revealed a regular cytoplasmic distribution of viral
212 RNA in every single cell from MΦP cultures, whereas the nucleoprotein N was observed with
213 variable expression and forming small or large aggregates (Figure 2a and 2b), in agreement with
214 morphology of inclusion bodies, previously described during hRSV replication [33]. We also
215 observed some cells with cytoplasmic hRSV-gRNA but undetectable expression of N protein
216 (Figure 2a). In merged images, red fluorescence from the DNA probes was deeply intense, whereas
217 green fluorescence from the anti-N antibody was in some cases almost imperceptible, mainly in
218 cells with low levels of N protein. As expected, mock-infected macrophages (MΦN) did not bind
219 either DNA probe against the hRSV-gRNA or the anti-N antibody.

220 Besides, we calculated the percentage of cells expressing the N protein in at least three different
221 microscopic fields from three independent MΦP cultures and such value was compared to that
222 obtained by flow cytometry; bright field was useful to improve visualization of cells with low N
223 protein expression (Figure 2b). Results showed higher percentage of hRSV-protein⁺ cells analyzed
224 by confocal microscopy than that by flow cytometry (Table 1), although this difference was not
225 statistically significant ($p=0.058$). It is important to consider that data from table 1 were calculated
226 with 358.1 ± 79.6 cells from each of the three independent MΦP cultures, whereas 10,000 events were
227 considered for analysis by flow cytometry. Thus, we observed hRSV-gRNA in all of the cells in
228 MΦP cultures, as expected in steady-state persistence, despite the fact that viral protein expression
229 was not always detected either by confocal microscopy or flow cytometry.

230
231
232
233
234
235
236
237
238
239
240
241
242
243
244

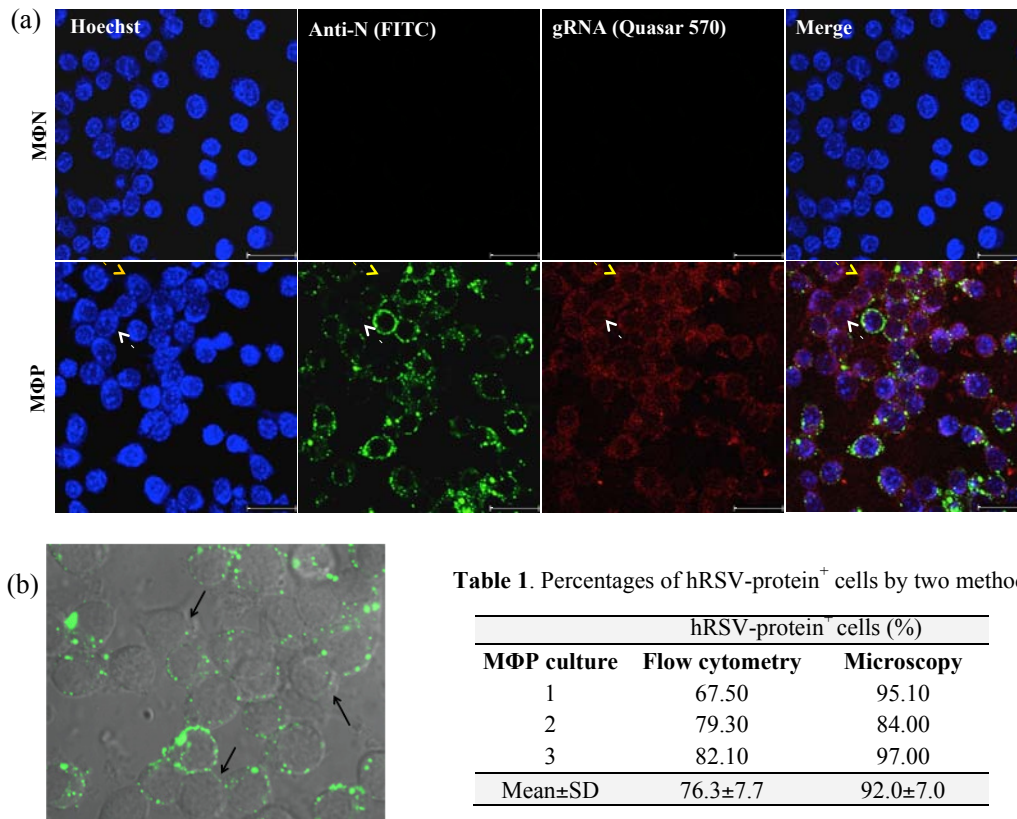


Table 1. Percentages of hRSV-protein⁺ cells by two methods

MΦP culture	hRSV-protein ⁺ cells (%)	
	Flow cytometry	Microscopy
1	67.50	95.10
2	79.30	84.00
3	82.10	97.00
Mean±SD	76.3±7.7	92.0±7.0

245

246

247

248

249

250

251

252

253

254

255

256

257

258

259

260

261

262

263

264

265

266

267

268

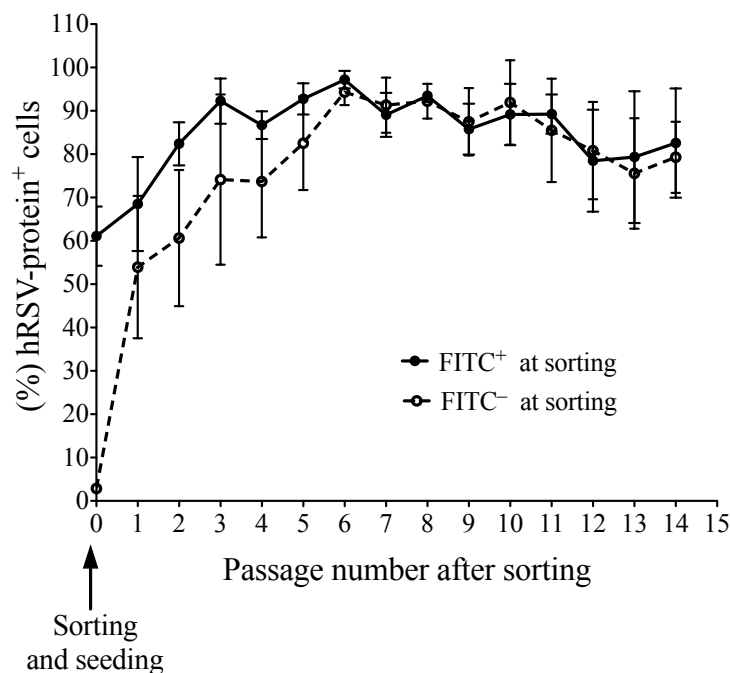
269

Figure 2. Intracellular distribution of hRSV genomic RNA (hRSV-gRNA) in MΦP cultures was analyzed by FISH and expression of the N protein determined by indirect immunofluorescence. Non-infected macrophages (MΦN) were used as negative control. (a) Nucleus staining was performed with Hoechst 33342 (blue), N-protein was detected with an anti-N antibody followed by a FITC-labeled secondary antibody (green) and the hRSV-gRNA detection was achieved with Quasar 570-labeled DNA probes directed against the N gene (red). White arrows point to a cell with low N protein expression, high level of hRSV-gRNA and imperceptible green signal in merge image. Yellow arrows point to a cell with undetectable N protein expression, even though hRSV-gRNA was distinguished. Images were captured with a 63× objective. Scale bars: 15 μm. (b) Bright field was used for contrast green fluorescence, in order to distinguish cells expressing low levels of N protein. Black arrows point to cells with few, tiny N protein aggregates; every cell with low or high expression of N protein was counted to calculate percentage of hRSV-protein⁺ cells by confocal microscopy and this value was compared to percentages obtained through flow cytometry (Table 1). Percentages were calculated from three independent MΦP cultures.

3.2. Flow cytometric cell sorting of hRSV-protein positive and hRSV-protein negative cells from MΦP cultures

Next, we used anti-hRSV-FITC antibodies to sort FITC⁻ and FITC⁺ cells from MΦP cultures by using flow cytometry; afterwards, cells were independently cultured to evaluate their behavior regarding viral protein expression throughout subsequent subcultures. High purity of FITC⁻ cells was achieved by sorting (96.4±1.2%), whereas purity of FITC⁺ cells was much lower (61.0±6.8%),

270 indicating that they were contaminated with negative cells (Figure 3). After their independent
 271 culture during four to five days, the first post-sorting passage was evaluated regarding hRSV
 272 protein expression. Under such condition, $53.9\pm 16.4\%$ of hRSV-protein⁺ cells were observed in the
 273 cultures sorted as FITC⁻ (hereafter called as csFITC⁻), with a progressive increase up to $94.3\pm 2.9\%$ at
 274 passage six and then, a slight but constant decrease up to $79.2\pm 8.2\%$ at passage 15 (Figure 3). In
 275 cultures sorted as FITC⁺ (hereafter called as csFITC⁺) $68.5\pm 10.8\%$ hRSV-protein⁺ cells were observed
 276 in the first post-sorting passage, with gradual augment to $97.2\pm 2.0\%$ at passage six and decline to
 277 $82.5\pm 12.6\%$ in the last passage. These results suggested that FITC⁻ cells harbored the hRSV-gRNA,
 278 whereas protein expression was low-to-undetectable but with potential to be reactivated to higher
 279 levels after sorting and independent culture.
 280



281

282

283

284

285

286

287

288

289

290

291

292

293

294

295

296

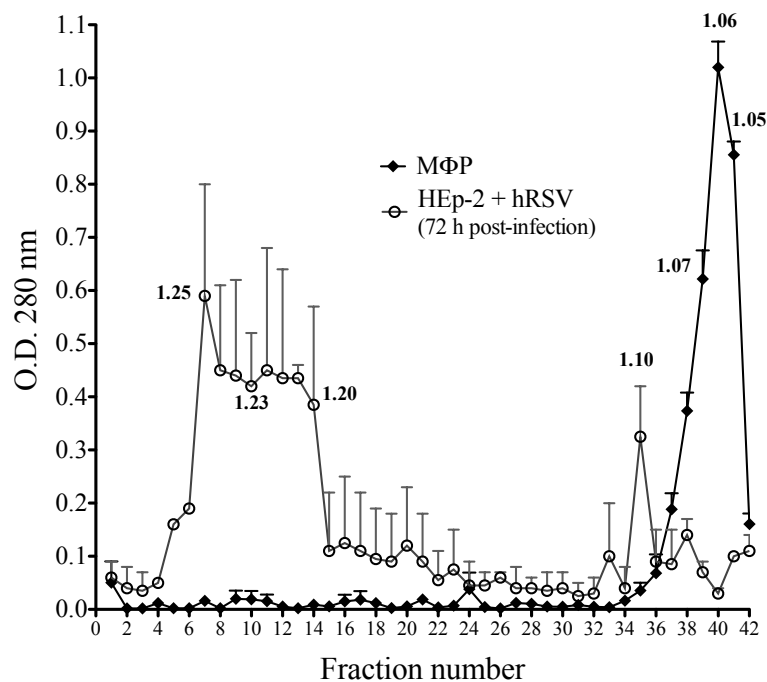
297

Figure 3. Sorting and independent culture of cells with positive and negative expression of hRSV proteins. Cells expressing or not hRSV proteins in MΦP cultures were identified by direct immunofluorescence and flow cytometry with anti-hRSV-FITC labeled antibodies. FITC⁻ and FITC⁺ cells were sorted, cultured independently and percentage of hRSV-protein⁺ cells was evaluated during 14 consecutive post-sorting passages. Percentage of FITC⁻ and FITC⁺ cells at time zero was determined according to purity of each cell population recovered. Data represent average±SD of the three independent MΦP cultures.

3.3. Buoyant density and titrating of persistent hRSV from MΦP cultures

In persistent carrier-cultures, infectious viruses are normally detected in supernatants [34,35]; therefore, we examined the presence of infectious hRSV in supernatants from MΦP cultures. Through titration in HEp-2 cells by limiting dilution (TCID₅₀), we did not detect infectious viruses in at least five different passages (120, 122, 135, 149 and 150), since cytopathic effect was undetectable. Nevertheless, titration in Vero E6 cells showed cytopathic effect sometimes in the first

298 \log_{10} dilution resulting in viral titers of 255.7 ± 202.6 TCID₅₀/ml, indicating infectious viruses were
 299 produced at low levels. Accordingly, we determined virus buoyant density by sucrose gradients.
 300 Reported buoyant density for hRSV is 1.17–1.20 g/ml [36] and we calculated average density of
 301 1.072 ± 0.009 g/ml for viruses in MΦP cultures (Figure 4), indicating primarily production of
 302 low-density, defective virus. As a control, we also determined buoyant density of hRSV produced
 303 in acutely infected HEp-2 cells (72 hours post infection), obtaining an average density of 1.195 ± 0.18
 304 g/ml, with low frequency of defective viruses (Figure 4); besides, viral titer during acute infection
 305 was of $2.40 \pm 0.55 \times 10^6$ TCID₅₀/ml. Accordingly, absence of infectious viruses support our previous
 306 observations that RSV established a steady-state persistence in macrophage-like cells.
 307
 308



309

310

311

312

313

314

315

316

317

318

319

320

321

322

323

324

325

Figure 4. Buoyant density of viral particles in MΦP cultures and in HEp-2 cells infected at m.o.i. of 0.5 for 72 h was determined through sucrose gradients. Supernatants from hRSV-infected cells were fractionated in sucrose gradients and buoyant density of each fraction was calculated; optical density at 280 nm was also evaluated. Buoyant densities are indicated in fractions that show absorbance at 280 nm. Data represent the average \pm SD of three independent MΦP or acutely infected HEp-2 cells.

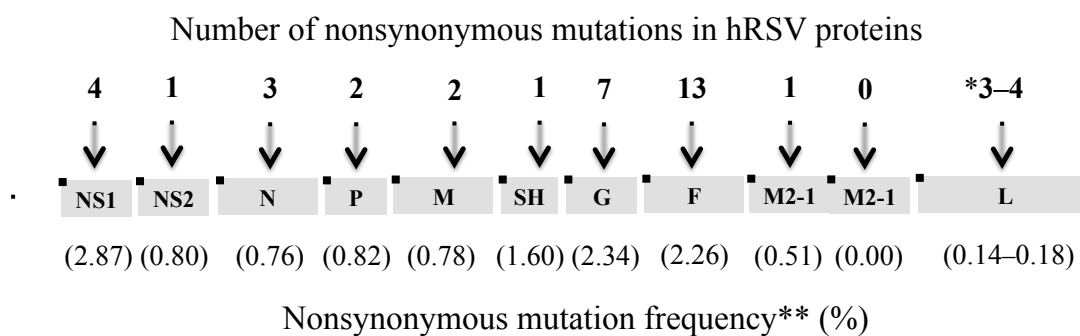
3.4. Sequencing of the persistent hRSV genome

Finally, we sequenced the persistent hRSV genome obtained from viral particles in supernatants of two independent MΦP cultures, csFITC⁻ and csFITC⁺. Supernatants were collected from both types of MΦP cultures along 10–15 post-sorting passages that showed approximately 80% hRSV-protein⁺ cells. After RNA was extracted from virus pellets, two sequencing libraries, Persistent_hRSV_F⁻ and Persistent_hRSV_F⁺, were constructed for samples from csFITC⁻ and csFITC⁺, respectively. One contig of 15,227 nucleotides per sample was obtained with 98% identity with respect to the

326 reference sequence, strain Long VR-26 (GeneBank accession no. AY911262.1), used to establish our
 327 persistently hRSV infected culture.

328 A total of 38 nonsynonymous mutations were detected in the persistent hRSV genome (Figure 5), of
 329 which, 34.2% occurred in protein F, 18.4% in protein G, 10.5% in protein NS1 and 7.9% or 10.5% in
 330 the polymerase L. Results were identical for the genome of virus collected from csFITC⁻ and
 331 csFITC⁺ cultures, except in protein L of virus from the last culture that showed an additional
 332 substitution (Q1112R, Table 2). Frequency of nonsynonymous mutations in each viral protein was
 333 calculated in regards to total amino acids (protein length), indicating similar mutation frequency for
 334 F and G proteins (Figure 5), while protein NS1 showed the higher mutation frequency with respect
 335 to all other viral proteins.

336
 337



338
 339

340 **Figure 5.** Schematic representation of hRSV genome and number of nonsynonymous mutations identified
 341 after sequencing the persistent viral genome of MΦP cultures. Viral RNA was obtained from hRSV recovered
 342 by ultracentrifugation of supernatants from two independent MΦP cultures (csFITC⁻ and csFITC⁺).
 343 Independent sequencing was performed and nonsynonymous mutations were identified. Numbers on the top
 344 of the diagram correspond to quantity of nonsynonymous mutations identified in the corresponding protein,
 345 while numbers into parenthesis represent the **frequency of nonsynonymous mutations, calculated as a
 346 percentage per total amino acid number of each viral protein. *3 and 4 mutations were observed in the
 347 polymerase L, in csFITC⁻ and csFITC⁺ respectively.

348
 349

350 We found previous reports describing biological effects of substitutions in eight of the 38 positions
 351 identified by us with nonsynonymous mutations (Table 2). Thereby, substitutions in proteins N
 352 (I270V), P (S116P), G (D6V) and F (K68Q, I79M, N126D, M526L, C550S), might alter viral assembly
 353 or budding, antibody recognition, triggering of virus-cell fusion and cell-cell fusion, as well as
 354 replication of the viral genome [24,37–42], in agreement with our observation of defective viruses.
 355 The other 30 substitutions, most of them located in proteins G and F, have not been described and
 356 their biological effect and contribution to hRSV persistence remains unknown; however, we
 357 included in table 2 commentary for some of them with regard to their localization or proximity to
 358 other characterized mutations.

359
 360
 361

362 **Table 2.** Substitutions observed in the persistent hRSV genome and potential biological effects.

Gen	Substitutions	Biological effect	Commentaries	References
NS1	E21K	Uncharacterized	–	–
	V82A	Uncharacterized	–	–
	E91G	Uncharacterized	–	–
	T123S	Uncharacterized	–NS1 α -helix-3 is constituted by residues 119-134. –Substitutions Y125, L132/L133 and α -helix-3 truncation, reduce NS1-mediated suppression of the antiviral response.	[55]
NS2	T90A	Uncharacterized	–P36, L52 and P92 residues are required for NS2 ubiquitination activity, targeting STAT2 for proteasomal degradation.	[57]
N	K60E	–	–	–
	H89Q	Uncharacterized	–	–
	I270V	Directly involved in interaction with viral P protein	–Core RSV polymerase complex consists of L and P, but N and M2-1 are also required. –I270A abrogates interaction with P protein and significantly reduces polymerase activity.	[37]
P	N75D	Uncharacterized	–	–
	S116P	Phosphorylation site	–S116, S117, S119, S232 and S237 are phosphorylation sites; mutation or dephosphorylation reduce N–P interaction and hRSV budding from infected HEp-2 cells. –M2-2-dependent transcriptional inhibition requires simultaneous phosphorylation of S116, S117, S119.	[47,50,51]
M	M43I	Uncharacterized	–	–
	T133I	Uncharacterized	–	–
SH	T38A	Uncharacterized	–	–
G	D6V	Involved in interaction with viral M protein	–D6A substitution reduced 3-fold the interaction of G with matrix M protein (cytoplasmic domain).	[38]
	G29C	Uncharacterized	–Position inside cytoplasmic domain	[50]
	I50T	Uncharacterized	–Position inside transmembrane domain	[50]
	T113I	Uncharacterized	–	–
	T133I	Uncharacterized	–	–
	I189V	Uncharacterized	–	–
	N294K	Uncharacterized	–	–
F	K68Q	Triggering of	–A positively charged residue in position 68 is	[39,46]

		membrane fusion and recognition by a neutralizing antibody	essential to mediate membrane fusion and viral entry. –K68N substitution is associated to low binding affinity of the neutralizing mAb MEDI8897.	
	I79M	Stability of the pre-fusion conformation	–I79A resulted in absence of membrane fusion, possibly by premature transition to the post-fusion conformation.	[40]
	N80K	Uncharacterized	–	–
	T101P	Uncharacterized	–	–
	N126D	N-glycosylation site	–N126Q substitution does not alter either F protein expression or membrane fusion (position within p27 peptide).	[41]
	I152T	Uncharacterized	–Position inside fusion domain	[54]
	I292V	Uncharacterized	–	–
	T323S	Uncharacterized	–	–
	Y391H	Uncharacterized	–	–
	E497A	Uncharacterized	–	–
	H515N	Uncharacterized	–	–
	M526L	Uncharacterized but M526I has been observed	–M526I substitution was observed in a SCID** patient with persistent RSV infection, after BM transplant and rising in CD8 T cell count.	[24]
	C550S	Palmitoylation site	–C550 is a palmitoylated residue of the cytoplasmic domain. –C550S does not alter F expression, although membrane fusion increased partially.	[42]
M2-1	T110A	Uncharacterized	–	–
M2-2	None	–	–	–
L	G412S	Uncharacterized	–Position inside **RdRp domain	[47]
	Q1112R*	Uncharacterized	–Position inside **PRNTase domain	
	V1124I	Uncharacterized	–Position inside **PRNTase domain	
	K1602R	Uncharacterized	–Position inside connector domain	

363 *Only observed in hRSV from csFITC⁺

364 **SCID, severe combined immune deficiency; RdRp, RNA-dependent RNA polymerase domain; PRNTase,
365 polyribonucleotidyl transferase or capping domain

366

367 4. Discussion

368 Considering that epithelial cells and macrophages are susceptible to hRSV infection in the
369 respiratory tract [1–3], we previously studied alterations in the biology of macrophage-like cells
370 during hRSV persistence and described some mechanisms related to maintenance of such long-term
371 viral infection [30–32]. Herein, we focused on features of the virus present in MΦP cultures after
372 several passages and present evidence that hRSV established a steady-state persistence, since
373 hRSV-gRNA was detected in all of the cells in culture, despite the fact that some of them displayed
374 low-to-undetectable N protein expression, according to flow cytometry and confocal microscopy.
375 We also observed a predominant production of defective viral particles and presented for the first
376 time the sequence of a persistent hRSV genome that has been maintained *in vitro* throughout 120
377 passages. The persistent hRSV genome showed 38 non-synonymous mutations distributed in ten
378 viral proteins; only eight substitutions have been previously studied and are mainly related to
379 alterations in viral assembly or budding, membrane fusion and possibly in evasion of the antiviral
380 response.

381 MΦP has been subcultured for more than 120 passages by means of repeated freezing and thawing;
382 normally we observe cultures with more than 90% of cells expressing hRSV proteins after thawing
383 from liquid nitrogen. However, we also detected some cultures from different passages with
384 relatively low percentage of infected cells ($\leq 70\%$) and such observation initially suggested that the
385 virus might have sometimes low rates of replication, allowing high proliferation index of the
386 uninfected cell population, as in a carrier-state persistence. However, detection of hRSV-gRNA by
387 FISH in the whole culture and the evidence of a small cell population without N protein expression,
388 suggested hRSV established a steady-state persistence in the macrophage-like cell line P388D1 and
389 we propose the hypothesis that some cells may preserve the viral genome in silent form. Actually,
390 we calculated by confocal microscopy up to $8.0 \pm 7.0\%$ hRSV-gRNA⁺ cells, with undetectable N
391 protein expression. Sorting and independent culture of FITC⁻ cells showed since the first
392 post-sorting passage, about 50% hRSV-protein⁺ cells and a progressive increase at subsequent
393 subcultures, supporting the evidence that this cell population preserved intracellularly the viral
394 genome. We do not discard that the sorted hRSV⁻ population may have included cells with very
395 low levels of viral proteins, essentially because we did not permeabilized them during
396 immunofluorescence to preserve viability, then, selection of FITC⁻ and FITC⁺ cells was set up
397 according to their surface protein expression. When we compared percentages of hRSV-protein⁺
398 cells analyzed by flow cytometry and confocal microscopy after cell permeabilization (Table 1), the
399 last method provided higher values though without statistical significance. As percentage of
400 hRSV-protein⁺ cells was determined by flow cytometry from 10,000 events, whereas percentage by
401 confocal microscopy was calculated from <500 cells, the former method could be considered more
402 reliable. However, overlapping between the autofluorescent cell population (control) and cells with
403 low expression of viral proteins by flow cytometry, could avoid accurate definition of positives and
404 negatives during analysis, resulting in underestimation of hRSV-protein⁺ cells.

405 It has been advised that numerous cycles of freezing and thawing could lead to phenotypic and
406 functional changes in cell lines, although mechanisms have not been described [43]; we consider
407 such effect as a possibility in MΦP, but if this was the case, alterations in hRSV-gRNA transcription
408 and translation were apparently reversible after independent culture of FITC⁻ cells.

409 Previous reports have shown that positive-sense single stranded RNA viruses maintain their
410 genome during persistence as double stranded RNA, in absence or with low level of viral protein
411 expression (e.g. porcine reproductive and respiratory syndrome virus, and Seneca virus A) [34,44].
412 In negative-sense RNA viruses, both dsRNA and structural viral proteins have been observed,
413 although studies have been performed only during acute infection [45]. We did not discard that
414 FITC⁻ cells from MΦP cultures might be silent reservoirs of hRSV-gRNA; therefore our observations
415 warrant further research to determine mechanisms associated to viral genome maintenance in the
416 host cell during persistence.

417 On the other hand, we previously reported that relative expression of hRSV genome is 11-fold
418 higher in MΦP at 24 h of culture with respect to acutely infected macrophages at 24 h post-infection,
419 and 2000-fold greater in MΦP compared with MΦN (non-infected control) [32]. Hence, despite
420 hRSV genome is actively replicated in MΦP, infectious viral particles are absent as we identified
421 only low-density defective virus (Figure 4). Such defective viruses were detected since early
422 passages of the MΦP culture (after passage 11; [25]); however, they were mixed with infectious
423 viruses displaying densities of 1.18 g/ml. Thus, after passage 120 we only identified viruses with
424 undetectable infectivity in HEp-2 cells and very low infectivity in Vero cells (which do not produce
425 type-I interferon), suggesting that progressive subculture of MΦP produced cumulative changes in
426 the viral genome.

427 Sequencing of the genomic RNA from defective viruses in MΦP supernatants, showed a full-length
428 genome with 38 nonsynonymous substitutions in ten of the eleven viral proteins, being F, G and
429 NS1 the proteins with higher mutation frequency (Figure 5); previous reports have described eight
430 of the 38 identified mutations [37–42,46,47].

431 Substitutions in the polymerase complex. The polymerase complex required for replication and
432 transcription of the hRSV genome consists of the large protein or L polymerase, the phosphoprotein
433 P, the nucleoprotein N and the processivity factor M2-1. N protein associates with nascent genomic
434 RNA possibly to modulate elongation during replication (increasing polymerase processivity) and
435 avoiding viral RNA destruction by cellular nucleases and/or recognition by the innate immune
436 system [48]. P protein is a fundamental polymerase-cofactor that tethers L polymerase to the N–
437 RNA complex. Other roles of P are as chaperone, preventing association of the recently synthesized
438 N with host cell RNAs, and recruiting of M2-1 to the polymerase complex for efficient transcription
439 [49]. Also, P protein has at least five phosphorylation sites of which, S116, S117 and S119 are
440 required for M2-2-mediated transcriptional inhibition [50], whereas this phosphorylated form of P
441 is also able to interact with N protein, contributing to viral assembly and budding from infected
442 cells [50,51].

443 We observed a total of ten nonsynonymous mutations in P, N, M2-1 and L proteins of which, only
444 two have been previously studied: 1) substitution I270A in N is related to diminished interaction
445 with P and reduced polymerase activity [37]. Our results showed the comparable substitution I270V
446 in protein N from the persistent hRSV; however, we have not evidence of altered polymerase
447 activity since, as mentioned before, hRSV genome is actively replicated in MΦP [32]. 2)
448 Substitutions S116L/A produce only a slight effect in P protein function, although S116D abolishes
449 completely its role during transcription and replication [47]; additionally, the former substitutions
450 partially affect N–P protein interaction [47,50]. We observed the substitution S116P in P protein and
451 we do not discard that such proline might be altering N–P interaction and, in consequence, viral

452 budding during hRSV persistence, although further experiments are necessary to determine
453 relevance of this particular mutation.

454 Unexpectedly, hRSV collected from csFITC⁺ showed a fourth mutation in the polymerase L with
455 respect to virus from csFITC⁻ that displayed only three mutations. Thus, virus from csFITC⁺
456 exhibited two mutations (Q1112R and V1124I) localized in the conserved region V (CRV, residues
457 956-1437) of the polymerase, involved in addition of a methylated cap to viral mRNAs [52]. Even
458 though we need to study biological relevance of having one or two mutations in the CRV, we
459 observed phenotypic differences between cells from csFITC⁺ and csFITC⁻, as the former culture
460 presented abundance of cells with a more rounded morphology and less firmly attached to surface
461 of culture dishes.

462 Substitutions in G protein. The attachment G protein is one of three hRSV envelope
463 glycoproteins (F and SH are the other two) and displays the highest variability with regards to
464 other proteins; for this reason it is a reference for virus classification into antigenic subtypes (A and
465 B) and genotypes [53]. Structurally, G is a type II glycoprotein with cytoplasmic and
466 transmembrane domains localized in the N-terminal region, and an extracellular domain displaying
467 only 44% of amino acid identity between subgroups [54,55]. A secreted form lacking the
468 cytoplasmic and part of the transmembrane (TM) domain is also produced in hRSV-infected cells
469 and escape mutations in these two domains have been observed in infected cultures under selective
470 pressure by a neutralizing anti-G antibody, resulting in reduced amounts of full-length G protein
471 on the cell-surface and into the viral envelope [38].

472 We found two nonsynonymous substitutions in the cytoplasmic domain of G (D6V and G29C) and
473 one localized in the TM domain (I50T); position D6 has been described as involved in interaction
474 with protein M during matrix assembly (located under the viral envelope), although it has been
475 reported that protein F has a redundant role through its direct interaction with M [38]. Considering
476 the three substitutions observed in the cytoplasmic and TM domains of G in viruses from MΦP
477 cultures, we do not discard main production of this glycoprotein in its soluble form and assembly
478 of virions with low levels of this envelope protein. Interestingly, virions released from cells infected
479 with a G-deleted hRSV, show up to 60% less quantity of SH protein in their envelope [56],
480 suggesting that a lack of G protein may alter hRSV assembly and possibly its buoyant density.

481 Substitutions in F protein. Fusion protein F is essential for viral entry through fusion of the
482 viral envelope with the host-cell plasma membrane, allowing access of the capsid to the cytoplasm
483 to initiate viral replication; also mediates cell-cell fusion and development of syncytia [57]. Protein F
484 is expressed in a pre-fusion state on the viral envelope and undergoes conformational changes to a
485 post-fusion form, upon binding to hRSV receptors that potentially are ICAM-I and nucleolin [58].
486 Five of the 13 sites with nonsynonymous mutations identified in the persistent hRSV-F protein have
487 been previously studied. Of relevance, K68 provides a positive charge that is essential for lipid
488 bilayer fusion [39]; our finding of the K68Q substitution might be related to absence of syncytia in
489 MΦP cultures and the low-to-undetectable viral infectivity. Also, I79 is related to stability of the
490 pre-fusion conformation and an earlier report indicates I79A substitution avoids membrane fusion,
491 probably by premature transition to the post-fusion conformation [40]; we observed the I79M
492 substitution, which may have similar consequences. It is also notable the uncharacterized
493 substitution I152T localized inside the fusion peptide [59], which might affect the hydrophobic
494 property of this domain, since threonine is a polar amino acid. In summary, substitutions K68Q,

495 I79M and I152T may be associated to altered viral-cell fusion and cell-cell fusion processes in MΦP
496 cultures.

497 Furthermore, a substitution M526I in F was reported in an infant with severe combined
498 immunodeficiency syndrome and persistent hRSV infection (>70 days virus detection in respiratory
499 samples), but only after bone marrow transplant [24]. Biological relevance of this substitution was
500 not studied; however, authors proposed it might be associated to specific or nonspecific immune
501 responses [24]. Considering it was observed a M526L substitution in the persistent hRSV from MΦP
502 cultures, we suggest it might be associated to innate immune pressure.

503 Substitutions in NS1. The two nonstructural proteins, NS1 and NS2, are hRSV molecules
504 responsible of suppressing the type I interferon (IFN-I)-mediated antiviral response [60]. Even
505 though the substitutions we observed in NS1 protein have not been previously characterized, it is
506 notable that the T123S (Table 2) is inside the NS1 helix α -3, which is a determinant domain for
507 innate immune modulation [61]. We previously reported that nuclear localization of IRF-3 and
508 synthesis of IFN- β are constitutive in MΦP, however, autocrine response to this cytokine is blocked,
509 and recombinant-IFN- β does not induce either STAT-1 phosphorylation or antiviral gene
510 transcription [31]. Further research is necessary to determine whether the T123S substitution in NS1
511 altered its role, as suppressor of IFN-I synthesis in MΦP, enabling NS2 as main antiviral effector
512 [62] contributing to maintenance of hRSV persistence. Notably, replication of defective viruses
513 (from supernatants of MΦP cultures) in HEp-2 cells was not significantly improved in Vero cells,
514 suggesting that mutations in NS1 and NS2 proteins were not principal determinants for lowering
515 infectious capacity, as may be mutations in proteins F and G.

516 5. Conclusions

517 Our results provided evidence that hRSV established a steady-state persistent infection in
518 macrophage-like cells, since all of the cells studied from MΦP cultures harbored the viral genome,
519 whereas non-infectious viral particles were mainly produced. However, it is still important to study
520 mechanisms associated to viral genome transmission and regulation of gene expression during
521 hRSV persistence. After sequencing the persistent viral genome isolated from virus particles from
522 MΦP culture supernatants we did not detect either gene deletions or insertions. However, the
523 nonsynonymous mutations identified and previously characterized, suggested that persistent hRSV
524 is defective in our *in vitro* model mainly by alterations at the level of viral assembly, viral budding
525 and membrane fusion; such alterations may be associated to the long-term infection. Further
526 characterization of the 30 novel nonsynonymous mutations would be useful to understand the
527 complex virus-host cell interaction related to hRSV persistence in macrophage-like cells, and as a
528 possibility, to identify molecular markers of persistent hRSV-infections.

529

530 **Author Contributions:** Conceptualization, ERT, JAVP; experiments XRG, ERT, JAVP, CSO, MEP, OFH;
531 confocal microscopy analysis, CM; data analysis, ERT, XRG, JAVP, JGB, BG; manuscript preparation ERT;
532 funding acquisition, ERT.

533 **Funding:** This research was supported by a grant from the School of Medicine of the National Autonomous
534 University of Mexico.

535

536 **Acknowledgments:** We thank Ana Flisser for providing the infrastructure and for review of this
537 manuscript. We thank María Jose Gómora Herrera for microscopy technical assistance. We thank Tanya Plett
538 Torres, Adriana Gaspar Rodríguez and Elizabeth Linares Alcántara for scientific discussions. Finally, we thank

539 Ricardo Alfredo Grande Cano for technical assistance in preparing samples for RNA-seq.

540

541 **Conflicts of Interest:** The authors declare no conflict of interest.

542

543 References

- 544 1. Panuska, J.R.; Hertz, M.I.; Taraf, H.; Villani, A.; Cirino, N.M. Respiratory Syncytial Virus
545 Infection of Alveolar Macrophages in Adult Transplant Patients. *Am Rev Respir Dis* **1992**, *145*, 934–
546 939, doi:10.1164/ajrccm/145.4_Pt_1.934.
- 547 2. Papin, J.F.; Wolf, R.F.; Kosanke, S.D.; Jenkins, J.D.; Moore, S.N.; Anderson, M.P.; Welliver, R.C.
548 Infant baboons infected with respiratory syncytial virus develop clinical and pathological changes
549 that parallel those of human infants. *American Journal of Physiology-Lung Cellular and Molecular*
550 *Physiology* **2013**, *304*, L530–L539, doi:10.1152/ajplung.00173.2012.
- 551 3. Johnson, J.E.; Gonzales, R.A.; Olson, S.J.; Wright, P.F.; Graham, B.S. The histopathology of fatal
552 untreated human respiratory syncytial virus infection. *Mod Pathol* **2007**, *20*, 108–119,
553 doi:10.1038/modpathol.3800725.
- 554 4. Gould, P.S.; Easton, A.J. Coupled Translation of the Respiratory Syncytial Virus M2 Open
555 Reading Frames Requires Upstream Sequences. *J. Biol. Chem.* **2005**, *280*, 21972–21980,
556 doi:10.1074/jbc.M502276200.
- 557 5. Cartee, T.L.; Wertz, G.W. Respiratory Syncytial Virus M2-1 Protein Requires Phosphorylation
558 for Efficient Function and Binds Viral RNA during Infection. *J. Virol.* **2001**, *75*, 12188–12197,
559 doi:10.1128/JVI.75.24.12188-12197.2001.
- 560 6. Cheng, X.; Park, H.; Zhou, H.; Jin, H. Overexpression of the M2-2 Protein of Respiratory
561 Syncytial Virus Inhibits Viral Replication. *JVI* **2005**, *79*, 13943–13952,
562 doi:10.1128/JVI.79.22.13943-13952.2005.
- 563 7. Sedeyn, K.; Schepens, B.; Saelens, X. Respiratory syncytial virus nonstructural proteins 1 and 2:
564 Exceptional disrupters of innate immune responses. *PLoS Pathog* **2019**, *15*, e1007984,
565 doi:10.1371/journal.ppat.1007984.
- 566 8. Shi, T.; McAllister, D.A.; O'Brien, K.L.; Simoes, E.A.F.; Madhi, S.A.; Gessner, B.D.; Polack, F.P.;
567 Balsells, E.; Acacio, S.; Aguayo, C.; et al. Global, regional, and national disease burden estimates of
568 acute lower respiratory infections due to respiratory syncytial virus in young children in 2015: a
569 systematic review and modelling study. *The Lancet* **2017**, *390*, 946–958,
570 doi:10.1016/S0140-6736(17)30938-8.
- 571 9. Sigurs, N.; Bjarnason, R.; Sigurbergsson, F.; Kjellman, B. Respiratory Syncytial Virus
572 Bronchiolitis in Infancy Is an Important Risk Factor for Asthma and Allergy at Age 7. *Am J Respir*
573 *Crit Care Med* **2000**, *161*, 1501–1507, doi:10.1164/ajrccm.161.5.9906076.
- 574 10. Sigurs, N.; Aljassim, F.; Kjellman, B.; Robinson, P.D.; Sigurbergsson, F.; Bjarnason, R.;
575 Gustafsson, P.M. Asthma and allergy patterns over 18 years after severe RSV bronchiolitis in the
576 first year of life. *Thorax* **2010**, *65*, 1045–1052, doi:10.1136/thx.2009.121582.
- 577 11. Schauer, U.; Hoffjan, S.; Bittscheidt, J.; Kochling, A.; Hemmis, S.; Bongartz, S.; Stephan, V. RSV
578 bronchiolitis and risk of wheeze and allergic sensitisation in the first year of life. *European*
579 *Respiratory Journal* **2002**, *20*, 1277–1283, doi:10.1183/09031936.02.00019902.

- 580 12. Stein, R.T.; Sherrill, D.; Morgan, W.J.; Holberg, C.J.; Halonen, M.; Taussig, L.M.; Wright, A.L.;
581 Martinez, F.D. Respiratory syncytial virus in early life and risk of wheeze and allergy by age 13
582 years. *The Lancet* **1999**, *354*, 541–545, doi:10.1016/S0140-6736(98)10321-5.
- 583 13. Zomer-Kooijker, K.; Uiterwaal, C.S.P.M.; van der Gugten, A.C.; Wilbrink, B.; Bont, L.J.; van der
584 Ent, C.K. Decreased lung function precedes severe respiratory syncytial virus infection and
585 post-respiratory syncytial virus wheeze in term infants. *European Respiratory Journal* **2014**, *44*, 666–
586 674, doi:10.1183/09031936.00009314.
- 587 14. Simões, E.A.F.; Carbonell-Estrany, X.; Rieger, C.H.L.; Mitchell, I.; Fredrick, L.; Groothuis, J.R.
588 The effect of respiratory syncytial virus on subsequent recurrent wheezing in atopic and nonatopic
589 children. *Journal of Allergy and Clinical Immunology* **2010**, *126*, 256–262, doi:10.1016/j.jaci.2010.05.026.
- 590 15. Sikkel, M.B.; Quint, J.K.; Mallia, P.; Wedzicha, J.A.; Johnston, S.L. Respiratory Syncytial Virus
591 Persistence in Chronic Obstructive Pulmonary Disease: *The Pediatric Infectious Disease Journal* **2008**,
592 *27*, S63–S70, doi:10.1097/INF.0b013e3181684d67.
- 593 16. Bramley, A.M.; Vitalis, T.Z.; Wiggs, B.R.; Hegele, R.G. Effects of respiratory syncytial virus
594 persistence on airway responsiveness and inflammation in guinea-pigs. *European Respiratory Journal*
595 **1999**, *14*, 1061–1067, doi:10.1183/09031936.99.14510619.
- 596 17. Estripeaut, D.; Torres, J.P.; Somers, C.S.; Tagliabue, C.; Khokhar, S.; Bhoj, V.G.; Grube, S.M.;
597 Wozniakowski, A.; Gomez, A.M.; Ramilo, O.; et al. Respiratory Syncytial Virus Persistence in the
598 Lungs Correlates with Airway Hyperreactivity in the Mouse Model. *J INFECT DIS* **2008**, *198*, 1435–
599 1443, doi:10.1086/592714.
- 600 18. Piedimonte, G.; Walton, C.; Samsell, L. Vertical Transmission of Respiratory Syncytial Virus
601 Modulates Pre- and Postnatal Innervation and Reactivity of Rat Airways. *PLoS ONE* **2013**, *8*, e61309,
602 doi:10.1371/journal.pone.0061309.
- 603 19. Schwarze, J.; O'Donnell, D.R.; Rohwedder, A.; Openshaw, P.J.M. Latency and Persistence of
604 Respiratory Syncytial Virus Despite T Cell Immunity. *Am J Respir Crit Care Med* **2004**, *169*, 801–805,
605 doi:10.1164/rccm.200308-1203OC.
- 606 20. Jartti, T.; Jartti, L.; Peltola, V.; Waris, M.; Ruuskanen, O. Identification of Respiratory Viruses in
607 Asymptomatic Subjects: Asymptomatic Respiratory Viral Infections. *The Pediatric Infectious Disease*
608 *Journal* **2008**, *27*, 1103–1107, doi:10.1097/INF.0b013e31817e695d.
- 609 21. Borg, I.; Rohde, G.; Löseke, S.; Bittscheidt, J.; Schultze-Werninghaus, G.; Stephan, V.; Bufe, A.
610 Evaluation of a quantitative real-time PCR for the detection of respiratory syncytial virus in
611 pulmonary diseases. *Eur Respir J* **2003**, *21*, 944–951, doi:10.1183/09031936.03.00088102.
- 612 22. Rezaee, F.; Gibson, L.F.; Piktel, D.; Othumpangat, S.; Piedimonte, G. Respiratory Syncytial
613 Virus Infection in Human Bone Marrow Stromal Cells. *Am J Respir Cell Mol Biol* **2011**, *45*, 277–286,
614 doi:10.1165/rcmb.2010-0121OC.
- 615 23. Cubie, H.A.; Duncan, L.A.; Marshall, L.A.; Smith, N.M. Detection of respiratory syncytial virus
616 nucleic acid in archival postmortem tissue from infants. *Pediatr Pathol Lab Med* **1997**, *17*, 927–938.
- 617 24. Grad, Y.H.; Newman, R.; Zody, M.; Yang, X.; Murphy, R.; Qu, J.; Malboeuf, C.M.; Levin, J.Z.;
618 Lipsitch, M.; DeVincenzo, J. Within-Host Whole-Genome Deep Sequencing and Diversity Analysis
619 of Human Respiratory Syncytial Virus Infection Reveals Dynamics of Genomic Diversity in the
620 Absence and Presence of Immune Pressure. *Journal of Virology* **2014**, *88*, 7286–7293,
621 doi:10.1128/JVI.00038-14.

- 622 25. Sarmiento, R.E.; Tirado, R.; Gómez, B. Characteristics of a respiratory syncytial virus
623 persistently infected macrophage-like culture. *Virus Research* **2002**, *84*, 45–58,
624 doi:10.1016/S0168-1702(01)00420-8.
- 625 26. Martínez, I.; Lombardía, L.; Herranz, C.; García-Barreno, B.; Domínguez, O.; Melero, J.A.
626 Cultures of HEp-2 cells persistently infected by human respiratory syncytial virus differ in
627 chemokine expression and resistance to apoptosis as compared to lytic infections of the same cell
628 type. *Virology* **2009**, *388*, 31–41, doi:10.1016/j.virol.2009.03.008.
- 629 27. Hobson, L.; Everard, M.L. Persistent of respiratory syncytial virus in human dendritic cells and
630 influence of nitric oxide. *Clin. Exp. Immunol.* **2008**, *151*, 359–366, doi:10.1111/j.1365-2249.2007.03560.x.
- 631 28. Ito, M.; Takeuchi, T.; Nishio, M.; Kawano, M.; Komada, H.; Tsurudome, M.; Ito, Y. Early Stage
632 of Establishment of Persistent Sendai Virus Infection: Unstable Dynamic Phase and Then Selection
633 of Viruses Which Are Tightly Cell Associated, Temperature Sensitive, and Capable of Establishing
634 Persistent Infection. *JVI* **2004**, *78*, 11939–11951, doi:10.1128/JVI.78.21.11939-11951.2004.
- 635 29. Woodbury, E.L. A review of the possible mechanisms for the persistence of foot-and-mouth
636 disease virus. *Epidemiol. Infect.* **1995**, *114*, 1–13, doi:10.1017/S0950268800051864.
- 637 30. Nakamura-López, Y.; Villegas-Sepúlveda, N.; Sarmiento-Silva, R.E.; Gómez, B. Intrinsic
638 apoptotic pathway is subverted in mouse macrophages persistently infected by RSV. *Virus Research*
639 **2011**, *158*, 98–107, doi:10.1016/j.virusres.2011.03.016.
- 640 31. Rivera-Toledo, E.; Torres-González, L.; Gómez, B. Respiratory Syncytial Virus Persistence in
641 Murine Macrophages Impairs IFN- β Response but Not Synthesis. *Viruses* **2015**, *7*, 5361–5374,
642 doi:10.3390/v7102879.
- 643 32. Santiago-Olivares, C.; Rivera-Toledo, E.; Gómez, B. Nitric oxide production is downregulated
644 during respiratory syncytial virus persistence by constitutive expression of arginase 1. *Arch Virol*
645 **2019**, *164*, 2231–2241, doi:10.1007/s00705-019-04259-0.
- 646 33. Lifland, A.W.; Jung, J.; Alonas, E.; Zurla, C.; Crowe, J.E.; Santangelo, P.J. Human Respiratory
647 Syncytial Virus Nucleoprotein and Inclusion Bodies Antagonize the Innate Immune Response
648 Mediated by MDA5 and MAVS. *Journal of Virology* **2012**, *86*, 8245–8258, doi:10.1128/JVI.00215-12.
- 649 34. Guo, R.; Shang, P.; Carrillo, C.A.; Sun, Z.; Lakshmanappa, Y.S.; Yan, X.; Renukaradhya, G.J.;
650 McGill, J.; Jaing, C.J.; Niederwerder, M.C.; et al. Double-stranded viral RNA persists in vitro and in
651 vivo during prolonged infection of porcine reproductive and respiratory syndrome virus. *Virology*
652 **2018**, *524*, 78–89, doi:10.1016/j.virol.2018.08.006.
- 653 35. Pinkert, S.; Klingel, K.; Lindig, V.; Dorner, A.; Zeichhardt, H.; Spiller, O.B.; Fechner, H.
654 Virus-Host Coevolution in a Persistently Coxsackievirus B3-Infected Cardiomyocyte Cell Line.
655 *Journal of Virology* **2011**, *85*, 13409–13419, doi:10.1128/JVI.00621-11.
- 656 36. Mbiguino, A.; Menezes, J. Purification of human respiratory syncytial virus: superiority of
657 sucrose gradient over percoll, renografin, and metrizamide gradients. *Journal of Virological Methods*
658 **1991**, *31*, 161–170, doi:10.1016/0166-0934(91)90154-R.
- 659 37. Esneau, C.; Raynal, B.; Roblin, P.; Brûlé, S.; Richard, C.-A.; Fix, J.; Eléouët, J.-F.; Galloux, M.
660 Biochemical characterization of the respiratory syncytial virus N⁰-P complex in solution. *J. Biol.*
661 *Chem.* **2019**, *294*, 3647–3660, doi:10.1074/jbc.RA118.006453.
- 662 38. Ghildyal, R.; Li, D.; Peroulis, I.; Shields, B.; Bardin, P.G.; Teng, M.N.; Collins, P.L.; Meanger, J.;
663 Mills, J. Interaction between the respiratory syncytial virus G glycoprotein cytoplasmic domain and

- 664 the matrix protein. *Journal of General Virology* **2005**, *86*, 1879–1884, doi:10.1099/vir.0.80829-0.
- 665 39. Hicks, S.N.; Chaiwatpongsakorn, S.; Costello, H.M.; McLellan, J.S.; Ray, W.; Peeples, M.E. Five
666 Residues in the Apical Loop of the Respiratory Syncytial Virus Fusion Protein F2 Subunit Are
667 Critical for Its Fusion Activity. *Journal of Virology* **2018**, *92*, 16.
- 668 40. Bermingham, I.M.; Chappell, K.J.; Watterson, D.; Young, P.R. The Heptad Repeat C Domain of
669 the Respiratory Syncytial Virus Fusion Protein Plays a Key Role in Membrane Fusion. *J. Virol.* **2017**,
670 JVI.01323-17, doi:10.1128/JVI.01323-17.
- 671 41. Leemans, A.; Boeren, M.; Van der Gucht, W.; Pintelon, I.; Roose, K.; Schepens, B.; Saelens, X.;
672 Bailey, D.; Martinet, W.; Caljon, G.; et al. Removal of the N-Glycosylation Sequon at Position N116
673 Located in p27 of the Respiratory Syncytial Virus Fusion Protein Elicits Enhanced Antibody
674 Responses after DNA Immunization. *Viruses* **2018**, *10*, 426, doi:10.3390/v10080426.
- 675 42. Branigan, P.J. The cytoplasmic domain of the F protein of Human respiratory syncytial virus is
676 not required for cell fusion. *Journal of General Virology* **2006**, *87*, 395–398, doi:10.1099/vir.0.81481-0.
- 677 43. Fazekas, J.; Grunt, T.W.; Jensen-Jarolim, E.; Singer, J. Long term storage in liquid nitrogen leads
678 to only minor phenotypic and gene expression changes in the mammary carcinoma model cell line
679 BT474. *Oncotarget* **2017**, *8*, 35076–35087, doi:10.18632/oncotarget.16623.
- 680 44. Maggioli, M.F.; Fernandes, M.H.V.; Joshi, L.R.; Sharma, B.; Tweet, M.M.; Noll, J.C.G.;
681 Bauermann, F.V.; Diel, D.G. Persistent Infection and Transmission of Senecavirus A from Carrier
682 Sows to Contact Piglets. *J Virol* **2019**, *93*, e00819-19, /jvi/93/21/JVI.00819-19.atom,
683 doi:10.1128/JVI.00819-19.
- 684 45. Mateer, E.; Paessler, S.; Huang, C. Confocal Imaging of Double-Stranded RNA and Pattern
685 Recognition Receptors in Negative-Sense RNA Virus Infection. *JoVE* **2019**, 59095, doi:10.3791/59095.
- 686 46. Zhu, Q.; Lu, B.; McTamney, P.; Palaszynski, S.; Diallo, S.; Ren, K.; Ulbrandt, N.D.; Kallewaard,
687 N.; Wang, W.; Fernandes, F.; et al. Prevalence and Significance of Substitutions in the Fusion
688 Protein of Respiratory Syncytial Virus Resulting in Neutralization Escape From Antibody
689 MEDI8897. *The Journal of Infectious Diseases* **2018**, *218*, 572–580, doi:10.1093/infdis/jiy189.
- 690 47. Lu, B.; Ma, C.-H.; Brazas, R.; Jin, H. The Major Phosphorylation Sites of the Respiratory
691 Syncytial Virus Phosphoprotein Are Dispensable for Virus Replication In Vitro. *JVI* **2002**, *76*, 10776–
692 10784, doi:10.1128/JVI.76.21.10776-10784.2002.
- 693 48. Fearn, R.; Deval, J. New antiviral approaches for respiratory syncytial virus and other
694 mononegaviruses: Inhibiting the RNA polymerase. *Antiviral Research* **2016**, *134*, 63–76,
695 doi:10.1016/j.antiviral.2016.08.006.
- 696 49. Gilman, M.S.A.; Liu, C.; Fung, A.; Behera, I.; Jordan, P.; Rigaux, P.; Ysebaert, N.; Tcherniuk, S.;
697 Sourimant, J.; Eléouët, J.-F.; et al. Structure of the Respiratory Syncytial Virus Polymerase Complex.
698 *Cell* **2019**, *179*, 193-204.e14, doi:10.1016/j.cell.2019.08.014.
- 699 50. Asenjo, A.; Villanueva, N. Phosphorylation of the human respiratory syncytial virus P protein
700 mediates M2-2 regulation of viral RNA synthesis, a process that involves two P proteins. *Virus*
701 *Research* **2016**, *211*, 117–125, doi:10.1016/j.virusres.2015.10.011.
- 702 51. Villanueva, N.; Navarro, J.; Cubero, E. Antiviral effects of xanthate D609 on the human
703 respiratory syncytial virus growth cycle. *Virology* **1991**, *181*, 101–108,
704 doi:10.1016/0042-6822(91)90474-P.
- 705 52. Braun, M.R.; Deflubé, L.R.; Noton, S.L.; Mawhorter, M.E.; Tremaglio, C.Z.; Fearn, R. RNA

- 706 elongation by respiratory syncytial virus polymerase is calibrated by conserved region V. *PLoS*
707 *Pathog* **2017**, *13*, e1006803, doi:10.1371/journal.ppat.1006803.
- 708 53. Do, L.A.H.; Wilm, A.; van Doorn, H.R.; Lam, H.M.; Sim, S.; Sukumaran, R.; Tran, A.T.;
709 Nguyen, B.H.; Tran, T.T.L.; Tran, Q.H.; et al. Direct whole-genome deep-sequencing of human
710 respiratory syncytial virus A and B from Vietnamese children identifies distinct patterns of inter-
711 and intra-host evolution. *Journal of General Virology* **2015**, *96*, 3470–3483, doi:10.1099/jgv.0.000298.
- 712 54. Kwilas, S.; Liesman, R.M.; Zhang, L.; Walsh, E.; Pickles, R.J.; Peeples, M.E. Respiratory
713 Syncytial Virus Grown in Vero Cells Contains a Truncated Attachment Protein That Alters Its
714 Infectivity and Dependence on Glycosaminoglycans. *JVI* **2009**, *83*, 10710–10718,
715 doi:10.1128/JVI.00986-09.
- 716 55. Collins, P.L. O glycosylation of glycoprotein G of human respiratory syncytial virus is
717 specified within the divergent ectodomain. *Journal of Virology* **1990**, *64*, 4007–4012,
718 doi:10.1128/JVI.64.8.4007-4012.1990.
- 719 56. Batonick, M.; Wertz, G.W. Requirements for Human Respiratory Syncytial Virus Glycoproteins
720 in Assembly and Egress from Infected Cells. *Advances in Virology* **2011**, *2011*, 1–11,
721 doi:10.1155/2011/343408.
- 722 57. Rossey, I.; McLellan, J.S.; Saelens, X.; Schepens, B. Clinical Potential of Prefusion RSV F-specific
723 Antibodies. *Trends in Microbiology* **2018**, *26*, 209–219, doi:10.1016/j.tim.2017.09.009.
- 724 58. Mastrangelo, P.; Hegele, R.G. Host and Viral Factors in Respiratory Syncytial Virus Infection.
725 *Curr Pediatr Rep* **2013**, *1*, 149–157, doi:10.1007/s40124-013-0019-3.
- 726 59. Sun, Z.; Pan, Y.; Jiang, S.; Lu, L. Respiratory Syncytial Virus Entry Inhibitors Targeting the F
727 Protein. *Viruses* **2013**, *5*, 211–225, doi:10.3390/v5010211.
- 728 60. Goswami, R.; Majumdar, T.; Dhar, J.; Chattopadhyay, S.; Bandyopadhyay, S.K.; Verbovetskaya,
729 V.; Sen, G.C.; Barik, S. Viral degradasome hijacks mitochondria to suppress innate immunity. *Cell*
730 *Res* **2013**, *23*, 1025–1042, doi:10.1038/cr.2013.98.
- 731 61. Chatterjee, S.; Luthra, P.; Esaulova, E.; Agapov, E.; Yen, B.C.; Borek, D.M.; Edwards, M.R.;
732 Mittal, A.; Jordan, D.S.; Ramanan, P.; et al. Structural basis for human respiratory syncytial virus
733 NS1-mediated modulation of host responses. *Nat Microbiol* **2017**, *2*, 17101,
734 doi:10.1038/nmicrobiol.2017.101.
- 735 62. Whelan, J.N.; Tran, K.C.; van Rossum, D.B.; Teng, M.N. Identification of Respiratory Syncytial
736 Virus Nonstructural Protein 2 Residues Essential for Exploitation of the Host Ubiquitin System and
737 Inhibition of Innate Immune Responses. *J. Virol.* **2016**, *90*, 6453–6463, doi:10.1128/JVI.00423-16.
- 738



© 2020 by the authors. Submitted for possible open access publication under the terms and conditions of the Creative Commons Attribution (CC BY) license (<http://creativecommons.org/licenses/by/4.0/>).



*"Lehninger Preparations"*Odra Noel

Capítulos de Libro

12. CAPÍTULOS DE LIBRO

- “*Proteomics of lignocellulosic substrates bioconversion in anaerobic digesters to increase the carbon recovery as methane*” Alicia Guadalupe Talavera-Caro, María Alejandra Sánchez-Muñoz, Inty Omar Hernández-De Lira, Lilia Ernestina Montañez-Hernández, Jesús Antonio Morlett-Chávez, **María de las Mercedes Esparza-Perusquía**, Nagamani Balagurusamy. Biological Approaches for the Management of Agro-industrial Residues Applied Environmental Science and Engineering for a Sustainable Future. (2020) Editor: Zainul Akmar Zakaria, Ramaraj Boopathy, Julian Rafael Dib, Reeta Rani Singhania. Springer, Cham. ISBN 978-3-030-39137-9.

Chapter 4

Proteomics of Lignocellulosic Substrates Bioconversion in Anaerobic Digesters to Increase Carbon Recovery as Methane



Alicia Guadalupe Talavera-Caro, María Alejandra Sánchez-Muñoz, Inty Omar Hernández-De Lira, Lilia Ernestina Montañez-Hernández, Ayerim Yedid Hernández-Almanza, Jesús Antonio Morlett-Chávez, María de las Mercedes Esparza-Perusquia, and Nagamani Balagurusamy

Abstract Anaerobic digestion (AD) is a cost-effective treatment for management of lignocellulosic substrates, viz., agricultural wastes and animal manures, which also aids in generation of methane as biofuel. Although the application of AD technology is increasing, one of the major limitations of the process is that the rate of fermentation is higher than the rate of methanogenesis, which significantly affects process stability and methane yield. Normally, the souring of digesters can be observed after 2–4 weeks after the initiation of the volatile fatty acids accumulation, which makes it difficult for early detection and consequently resulting in acidification of digesters. Of late, metagenomic approaches are gaining importance due to their ability to reveal the microbial diversity and their dynamics in a relatively short time. However, their functional nature could not be clearly explained due to the lack of data on their activity. Recent advances in proteomic studies show its potential as a complementary technology to metagenomic studies for efficient management of digesters. Metaproteomic analyses aid in identifying a shift in metabolic paths and in metabolic networks under stress conditions. This provides insights on functionality, microbial interactions, and provides data on spatiotemporal variations and their dynamics of proteins crucial for efficient performance of the digester. Besides, this technique has

A. G. Talavera-Caro · M. A. Sánchez-Muñoz · I. O. H.-D. Lira · L. E. Montañez-Hernández · A. Y. Hernández-Almanza · N. Balagurusamy (✉)
Facultad de Ciencias Biológicas, Laboratorio de Bioremediación, Universidad Autónoma de Coahuila, Torreón, Mexico
e-mail: bnagamani@uadec.edu.mx

J. A. Morlett-Chávez
Facultad de Ciencias Químicas, Laboratorio de Biología Molecular, Universidad Autónoma de Coahuila, Saltillo, Mexico

M. d. I. M. Esparza-Perusquia
Facultad de Medicina, Departamento de Bioquímica, Universidad Nacional Autónoma de México, Ciudad de México, Mexico

© Springer Nature Switzerland AG 2020

Z. A. Zakaria et al. (eds.), *Valorisation of Agro-industrial Residues – Volume I: Biological Approaches*, Applied Environmental Science and Engineering for a Sustainable Future, https://doi.org/10.1007/978-3-030-39137-9_4

led to identify novel phylotypes with novel functions among the microbial communities of the anaerobic digesters, which suggest the potential of proteomics in bioprospection of novel enzymes for industrial purposes. How proteomics along with metagenomics and transcriptomics data could aid in early detection of disturbances in the digesters helps in formulating recovery strategies as well as to increase the methane content of biogas will be discussed in this chapter.

Keywords Anaerobic digestion · Metabolic networks · Methane · Proteomics

4.1 Introduction

The recent use of lignocellulosic biomass as a renewable energy source has been of increasing interest due to the environmental crisis and alarming decline in fossil fuel reserves. In the next few decades, bioenergy will be considered as one of the potential renewable energy sources, in addition to other renewable energy sources, e.g., wind and solar. Wide-scale practice of these technologies depends on the economics involved in their infrastructure and maintenance. Among all, bioenergy from biomass is constantly investigated due to their easiness in installation and operation. Anaerobic digestion (AD) is one of the processes widely used to recover energy from biomass sources, like animal manures, solid municipal wastes, paper industry wastes, energy crops, or agricultural wastes, in the form of methane (Nallathambi Gunaseelan 1997).

Anaerobic digestion process degrade/oxidize organic matter under anaerobic conditions by several consortia of different metabolic groups of microorganisms, where methane (60–70%) and carbon dioxide (30–40%), and other trace gases (<1% hydrogen, nitrogen, ammonia, and hydrogen sulfide) are major end products. However, methane is the most valuable product because it can be used to generate electricity and heat (Angelidaki et al. 2003). Methane production in AD process involves four different steps: hydrolysis, acidogenesis, acetogenesis, and methanogenesis.

Nevertheless, microorganisms carrying out this degradation/transformation reactions differs in their physiology, nutritional requirement, growth kinetics, and are sensitive to the environment. This characteristics lead to a delicate balance between all group of microorganisms involved in AD, and any modification can cause instability and consequently, low methane yield (Adekunle and Okolie 2015). For this reason, over the last decade, there has been a rapid development in state-of-the-art techniques to understand the microbial community dynamics, interactions, and functionality to achieve a proper digester efficiency and stability. Besides, it is necessary to study the non-culturable microorganisms involved in the process and its proteome to fill the knowledge gaps in our understanding of the complex microbial interplay and functionality in AD process.

The study of microbial diversity and gene expression in AD, through metagenomic and metatranscriptomic analysis, has helped us to reveal “black box” contents and their role to a certain level. Still, there is limited understanding of all the possible metabolic pathways that are active throughout the biomethanation process

and without which, successful operation and maintenance of biodigesters for higher methane yield. Hence, the interest on metaproteomics of digesters is gaining attention. This tool can evaluate growth and activity of different microorganisms in relation to their environment (protein expression and localization), to identify posttranslational modification, to infer certain protein–protein interactions, amino acid sequences, and genotypes, besides protein identification (Vanwonderghem et al. 2014). As well, metaproteomic databases can permit to examine targeted biomarkers from microbial communities for evaluation of the biodigester functioning. In this chapter, we focus on the contribution of metaproteomic approaches to gain an insight on the composition of microorganisms sharing similar metabolic structure, and the shift in their dynamics and functions under certain environmental or induced conditions in biodigesters employing lignocellulosic substrates as main feedstock.

4.2 Anaerobic Digestion of Lignocellulosic Substrates

Global annual production of available lignocellulosic biomass is 181.5 billion tonnes. In USA alone, about 1.25 billion tonnes of lignocellulosic biomass is produced annually, while in Canada, about 69.25 million tonnes are generated (Paul and Dutta 2018). The use of biomass residues as sources of renewable energy has increased. Recently, the lignocellulosic-rich biomass feedstocks such as fibrous food wastes, animal manures, paper industry wastes, agro residues, and energy crops are mostly used as feedstocks for bioenergy production (Sawatdeenarunat et al. 2015). Apart from biogas production, ethanol and butanol production from lignocellulosic biomass, such as wheat straw, corn cob, and sugarcane bagasse is also being studied (Jiang et al. 2017).

The major components of the lignocellulosic biomasses are cellulose, hemicellulose, and lignin, which are hydrolyzed through a series of reactions by microorganisms. Cellulose and hemicellulose are the predominant polysaccharides in these biomass materials. Whereas, lignin is conformed of phenolic polymers, which add recalcitrance to the complex structure of lignocellulose substrates and limits the accessibility of polysaccharides by microbial enzymes (Isikgor and Becer 2015; Liu and Chen 2015). Li et al. (2018) reported the interaction of cellulose, hemicellulose, and lignin components on biodegradability of different lignocellulosic biomasses and observed that methane production was favored and correlated with decomposition of substrates rich in cellulose and hemicellulose, whereas, lignin was not completely digested (Li et al. 2018).

Nevertheless, the lignocellulosic biomass shows low rate of polysaccharide hydrolysis due to the presence of lignin (Cesarino et al. 2012). Therefore, to increase hydrolysis rate, methods of pretreatment have been developed (Ariunbaatar et al. 2014) and becoming crucial to anaerobic digestion process. Pretreatments aid to overcome limitations and eliminate the barriers to access polysaccharides for degradation, augment digestibility, and consequently increase biogas production from lignocellulosic biomass residues (Chen et al. 2014). Pretreatment techniques such as physical (steam explosion, hydro-thermolysis, thermochemical), chemical (alkalis,

acids, oxidants as organic solvents), nonconventional (ionic liquids), and biological processes are mostly applied to polysaccharide decomposition (Singh et al. 2015; Carrere et al. 2016).

Enhancement in methane yield has been reported for several lignocellulosic residues, which reveal the significant improvements on lignin depolymerization. However, type of pretreatment depends on the composition of lignocellulosic feedstocks (Table 4.1), since the type and accumulation of products after pretreatment process can either be beneficial or harmful to the microbial consortium of AD process (Poudel et al. 2012; Ahring et al. 2015).

Additionally, C:N ratio of lignocellulosic-rich substrates is an important parameter as high and low ratios were found to have negative impact on the process by altering pH, and consequently inhibiting growth and activity of microbial communities in the biodigester (Rahman et al. 2017). In general, to overcome the limitations due to C:N ratios, the addition of a co-substrate rich in carbon or nitrogen provide optimum conditions for biomethanation and this process is known as co-digestion. Selection of suitable co-substrate is important, in order to enhance synergisms, dilute detrimental compounds, and optimize the methane yield without affecting digestate quality (Mata-Alvarez et al. 2014; Siddique and Wahid 2018). Hence, research on the AD process evolves continuously to identify optimum operational conditions and their relation to the microbial diversity, their function to increase methane yield.

4.3 Recognizing Important Pathways of AD

In terms of energy, anaerobic digestion is a green technology, where biogas production is a more efficient method for energy generation from biomass than other biological and thermochemical conversion processes (Deublein 2009). AD is an alternative to landfills as a means of organic waste management as AD process generates energy apart from reducing methane emissions. Similarly, traditional management of burning conventional forage residues results in atmospheric pollution and the application of AD process can recover energy from these lignocellulosic biomass (Braun et al. 2008). The conversion of agricultural waste is commonly performed in large parallel or serial biodigester systems of different sizes and designs, known as biogas plants (BGPs). The biodigesters are classified depending on some conditions; such as temperature of the process (psychrophilic, mesophilic, or thermophilic), the type of substrate (e.g., silage, animal manure, or dung), and consistency (e.g., Wet process with low solid content or Dry digestion process with high solids content) (Mcinerney et al. 1979; Weiland 2010; Angelidaki et al. 2005).

AD is a complex multistep process that is performed by a large consortium of microorganisms composed of four major groups as mentioned previously, hydrolytic, fermentative, syntrophic acetogenic bacteria, and methanogenic archaea (Fig. 4.1) (Ferry 1993; Zheng et al. 2014).

First, hydrolytic bacteria hydrolyze biopolymers (lipids, proteins, and carbohydrates) to soluble oligomers and monomers (long-chain fatty acids, glycerol, amino

Table 4.1 Biochemical composition of different lignocellulosic substrates and their potential methane production

Type of substrate	Reactor volume (L)	Cellulose (%)	HC (%)	Lignin (%)	C (%)	N (%)	C:N	TS (%)	VS (%)	Methane production (mL CH ₄ /g VS)	References
Rice straw	1	35–44	27–34	12–13	39.7	0.9	47–67	92.9	81.6	281	Paul and Dutta (2018), Sawatdeenarunat et al. (2015), Li et al. (2013a)
Wheat straw	1	38–42	20–27	20–22	39.9	0.4	50–60	90.5	77.9	245	
Corn stover	1	40	25–31	14–17	43.2	0.8	50–63	84.9	76.9	241	Paul and Dutta (2018), Sawatdeenarunat et al. (2015), Singh et al. (2015), Li et al. (2013b)
Corn cob	0.575	45	25	15	41.26	0.45	123	^a	81.22	254.2	Paul and Dutta (2018), Pérez-Rodríguez et al. (2016), Kanwal et al. (2019)
Sugarcane bagasse	2	40–45	20–24	25–30	46.08	0.74	118–150	75–16	73.55	84.75	Paul and Dutta (2018), Inyang et al. (2010), Mustafa et al. (2018)
Switchgrass	1	36–45	28–30	12–26	43.6	0.4	90	91.3	87.4	246	Paul and Dutta (2018), Li et al. (2013b)
Chicken manure	1	20	23.2	1.6	35.9	3.4	10.9	25.9	19.5	295	Paul and Dutta (2018), Li et al. (2013b)
Dairy manure	1	19.5	15.2	17.4	37.6	2.8	13.4	38.5	28.8	51	Li et al. (2013b)
Swine manure	1	11.3	27.7	4.3	34.8	2.2	15.8	30.4	22	322	Li et al. (2013b)
Food waste	1	12	5.9	7.9	43.3	3.3	3–17	3.7	3.3	342	Li et al. (2013b), Divya et al. (2015)

HC Hemicellulose

^aNot determined

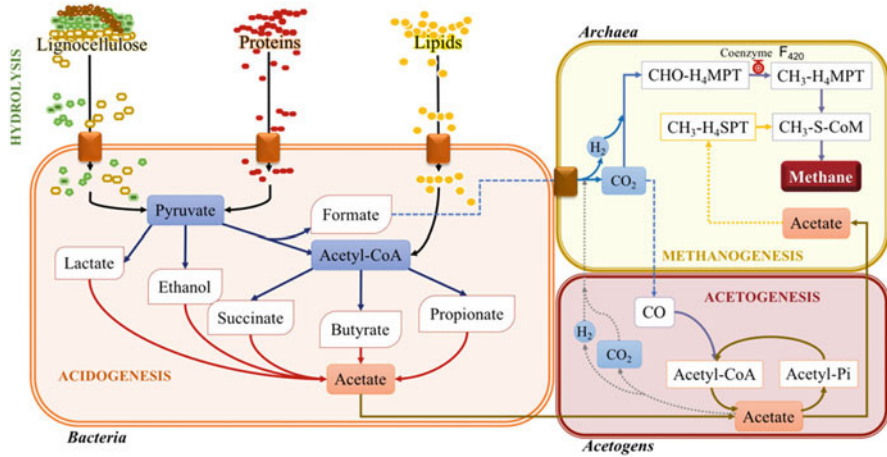


Fig. 4.1 General map of the four main stages of anaerobic digestion with the most abundant intermediates influencing methane yield

acids, and monosaccharides) by extracellular enzymes. These compounds are further converted to volatile fatty acids (VFAs; butyrate, propionate, acetate, among others), alcohol (ethanol and methanol), H₂, and CO₂ by fermentative bacteria. Eventually, VFAs greater than C₂ and alcohols are oxidized to acetate, hydrogen (H₂), formate, and CO₂ by syntrophic acetogens. Finally, the last group of methanogenic archaea converts acetate and CO₂ to methane (Gujer and Zehnder 1983).

In the last AD step (methanogenesis), a complex interplay among different functional microorganisms occurs. Hydrogenotrophic methanogens oxidize H₂ into methane (CH₄) by using CO₂. While the methyl group of acetate or methylamines is reduced to CH₄ by acetoclastic methanogenesis (Schink 1997). Syntrophic acetate oxidation (SAO) (Schnürer et al. 1999) also occurs under anaerobic conditions, yielding CO₂ and H₂, which feed the hydrogenotrophic methanogens (Fig. 4.1). Methanogenic stage is one of the rate-limiting steps as the growth rate of methanogens is low as well as they are sensible to environmental fluctuations such as pH, temperature, and VFAs concentration (Chen et al. 2008). In addition, several other factors influence biogas yield, mainly the recalcitrant nature of the substrate, the binding of bacteria on the substrate during the hydrolysis stage (Angelidaki et al. 2011) and high ammonia concentrations (Appels et al. 2011).

It is worth to mention, methanogenesis involve an optimal organization and interaction among different bacterial and archaeal communities, specific syntrophic interactions, and an imbalance can affect growth and activity of the microbial communities and could cause a deterioration in reactor performance, and thereby decreasing the methane yield (Krause et al. 2008; Rastogi et al. 2008; Akuzawa et al. 2011). Understanding the structure of microbial communities, the possible interactions among different microbial groups, and the active metabolic pathways could help in improving the methane yield. As mentioned earlier, the metaproteomics is a useful

tool that can provide information on transcription and translation, giving discernment between regulation of gene expression, protein synthesis, stability, and turnover of mRNA and proteins synthesized in situ. Of late, this approach has been successfully applied to laboratory- and full-scale anaerobic systems with potential in biogas production from lignocellulose substrates, as seen in Table 4.2.

Laboratory-scale digesters systems are scaled-down models to investigate new different substrate composition, microbial diversity, and its efficiency on organic matter removal and consequently methane yield potential and for testing new reactor configurations (Herrmann et al. 2011). These systems allow us to add control tools to handle several operational parameters and to control a malfunction, if there is any. In contrast, full-scale BGP represents a bigger challenge in operation and maintenance and some disturbances are hard to manipulate (Gerardi 2003).

Table 4.2 Overview of metaproteomic studies on AD of lignocellulosic biomass

Reactor type	Substrate	Major findings	References
<i>Laboratory-scale reactors</i>			
Thermophilic 8 L-stirred tank reactor (55 °C)	Mixture of beet silage (95%) and chopped rye (5%)	Proteins involved in acetoclastic and hydrogenotrophic methanogenesis, energy conservation, and a heat shock protein were identified. Most of them belong to <i>Methanosarcinales</i> , and others to <i>Methanomicrobiales</i> and <i>Synergistales</i>	Hanreich et al. (2012)
Mesophilic 2 L digester under acid stress conditions (35 °C)	Blended Taihu blue algae	Proteins involved in methane production and energy metabolism were identified (MCR: methyl-coenzyme M reductase, alcohol dehydrogenase, coenzyme-B sulfoethyl thiotransferase) from <i>Methanosarcinales</i> , <i>Methanomicrobiales</i> , and <i>Clostridiales</i>	Yan et al. (2012)
Mesophilic 500 mL batch digesters (38 °C)	Cut straw and hay	Members of <i>Bacteroidetes</i> were responsible for carbohydrate metabolism, while flagellins from <i>Firmicutes</i> showed its prevalence among the community. Otherwise, abundant enzymes from methanogenesis were detected from <i>Methanobacteriales</i> , <i>Methanosarcinales</i> , and <i>Methanomicrobiales</i>	Hanreich et al. (2013)

(continued)

Table 4.2 (continued)

Reactor type	Substrate	Major findings	References
Thermophilic 1 L digester (55 °C)	Unprinted office paper and anaerobic sludge from thermophilic industrial digester fed with municipal solid wastes	Cellulose and hemicellulose hydrolysis and fermentation enzymes were strongly related to <i>Caldicellulosiruptor</i> spp. and <i>Clostridium thermocellum</i> . Hydrogenotrophic pathway enzymes assigned to <i>Methanobacteriales</i> . <i>Coprothermobacter proteolyticus</i> recognized to perform proteolysis and fermentation	Lü et al. (2014)
Mesophilic 5 L continuous stirred tank reactors (CSTRs, 37 °C) designed as a “bovid-like” digestive system	Aerobic sludge from a wastewater treatment plant inoculated with cow digestive tract contents (RU) and cow manure (CO)	Glycogen-accumulating microorganisms (<i>Competibacteraceae</i> with two-phase metabolism from aerobic to anaerobic) dominated the CSTRs. Hydrogenotrophic methanogenic proteins dominated the RU. While CO reactor was affiliated to subunits from acetyl-CoA decarboxylase/synthase (ACDS) complex and acetate kinase from <i>Methanosarcinales</i> and <i>Methanomicrobiales</i>	Bize et al. (2015)
Thermophilic digester (2 L; 55 °C)	Fresh and digested swine manure	The most abundant proteins belong to energy production and conversion, carbohydrates, lipids, and amino acid metabolism, followed by information storage and cellular processing proteins. The proteins related to energy production were ATPases subunits, MCR, and acetyl CoA decarboxylase	Lin et al. (2016)
Mesophilic and thermophilic anaerobic digesters (5 L); 37 and 55 °C)	Acidified grass	Both mesophilic and thermophilic reactors contained high abundance of glycolytic proteins, sugar transport systems, and phosphotransferase systems affiliated to <i>Firmicutes</i> . While in thermophilic conditions chaperons and heat shock proteins were overexpressed	Abendroth et al. (2017)

(continued)

Table 4.2 (continued)

Reactor type	Substrate	Major findings	References
Mesophilic 2 L batch reactors (37 °C)	Reed straw (pretreated with cellulase) and swine manure sludge	Bacterial proteins (<i>Firmicutes</i> , <i>Proteobacteria</i> , <i>Actinobacteria</i> , and <i>Bacteroidetes</i>) were mainly affiliated to polymer metabolism. Ferredoxin-NADP reductase for H ₂ production was assigned to <i>Azotobacter</i> . The most abundant metaproteins were acetyl-CoA decarboxylase, MCR, and acetate pathway from <i>Methanosarcinales</i>	Jia et al. (2017a)
Mesophilic 2 L reactors (35 °C)	Food waste with short-term hydrothermal pretreatment	Carbohydrate and energy metabolism were the most active functions during the H ₂ production stage of <i>Firmicutes</i> and <i>Bacteroidetes</i> . Proteins from acetate metabolism, methylotrophic and acetoclastic pathways increased during the methanogenic stage were assigned to <i>Methanosarcinales</i> , <i>Methanobacteriales</i> , and <i>Methanotococcales</i>	Jia et al. (2017b)
Mesophilic (R1-2), thermophilic (R3-4), and high ammonia levels (R5-6) of multibioreactor system (500 mL)	Sludge from BGP fed with corn, silage, pressed and pulp turnip, chicken dung, liquid manure, and iron sludge	Enzymes of glycolysis and amino acid biosynthesis were found in R1. In reactors 3 and 4 decreased MCR from <i>Methanosarcinales</i> and <i>Methanobacteriales</i> . While in R5-6 increased the expression of 5,10-ethylene H ₄ MTP reductase and subunits of ACDS complex from <i>Methanobacteriales</i> and <i>Methanosarinales</i>	Kohrs et al. (2017)
Mesophilic 500 mL reactor	Cut filter paper	The most upregulated proteins included carbohydrates hydrolases, ABC transporter proteins, outer binding proteins, copper amine oxidases, translation elongation factors, carboxyl transferase, glyceraldehyde 3-phosphate dehydrogenase, and flagellins, mostly belonging to <i>Firmicutes</i> , <i>Synergistetes</i> , and <i>Bacteroidetes</i>	Speda et al. (2017)

(continued)

Table 4.2 (continued)

Reactor type	Substrate	Major findings	References
Mesophilic 4 L leach bed reactors (37 °C)	Acidified ensiled rye-grass and granular sludge	Proteins related to carbohydrate hydrolysis, glycolysis, and transport proteins were assigned to <i>Firmicutes</i> , <i>Bacteroidetes</i> , <i>Spirochaetes</i> , and <i>Proteobacteria</i> . ATPases and oxidoreductases belong mostly to <i>Firmicutes</i> , <i>Proteobacteria</i> , and <i>Bacteroidetes</i> . Meanwhile, proteins from lipid and amino acid metabolisms and environmental stress were affiliated to <i>Firmicutes</i> and <i>Bacteroidetes</i>	Joyce et al. (2018)
Mesophilic 10 L stirred tank reactor (37 °C)	Dried distiller grains feedstock under trace element deprivation	Trace element (TE) deprivation causes a decrease of hydrogenotrophic metaproteins from <i>Methanomicrobiales</i> . Only coenzyme F ₄₂₀ -reducing hydrogenase and methyl-H ₄ MTP increased its abundance upon the addition of TE. Methylophilic and acetoclastic metaproteins decreased while formylmethanofuran dehydrogenase from <i>Methanosarcinales</i> increased	Wintsche et al. (2018)
<i>Full-scale biogas plant</i>			
Mesophilic biogas plants (BGPs; 270–2280 m ³)	Corn-/grass-/rye whole crop silages Piglet manure/cattle manure/cattle slurry	Peptidases, glycolytic enzymes, glucose transporters, ribosomal proteins, chaperons, amino acid metabolism, and energy conservation proteins were identified from bacteria. No cellulolytic enzymes were detected. For Archaea, hydrogenotrophic and acetoclastic metaproteins from <i>Methanobacteriales</i> and <i>Methanosarcinales</i> were identified. Changes in protein profiles correlated to MCR decrease upon acidification	Heyer et al. (2013)

(continued)

Table 4.2 (continued)

Reactor type	Substrate	Major findings	References
Mesophilic (43 °C) and thermophilic (52 °C) BGPs (1500–1600 m ³)	M: Whole crop silages of maize, forage rye, cattle manure, and slurry T: Mix of maize whole crop silage and poultry manure	Carbohydrate hydrolases, sugar transporters, glycolytic enzymes, and primary fermentation enzymes were identified. Most of the mesophilic proteins were affiliated to <i>Methanosarcinales</i> . Whereas <i>Firmicutes</i> and <i>Thermotogales</i> were assigned to thermophilic BGP, as well as <i>Methanobacteriales</i>	Kohrs et al. (2014)
Mesophilic BGP (43 °C; 1500 m ³)	Whole crop silages of maize and rye, cattle manure and cattle slurry	Proteins as H ₄ MPT S-methyltransferase, V-type H ⁺ -transporting ATPase and MCR from both acetoclastic and hydrogenotrophic pathways were dominant and belonged to <i>Methanomicrobiales</i> and <i>Methanosarcinales</i> . Subunits of ACDS complex were affiliated to <i>Methanosarcinales</i>	Theuerl et al. (2015)
35 mesophilic and thermophilic BGPs (min. 33 °C, max. 55 °C; 20–4000 m ³)	Agricultural substrates, industrial wastes, slaughterhouse wastes, sewage sludge, municipal waste, mixed and unknown substrates	The 40 BGPs were dominated by methanogenic enzymes related to nutrient transport and one-carbon metabolism. The most abundant metaproteins (MCR and 5,10-methylene H ₄ MTP reductase) belonged to <i>Methanobacteriales</i> and <i>Methanosarcinales</i> . At 33 °C, proteins from short fatty acid metabolism, lipid and one-carbon metabolism were abundant. At 55 °C, proteins from DNA recombination and repair, and amino acid biosynthesis were abundant	Heyer et al. (2016)
Mesophilic and thermophilic BGPs (1–3: 37 and 4: 54 °C; 105 m ³)	BGP1: Maize silage, sugar beet, and poultry manure. BGP2: Maize silage, grass, and pig/cattle manure. BGP3: Maize silage and pig manure. BGP4: Maize silage, grass, and pig manure	ABC transporters, carbon and methane enzymes were assigned to BGP3. ABC transporters were highly expressed and affiliated to <i>Firmicutes</i> and <i>Bacteroidetes</i> , as well as, hypothetical substrate-binding proteins. Glycolytic enzymes were identified from <i>Firmicutes</i> and <i>Bacteroidetes</i> . While members of <i>Methanosarcinales</i> and	Ortseifen et al. (2016)

(continued)

Table 4.2 (continued)

Reactor type	Substrate	Major findings	References
		<i>Methanomicrobiales</i> were responsible for hydrogenotrophic and methylotrophic methanogenesis	
Thermophilic industrial biogas reactor (60 °C; 2200 m ³)	Food waste with high levels of free ammonia	<i>Dictyoglomales</i> and <i>Planctomycetes</i> were highly active in polysaccharide hydrolysis. Proteins from obligate hydrogenotrophic methanogens dominated over acetoclastic methanogens. Novel phylotypes of SAO-bacteria (<i>unFi_c1</i> and <i>unFi_c2</i>) were identified and perform β -oxidation of butyrate and other longer chain fatty acids, as well as in acetate oxidation	Hagen et al. (2017)

4.4 Metaproteomics in AD of Lignocellulosic Substrates

Metaproteomics was first defined by Wilmes and Bond (2004) as “the large-scale characterization of the entire protein complement of environmental microbiota at a given point of time.” Through the years several denominations have been used depending on the different experimental procedure, the complexity of the environmental sample or the outcomes. Terms include *environmental proteomics*, *metaproteomics*, *community proteomics*, *proteogenomics*, and *proteotyping*. However, not all are synonyms. Schneider and Riedel (2010) mentioned that *environmental proteomics* refers to the proteome analysis of environmental samples, while *metaproteomics* is the study of highly complex biological systems containing a large number of proteins, which is hard to assign to species within a phylotype. In contrast, *community proteomics* infers that most of the proteins identified are assigned specifically to members of the community. *Proteogenomics* links the gene function to the identified protein, giving the accurate information about a biological system functionality. On the other hand, *proteotyping* refers to a gel-free approach, supported by the rapid protein resolution by mass spectrometers for the characterization of mixed microbial communities (Kohrs et al. 2017). Despite several definitions, proteomics englobes a large-scale study of proteins, which allows the understanding the metabolic networks, syntrophic interactions, carbon and nitrogen fluxes, and novel pathways.

Several analytical methods have been applied to provide an insight into microbial communities in AD, commonly genomic approaches. Cloning and sequencing of

DNA or fingerprint target of 16S rRNA gene have been usually applied to explore communities of *Archaea* and *Bacteria* (Clement et al. 1998; Schlüter et al. 2008). However, metaproteomics emerged as a complementary approach to give a full vision of the physiological and biochemical functions of microbial population. General metaproteomic workflow comprises biogas community sampling, protein extraction, protein gel separation, tryptic digestion of proteins, mass spectrometry of resulting peptides, and database searching of mass spectra (Hassa et al. 2018). However, as mentioned before, new gel-free approaches have led to rapid resolving mass spectrometers (MS) for rapid identification and characterization of microbial communities employing tandem MS and MS/MS-based shotgun proteomics (Karlsson et al. 2015).

4.4.1 Hydrolysis

As mentioned previously, microbial communities degrade polymeric biomass into monomers by hydrolytic enzymes during the first step of AD process in order that simpler compounds are available for the next steps of biomethanation process. The three primary substrates for hydrolysis are polysaccharides, lipids, and proteins, which are generally present in majority of the wastes or feedstocks of anaerobic digesters (Tong et al. 1990). In the case of polysaccharides, there exist two basic types of enzyme system for its hydrolysis: complex systems as cellulosomes, produced by anaerobic bacteria and nonassociated, free enzyme systems produced by aerobic microorganisms (Fig. 4.2) (Felix and Ljungdahl 1993).

The first metaproteomic study conducted by Hanreich et al. (2013), demonstrated the presence of α -amylase and glycoside hydrolase only. α -amylase is an endoamylase, which acts on α -1,4 glycosidic bonds in amylose or amylopectin of starch, releasing oligosaccharides of different length. While, glycoside hydrolases are capable of hydrolyzing cellulose, hemicellulose, and starch. This study employed maize-digestate from a biogas plant fermenting maize and a mix of cut straw and hay as feedstock. The metaproteome was dominated only for few proteins from genus *Thermoanaerobacterum* and *Microscilla* and in less abundance, the proteins of *Cytophaga*, which synthesizes pectate lyase. This enzyme catalyzes the eliminative cleavage of pectate, a main component of cell walls in plants. In contrast, a study of a biogas plant treating silage or whole maize crop showed a set of hydrolytic enzymes performing degradation of high-molecular carbohydrates like cellulose, hemicellulose, xylan, and arabinan (Heyer et al. 2013).

Other nonagricultural substrates, as waste papers, with a composition of about 70% of cellulose and 30% of hemicellulose has led to the identification of structural and catalytic components of *C. thermocellum* cellulosome; CelS and CelJ, as well as hydrolytic enzymes degrading high-molecular carbohydrates. Other enzymes as β -mannanase, acetyl xylan esterase, and endoxylanase, specialized in hemicellulose degradation were related to *Caldicellulosiruptor* genus (Lü et al. 2014). On the other hand, food wastes as feedstock, with high levels of free ammonia, indicated that an

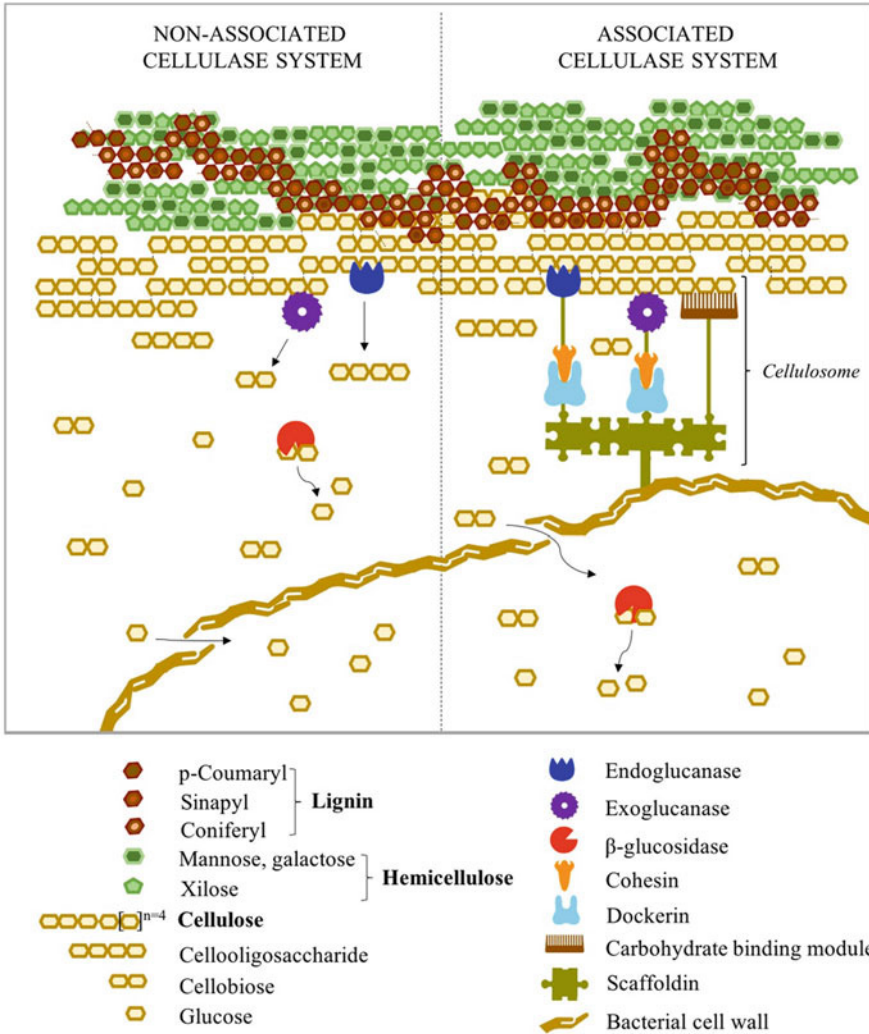


Fig. 4.2 Schematic diagram of the nonassociated and associated cellulase systems. Most aerobic microorganisms degrade cellulose by secreting a set of complex enzymes viz., endoglucanase, exoglucanase, and β-glucosidase. On the contrary, most of the anaerobic microorganisms produce cellulosomes. The cellulosome is an extracellular multienzymatic complex present on the cell wall and binds to the substrate for its hydrolysis. It can incorporate several hydrolases through cohesin–dockerin interaction, while the carbohydrate-binding module keeps the cellulosome attached to the lignocellulosic substrate. This figure was modified from Zhu and McBride (2017)

uncultured *Atribacteria* was mainly responsible for the hydrolysis of polysaccharides synthesizing enzymes as β-glucosidase, galactose mutarotase, L-fucose isomerase, and xylose isomerase potentially related with hemicellulose degradation.

For protein hydrolysis, proteases, and endopeptidases belonging to *C. proteolyticus* are reported frequently, when protein-rich biomass is treated in

thermophilic biodigester (Heyer et al. 2013). Other enzymes also related to protein degradation are trypsin-like serine protease and it is reported that *Planctomycetes* and *Atribacteria* groups are metabolically active in carbohydrate and protein degradation (Hagen et al. 2017).

Recently, metaproteomics is employed as a bioprospecting tool for identifying novel enzymes. Speda et al. (2017) showed this tool is useful to identify and select novel enzymes from consortia, that are specifically upregulated upon its induction. Cellulolytic activity was targeted in a defined medium containing filter paper, instead of glucose, and compared with a non-induced sample. Cellulose induction led to the identification of 1,4 β -cellobiosidase, 1,4 β -xylanase, cellobiose phosphorylase, β -glucosidase, and hypothetical Ig domain proteins from several species.

4.4.2 Nutrient Transport

Substrate transporter systems are of great relevance for the following steps of methanogenesis. The main mechanism by which a microorganism can obtain nutrients from the environment is by means of these proteins. Diverse studies have evidenced transport proteins in anaerobic reactors. Two classes of proteins involved in nutrient transport are TonB-dependent receptors and ATP-binding cassette (ABC) transporters. These proteins have been previously reported in AD from several members of *Bacteroidetes* and *Spirochaetes* phylum (Hanreich et al. 2013). The TonB-dependent transporter (TBDT) is a bacterial outer protein that can actively transport siderophores, as well as, vitamin B12, nickel complexes, and carbohydrates. This receptor is part of a starch utilization system that has been recognized by its efficiency to transport oligosaccharides to its further degradation. As mentioned before, TBDT is deployed for more complex substrates and uses a proton motive force for the uptake of oligomers that are too large to diffuse via porins (Lü et al. 2014). Interestingly, TBDT also can degrade polymers as polysaccharides, proteins, proteoglycans and via substrate-binding hydrolytic proteins.

In contrast, ABC proteins are a family of primary transporters that hydrolyzes ATP to transport organic and inorganic compounds. ABC systems are bioenergetically expensive as ATP hydrolysis is needed to translocate the substrate across the membrane. Consequently, investment of ATP in this transport mechanism limits binding and transport, especially when higher concentration metabolites are present. ABC transporters have been reported to be related to peptide transport, maltose, and other metabolites, such as glycerol 3-phosphate (Speda et al. 2017; Kohrs et al. 2014; Hagen et al. 2017). Ortseifen and colleagues (2016) showed in an integrated metagenome-proteome research digesting maize silage and pig manure, that mostly ABC-transporters of peptides, oligopeptides, monosaccharides, and iron of the phylum *Firmicutes* were upregulated, and as well as other translocating proteins from *Spirochaetes*, *Thermotogae*, and *Thermococcus* phylum. While Jia and coworkers (2017a) made an extensive work of the metaproteome evaluating the four different stages of methanogenesis (peak stage of hydrogen production, late

stage of hydrogen production, peak methanogenic stage, and late methanogenic stage) in a bioreactor fed with cellulase-pretreated reed straw. They found ABC protein expression increased during the peak methanogenic stage where methane production potentials and methane production rate reached 2709.94 mL and 9.71 mL/h.

Otherwise, components of sugar transport systems (like the phosphotransferase system) were identified mainly from *Firmicutes* species, in a biodigester fed with grass, and with a separate acidification step at thermophilic and mesophilic conditions (Abendroth et al. 2017). This active transport is used by bacteria for uptake of carbohydrates, particularly hexoses, hexitols, and disaccharides, where the source of energy is from phosphoenolpyruvate (Roseman 1969).

4.4.3 Acidogenesis

After hydrolysis and nutrient transport, monosaccharides and amino acids are the most abundant substrates for fermentation and a wide range of microorganisms can metabolize both, mostly *Clostridia* and other Gram-positive bacteria (Madigan et al. 2008; Ramsay and Pullammanappallil 2001).

Monosaccharides are channeled to catabolic pathways for the production of pyruvate via the Embden–Meyerhof–Parnas (EMP; glycolysis) or Entner Doudoroff (ED) pathway. During glycolysis, reducing equivalents like NADH and H₂ are produced, and pyruvate is further metabolized to acetate, CO₂, and H₂ (at low partial pressure) or subsequently to C₃ products (lactate or propionate), or C₂/C₄/C₆ products (acetate/butyrate/caproate) via acetyl-CoA (at high partial pressure). At low partial pressure of H₂, the flow of electrons (NADH) lead to H₂ production which leads to pyruvate degradation. As partial pressure increases, the flow of electrons shift to the generation of reduced electron fermentation products (volatile fatty acids, VFAs) such as propionate and long-chain fatty acids, lactate, or ethanol. Thus, in a system where methanogens are effectively consuming H₂, low concentrations of ethanol, lactate, and butyrate are maintained (Bräsen et al. 2014).

At first evaluation of a full-scale agricultural BGP metaproteome, Heyer et al. (2013) demonstrated the identification of metabolic enzymes involved in glycolysis as glyceraldehyde-3-phosphate dehydrogenase (G3PD), enolase, phosphoglycerate kinase, glycerol kinase, and lactate dehydrogenase (LDH), mostly associated to *Clostridia*. Similar results were found in agricultural BGPs in mesophilic and thermophilic conditions assigning proteins from glycolysis as 6-phosphofructokinase, aldolase, G3PD, 3-phosphoglycerate kinase, phosphoglycerate mutase, and enolase, as well as enzymes from the primary fermentation: LDH (assigned to *Lactobacillus*), NADP-dependent isopropanol dehydrogenase, and aldehyde dehydrogenase also related to *Clostridia* (Kohrs et al. 2017). Jia et al. (2017a) also demonstrated the presence of LDH in *Streptococcus* during the hydrogen production stage.

Other BGP digesting maize silage and pig manure revealed highly abundant proteins in fermentation. In spite of the low abundance reported, the use of an

integrated approach for combining metaproteomics and metagenomics tools aid in the identification of glycolysis enzymes (enolase, aldolase, and G3PD) (Ortseifen et al. 2016). Similar results were found in a case study evaluating a proteome from a thermophilic reactor degrading swine manure, where enolase from different species of phyla *Proteobacteria* were identified (Lin et al. 2016).

On the other hand, an industrial biogas reactor predominantly fed with food waste and high levels of free ammonia, few enzymes from glycolysis were identified, and attributed to uncultured phylotypes *Atribacteria*, *Planctomycetes*, and *Dictyoglomus* (Hagen et al. 2017). In contrast, a mesophilic reactor containing pretreated food waste (under short-term hydrothermal) recorded a higher proportion of proteins of carbohydrate metabolism to *Proteobacteria*, *Firmicutes*, *Actinobacteria*, *Bacteroidetes*, and *Cyanobacteria*. The proteins involved belong to glycolysis, pyruvate, propionate, glyoxylate, and dicarboxylate metabolism (Jia et al. 2017b).

In lab-scale models, anaerobic digestion of office paper, led to the identification and assignment of all glycolytic enzymes to *C. thermocellum*, *C. proteolyticus*, and *Caldicellulosiruptor* genus. Also, proteins involved in the synthesis of fermentation products such as lactate, ethanol, butanol, acetate, formate, and butanoate were also assigned to the same genus (Lü et al. 2014). Corresponding to the metabolism of grass, as lignocellulosic biomass, a set of glycolytic enzymes were identified specifically in the phase of sugar assimilation (Abendroth et al. 2017). Speda et al. (2017) were able to identify carboxyl transferase (gluconeogenesis) and G3PD (glycolysis) in a cellulose-rich (paper filter) biodigester. These findings showed that the EMP is one of the key glycolytic pathways functional during anaerobic digestion, as well as in the formation of intermediary products of fermentation, leading to the next step of methane production (Wilmes and Bond 2009; Abram et al. 2009).

4.4.4 Acetogenesis

During this stage, syntrophic bacteria oxidize VFAs greater than C_2 to produce key intermediates (25% acetate and 11% H_2) of the process. In this acetogenesis step, obligatory hydrogen forming syntrophic bacteria can cause toxic effects by accumulating high hydrogen pressure on the system. Consequently, the microbial consortium is not capable to survive under those conditions. Hence, symbiosis, as a syntrophic relationship, is necessary between acetogenic bacteria and autotrophic methanogens or sulfate-reducing bacteria for hydrogen consumption. The hydrogenotrophic methanogens keep the hydrogen pressure low, which contributes to a thermodynamically controlled condition for the fermentative bacteria to continue oxidizing the organic compounds (e.g., ethanol, propionate, and butyrate into acetate) (Barua and Dhar 2017). This oxidizing activity is related to the genera of *Syntrophomonas* and *Syntrophobacter*, as well to *Chloroflexi*, *Actinobacteria*, and *Spirochaetes*. Nonetheless, more or less abundance is related as well to *Gelria*, *Lachnospiraceae* (uncultured), *Ruminococcaeae*, *Incertae sedis*, *Sporanaerobacter*, and *Petrobacter* (Ziemiński and Fraç 2012; Wang et al. 2017; Jain et al. 2015).

In the case of butyrate, the oxidizing pathways are through the β -oxidation, for propionate oxidation will proceed through the methyl-malonyl-CoA (MMC) pathway and for syntrophic oxidation will be associated to the Wood-Ljungdahl (WL) pathway. According to Hagen et al. (2017), *Syntrophomonas* genus is the major phylotype in AD, where *S. wolfei* required all classes of the β -oxidation enzymes (acyl-CoA dehydrogenase, enoyl-CoA hydratase, 3-hydroxyacyl-CoA dehydrogenase, and 3-ketoacyl-CoA thiolase). While for the propionate degradation, *Pelotomaculum thermopropionicum* identification suggests the requirement of the methyl-malonyl-CoA (MMC) cluster and propionate CoA transferase (PCT) cluster in high abundance. Further, this study reported that *Thermoacetogenium phaeum* for acetate oxidation by WL pathway (formyltetrahydrofolate synthase, 5,10-methylenetetrahydrofolate dehydrogenase, methylenetetrahydrofolate reductase, trimethylamine:corrinoid methyltransferase, carbon monoxide dehydrogenase/acetyl-CoA, phosphotransacetylase, and acetate kinase) (Hagen et al. 2017).

Role of all enzymes participating in AD has been poorly reported, due to the large amounts of proteins and other interfering substances present in the sample. Nevertheless, a relatively high abundance of proteins involved in acetogenesis has been revealed. Mostly, WL-like formyltetrahydrofolate synthase, 5,10-methylenetetrahydrofolate dehydrogenase, methylenetetrahydrofolate reductase, trimethylamine-corrinoid methyltransferase, carbon monoxide dehydrogenase-acetyl CoA, phosphotransacetylase, and acetate kinase have been identified as crucial for energy transport and microbial interactions performed mainly in syntrophic acetate oxidizers. A protein cluster encoding Fe-S oxidoreductase and an electron transfer flavoprotein were also identified, both related as well as electron transfer mechanisms (Hagen et al. 2017).

4.4.5 Interspecies Hydrogen Transfer in Syntrophs

Interspecies hydrogen transfer mechanism is vital in syntrophic relationships, where the latter groups such as hydrogen consumers are strongly influencing the syntrophic bacteria (Gomez Camacho and Ruggeri 2018). Acetate produced in the process could be converted to methane either directly by methyl reduction or by following a two-step reaction, where acetate is first oxidized to CO_2 and H_2 , by syntrophic acetate oxidation (SAO), and then this hydrogen is used to reduce CO_2 into CH_4 (Mulat et al. 2014). Heyer et al. (2019) studied the interactions between microorganisms and the metabolic interchangeability of the different microorganisms. This work suggested that under specific anaerobic digestion conditions the thermodynamic equilibrium of CO_2 , H_2 , and acetate will decide on the metabolic pathway shift, either between SAO or homoacetogenesis. Understanding this will explain how some archaeal species have major enzyme affinity on acetate and could suppress other acetate-consuming phylotypes.

Thus, competition on the substrate between certain microorganisms such as *Methanosaetaceae* may kill or suppress other species due to the expression of bacteriocins, which inhibit the competitor (Heyer et al. 2019). The H_2 produced by

non-methanogenic syntrophic microorganisms from key fermentation products (ethanol and C_2 and greater than C_2 volatile fatty acids) are reduced to methane by hydrogenotrophic methanogens or to H_2S by sulfate-reducing bacteria. This interspecies microbial exchange of hydrogen suggests that syntrophs are incapable of independently oxidizing alcohols and C_2 and greater than C_2 volatile fatty acids under anaerobic conditions and need a partner that consumes hydrogen to keep the partial pressure of hydrogen under control and facilitate their metabolic activity. Syntrophic interactions consist generally on the intercellular transport of reducing equivalents, like H_2 and/or formate, coupled with H_2 /formate consumers, also referred as interspecies hydrogen transfer (IHT) (Shrestha and Rotaru 2014; Summers et al. 2010).

In addition, formate often serves as a substitute for H_2 in interspecies electron transfer. The electron reduced carriers on this type of mechanism are additionally regenerated to an oxidized state (Shrestha and Rotaru 2014; Kouzuma et al. 2015). Westerholm et al. (2016) reported that SAO bacteria are principally classified in the group of homoacetogens, which perform the Wood Ljungdahl (WL) pathway during growth, in presence of autotrophic and/or heterotrophic substrates, and produce acetate as main by-product. In this pathway, they suggest that the gene *fhs* encodes the enzyme formyl tetrahydrofolate synthetase (FTHFS) to catalyze the ATP-dependent activation of formate, postulating as well, the reverse WL performance for acetate oxidation. Interestingly, the *Pseudothermotoga lettingae* acetate oxidizer can combine the methyl branch of the latter pathway with a glycine cleavage system (Westerholm et al. 2016).

Recent discoveries reported that some bacteria could directly transfer electrons to methanogens, as a unique cell-to-cell electron transfer mechanism, in a thermodynamically efficient manner (Cheng and Call 2016). The electron transfer, between microorganisms mediating electron carriers, is referred as direct interspecies electron transport (DIET), where three mechanisms have recently been suggested: (1) the via conductive pili, by association from two bacteria with a conductive pili (conductive nanowires), (2) the membrane-bound mechanism with electron transport proteins, by electron transmission which represents close cell connections by using a multiheme outer surface cytochrome (OmcZ), and finally (3), the more recently studied the magnetite particle which form chains for electrically connecting cells involved in DIET (Park et al. 2018).

4.4.6 Methanogenesis

Methanogenesis is one of the critical steps in the process of AD, characterized by slow reaction rate on the energy workflow. Syntrophic interactions between acetogenic bacteria and methanogens as well as methyl group reduction are essential to CH_4 production. Thus, understanding the microbial community involved in electron transferring dynamics is key to biogas production improvement. Archaeal methanogens are dominant groups in this phase, generally performing the aceticlastic, hydrogenotrophic

and methylotrophic pathways. The microorganisms usually found are the strict hydrogenotrophic *Methanomicrobiales*, *Methanobacteriales*, *Methanococcales*, and the acetate-utilizing microorganisms *Methanosarcinales* with specific predominance of *Methanosarcina* and *Methanosaeta*. Methanogens are quite sensitive for changes in environmental and operational conditions of AD process and many factors (i.e., high concentrations of volatile fatty acids, ammonium, sulfide, sodium and heavy metals) could inhibit the process (Al Seadi et al. 2008; Ziganshin et al. 2016).

As mentioned earlier, methane can be produced either by hydrogenotrophic pathway by reducing CO₂ using hydrogen, the methylotrophic pathway where methylated compounds like methanol or methylamine are reduced, and in acetoclastic pathway, methyl group of acetate is directly reduced to methane. Recently, the class of *Thermoplasmata* has been described to be capable to reduce methanol with H₂ and may use methylamines as well, suggesting that methanogenic diversity could be higher (Wintsche et al. 2018).

From the above three pathways, studies were performed using isotope assays to know the metabolic contribution from each one. It was reported that syntrophic acetogenic process and hydrogenotrophic methanogenesis accounted for 41 and 50% of methane formation at 37 °C and 55 °C, respectively (Yin et al. 2018). Another study using isotopes indicated that the non-acetoclastic oxidizers performed, approximately 80% of the pathway of the acetate decomposition in the reactor, which indicated the role of syntrophic acetate-oxidizing bacteria. *Pseudothermotoga lettingae* (previously as *Termotoga lettingae*) strain was reported to show syntrophic acetate oxidizing activity without sulfate ions and under co-culture conditions in relation with hydrogenotrophic methanogens (Sasaki et al. 2011).

Identification of the pathways and enzymes involved in the methanogenesis networks via metaproteomic approach has been carried out (Table 4.2). During the hydrogenotrophic pathway, CO₂ is reduced to methane through the intermediates formyl, methylene, and methyl. These residues are transferred to the coenzyme M, forming a methyl-CoM molecule further reduced to CH₄ by the key methyl coenzyme M reductase (MCR). Meanwhile, the energetically coenzyme F₄₂₀ acts as an electron acceptor for hydrogenase, formate dehydrogenase, and carbon monoxide dehydrogenase, as well as donor electron for reductase NADP⁺. Moreover, this coenzyme utilize H₂ and formic acid, as electron donor to produce the methane by CO₂ reduction (Jia et al. 2017b). In the acetoclastic pathway, methyl group of acetate is reduced to methane by methyl reductase enzyme. In the case of methylotrophic pathway, the methyl groups are transferred to a methanol-specific corrinoid protein, then reduced by the MCR (Jia et al. 2017b; Guo et al. 2015). It is important to highlight that methyl-coenzyme M (methyl-CoM) reductase is active for all the three pathways (Hanreich et al. 2012).

In a full-scale BGP, CODH/ACS and energy-converting hydrogenase (Ech), proteins, and enzymes involved in metabolism of methanol and methylated amines, as well as, V-type ATP synthase for energy conversion were assigned to *Methanosarcinales*. While F₄₂₀-dependent N₅,N₁₀-methyleneH₄MPT reductase (Mer), Mtr, and F₄₂₀ reducing hydrogenase (Frh) were assigned to *Methanobacteriales* (Heyer et al. 2016). In the hydrogenotrophic pathway, Lü et al. (2014) found proteins from strains of

Methanothermobacter as H₂-forming methylene H₄MPT dehydrogenase, F₄₂₀-dependent methyleneH₄MPT dehydrogenase, Mtr, Mer, MCR, Frh, and heterodisulfide reductase. As well as from the methylotrophic pathway, monomethylamine methyltransferase, and a large subunit of the corrinoid/iron–sulfur protein and methylcobamide:CoM methyltransferase were detected. In contrast, none of acetoclastic enzymes were identified in this study.

Furthermore, trace elements on the anaerobic digestion have an impact on the performance process to carry out cell metabolisms and is critical to the final stage of the methane yield. For methanogens, the presence of Fe, Zn, Ni, Cu, Co, Mo, and Mn are essential. First, Fe, is important in stimulant as growth factor and formation of cytochromes and ferroxins vital for energy metabolism. Additionally, trace elements form the active site in metalloproteins, act as a cofactor and give the structure. Enzymes such as Mtr and MCR require Co and a nickel-containing cofactor F₄₃₀ in their active sites, respectively (Choong et al. 2016). Trace element deprivation has shown to decrease hydrogenotrophic metaproteins abundance from *Methanomicrobiales* and methylotrophic and aceticlastic metaproteins from *Methanosarcinales*. However, trace elements may have negative impact when present in high concentrations. It has been demonstrated to cause enzyme disruptions and changes on functional structure, and microbial composition as well. Therefore, effectiveness of the anaerobic digestion performance by using trace elements will further depend on its optimum bioavailability fraction (Bourven et al. 2017).

4.5 Stress Responses and Biomarkers

Although AD is an economic way of waste management combining with renewable energy production in the form of methane, the process has certain thresholds and one of them is high sensitivity to the presence of certain substances at high concentrations during the process. Most frequently, a reactor turns “sour” due to accumulation of volatile fatty acids (VFAs). Further, ammonia, high partial pressure of H₂ have recorded negative effects on AD process, among several other factors (Chen et al. 2014). Therefore, several studies have focused on efforts to overcome stress conditions by detecting different key enzymes to those conditions in the reactor (Table 4.3).

Formerly, when the process contains simple sugars, which are easy to degrade, VFAs are accumulated and decrease in pH results in the imbalance of AD process. Interestingly, under this condition, Theuerl et al. (2015) could detect proteins involved on aceticlastic and hydrogenotrophic methanogenesis from *Methanosarcinales*, *Methanobacteriales*, and *Methanomicrobiales*, with an abundance ranging from 55 to 77%.

On the other hand, high concentrations of total ammonia nitrogen due to the high rate of protein hydrolysis could negatively affect reactor operation. Nevertheless, lignocellulosic-rich matter is a convenient substrate to slow the rates of process start-up, diminishing the possible ammonia accumulation. Also, trace elements have demonstrated to overcome such problems. It has demonstrated that nickel which is contained in coenzyme F₄₃₀ enhanced methane potential and overcome such

Table 4.3 General overview on protein abundance under varying environmental and operational conditions

Reactor	Key enzyme/ biomarkers	Functional role	RA	Species related to expression	References
Lab-scale anaerobic moving bed reactor at 37 °C	Cofactor F ₄₃₀	Nickel hydrocorrinoid prosthetic group of the methyl-CoM reductase. It decreases the toxic effect of higher VFAs content and increases methane production	++	<i>Methanococcus jannaschii</i> <i>Methanococcus maripaludis</i> <i>Methanococcus vaneilii</i>	Passaris et al. (2018)
Lab-scale mesophilic digester treating starch	Methyl coenzyme-M reductase	It reduces the methyl CoM with hydrogen for methane production	+	<i>Methanobacterium</i> <i>Methanosaeta</i>	Zhang et al. (2018)
Low-temperature granular sludge reactor operated at 15 °C	^a Oxygen-sensitive alcohol dehydrogenase	Interconversion from alcohol to acetaldehyde	++	<i>P. propionicus</i>	Abram et al. (2011)
	^a Transketolase	Constitutes the reversible link between glycolysis and pentose phosphate pathways	+ + +		
Sequencing batch reactor with alterations in phosphorus level	^a Peroxiredoxin	Protects the cell against reactive oxygen species	++ +	<i>Accumulibacter phosphatis</i>	Wilmes and Bond (2009)
	^a Thioredoxins/ chaperon proteins	Responsible to maintain disulfide bonds within the cytoplasmatic proteins in a reduced state	+ + +		

RA Relative abundance

^aAbundance of proteins depending on the stress condition or inhibitory factor

+ low abundance, ++ medium abundance, +++ high abundance

problems (Capson-Tojo et al. 2017). Additionally, under concentrations of 6–7 g-N/L ammonium, inhibition of *Methanomicrobiales* and *Methanosaetacea* activities was observed along with a shift in microbial community (Lü et al. 2014).

The lignocellulosic-rich feedstocks with high lignin content could also cause inhibitory stress conditions. The negative impacts on these types of substrate, especially due to the by-products of lignin decomposition, inhibitory aromatic compounds. These are mainly composed of furanic acid (5-HMF, fufural) and phenolic compounds leading to a metabolic shift of the H₂-producing pathways to a nonproducing pathway (Monlau et al. 2014). However, several numbers of enzymes are involved in the catabolic pathway of lignocellulosic compounds. The

benzoyl-CoA reductase class II (BamBCDEFGHI) could function as a functional marker, which is expressed and detected when mono-aromatic compounds are degraded (von Netzer et al. 2016).

A well-studied biomarker to understand methane production is the expression of *mcrA* gene, which encodes the key enzyme methyl coenzyme M reductase (MCR). MCR catalyses the last step of methanogenesis and related to methane yield. This biomarker can provide useful information and by monitoring its activity functional performance of a bioreactor can be studied (Morris et al. 2014). Expression of *mcrA* has been found related to the presence of concentration of volatile fatty acid such as acetate and propionate (Aguinaga Casañas et al. 2015). However, new protein biomarkers are drawing attention, as proteins can be synthesized and then folded immediately after a stimulus, which could vary under different conditions. Hence, protein identification with potential in biomarker fingerprint could be revealing tool for instant physiological responses (Lacerda et al. 2007).

4.6 Challenges and Future Perspectives

Metaproteomics analysis is the most recently developed tool, which indicates the protein assignment to specific microorganisms and contributes to understand the relationship between phylogenetic analyses and the proteome (Abram et al. 2011). However, its application has not been completely exploited since there is still more “black holes” and methodological challenges to solve the whole metabolic pathways (Wilmes et al. 2015).

Principal problems are related to methodological issues involved in the correct isolation of the proteome, since humic acids and their impurities make the quantification and separation of the proteins very challenging. Humic acids are commonly present in environmental samples and bind to the proteins which hamper protein separation (Wilmes and Bond 2004). Fractioning proteins by gel separation, also involves several difficulties, as poor separation of acidic, alkaline, and hydrophobic proteins and a low load capacity, which affects the resolution and analysis of the gel (Li et al. 2016).

Secondly, peptides’ identification is one of the most challenging steps in metaproteomics. Some proteins’ sequences are among the most highly conserved across different microorganisms, which entails the same peptide sequences from several different species. These leads to have many proteins identified in the same information storage and processing group. Besides, MS/MS data uses the top of the 10–20 most abundant peptide ions acquired and does not cover all available peptide ions, which misses a plenty of valuable information (Heyer et al. 2017). Thus, metaproteomic approaches have to overcome the cleanup and characterization of peptides and proteins by intensive purification and pre-fractionation methods (Wenzel et al. 2018).

The key to the metaproteomic studies is the resolution level of the peptide identification. In future, considerations on the use of the best algorithm which

could identify the proteins covered on the database to evaluate for de novo results (Heyer et al. 2015). The molecular techniques could provide the microbial information and linking the species on the proteomic data by complementary studies of the microbial consortium, could aid to overcome the challenges encountered in the coverage of the samples. Further, improvement in methodologies to identify proteins along with improvement in methods of data analyses are essential to apply metaproteomics as an effective tool to understand the microbial diversity and their function of biodigesters (Herbst et al. 2016).

References

- Abendroth C, Simeonov C, Peretó J, Antúnez O, Gavidia R, Luschnig O, Porcar M (2017) From grass to gas: microbiome dynamics of grass biomass acidification under mesophilic and thermophilic temperatures. *Biotechnol Biofuels* 10:171. <https://doi.org/10.1186/s13068-017-0859-0>
- Abram F, Gunnigle E, O'Flaherty V (2009) Optimisation of protein extraction and 2-DE for metaproteomics of microbial communities from anaerobic wastewater treatment biofilms. *Electrophoresis* 30:4149–4151. <https://doi.org/10.1002/elps.200900474>
- Abram F, Enright A-M, O'Reilly J, Botting CH, Collins G, O'Flaherty V (2011) A metaproteomic approach gives functional insights into anaerobic digestion. *J Appl Microbiol* 110:1550–1560. <https://doi.org/10.1111/j.1365-2672.2011.05011.x>
- Adekunle KF, Okolie JA (2015) A review of biochemical process of anaerobic digestion. *Adv Biosci Biotechnol* 06:205. <https://doi.org/10.4236/abb.2015.63020>
- Aguinaga Casañas MA, Rangkasene N, Krattenmacher N, Thaller G, Metges CC, Kuhla B (2015) Methyl-coenzyme M reductase A as an indicator to estimate methane production from dairy cows. *J Dairy Sci* 98:4074–4083. <https://doi.org/10.3168/jds.2015-9310>
- Ahring BK, Biswas R, Ahamed A, Teller PJ, Uellendahl H (2015) Making lignin accessible for anaerobic digestion by wet-explosion pretreatment. *Bioresour Technol* 175:182–188. <https://doi.org/10.1016/j.biortech.2014.10.082>
- Akuzawa M, Hori T, Haruta S, Ueno Y, Ishii M, Igarashi Y (2011) Distinctive responses of metabolically active microbiota to acidification in a thermophilic anaerobic digester. *Microb Ecol* 61:595–605. <https://doi.org/10.1007/s00248-010-9788-1>
- Al Seadi T, Rutz D, Prassl H, Köttner M, Finsterwalder T, Volk S, Janssen R (2008) Biogas handbook. University of Southern Denmark Esbjerg, Esbjerg
- Angelidaki I, Ellegaard L, Ahring BK (2003) Applications of the anaerobic digestion process. *Adv Biochem Eng Biotechnol* 82:1–33. https://doi.org/10.1007/3-540-45838-7_1
- Angelidaki I, Boe K, Ellegaard L (2005) Effect of operating conditions and reactor configuration on efficiency of full-scale biogas plants. *Water Sci Technol* 52:189–194. <https://doi.org/10.2166/wst.2005.0516>
- Angelidaki I, Karakashev D, Batstone DJ, Plugge CM, Stams AJM (2011) Biomethanation and its potential. *Methods Enzymol* 494:327–351. <https://doi.org/10.1016/B978-0-12-385112-3.00016-0>
- Appels L, Lauwers J, Degève J, Helsen L, Lievens B, Willems K, Van Impe J, Dewil R (2011) Anaerobic digestion in global bio-energy production: potential and research challenges. *Renew Sust Energ Rev* 15:4295–4301. <https://doi.org/10.1016/j.rser.2011.07.121>
- Ariunbaatar J, Panico A, Esposito G, Pirozzi F, Lens PNL (2014) Pretreatment methods to enhance anaerobic digestion of organic solid waste. *Appl Energy* 123:143–156. <https://doi.org/10.1016/j.apenergy.2014.02.035>

- Barua S, Dhar BR (2017) Advances towards understanding and engineering direct interspecies electron transfer in anaerobic digestion. *Bioresour Technol* 244:698–707. <https://doi.org/10.1016/j.biortech.2017.08.023>
- Bize A, Cardona L, Desmond-Le Quémener E, Battimelli A, Badalato N, Bureau C, Madigou C, Chevret D, Guillot A, Monnet V, Godon J-J, Bouchez T (2015) Shotgun metaproteomic profiling of biomimetic anaerobic digestion processes treating sewage sludge. *Proteomics* 15:3532–3543. <https://doi.org/10.1002/pmic.201500041>
- Bourven I, Casellas M, Buzier R, Lesieur J, Lenain J-F, Faix A, Bressolier P, Maftah C, Guibaud G (2017) Potential of DGT in a new fractionation approach for studying trace metal element impact on anaerobic digestion: the example of cadmium. *Int Biodeterior Biodegrad* 119:188–195. <https://doi.org/10.1016/j.ibiod.2016.11.007>
- Bräsen C, Esser D, Rauch B, Siebers B (2014) Carbohydrate metabolism in archaea: current insights into unusual enzymes and pathways and their regulation. *Microbiol Mol Biol Rev* 78:89–175. <https://doi.org/10.1128/MMBR.00041-13>
- Braun R, Weiland P, Wellinger A (2008) Biogas from energy crop digestion. IEA Bioenergy Task 37:1–20
- Capson-Tojo G, Ruiz D, Rouez M, Crest M, Steyer J-P, Bernet N, Delgenès J-P, Escudé R (2017) Accumulation of propionic acid during consecutive batch anaerobic digestion of commercial food waste. *Bioresour Technol* 245:724–733. <https://doi.org/10.1016/j.biortech.2017.08.149>
- Carrere H, Antonopoulou G, Affes R, Passos F, Battimelli A, Lyberatos G, Ferrer I (2016) Review of feedstock pretreatment strategies for improved anaerobic digestion: from lab-scale research to full-scale application. *Bioresour Technol* 199:386–397. <https://doi.org/10.1016/j.biortech.2015.09.007>
- Cesarino I, Araújo P, Domingues Júnior AP, Mazzafera P (2012) An overview of lignin metabolism and its effect on biomass recalcitrance. *Braz J Bot* 35:303–311. <https://doi.org/10.1590/S0100-84042012000400003>
- Chen Y, Cheng JJ, Creamer KS (2008) Inhibition of anaerobic digestion process: a review. *Bioresour Technol* 99:4044–4064. <https://doi.org/10.1016/j.biortech.2007.01.057>
- Chen JL, Ortiz R, Steele TWJ, Stuckey DC (2014) Toxicants inhibiting anaerobic digestion: a review. *Biotechnol Adv* 32:1523–1534. <https://doi.org/10.1016/j.biotechadv.2014.10.005>
- Cheng Q, Call DF (2016) Hardwiring microbes via direct interspecies electron transfer: mechanisms and applications. *Environ Sci Process Impacts* 18:968–980. <https://doi.org/10.1039/C6EM00219F>
- Choong YY, Norli I, Abdullah AZ, Yhaya MF (2016) Impacts of trace element supplementation on the performance of anaerobic digestion process: a critical review. *Bioresour Technol* 209:369–379. <https://doi.org/10.1016/j.biortech.2016.03.028>
- Clement BG, Kehl LE, DeBord KL, Kitts CL (1998) Terminal restriction fragment patterns (TRFPs), a rapid, PCR-based method for the comparison of complex bacterial communities. *J Microbiol Methods* 31:135–142. [https://doi.org/10.1016/S0167-7012\(97\)00105-X](https://doi.org/10.1016/S0167-7012(97)00105-X)
- Deublein S (2009) Biogas from waste and renewable resources: an introduction. *Choice Rev Online* 46:2682–2682. <https://doi.org/10.5860/CHOICE.46-2682>
- Divya D, Gopinath LR, Merlin Christy P (2015) A review on current aspects and diverse prospects for enhancing biogas production in sustainable means. *Renew Sust Energ Rev* 42:690–699. <https://doi.org/10.1016/j.rser.2014.10.055>
- Felix CR, Ljungdahl LG (1993) The cellulosome: the exocellular organelle of *Clostridium*. *Annu Rev Microbiol* 47:791–819. <https://doi.org/10.1146/annurev.mi.47.100193.004043>
- Ferry JG (1993) Fermentation of acetate. In: Ferry JG (ed) *Methanogenesis: ecology, physiology, biochemistry and genetics*. Springer, Boston, pp 304–334
- Gerardi MH (2003) *The microbiology of anaerobic digesters*. Wiley-Intersciences, Canada
- Gomez Camacho CE, Ruggeri B (2018) Syntrophic microorganisms interactions in anaerobic digestion (AD): a critical review in the light of increase the energy production. *Chem Eng Trans* 64:391–396. <https://doi.org/10.3303/CET1864066>

- Gujer W, Zehnder AJB (1983) Conversion processes in anaerobic digestion. *Water Sci Technol* 15:127–167. <https://doi.org/10.2166/wst.1983.0164>
- Guo J, Peng Y, Ni B-J, Han X, Fan L, Yuan Z (2015) Dissecting microbial community structure and methane-producing pathways of a full-scale anaerobic reactor digesting activated sludge from wastewater treatment by metagenomic sequencing. *Microb Cell Factories* 14:33. <https://doi.org/10.1186/s12934-015-0218-4>
- Hagen LH, Frank JA, Zamanzadeh M, Eijsink VG, Pope PB, Horn SJ, Arntzen MØ (2017) Quantitative metaproteomics highlight the metabolic contributions of uncultured phylotypes in a thermophilic anaerobic digester. *Appl Env Microbiol* 83:e01955–e01916. <https://doi.org/10.1128/AEM.01955-16>
- Hanreich A, Heyer R, Benndorf D, Rapp E, Pioch M, Reichl U, Klocke M (2012) Metaproteome analysis to determine the metabolically active part of a thermophilic microbial community producing biogas from agricultural biomass. *Can J Microbiol* 58:917–922. <https://doi.org/10.1139/w2012-058>
- Hanreich A, Schimpf U, Zakrzewski M, Schlüter A, Benndorf D, Heyer R, Rapp E, Pühler A, Reichl U, Klocke M (2013) Metagenome and metaproteome analyses of microbial communities in mesophilic biogas-producing anaerobic batch fermentations indicate concerted plant carbohydrate degradation. *Syst Appl Microbiol* 36:330–338. <https://doi.org/10.1016/j.syapm.2013.03.006>
- Hassa J, Maus I, Off S, Pühler A, Scherer P, Klocke M, Schlüter A (2018) Metagenome, metatranscriptome, and metaproteome approaches unraveled compositions and functional relationships of microbial communities residing in biogas plants. *Appl Microbiol Biotechnol* 102:5045–5063. <https://doi.org/10.1007/s00253-018-8976-7>
- Herbst F-A, Lünsmann V, Kjeldal H, Jehmlich N, Tholey A, von Bergen M, Nielsen JL, Hettich RL, Seifert J, Nielsen PH (2016) Enhancing metaproteomics—the value of models and defined environmental microbial systems. *Proteomics* 16:783–798. <https://doi.org/10.1002/pmic.201500305>
- Herrmann C, Heiermann M, Idler C (2011) Effects of ensiling, silage additives and storage period on methane formation of biogas crops. *Bioresour Technol* 102:5153–5161. <https://doi.org/10.1016/j.biortech.2011.01.012>
- Heyer R, Kohrs F, Benndorf D, Rapp E, Kausmann R, Heiermann M, Klocke M, Reichl U (2013) Metaproteome analysis of the microbial communities in agricultural biogas plants. *New Biotechnol* 30:614–622. <https://doi.org/10.1016/j.nbt.2013.01.002>
- Heyer R, Kohrs F, Reichl U, Benndorf D (2015) Metaproteomics of complex microbial communities in biogas plants. *Microb Biotechnol* 8:749–763. <https://doi.org/10.1111/1751-7915.12276>
- Heyer R, Benndorf D, Kohrs F, De Vrieze J, Boon N, Hoffmann M, Rapp E, Schlüter A, Sczyrba A, Reichl U (2016) Proteotyping of biogas plant microbiomes separates biogas plants according to process temperature and reactor type. *Biotechnol Biofuels* 9:155. <https://doi.org/10.1186/s13068-016-0572-4>
- Heyer R, Schallert K, Zoun R, Becher B, Saake G, Benndorf D (2017) Challenges and perspectives of metaproteomic data analysis. *J Biotechnol* 261:24–36. <https://doi.org/10.1016/j.jbiotec.2017.06.1201>
- Heyer R, Schallert K, Siewert C, Kohrs F, Greve J, Maus I, Klang J, Klocke M, Heiermann M, Hoffmann M, Püttker S, Calusinska M, Zoun R, Saake G, Benndorf D, Reichl U (2019) Metaproteome analysis reveals that syntrophy, competition, and phage-host interaction shape microbial communities in biogas plants. *Microbiome* 7:69. <https://doi.org/10.1186/s40168-019-0673-y>
- Inyang M, Gao B, Pullammanappallil P, Ding W, Zimmerman AR (2010) Biochar from anaerobically digested sugarcane bagasse. *Bioresour Technol* 101:8868–8872. <https://doi.org/10.1016/j.biortech.2010.06.088>
- Isikgor FH, Becer CR (2015) Lignocellulosic biomass: a sustainable platform for the production of bio-based chemicals and polymers. *Polym Chem* 6:4497–4559. <https://doi.org/10.1039/c5py00263j>

- Jain S, Jain S, Tim Wolf I, Lee J, Wah Tong Y (2015) A comprehensive review on operating parameters and different pretreatment methodologies for anaerobic digestion of municipal solid waste. *Renew Sust Energ Rev* 52:142–154. <https://doi.org/10.1016/j.rser.2015.07.091>
- Jia X, Xi B-D, Li M-X, Yang Y, Wang Y (2017a) Metaproteomics analysis of the functional insights into microbial communities of combined hydrogen and methane production by anaerobic fermentation from reed straw. *PLoS One* 12:e0183158. <https://doi.org/10.1371/journal.pone.0183158>
- Jia X, Xi B, Li M, Liu D, Hou J, Hao Y, Meng F (2017b) Metaproteomic analysis of the relationship between microbial community phylogeny, function and metabolic activity during biohydrogen-methane coproduction under short-term hydrothermal pretreatment from food waste. *Bioresour Technol* 245:1030–1039. <https://doi.org/10.1016/j.biortech.2017.08.180>
- Jiang Y, Xin F, Lu J, Dong W, Zhang W, Zhang M, Wu H, Ma J, Jiang M (2017) State of the art review of biofuels production from lignocellulose by thermophilic bacteria. *Bioresour Technol* 245:1498–1506. <https://doi.org/10.1016/j.biortech.2017.05.142>
- Joyce A, Ijaz UZ, Nzetue C, Vaughan A, Shirran SL, Botting CH, Quince C, O’Flaherty V, Abram F (2018) Linking microbial community structure and function during the acidified anaerobic digestion of grass. *Front Microbiol* 9:540. <https://doi.org/10.3389/fmicb.2018.00540>
- Kanwal S, Chaudhry N, Munir S, Sana H (2019) Effect of torrefaction conditions on the physico-chemical characterization of agricultural waste (sugarcane bagasse). *Waste Manag* 88:280–290. <https://doi.org/10.1016/j.wasman.2019.03.053>
- Karlsson R, Gonzales-Siles L, Boulund F, Svensson-Stadler L, Skovbjerg S, Karlsson A, Davidson M, Hulth S, Kristiansson E, Moore ERB (2015) Proteotyping: proteomic characterization, classification and identification of microorganisms – a prospectus. *Syst Appl Microbiol* 38:246–257. <https://doi.org/10.1016/j.syapm.2015.03.006>
- Kohrs F, Heyer R, Magnussen A, Benndorf D, Muth T, Behne A, Rapp E, Kausmann R, Heiermann M, Klocke M, Reichl U (2014) Sample prefractionation with liquid isoelectric focusing enables in depth microbial metaproteome analysis of mesophilic and thermophilic biogas plants. *Anaerobe* 29:59–67. <https://doi.org/10.1016/j.anaerobe.2013.11.009>
- Kohrs F, Heyer R, Bissinger T, Kottler R, Schallert K, Püttker S, Behne A, Rapp E, Benndorf D, Reichl U (2017) Proteotyping of laboratory-scale biogas plants reveals multiple steady-states in community composition. *Anaerobe* 46:56–68. <https://doi.org/10.1016/j.anaerobe.2017.02.005>
- Kouzuma A, Kato S, Watanabe K (2015) Microbial interspecies interactions: recent findings in syntrophic consortia. *Front Microbiol* 6:477. <https://doi.org/10.3389/fmicb.2015.00477>
- Krause L, Diaz NN, Edwards RA, Gartemann K-H, Krömeke H, Neuweiger H, Pühler A, Runte KJ, Schlüter A, Stoye J, Szczepanowski R, Tauch A, Goesmann A (2008) Taxonomic composition and gene content of a methane-producing microbial community isolated from a biogas reactor. *J Biotechnol* 136:91–101. <https://doi.org/10.1016/j.jbiotec.2008.06.003>
- Lacerda CMR, Choe LH, Reardon KF (2007) Metaproteomic analysis of a bacterial community response to cadmium exposure. *J Proteome Res* 6:1145–1152. <https://doi.org/10.1021/pr060477v>
- Li Y, Zhang R, Liu X, Chen C, Xiao X, Feng L, He Y, Liu G (2013a) Evaluating methane production from anaerobic mono- and co-digestion of kitchen waste, corn stover, and chicken manure. *Energy Fuel* 27:2085–2091. <https://doi.org/10.1021/ef400117f>
- Li Y, Zhang R, Liu G, Chen C, He Y, Liu X (2013b) Comparison of methane production potential, biodegradability, and kinetics of different organic substrates. *Bioresour Technol* 149:565–569. <https://doi.org/10.1016/j.biortech.2013.09.063>
- Li R, Wu Z, Wang Y, Ding L, Wang Y (2016) Role of pH-induced structural change in protein aggregation in foam fractionation of bovine serum albumin. *Biotechnol Rep* 9:46–52. <https://doi.org/10.1016/j.btre.2016.01.002>
- Li W, Khalid H, Zhu Z, Zhang R, Liu G, Chen C, Thorin E (2018) Methane production through anaerobic digestion: participation and digestion characteristics of cellulose, hemicellulose and lignin. *Appl Energy* 226:1219–1228. <https://doi.org/10.1016/j.apenergy.2018.05.055>

- Lin Y-W, Tuan N, Huang S-L (2016) Metaproteomic analysis of the microbial community present in a thermophilic swine manure digester to allow functional characterization: a case study. *Int Biodeterior Biodegrad* 115:64–73. <https://doi.org/10.1016/j.ibiod.2016.06.013>
- Liu Z-H, Chen H-Z (2015) Xylose production from corn stover biomass by steam explosion combined with enzymatic digestibility. *Bioresour Technol* 193:345–356. <https://doi.org/10.1016/j.biortech.2015.06.114>
- Lü F, Bize A, Guillot A, Monnet V, Madigou C, Chapleur O, Mazéas L, He P, Bouchez T (2014) Metaproteomics of cellulose methanisation under thermophilic conditions reveals a surprisingly high proteolytic activity. *ISME J* 8:88–102. <https://doi.org/10.1038/ismej.2013.120>
- Madigan M, Martinko J, Dunlap PV, Clark DP (2008) Brock biology of microorganisms. *Int Microbiol* 11:65–73
- Mata-Alvarez J, Dosta J, Romero-Güiza MS, Fonoll X, Peces M, Astals S (2014) A critical review on anaerobic co-digestion achievements between 2010 and 2013. *Renew Sust Energy Rev* 36:412–427. <https://doi.org/10.1016/j.rser.2014.04.039>
- Mcinerney M, Bryant MP, Pfennig N (1979) Anaerobic bacterium that degrades fatty acids in syntrophic association with methanogens. *Arch Microbiol* 122:129–135. <https://doi.org/10.1007/BF00411351>
- Monlau F, Sambusiti C, Barakat A, Quéméneur M, Trably E, Steyer J-P, Carrère H (2014) Do furanic and phenolic compounds of lignocellulosic and algae biomass hydrolyzate inhibit anaerobic mixed cultures? A comprehensive review. *Biotechnol Adv* 32:934–951. <https://doi.org/10.1016/j.biotechadv.2014.04.007>
- Morris R, Schauer-Gimenez A, Bhattad U, Kearney C, Struble CA, Zitomer D, Maki JS (2014) Methyl coenzyme M reductase (mcrA) gene abundance correlates with activity measurements of methanogenic H₂/CO₂-enriched anaerobic biomass. *Microb Biotechnol* 7:77–84. <https://doi.org/10.1111/1751-7915.12094>
- Mulat DG, Ward AJ, Adamsen APS, Voigt NV, Nielsen JL, Feilberg A (2014) Quantifying contribution of syntrophic acetate oxidation to methane production in thermophilic anaerobic reactors by membrane inlet mass spectrometry. *Environ Sci Technol* 140130145609003. <https://doi.org/10.1021/es403144e>
- Mustafa AM, Li H, Radwan AA, Sheng K, Chen X (2018) Effect of hydrothermal and Ca(OH)₂ pretreatments on anaerobic digestion of sugarcane bagasse for biogas production. *Bioresour Technol* 259:54–60. <https://doi.org/10.1016/j.biortech.2018.03.028>
- Nallathambi Gunaseelan V (1997) Anaerobic digestion of biomass for methane production: a review. *Biomass Bioenergy* 13:83–114. [https://doi.org/10.1016/S0961-9534\(97\)00020-2](https://doi.org/10.1016/S0961-9534(97)00020-2)
- Ortseifen V, Stolze Y, Maus I, Sczyrba A, Bremges A, Albaum SP, Jaenicke S, Fracowiak J, Pühler A, Schlüter A (2016) An integrated metagenome and-proteome analysis of the microbial community residing in a biogas production plant. *J Biotechnol* 231:268–279. <https://doi.org/10.1016/j.jbiotec.2016.06.014>
- Park J, Lee B, Shi P, Kwon H, Jeong SM, Jun H (2018) Methanol metabolism and archaeal community changes in a bioelectrochemical anaerobic digestion sequencing batch reactor with copper-coated graphite cathode. *Bioresour Technol* 259:398–406. <https://doi.org/10.1016/j.biortech.2018.03.009>
- Passaris I, Van Gaelen P, Cornelissen R, Simoens K, Grauwels D, Vanhaecke L, Springael D, Smets I (2018) Cofactor F430 as a biomarker for methanogenic activity: application to an anaerobic bioreactor system. *Appl Microbiol Biotechnol* 102:1191–1201. <https://doi.org/10.1007/s00253-017-8681-y>
- Paul S, Dutta A (2018) Challenges and opportunities of lignocellulosic biomass for anaerobic digestion. *Resour Conserv Recycl* 130:164–174. <https://doi.org/10.1016/j.resconrec.2017.12.005>
- Pérez-Rodríguez N, García-Bernet D, Domínguez JM (2016) Effects of enzymatic hydrolysis and ultrasounds pretreatments on corn cob and vine trimming shoots for biogas production. *Bioresour Technol* 221:130–138. <https://doi.org/10.1016/j.biortech.2016.09.013>
- Poudel BN, Paudel KP, Timilsina G, Zilberman D (2012) Providing numbers for a food versus fuel debate: an analysis of a future biofuel production scenario. *Appl Econ Perspect Policy* 34:637–668. <https://doi.org/10.1093/aepp/pps039>

- Rahman MA, Møller HB, Saha CK, Alam MM, Wahid R, Feng L (2017) Optimal ratio for anaerobic co-digestion of poultry droppings and lignocellulosic-rich substrates for enhanced biogas production. *Energy Sustain Dev* 39:59–66. <https://doi.org/10.1016/j.esd.2017.04.004>
- Ramsay IR, Pullammanappallil PC (2001) Protein degradation during anaerobic wastewater treatment: derivation of stoichiometry. *Biodegradation* 12:247–256. <https://doi.org/10.1023/A:1013116728817>
- Rastogi G, Ranade DR, Yeole TY, Patole MS, Shouche YS (2008) Investigation of methanogen population structure in biogas reactor by molecular characterization of methyl-coenzyme M reductase A (*mcrA*) genes. *Bioresour Technol* 99:5317–5326. <https://doi.org/10.1016/j.biortech.2007.11.024>
- Roseman S (1969) The transport of carbohydrates by a bacterial phosphotransferase system. *J Gen Physiol* 54:138–184. <https://doi.org/10.1085/jgp.54.1.138>
- Sasaki D, Hori T, Haruta S, Ueno Y, Ishii M, Igarashi Y (2011) Methanogenic pathway and community structure in a thermophilic anaerobic digestion process of organic solid waste. *J Biosci Bioeng* 111:41–46. <https://doi.org/10.1016/j.jbiosc.2010.08.011>
- Sawatdeenarunat C, Surendra KC, Takara D, Oechsner H, Khanal SK (2015) Anaerobic digestion of lignocellulosic biomass: challenges and opportunities. *Bioresour Technol* 178:178–186. <https://doi.org/10.1016/j.biortech.2014.09.103>
- Schink B (1997) Energetics of syntrophic cooperation in methanogenic degradation. *Microbiol Mol Biol Rev* 61:262–280
- Schlüter A, Bekel T, Diaz NN, Dondrup M, Eichenlaub R, Gartemann K-H, Krahn I, Krause L, Krömeke H, Kruse O, Mussgnug JH, Neuweger H, Niehaus K, Pühler A, Runte KJ, Szczepanowski R, Tauch A, Tilker A, Viehöver P, Goesmann A (2008) The metagenome of a biogas-producing microbial community of a production-scale biogas plant fermenter analysed by the 454-pyrosequencing technology. *J Biotechnol* 136:77–90. <https://doi.org/10.1016/j.jbiotec.2008.05.008>
- Schneider T, Riedel K (2010) Environmental proteomics: analysis of structure and function of microbial communities. *Proteomics* 10:785–798. <https://doi.org/10.1002/pmic.200900450>
- Schnürer A, Zellner G, Svensson BH (1999) Mesophilic syntrophic acetate oxidation during methane formation in biogas reactors. *FEMS Microbiol Ecol* 29:249–261. <https://doi.org/10.1111/j.1574-6941.1999.tb00616.x>
- Shrestha PM, Rotaru A-E (2014) Plugging in or going wireless: strategies for interspecies electron transfer. *Front Microbiol* 5:237. <https://doi.org/10.3389/fmicb.2014.00237>
- Siddique MNI, Wahid ZA (2018) Achievements and perspectives of anaerobic co-digestion: a review. *J Clean Prod* 194:359–371. <https://doi.org/10.1016/j.jclepro.2018.05.155>
- Singh S, Cheng G, Sathitsuksanoh N, Wu D, Varanasi P, George A, Balan V, Gao X, Kumar R, Dale BE, Wyman CE, Simmons BA (2015) Comparison of different biomass pretreatment techniques and their impact on chemistry and structure. *Front Energy Res* 2:62. <https://doi.org/10.3389/fenrg.2014.00062>
- Speda J, Jonsson B-H, Carlsson U, Karlsson M (2017) Metaproteomics-guided selection of targeted enzymes for bioprospecting of mixed microbial communities. *Biotechnol Biofuels* 10:128. <https://doi.org/10.1186/s13068-017-0815-z>
- Summers ZM, Fogarty HE, Leang C, Franks AE, Malvankar NS, Lovley DR (2010) Direct exchange of electrons within aggregates of an evolved syntrophic coculture of anaerobic bacteria. *Science* 330:1413–1415. <https://doi.org/10.1126/science.1196526>
- Theuerl S, Kohrs F, Benndorf D, Maus I, Wibberg D, Schlüter A, Kausmann R, Heiermann M, Rapp E, Reichl U, Pühler A, Klocke M (2015) Community shifts in a well-operating agricultural biogas plant: how process variations are handled by the microbiome. *Appl Microbiol Biotechnol* 99:7791–7803. <https://doi.org/10.1007/s00253-015-6627-9>
- Tong X, Smith LH, McCarty PL (1990) Methane fermentation of selected lignocellulosic materials. *Biomass* 21:239–255. [https://doi.org/10.1016/0144-4565\(90\)90075-U](https://doi.org/10.1016/0144-4565(90)90075-U)

- Vanwonterghem I, Jensen PD, Ho DP, Batstone DJ, Tyson GW (2014) Linking microbial community structure, interactions and function in anaerobic digesters using new molecular techniques. *Curr Opin Biotechnol* 27:55–64. <https://doi.org/10.1016/j.copbio.2013.11.004>
- von Netzer F, Kuntze K, Vogt C, Richnow HH, Boll M, Lueders T (2016) Functional gene markers for fumarate-adding and dearomatizing key enzymes in anaerobic aromatic hydrocarbon degradation in terrestrial environments. *J Mol Microbiol Biotechnol* 26:180–194. <https://doi.org/10.1159/000441946>
- Wang D, Liu Y, Ngo HH, Zhang C, Yang Q, Peng L, He D, Zeng G, Li X, Ni B-J (2017) Approach of describing dynamic production of volatile fatty acids from sludge alkaline fermentation. *Bioresour Technol* 238:343–351. <https://doi.org/10.1016/j.biortech.2017.04.054>
- Weiland P (2010) Biogas production: current state and perspectives. *Appl Microbiol Biotechnol* 85:849–860. <https://doi.org/10.1007/s00253-009-2246-7>
- Wenzel L, Heyer R, Schallert K, Löser L, Wünschiers R, Reichl U, Benndorf D (2018) SDS-PAGE fractionation to increase metaproteomic insight into the taxonomic and functional composition of microbial communities for biogas plant samples. *Eng Life Sci* 18:498–509. <https://doi.org/10.1002/elsc.201800062>
- Westerholm M, Moestedt J, Schnürer A (2016) Biogas production through syntrophic acetate oxidation and deliberate operating strategies for improved digester performance. *Appl Energy* 179:124–135. <https://doi.org/10.1016/j.apenergy.2016.06.061>
- Wilmes P, Bond PL (2004) The application of two-dimensional polyacrylamide gel electrophoresis and downstream analyses to a mixed community of prokaryotic microorganisms. *Environ Microbiol* 6:911–920. <https://doi.org/10.1111/j.1462-2920.2004.00687.x>
- Wilmes P, Bond PL (2009) Microbial community proteomics: elucidating the catalysts and metabolic mechanisms that drive the Earth's biogeochemical cycles. *Curr Opin Microbiol* 12:310–317. <https://doi.org/10.1016/j.mib.2009.03.004>
- Wilmes P, Heintz-Buschart A, Bond PL (2015) A decade of metaproteomics: where we stand and what the future holds. *Proteomics* 15:3409–3417. <https://doi.org/10.1002/pmic.201500183>
- Wintsche B, Jehmlich N, Popp D, Harms H, Kleinstüber S (2018) Metabolic adaptation of methanogens in anaerobic digesters upon trace element limitation. *Front Microbiol* 9:405. <https://doi.org/10.3389/fmicb.2018.00405>
- Yan Q, Li Y, Huang B, Wang A, Zou H, Miao H, Li R (2012) Proteomic profiling of the acid tolerance response (ATR) during the enhanced biomethanation process from Taihu Blue Algae with butyrate stress on anaerobic sludge. *J Hazard Mater* 235–236:286–290. <https://doi.org/10.1016/j.jhazmat.2012.07.062>
- Yin D-M, Westerholm M, Qiao W, Bi S-J, Wandera SM, Fan R, Jiang M-M, Dong R-J (2018) An explanation of the methanogenic pathway for methane production in anaerobic digestion of nitrogen-rich materials under mesophilic and thermophilic conditions. *Bioresour Technol* 264:42–50. <https://doi.org/10.1016/j.biortech.2018.05.062>
- Zhang W, Dai K, Xia X-Y, Wang H-J, Chen Y, Lu Y-Z, Zhang F, Zeng RJ (2018) Free acetic acid as the key factor for the inhibition of hydrogenotrophic methanogenesis in mesophilic mixed culture fermentation. *Bioresour Technol* 264:17–23. <https://doi.org/10.1016/j.biortech.2018.05.049>
- Zheng Y, Zhao J, Xu F, Li Y (2014) Pretreatment of lignocellulosic biomass for enhanced biogas production. *Prog Energy Combust Sci* 42:35. <https://doi.org/10.1016/j.pecs.2014.01.001>
- Zhu Y, McBride MJ (2017) The unusual cellulose utilization system of the aerobic soil bacterium *Cytophaga hutchinsonii*. *Appl Microbiol Biotechnol* 101:7113–7127. <https://doi.org/10.1007/s00253-017-8467-2>
- Ziemiński K, Fraç M (2012) Methane fermentation process as anaerobic digestion of biomass: transformations, stages and microorganisms. *Afr J Biotechnol* 11:4127–4139. <https://doi.org/10.5897/AJBX11.054>
- Ziganshin AM, Ziganshina EE, Kleinstüber S, Nikolausz M (2016) Comparative analysis of methanogenic communities in different laboratory-scale anaerobic digesters. *Archaea* 2016:1–12. <https://doi.org/10.1155/2016/3401272>